DOE/BC/14651-20
Distribution Category UC-122

RESERVOIR CHARACTERIZATION OF PENNSYLVANIAN SANDSTONE RESERVOIRS

Final Report

By
Mohan Kelkar

February 1995

Work Performed Under Contract No. DE-AC22-90BC14651

Prepared for
U.S. Department of Energy
Assistant Secretary for Fossil Energy

Rhonda Lindsey, Project Manager
Bartlesville Project Office
P.O. Box 1398
Bartlesville, OK 74005

Prepared by
University of Tulsa
Department of Petroleum Engineering
Tulsa, OK 74104

DISCLAIMER

CONTENTS

LIST OF FIGURES

LIST OF TABLES

ACKNOWLEDGMENT

The research effort described in this report was supported by the U.S. Department of Energy under contract DE-AC22-90BC14651 and by Tulsa University Petroleum Reservoir Exploitation Projects (TUPREP) member companies: Amoco, Arco, Aramco, Conoco, Chevron, Marathon, Mobil, Pertamina, Petrobras and Unocal. Additionally, the computer facilities and the lab space was provided by the University of Tulsa. We gratefully acknowledge all this support.

Our special thanks go to Rhonda Patterson, representative of the contracting officer for this project, for her enthusiasm, willingness to interact, and valuable suggestions. We also acknowledge the comments and suggestions provided by the representatives of the member companies during our bi-annual meetings.

Mohan Kelkar
October 1994

ABSTRACT

This final report summarizes the progress during the three years of a project on Reservoir Characterization of Pennsylvanian Sandstone Reservoirs. The report is divided into three sections:

(i) reservoir description
(ii) Scale-up procedures
(iii) Outcrop investigation

The first section describes the methods by which a reservoir can be described in three dimensions. In this section we apply the technique of simulated annealing to incorporate dynamic information. Dynamic information includes any information which is a result of flow performance of the reservoir. The two types of dynamic information included are well test data and production data. To include the dynamic data more efficiently, we first convert the information into equivalent static information. For well test data, we show that, using an analytical solution for radial geometry and combining it with the Cartesian coordinate system, we can generate reservoir description which honors the well test pressure data as well as the pressure derivative data. The technique is also extended to include the porosity heterogeneities as well as permeability anisotropy. When applied to multiwell well testing problem, we observe that the constructed reservoir description is superior to the description created using only conventional univariate and spatial constraints. For inclusion of production data, we develop equivalent static constraints for primary recovery as well as secondary recovery. We observe that primary constraints which have the most influence on reservoir flow performance are the near well permeability value and near well bore pore volumes. For secondary recovery performance, the connectivity between injectors and producers is a significant parameter in determining the flow performance. The developed technique is extended to a full field scale simulation to show its effectiveness in capturing the overall field as well as individual well performance.

The next step in reservoir description is to scale up reservoir properties for flow simulation. The second section addresses the issue of scale-up of reservoir properties once the spatial descriptions of properties are created. A new analytical method is proposed to estimate a permeability tensor based on small scale

permeability variations. In the previous report, a method which captures the scale of small scale permeabilities in two dimensions was proposed. This report extends the method to three dimensions. The method has been validated by comparing the results with the numerical results.

An ideal environment to test many of these techniques is to use outcrop data. One of the reasons is that we can collect detailed information on a smaller scale. The last section describes the investigation of an outcrop. The outcrop is an analog of Bartlesville sandstone. We collected extensive data on the outcrop. The collected data were analyzed and interpreted. We observe that geologically the data can be divided into four discrete genetic interval (DGI) units. Three of these units (channel fill) are further divided into three subfacies - upper, middle and lower. Using the geological description, a three dimensional description of the outcrop was created which honors the observed geological information as well as the petrophysical data. Preliminary flow simulation results indicate that the large scale geological description has a stronger impact on the flow performance than the small scale variations in petrophysical properties. Further, collection of vertical connectivity is very critical in honoring the reservoir performance.

EXECUTIVE SUMMARY

This final report contains three sections related to Reservoir Characterization of Pennsylvanian sandstone reservoirs. The first section discusses the reservoir description process of including dynamic information. The second section describes the scale up of reservoir properties generated by reservoir description process. The last section explains the investigation of an analogous outcrop.

Chapter One, titled "Inclusion of Production Data for Reservoir Description," describes a method to incorporate the production data in the simulated annealing process to generate the reservoir descriptions. Production data are readily available compared to many other types of data. It is critical that dynamic information such as production data should be included as part of the reservoir description process. In this section, we describe a method of incorporating two types of dynamic data: well test data and production data. The approach for including the two types of data is the same. First convert the dynamic information into equivalent static information; then include the static information as part of the constraint in reservoir description process. We use a method of simulated annealing to include these static constraints. Although computationally demanding, this method is chosen because of its flexibility and robustness.

One of the most important constraints in reservoir description process is the well test data. To define the proper constraint for incorporating the well test data, we first need to identify a proper averaging technique which represents the well test data. We have observed that Oliver's approach (SPEFE, Sept. 1990, pp. 319-24) is adequate to determine the proper averaging functions to describe the well test data. If the reservoir is divided into several concentric rings, and we calculate the geometric averages of permeability values within each ring, we can then apply Oliver's weighting functions to estimate instantaneous permeability value represented by the pressure transient data. This method can be applied at many different times so that the pressure transient characteristics can be reproduced when the generated description is used to simulate the well test data. We have observed that the inclusion of this constraint can successfully reproduce the pressure as well as pressure derivative characteristics of the well data. We have investigated the synthetic data over a wide range of heterogeneities and have observed that the

method works for wide ranging conditions. In addition to using Oliver's method, we have investigated the method proposed by Feitosa et al. (1993). The results indicate that this method can also be used to properly incorporate the well test permeability data. An added advantage of using this method is that the computation speed of simulated annealing method is also enhanced.

In addition to investigating variations in permeability values, we also investigate the variations in porosity on well testing performance. We observe that the effect of porosity on the pressure response is secondary and can be ignored. We also investigate the effect of permeability anisotropy on pressure response. We develop a method which, by transforming the grid dimensions to reflect the anisotropy, can appropriately account for the permeability anisotropy.

In the second part of the section, we discuss the inclusion of production data during both primary and secondary recovery processes. No methods currently exist which will allow incorporation of production data in reservoir description. To decide an in fill well location, it is very important to understand the reservoir continuities. More continuous the reservoir, less is the need to drill an additional well. The type of information typically available is oil rates, gas oil ratio as well as water oil ratio, oil production and water injection rates during secondary oil recovery. We present a method to incorporate the production information related to both primary and secondary production. Based on several numerical experiments, it is observed that the primary production rate is closely tied to the near well bore permeability values. Also, over the life of the primary production, the pore volume drained by the well can also play a significant role in deciding the future performance. During secondary oil recovery, the connectivity between injector and producer is important for properly defining the inter well distributions of reservoir properties. By including these parameters, the uncertainty in the production performance can be significantly reduced. We extend this work to a full scale field study and show that the technique is equally useful for the field scale simulation as well. Essentially, all the producing curves from different realizations collapse into a single curve. In addition, with the help of these constraints, uncertainties with respect to inter well distributions of reservoir properties are considerably reduced. This should help us in better planning of in fill wells.

Chapter Two, titled "Effective Properties of Reservoir Simulator Grid Blocks," presents the analytical method to upscale the small scale distributions in three

dimensional grid blocks. First, we briefly describe that small scale permeabilities present within two dimensional grid can be effectively up scaled through permeability tensor. The results are validated through both single phase and two phase reservoir simulations and comparing the results of detailed simulations with the simulations using up scaled properties. Although useful, in field scale simulations, we need an ability to describe the effective permeability tensor for a three dimensional gird block. This report presents preliminary results on up scaling procedure in three dimensions. As a first step, we have only considered small scale permeability values to be isotropic with the non diagonal elements to be zero. Following the method for the two dimensional grid blocks, an analytical procedure is established by considering the flow in one direction at a time and assuming no flow in any other two directions. Under steady state conditions, with some additional assumptions with respect to cross flow, an analytical solution can be established for a full permeability tensor which includes nine elements. A comparison between the analytical and numerical results is very encouraging for this case. We believe that the method can be easily extended to other complex permeability distributions for a proper up scaling in three dimensions.

In Chapter Three, titled "Outcrop Studies," we discuss in great detail the investigation of Bartlesville outcrop which involved both geological and engineering studies. Data were collected on the surface of the outcrop as well as by drilling ten wells behind the outcrop. Wells were cored, logged and scanned using gamma ray logs. Permeability measurements were taken using minipermeameter as well as conventional core analysis methods. Using all the available data, first, the geological description was created. This description identified four distinct geological units, three channel fill and one splay. These four units were mapped using facies biased procedure. The channel fill was further divided into three subfacies - upper, middle and lower. The analysis of vertical variograms revealed that part of the geological description can be quantified using the variogram structure, especially, the hole effect and periodic behavior of the data. Using the geologic information, a two step conditional simulation procedure was used to construct petrophysical properties description which honors both the geological and engineering data. The description was used to study the flow performance in this simulated reservoir. We observed that the geological description has a bigger impact on the flow performance than the variations in the petrophysical properties.

Also, one of the biggest uncertainties in reservoir descriptions, which has a significant impact on the flow performance, is observed to be vertical permeability.

To summarize the conclusions based on this project, we have accomplished all the tasks we intended to complete. We developed a procedure to generate a three dimensional description of the rock properties using a simulated annealing procedure. We were able to incorporate dynamic data as part of the reservoir description. This allowed us to better describe the interwell distributions of reservoir properties, and hence potential in fill well locations. We tested the application of fractal methods for characterizing the reservoir properties. We established a method to scale up permeability for a two as well as a three dimensional grid blocks. Finally, we investigated the application of the outcrop data for detailed reservoir description.

CHAPTER 1

Inclusion of Production Data for Reservoir Description

R. Sagar, K. Hird and M. Kelkar

Reservoir description requires inclusion of various types of qualitative and quantitative information in assigning reservoir properties at unsampled locations. One of the most difficult types of data to incorporate is dynamic data. Incorporation of dynamic production data for describing reservoir properties and parameters requires an inverse modeling technique. Primary and secondary production parameters and the pressure response during a well test are measures of dynamic properties of a reservoir. A dynamic property of a reservoir that most influences its performance is the permeability and the distribution of permeability is a measure of heterogeneity of the reservoir. It is easier to effectively incorporate production information, specifically primary and secondary performance and the pressure response during a well test, if it can be converted into equivalent static information. This chapter discusses the procedures of incorporating the well test and the production data as part of the reservoir description. In the first section, we present the forward problem - how can production performance parameters (such as water-oil ratios and break through times) and the pressure response of a reservoir/well be represented as equivalent static information.[1.1, 1.2] This will allow us to describe the permeability heterogeneity consistent with the production data. In the second section, we discuss the method used for incorporating production data as part of the reservoir description. The method used is simulated annealing which has the flexibility to incorporate various constraints. In the last section, we present the results of incorporating dynamic information as part of the reservoir description. A significant improvement in reservoir description is observed after the dynamic information is incorporated. This will allow us to better describe inter well distributions of reservoir properties, which will further help in deciding in fill well locations.

In this section, we describe the procedures used for transforming dynamic information into equivalent static information. In the first part, we describe the transformation of well test data into equivalent permeability distribution. In the second part, we present transformation of primary and secondary data into equivalent static information.

1.1.1 Well Test Permeability

The effective radial permeability calculated by well test analysis is based on a classical analytical solution to the diffusivity equation. The solution for the infinite-acting or transient flow period can be written as:[1.3]

$$p_{wf} = p_i - \frac{162.6qB\mu}{\bar{k}_{wt}h}\left[\log t + \log\left(\frac{\bar{k}_{wt}}{\phi\mu c_t r_w^2}\right) - 3.2275 + .86859s\right] \qquad (1.1)$$

where the symbols used are standard and defined in the nomenclature. The slope (m) of the semilog straight line plot of pressure vs. time determines the well test permeability,

$$\bar{k}_{wt} = -162.6\frac{qB\mu}{mh} \qquad (1.2)$$

This solution is based on the assumption that the reservoir is homogeneous; however, no reservoir is homogeneous and the degree of heterogeneity is a function of the lithology, and the depositional and post-depositional environment of the reservoir. For practical purposes, it is assumed that the permeability determined by well test analysis is an effective permeability representing some *average* within a radius of investigation or drainage radius, which is influenced by the producing well. The classical definition of radius of influence is given by Van Poolen.[1.4] In physical terms it defines the radius over which all the reservoir properties have influenced the well flowing pressure.[1.5] It is given by the following equation:

$$r = A\sqrt{\frac{\bar{k}_{wt}t}{\phi\mu c_t}} \qquad (1.3)$$

Various authors have derived different values for the coefficient, A. Lee[1.5] defines A to be 0.03248. As the time of the test increases more of the reservoir is influenced by the well and the radius of drainage increases. However, this definition of radius of drainage is questionable in the presence of heterogeneities.[1.6]

In order to effectively incorporate well test data for the purpose of description of small scale permeability heterogeneities, one must first address the forward problem - what kind of average does the well test derived permeability represent and over what region of the reservoir is this average valid?

The analytical solutions for a heterogeneous reservoir begin by addressing the forward problem, e.g., for a well producing a single-phase fluid in an infinite acting reservoir. First we present a mathematical solution of the diffusivity equation for heterogeneous reservoirs.

In this work we consider the mathematical solutions presented by Oliver[1.7] and Feitosa.[1.8] The analytical solutions are based on the following assumptions:

- constant rate production,
- uniformly thick reservoir with closed upper and lower boundaries,
- areally infinite reservoir,
- negligible wellbore storage and skin effect,
- constant porosity, thickness and rock compressibility,
- single phase fluid with constant viscosity and compressibility,
- uniform initial pressure throughout the reservoir,
- negligible gravity and capillary pressure effects,
- fully penetrating well, and
- rock and fluid properties independent of pressure.

The governing equations describing the forward problem of the pressure response in an areally heterogeneous reservoir producing a slightly compressible fluid through a single well are given by the following[1.8] Initial Boundary Value Problem:

$$\frac{1}{r_D}\frac{\partial}{\partial r_D}\left[r_D k_D(r_D,\theta)\frac{\partial p_D}{\partial r_D}\right]+\frac{1}{r_D^2}\frac{\partial}{\partial \theta}\left[k_D(r_D,\theta)\frac{\partial p_D}{\partial \theta}\right]=\frac{\partial p_D}{\partial t_D} \qquad (1.4)$$

$$\left[p_D(r_D,\theta,t_D=0)\right]=0 \qquad (1.5)$$

$$\frac{1}{2\pi}\left[\int_0^{2\pi} k_D(r_D,\theta) r_D \frac{\partial p_D}{\partial r_D} d\theta\right]_{r_D=1} = -1 \tag{1.6}$$

$$\left[\frac{\partial p_D}{\partial \theta}\right]_{r_D=1} = 0 \tag{1.7}$$

$$\lim_{r_D \to \infty} p_D(r_D,\theta,t_D) = 0 \tag{1.8}$$

$$p_D(r_D,\theta=0,t_D) = p_D(r_D,\theta=2\pi,t_D) \tag{1.9}$$

$$\left[\frac{\partial p_D}{\partial \theta}\right]_{\theta=0} = \left[\frac{\partial p_D}{\partial \theta}\right]_{\theta=2\pi} \tag{1.10}$$

where the dimensionless terms are defined as:

dimensionless radius, r_D:

$$r_D = \frac{r}{r_w} \tag{1.11}$$

dimensionless time, t_D:

$$t_D = \frac{0.006328 k_{ref} t}{\phi \mu c_t r_w^2} \tag{1.12}$$

dimensionless pressure drop, p_D:

$$p_D = \frac{k_{ref} h}{141.2 q B \mu}\left[p_i - p(r,\theta,t)\right] \tag{1.13}$$

and

$$k_D = \frac{k(r,\theta)}{k_{ref}} \tag{1.14}$$

where the time is measured in days and k_{ref} is an arbitrary reference value of permeability.

Oliver's Solution

Oliver[1.7] investigated the averaging process of permeability variations in r and θ coordinates. He solved the diffusion equation for the pressure response of a well situated in an infinite reservoir where permeability is an arbitrary function of position, he assumed small permeability variations about some mean. Some type of averaging is inherently present when an effective permeability is determined from the slope of the semilog plot; therefore, the *averaged permeability* of the small scale permeabilities within the area of investigation is determined from the slope of the semilog plot at any instant. Oliver's solution only allows for small variations about a mean value since the overall solution is determined by a first order perturbation technique to the generalized problem. Neglecting wellbore storage and skin, the dimensionless pressure derivative for a heterogeneous reservoir is given in a dimensionless radial[1.8] form by:

$$p'_{wD} = \frac{\partial p_D}{\partial \ln t_D} = \frac{1}{2} - \int_1^{\infty} K(r_D, t_D)\left(\frac{1}{2\pi}\int_{-\pi}^{+\pi}\left[1 - \frac{1}{k_D(r_D,\theta)}\right]d\theta\right)dr_D \qquad (1.15)$$

For our investigation, we consider only the transient flow period for which this solution is valid, and analyze the appropriate time versus pressure data. Note that for a homogeneous reservoir $k_D(r_D,\theta) = 1$, and Eq. 1.15 gives the dimensionless pressure derivative for a homogeneous reservoir, i.e., $p'_{wD} = \frac{1}{2}$. It can be shown that the integral over a region is a normalized form of the harmonic average of permeabilities over a region. $K(r_D, t_D)$ is the weighting or kernel function and is given by:

$$\sqrt{t_D}K(r_D,t_D) = 0.5\sqrt{\frac{\pi r_D^2}{t_D}}\exp\left(-\frac{r_D^2}{2t_D}\right)W_{1/2,1/2}\left(\frac{r_D^2}{t_D}\right) \qquad (1.16)$$

Eq. 1.16 is valid for dimensionless times greater then 100 and $W_{1/2,1/2}$ is the Whittaker function defined in Reference 1.9. For further details on this solution see Reference 1.7. Of more importance, is the physical significance of the weighting function. The shape of this function (Fig. 1.1) is used to determine the area of investigation. The inner and outer radii of the area of investigation are defined as

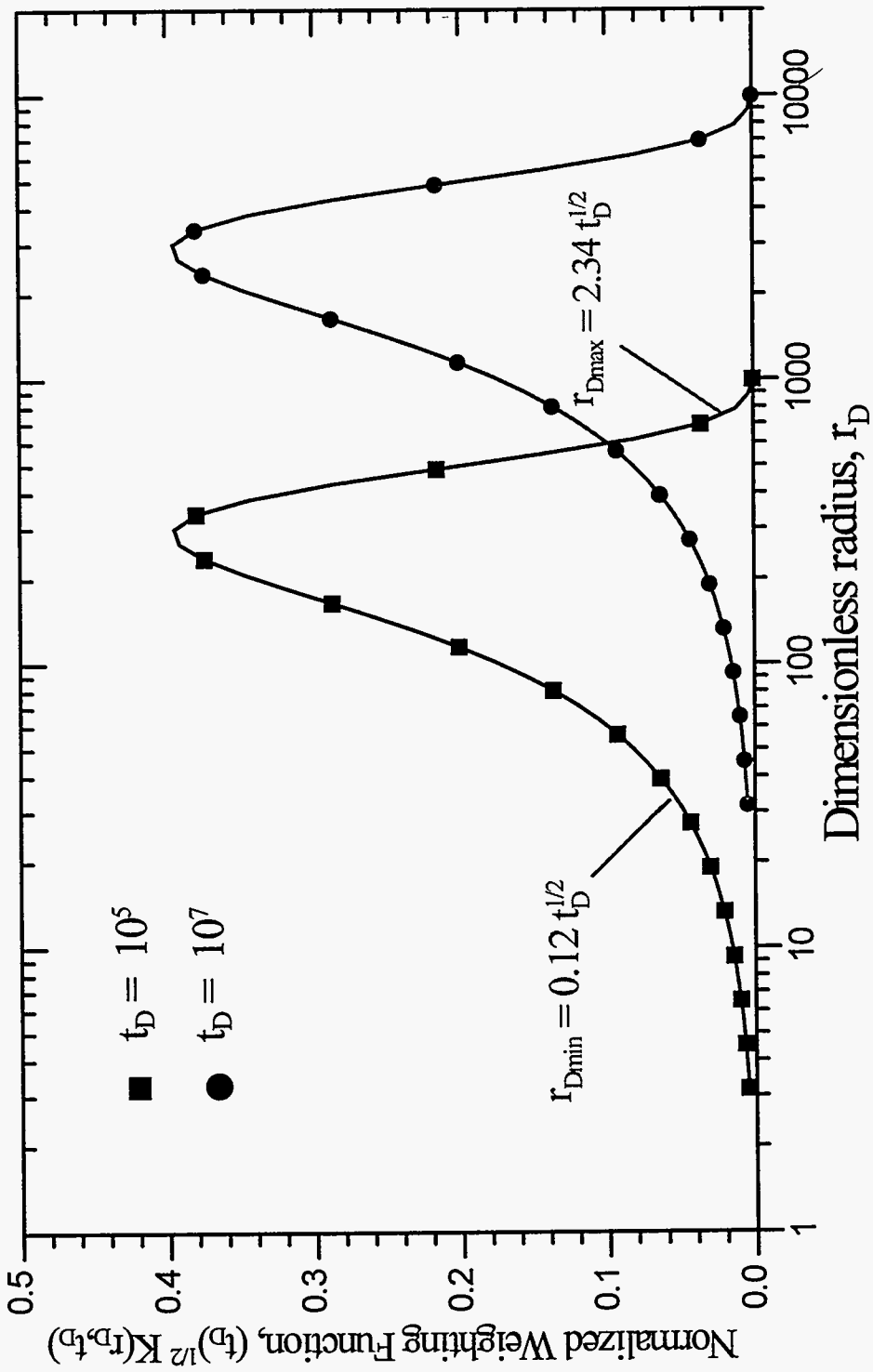

Figure 1.1: Weighting or kernal function defining the radii of investigation, after Oliver.[1.7]

the minimum and maximum radii at which the weighting function becomes so small that the permeabilities outside the region do not contribute to the slope of the semilog plot. A normalized plot of the weighting function (Fig. 1.1) shows that 98% of the contribution of the weighting function comes from the area encompassed by the dimensionless radii of $r_D = 0.12\sqrt{t_D}$ and $2.34\sqrt{t_D}$. Thus, the kernel function gives the weighted average of the well test permeability within these radii. Oliver claims that by using the appropriate weighting function, the average radial permeability can be estimated and that the area under the curve is a measure of the cumulative contribution to the permeability estimate.

Reference 1.8 has shown that Eq. 1.15 can be represented as:

$$\frac{1}{\hat{k}} = \sum_{j=2}^{N_r} \left[\frac{\int_{r_{Dj-1}}^{r_{Dj}} K(r_D, t_D) dr_D}{\int_{1}^{\infty} K(r_D, t_D) dr_D} \right] \frac{1}{\bar{k}_j(r_{Dj})} \tag{1.17}$$

where, $\hat{k}$, is the instantaneous permeability defined by:

$$\hat{k} = \frac{1}{2}\left[\frac{141.2 qB\mu}{h\Delta p'_w}\right] \tag{1.18}$$

and the instantaneous pressure derivative is:

$$\Delta p'_w = \frac{\partial \Delta p_w}{\partial \ln t} \tag{1.19}$$

and the pressure drop is,

$$\Delta p_w = p_i - p_{wf} \tag{1.20}$$

$\bar{k}(r_{Dj})$ is some arbitrary permeability average of grid block permeabilities within an annular region around r_{Dj} for $j = 1, \ldots N_r$. Eq. 1.17 is important and fundamental to the preceeding work because it explicitly relates the instantaneous well test permeability, $\hat{k}$, to the kernel function and a radially-distributed arbitrary permeability average in the theta-direction. It implies that the area under the kernel function represents the weight applied to each of the permeability averages in the

annular regions $\left(r_{j-1} \rightarrow r_j\right)$, and the weighted harmonic average of the effective radial permeability averages is a measure of the cumulative contribution to the instantaneous well test permeability, $\hat{k}$.

The Inverse Solution Algorithm (*ISA*)

Feitosa[1.8] extended Oliver's solution and developed an Inverse Solution Algorithm (*ISA*) to estimate the equivalent radial permeability distribution as a function of distance from the well. The *ISA* algorithm has the advantage over Oliver's solution in that it can be applied to large radial variations in permeability. Instead of using a reference permeability, k_{ref}, to define the dimensionless time, t_D, it is defined in terms of an instantaneous permeability determined from instantaneous pressure derivative:

$$\hat{t}_D = \frac{0.006328\hat{k}t}{\phi\mu c_t r_w^2} \tag{1.21}$$

where,

$$\hat{k} = \frac{1}{2}\left[\frac{141.2qB\mu}{h\Delta p_w'}\right] \tag{1.22}$$

and

$$\Delta p_w' = \frac{\partial \Delta p_w}{\partial \ln t} \tag{1.23}$$

ISA sequentially determines the equivalent radial permeability distribution for each zone using the following relationships:

$$\Delta\left(\frac{1}{k_{ISAn}}\right) = \frac{\frac{1}{\hat{k}_n} - \frac{1}{k_{ISAn-1}} + \sum_{i=2}^{n-1}\left[\Delta\left(\frac{1}{k_i}\right)\int_{\hat{z}_{0D}}^{\hat{z}_{i-1D}}\Omega(\hat{z}_D)d\hat{z}_D\right]}{1 - \int_{\hat{z}_{0D}}^{\hat{z}_{n-1D}}\Omega(\hat{z}_D)d\hat{z}_D} \tag{1.24}$$

where,

$$\hat{z}_{0D} = \min\left\{\frac{1}{\sqrt{\hat{t}_D}}, 0.12\right\} \tag{1.25}$$

$$\Omega\hat{z}_D = \sqrt{\pi}\ \ \hat{z}_D \exp\left(-\frac{\hat{z}_D^2}{2}\right) W_{\frac{1}{2},\frac{1}{2}}\left(\hat{z}_D^2\right) \tag{1.26}$$

$$\hat{z}_{0D} = \frac{1}{\sqrt{\hat{t}_D}} \tag{1.27}$$

and

$$\hat{z}_{jD} = \frac{r_{jD}}{\sqrt{\hat{t}_D}} \tag{1.28}$$

Once $\Delta(1/k_{ISAn})$ is calculated the permeability at zone n is determined by:

$$k_{ISAn} = \frac{1}{\frac{1}{k_{ISAn-1}} + \Delta\left(\frac{1}{k_{ISAn}}\right)} \tag{1.29}$$

The radius of investigation for the solution at zone n is defined as:

$$r_n = 2\sqrt{\frac{0.006328\hat{k}_n t}{\phi\mu c_t r_w^2}} \tag{1.30}$$

Comparisons of simulation results using the calculated radial permeability distribution and actual permeability distribution have resulted in excellent agreement between computed pressures, pressure derivatives, and permeability distributions.[1.8]

Feitosa also presented analysis of the solution to areally heterogeneous reservoirs, where permeability varies in (r, θ) and (x, y). He analyzed the pressure derivatives of such distributions and determined equivalent radial permeability distributions that honor the original pressure behavior of the reservoir during a well test.

To effectively use a well test derived permeability in a stochastic conditional simulation method, the well test permeability must impose a deterministic constraint on the distribution of surrounding small-scale permeabilities within the area of

investigation. Therfore, an averaging model that defines the permeability distribution within the annulus of investigation has to be developed. The pressure bahavior of numerous permeability fields, with varying degrees of heterogeneity are used along with analytical solutions proposed by Oliver[1.7] and Feitosa[1.8] to determine the averaging process and the region of investigation.

The Base Case

The first step is to generate synthetic permeability distributions and numerically simulate pressure drawdown tests. We assume that these distributions and pressure responses are the *truth* or *base* cases. A two dimensional permeability field is generated using the Turning Bands Method (TBM).[1.10, 1.11] TBM generates an unconditional correlated distribution. The distribution is unconditional since there are no available data at grid blocks that must be honored. The specified univariate and spatial statistics of the distribution are honored. For simplicity a square reservoir with square grid blocks is considered. An example of a permeability field generated using this method is shown as a greyscale map in Fig. 1.2. In order to draw general conclusions, we generate numerous base cases with varying degrees of heterogeneity. A summary of the univariate and spatial statistics of the generated distributions is given in Table 1.1. Using this permeability field, a numerical fluid flow simulation of a drawdown is performed on the reservoir. It is assumed that all other reservoir properties are constant and only the distribution of permeabilities is varied. The reservoir properties are given in Table 1.2.

A well producing at a constant rate is placed at the center of the grid block at the center of the reservoir. A finite difference numerical fluid flow simulation of the reservoir is performed using ECL 100,[1.12] a commercial reservoir simulation package. ECL 100 corrects grid block pressures to well flowing pressures using Peaceman's approximation.[1.13]

The pressure and pressure derivative responses for the permeability field shown in Fig. 1.2 are shown in Fig. 1.3. To draw general conclusions, numerous base cases are investigated. Our objective is to generate a reservoir description such that the univariate and spatial statistics, and the simulated pressures and pressure derivatives are reproduced to match the base case study.

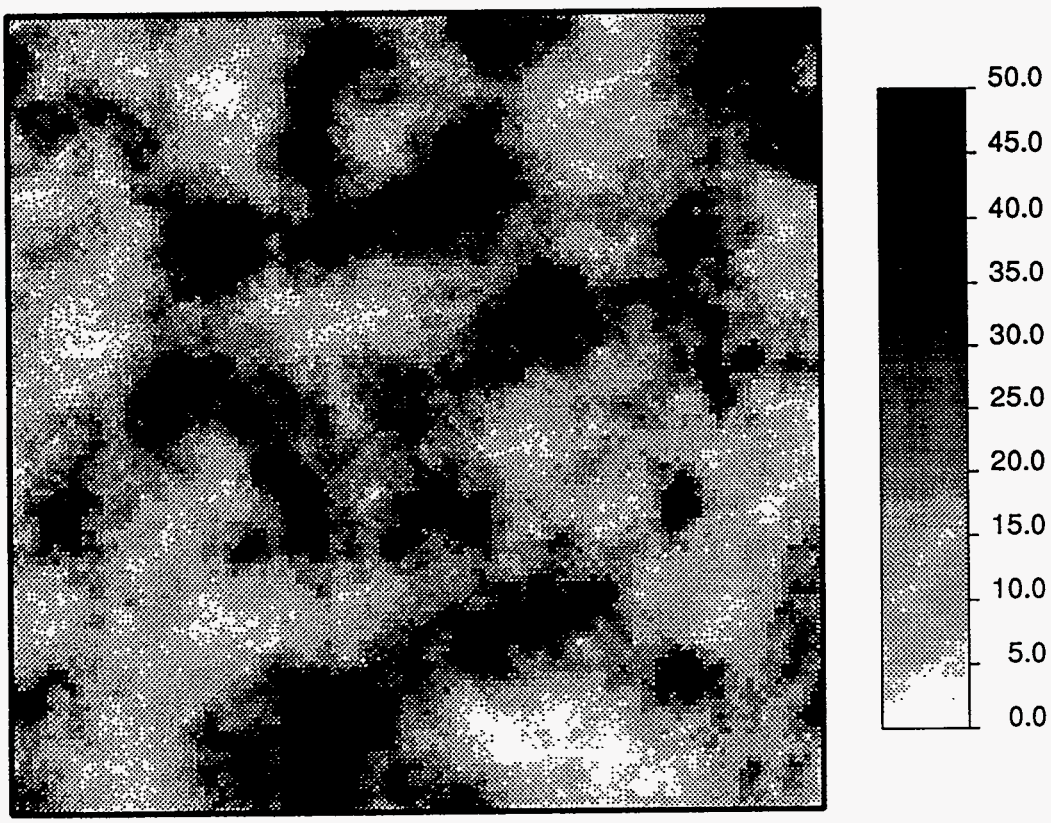

Figure 1.2: Base case permeability distribution generated by Turning Bands (range = 600 feet, $\sigma^2_{\ln k} = 0.92$, mean = 20 md).

Table 1.1: Summary of comparison for different permeability averaging techniques using Oliver's solution. The permeability derived from the best fit semi-log straight line is used to calculate t_D.

Turning Bands input parameters, μ_k = 20 md			Measures of heterogeneity		Relative error			Absolute relative error		
seed	$\sigma^2_{\ln k}$	Range ft	HI	V	err$(\bar{k}_{he})$	err$(\bar{k}_{ge})$	err$(\bar{k}_{ae})$	aerr$(\bar{k}_{he})$	aerr$(\bar{k}_{ge})$	aerr$(\bar{k}_{ae})$
-15	0.4	2000	0.0795	0.33	-0.09036	-0.31868	-0.54748	0.513138	0.392082	0.547485
-4	0.25	3200	0.0497	0.22	-0.43524	-0.45448	-0.47404	0.435235	0.454482	0.474038
-3	0.5	2000	0.1242	0.39	0.222823	-0.74244	-1.80654	0.723932	0.742444	1.806539
-10	0.5	500	0.0311	0.39	1.18261	0.133535	-0.99903	1.272835	0.788592	1.225603
-22	0.92	595.41	0.1242	0.6	2.475823	0.057403	-2.89076	3.141266	1.3344	1.418949
-20	0.92	2143.84	0.4472	0.6	-0.3347	-0.4562	-0.57784	0.511436	0.542633	0.601231
-18	0.92	958.78	0.2	0.6	0.326066	-0.16675	-0.66303	0.61267	0.466313	0.697861
-16	0.92	1072	0.2236	0.6	5.276271	1.74461	-2.74124	5.366854	1.999967	2.741241
-12	0.75	1250	0.1747	0.53	3.799674	1.607549	-0.95948	3.955623	1.855726	1.272401
-11	0.75	3200	0.4472	0.53	-0.09421	-0.38604	-0.72328	0.269079	0.386039	0.723275
-7	0.75	1600	0.2236	0.53	0.666887	-0.05145	-0.74134	0.870897	0.250329	0.741335
-8	0.75	2000	0.2795	0.53	4.258866	1.719957	-1.07827	4.56714	2.142425	1.079453
-9	0.75	1000	0.1398	0.53	3.157713	0.543653	-2.01837	3.65774	2.508632	2.0854
-26	1.2	1241.69	0.4472	0.7	10.85558	3.762324	-6.27113	11.14859	4.272174	6.271128
-25	1.2	555.32	0.2	0.7	1.794496	-0.48399	-3.86832	2.291219	0.654822	3.868322
-24	1.2	220.74	0.0795	0.7	2.587599	-0.44731	-6.67754	2.690726	0.727924	6.677539
-23	1.61	193	0.1242	0.8	3.260873	-0.42692	-10.373	3.286525	0.554495	10.37296
-21	1.61	694.93	0.4472	0.8	1.478112	-0.3463	-4.50955	1.705823	0.368285	4.509553
-19	1.61	310.8	0.2	0.8	3.392921	0.70958	-4.32311	3.392921	0.719254	4.323115
-17	1.61	347.5	0.2236	0.8	1.533938	-0.00949	-4.29839	1.662844	0.493295	4.29839
Cumulative errors					2.174269	0.242667	-2.93269	2.508204	1.020205	4.194824

where,

Seed = turning bands seed number

$\sigma^2_{\ln k}$ =standard devation on a log normal scale $\mu_{k=}$ mean permeaility

HI = Heterogeneity Index = $(\sigma^2_{\ln k} range / \Delta x \times N_Y)$ V = Dykstra Parsons coefficient = $1 - 1/\exp(\sigma^2_{\ln k})$

Number of grid blocks (x,y,z)	115x115x1
Block dimensions ($\Delta x, \Delta y, \Delta z$)	35*ft* x 35*ft* x 10*ft*
Porosity	0.3
Wellbore radius	0.5 *ft*
Total compressibility	4.9×10^{-7} psi^{-1}
Oil formation volume factor	1.2 *bbl/STB*
Oil viscosity	0.4 *cp*
Oil rate	106.3 *STB/D*
Initial pressure	2000 *psia*
No flow upper and lower boundaries	
Negligible well bore storage and skin	
Negligible gravity and capillary effects	
Fully penetrating well	

Table 1.2: Reservoir properties

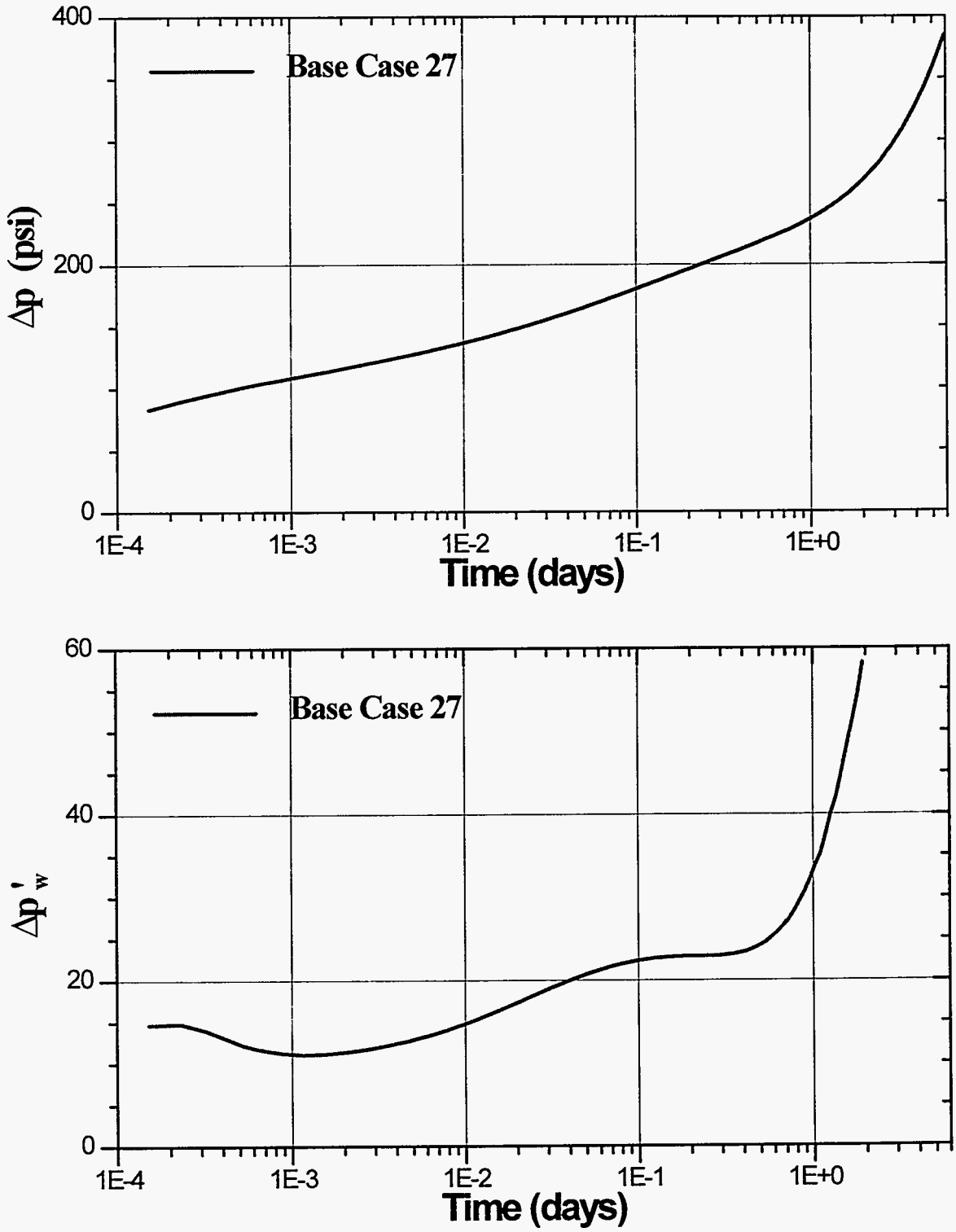

Figure 1.3: Pressure and pressure derivative response for the permeability field shown in Figure 1.2.

Application of Oliver's Solution to an Areally (x-y) Heterogeneous Reservoir

In this section, we consider the application of Oliver's solution (in specific Eq. 1.17) to an areally $(x-y)$ heterogeneous reservoir. A method that discretizes Eq. 1.17 and applies the radial solution to an equivalent areal $(x-y)$ reservoir is presented.

For a dimensionless time, t_D, the kernel function is non-negligible between the dimensionless radii, $r_D = 0.12\sqrt{t_D}$ and $2.34\sqrt{t_D}$, where,

$$t_D = 2.637\times10^{-4}\frac{\bar{k}_{wt}t}{\phi\mu c_t r_w^2} \tag{1.31}$$

and $\bar{k}_{wt}$ is the permeability calculated from the best fit semilog straight line equation.

In order to discretize Oliver's solution, the reservoir is divided into annular rings defined by Coats'[1.14] grid:

$$r_j = \alpha^j r_o, \qquad j = 1,2,\ldots\ldots,N_r \tag{1.32}$$

where,

$$r_o = \frac{r_w \ln\alpha}{(\alpha-1)},\quad \alpha = (r_e/r_w)^{1/N_r} \quad \text{and} \quad r_e = \min\left(\frac{\Delta x\times N_X}{2},\frac{\Delta y\times N_Y}{2}\right).$$

For our study we assumed N_r to be 50.

It should be noted that for a heterogeneous reservoir, there is no clear transition between the transient and pseudo-steady state flow period. Heterogeneous systems exhibit permeability streaks. The resulting fluid flow through the reservoir causes one or more of the boundaries that are closer to high permeability streaks, to be felt sooner than others. This would be especially evident in anisotropic permeability fields. The equipotential lines are not circular as they are in homogeneous reservoir. For the isotropic case studies investigated, we assume that transient flow ends when for a given flow period (time), the maximum radius of investigation defined by Oliver's solution, $r_{D\max}$, is approximately equal to the outer radius, r_e, of the reservoir, i.e., the end of the transient period is defined by:

$$r_{D\max} = 2.34\sqrt{t_D} \le \frac{r_e}{r_w} \tag{1.33}$$

At each time value, an annulus of investigation is defined based on the non negligible region of the kernel function.[1.7] Since the reservoir annular rings have been pre-defined by Coats' grid, we define the minimum and maximum radii for the annulus of investigation at each t_D by the following criteria:

$$\begin{aligned} r_{D\min} &= r_{Dj-1}, \quad r_{Dj-1} \le 0.12\sqrt{t_D} < r_{Dj} \\ r_{D\max} &= r_{Dj}, \quad r_{Dj-1} < 2.34\sqrt{t_D} \le r_{Dj} \end{aligned} \tag{1.34}$$

Note that since the kernel function is negligible at $r_D < 0.12\sqrt{t_D}$, it must also be negligible at the Coats radius r_{Dj}. A similar argument is valid for the upper limit. A numerical integration of the kernel function using Simpson's rule[1.15] gives the area under the curve between $r_{D\min}$ and $r_{D\max}$. The weight of each annular region is given by:

$$w_j = \frac{\int_{r_{j-1}}^{r_j} K(r_D, t_D)}{\int_{r_{D\min}}^{r_{D\max}} K(r_D, t_D)}, \quad \text{for } j = j_{\min}, j_{\min+1}, \cdots j_{\max} \tag{1.35}$$

where, $r_{j\min}$ and $r_{j\max}$ correspond to the minimum and maximum radii defined by Eq. 1.34.

A single well draining a reservoir imposes radial flow and consequently a radial solution to this problem. Permeability or reservoir properties, however, are not distributed radially but areally $(x - y)$. Thus we must impose the radial solution on an areal permeability distribution. We need to first evaluate the correct type of averaging of grid block permeabilities within the annular rings. Note that in Oliver's solution this averaging is harmonic. In our work we test alternate averaging methods for grid block permeabilities in the θ-direction.

An area-based power averaging scheme is considered. It accounts for segments of grid blocks that only partially lie within the annulus under consideration. The equation to calculate this average permeability, $\bar{k}$, is:

$$(\bar{k}A_r)^{\omega} = \sum_{\vec{s}\in A_r} \left(k_{\vec{s}}A_{\vec{s}}\right)^{\omega} \tag{1.36}$$

where, $\vec{s}$ is the location vector of the grid block, A_r is the radial area between the r_{j-1} and r_j interval and $A_{\vec{s}}$ is the area of the grid block that falls in between these radii. The procedure used to calculate the area of such a grid block is given in Appendix A of Reference 1.1. The nomenclature is clearly illustrated in Fig. 1.4. For $\omega = 1$ the arithmetic average is calculated and when $\omega = -1$ the harmonic average, i.e., the average suggested by Oliver's solution, is calculated. However, when $\omega = 0$ the geometric average cannot be calculated by Eq. 1.36; instead, the following area-based geometric averaging equation is used:

$$A_r \ln \bar{k}_g = \sum_{\vec{s}\in A_r} A_{\vec{s}} \ln k_{\vec{s}} \tag{1.37}$$

Note that if the grid block permeability, $k_{\vec{s}}$, is 0 the permeability average cannot be defined; therefore, we constrain our distribution such that permeability values are greater than 0. Eq. 1.17 shows that the instantaneous permeability, $\hat{k}$, can be represented by an integral of the inverse of the radial permeability distribution within the annulus of investigation, i.e., a harmonic average of the θ-averaged radial permeability average within an annular region weighted by the function defined in Eq. 1.35. In order to represent the discrete form of Eq. 1.17, for an areal $(x-y)$ heterogeneous reservoir, the instantaneous permeability, $\hat{k}$, is replaced by the equivalent permeability, $\bar{k}_e$. Therefore, the discrete form of Eq. 1.17 is written as:

$$\frac{1}{\bar{k}_e} = \sum_{j=1}^{N_r} w_j \frac{1}{\bar{k}_j} \tag{1.38}$$

where $\bar{k}_j$ is an area based permeability average in the theta direction and determined in the next part of this report. w_j is weight contribution of each radial permeability distribution defined by Eq. 1.35.

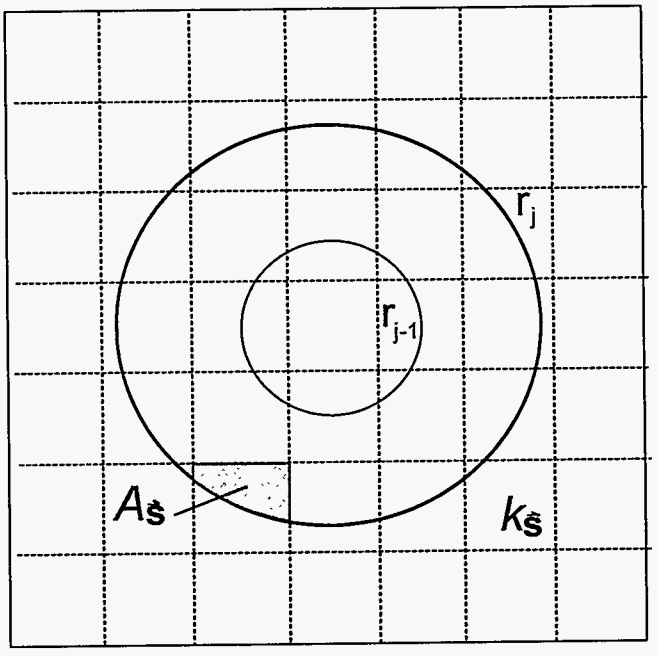

Figure 1.4: Illustration of the nomenclature used to calculate the area based power average of grid block permeabilities in annular rings.

Numerical Experiments to Determine the Best Averaging Technique in the θ-Direction for Oliver's Solution

In Oliver's solution the averaging process in the theta direction is defined as a harmonic mean for small permeability variations about a base value. This is done so that the perturbation theory technique facilitates a solution to the generalized problem (Eq. 1.4 through Eq. 1.10). However, in the areal permeability distributions, permeability is log-normally distributed with varying degrees of heterogeneity and does *not* vary slightly about a base value. We, therefore, investigate different averaging techniques in the θ-direction using Eq. 1.36 or Eq. 1.37. The instantaneous well test permeability, $\hat{k}$, (Eq. 1.18) is compared to the equivalent permeability, $\bar{k}_e$, (Eq. 1.38). Numerical experiments on the synthetic permeability distribution and pressure data have shown that a geometric average of grid block permeabilities in the theta direction, followed by a harmonic average, weighted by the kernel function, in the radial direction give a good approximation of $\hat{k}$. Fig. 1.5, Fig. 1.6, and Fig. 1.7 show the comparisons between harmonic, geometric, and arithmetic averaging methods in the theta direction to the instantaneous well test permeability, respectively. The results are summarized in Table 1.1. The errors are defined as:

$$err(\bar{k}_{he}) = \frac{1}{N_t}\sum_{i=1}^{N_t}\bar{k}_{he_i} - \hat{k}_i \tag{1.39}$$

where $\bar{k}_{he}$ is the equivalent permeability calculated by averaging harmonically in the θ-direction (Eq. 1.36) and harmonically in the radial direction (Eq. 1.36).

$$err(\bar{k}_{ge}) = \frac{1}{N_t}\sum_{i=1}^{N_t}\bar{k}_{ge_i} - \hat{k}_i \tag{1.40}$$

where $\bar{k}_{ge}$ is the equivalent permeability calculated by averaging geometrically in the θ-direction (Eq. 1.37) and harmonically in the radial direction (Eq. 1.36).

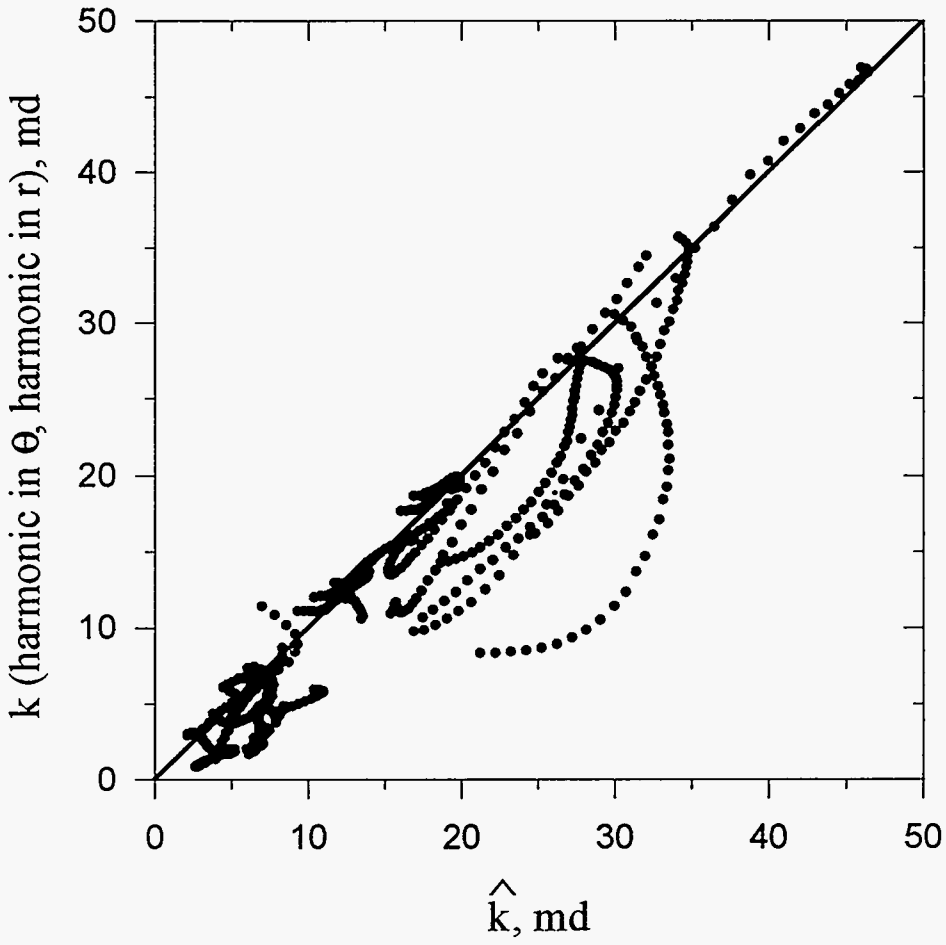

Figure 1.5: Grid block permeabilities averaged harmonically in θ and harmonically in r compared to the instantaneous well test permeability, $\hat{k}$.

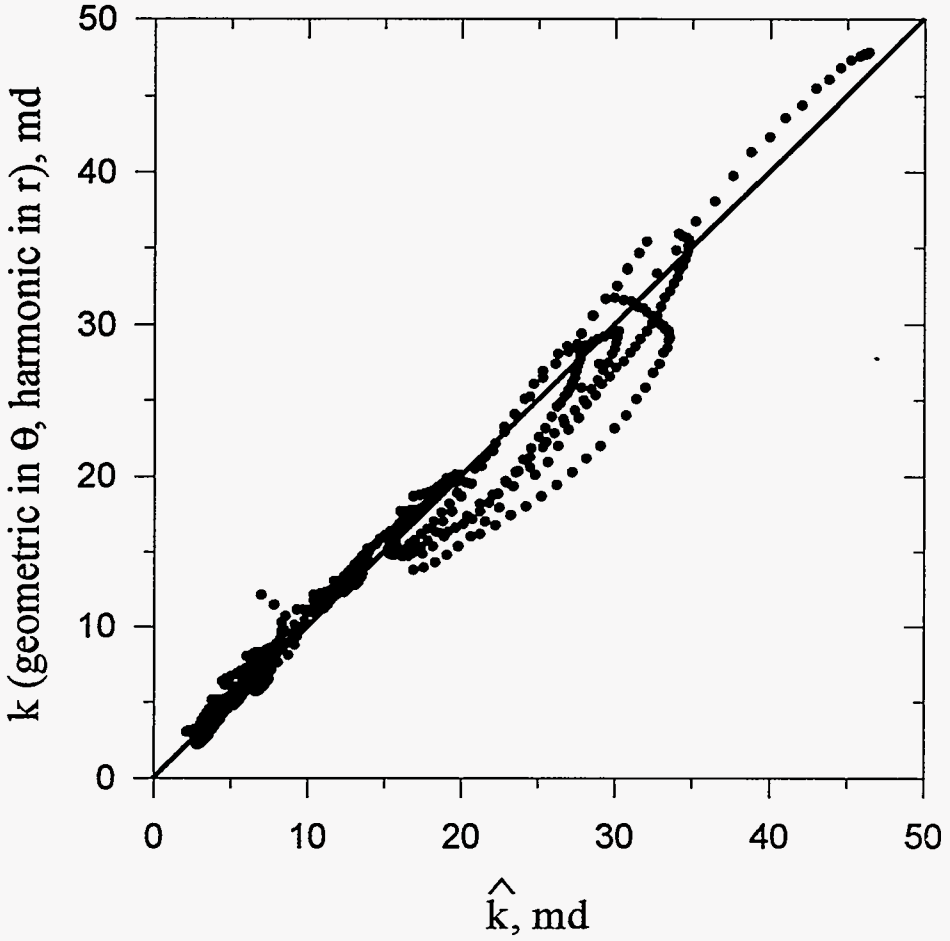

Figure 1.6: Grid block permeabilities averaged geometically in θ and harmonically in r compared to the instantaneous well test permeability, $\hat{k}$.

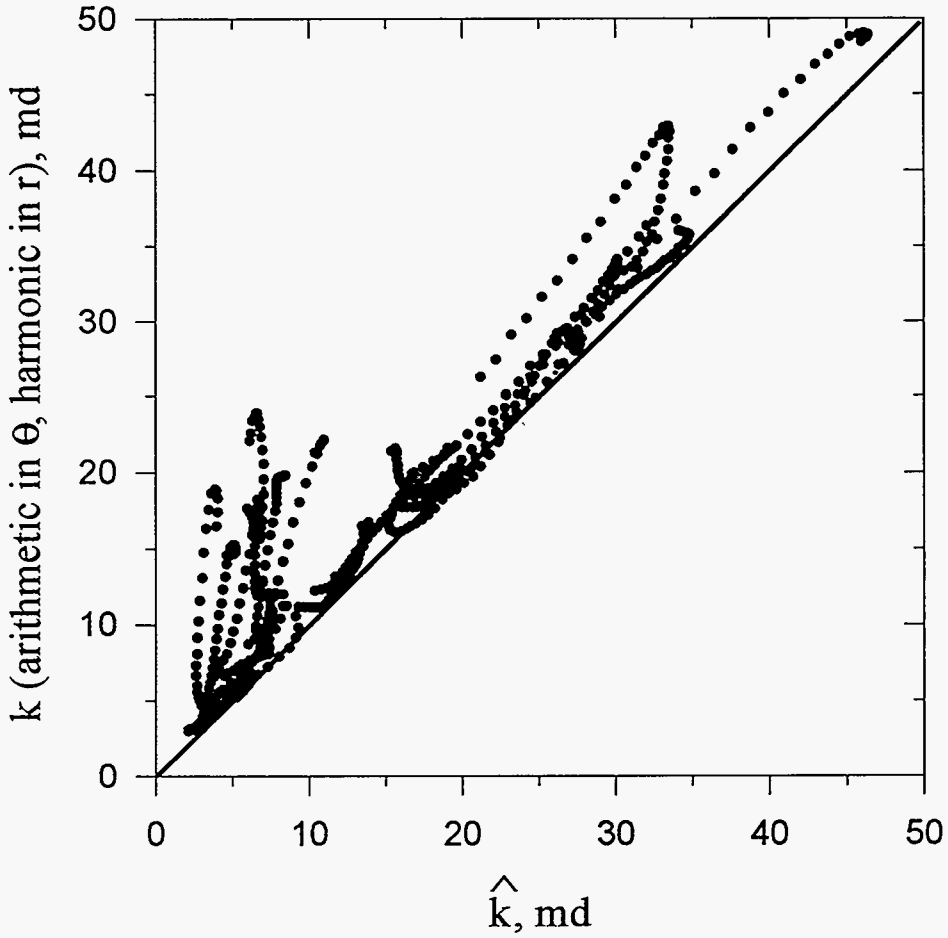

Figure 1.7: Grid block permeabilities averaged arithmetically in θ and harmonically in r compared to the instantaneous well test permeability, $\hat{k}$.

$$err(\bar{k}_{ae}) = \frac{1}{N_t}\sum_{i=1}^{N_t} \bar{k}_{ae_i} - \hat{k}_i \tag{1.41}$$

where $\bar{k}_{ae}$ is the equivalent permeability calculated by averaging arithmetically in the θ-direction (Eq. 1.36) and harmonically in the radial direction (Eq. 1.36). The absolute relative errors are calculated by:

$$aerr(\bar{k}_{he}) = \frac{1}{N_t}\sum_{i=1}^{N_t} \left|\bar{k}_{he_i} - \hat{k}_i\right| \tag{1.42}$$

$$aerr(\bar{k}_{ge}) = \frac{1}{N_t}\sum_{i=1}^{N_t} \left|\bar{k}_{ge_i} - \hat{k}_i\right| \tag{1.43}$$

and

$$aerr(\bar{k}_{ae}) = \frac{1}{N_t}\sum_{i=1}^{N_t} \left|\bar{k}_{ae_i} - \hat{k}_i\right| \tag{1.44}$$

Note that the harmonic average underpredicts the instantaneous well test permeability and the arithmetic average overpredicts the permeability. A geometric average in the θ-direction and a harmonic average in the radial direction best approximates the instantaneous well test permeability, $\hat{k}$. Therefore, Eq. 1.38, in which an area-based geometric average represents the θ-direction permeability average, is the best approximation for the discretized form of Eq. 1.17.

To develop his Inverse Solution Algorithm (*ISA*), Feitosa[1.8] uses the instantaneous permeability, $\hat{k}$, to calculate an "instantaneous" dimensionless time $\hat{t}_D$ (Eq. 1.21). His numerical experiments show that by using these "instantaneous" parameters a more accurate evaluation of the kernel function is obtained which reproduces the pressure response and permeability distribution. In this method, a pressure derivative which has large variations may result in a kernel function whose minimum radius is not guaranteed to shift forward in the domain of the reservoir for successive pressure derivative values.

Based on numerical experiments, we observed that using $\hat{k}$, instead of the permeability derived from the best fit of the semi-log straight line to calculate the dimensionless time, t_D, made no noticeable improvements in our results. This is

probably due to the fact that the pressure derivatives of our base cases do not vary extremely. The comparison results are summarized in Table 1.3.

Application of *ISA* to Areally (*x*-y) Heterogeneous Reservoir

For the pressure response showm in Fig. 1.3, *ISA* (Eq. 1.21 through Eq. 1.30) generates an equivalent radial permeability distribution. The permeability distribution, generated by *ISA* is a piecewise linear polynomial (Fig. 1.8). In our application to an areal permeability field, we must define the equivalent *ISA* permeability within an inner and outer radius of investigation. We define k'_{ISAn} as the permeability which is linearly interpolated between k_{ISAn-1} and k_{ISAn}, for the inner and outer radius of investigation, r_{n-1} and r_n, respectively (see Fig. 1.8). Therefore, for each annular region over which k'_{ISAn} is defined, the minimm radius, is defined by r_{n-1} and the maximum radius is defined by r_n.

Feitosa showed an example in which permeability is varied in r and θ. A numerical fluid flow simulation is performed using a $r-\theta$ flow simulator. He observed that if he replaces the areally $(r-\theta)$ heterogeneous reservoir with a radial reservoir where the permeability in each Coat's grid annulus was computed as the geometric average of the grid block permeabilities within the annulus, he obtained a pressure derivative that best matches the pressure derivative from the areally heterogeneous reservoir.

Numerical Experiments to Determine the Best Averaging Technique in the θ -Direction for *ISA*

We study the application of *ISA*-derived radial permeabilities to our areal $(x-y)$ permeability distribution. A procedure similar to the one used to determine the best type of average for Oliver's solution is used. Eq. 1.36 and Eq. 1.37 are used to calculate the arithmetic, harmonic, and geometric permeability averages within the *ISA* defined radii of investigation. Fig. 1.9 through Fig. 1.11 compare the different averaging techniques to the *ISA* permeability distribution. The errors are defined as:

Turning Bands input parameters, μ_x = 20 md			Measures of heterogeneity		Relative error		Absolute relative error	
seed	$\sigma^2_{ln_x}$	Range ft	HI	V	$err(\bar{k}_{he})$	$err(\bar{k}_{ge})$	$aerr(\bar{k}_{he})$	$aerr(\bar{k}_{ge})$	$aerr(\bar{k}_{ae})$
-15	0.4	2000	0.0795	0.33	-0.134	-0.356	0.546	0.427	0.577
-4	0.25	3200	0.0497	0.22	-0.458	-0.477	0.458	0.477	0.496
-3	0.5	2000	0.1242	0.39	0.304	-0.565	0.629	0.565	1.520
-10	0.5	500	0.0311	0.39	1.634	0.623	1.643	1.085	1.341
-22	0.92	595.41	0.1242	0.6	3.971	1.453	-1.619	3.971	1.498	2.063
-20	0.92	2143.84	0.4472	0.6	-0.547	-0.637	-0.727	0.547	0.637	0.727
-18	0.92	958.78	0.2	0.6	0.286	-0.176	-0.645	0.580	0.535	0.692
-16	0.92	1072	0.2236	0.6	5.955	2.081	-2.838	5.963	2.266	2.838
-12	0.75	1250	0.1747	0.53	4.041	1.710	-1.020	4.081	1.810	1.081
-11	0.75	3200	0.4472	0.53	-0.184	-0.450	-0.757	0.299	0.450	0.757
-7	0.75	1600	0.2236	0.53	0.647	-0.085	-0.782	0.895	0.267	0.782
-8	0.75	2000	0.2795	0.53	4.933	2.147	-0.948	5.111	2.414	0.948
-9	0.75	1000	0.1398	0.53	5.858	2.943	0.084	5.932	3.244	1.389
-26	1.2	1241.69	0.4472	0.7	12.200	4.254	-6.825	12.21	4.507	6.825
-25	1.2	555.32	0.2	0.7	1.487	-0.515	-3.464	2.014	0.688	3.464
-24	1.2	220.74	0.0795	0.7	2.461	-0.430	-6.371	2.635	0.724	6.371
-23	1.61	193	0.1242	0.8	3.147	-0.408	-10.09	3.263	0.524	10.088
-21	1.61	694.93	0.4472	0.8	NO SOLUTION					
-19	1.61	310.8	0.2	0.8	0.349	0.729	-4.752	3.563	0.737	4.752
-17	1.61	347.5	0.2236	0.8	1.790	0.231	-3.727	1.848	0.597	3.727
Cumulative errors					2.627	0.588	-2.617	2.902	1.196	3.711

Table 1.3: Summary of comparison for different permeability averaging techniques using Oliver's solution. The instantaneous permeability, $\hat{k}$, is used to determine $\hat{t}_D$.

where,
Seed = turning bands seed number

$\sigma^2_{ln_k}$ =standard deviation on a log normal scale

μ_k= mean permeability

HI = Heterogeneity Index = $(\sigma^2_{ln_k} range/\Delta x \times N_x)$

V = Dykstra Parsons Coefficient = $1-1/\exp(\sigma^2_{ln_k})$

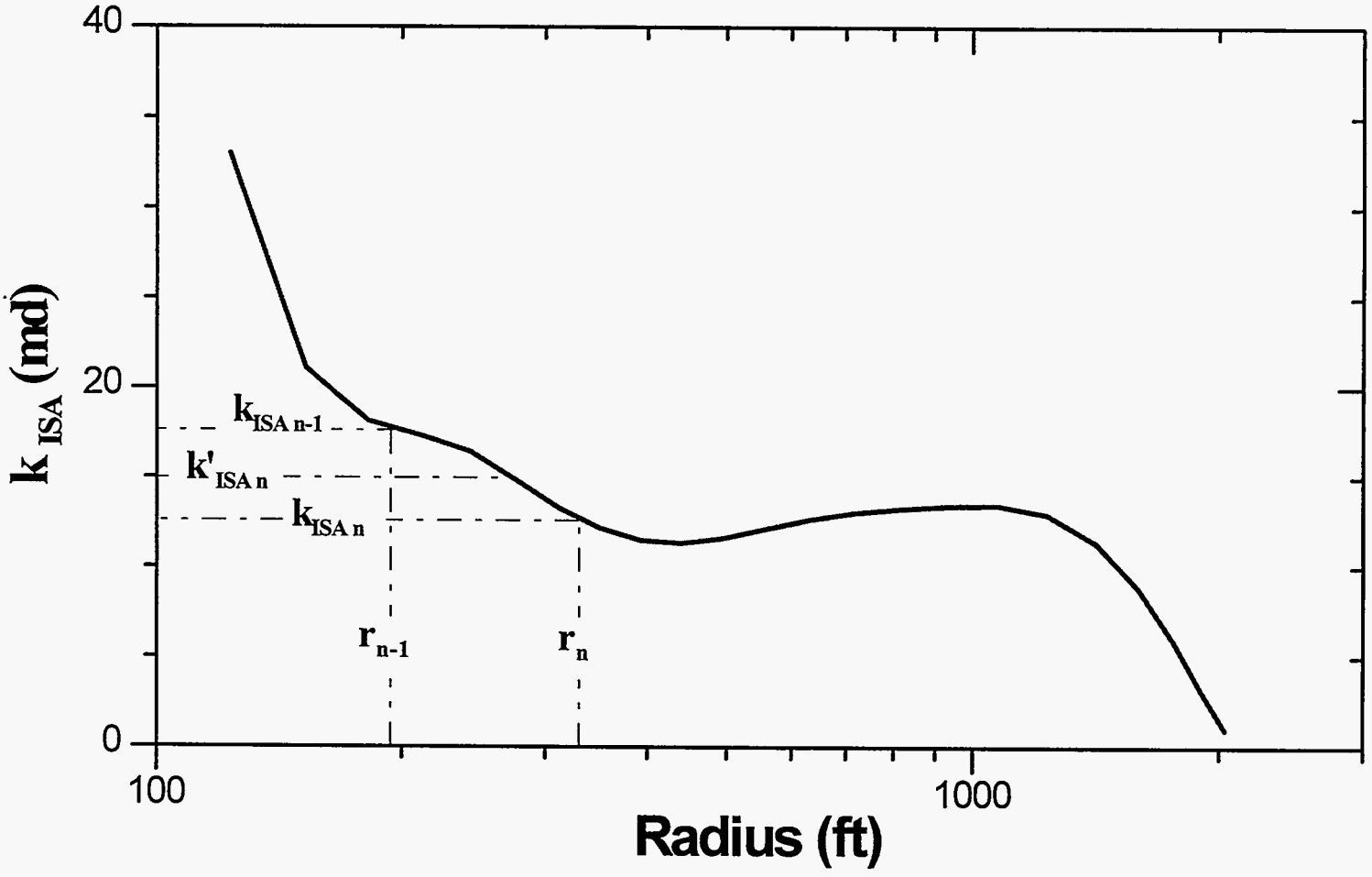

Figure 1.8: Equivalent radial permeability distribution determined by *ISA* for the pressure response shown in Figure 1.3.

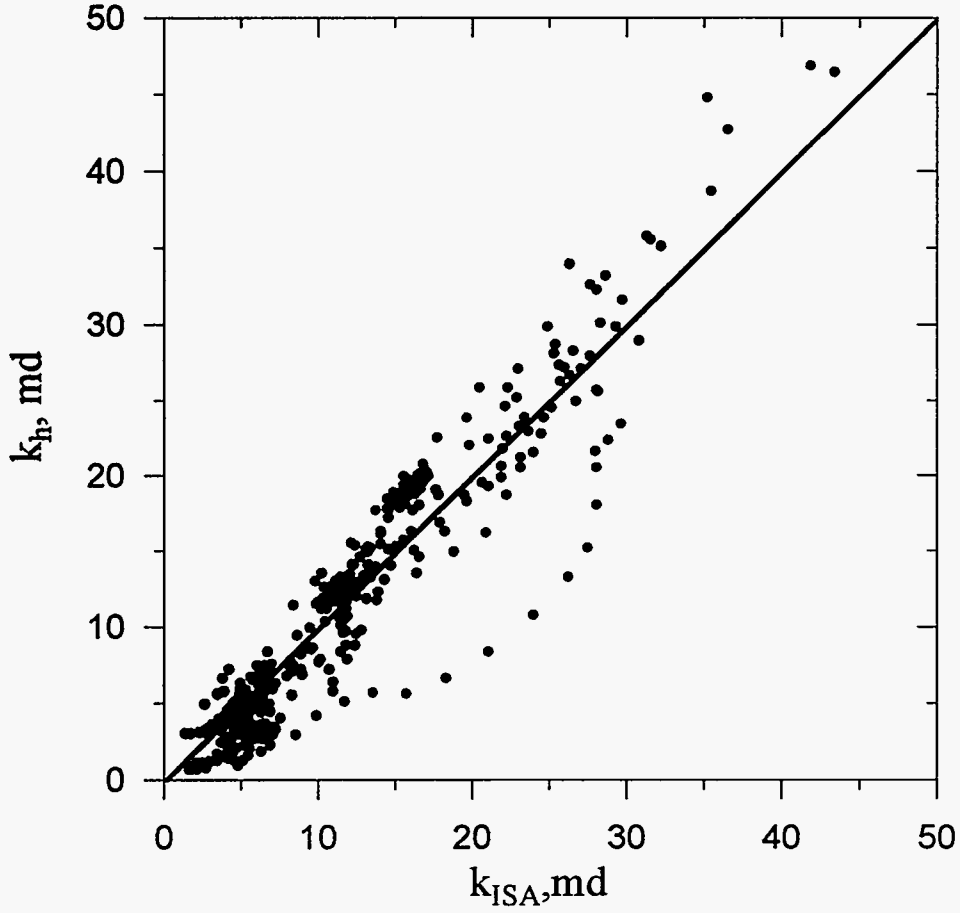

Figure 1.9: Grid block permeability averaged harmonically in θ compared to the *ISA* well test permeability distribution, k_{ISA}.

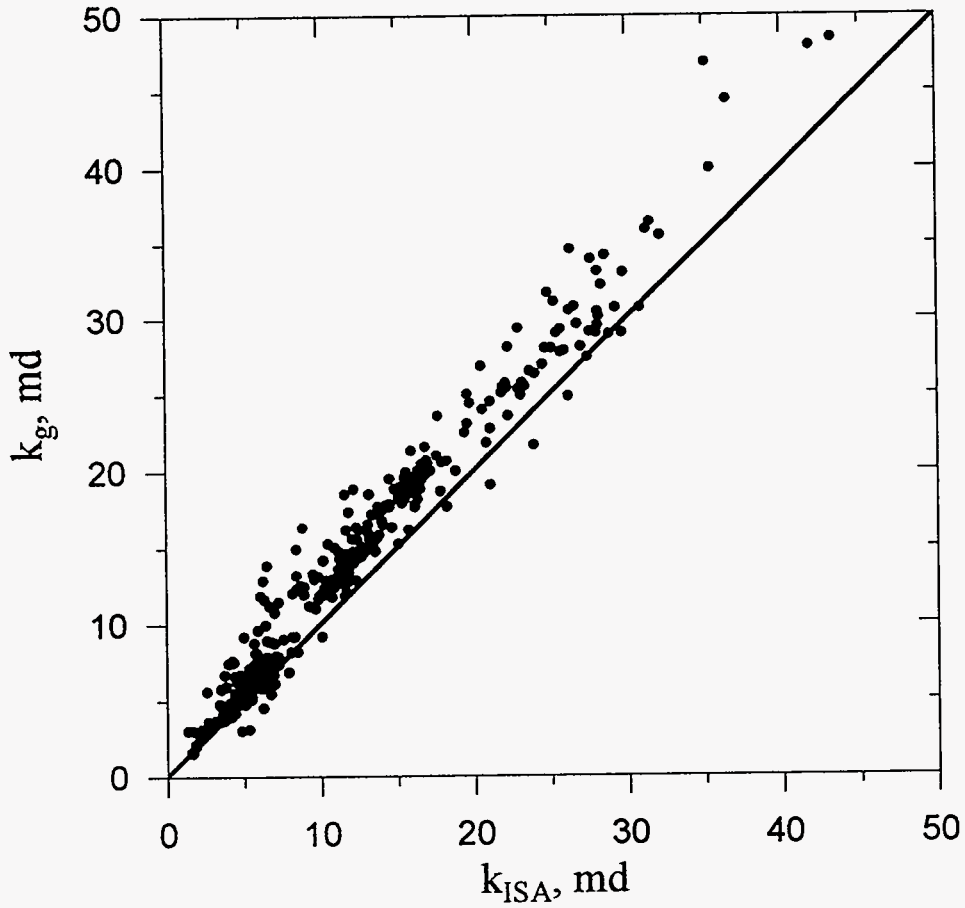

Figure 1.10: Grid block permeabilities averaged geometrically in θ compared to the *ISA* well test permeability distribution, k_{ISA}.

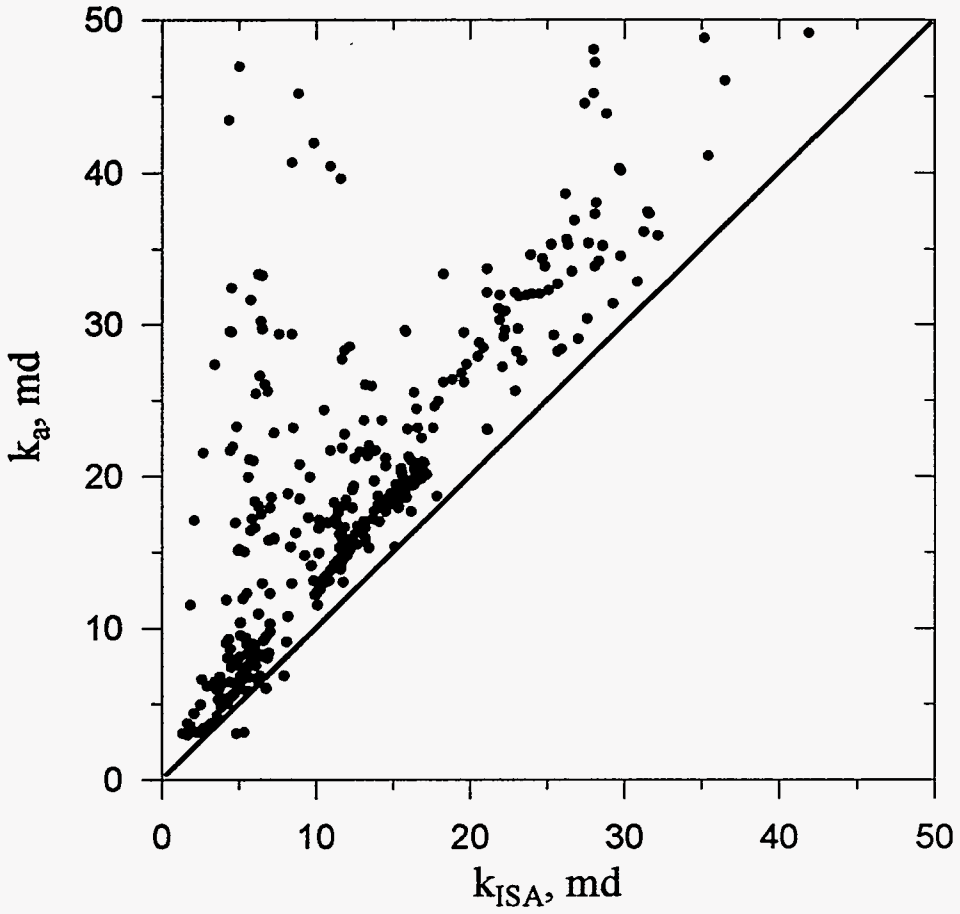

Figure 1.11: Grid block permeabilities averaged arithmetically in θ compared to the *ISA* well test permeability distribution, k_{ISA}.

$$err(\bar{k}_h) = \frac{1}{N_r}\sum_{j=1}^{N_r}\bar{k}_{hj} - k_{ISAj} \tag{1.45}$$

where $\bar{k}_h$ is the harmonic average of grid block permeabilities in the θ-direction (Eq. 1.36) between the inner and outer radii of investigation.

$$err(\bar{k}_g) = \frac{1}{N_r}\sum_{j=1}^{N_r}\bar{k}_{gj} - k_{ISAj} \tag{1.46}$$

where $\bar{k}_g$ is the geometric average of grid block permeabilities in the θ-direction (Eq. 1.37) between the inner and outer radii of investigation.

$$err(\bar{k}_a) = \frac{1}{N_r}\sum_{j=1}^{N_r}\bar{k}_{aj} - k_{ISAj} \tag{1.47}$$

where $\bar{k}_a$ is the arithmetic average of grid block permeabilities in the θ-direction (Eq. 1.36) between the inner and outer radii of investigation. The absolute relative errors are calculated by:

$$aerr(\bar{k}_h) = \frac{1}{N_r}\sum_{j=1}^{N_r}\left|\bar{k}_{hj} - k_{ISAj}\right| \tag{1.48}$$

$$aerr(\bar{k}_g) = \frac{1}{N_r}\sum_{j=1}^{N_r}\left|\bar{k}_{gj} - k_{ISAj}\right| \tag{1.49}$$

and

$$aerr(\bar{k}_a) = \frac{1}{N_r}\sum_{j=1}^{N_r}\left|\bar{k}_{aj} - k_{ISAj}\right| \tag{1.50}$$

Note that both harmonic and geometric averaging in the θ-direction of the areal permeability field give good approximations to the *ISA* radial permeability distribution. The best averaging technique for *ISA* is studied further in Section 1.3, where the inverse problem is solved; i.e. an areal permeability distribution honoring geostatistical and *ISA* equivalent permeabilities is generated. The pressure response of permeability fields honoring *ISA* by performing both harmonic and geometric averaging in the θ-direction are compared to the base case pressure response.

To summarize the findings, the well test data can be represented by equivalent static permeability distribution. Both Oliver[1.7] and Feitosa[1.8] provide appropriate solutions for representing dynamic well test data as radially heterogeneous permeability distributions.

1.1.2 Incorporation of Production Performance Constraints

In this section the primary and secondary performance parameters are investigated to identify the quatifiable spatial charateristics of petrophysical propeties which impact performance. These indirect performance constraints are identified by studying synthetic heterogeneous reservoirs and the flow simulation results of primary and seccondary recovery. In Section 1.2 we show how some of these constraints are included in the simulated annealing algorithm.

Primary Performance Constraints

The correlation between primary well performance parameters and spatial distributions of porosity and permeability is investigated. In reservoir modeling, it is advantageous to identify as early as possible well performance characteristics which are influenced by heterogeneities. Such information can be used to better define internal reservoir architecture and optimize operating and development plans early in the life of a reservoir. With synthetic data sets, we show that the primary production performance is closely related to the near-well bore permeability distribution.

Flow Simulation Comparisons

To understand the relationship between the primary performance and static parameters, we used synthetic permeability distributions. Conventional simulated annealing, (discussed in Section 1.2) without near well bore permeability constraints, was used to generate 21 areal distributions of permeability. A log normal distribution was used having a mean log (k), $\mu_{\log(k)}$, of 2.0 (100 md) and a standard deviation, $\sigma_{\log(k)}$, of 0.40. For this $\mu_{\log(k)}$ and λ_D, 68% of the values lie between 1.6 (40 md) and 2.4 (250 md). The Dykstra-Parsons coefficient is 0.60. An omnidirectional spherical variogram model having a relative nugget of 20% and a range of 1,200 feet was used for all conditional simulations. The 5,280 feet × 5,280 feet system was discretized into a 60 × 60 grid mesh, each grid block having

88 feet side lengths. Well grid blocks were distributed on regularly spaced 80 acre patterns, resulting in a 13 well system (Fig. 1.12). A dimensionless correlation length, λ_D, of 0.643 is obtained when the variogram range (1,200 feet) is divided by the drainage area side length (1,867 feet). Well block permeabilities were considered as conditioning data and remained unchanged for all 21 conditional simulations.

Flow simulations were performed for each of the 21 permeability realizations. The only parameter varied between flow simulations was the permeability field. Reservoir porosity and thickness were assumed to be constant and equal to 25% and 30 feet, respectively. A uniform initial pressure of 1200 psi was used; bubble point pressure of the black oil was 1024 psi. The wells were operated at a 200 psi constant bottomhole pressure; well flow rates were dictated by the reservoir. A total of ten years of primary production was simulated. A finite-difference fluid flow simulator was used.[1.16] Flow simulation input parameters are summarized in Table 1.4.

Flow simulation results for all 21 cases are summarized in Fig. 1.13. Note the wide spread in rates and gas-oil ratios (GOR's). Initial rates vary from 1100 STB/D to 3100 STB/D. The large spread in producing rates at early times continues to grow throughout the ten year period. Although all 21 cases have equal pore volumes and permeability frequency distributions, cumulative recoveries at the end of 10 years vary significantly. The permeability fields, although having the same conditioning data and spatial correlation structure, have enough significant differences to result in a wide spread in well performance. It is obvious that additional conditional simulation constraints are required before realizations can be generated which are "equally probable" from a well/reservoir performance viewpoint. Considering that the majority of the performance differences develop at the very start of the simulation, it is reasonable to infer that variations in near well permeability may be the primary reason for the wide variations.

The impact of near well permeability on well performance is further illustrated in Fig. 1.14. Here, the initial producing rate (average rate for the first month) of the central producer for each of the 21 flow simulations is plotted as a function of the

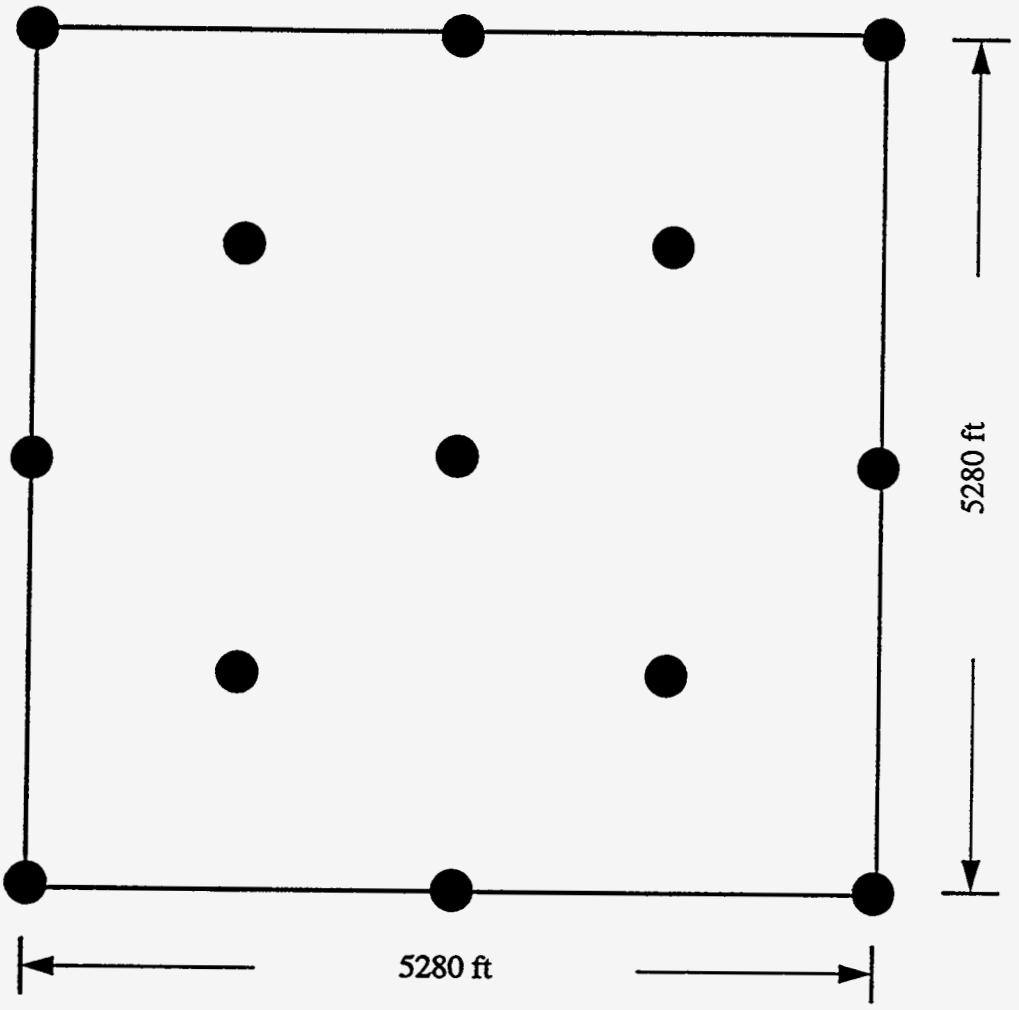

Figure 1.12: Schematic of 13 well, 80 acre well spacing reservoir system.

Type of Simulation	2D Primary
Well spacing	80 Ac
Initial pressure	1200 psi
Bottomhole producing pressure	200 psi
Bubble point pressure	1024 psi
Initial gas saturation	0%
Formation thickness	30 ft
Porosity	0.25, variable
Permeability	100 md, variable

Table 1.4: Primary production flow simulation data.

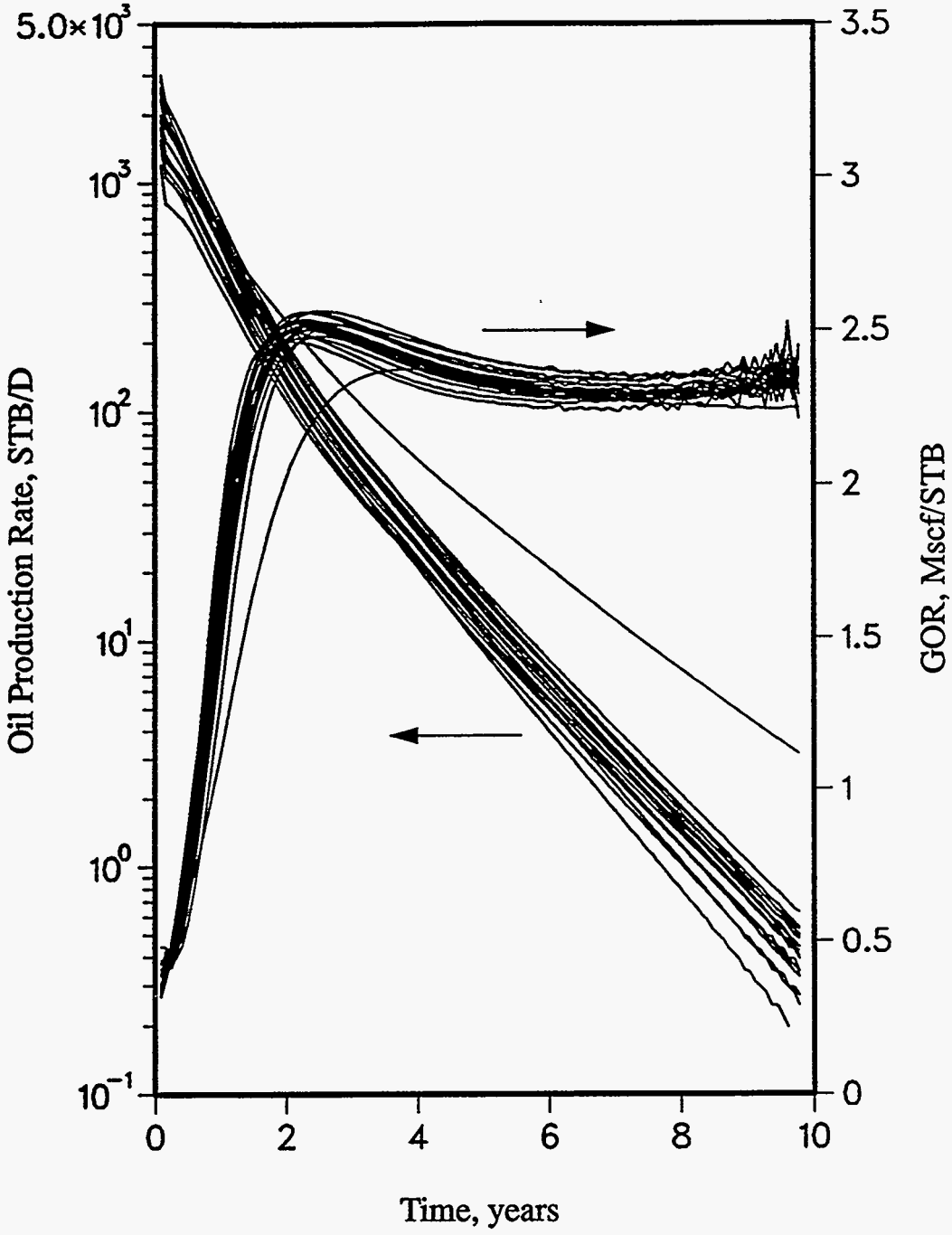

Figure 1.13: Primary performance of central producer for base case realizations; more heterogeneous permeability distribution.

effective near-well permeability, k_{NW}. The effective near-well permeability was computed using a geometric average of the well block and the adjacent eight grid blocks (3 × 3 region). As shown in Fig. 1.14, the correlation is excellent with the correlation coefficient being 0.98. Effective nearwell permeability was calculated for a variety of near-well areas ranging from 3 x 3 grid blocks (264 feet × 264 feet, or 1.6 acres) to 27 × 27 grid blocks (2,376 feet × 2,376 feet, or 130 acres). The correlation coefficient of initial producing rate vs. k_{NW} is plotted as a function of fractional drainage in Fig. 1.15, where the fractional drainage area is the area included in the computation normalized by the well drainage area (80 acres). The correlation coefficient exceeds 0.95 for fractional drainage areas less than 0.30. The above results are sufficient to conclude that k_{NW} has a strong impact on well performance and thus should be implemented as a constraining parameter.

Secondary Performance Constraints

The above analysis indicates that primary performance is closely related to near-well bore permeability distribution. In this section, we examine the impact of secondary recovery (water flooding) performance on relevant static parameters. The following case studies assume sufficient secondary performance data is available to make accurate estimates of the secondary performance constraints. We would like to define the constraints such that they incorporate the connectivity between the injector and the producer.

Waterflood Constraints

As shown before, primary performance is rather insensitive to areal reservoir heterogeneities, the exception being the near-well region (and faults/fractures). There are several differences between primary and secondary recovery regarding well-to-well interactions. Primary individual well recoveries cannot be improved by placement of offset primary wells - only reduced as a result of interference (this does not imply that primary field recovery is not improved by infill drilling). Fluid recovery is strictly dependent on the rock properties existing between the location of the fluid and each offset well (i.e., well "fluid pulling" characteristics). These characteristics of primary recovery do not apply to secondary recovery operations.

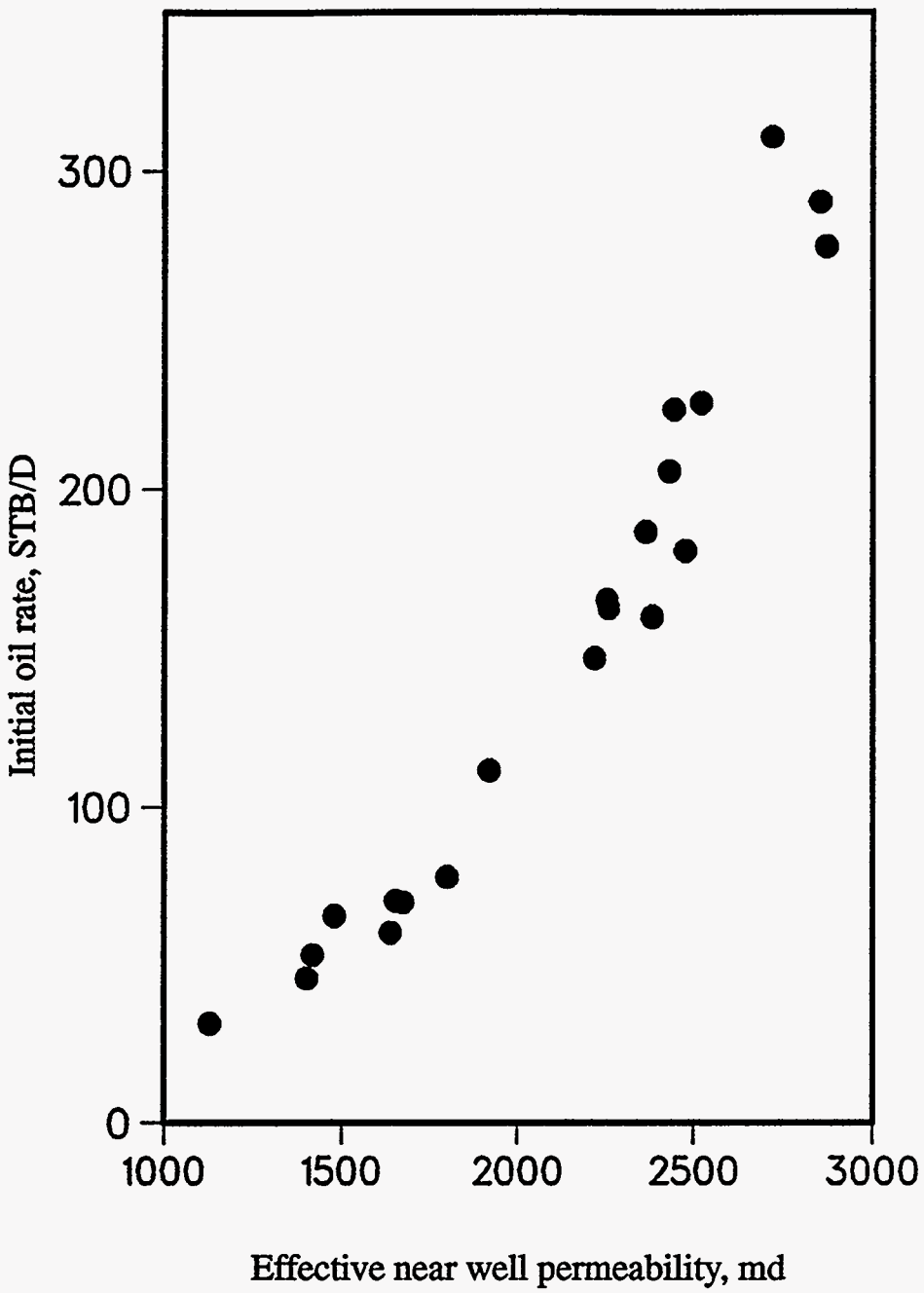

Figure 1.14: Correlation of initial oil production rate to effective near well permeability.

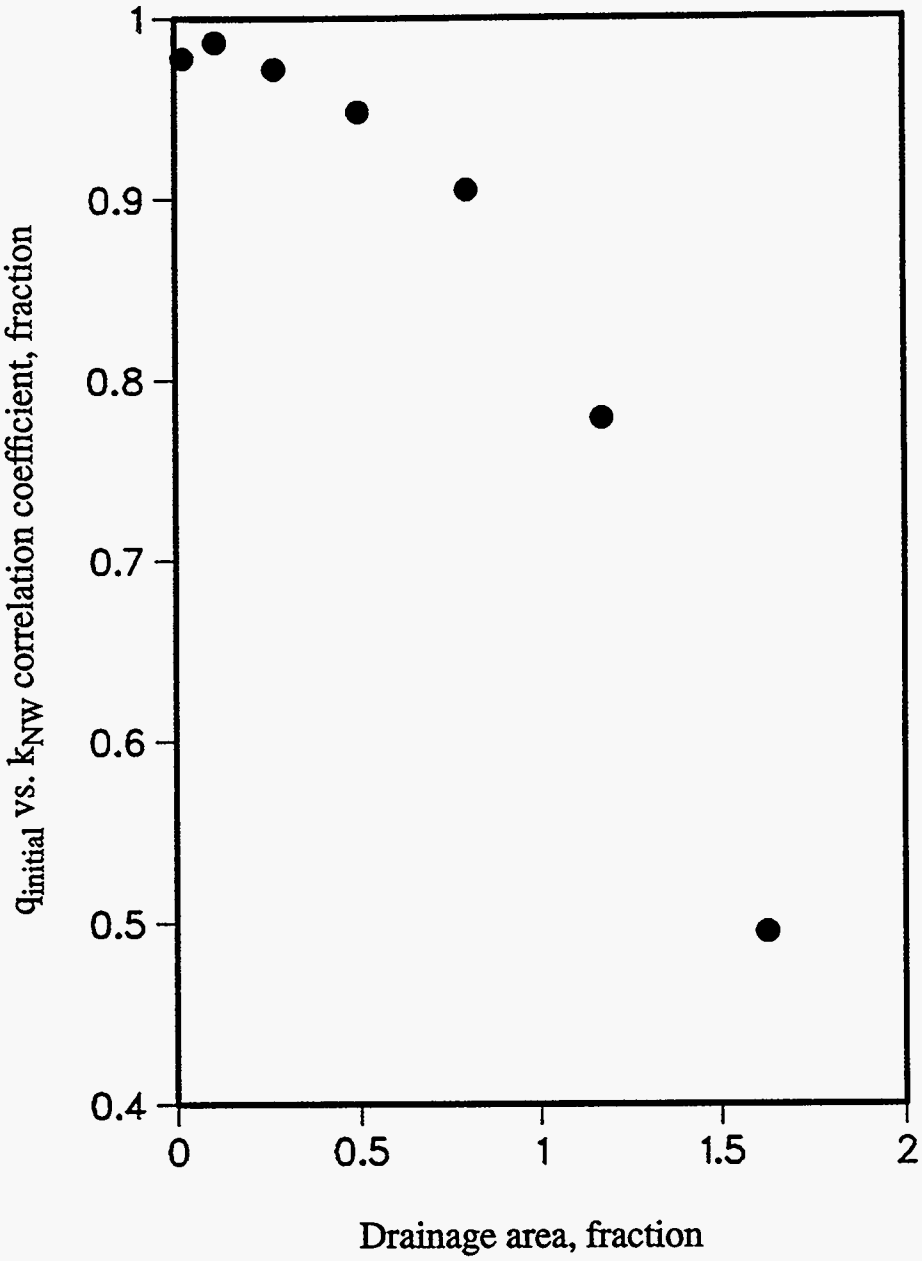

Figure 1.15: Correlation coefficient of initial oil production rate vs. near well effective permeability as a function of fractional drainage area.

Interwell reservoir characteristics become much more important. Secondary recovery efficiency is strongly influenced by local reservoir connectivity between each injector/producer pair (i.e., well "fluid pulling and pushing" characteristics).

The importance of interwell reservoir connectivity on secondary performance is the primary consideration in defining static parameters. Reservoir connectivity measures will be defined based on the spatial arrangement of permeability. This approach is used since permeability typically has a stronger influence on flow characteristics than any other variable. The techniques developed in this study quantify reservoir connectivity relative to specific well locations. Although existing definitions of connectivity may be used to improve predictions of overall field rates and recoveries, local measures of connectivity are required to better predict interactions between specific wells.

Fractional Connectivity Function

For the first method, connectivity is defined by a functional relationship between fractional area connected and permeability percentile cutoffs. Both connectivity of high permeabilities and low permeabilities are considered. A description of the procedure used to define the connectivity function for a given permeability field follows. Grid block permeability values are transformed to binary indicators (i.e., 0's and 1's) depending on whether they are equal to or greater than the cutoff values (1's) or less than the cutoff values (0's). For the connectivity of high values, two adjacent grid blocks are considered as being "connected" if their permeability indicators are both 1's. Conversely, adjacent blocks having 0's as permeability indicators are defined as being "connected" for the connectivity of low values. For both cases, a "connected path" is defined as a series of connected blocks which extend from an injector to an offset producer (or vice versa). The "fractional area connected" is obtained by dividing the number of connected grid blocks by the total number of grid blocks. Only horizontal and vertical directions (not diagonal) are considered for connectivity computations in this study. The relationship between permeability percentile cutoff and fractional area connected for both high permeabilities, C_H, and low permeabilities, C_L, is considered to completely define the connectivity characteristics of the injector/producer pair.

An example is presented to illustrate this concept. Fig. 1.16 is a greyscale image of permeability for one-quarter of a five-spot pattern generated using conventional simulated annealing. The 1st through 6th permeability deciles of this image are 61 md, 142 md, 165 md, 215 md, 374 md and 445 md, respectively. Fig. 1.17 displays the indicator greyscale maps corresponding to the six percentile cutoffs. The grid blocks with permeabilities exceeding each respective cutoff are shaded black. Assuming the injection well is located in the lower left corner and the producer is in the upper right corner, the connectivity of high values is determined by computing the fraction of blocks which have an indicator value of 1 and are part of a connected path (defined above) extending between the injector and the producer. The upper limit of connectivity is equal to the fraction of blocks having an indicator of 1 while the lower limit is 0. The existence of isolated or unconnected grid blocks of value 1 will result in the percentage of connected blocks being less than the cutoff percentile. Fig. 1.18 shows the connected (shaded black), isolated (shaded gray) and dead end (unshaded) grid blocks for these six percentiles. The fractional connectivity function shown in Fig. 1.19 is obtained by evaluating the connectivity of highs and lows at each percentile. The permeability percentile at which connectivity is first reduced to zero is defined as the permeability percentile threshold, p_t. In Fig. 1.19, the thresholds for the connectivity of high values, p_{tH}, and low values, p_{tL}, are the 54th percentile (400 md) and the 76th percentile (621 md), respectively. Note that whereas most of the previously published definitions of connectivity refer to global reservoir connectivity characteristics, the fractional connectivity function defined above is dependent on the locations of the injector and producer. A different connectivity function would be obtained if the wells were located elsewhere.

The determination of the connectivity function can be computationally intensive and cannot be easily updated. Fortunately, it was found that the characteristic of the connectivity function which most strongly influences waterflood performance for the cases considered is p_{tH}. This value represents the largest minimum permeability value of all paths which connect the injector to the producer. Other paths may contain more higher permeability values, but in each case contain at least one permeability which falls below the permeability represented by p_{tH}. The determination of p_{tH} is much easier than computing the entire connectivity function;

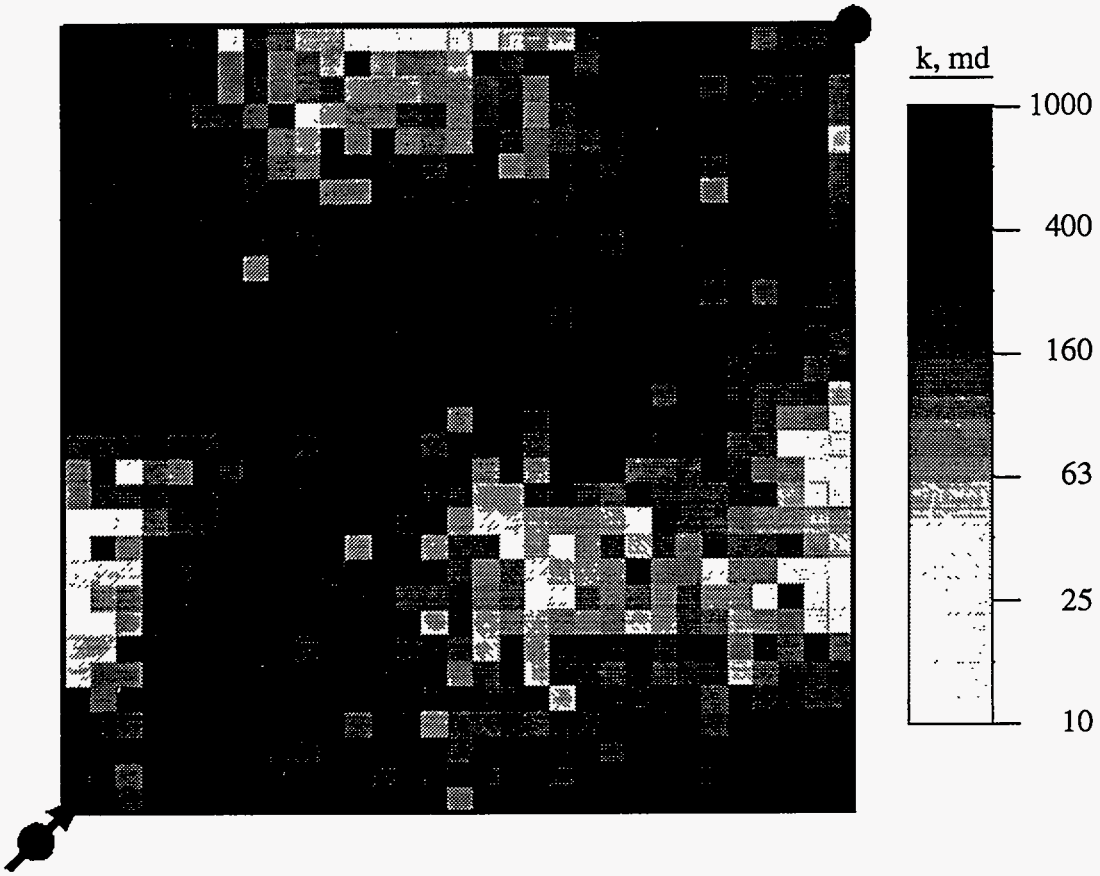

Figure 1.16: Example permeability field for one-quarter of a five-spot pattern.

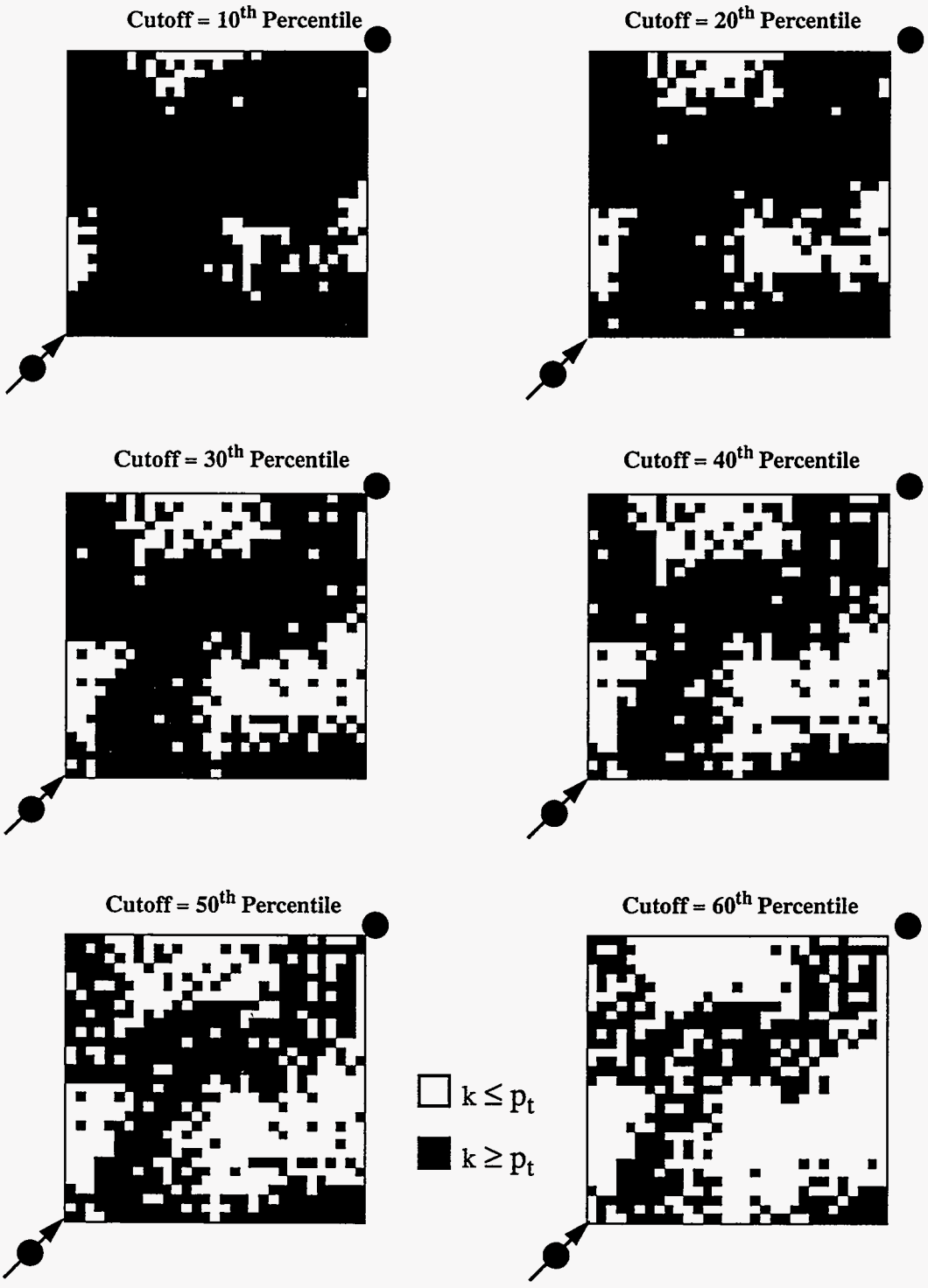

Figure 1.17: Connectivity indicators at various permeability percentile cutoffs.

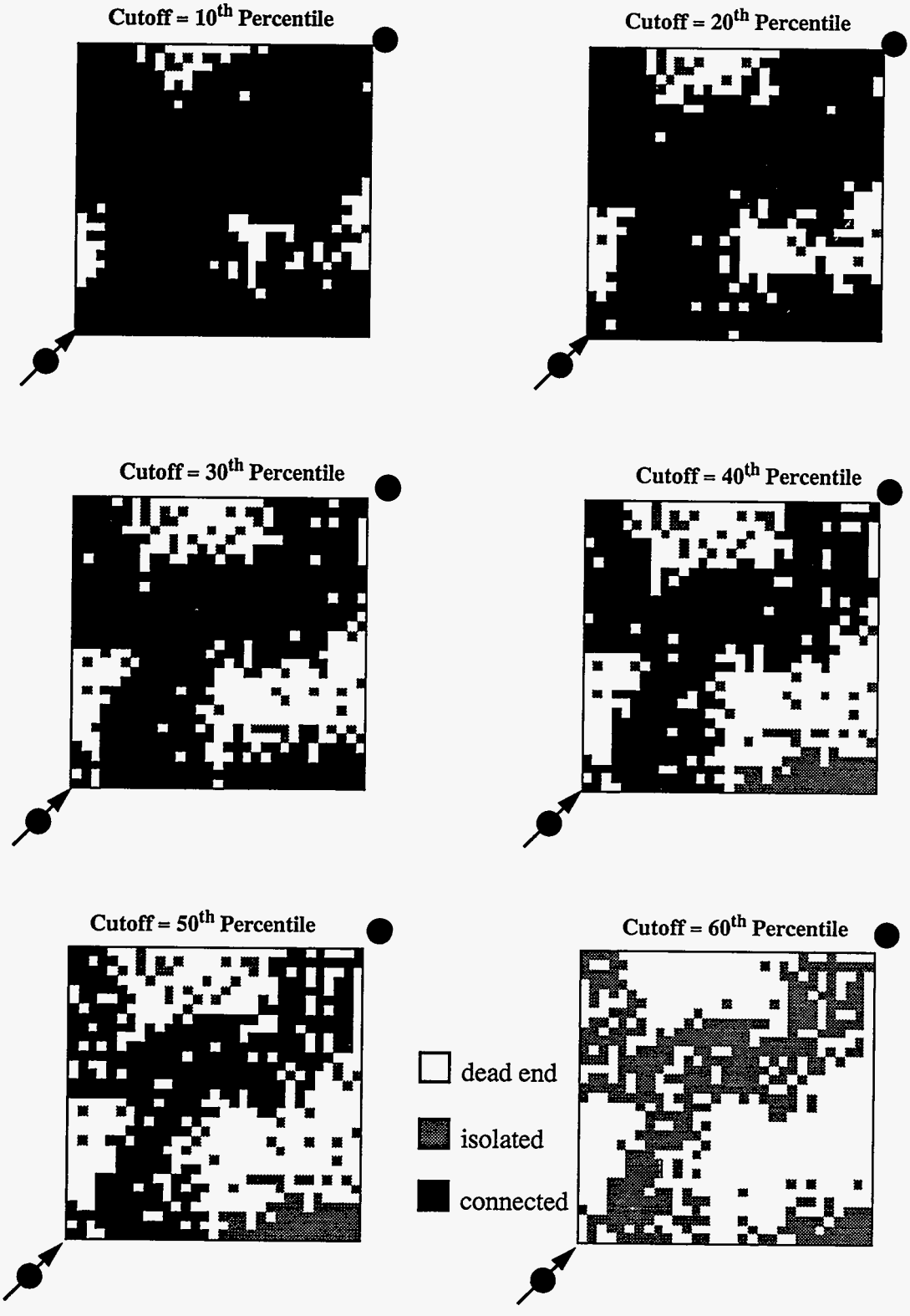

Figure 1.18: Identification of connected, isolated and dead end grid blocks.

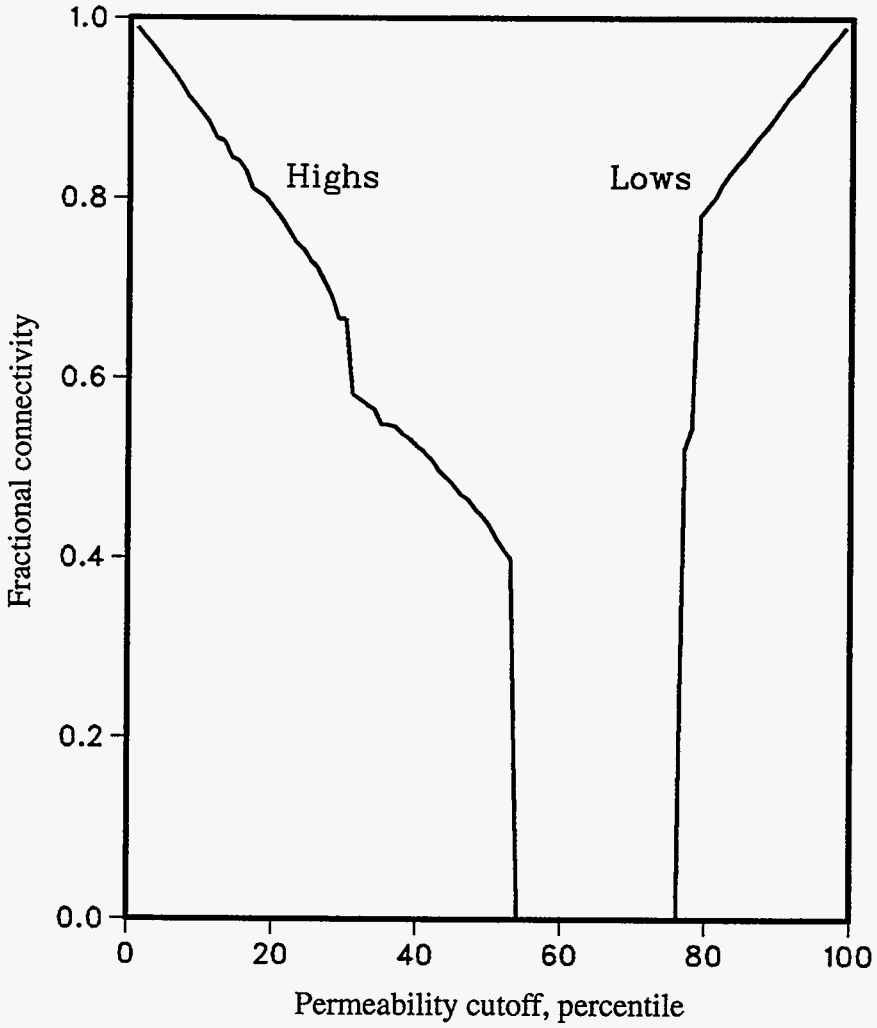

Figure 1.19: Fractional connectivity function for simulated annealing example.

only one path rather than all possible paths needs to be identified. Systematically searching for a connected path was found to be more efficient than using a random walk approach. Beginning at one of the wells, the perimeter of the connected area between a injector/producer pair is traced. Connectivity exists if the second well is visited prior to revisiting the first well. If connectivity doesn't exist, p_{IH} has been exceeded, thus the actual threshold is a smaller value.

Flow Pattern Permeability Coefficient

The second connectivity parameter investigated incorporates curvilinear fluid flow geometry. Idealized unit mobility streamlines for a homogeneous five-spot pattern were used to determine the effective permeability of the flow pattern segments (i.e., streamtubes). This second parameter, referred to as CV_{k*}, represents the coefficient of variation (standard deviation divided by the mean) of a distance-normalized flow pattern segment permeability, $k*$:

$$CV_{k*} = \frac{\sigma_{k*}}{\mu_{k*}} \tag{1.51}$$

where $k*$ is defined for the n^{th} flow pattern segment as

$$k* = \frac{k(n)}{l_D^2(n)} \tag{1.52}$$

and

$$\sigma_{k*} = \sqrt{\frac{1}{N_s}\sum_{n=1}^{N_s}(k*_n - \mu_{k*})^2} \tag{1.53}$$

$$\mu_{k*} = \frac{1}{N_s}\sum_{n=1}^{N_s}\frac{k(n)}{l_D^2(n)} \tag{1.54}$$

$$l_D(n) = \frac{l(n)}{l_o} \tag{1.55}$$

The variables $k(n)$ and $l(n)$ represent the effective permeability and average length, respectively, of the n^{th} flow pattern segment. Note that a value for the permeability parameter $k*$ is obtained for each flow pattern segment. The mean and standard

deviation of $k*$ are then used to compute CV_{k*}. The effective permeability $k(n)$ is calculated from the grid block permeabilities located within the n^{th} flow pattern segment. The line bisecting the n^{th} flow pattern segment is used to estimate $l(n)$. The total number of segments used for each one-quarter of a five-spot pattern was 8 ($N_s = 8$). As indicated by Eq. 1.55, flow pattern segment lengths are normalized by the interwell diagonal length, l_o. High permeability streaks existing directly between the injector and the producer influence waterflood response more so than indirect high permeability paths. This effect was accounted for by normalizing the flow pattern segment permeabilities by the square of the dimensionless flow pattern length, $l_D(n)$. This measure of connectivity has an advantage over the fractional connectivity function in that the intensity of high and/or low permeability streaks can be accounted for. Flow pattern segment permeabilities were estimated using a geometric average of the grid block permeabilities. The geometric average was selected because it can be updated easily and it gives acceptable results. Similarly, a more rigorous method of computing flow pattern segment geometry could have been used instead of assuming idealized ones. This would have required costly recomputations during the annealing process. Considering the high quality of the results obtained using idealized flow pattern segments, it was decided not to pursue the rigorous approach.

Thus, the process for determining CV_{k*} for each injector/producer one-quarter five-spot pattern is as follows. Idealized unit mobility streamlines are determined given the injector/producer locations. Grid block permeability values are assigned to all flow pattern segments for which the grid blocks are members. The effective permeability parameter $k*$ is then computed (using Eq. 1.52) for each of the n flow pattern segments comprising the injector/producer one-quarter five-spot pattern. The value of CV_{k*} can then be determined from the standard deviation (using Eq. 1.53) and mean (using Eq. 1.54) of $k*$. This process is repeated until a value of CV_{k*} is obtained for each injector/producer one-quarter five-spot pattern.

Procedure

Based on previous results, it was decided to investigate only the effect of areal permeability heterogeneities on secondary well performance; reservoir porosity and thickness are assumed to be constant. Permeability is assumed to be a stationary random function with a known log-normal frequency distribution and spatial

correlation structure. Two permeability frequency distributions were investigated. The first is the same as was used in the primary performance work, i.e., $\mu_{\log(k)}$ and $\sigma_{\log(k)}$ are 2.0 (100 md) and 0.40, respectively. The second permeability frequency distribution is characterized by $\mu_{\log(k)}$ and $\sigma_{\log(k)}$ values of 2.5 (250 md) and 0.2, respectively. As previously mentioned, 68% of the permeabilities lie between 40 md and 250 md for the first distribution. For the second, less heterogeneous distribution, 68% of the values lie between 200 md and 500 md. These two distributions will be referred to as the less heterogeneous permeability distribution ($\sigma_{\log(k)} = 0.2$) and the more heterogeneous permeability distribution ($\sigma_{\log(k)} = 0.4$) throughout the remainder of this section. The variogram model used was an omnidirectional spherical model having a relative nugget of 20% and a correlation length of 1000 ft. This represents a λ_D of 0.536 for 80-acre well spacing. All permeability fields were generated using simulated annealing.

Waterflood response for one-quarter, full and extended five-spot patterns were simulated using the black-oil option of a finite-difference fluid flow simulator.[1.16] In each case, 80-acre well spacing and 160-acre five-spot patterns were used. Grid block dimensions were 40 ft for the one-quarter and full five-spot patterns cases and 88 ft for the extended five-spot simulations. Initial conditions of all flow simulations assumed depleted primary conditions with a uniform initial reservoir pressure of 300 psi and a uniform initial gas saturation of 20%. Injection wells and producers were pressure-constrained at 2000 psi and 200 psi, respectively. A slightly favorable mobility ratio of 0.96 was used. Pertinent flow simulation data are summarized in Table 1.4.

To understand the effectiveness of the various constraints we compared simulated waterflood performance of 20 flow simulations to "truth" case results. The truth case permeability field and corresponding simulated reservoir performance were considered to be the actual permeability distribution and performance of the reservoir. The permeability field was the only input variable changed for each flow simulation. The same well block permeabilities were assumed to be conditioning data for all cases. The waterflood performance of 20 flow simulations obtained using conventional simulated annealing constraints was assumed to represent the base case, i.e., they represent typical results using a conventional approach. Five-

spot segment synthetic case studies were performed using both of the permeability frequency distributions described previously.

One-Quarter Five-Spot Pattern

Producer and injector grid block permeabilities were assumed to be 250 md and 125 md, respectively, for the more heterogeneous permeability distribution. For the second, less heterogeneous permeability frequency distribution, respective producer and injector grid block values were 250 md and 355 md. Base case and truth case results for both permeability frequency distributions will be presented.

Base Case Results

A total of 21 permeability realizations were generated using the conventional simulated annealing algorithm (described in Section 1.2) and the variogram model described previously. A greyscale map of the realization selected as the first "truth" case is depicted in Fig. 1.20. The permeability fields were used to simulate waterflood performance over a 20-year period. Waterflood performance for the 21 flow simulations, based on water injection rates, oil producing rates, water producing rates and WOR's is presented in Fig. 1.21. Performance is seen to vary significantly between flow simulations. For example, initial water injection rates vary from 410 to 1200 STB/D, water breakthrough times range from 2.0 years to 5.1 years and peak oil responses vary from 170 to 600 STB/D. At the end of the 20-year simulation period, WOR's range from 19 to 50 STB/STB. It is obvious that additional constraints are required before these reservoir descriptions can be considered as being "equally probable." Note that the performance of the first truth case has been highlighted (using x's). Its permeability spatial characteristics and waterflood performance will be used to test the effectiveness of connectivity and near-well effective permeability constraints.

This particular permeability realization was selected to represent the first truth case because it has an anomalous WOR trend. A large increase in WOR occurs approximately two years after water breakthrough. Also, the near-well effective permeability surrounding the injector (approximately 400 md) is significantly greater than that surrounding the producer (approximately 200 md). However, as previously stated, the injection well grid block permeability (125 md) is less than

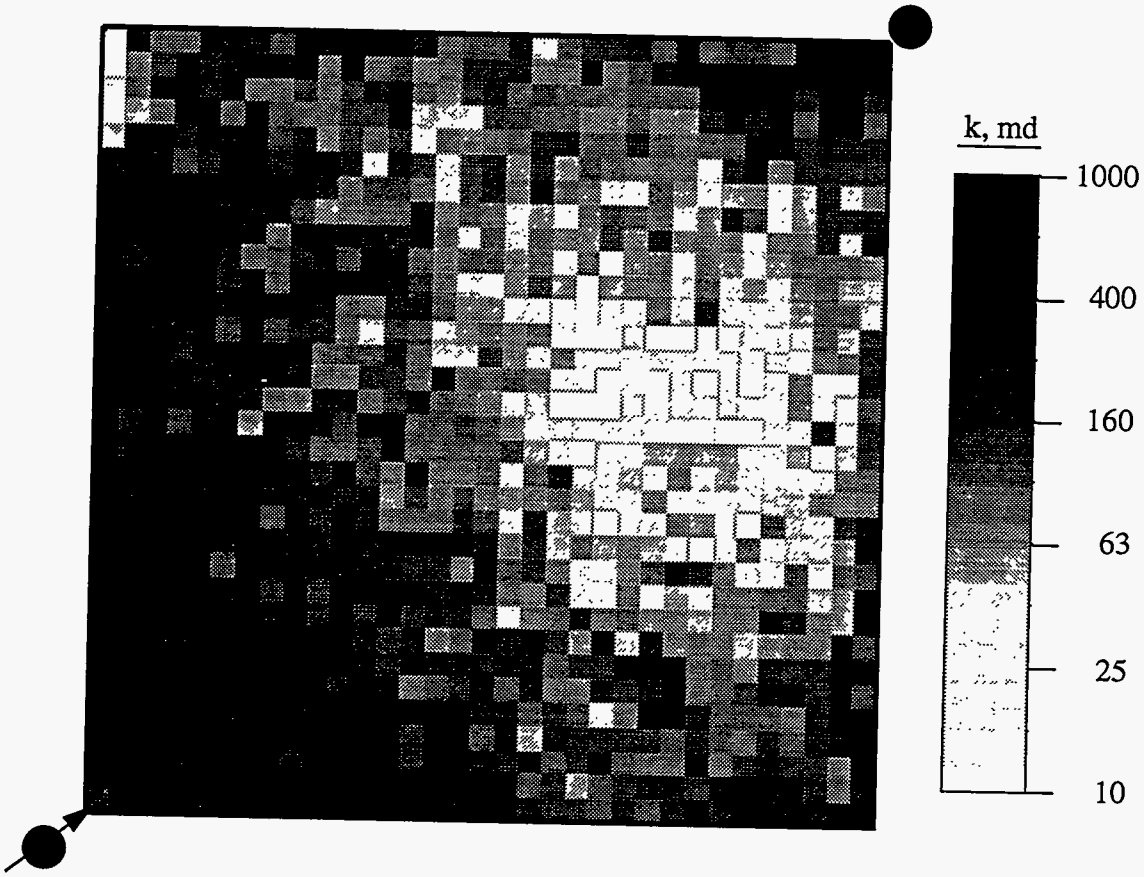

Figure 1.20: Permeability field for the first one-quarter five-spot pattern truth case.

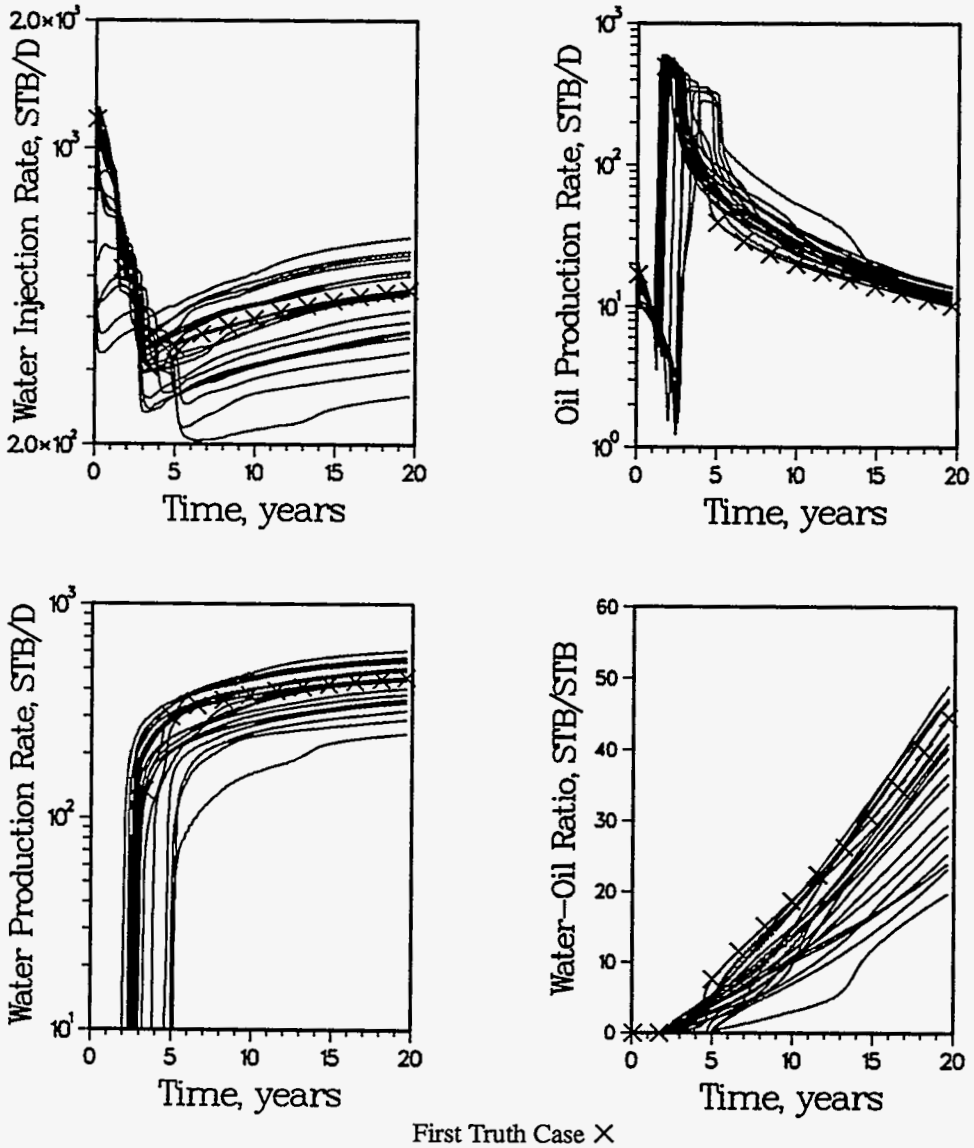

Figure 1.21: Simulated waterflood performance of the first truth case and the 20 first base flow simulations; one-quarter five-spot pattern system.

the producer grid block value (250 md). This anomaly is apparent in the performance data, with the initial injection rate for the first truth case being greater than any other run. Perhaps even more of an anomaly is the existence of a low permeability region just offset to the high permeability near-well region surrounding the injector.

Base case permeability realizations and corresponding waterflood performance were also generated using the second, less heterogeneous permeability distribution. The permeability realization selected to be the second truth case is shown in Fig. 1.22. Note that the permeability surrounding the injection well (approximately 600 md) is greater than the permeability surrounding the producer (approximately 350 md). This is consistent with the well block permeability relationships. Fig. 1.23 depicts the flow rates and WOR trends based on flow simulations using the second truth case and the other 20 permeability realizations. The variations in waterflood performance are less than that observed for the first base case because of the smaller degree of heterogeneity, but are still much greater than the desirable range. Note that the initial injectivity of the second truth case is greater than any other base case run.

It is obvious that conventional constraints are not enough to capture the performance of the "truth" case. Additional constraints are needed to capture the dynamic performance. In Section 1.3.2, we discuss the effectiveness of p_{tH}, CV_{k*} and k_{NW} in capturing the dynamic performance of the reservoir.

To summarize, conventional static constriants such as variogram and univariate statistics may not be enough to capture the production data adequately. Additional static parameters such as p_{tH}, CV_{k*} and k_{NW} are defined which may be more effective in capturing produciton data.

1.2 Simulated Annealing

In this section, we present the method used for generating reservoir description. The desirable characteristics of any method are: the ability to generate alternate descriptions to quatify uncertainty, computational efficiency, and flexibility to

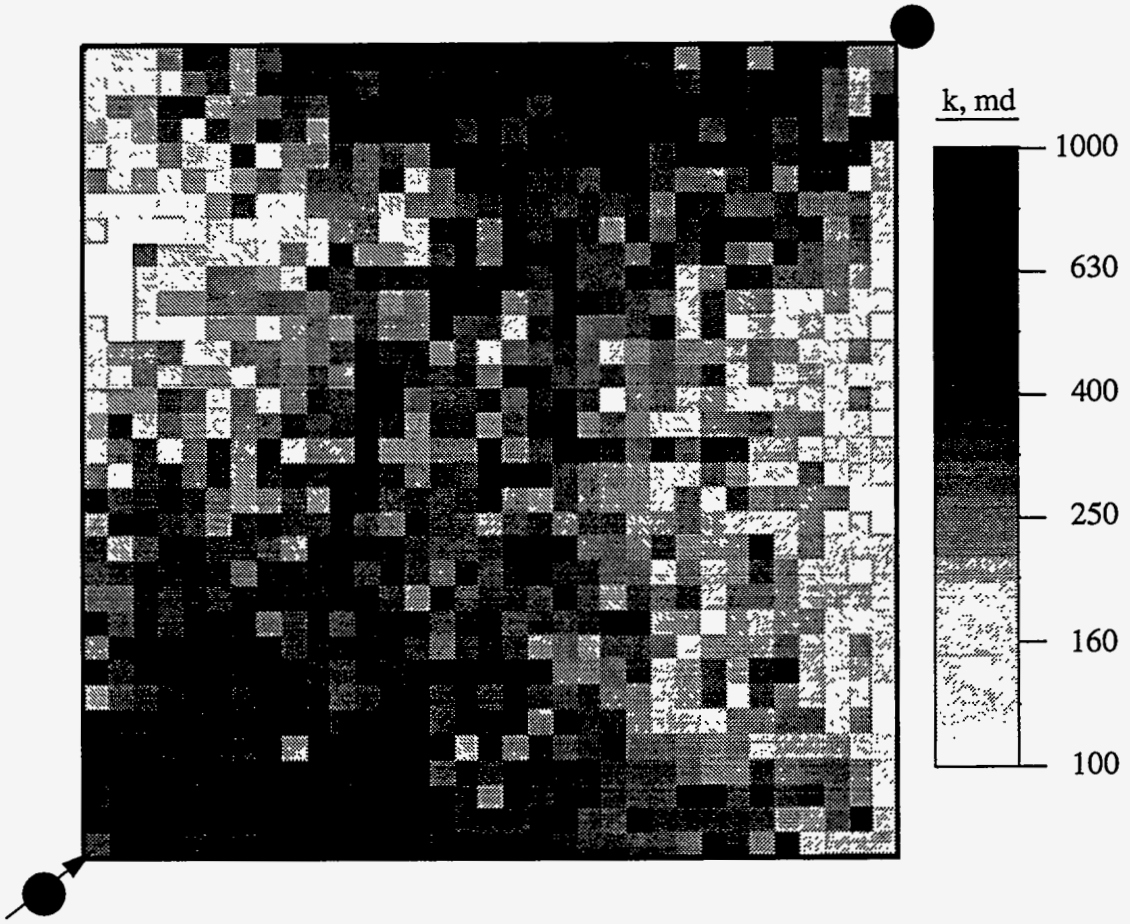

Figure 1.22: Permeability field for the second one-quarter five-spot pattern truth case.

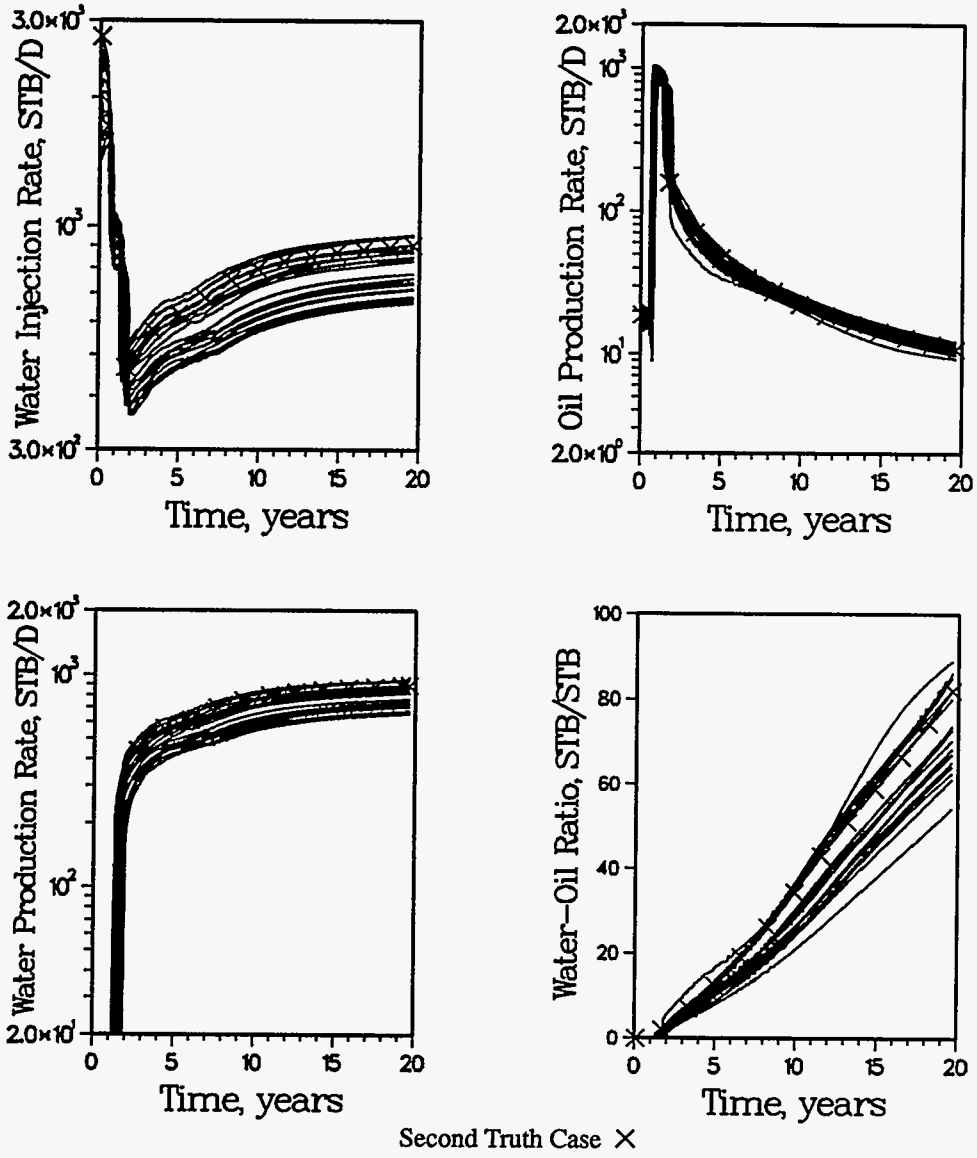

Figure 1.23: Simulated waterflood performance of the second truth case and the 20 second base case flow simulations; one-quarter five-spot pattern system.

incorporate multiple constraints. We have selected the method of simulated annealing which is a conditional simulation method.

Stochastic conditional simulation methods are used to generate possible descriptions of reservoir properties. The methods are stochastic since reservoir properties are represented by random variables; they are conditional since available data are honored at sampled locations; and the methods simulate several equiprobable distributions of a property in the reservoir. There are several conditional simulation techniques available in the literature. The methods range from Sequential Indicator Simulation (SIS),[1.17] Sequential Gaussian Simulation (SGS),[1.18] Fractal techniques,[1.19] Turning Bands Method (TBM),[1.10, 1.11] and combinatorial optimization algorithms.[1.1, 1.2, 1.20-1.25]

In recent years, combinatorial optimization techniques for the purpose of reservoir description have become extremely popular as evidenced by the large number of studies performed and papers presented on this subject. Although these techniques are computationally demanding, the methods show promise in their robustness and flexibility to allow the incorporation of multiple constraints that can be imposed on a reservoir description when data is obtained from many sources. The methods are listed below with appropriate references for petroleum engineering applications:

- Genetic Algorithms[1.21, 1.22]
- Simulated Annealing[1.1, 1.2, 1.20, 1.21-1.25]
- Maximum A Posteriori (MAP)[1.26]
- Stochastic Hill Climbing[1.20]
- Neural Networks (applications are restricted to pattern recognition in well testing and log interpretations)

Huang[1.21] and Sen et al.[1.22] studied and compared some of the combinatorial optimization methods for the purpose of reservoir description. This study will focus on the method of simulated annealing.

Simulated annealing is an algorithmic approach to solving optimization problems and has its origins in the area of statistical mechanics.[1.27] As the name implies, simulated annealing simulates the physical process of annealing, i.e., a metal is cooled from a state of high temperature or energy to a lower temperature. The

application of method for reservoir description was first proposed by Farmer.[1.23] The method was extended by others[1.1, 1.2, 1.20, 1.24, 1.25] to develop reservoir descriptions that honor static information (log and core data) and/or dynamic information (production and well test data).

In this section we present a general outline of the simulated annealing algorithm to solve the inverse problem of describing reservoir properties constrained to static and/or dynamic information. We first describe the calculation of important components of the simulated annealing algorithm. Then the actual simulation process is described.

1.2.1 Generation of the Simulation Grid

A simulation grid with N_x grid blocks in the x-direction, N_y grid blocks in the y-direction and N_z grid blocks in the z-direction is defined. The size of each grid block is $\Delta x \times \Delta y \times \Delta z$. The coordinates of the center of the grid block (x_i, y_j, z_k) are

$$x_i = O_x + i\Delta x, \quad \text{for } i = 1,2,\ldots N_x \tag{1.56}$$

$$y_j = O_y + j\Delta y, \quad \text{for } j = 1,2,\ldots N_y, \tag{1.57}$$

and

$$z_k = O_z + k\Delta z, \quad \text{for } k = 1,2,\ldots N_z, \tag{1.58}$$

where, (O_x, O_y, O_z) are the coordinates of the origin of the simulation grid.

In the simulated annealing algorithm, the grid block location vector, $\vec{s} = (x_i, y_j, z_k)$, is referenced by a single index, l, which defines the grid-block location index (i, j, k) in the algorithm:

$$\begin{aligned} k &= 1 + \text{INT}\left[\frac{l-1}{N_x N_y}\right] \\ j &= 1 + \text{INT}\left[\frac{l-(k-1)N_x N_y - 1}{N_x}\right] \end{aligned} \tag{1.59}$$

and

$$i = l - (k-1)N_x N_y - (j-1)N_x$$

where, $l = 1,2...N_s$ and N_s is the total number of simulation points, i.e., $N_x \times N_y \times N_y$. INT truncates the number in brackets to an integer value.

The simulation variable is defined at the location vector, $\vec{s}$, as $V_{\vec{s}}$. The value of each grid block permeability is assigned by sampling the cumulative distribution function (cdf). The discrete cdf can be represented as C_j classes, for $j = 1,...,N_f$ class intervals. By sequentially visiting each grid block in the domain, the simulation variable value at each grid block is assigned:

$$V_{\vec{s}} = C_{iR} - \left(C_{iR} - C_{iR-1}\right)\left[\frac{iR}{N_f} - R\right]N_f \tag{1.60}$$

where

$$iR = \mathrm{INT}\left(R \times N_f\right) + 1 \tag{1.61}$$

and R is a random number sampled from a uniform distribution between [0,1]. The above equations form the constraint for the cdf.

The conditioning data constraint is specified by assigning the simulation variable at specified locations, i.e.,

$$V_{\vec{s},c} = V(c)_{\vec{s}} \tag{1.62}$$

where $V(c)_{\vec{s}}$ is the sampled variable at the conditioning point location. The values of the conditioning points remain fixed throughout the simulation.

This procedure yields an initial uncorrelated distribution that honors the cdf and the conditioning data.

1.2.2 Sample Variogram

The sample variogram of the distribution is calculated by:

$$\gamma_s\left(\vec{h}_{l,i}\right) = \frac{1}{2N_p\left(\vec{h}_{l,i}\right)} \sum_{j=1}^{N_p\left(\vec{h}_{l,i}\right)} \left[V\left(\vec{s}_j + \vec{h}_{l,i}\right) - V\left(\vec{s}_j\right)\right]^2 \tag{1.63}$$

where $\vec{h}_{l,i}$ is the lag distance vector (or separation distance between points), $N_p(\vec{h}_{l,i})$ is the number of pairs within the simulation grid corresponding to the lag $\vec{h}_{l,i}$, $\vec{s}_j$ is the location vector of the grid block. The index i refers to the direction and the index l refers to the lag distance considered for a given direction. Spatial relations can be defined in the three principle directions and anisotropy is considered such that three-dimensional anisotropic realizations are generated.

A variogram model, γ_o, is defined by fitting one of the conventional models (e.g., spherical, exponential, Gaussian, etc.) to the available data.

1.2.3 Objective Function

Simulated annealing is an optimization algorithm. The basic goal of the simulated annealing algorithm is to describe a configuration of variables such that a global minimum of the objective or energy function is obtained.

The objective function defines the difference between a function of sample data and a desired model that the sample data must fit. The objective function can have several components depending on the constraints imposed in describing the reservoir properties. For example, a component can be the difference between the sample and model variograms or the difference between the permeability derived from pressure transient data and some averaging process of permeabilities. When multiple constraints are imposed on the reservoir description the objective function is divided into principle components that describe each imposed constraint. In our study, the objective functions or energies for the following constraints are defined: (i) the energy of the variogram component and/or (ii) the energy of the constraint imposed by the production information.

Energy Function - Variogram Constraint

The variogram energy function, E_1^k, is calculated as the square root of the sum in N_d directions and for N_h lags of the normalized difference between the model variogram and sample variogram at the k^{th} iteration step of the algorithm:

$$E_1^k = \sqrt{\sum_{i=1}^{N_d}\sum_{l=1}^{N_M}\left[\frac{\gamma_s^k(\vec{h}_{l,i}) - \gamma_o(\vec{h}_{l,i})}{\gamma_o(\vec{h}_{l,i})}\right]^2} \qquad (1.64)$$

$\gamma_s^k\left(\vec{h}_{l,i}\right)$ is the variogram of the permeability distribution at the iteration level k calculated by Eq. 1.62. $\gamma_o\left(\vec{h}_{l,i}\right)$ is the model variogram that the sample variogram must ultimately match.

A normalizing constant of the variogram energy function, E_{01} is also defined. It is the normalizing constant of the variogram constraint and is determined in the initial part of the algorithm. It is determined by calculating the energy of the variogram at initial conditions:

$$E_{01}=\sqrt{\sum_{i=1}^{N_d}\sum_{l=1}^{N_{hi}}\left[\frac{\gamma_s^o\left(\vec{h}_{l,i}\right)-\gamma_o\left(\vec{h}_{l,i}\right)}{\gamma_o\left(\vec{h}_{l,i}\right)}\right]^2} \tag{1.65}$$

$\gamma_s^o\left(\vec{h}_{l,i}\right)$ is the variogram of the simulation variable for the initial uncorrelated distribution.

Energy Function - Production Information

The second energy function component E_2 describes the well test constraint or the production performance constraint. The components, E_2, the normalizing constants, E_{02}, for the respective components are described in the following section.

Energy Function - Well Test Constraint (Oliver's Method)

In Section 1.1.1 we concluded that for Oliver's solution the equivalent permeability, $\bar{k}_e$, (Eq. 1.38) is approximately equal to the instantaneous well test permeability, $\hat{k}$ (Eq. 1.18). Based on this observation, if we simulate the annealing procedure until $\bar{k}_e \approx \hat{k}$ for each t_D, we should be able to reproduce the pressure response of the reservoir. For our sets of pressure derivative data, we compute N_t associated regions of investigation. Each region is defined in the limits of $r_{D\min}=0.12\sqrt{t_D}$ and $r_{D\max}=2.34\sqrt{t_D}$. Note that since $r_{D\min}$ for the current pressure derivative data point may be less than $r_{D\max}$ for the previous pressure derivative data point, i.e., $r_{D\min i} < r_{D\max i-1}$ for $i=1,2...N_t$, there may be some overlap between the different radii of investigation.

The energy function of the well test constraint imposed by Oliver's method is calculated by:

$$E_2^k = \sqrt{\sum_{i=1}^{N_t} \left[\frac{\left[\bar{k}_e^k - \hat{k}_i \right]}{\hat{k}_i} \right]^2} \tag{1.66}$$

where $\bar{k}_e^k$ is the equivalent permeability determined by Eq. 1.38 at the k^{th} iteration level of the simulation. $\hat{k}$ is the instantaneous permeability derived from the instantaneous pressure derivative.

The initial energy function for Oliver's method incorporating the well test component, E_{02}, is defined as:

$$E_{02} = \sqrt{\sum_{i=1}^{N_t} \left[\frac{\left[\bar{k}_{e,i}^o - \hat{k}_i \right]}{\hat{k}_i} \right]^2} \tag{1.67}$$

where $\bar{k}_e^o$ is the equivalent permeability for the initial uncorrelated distribution calculated by Eq. 1.38.

Energy Function -Well Test Constraint (ISA)

In Section 1.1.1 we observed that the *ISA* equivalent permeability, k_{ISA}, (Eq. 1.21 through Eq. 1.30) is best approximated by either the area-based geometric (Eq. 1.37) or harmonic average (Eq. 1.36) of grid block permeabilities between the annulus of investigation. The component of the energy function incorporating the equivalent *ISA* radial permeability distribution is given by:

$$E_2^k = \sqrt{\sum_{j=1}^{N_r} \left[\frac{\left[\bar{k}_j^k - k_{ISAj} \right]}{k_{ISAj}} \right]^2} \tag{1.68}$$

where $\bar{k}_j^k$ is either the area-based geometric (Eq. 1.37) or harmonic (Eq. 1.36) average of grid block permeabilities within the pre-defined annular regions at the k^{th} iteration level of the simulation and k_{ISA} is the equivalent *ISA* radial permeability distribution given by Eq. 1.21 through Eq. 1.30.

The normalizing coefficient of the energy function incorporating *ISA* is given by:

$$E_{02} = \sqrt{\sum_{j=1}^{N_r} \left[\frac{\bar{k}_j^o - k_{ISAj}}{k_{ISAj}} \right]^2} \tag{1.69}$$

where $\bar{k}_j^o$ is either the area-based geometric or harmonic average of grid block permeabilities for the initial uncorrelated distribution.

Energy Function -Production Performance Constriants

In addition to using conventional spatial statistics, we observed that near well bore permeability is very important in honoring primary production data.

We assume that the geometric mean of near-well bore values represents the effective permeability. Although more sophisticated approaches give better results for anisotropic, spatially-correlated permeable mediums, such approaches cannot be updated - a highly desirable characteristic for simulated annealing applications.

The geometric averaged effective permeability, k_e, is defined as:

$$k_e = \left[\prod_{i=1}^{N_b} k_i \right]^{\frac{1}{N_b}} \tag{1.70}$$

where k_i is the fine-scale permeability of the N_b locations comprising the large-scale region. Frequently, stochastic modeling of permeability is performed based on the spatial correlation of the logarithmic permeability transform, $\log(k_e)$. In that case, the geometric average is simply the arithmetic average of the permeability logarithms:

$$\log(k_e) = \frac{1}{N_b} \sum_{i=1}^{N_b} \log(k_i) \tag{1.71}$$

The objective function which includes the local permeability can be defined as:

$$E_2^k = \sum_{n=1}^{N_w} \frac{\left[k_{e,a}^k(n) - k_{e,t}(n) \right]^2}{E_{02}} \tag{1.72}$$

where $k_{e,a}^{k}$ and $k_{e,t}$ represent the effective peremeability at k^{th} iteration and true effective permeabilities, respectively, and E_{02} is the initial objective function of the effective permeability function:

$$E_{02} = \sum_{n=1}^{N_w} \frac{\left[k_{e,a}^{o}(n) - k_{e,t}(n)\right]^2}{k_{e,t}(n)} \tag{1.73}$$

Similar equations can also be written when connectivity constraints are included as part of the objective function.[1.2]

1.2.4 Objective Function Weights

Combinatorial optimization techniques allow us to incorporate additional constraints into the objective function. This is done by dividing the objective function into components describing each constraint that must be honored. In order to simultaneously honor the variogram and the production information constraints, the energies of the two components are weighted and added together, to yield the overall energy function:

$$E^{k} = \frac{\psi_1}{E_{01}} E_1^{k} + \frac{\psi_2}{E_{02}} E_2^{k} \tag{1.74}$$

E_{01} (Eq. 1.65) and E_{02} (Eq. 1.67 or Eq. 1.69 or Eq. 1.73) are the normalizing constants of the variogram and production components of the energy function, respectively. E_1^{k} (Eq. 1.64) and E_2^{k} (Eq. 1.66 or Eq. 1.68 or Eq. 1.72) are the energy functions of the variogram and production information components, respectively.

ψ_1 and ψ_2 are the weights assigned to each component of the energy function. The weights may be defined arbitrarily such that one component is weighted more than the other or they may be weighted such that on average each component contributes equally to the change in the overall objective function. For equal weighting of component energy functions, the weights are computed numerically in the initial phase of the algorithm by performing sufficient, M, interchanges such that stable estimates of the weights are obtained. The equation to calculate the weight for the production constraint, ψ_2, is given by:

$$\psi_2 = \frac{\frac{1}{M}\sum_{k=1}^{M}\frac{|E_1^k - E_{01}|}{E_{01}}}{\frac{1}{M}\sum_{k=1}^{M}\frac{|E_1^k - E_{01}|}{E_{01}} + \frac{1}{M}\sum_{k=1}^{M}\frac{|E_2^k - E_{02}|}{E_{02}}} \tag{1.75}$$

The weight for the first (variogram) constraint, ψ_1, is similarly determined:

$$\psi_1 = \frac{\frac{1}{M}\sum_{k=1}^{M}\frac{|E_2^k - E_{02}|}{E_{02}}}{\frac{1}{M}\sum_{k=1}^{M}\frac{|E_2^k - E_{02}|}{E_{02}} + \frac{1}{M}\sum_{k=1}^{M}\frac{|E_1^k - E_{01}|}{E_{01}}} \tag{1.76}$$

In order to achieve a general value of the minimum number of iterations to achieve a stable estimate of the weighting functions, the iterations are normalized by dividing the iterations by the total number of simulation points, N_s, to determine the number of cycles.

Fig. 1.24 shows the example for which the variogram and well test component of the energy function are considered. Note that after 0.06 cycles of iterations, weights which converge to a stable value are obtained. Note that the weight for the well test energy function is less than that for the variogram.

The simulated annealing algorithm must simultaneously satisfy the variogram, the conditioning data constraints, and the production data information. The overall energy function (Eq. 1.74) must converge to a value of 0 within some tolerance.

1.2.5 The Interchange Mechanism

In order to allow for convergence of the objective function, perturbations are made to the simulation domain. The perturbation can be a two-point or single-point swap.

For the two-point swap the exchange points in the reservoir are randomly selected as follows:

$$I_1 = 1 + \mathrm{INT}(N_s R_1) \tag{1.77}$$

and

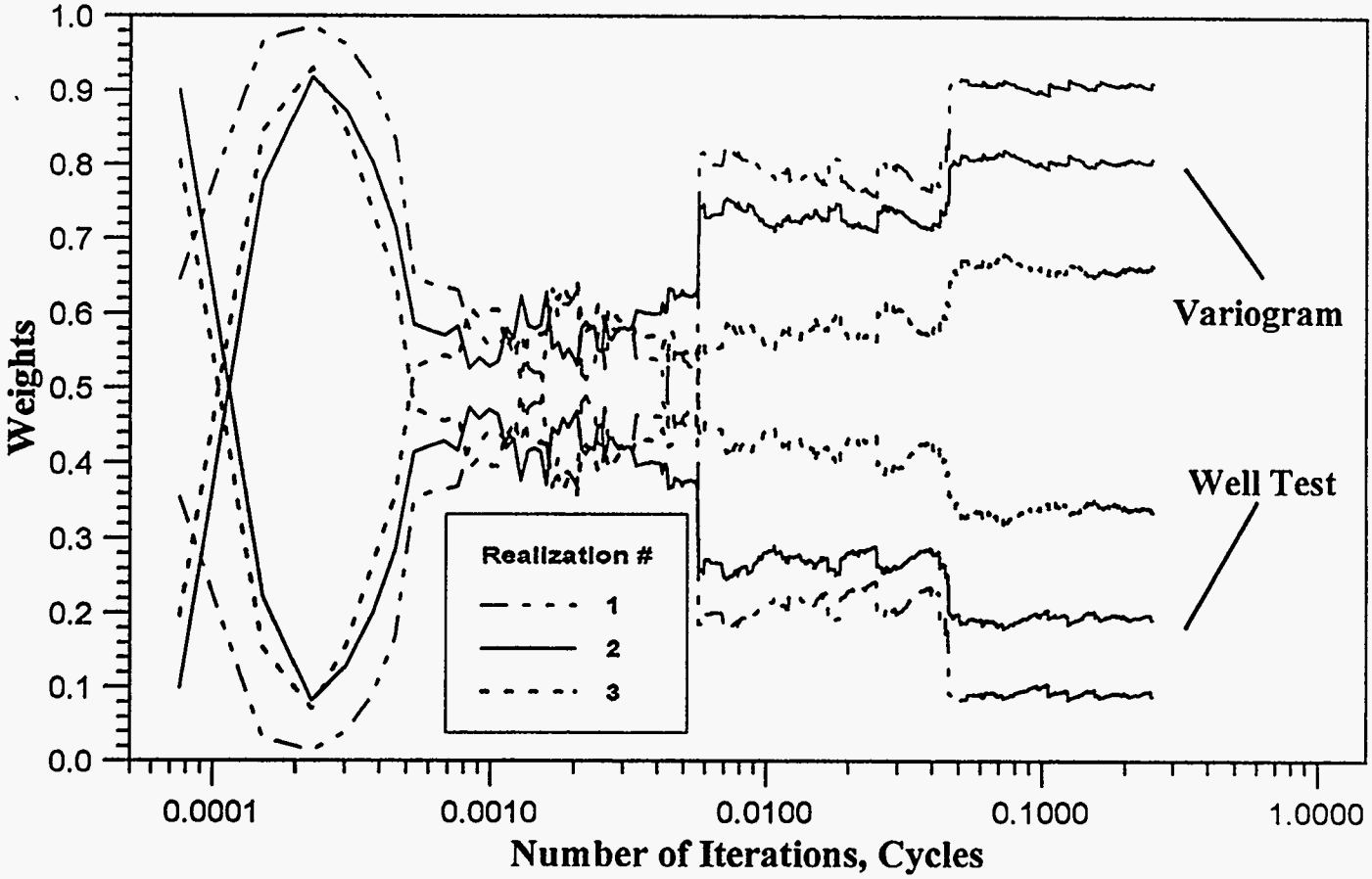

Figure 1.24: Estimated objective function weights for a different number of iterationa cycles and realizations.

$$I_2 = 1 + \mathrm{INT}(N_s R_2) \tag{1.78}$$

where R_1 and R_2 are random numbers generated from a uniform distribution in the range [0,1] and INT truncates the number in brackets to an integer. The two permeability values located at these two random locations are swapped. For the single-point swap only one exchange point is randomly selected by using either of the above equations. The algorithm also ensures that the selected swap point or points do not coincide with any of the conditioning data.

For the single-point swap a possible new permeability value is determined by sampling the original cdf. Eq. 1.60 and Eq. 1.61 are used to calculate the new value of the simulation variable. Since the variable at the exchange point must make a significant change on the objective function, the algorithm also ensures that the value of the variable at the selected grid block is significantly different from the original permeability. This is achieved by ensuring that the difference between the original permeability value and the new permeability value at the swap point is greater than the smallest magnitude of the difference between consecutive class limits, i.e.,

$$\left|V(\vec{s}_{l_1}) - V(\vec{s}_{l_2})\right| > \mathrm{MIN}(C_i - C_{i-1}), \quad \text{for } i = 1,2,\ldots N_f \tag{1.79}$$

A similar criterion can be defined for the single-point swap.

1.2.6 Metropolis Condition

Variables in the system are *interchanged* or *swapped* until the objective function is minimized. Variations of the simulated annealing algorithm as applied to reservoir description exist in the literature. The differences are based on the acceptance criteria of a swap. These include the greedy algorithm, the heat bath algorithm, and the Metropolis condition.[1.20, 1.22] In this work only the Metropolis acceptance criteria[1.28] will be considered and are described as follows. The exchange of two points or the swap is accepted if the value of the energy function is reduced. The exchange may also be accepted if the energy function is increased. The Metropolis condition calculates the probability of the transition between two states of the objective function:

$$P(\Delta E^k, T_r) = \begin{cases} 1, & \Delta E^k \le 0 \\ \exp\left(\dfrac{-\Delta E^k}{T^r}\right) & \Delta E^k > 0 \end{cases} \tag{1.80}$$

where the index k denotes an iteration within a step, represented by index r. The change in the objective function, ΔE_k, due to one interchange is:

$$\Delta E^k = E' - E^k \tag{1.81}$$

where E' is the updated value after the perturbation (see Eq. 1.94). T^r is the control parameter calculated by:

$$T^r = \alpha T^{r-1} \tag{1.82}$$

α is the convergence rate factor and is a constant value in the range $0 < \alpha < 1$.

If $\Delta E^k \le 0$ the exchange is always accepted according to Eq. 1.80. However, if $\Delta E^k \ge 0$, then a random number, R, from a uniform distribution in the range [0,1] is compared to $P\left(\Delta E^k, T^r\right)$ (Eq. 1.80). If $R \le P\left(\Delta E^k, T^r\right)$ the proposed interchange is accepted.

The use of the Metropolis condition ensues the convergence of the algorithm to a global rather than a local minimum.

1.2.7 The Initial Control Parameter

The effect of the control parameter, T_r, is evident from the Metropolis condition; if the value of the control parameter is high then more of the iterations proposed by the interchange mechanism will be accepted. The initial control parameter, T°, is determined for the first step ($r = 1$), numerically in the initial phase of the algorithm. The value of the initial control parameter determines the performance and efficiency of simulated annealing. If the control parameter is too high then most of the swaps are accepted leaving the simulation variable essentially uncorrelated. If its value is too low, then the simulation may converge to a local minimum. An appropriate value for T° is derived by Aarts and Korst.[1.29] It is determined in the initial phase of the algorithm and is given by:

$$T^{\circ} = \frac{\overline{\Delta E}^{+}}{\ln\left[\frac{m_2}{\chi_{initial} m_2 - (1-\chi_{initial}) m_1}\right]} \tag{1.83}$$

$\overline{\Delta E}^{+}_{initial}$ is the mean of m_2 positive changes in the objective function

$$\overline{\Delta E}^{+}_{initial} = \frac{1}{m_2} \sum_{i=1}^{m_2} \Delta E^{+}_{initial} \tag{1.84}$$

$\Delta E^{+}_{initial}$ represents a positive change in the energy function. This is numerically determined by performing sufficient iterations in the initial phase of the algorithm. The change in the objective function at each iteration is given by:

$$\Delta E^{k}_{initial} = E^{k}_{initial} - E_o \tag{1.85}$$

for $k = 1,\ldots,M_{initial}N_s$ where E° is the initial objective function. For the total number of iterations there are m_1 iterations for $\Delta E^{k}_{initial} \leq 0$ and m_2 iterations for $\Delta E^{k}_{initial} > 0$.

By performing numerical experiments, Pérez[1.20] determined that $M_{initial} = 0.25$ is sufficiently large to allow for a stable estimate of the mean change in the objective function. He also defines the initial acceptance ratio, $\chi_{initial}$, to be 0.99 which is sufficiently large such that most of the proposed exchanges are accepted.

1.2.8 Maximum Number of Iterations Per Step

The method developed by Pérez[1.20] to calculate the maximum number of total iterations per step is outlined. The method calculates the maximum number of iterations per step by estimating the acceptance ratio for the subsequent step. The maximum number of steps defined by Pérez is 1000. The acceptance ratio for subsequent step is observed to be:

$$\chi^{r+1} = \frac{(\chi^{r})^2}{\chi^{r-1}} \tag{1.86}$$

for $r = 1,2,\ldots1000$ and for $r = 1$, $\chi^{1} = 1$.

The maximum number of iterations per step are calculated by:

$$M_t^{r+1} = M_a \frac{\chi^{r-1}}{\left(\chi^r\right)^2} \tag{1.87}$$

where the recommended value for M_a is $5.0N_s$. Numerical experiments recommend the coefficient value of 5.0 is ideal and allows for sufficient iterations per step.

1.2.9 Energy Function Update Mechanism

In the simulated annealing algorithm most of the computational effort is spent on updating the constraints imposed by the variogram and well test information, once a perturbation or swap has been made. Thus the update code must be efficient with minimum computations to reduce the overall computational cost. The permeabilities at the swap points, $\vec{s}_{l1}$ and $\vec{s}_{l2}$, result in a change in the energy function for each component. We present the update formulations for the two point swap for the variogram and well test components of the energy function and the update formulations for the single point swap for only the variogram component. The update formulations presented here allow us to determine the new variogram and permeability average efficiently with minimal computational cost.

Variogram Energy Function Update

The update mechanism for the variogram component of the energy function was described by Pérez[1.20] and presented here for the sake of completeness. The new sample variogram, $\gamma_s'\left(\vec{h}_a\right)$, calculated at an arbitrary lag distance, $\vec{h}_a$ is

$$\gamma_s'\left(\vec{h}_a\right) = \gamma_s\left(\vec{h}_a\right) + \lambda\left(\vec{h}_a\right) \tag{1.88}$$

where $\gamma_s\left(\vec{h}_a\right)$ is the original variogram value at $\vec{h}_a$. $\lambda\left(\vec{h}_a\right)$ is the variogram correction term which consists of removing the contribution to the variogram of the permeability at one exchange point and adding the contribution of permeability at the other exchange point for the two point swap or the permeability sampled from the cdf for the single point swap.

The correction term at the lag distance, $\vec{h}_a$ is

$$\lambda\left(\vec{h}_a\right) = \frac{1}{2N_p\left(\vec{h}_a\right)}\left[\lambda_{I1}^{+} + \lambda_{I1}^{-} + \lambda_{I2}^{+} + \lambda_{I2}^{-}\right] \tag{1.89}$$

where, N_p is the number of pairs for the lag, $\vec{h}_a$. For the single point swap $\lambda_{I2}^{+} = 0$ and $\lambda_{I2}^{-} = 0$.

For the exchange at $\vec{s}_{I1}$ the correction components are:

$$\begin{aligned} &\lambda_{I1}^{+} = -d_{1,2}k\left(\vec{s}_{I1} + \vec{h}_a\right) + D_{1,2} \\ &\text{and} \\ &\lambda_{I1}^{-} = -d_{1,2}k\left(\vec{s}_{I1} - \vec{h}_a\right) + D_{1,2} \end{aligned} \tag{1.90}$$

For the exchange at $\vec{s}_{I2}$ the correction components are:

$$\begin{aligned} &\lambda_{I2}^{+} = -d_{1,2}k\left(\vec{s}_{I2} + \vec{h}_a\right) + D_{1,2} \\ &\text{and} \\ &\lambda_{I2}^{-} = -d_{1,2}k\left(\vec{s}_{I2} - \vec{h}_a\right) + D_{1,2} \end{aligned} \tag{1.91}$$

where

$$D_{1,2} = \left[k_{\vec{s}I1} + k_{\vec{s}I2}\right]\left[k_{\vec{s}I1} - k_{\vec{s}I2}\right] \tag{1.92}$$

and

$$d_{1,2} = 2\left[k_{\vec{s}I1} - k_{\vec{s}I2}\right] \tag{1.93}$$

Note that for the single point swap, $k_{\vec{s}I2}$ is substituted by the value sampled from the cdf.

Most of the computational cost in the simulated annealing algorithm is due to the update of the energy function. Since the number of computations for the single point swap are less than that of the two point swap, the single point swap formulation speeds up the algorithm. However, note that for the single point swap the cdf constraint of the algorithm is no longer satisfied.

The new variogram objective function due to the swap is written as:

$$E_1' = \sqrt{\sum_{i=1}^{N_d}\sum_{l=1}^{N_{hd}}\left[\frac{\gamma_s^k\left(\vec{h}_{l,i}\right)+\lambda^k\left(\vec{h}_{l,i}\right)-\gamma_o\left(\vec{h}_{l,i}\right)}{\gamma_o\left(\vec{h}_{l,i}\right)}\right]^2} \tag{1.94}$$

Well Test Component Update

The correction term for the well test component is a correction to the geometric permeability average in the theta direction, $\bar{k}_{gj}$, for each pressure derivative data point considered. The correction removes the contribution of permeability at one exchange point and adds the contribution of permeability to the other exchange point. This equation can be written to account for the change of two exchanged locations $\vec{s}_{l1}$ and $\vec{s}_{l2}$ on the geometric permeability average, $\bar{k}_{gj}$:

$$\begin{aligned}\bar{k}_{gj}' = \exp[(&A_{rj}\ln\bar{k}_{gj} + A_{\bar{s}_{l2},j}\ln k_{\bar{s}_{l1}} - A_{\bar{s}_{l2},j}\ln k_{\bar{s}_{l2}} \\ &+A_{\bar{s}_{l1},j}\ln k_{\bar{s}_{l2}} - A_{\bar{s}_{l1},j}\ln k_{\bar{s}_{l1}}) / A_{rj}]\end{aligned} \tag{1.95}$$

where $j = 1,2,3,\ldots N_r$.

If the grid block at $\vec{s}$ falls completely outside the annular region between $j-1$ and j, then since $A_{\bar{s},j} = 0$, the contribution of the permeability $k_{\bar{s}}$, to the permeability average is 0. We then calculate the equivalent permeability, $\bar{k}_e$, for the correction term:

$$\frac{1}{\bar{k}_e'} = \sum_{j=1}^{N_r} w_j \frac{1}{\bar{k}_{gj}'} \tag{1.96}$$

For Oliver's method the well test component of the energy function is calculated by the following equation:

$$E_2' = \sqrt{\sum_{i=1}^{N_t}\left[\frac{\bar{k}_e' - \hat{k}_i}{\hat{k}_i}\right]^2} \tag{1.97}$$

If the harmonic average is used to approximate the *ISA* permeability distribution then the following update equation is used:

$$\bar{k}_{hj}' = \frac{A_{rj}}{A_{rj}\bar{k}_{hj} + A_{\bar{s}_{l2},j}k_{\bar{s}_{l1}} - A_{\bar{s}_{l2},j}k_{\bar{s}_{l2}} + A_{\bar{s}_{l1},j}k_{\bar{s}_{l2}} - A_{\bar{s}_{l1},j}k_{\bar{s}_{l1}}} \tag{1.98}$$

For *ISA* the well test component of the energy function is calculated by:

$$E_2' = \sqrt{\sum_{j=1}^{N_r} \left[\frac{\bar{k}_j' - \hat{k}_j}{\hat{k}_{ji}} \right]^2} \tag{1.99}$$

where $\bar{k}'$ is either the area-based geometric or harmonic average of grid block permeabilities in annular rings defined by Eq. 1.37 or Eq. 1.36, respectively.

Update of Production Performance Energy Function Constraint

In the context of simulated annealing, the logarithm of effective permeability can be updated after a swap as follows:

$$\log(k_e') = \frac{N_b \log(k_e) - \log(k_i) + \log(k_{i'})}{N_b} \tag{1.100}$$

where log (k_e) is the value prior to the swap and log (k_e') represents the updated value after replacing log (k_i) with ($k_{i'}$). The new energy function (E_e') is then calculated by:

$$E_2' = \sqrt{\sum_{n=1}^{N_w} \left[\frac{k_e' - k_e}{k_e} \right]} \tag{1.101}$$

1.2.10 Simulation Process

In this section we present a step by step outline of the simulated annealing algorithm. The algorithm is summarized in the flow chart shown in Fig. 1.25. Numbers in the flow chart indicate steps in the algorithm below.

1. Generate the initial uncorrelated permeability distribution by the method described in Section 1.2.1.

2. Calculate the sample variogram (Section 1.2.2) and the initial well test information for the initial distribution. The initial well test information includes (i) the area of each grid block within the predefined radial grid (ii) the area-based geometric or harmonic grid block permeabilities within each annular region and/or (iii) for Oliver's method only, the equivalent permeability and corresponding weights determined by the kernel function.

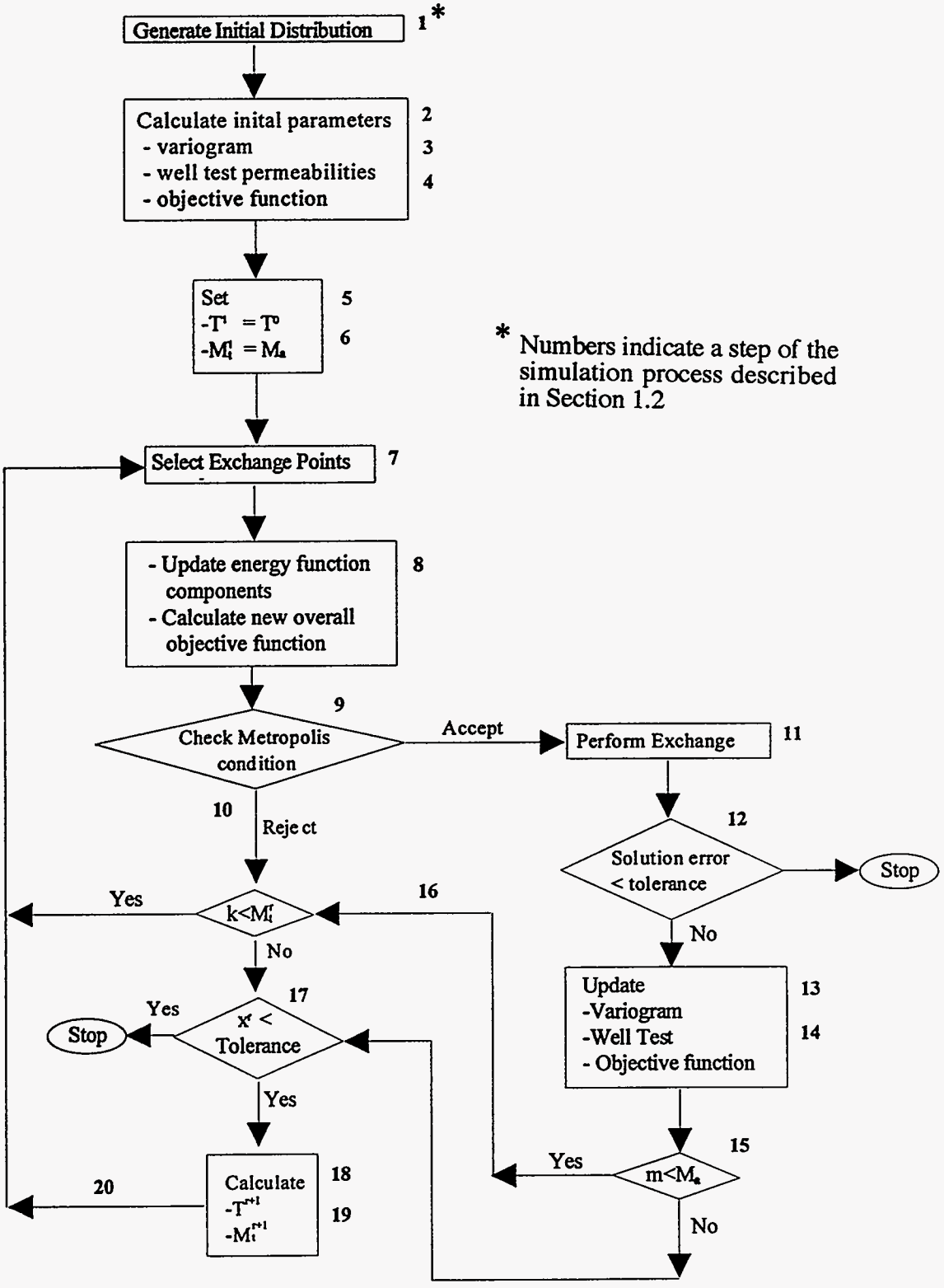

Figure 1.25: Simulated annealing flow chart, incorporating geostatistical and well test information.

3. Calculate each of the normalizing constants for each of the component objective functions (Section 1.2.3).

4. Calculate the component objective function weights by the procedure given in Section 1.2.4.

5. Calculate the value of the initial control parameter, T^o (Section 1.2.7) and set $T^1 = T^o$.

6. For the first step, set the maximum number of iterations per step equal to M_a, i.e., $M_{t^1} = M_a$ (Section 1.2.8).

7. Using the interchange mechanism described in Section 1.2.5 select two random locations in the simulation domain, $\vec{s}_{I1}$ and $\vec{s}_{I2}$.

8. Calculate the update of each component of the energy function (variogram and well test) using the procedure outlined in Section 1.2.9 and calculate the new overall energy function (Section 1.2.4).

9. By the procedure outlined in Section 1.2.6 check if the Metropolis condition accepts the proposed interchange.

10. If the interchange is not accepted return to step 7.

11. If the interchange is accepted, then permanently exchange the permeabilities at the two selected swap points by assigning the original permeabilities at the swap points to temporary variables, i.e., $TV_1 = k_{\vec{s}I1}$ and $TV_2 = k_{\vec{s}I2}$. Then assign the permeability values at the new location: $k_{\vec{s}I1} = TV_2$ and $k_{\vec{s}I2} = TV_1$.

12. Check for convergence; if the tolerance condition of the objective function is satisfied. For Oliver's method this convergence criterion is,

$$\frac{E_1^k}{\sum_{i=1}^{N_d} N_{h,i}} + \frac{E_2^k}{N_{wt} + N_r} \leq \varepsilon_v \qquad (1.102)$$

For *ISA* the convergence criterion is

$$\frac{E_1^k}{\sum_{i=1}^{N_d} N_{h,i}} + \frac{E_2^k}{N_r} \le \varepsilon_v \tag{1.103}$$

Similarily the convergence criteria for the near well-bore permeabiltity, for the production performance can be defined as:

$$\frac{E_1^k}{\sum_{i=1}^{N_d} N_{h,i}} + \frac{E_2^k}{N_w} \le \varepsilon_v \tag{1.104}$$

ε_v is a convergence tolerance close to 0. If the convergence criteria are satisfied, then the simulation is stopped.

13. Update the sample variogram and corresponding variogram energy function for the next iteration level:

$$\gamma_s^{k+1}\left(\vec{h}_{l,i}\right) = \gamma_s'\left(\vec{h}_{l,i}\right) \quad \text{for} l = 1,\ldots N_{h,i} \text{ and } i = 1,\ldots N_d \tag{1.105}$$

and

$$E_1^{k+1} = E_1' \tag{1.106}$$

14a. For Oliver's method, update the area-based geometric average of the grid block permeabilities within annular regions, the equivalent permeability and the corresponding energy function:

$$\overline{k}_{g,j}^{k+1} = \overline{k}_{g,j}', \quad \text{for} j = 1,\ldots,N_r \tag{1.107}$$

$$\overline{k}_{e,i}^{k+1} = \overline{k}_{e,i}', \quad \text{for} i = 1,\ldots N_t \tag{1.108}$$

and

$$E_2^{k+1} = E_2' \tag{1.109}$$

14b. For *ISA* update the area-based geometric or harmonic average of the grid block permeabilities within annular regions and the corresponding energy function:

$$\overline{k}_{g,j}^{k+1} = \overline{k}_{g,j}', \quad \text{for} j = 1,\ldots,N_r \tag{1.110}$$

or

$$\overline{k}_{h,j}^{k+1} = \overline{k}_{h,j}', \quad \text{for} j = 1,\ldots,N_r \tag{1.111}$$

and

$$E_2^{k+1} = E_2' \tag{1.112}$$

14c. For near-well permeability constraint, k_{nw}, the updated values are:

$$k_e^{k+1} = k_e', \quad \text{for} j = 1,\ldots,N_w \tag{1.113}$$

and

$$E_2^{k+1} = E_2' \tag{1.114}$$

15. Check if the number of iterations is less than the maximum number of allowable iterations, if $m > M_a$ go to 17 or if $m \le M_a$ go to 16.

16. Check if the number of iterations in a step r does not exceed the maximum number of total iterations per step, M_t^r. If $k \ge M_t^r$ then go to step 17. If $k < M_t^r$ then go to step 7.

17. Check the acceptance ratio tolerance for the current step. The acceptance ratio is the fraction of the total iterations in a step which were accepted by the Metropolis condition (Section 1.2.6) and is given by

$$\chi^r = \frac{m}{k} \tag{1.115}$$

where m is the number of accepted iterations in the step r and k is the total number of iterations. The convergence criteria is

$$\chi^r \le \varepsilon_a \tag{1.116}$$

ε_a is a convergence tolerance close to 0. If the convergence criterion is satisfied the simulation is stopped. This convergence does not imply a convergence of the objective function but ensures the algorithm does not run for extremely long times.

18. Calculate the control parameter for the next step using the procedure outlined in Section 1.2.6.

19. Calculate the maximum number of iterations for the next step as described in Section 1.2.7.

20. Proceed to step 7.

1.3 Inclusion of Dynamic Data in Reservoir Description - Results

In this part of the report, we apply the simulated annealing algorithm to develop reservoir descriptions that simultaneously honor the spatial statistics (variogram) and the well test information or the production performance constraints.

For the production performance constraints we investigate synthetic inverted 5-spot heterogeneous reservoirs and demonstrate the importance of the identified parameters in improving our ability to predict reservoir performance. We show the importance of near-well bore permeability in predicting primary and secondary recovery performance and the importance of CV_{k*} and threshold connectivity functions for improving the prediction of secondary recovery performance.

We also show that porosity heterogeneties are not crucial for improving performance prediction.

Finally an actual field case under primary and secondary recovery is investigated and it is demonstrated that by including the additional constraints the performance prediction of the field is greatly improved.

From the pressure transient response of a single well producing during a drawdown test in a heterogeneous reservoir, both Oliver's method and *ISA* are used to reproduce the permeability distribution. The reproduced reservoir images and their pressure and pressure derivatives are compared to their respective base cases. We also investigate the efficiency, in terms of computational cost, for both methods.

The effect of porosity variations on the pressure response for a single well producing in a heterogeneous porous medium is also investigated.

We consider the effect of anisotropy on the pressure response during a drawdown test. A gridding scheme for simulated annealing is developed; it allows for the incorporation of the pressure response due to anisotropy into an equivalent isotropic domain.

1.3.1 Incorporation of Well Test Data

Using the simulated annealing algorithm described in Section 1.2, permeability fields are reproduced such that the spatial and univariate statistics and the pressure transient data of the synthetic base case are honored. A numerical fluid flow drawdown simulation of the regenerated permeability field is performed using ECL 100. The reservoir properties are the same as in the base cases and are summarized in Table 1.2. The pressures and pressure derivatives are compared to the base case pressure responses. The input parameters for the simulated annealing algorithm are:

- the univariate statistics (cdf),
- the spatial statistics (variogram),
- the conditioning data,
- the instantaneous permeability, $\hat{k}$, for N_t time steps for Oliver's solution, or
- the equivalent radial permeability distribution, $\bar{k}_{ISA}$, determined by *ISA*.

Each distribution is conditioned such that the center grid block permeability where the well is located is the permeability of the base distribution. It should be noted that Turning Bands does a poor job of reproducing the input variogram. Therefore, the variogram of the base distribution was recalculated using the Xgam program in GSLIB.[1.18] We present both the Oliver's solution and *ISA* results.

Oliver's Solution Results

Example 1

In the first example, we consider the permeability field shown in Fig. 1.2 and corresponding pressure response shown in Fig. 1.3 as the truth case. From a qualitative global radial perspective we observe that the permeability field in this example exhibits a region of higher permeability near the flowing well located at the center of the reservoir and reduced permeability nearer the outer no-flow boundaries. This effect is also shown by the pressure derivative which has a lower

value at early times and a higher value at later times. Typical well test interpretation of the pressure derivative would indicate the behavior of two-zone composite reservoir.

The input parameters for the simulated annealing algorithm are summarized in Table 1.5. Multiple realizations, honoring the same constraints, are generated by changing only the seed value to generate random numbers. Fig. 1.26a is the base case permeability distribution and Fig. 1.26b through Fig. 1.26f are multiple realizations honoring the same constraints. A comparison between the pressures and pressure derivatives of the base case and simulated cases are shown in Fig. 1.27.

The match between the pressures and the pressure derivatives of the base case and simulated cases show a good agreement. The simulation statistics also show an excellent match between the input and simulated variogram. Fig. 1.28 shows the pressures and pressure derivatives of realizations generated by constraining them only to the univariate and spatial statistics, but *not* to pressure transient data. Note that for these cases the pressure response is reproduced poorly.

Example 2

We also present a second case study, where the permeability has a higher variance indicating a higher degree of heterogeneity. The base case permeability field is shown in Fig. 1.29a and the reproduced permeability distributions are shown in Fig. 1.29b through Fig. 1.29c. Fig. 1.30 shows the fluid flow simulation results of the pressure responses compared to the base case pressure response. Fig. 1.31 shows pressure responses of reproduced permeability fields that do not honor the well test constraint. Once again, we observe that the pressure response is more effectively reproduced when the well test constraint is taken into consideration.

Example 3

Fig. 1.32a shows the base case permeability field for this example and Fig. 1.32b through Fig. 1.32c show simulated permeability fields honoring the spatial statistics and well test information constraints. Note that for this particular example the correlation range of the variogram is 2100 ft which is half the length of one side of

Number of grid blocks (x,y,z)	115x115x1
Block dimensions ($\Delta x, \Delta y, \Delta z$)	35*ft* x 35*ft* x 10*ft*
Variogram type	Spherical - isotropic
Sill	440.0
Range	590.0 *ft*

Well Test Information

n	t (days)	r_{min}	r_{max}	$\hat{k}$
1	1.16×10^{-3}	5.4	105.6	32.41
2	2.29×10^{-3}	7.6	148.3	31.22
3	4.37×10^{-3}	10.5	204.9	28.60
4	9.08×10^{-3}	15.1	295.4	24.86
5	1.93×10^{-2}	22.1	430.7	20.98
6	3.46×10^{-2}	29.6	576.3	18.54
7	5.71×10^{-2}	38.0	740.5	17.08
8	8.74×10^{-2}	47.0	916.3	16.29
9	1.25×10^{-1}	56.1	1093.5	15.92
10	2.19×10^{-1}	74.3	1449.5	15.76
11	2.90×10^{-1}	85.6	1668.4	15.71
12	4.12×10^{-1}	102.0	1988.6	15.38

Conditioning Data	$x(ft)$	$y(ft)$	$z(ft)$	$k_z(md)$
	2012.5	2012.5	17.5	34.3

Table 1.5: Simulated annealing input data - Oliver's solution

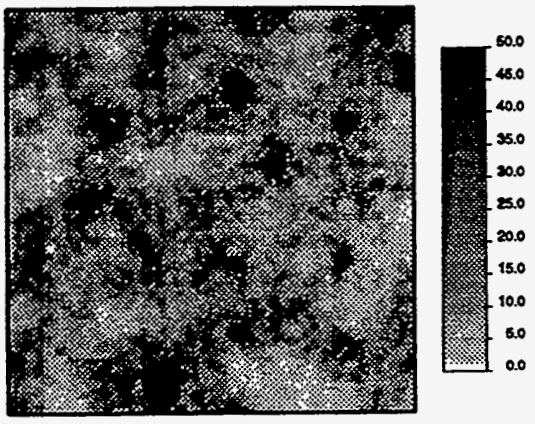

Figure 1.26a: Base case permeability distribution generated by Turning Bands (range = 600 feet, $\sigma^2_{\ln k} = 0.92$).

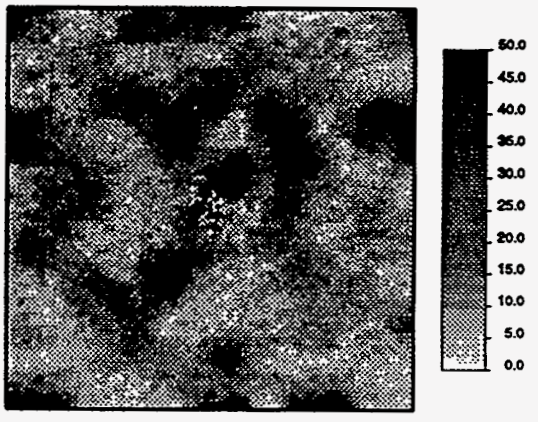

Figure 1.26b: (seed = 107935).

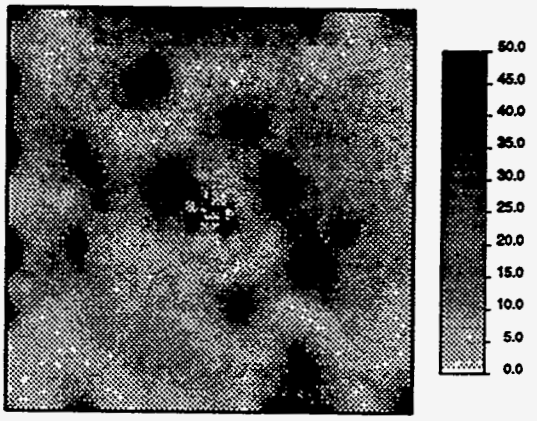

Figure 1.26c: (seed - 1079602).

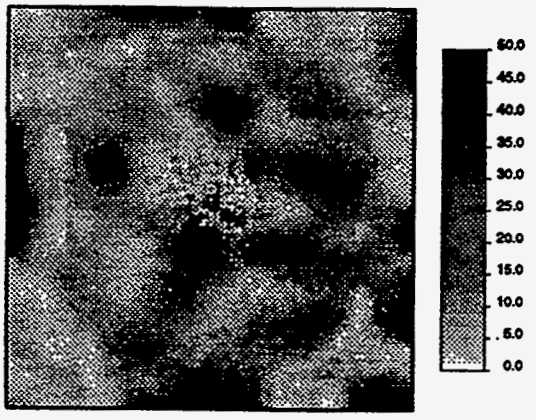

Figure 1.26d: (seed = 1079623).

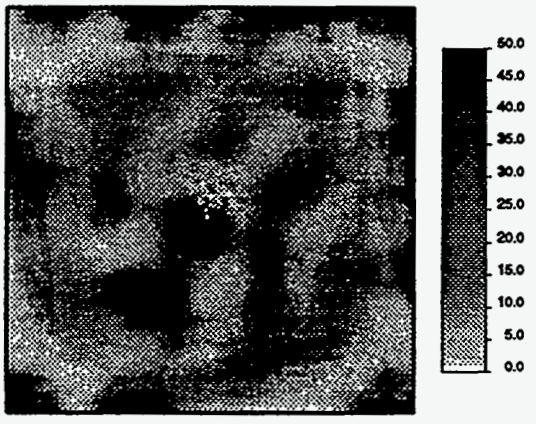

Figure 1.26e: (seed = 1079635).

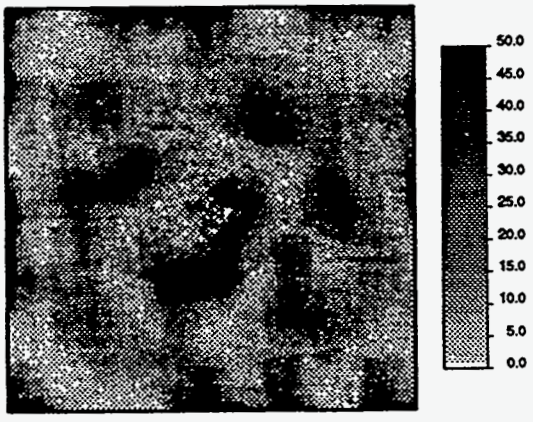

Figure 1.26f: (seed - 1079602).

Figure 1.26b-f: Simulated permeability distributions honoring variogram and well test constraints (Oliver's solution).

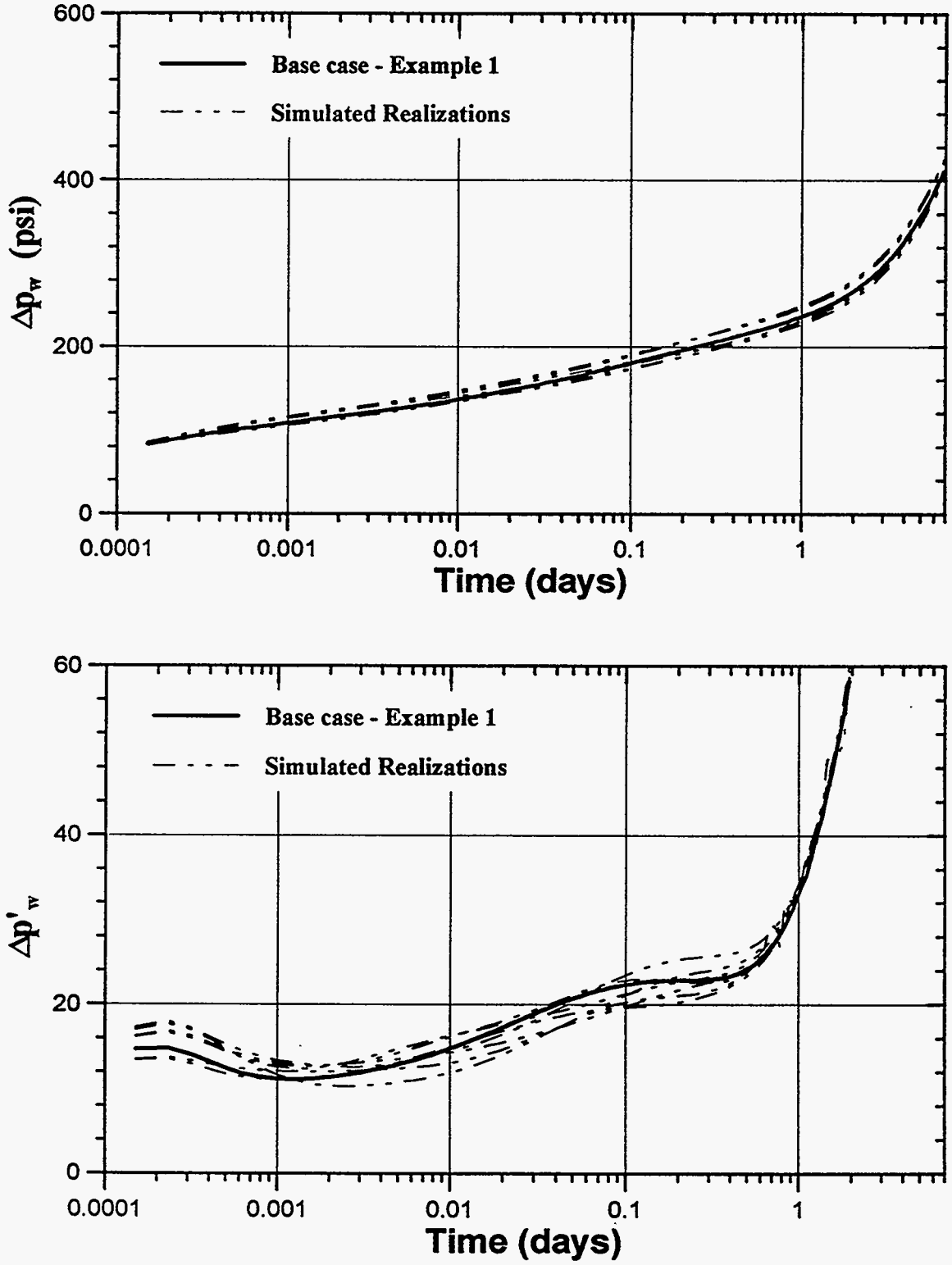

Figure 1.27: Pressures and pressure derivatives of simulated permeability realizations honoring variogram and well test constraints compared to the base case response for Example 1.

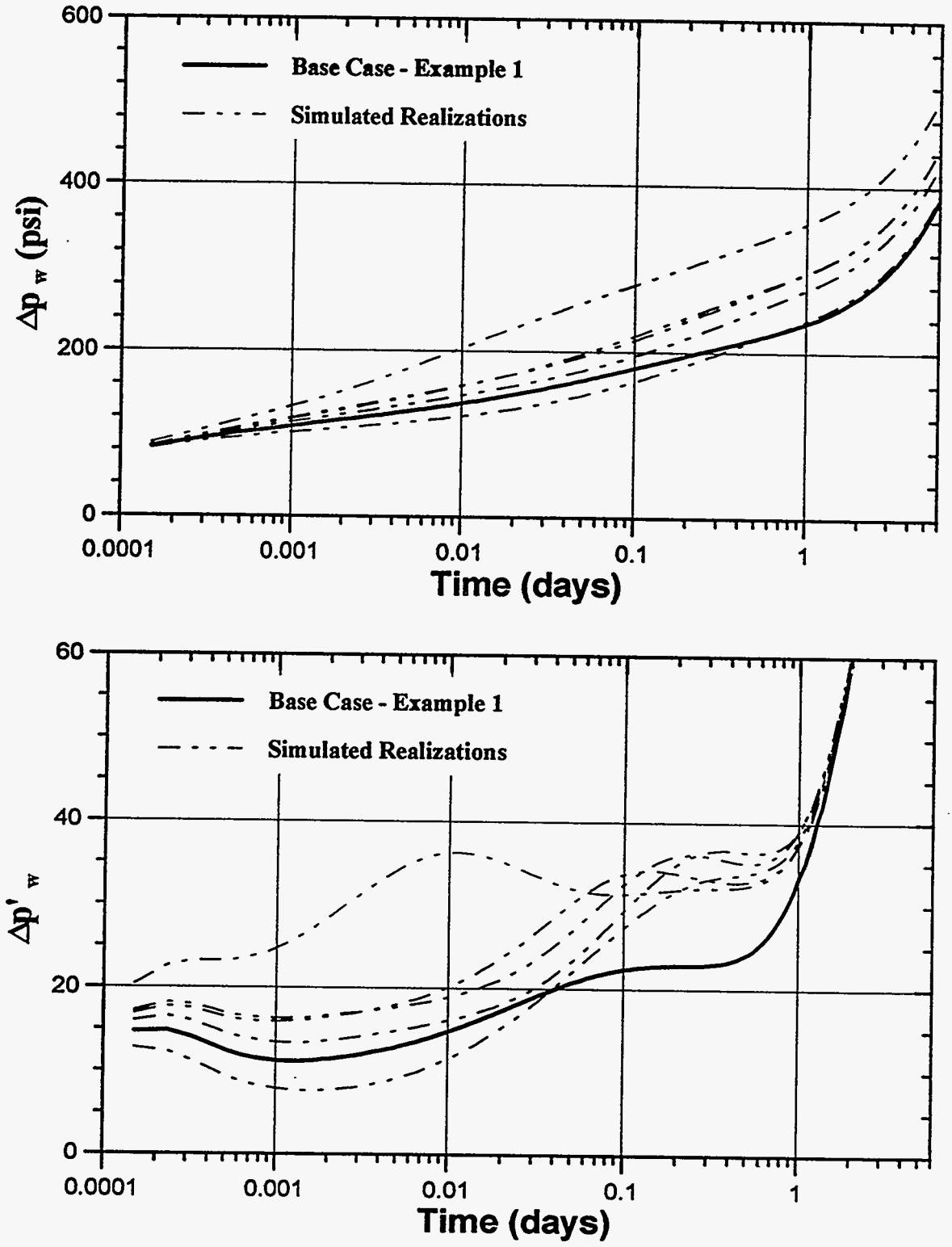

Figure 1.28: Pressures and pressure derivatives of simulated permeability realizations honoring only the variogram constraint compared to the base case response for Example 1.

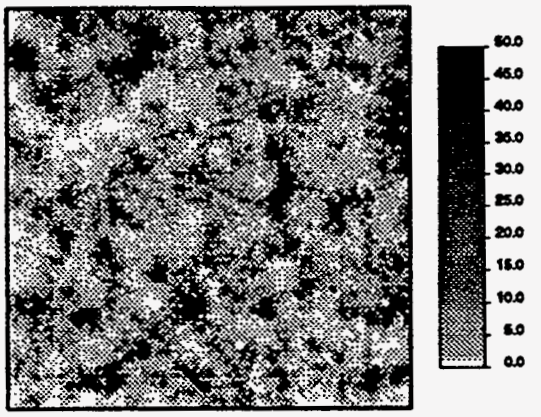

Figure 1.29a: Base case permeability distribution generated by Turning Bands (range = 310 feet, $\sigma^2_{\ln k} = 1.61$).

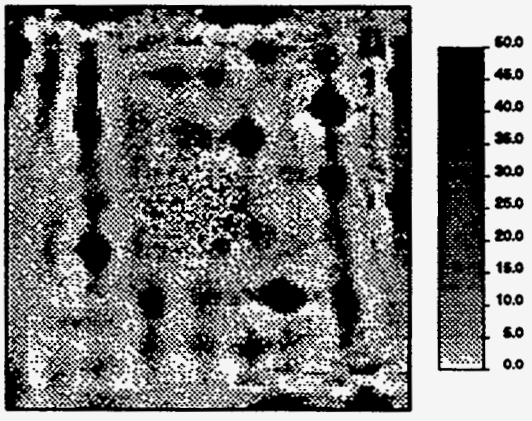

Figure 1.29b: (seed = 1079601).

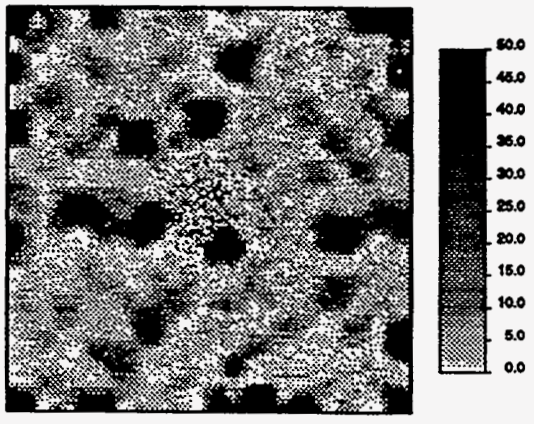

Figure 1.29c: (seed - 1079616).

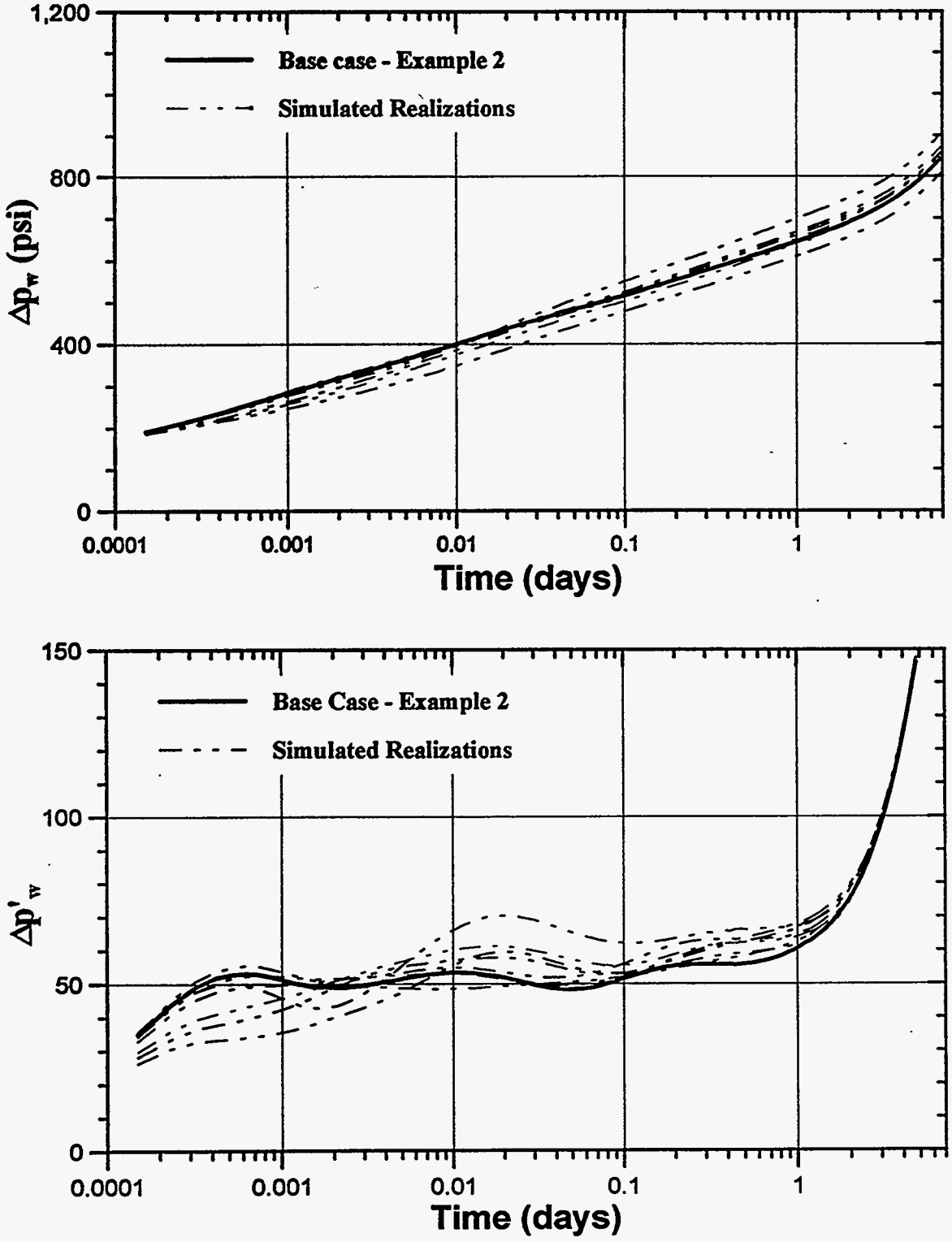

Figure 1.30: Pressures and pressure derivatives of simulated permeability realizations honoring variogram and well test constraints compared to the base case response for Example 2.

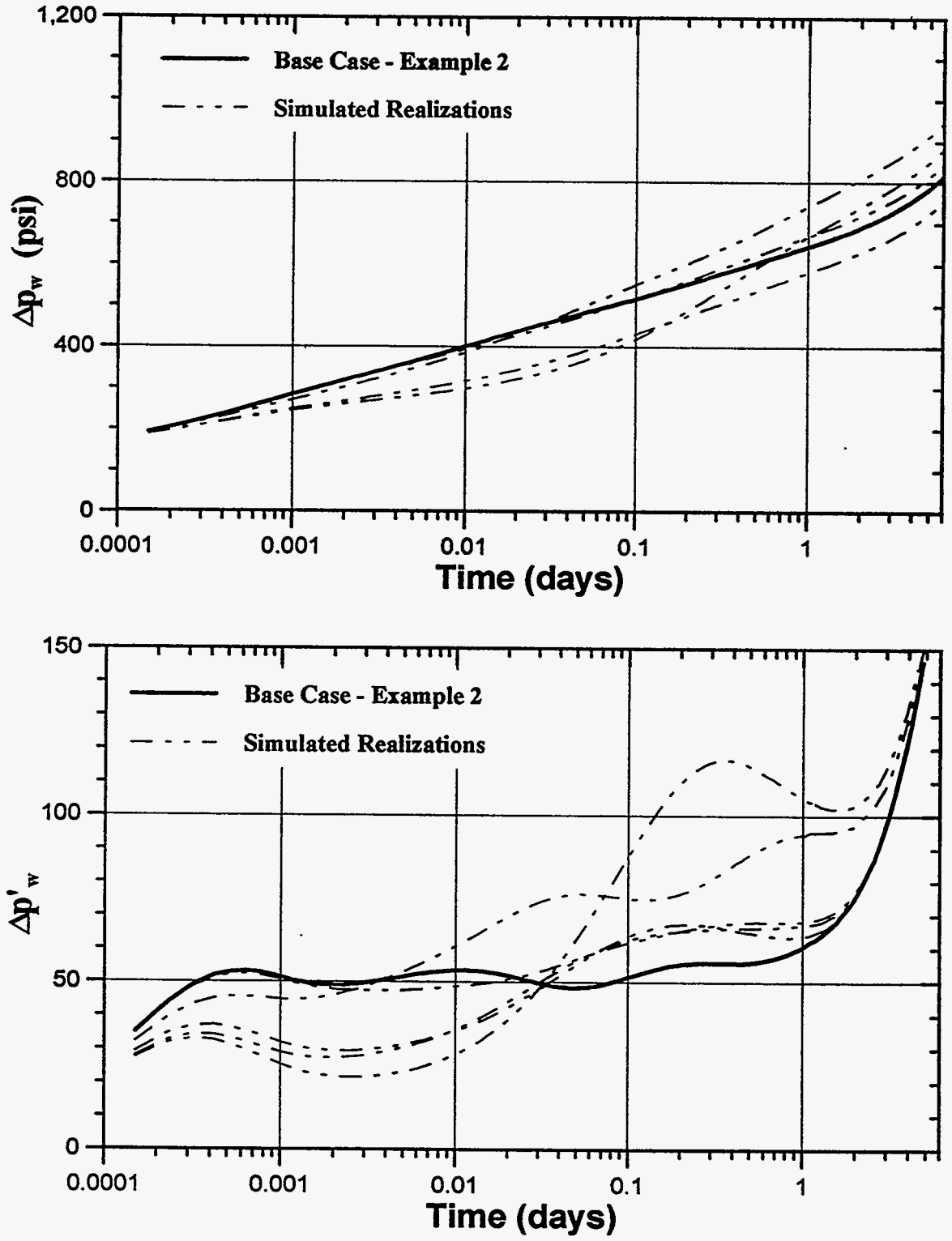

Figure 1.31: Pressures and pressure derivatives of simulated permeability realizations honoring only the variogram constraint compared to the base case response for Example 2.

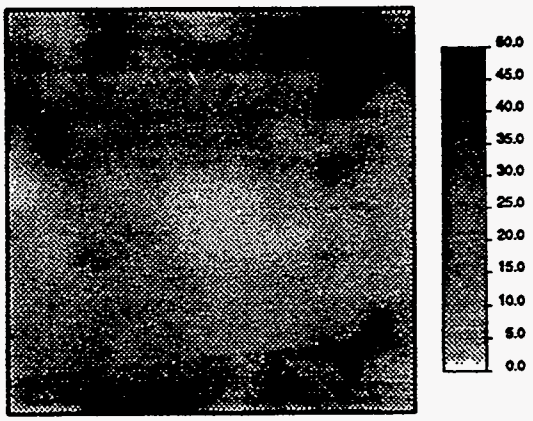

Figure 1.32a: Base case permeability distribution generated by Turning Bands (range = 2100 feet, $\sigma^2_{\ln k} = 0.92$).

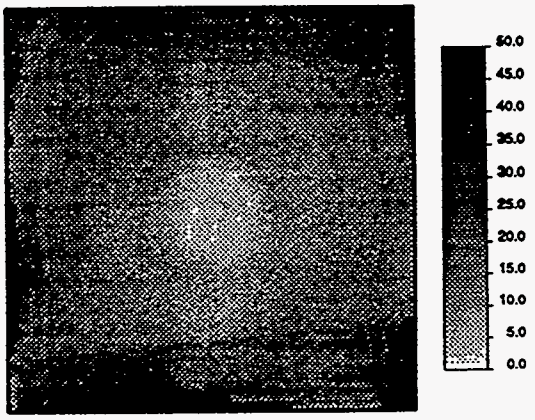

Figure 1.32b: (seed = 1079613).

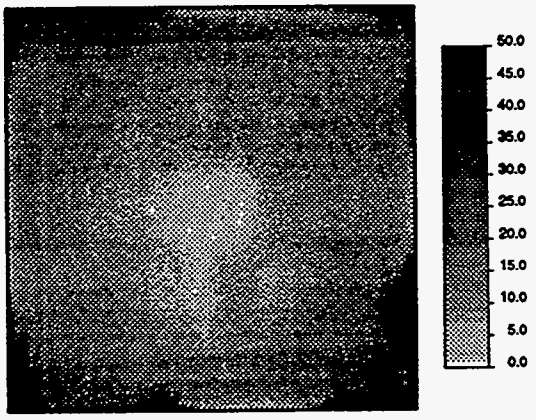

Figure 1.32c: (seed - 1079608).

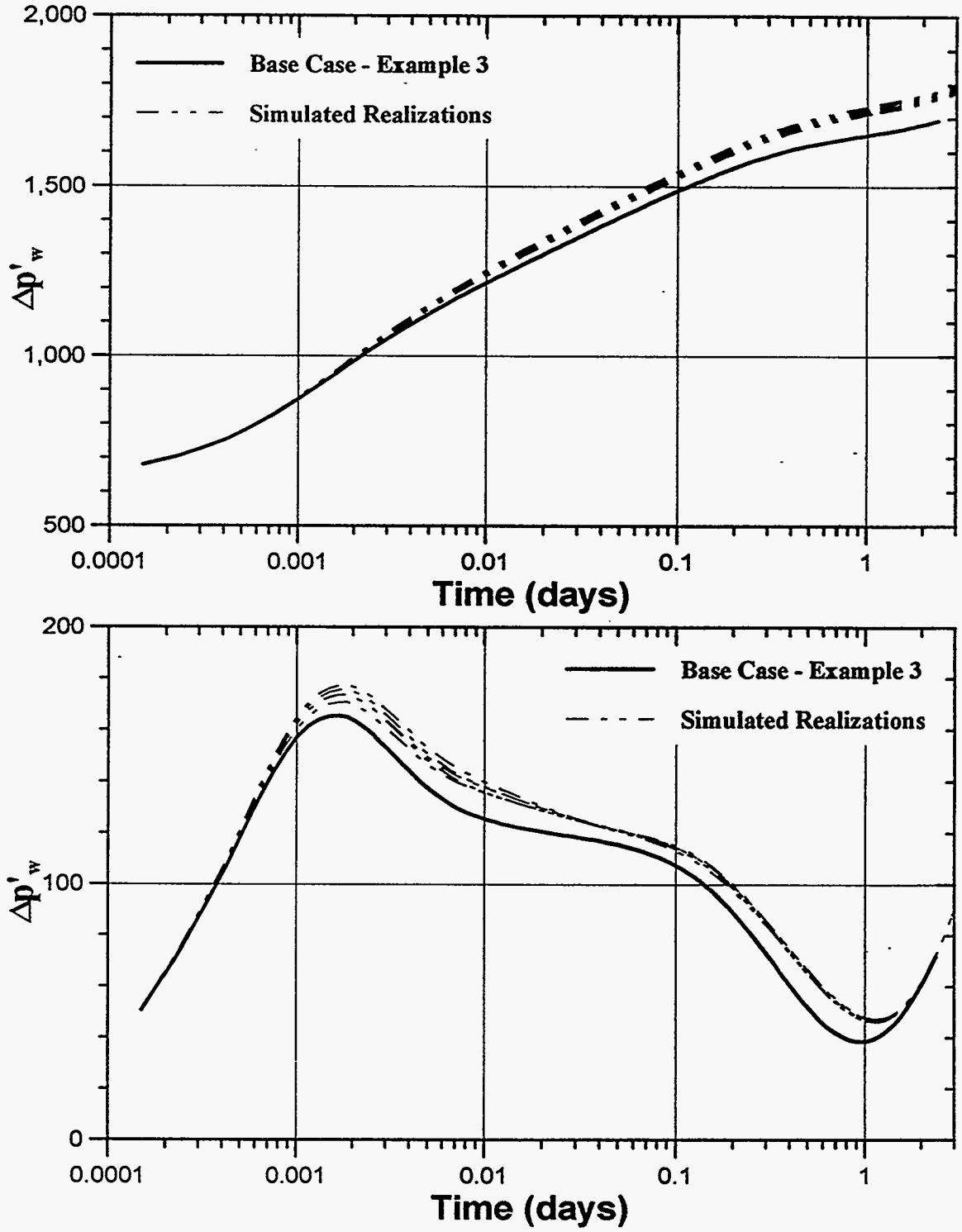

Figure 1.33: Pressures and pressure derivatives of simulated permeability realizations honoring variogram and well test constraints compared to the base case response for Example 3.

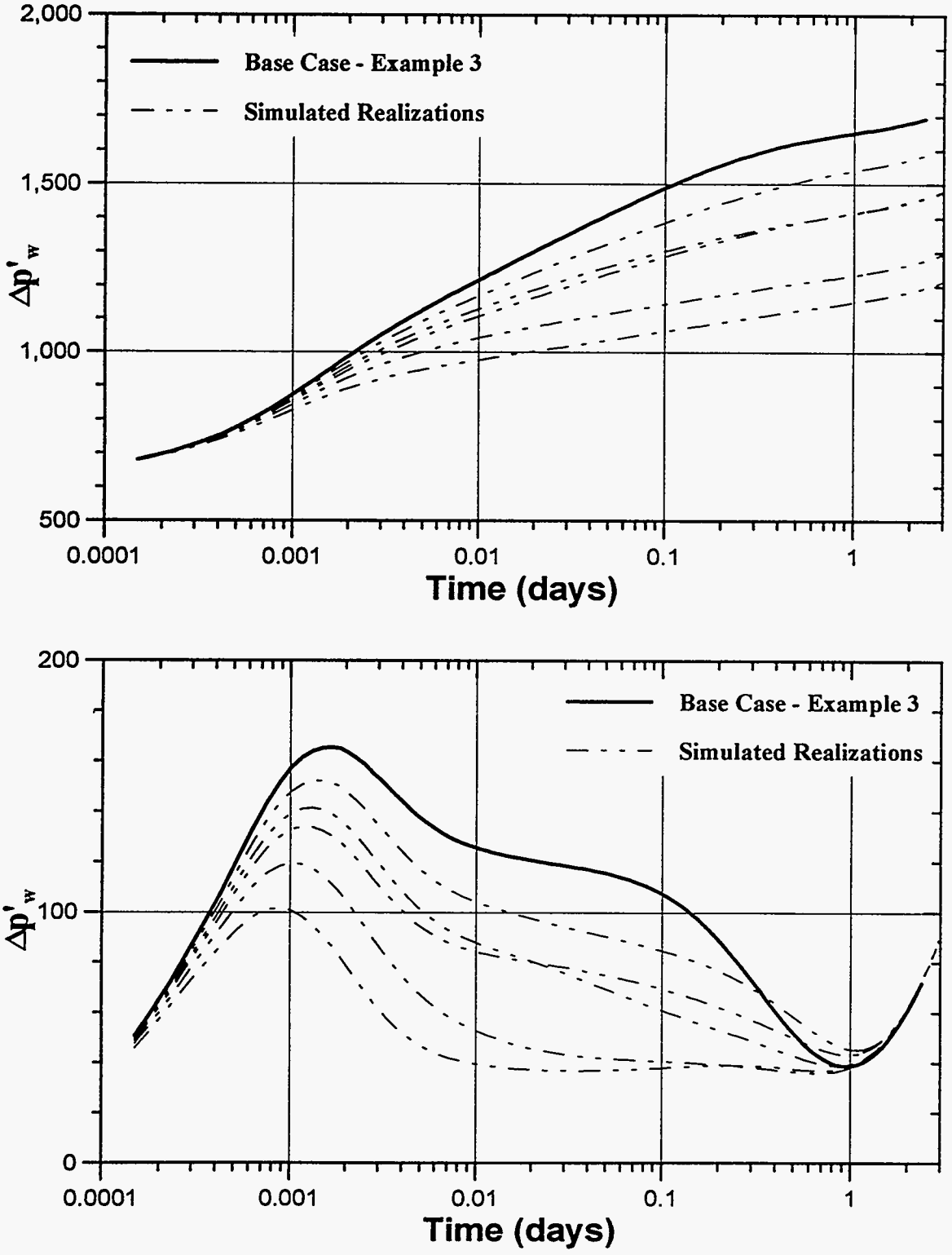

Figure 1.34: Pressures and pressure derivatives of simulated permeability realizations honoring only the variogram constraint compared to the base case response for Example 3.

the reservoir. From a qualitative perspective the permeability values near the center of the reservoir appear to be lower than those further away and the distribution of permeabilities have a radial characteristic. A comparison of pressures and pressure derivatives to the base case are shown in Fig. 1.33. Fig. 1.34 shows pressure responses for the same case for which the well test information is not honored and only the variogram is honored in regenerating the distribution. The pressure response for these cases is reproduced poorly.

The heterogeneity parameters for the three examples are given in Table 1.6.

Table 1.6
Summary of Heterogeneity Parameters for the Examples Investigated

0	$\sigma^2_{\ln k}$	Range (ft)	*HI*	*V*
Example 1	0.92	600	0.124	0.6
Example 2	1.61	310	0.20	0.8
Example 3	0.92	2100	0.45	0.6

The heterogeneity index is defined in Reference 1.31 as:

$$H.I. = \frac{\sigma^2_{\ln k} range}{\Delta x N_x} \tag{1.117}$$

Reference 1.30 defines the Dykstra Parson's coefficient, V, as:

$$V = 1 - \frac{1}{\exp\left(\sigma^2_{\ln k}\right)} \tag{1.118}$$

Note that for examples 1 and 3 the multiple realizations generated consistently reproduce the pressures and pressure derivatives that match the base case pressure response. However, in example 2, the pressure responses of the simulated cases are not as consistent in reproducing the base case response. Note that, in example 2 the variance of the distribution is high and the range is low. For practical purposes, the pressure derivative shown in Fig. 1.30, for this example may be considered as that of a homogeneous reservoir. The "homogeneous" pressure response is also observed for reservoirs in which the permeability distribution is completely random, i.e., the permeability distribution has no spatial correlation. This effect

may apply to example 2 - the base case permeability distribution with the low correlation range shown in Fig. 1.29a results in a relatively constant instantaneous well test permeability, $\hat{k}$, as shown in Fig. 1.35. The equivalent permeability, $\bar{k}_e$, calculated by Oliver's method is also relatively constant as shown in Fig. 1.35. The overall effect is that the pressure response is that of a homogeneous or completely random heterogeneous reservoir. This can be attributed to the low correlation range of the variogram used to develop the description and the reservoir image can interpreted to be that of a permeability distribution that is completely random (see Fig. 1.29a).

ISA Results

In Section 1.1.1, it was observed that both the area-based geometric average, $\bar{k}_g$, and the area-based harmonic average, $\bar{k}_h$, give reasonable approximations to the *ISA* radial permeability distribution, k_{ISA}. We consider examples in which both averaging techniques are used to generate the areal permeability distribution using the simulated annealing procedure given in Section 1.2. The equivalent radial permeability distribution derived by *ISA*, k_{ISA}, the conditioning data, and the univariate and spatial statistics are honored in the annealing algorithm.

The input parameters for the first example are given in Table 1.8. The truth case is the areal permeability distribution shown in Fig. 1.2 with the pressure response shown in Fig. 1.3.

Fig. 1.36b and Fig. 1.36c show the reproduced permeability fields honoring the input constraints. Fig. 1.36a shows the base case for this example. The area based geometric average, $\bar{k}_g$, is used to approximate the *ISA* equivalent permeability, k_{ISA}. Fig. 1.37 compares the pressure responses of the multiple realizations to the base case pressure response.

Fig. 1.38a through Fig. 1.38c shows the reproduced permeability distributions, where the area-based harmonic average, $\bar{k}_h$, is used to approximate k_{ISA}. The base case permeability field is shown in Fig. 1.36a. Fig. 1.39 compares the pressure response of the multiple realizations to the base case pressure response.

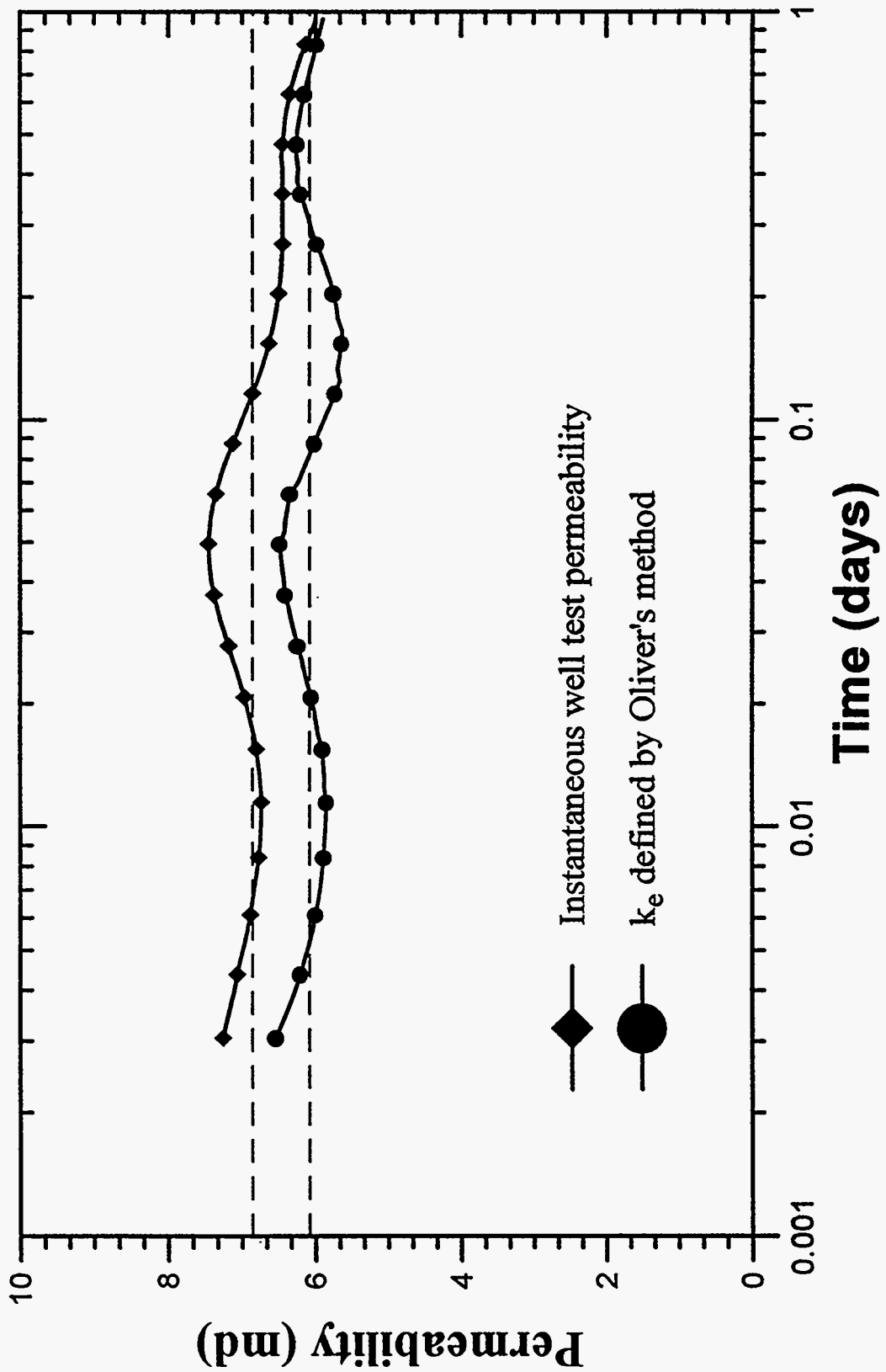

Figure 1.35: Illustrations of the instantaneous well test permeability and the Oliver derived permeability, k_e, for Example 2.

Number of grid blocks (x,y,z)	115x115x1
Block dimensions ($\Delta x, \Delta y, \Delta z$)	35*ft* x 35*ft* x 10*ft*
Variogram type	Spherical - isotropic
Sill	440.0
Range	590.0 *ft*

Well Test Information

n	r_{min}	r_{max}	k_{ISA}
1	64.53	91.40	33.18
2	91.40	115.8	34.28
3	115.8	138.24	23.04
4	138.24	159.92	20.33
5	159.92	181.71	19.72
6	181.71	203.98	19.13
7	203.98	227.00	18.00
8	227.00	250.92	16.51
9	250.92	275.96	15.02
10	275.96	302.98	13.75
11	302.98	330.19	12.74
12	330.19	360.05	12.04
13	360.05	392.24	11.60
14	392.24	427.29	11.40
15	427.29	465.88	11.43
16	465.88	508.73	11.69
17	508.73	556.52	12.05
18	556.52	610.10	12.42
19	610.10	670.46	12.74
20	670.46	738.57	12.99
21	738.57	815.63	13.17
22	815.63	902.83	13.33
23	902.83	1001.22	13.45
24	1001.22	1111.72	13.47
25	1111.72	1234.12	13.23
26	1234.12	1366.35	12.43
27	1366.35	1504.50	10.98

Conditioning Data	$x(ft)$	$y(ft)$	$z(ft)$	$k_{\bar{s}}(md)$
	2012.5	2012.5	17.5	34.3

Table 1.7: Simulated annealing input data - *ISA*.

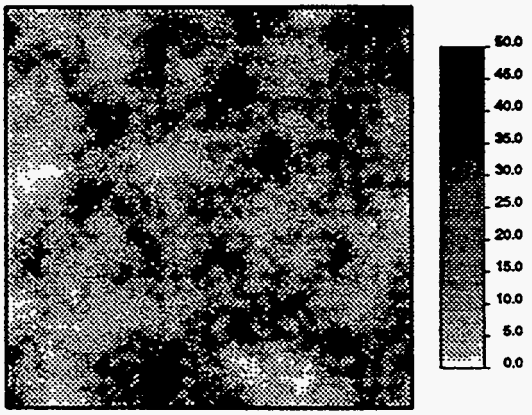

Figure 1.36a: Base case permeability distribution generated by Turning Bands (range = 600 feet, $\sigma^2_{\ln k} = 0.92$).

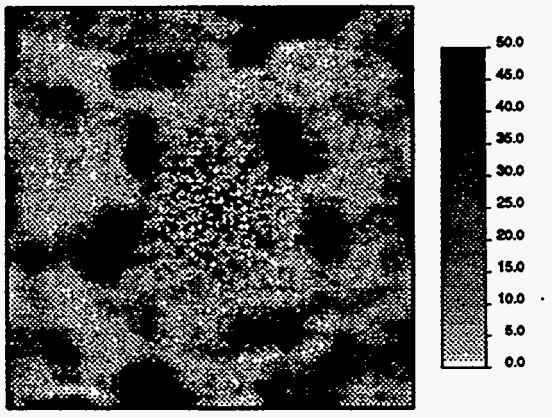

Figure 1.36b: (seed = 1079607).

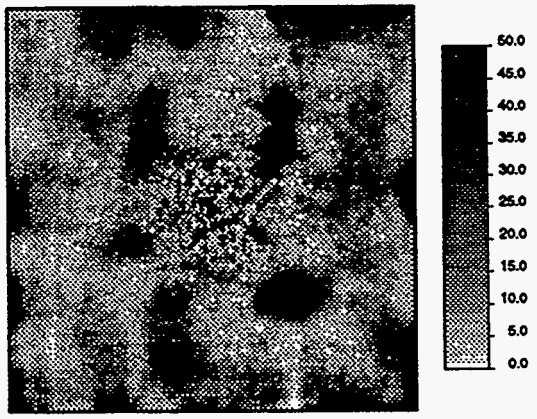

Figure 1.36c: (seed - 1079622).

Figure 1.36b-c: Simulated permeability distributions honoring variogram and *ISA* permeability distribution with a geometric area based permeability average.

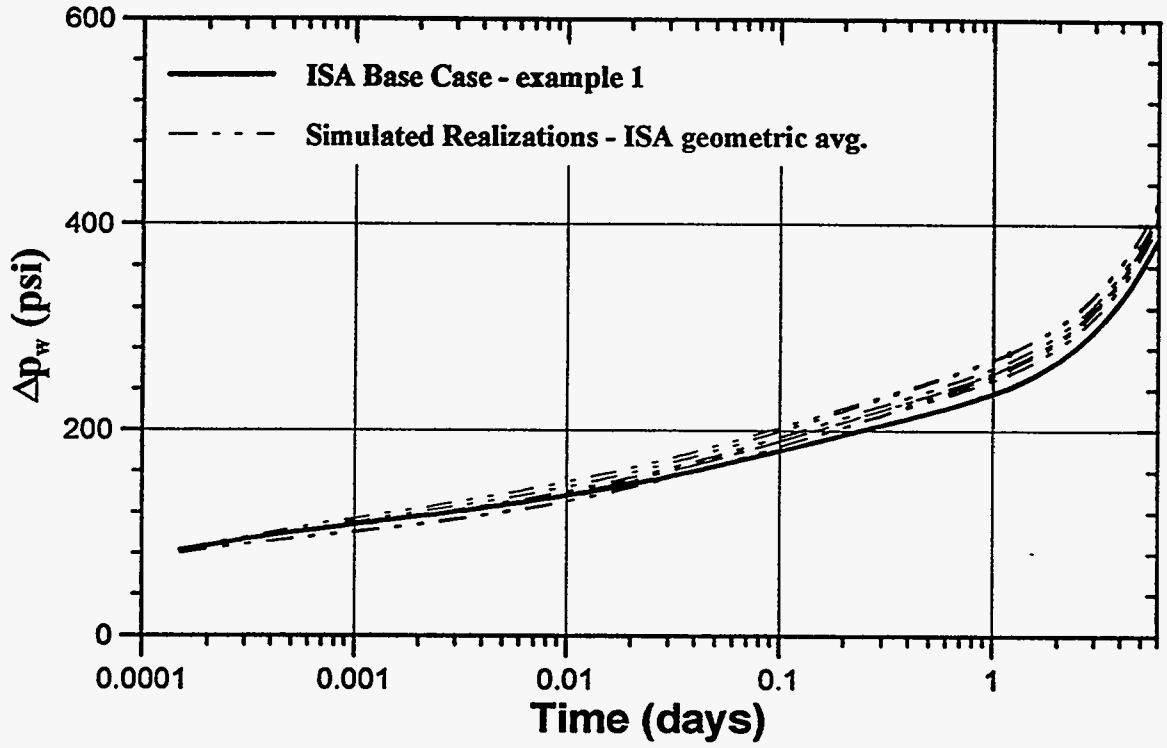

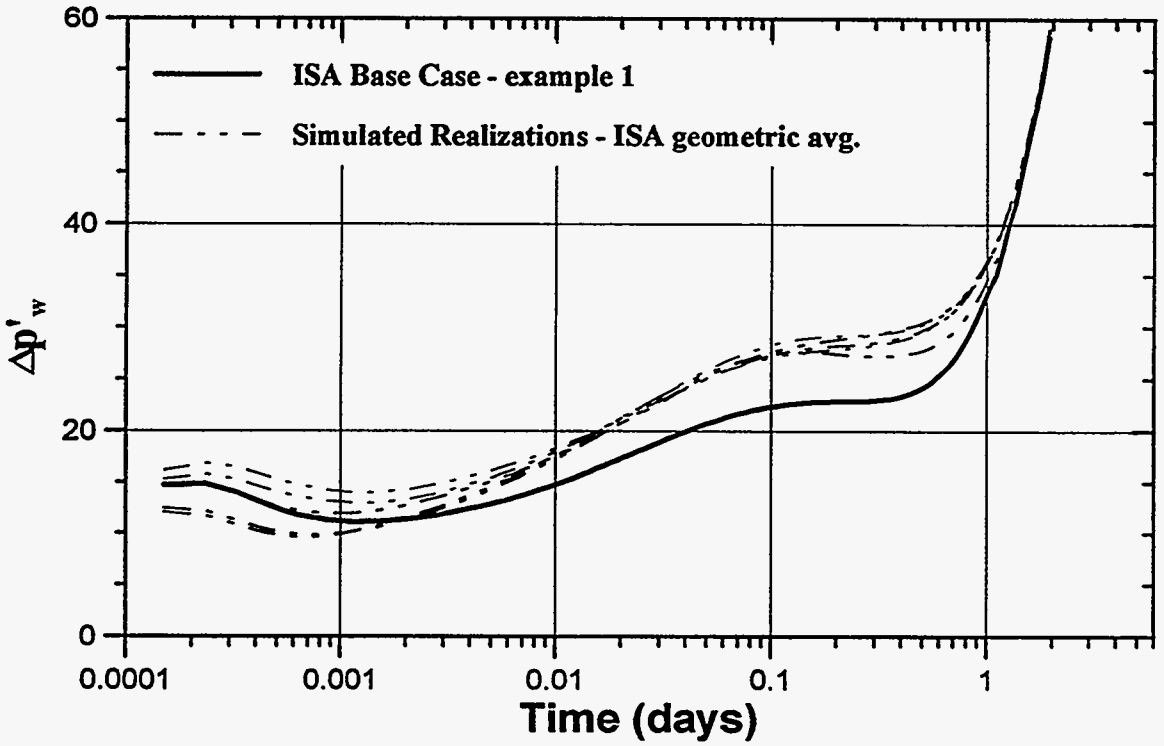

Figure 1.37: Pressures and pressure derivatives of simulated permeability fields honoring variogram and well test constraints compared to the base case response. k_{ISA} is approximated by $\bar{k}_g$.

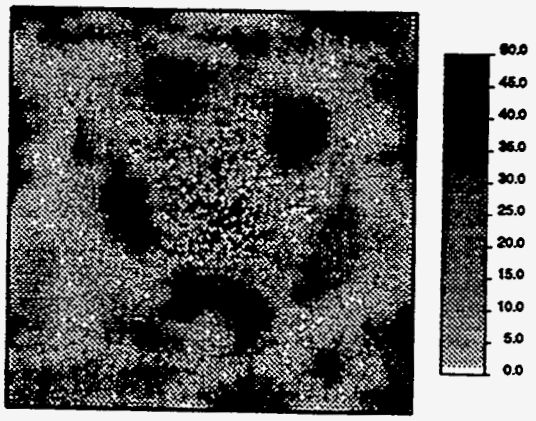

Figure 1.38a: (seed = 1079613).

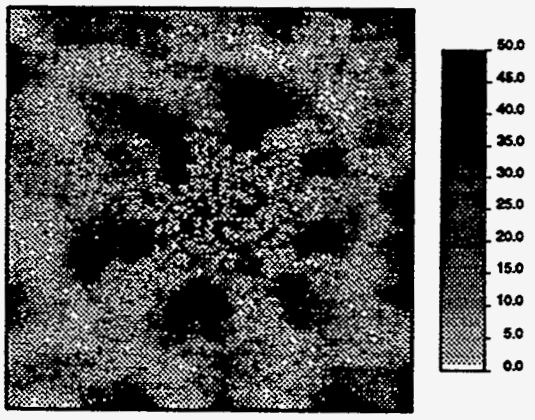

Figure 1.38b: (seed = 1079630).

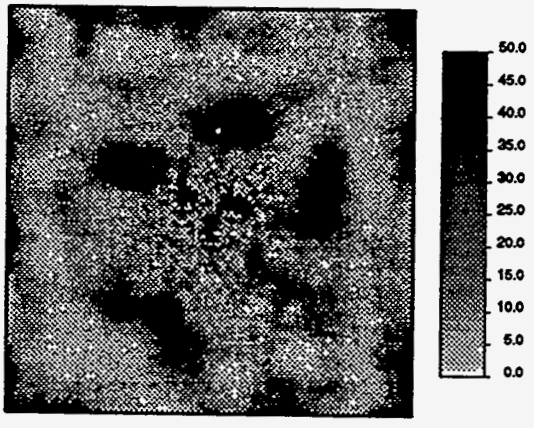

Figure 1.38c: (seed - 1079614).

Figure 1.38a-c: Simulated permeability distributions honoring the variogram and the *ISA* radial permeability distribution with an area based harmonic permeability average.

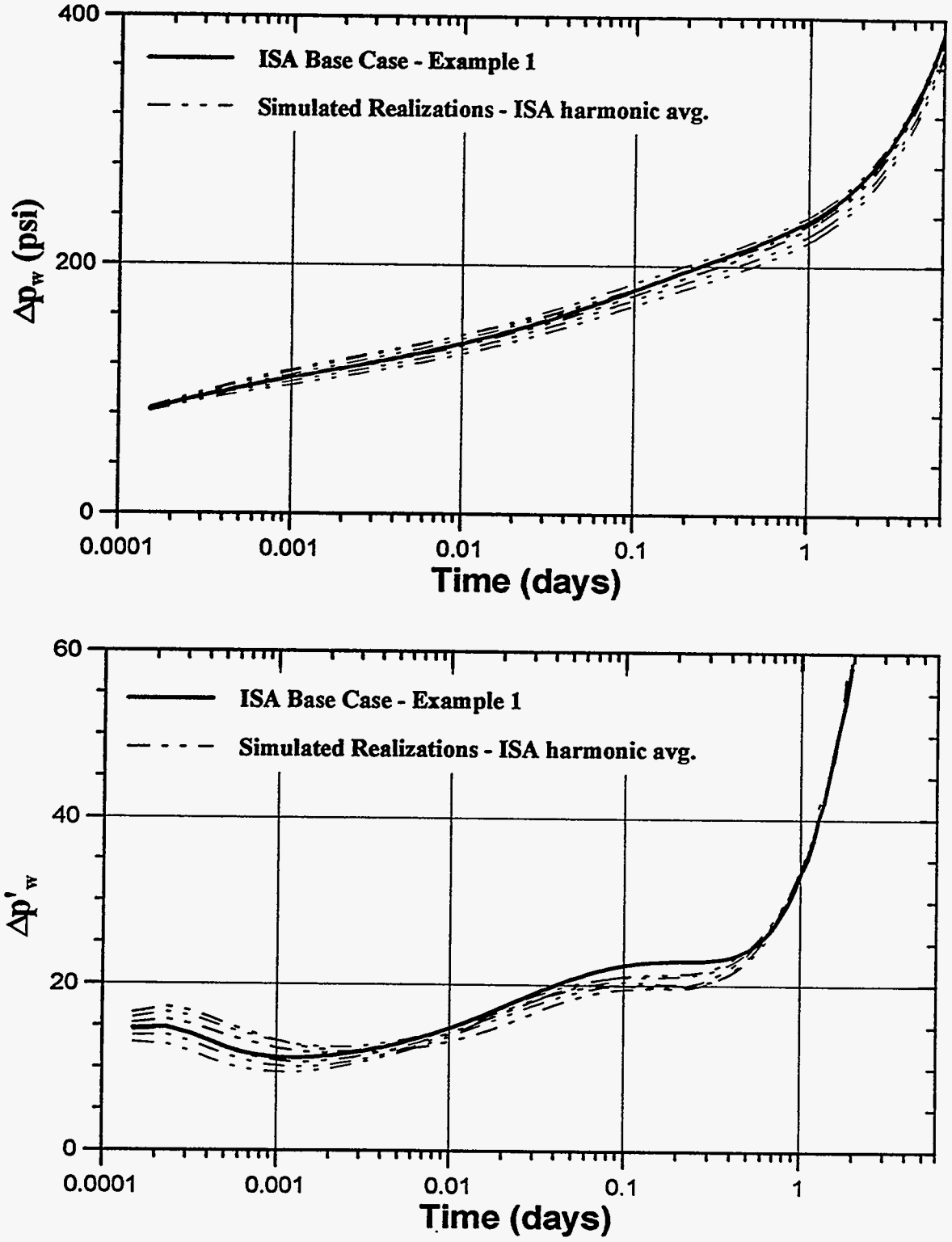

Figure 1.39: Pressures and pressure derivatives of simulated permeability realizations honoring variogram and well test constraints compared to the base case response. k_{ISA} is approximated by $\bar{k}_h$.

For this example, we observe that when we perform harmonic averaging of grid block permeabilities within our radii of investigation to produce our distribution, the resulting pressure response matches the base case pressure response better than geometric averaging of grid block permeabilities.

Fig. 1.40 shows the pressure and pressure derivative response compared to the base response for a second example. In this case geometric averaging of grid block permeabilities was used. Fig. 1.41 shows the pressure response for the same example, where harmonic averaging of grid block permeabilities is used. When harmonic averaging is used the pressure derivative is better reproduced; however, the geometric averaging reproduces the pressure better.

In general, for all the realizations generated by the two methods to incorporate well test information (Oliver or *ISA* procedure), we observe that the reproduced images of the permeability distribution do not agree with the base case images. We also observe that the reproduced permeability images are characteristically radial in appearance. This is expected, since the simulated annealing algorithm is constrained only to the variogram and a radial permeability distribution. In order to generate a more realistic image we would have to include more constraints, such as more conditioning data and production data.

Computational Cost of Each Method

The advantage of using the *ISA* algorithm is that the simulated annealing procedure considering *ISA* is faster than that considering the Oliver procedure. This is clearly illustrated in Fig. 1.42; for the same convergence tolerance, the Oliver procedure requires greater CPU time. We also observe that for the *ISA* procedure the update of the well test component of the energy function consumes less time than the update of the variogram component, where as in the Oliver method the well test update consumes the most time. This is because *ISA* defines an equivalent permeability within an inner and outer radius of investigation and there is no overlap of the different radii of investigation.

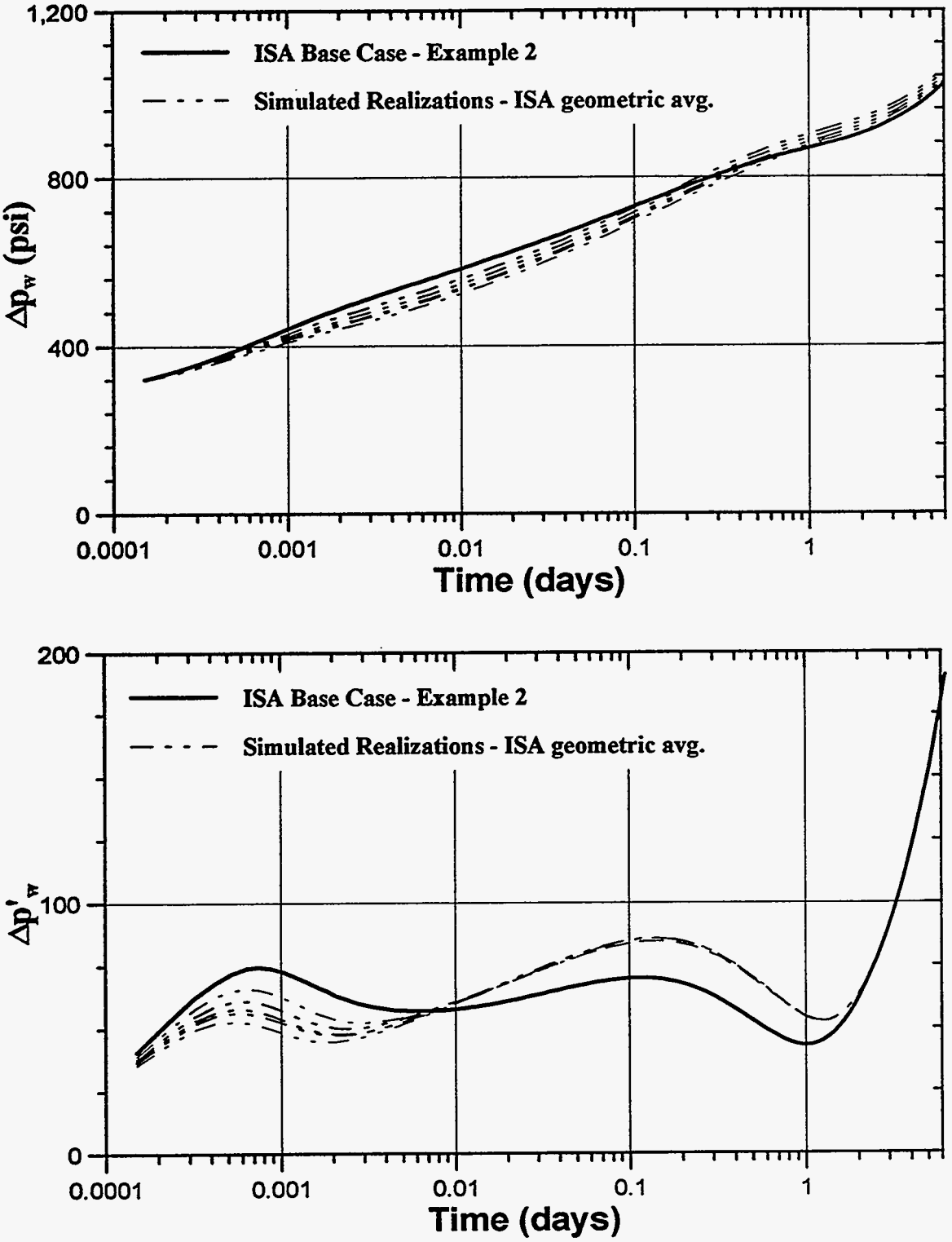

Figure 1.40: Pressures and pressure derivatives of simulated permeability realizations honoring variogram and well test constraints compared to the base case response. k_{ISA} is approximated by $\bar{k}_g$.

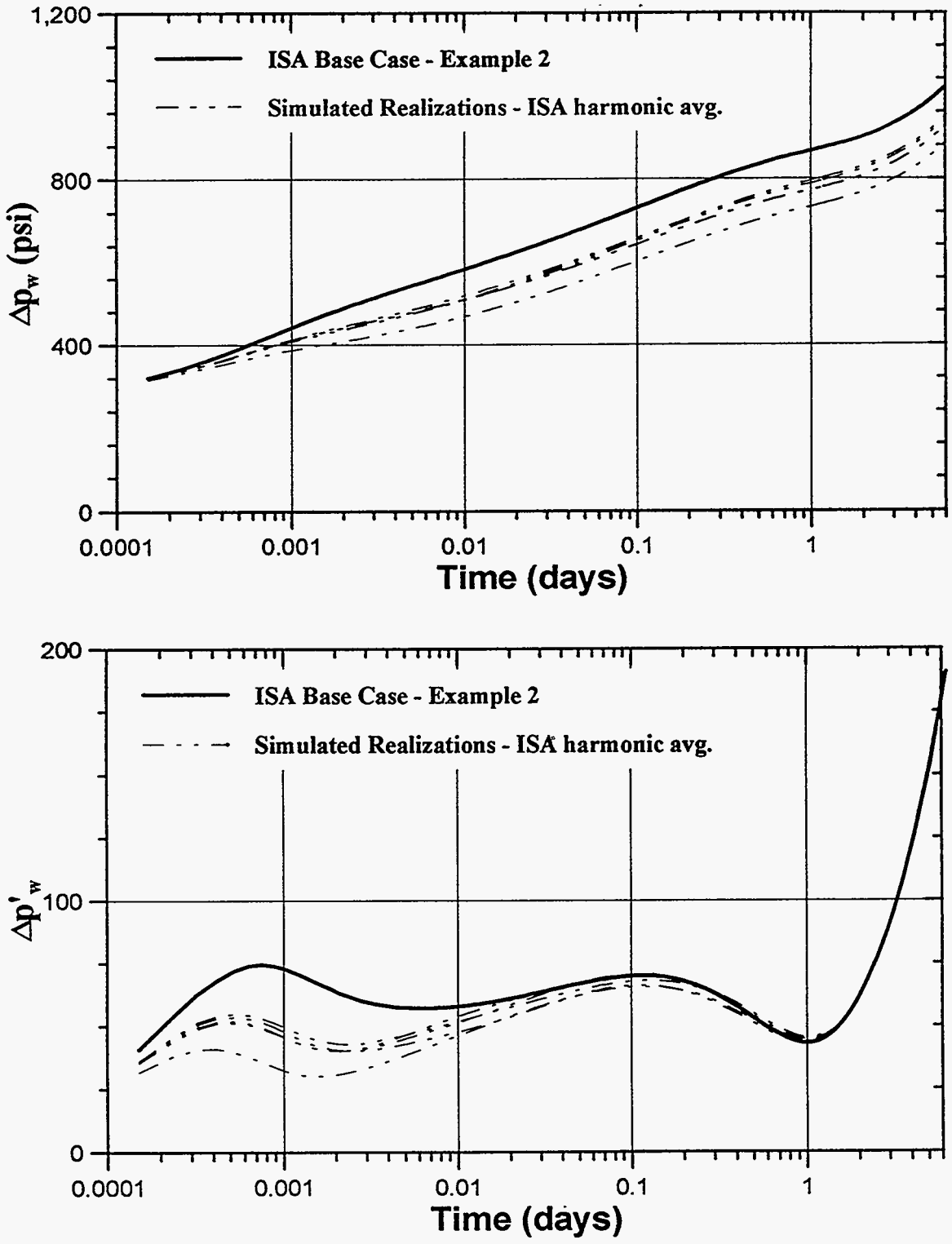

Figure 1.41: Pressures and pressure derivatives of simulated permeability realizations honoring variogram and well test constraints compared to the base case response. k_{ISA} is approximated by $\bar{k}_h$.

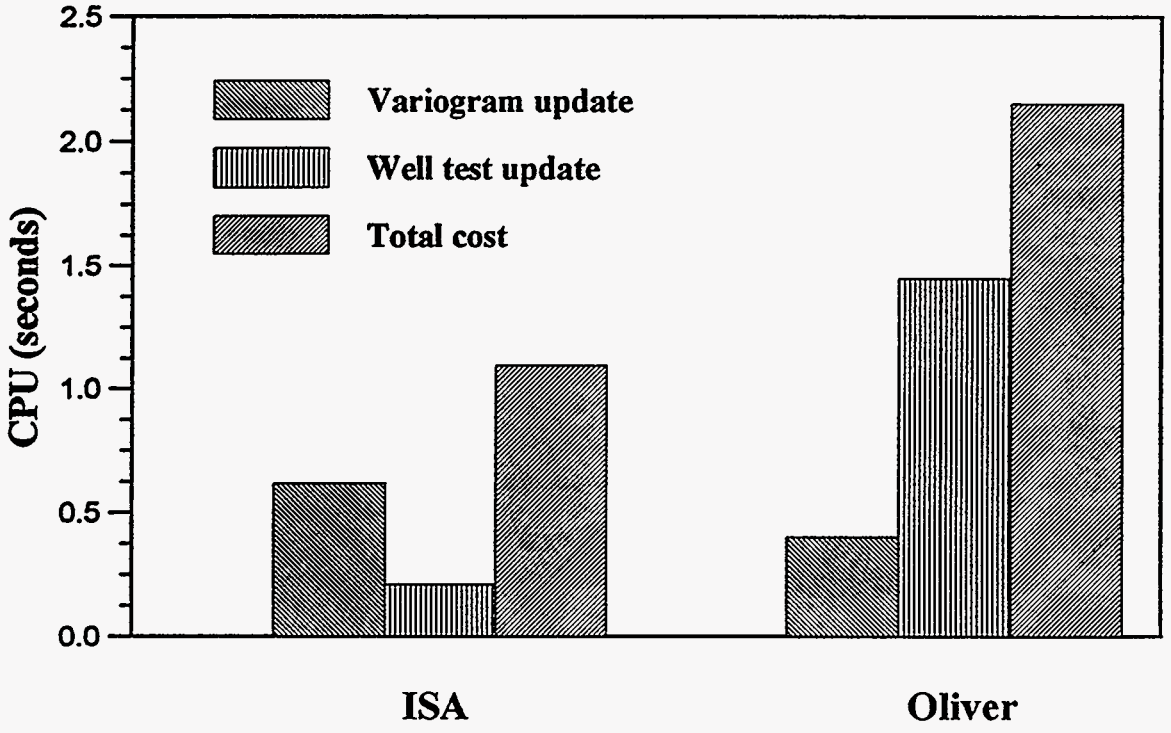

Figure 1.42: Illustration of the CPU consumption of the simulated annealing algorithm for the *ISA* and Oliver method.

Effect of Porosity Variation

So far, we have presented cases in which we have studied heterogeneous reservoirs with variations in permeability only. In this section, we investigate the effect of porosity variations on the pressure response of a reservoir during a drawdown test. In our analysis we consider a procedure similar to that outlined by Feitosa.[1.8] He considered permeability and porosity heterogeneities for an $r-\theta$ distribution. We consider permeability heterogeneities for an x-y areal distribution.

We generate two base case heterogeneous systems. For the first case, we generate a heterogeneous reservoir with variable permeability and porosity. The base case permeability distribution is shown in Fig. 1.43 and the histogram of the distribution in Fig. 1.44. A permeability-porosity transform is performed using the following equation given in Reference 1.32:

$$\phi = \left[\frac{\sqrt{k}S_{wi}}{100}\right]^{1/2.25} \tag{1.119}$$

where S_{wi} is the irreducible water saturation, which in our case is assumed to be 0.3.

In the second case, we consider the same permeability distribution shown in Fig. 1.43 with a constant porosity of 0.144. This is the average porosity of the transformed porosity distribution determined by Eq. 1.119.

For both cases a fluid simulation is performed in the heterogeneous medium using ECL 100. The resulting pressures and pressure derivatives are shown in Fig. 1.45. Observe that the differences in the pressure and pressure derivative between the two simulations are relatively small.

We also consider an example in which we examine heterogeneities in porosity and a constant permeability of 20 md. The fluid simulation of a drawdown in this heterogeneous medium is shown in Fig. 1.46. Note that the pressure derivative is approximately constant.

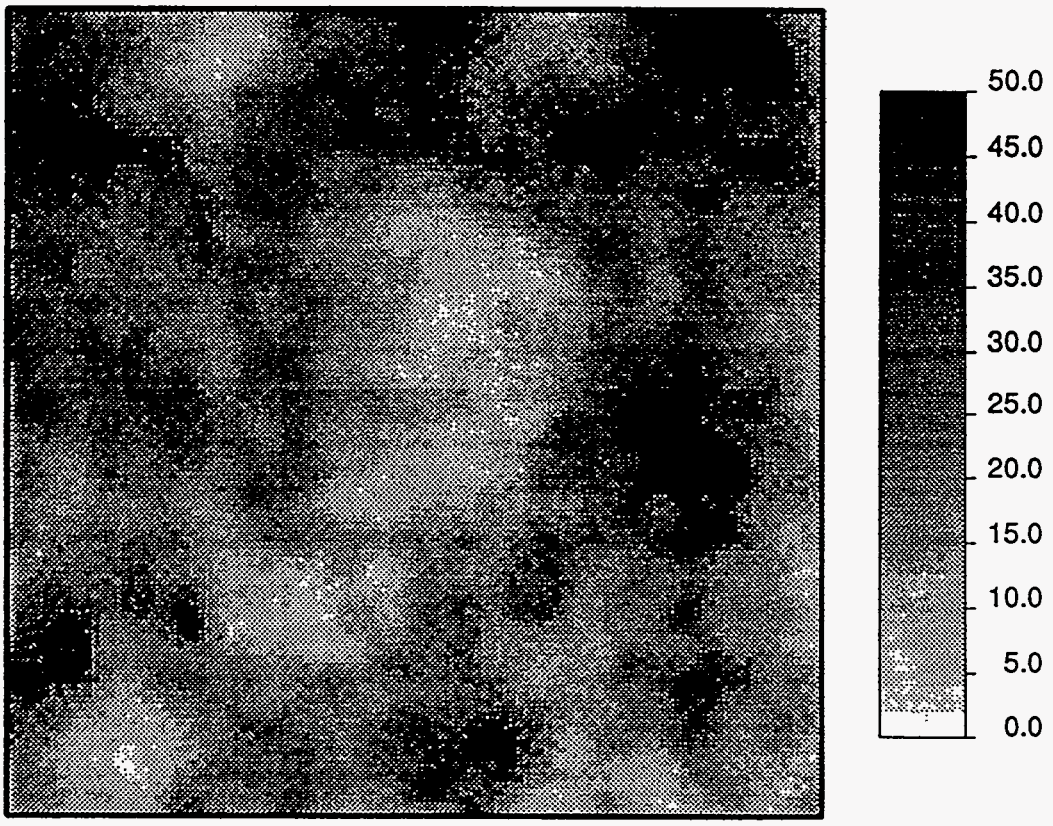

Figure 1.43: Base case permeability distribution, for investigating the effect of porosity. Generated by Turning Bands (seed = -18, range = 960 feet, $\sigma^2_{\ln k} = 0.92$, $\bar{k} = 20$ md).

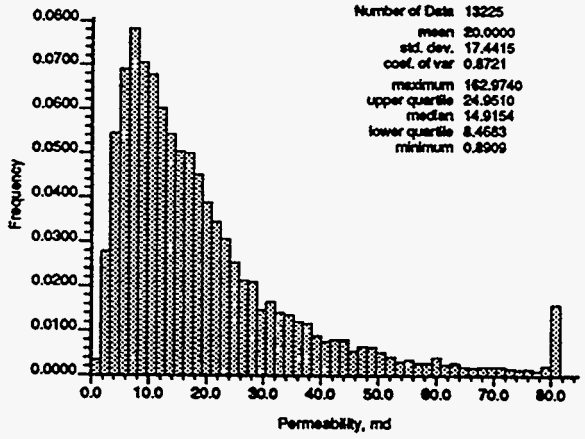

Permeability histogram

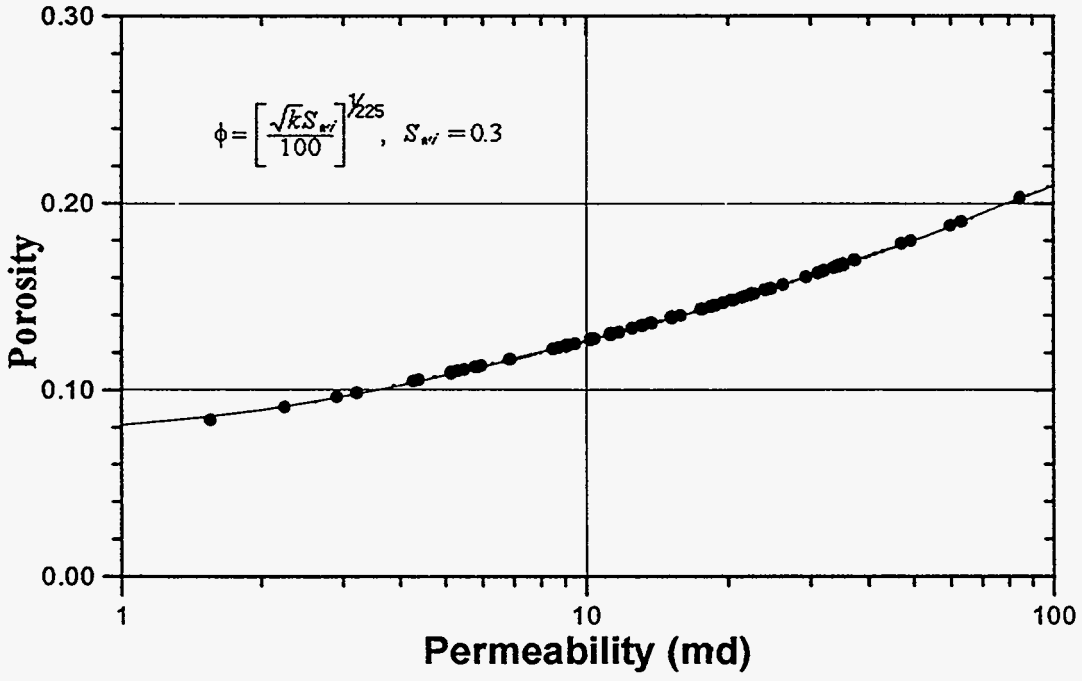

Figure 1.44: Permeability - porosity transformations.

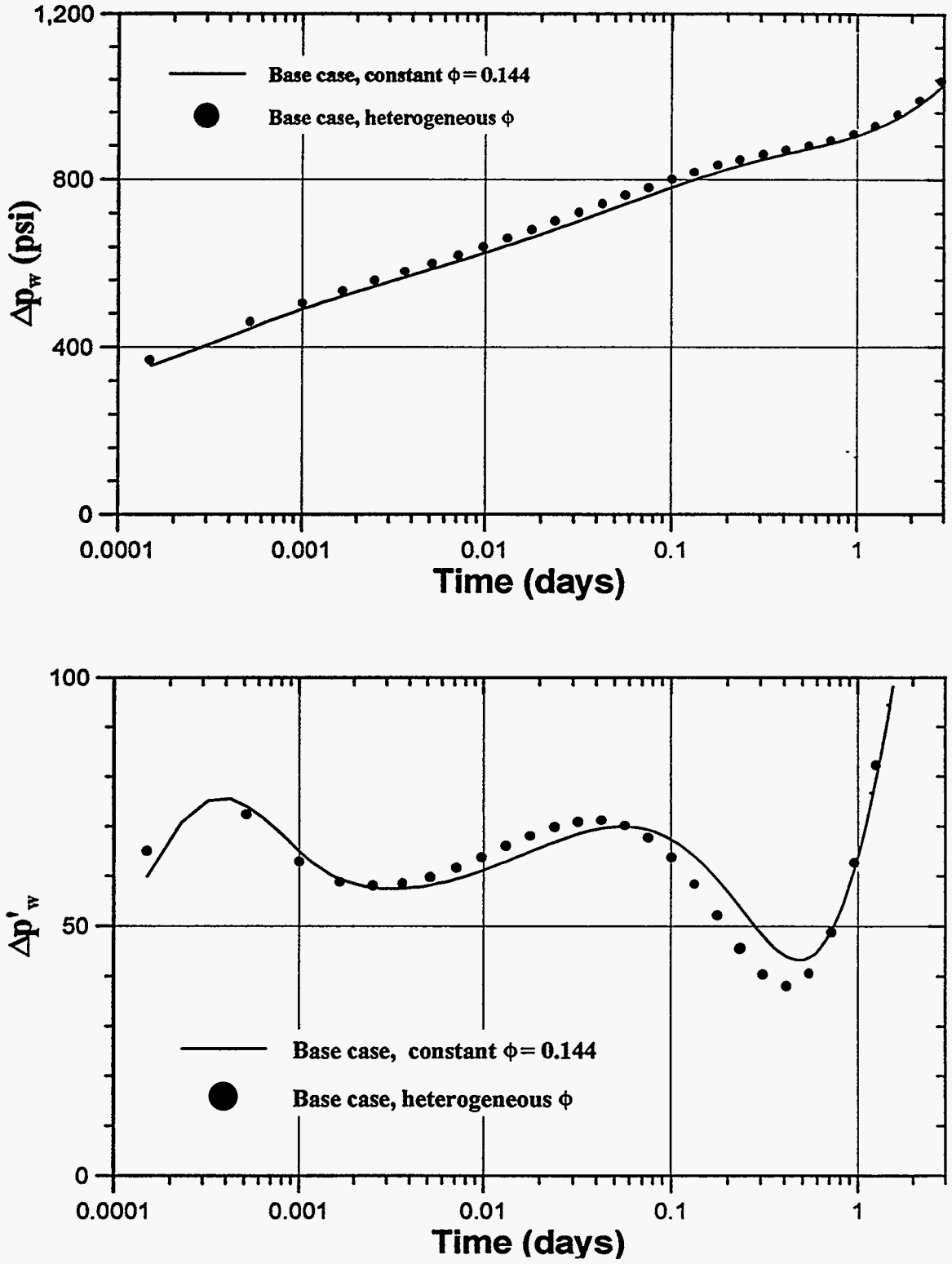

Figure 1.45: Comparison of pressures and pressure derivatives between heterogeneious distributions with a variation in permeability and porosity, and only permeability.

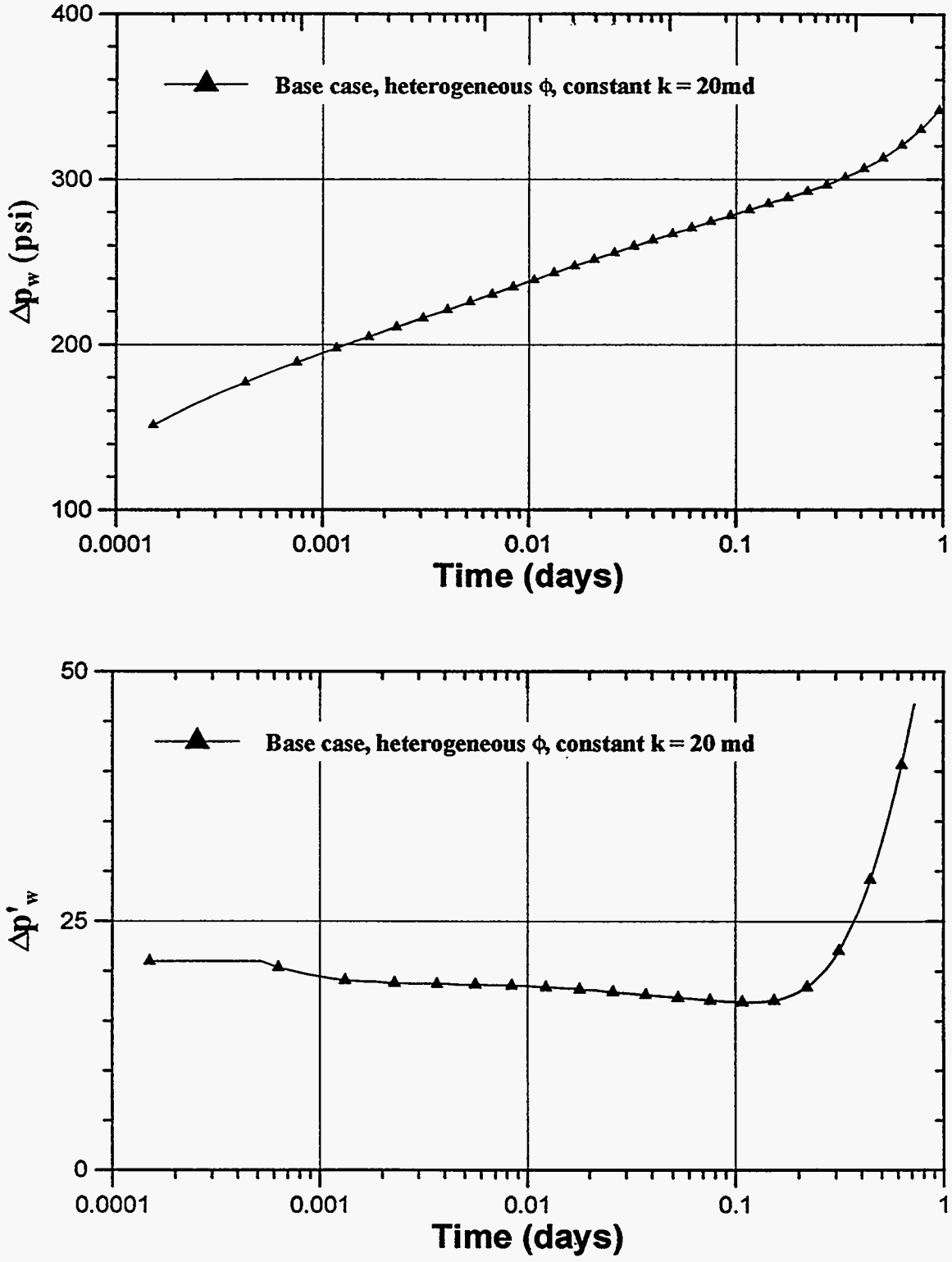

Figure 1.46: Pressures and pressure derivatives of a heterogeneous medium with variable porosity and a constant permeability of 20 md.

We solve the inverse problem of describing the permeability distribution assuming that univariate and spatial statistics, and the pressure response during a drawdown of the reservoir are known. We use the pressure response of the reservoir in which both the permeability and porosity vary.

The method of simulated annealing using Oliver's solution is used to develop the permeability distribution. The input parameters to the simulated annealing algorithm are given in Table 1.8. The resulting permeability field is shown in Fig. 1.47. Porosity values are assigned to corresponding grid blocks using the transform equation (Eq. 1.119). A fluid flow simulation is then performed in the heterogeneous porous medium. The results of the pressure responses for the case in which both permeability and porosity vary and also the case for which only permeability varies and porosity is constant at 0.144 are shown in Fig. 1.48. These are compared to the base case pressure response.

From our analysis, we can conclude that, for practical purposes, porosity variations have a minimal effect on the pressure response of a reservoir. This is important, since reservoir descriptions must not only describe heterogeneities in permeability but also in porosity; therefore, the effect of porosity in the use of describing reservoir heterogeneity with well test information must be minimal.

Effect and Incorporation of Anisotropy

The application of anisotropy to geostatistics is defined by the variogram model. Variogram models define zonal and/or geometric anisotropy (Fig. 1.49).[1.33] A zonal anisotropy is one in which the sill value changes in direction and the range remains constant. In geometric anisotropy, the sill remains constant and the range varies - see Fig. 1.49. Variogram anisotropy may be observed in river channel deposits, where the spatial continuity of reservoir properties is greater in one direction than another. The effect of anisotropy on the fluid flow in a reservoir will affect the pressure response of a well test. In this study we consider an anisotropic reservoir drained by a single well producing at a constant rate at the center of the reservoir. In order to incorporate the effect of anisotropy on the pressure response, we develop a gridding scheme for the simulated annealing algorithm which allows for the incorporation of anisotropy in an isotropic domain.[1.1]

Number of grid blocks (x,y,z)	115x115x1
Block dimensions ($\Delta x, \Delta y, \Delta z$)	35*ft* x 35*ft* x 10*ft*
Variogram type	Spherical - isotropic
Sill	263.0
Range (*ft*)	600.0

Well Test Information

n	t (days)	r_{min}	r_{max}	$\hat{k}$
1	1.67×10^{-3}	5.4	106.1	6.14
2	3.06×10^{-3}	7.4	143.7	6.21
3	5.62×10^{-3}	10.0	195.0	5.98
4	1.24×10^{-2}	14.8	288.8	5.52
5	2.56×10^{-2}	21.4	418.2	5.14
6	4.95×10^{-2}	29.7	578.2	5.09
7	9.38×10^{-2}	40.8	796.2	5.57
8	1.54×10^{-1}	52.3	1019.4	6.52
9	2.35×10^{-1}	64.6	1259.2	7.90
10	3.33×10^{-1}	77.0	1501.1	9.15
11	4.42×10^{-1}	88.6	1727.4	9.43
12	5.45×10^{-1}	98.4	1919.1	8.87

Conditioning Data	$x(ft)$	$y(ft)$	$z(ft)$	$k_z(md)$
	2012.5	2012.5	17.5	6.95

Table 1.8: Simulated annealing input data - example considering heterogeneous medium in porosity and permeability.

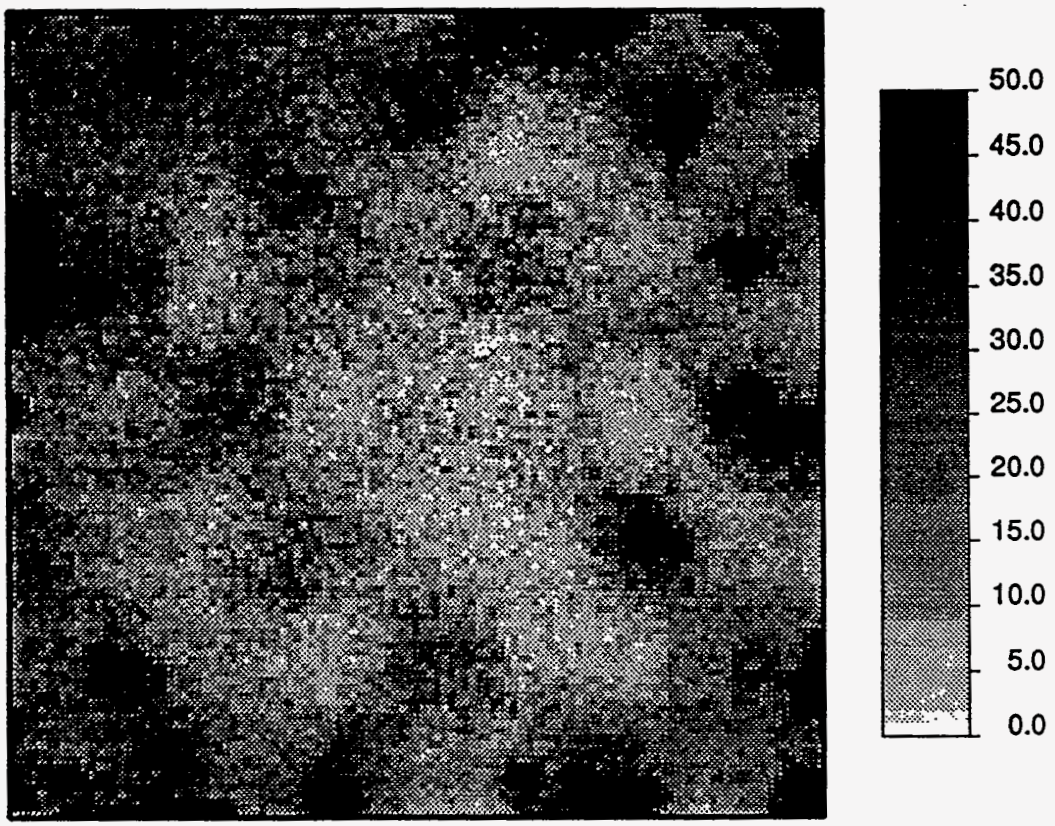

Figure 1.47: Simulated permeability distribution honoring the constraints given in Table 1.8.

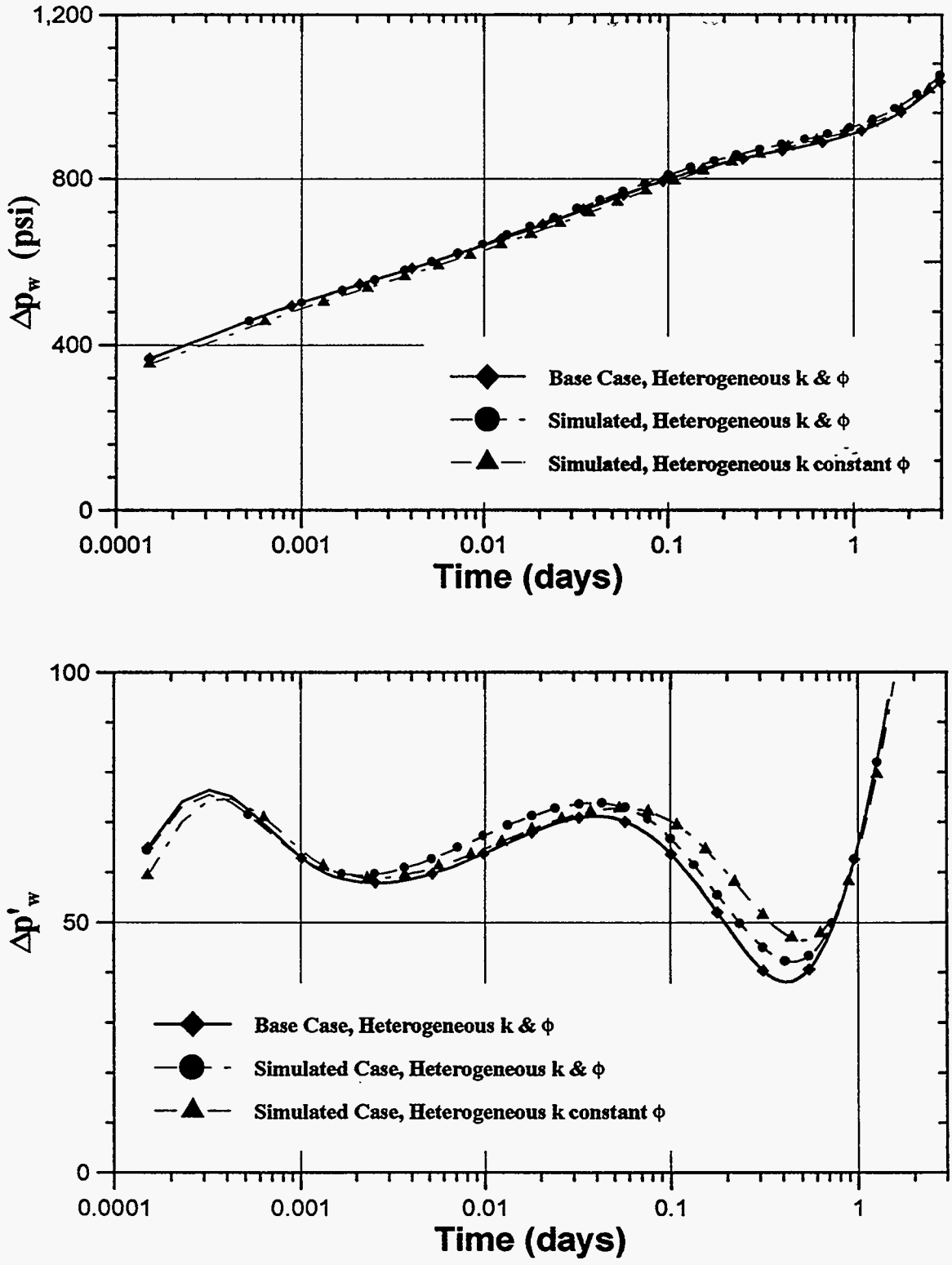

Figure 1.48: Comparison of the pressure response between the base case and simulated heterogeneous systems.

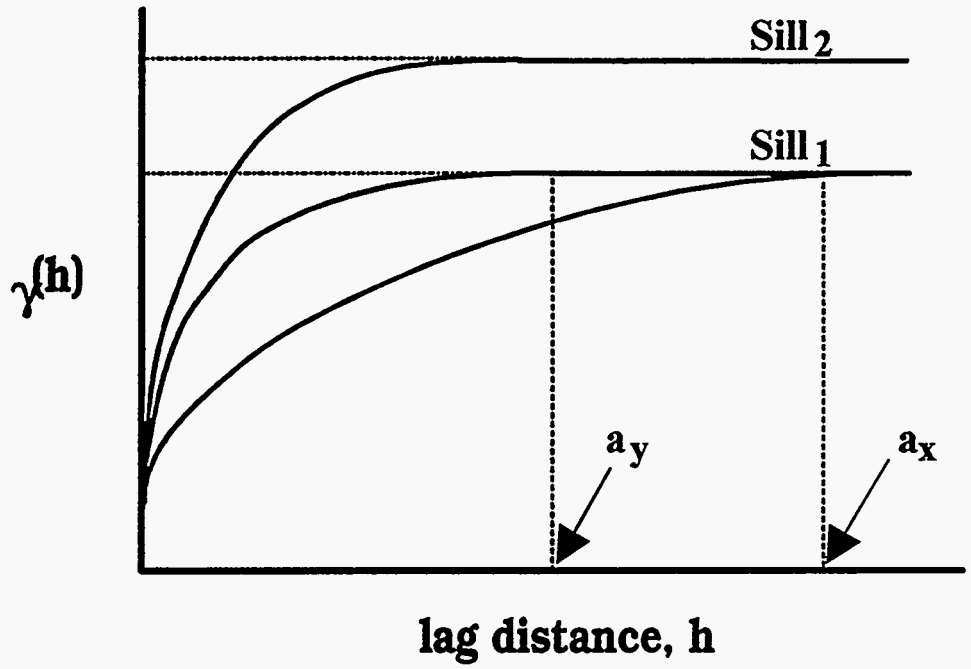

Figure 1.49: Variogram models illustrating zonal and geometric anisotropy.

Base Cases

Base case reservoir descriptions, considering geometric anisotropy, are developed using the simulated annealing algorithm. The reservoir dimensions and anisotropic variogram models for base case permeability distributions are given in Table 1.9.

Table 1.9
Summary of Variogram Parameters used to Generate the Base Case Anisotropic Permeability Distributions

	Range in x-direction (ft)	Range in y-direction (ft)	Sill x-direction	Sill y-direction
Example 1	1500	550	350	350
Example 2	3200	550	400	400
Example 3	3200	420	150	150

We consider only geometric anisotropy in these examples. In order to be able to incorporate the permeability information from a well test into the simulated annealing algorithm, we consider a variogram model in which the range in the x-direction is greater than that in the y-direction $(a_x > a_y)$. This simplifies the inverse problem. The base case permeability distributions for the three examples are shown in Fig. 1.50. The corresponding pressure and pressure derivative response for these examples are shown in Fig. 1.51. For these examples, the reservoir descriptions are created by forcing a permeability streak along the x-direction such that the producing well lies within the streak. This was achieved by using high permeability values along the location of the streak as conditioning values. The resulting permeability distribution resembles that of a channel sand reservoir. Fig. 1.52 and Fig. 1.53 show equipotential contours of the flow simulation, for example 1, at 0.15 days and 0.29 days, respectively. Note that the equi-potential pressure profile in the reservoir is approximately circular closer to the center of the reservoir and elliptical further away. The major axis of the ellipse is along the x-direction.

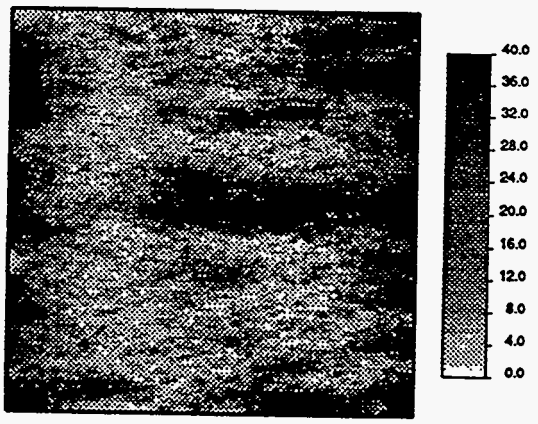

Example 1 - $a_x = 1500$ ft, $a_y = 550$ ft

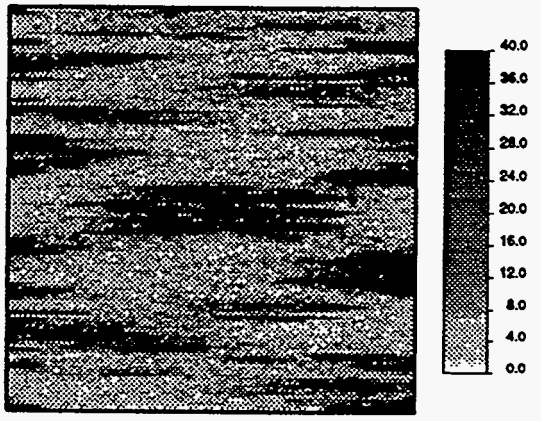

Example 2 - $a_x = 3200$ ft, $a_y = 550$ ft

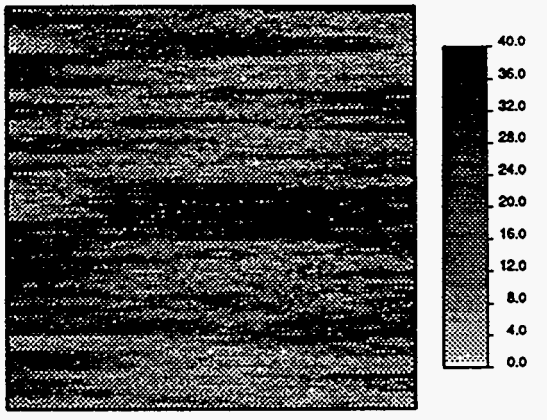

Example 3 - $a_x = 3200$ ft, $a_y = 450$ ft

Figure 1.50: Base case anisotropic permeability distributions.

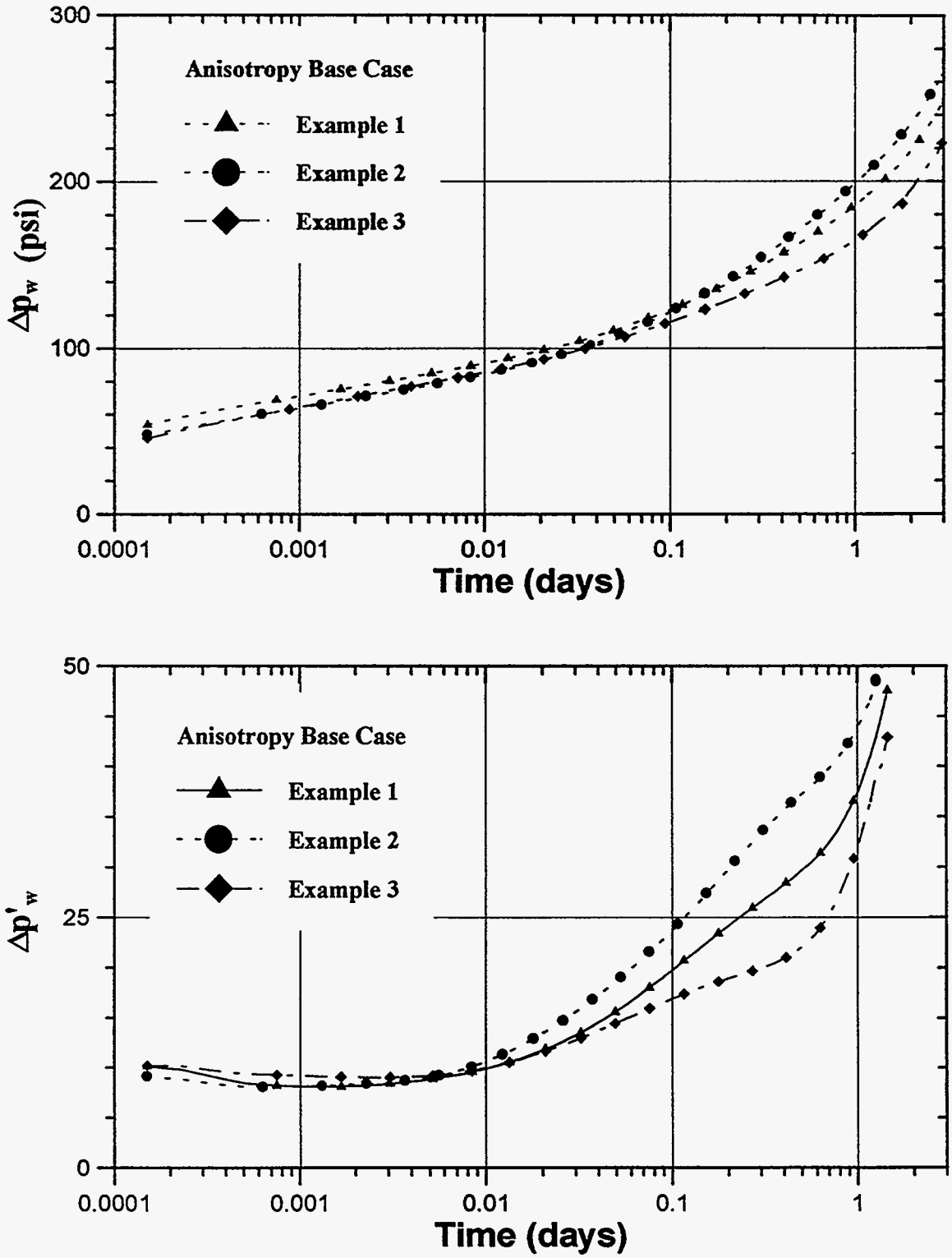

Figure 1.51: Pressures and pressure derivative for the anisotropic permeability fields shown in Figure 1.50.

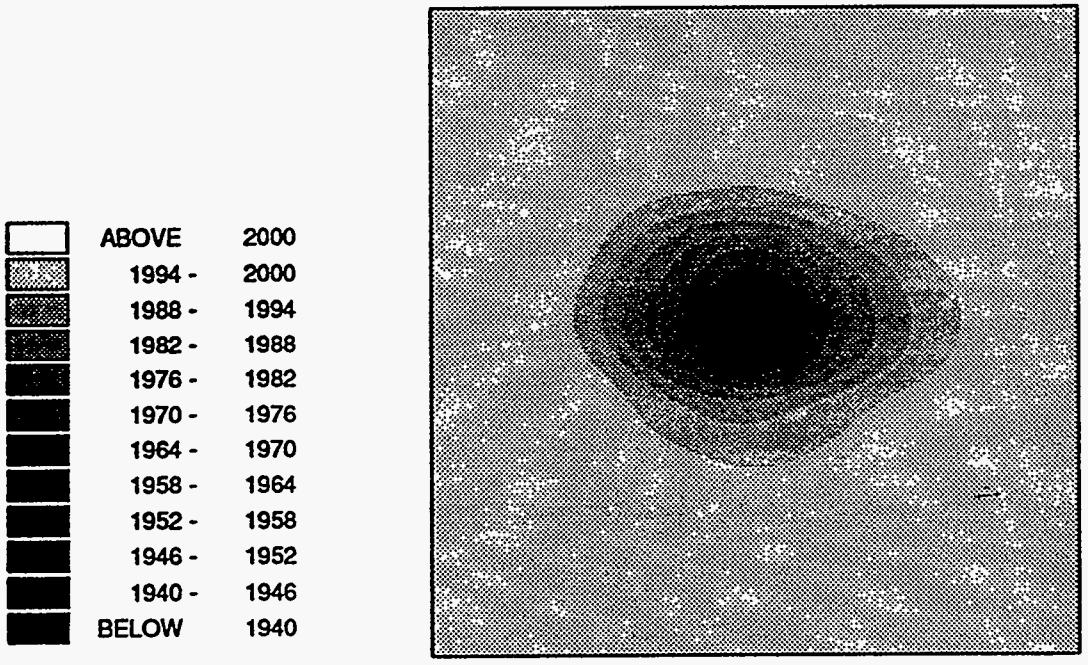

Figure 1.52: Pressure contours for the permeability field shown in Example 1 at a time step of 0.15 days during the flow simulation.

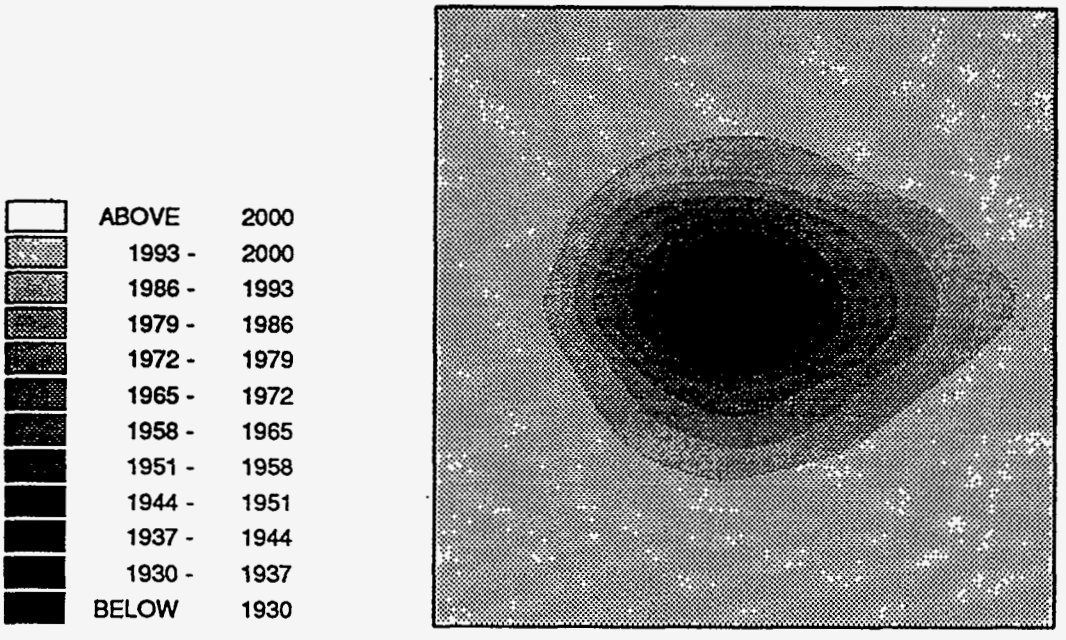

Figure 1.53: Pressure contours for the permeability field in Example 1 at a time step of 0.29 days during the flow simulation.

Reservoir Description Incorporating Anisotropy

The method of simulated annealing along with Oliver's solution is used to develop reservoir descriptions that honor anisotropy. The method must honor the anisotropic variogram models and the permeability information obtained from the pressure response of an anisotropic reservoir.

In order to facilitate a solution to the problem, we only consider anisotropy defined in two principle directions: x and y. Fig. 1.52 and Fig. 1.53 show that a reservoir drained by a single well, in which the range of the variogram in the x-direction is greater than that in the y-direction causes the equipotential profile to be elliptical. The major axis of the drainage ellipse is along the variogram direction of higher range.

For a steady state anisotropic problem, Muskat[1.34] considers an anisotropic medium in which $k_x \neq k_y$. Muskat claims that the effect of anisotropy in a porous media can be replaced by an equivalent *shrinking* or *expansion* of the coordinate system, for which the transformed coordinates from (x, y) to (x', y') are defined by:

$$x' = \frac{x}{\sqrt{k_x}} \text{ and } y' = \frac{y}{\sqrt{k_y}} \tag{1.120}$$

By analogy we hypothesize that a similar transformation of coordinates should apply to an areally heterogeneous anisotropic medium. For our study we consider geometric anisotropy in which the range of the x-direction variogram (a_x) is different from the range of the y-direction variogram (a_y). Note that for our example in which $a_x > a_y$ results in the elliptical drainage profile. This effect will also be observed if $k_x > k_y$. Although on a local scale (individual grid blocks) we have an isotropic medium, on a larger scale, due to variogram anisotropy, we have an apparent anisotropic permeability medium. We hypothesize that this variogram anisotropy ratio is representative of the apparent large scale permeability anisotropy. By analogy to Eq. 1.120 we assume the following transformation of grid block dimensions:

$$\Delta x' = \frac{\Delta x}{\sqrt{a_x}} \text{ and } \Delta y' = \frac{\Delta y}{\sqrt{a_y}} \tag{1.121}$$

For our study since $\Delta x = \Delta y$ the anisotropy factor can be defined as:

$$a_f = \frac{\Delta y'}{\Delta x'} = \sqrt{\frac{a_x}{a_y}} \tag{1.122}$$

In order to incorporate the anisotropy effect, due to the pressure response, the grid dimensions are modified as illustrated in Fig. 1.54 and are redefined by:

$$\Delta x' = \Delta x \text{ and } \Delta y' = a_f \Delta y \tag{1.123}$$

The grid dimension modifications are only for permeability averaging within annular regions, and do *not* apply when the spatial statistics are honored. Fig. 1.54 shows that if the major axis of the ellipse is along the x-direction and the minor axis of the ellipse is along the y-direction, then the reservoir, for the purpose of radial permeability averaging, is elongated in the y-direction. The overall effect is the incorporation of an elliptical drainage of the reservoir.

Results and Discussions on the Incorporation of Anisotropy

The grid dimensions modifications in permeability averaging are incorporated with Oliver's procedure in the simulated annealing algorithm to reproduce permeability distributions. We present one example in this report (Example 1 in Table 1.9). The details regarding other examples can be found elsewhere.[1.1]

Eq. 1.122 is used to calculate the anisotropy factor. For example 1 ($a_x = 1500$ and $a_y = 550$) $a_f = 1.65$. In the simulated annealing procedure the grid dimensions for the purpose of radial permeability averaging are modified by Eq. 1.123. Fig. 1.55 shows examples of permeability fields generated honoring the anisotropic variogram and pressure response of the anisotropic reservoir in example 1. In Fig. 1.56 the pressures and pressure derivatives of the simulated cases are compared to the base case pressure. We also consider the pressure response of simulated permeability fields where anisotropy in permeability averaging is not considered, i.e., an anisotropy factor of 1.0 is used. The pressure responses of these simulations are shown in Fig. 1.57.

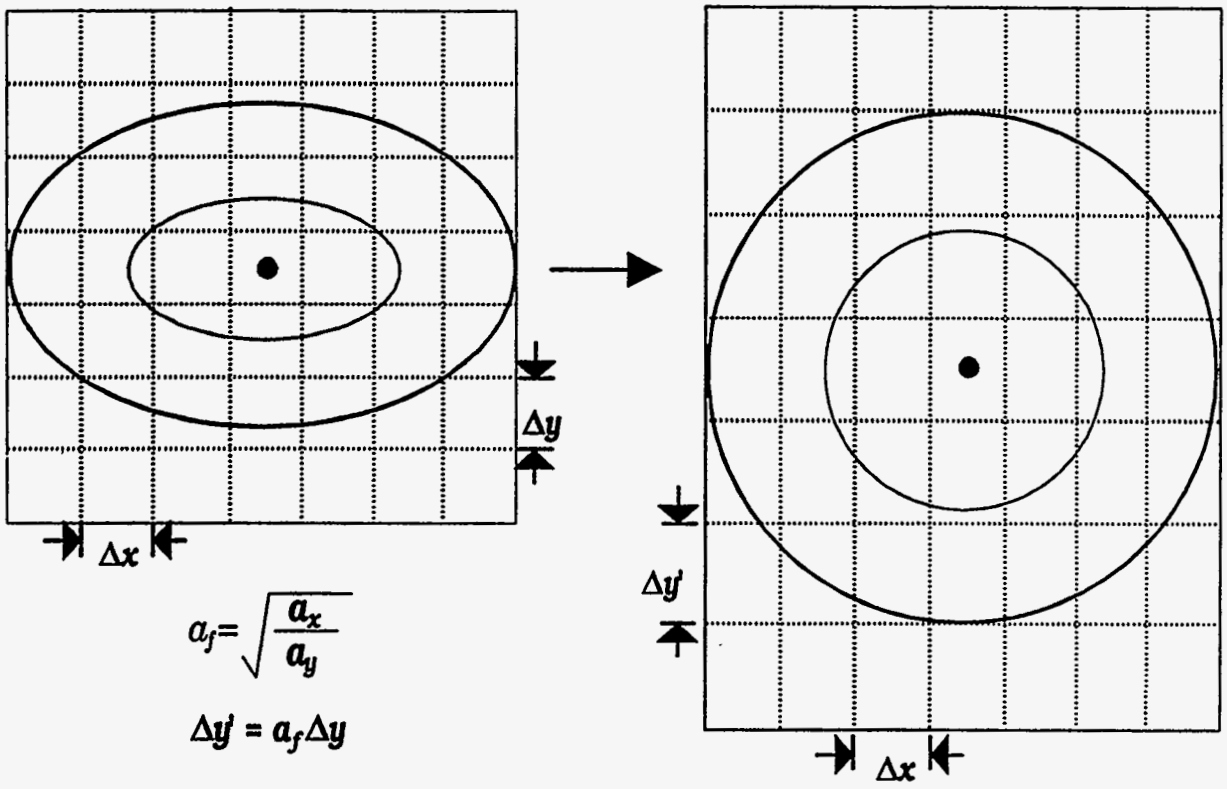

Figure 1.54: Transformation of areal grid to incorporate anisotropy from well-test information.

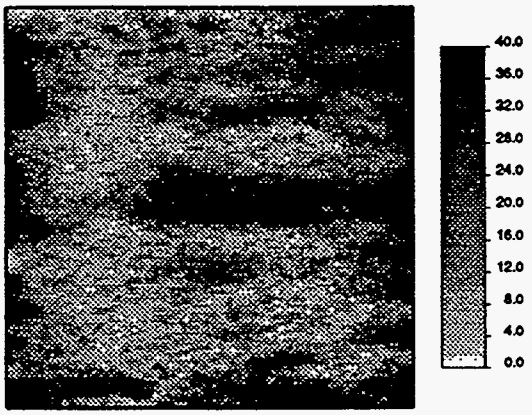

Figure 1.55a: Base case permeability distribution a_x = 1500 feet, a_y = 550 feet.

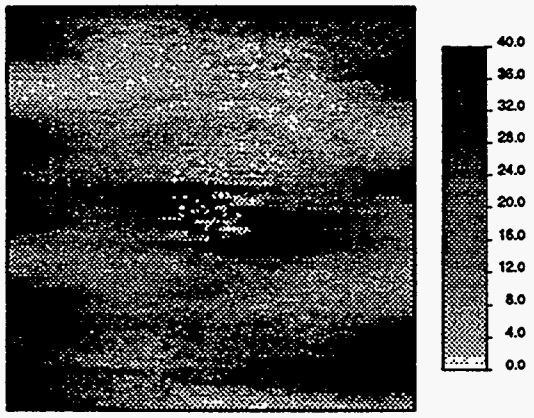

Figure 1.55b: (seed = 1079614).

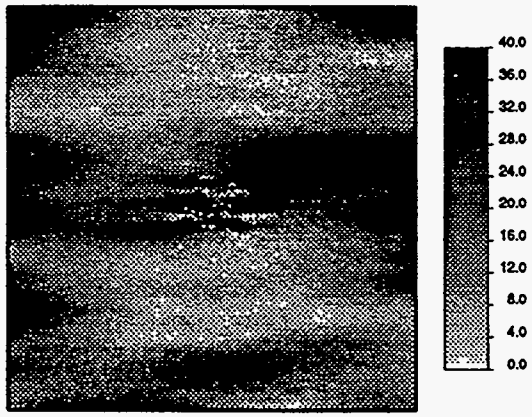

Figure 1.55c: (seed - 1079618).

Figure 1.55a-c: Base case and simulated permeability distributions incorporating well test and variogram anisotropy for Example 1.

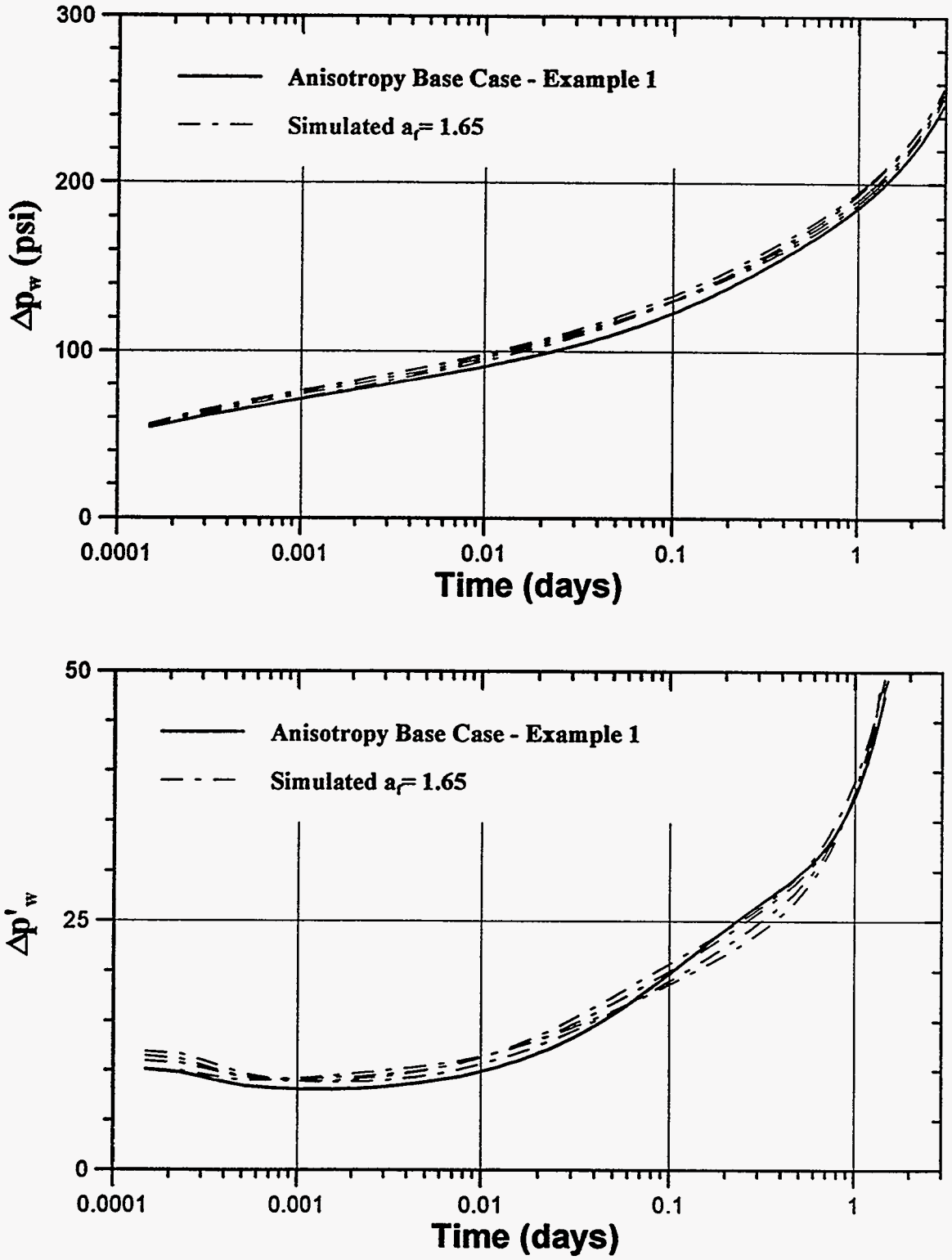

Figure 1.56: Comparison of pressure and pressure derivatives between the base case and simulated distributions honoring anisotropic variogram and radial anisotropy well test information (a_f = 1.65) for Example 1.

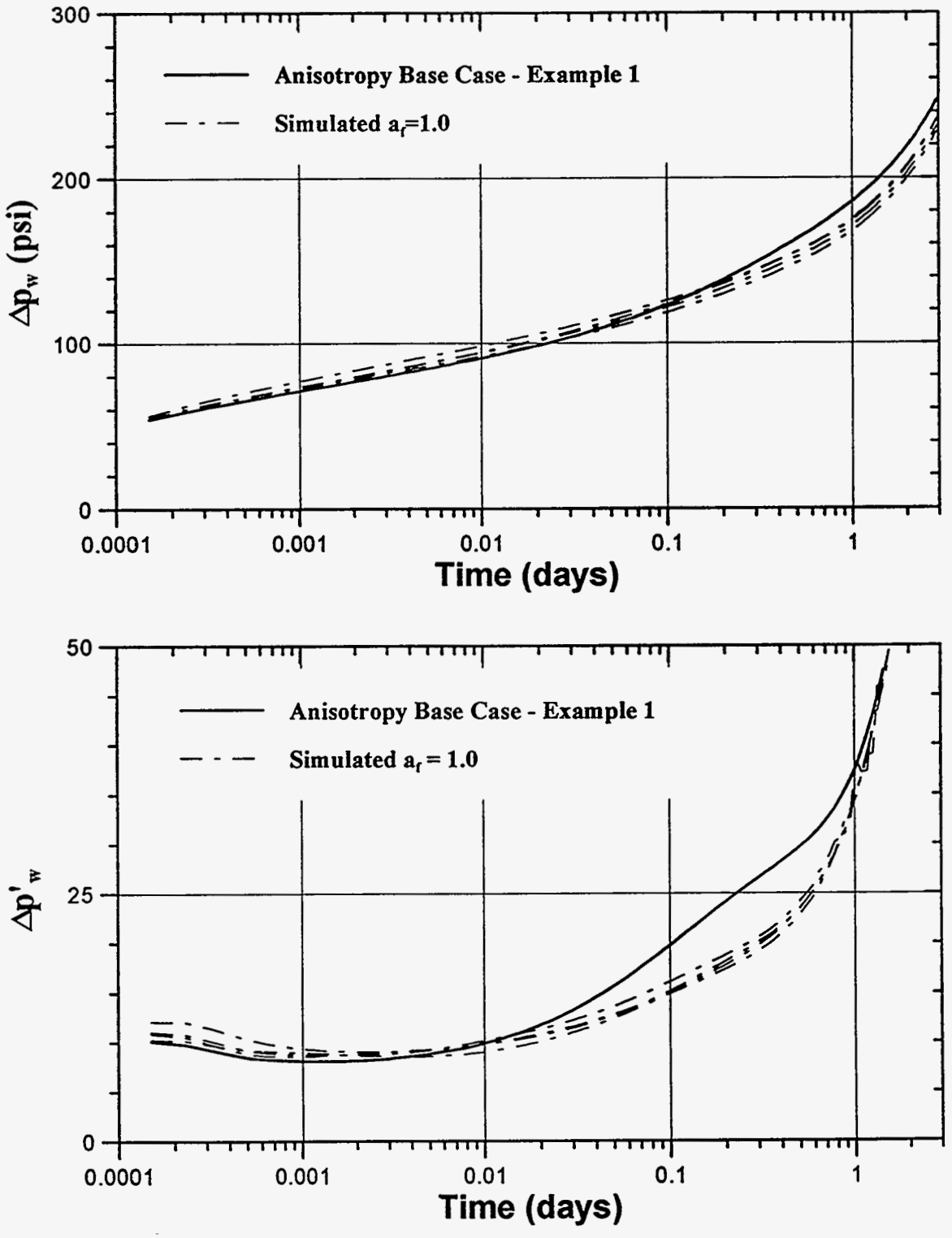

Figure 1.57: Comparison of pressure and pressure derivatives between the base case and simulated distributions honoring anisotropic variogram and radial anisotropy well test information (a_f = 1.0) for Example 1.

For the example studied, we observe that the pressure response is consistent from simulation to simulation. Note from the example that, when the anisotropy effect due to the pressure response is considered in permeability averaging, the pressure response matches the base case pressure response better than when anisotropy is not considered. The improvement in the match is especially noticeable at later times, before pseudo steady-state flow occurs. This implies that, for this and other examples, we were better able to capture the elliptical flow phenomena due to anisotropy by considering the defined anisotropy ratio in the radial permeability averaging.

Overall, for the three examples investigated, the inclusion of anisotropy in permeability averaging during the simulated annealing process improves the reproduction of the pressure response. Therefore, the effect of variogram anisotropy on the pressure response can be properly accounted for.

1.3.2 Incorporation of Production Performance

Primary Production Performance

The synthetic example studied is the same as that given in Section 1.1.2 of this report. The reservoir properties and dimensions are given in Table 1.4. The simulated annealing objective function was modified to include both effective near-well permeability and the permeability variogram as constraints.

Twenty-one permeability realizations were generated, all honoring conventional constraints (well block permeabilities, the permeability frequency distribution and variogram) and the additional k_{NW} constraint. The permeability fields were then used to simulate 10 years of primary performance for the 13-well system previously defined. The resulting performance of the central producer, for all 21 cases, is shown in Fig. 1.58. A comparison of Fig. 1.13 and Fig. 1.58 demonstrates the impact of k_{NW} on well performance. Inclusion of k_{NW} as a conditional simulation constraint is seen to result in permeability fields which have essentially the same primary performance characteristics. These permeability realizations truly can be referred to as "equally probable" since they honor all of the existing data. Uncertainty in future reservoir performance has been minimized, thus a more

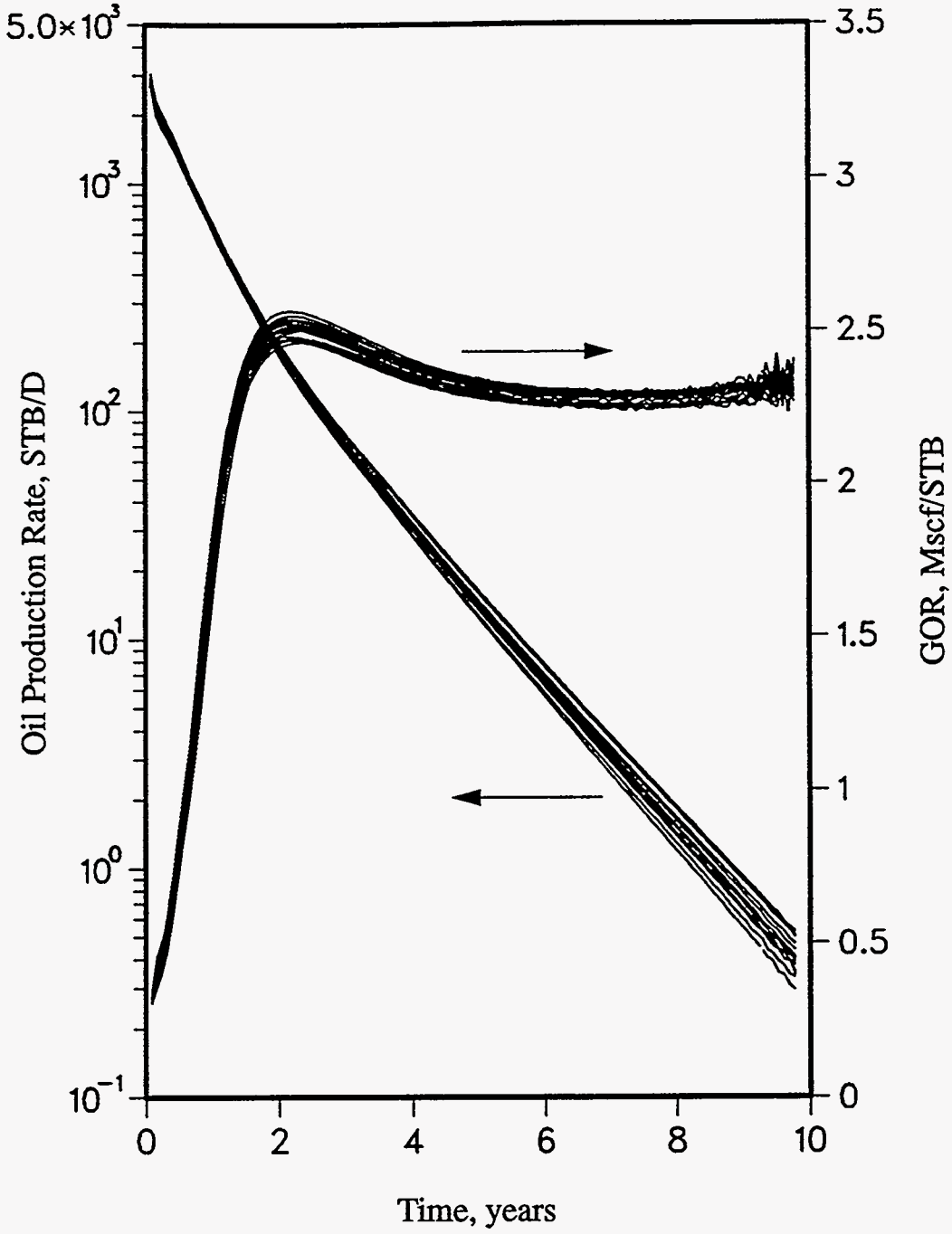

Figure 1.58: Primary performance of central producer for k_{NW} contrained realizations; more heterogeneous permeability distribution.

realistic reservoir modeling study can be performed for quantifying uncertainty. Fortunately, not only can good estimates of k_{NW} be obtained via well tests, but such information is typically available early in the life of a well.

Porosity Heterogeneities

The impact of porosity heterogeneities on well performance was also investigated. Heterogeneous porosity fields were generated by transforming the two sets of 21 permeability fields described above using the following information:

$$\varphi(i,j) = \frac{\left[\log\left(\left[k(i,j)\right] - 0.667\right)\right]}{6.667} \tag{1.124}$$

where $\varphi(i,j)$ and $k(i,j)$ represent the porosity and permeability, respectively, for the ith column and jth row. This normal distribution has a mean of 0.20 and a standard deviation of 0.060; 68% of the values lie between 0.14 and 0.26.

Analogous to the k_{NW} study, flow simulations were performed for each of the 21 porosity fields. A uniform permeability of 100 md was used in each case. The central producer oil rate and GOR vs. time profiles for all 21 flow simulations are presented in Fig. 1.59. The spread in primary performance between each case is very small - certainly not large enough to be able to quantify porosity heterogeneities from well performance characteristics. It can be concluded that a porosity heterogeneity constraint cannot be developed because of the insensitivity of primary well performance to porosity heterogeneities.

A global multiplier of 1.20 was applied to each $\varphi(i,j)$ for all 21 porosity fields to increase the average porosity from 0.20 to 0.24. Flow simulations were once again made using the revised porosity fields. Fig. 1.60 compares the primary performance of the central producer for both sets of porosity fields (average porosities of 0.20 and 0.24). It can be seen that there is significant difference between the two sets of runs, but an insignificant difference within each set. Although porosity heterogeneities cannot be identified from primary performance, an estimate of drainage area average porosity/pore volume is often obtainable from a

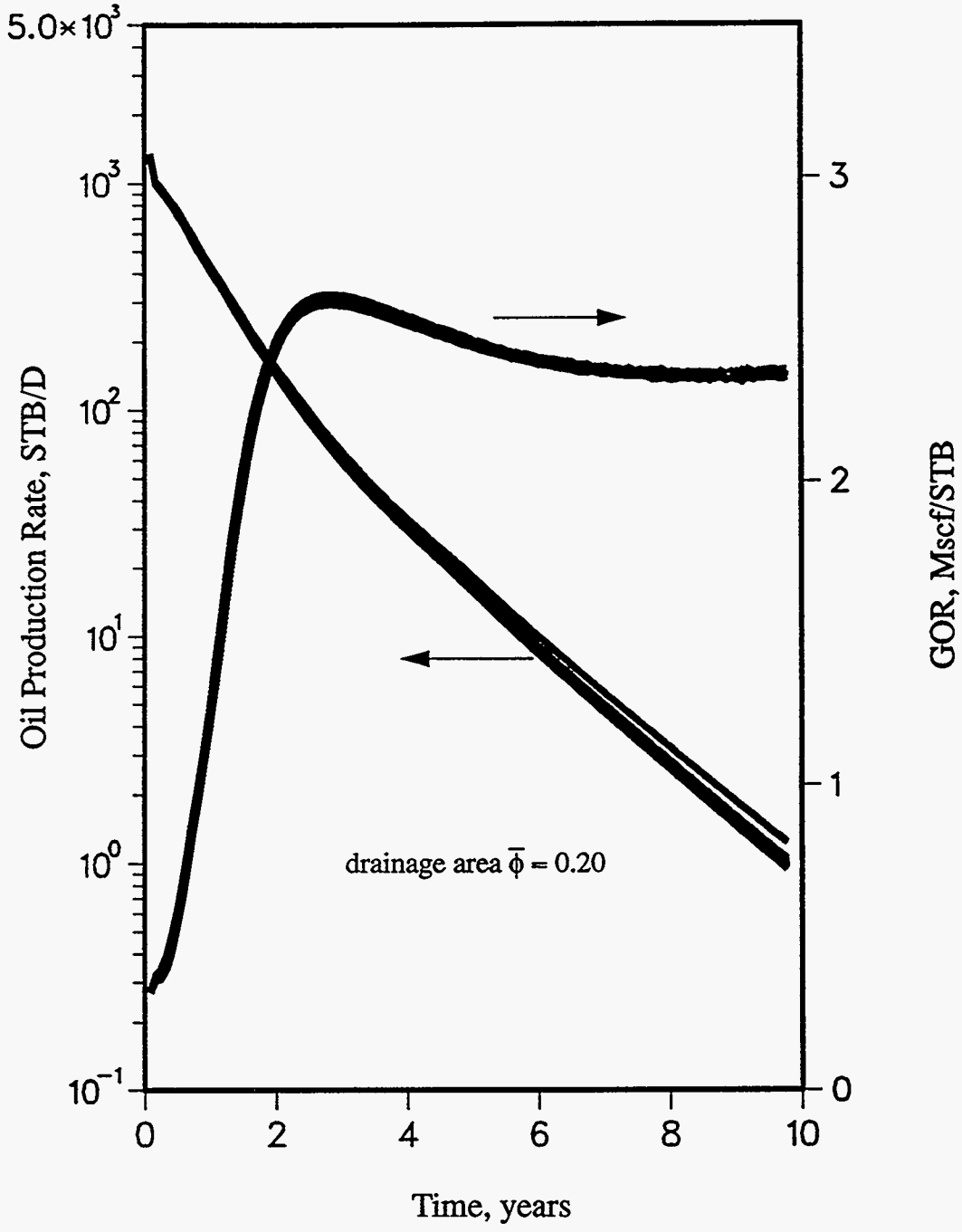

Figure 1.59: Primary performance of central producer for porosity heterogeneous realizations; drainage area average porosity equals 0.20.

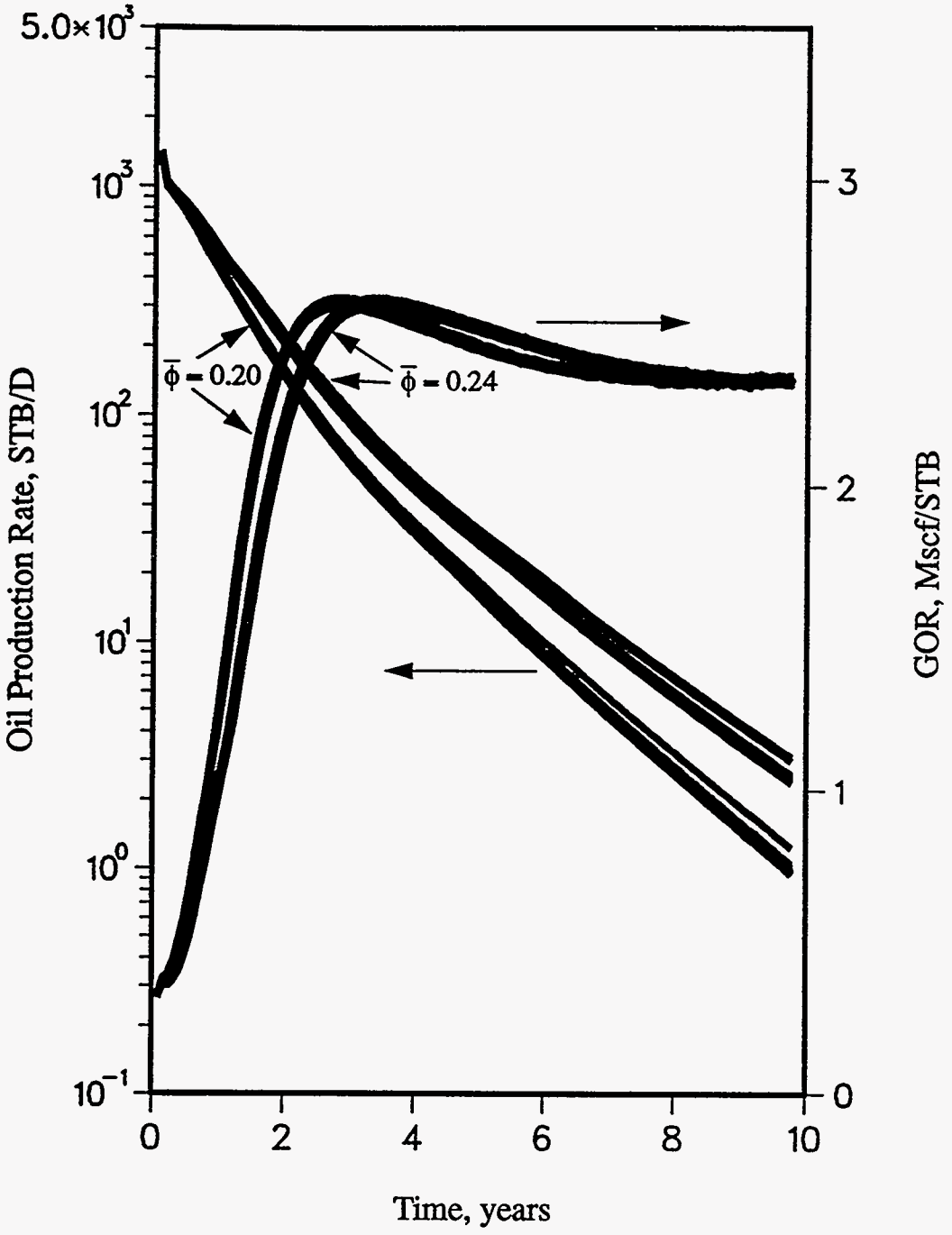

Figure 1.60: Comparison of central producer primary performance for porosity heterogeneous realizations with average porosities of 0.20 and 0.24.

historical rate profile and thus should be used as a conditioning parameter. Pore volume estimates via material balance or volumetric calculations are often obtainable early in the life of a well using rate and pressure data.

Summary of Results - Primary Production

The effective permeability of the near-well region was found to be a dominating reservoir characteristic during primary production. This was illustrated analytically for radially homogeneous and composite reservoir systems and numerically for heterogeneous solution gas drive reservoirs. The correlation coefficient of initial producing rate vs. near-well effective permeability for the central producer in a five-well heterogeneous system was found to be 0.98. The spread in simulated primary performance between permeability realizations was greatly reduced when near-well effective permeability was combined with conventional conditional simulation constraints. A geometric mean was found to be a sufficient estimate of effective permeability for the near-well region. It was not possible to identify other spatial permeability distribution characteristics from primary performance data.

Porosity heterogeneities were found to have an insignificant impact on primary production characteristics. Hence, porosity heterogeneities cannot be quantified from primary performance. The benefit of including pore volume conditional simulation constraints was demonstrated.

Fortunately, both near-well effective permeability and drainage area pore volume often can be estimated from well test and/or production data.

Secondary Production Performance

Connectivity Threshold Constraint Results

The value of p_{tH} for the first truth case was determined to be 0.319; (discussed in Section 1.1.2) i.e., the largest minimum permeability value of all connected paths between the injector and producer is greater than or equal to 31.9% of all permeability values. The simulated annealing with connectivity algorithm was used to generate 20 permeability realizations, all having a p_{tH} of 0.319. Although all permeability realizations have the same interwell connectivity, inspection of their spatial structures shows that the locations of high and low permeability regions vary

from realization to realization. Waterflood performance for the first truth case and the 20 flow simulations are included in Fig. 1.61. A comparison of Fig. 1.21 and Fig. 1.61 indicates that although the inclusion of the connectivity constraint reduced the spread in waterflood performance, the results appear to be biased. None of the 20 flow simulations reproduced the WOR trend exhibited by the first truth case. This biased behavior is evident also in the producing oil rate history.

The value of p_{tH} for the second truth case is 0.298. This value was used to generate 20 additional permeability realizations using the simulated annealing with connectivity algorithm. Once again, although connectivity is preserved, the location of high and low permeability regions change from realization to realization. Many of the realizations exhibit a region of high permeability surrounding the injector because of its high wellblock permeability. Inspection of the corresponding performance plots (Fig. 1.62) shows that the resulting trends are unbiased with respect to the second truth case. Also, the spread in performance has been reduced somewhat in comparison to the base case results (Fig. 1.23). These variations in performance could be reduced if the initial injectivity and productivity were better constrained.

k_{NW} and p_{tH} Constraints Results

The simulated annealing with connectivity algorithm was extended to include the additional constraint of k_{NW} (near-well bore permeability). Two more synthetic case studies were performed, using properties from the two previously discussed truth cases as the specified constraints.

For the first truth case, the producer $k_{NW}(k_{NWp})$ and the injector $k_{NW}(k_{NWi})$ are 190 md and 370 md, respectively. Once again, 20 permeability realizations were generated, this time using k_{NW} constraints in addition to the p_{tH} and conventional constraints. Waterflood performance plots of the corresponding flow simulations (and the first truth case) are illustrated in Fig. 1.63. The improvement resulting from including k_{NW} as a constraint can be observed by comparing the performance curves shown in Fig. 1.63 with the base case curves (Fig. 1.21) and the results obtained when excluding the k_{NW} constraint (Fig. 1.61). It can be seen that the spread in waterflood performance is significantly reduced, especially during early

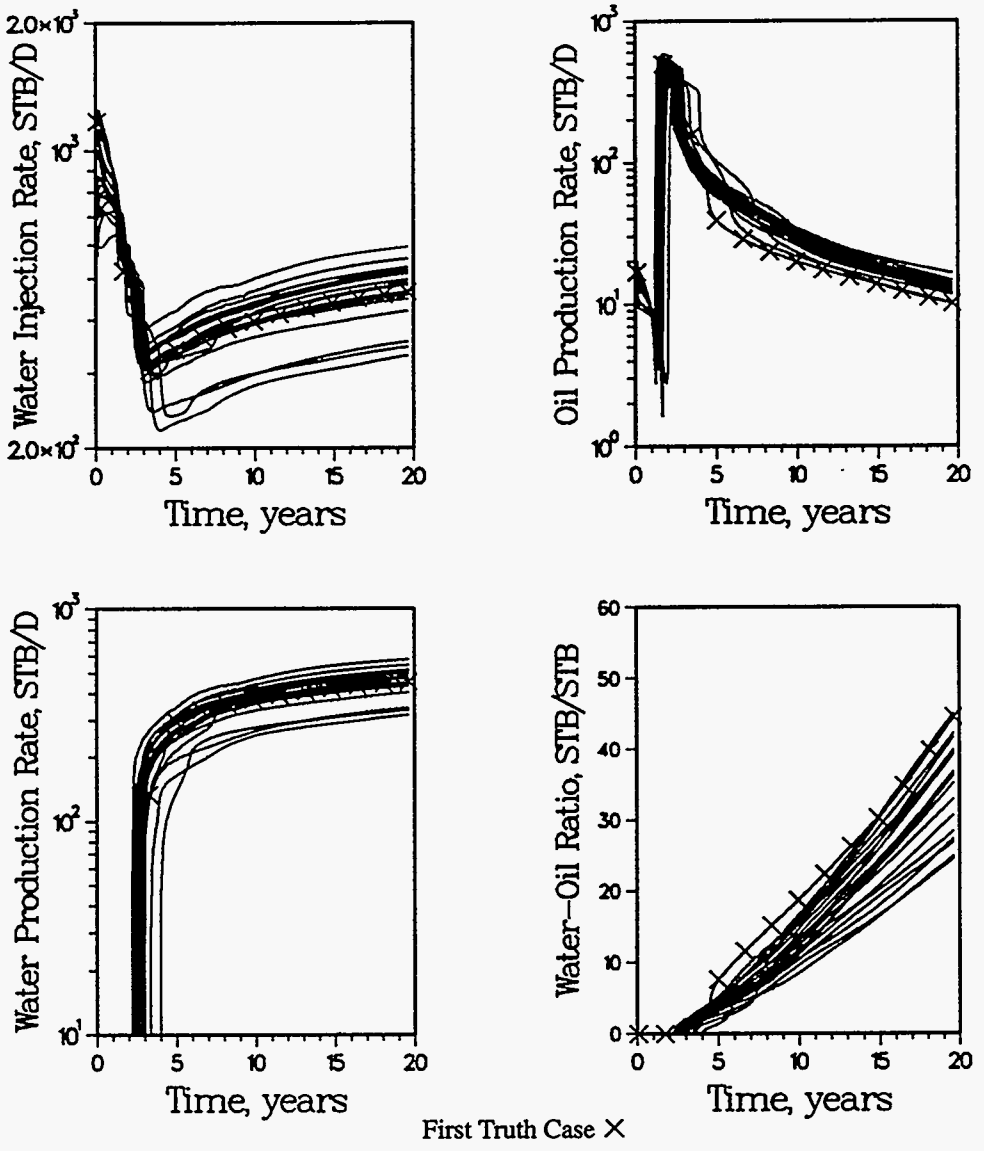

Figure 1.61: Simulated waterflood performance comparing the first trugh case and 20 flow simulations based on p_{tH} = 0.319; one-quarter five-spot pattern system.

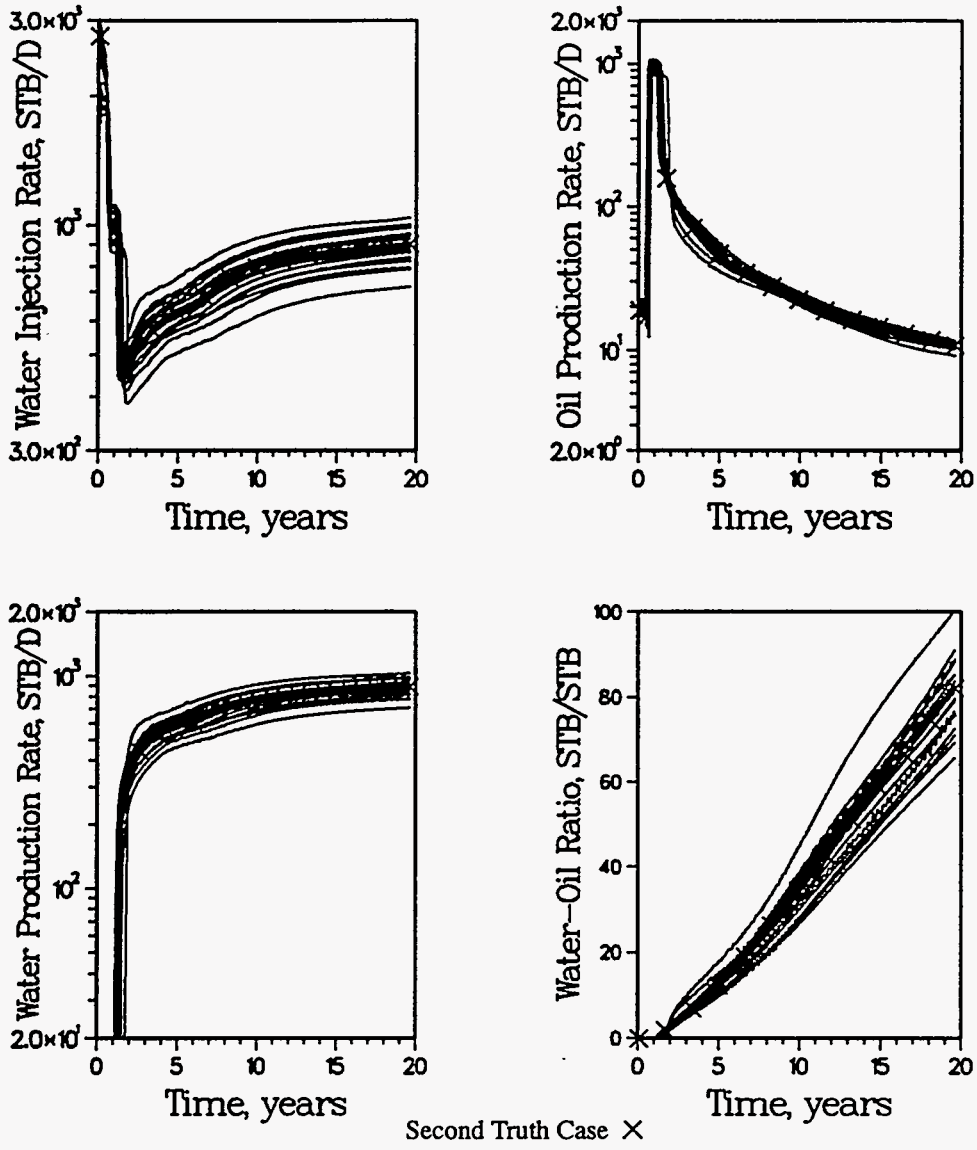

Figure 1.62: Simulated waterflood performance comparing the second truth case and 20 flow simulations based on p_{tH} = 0.298; one-quarter five-spot pattern system.

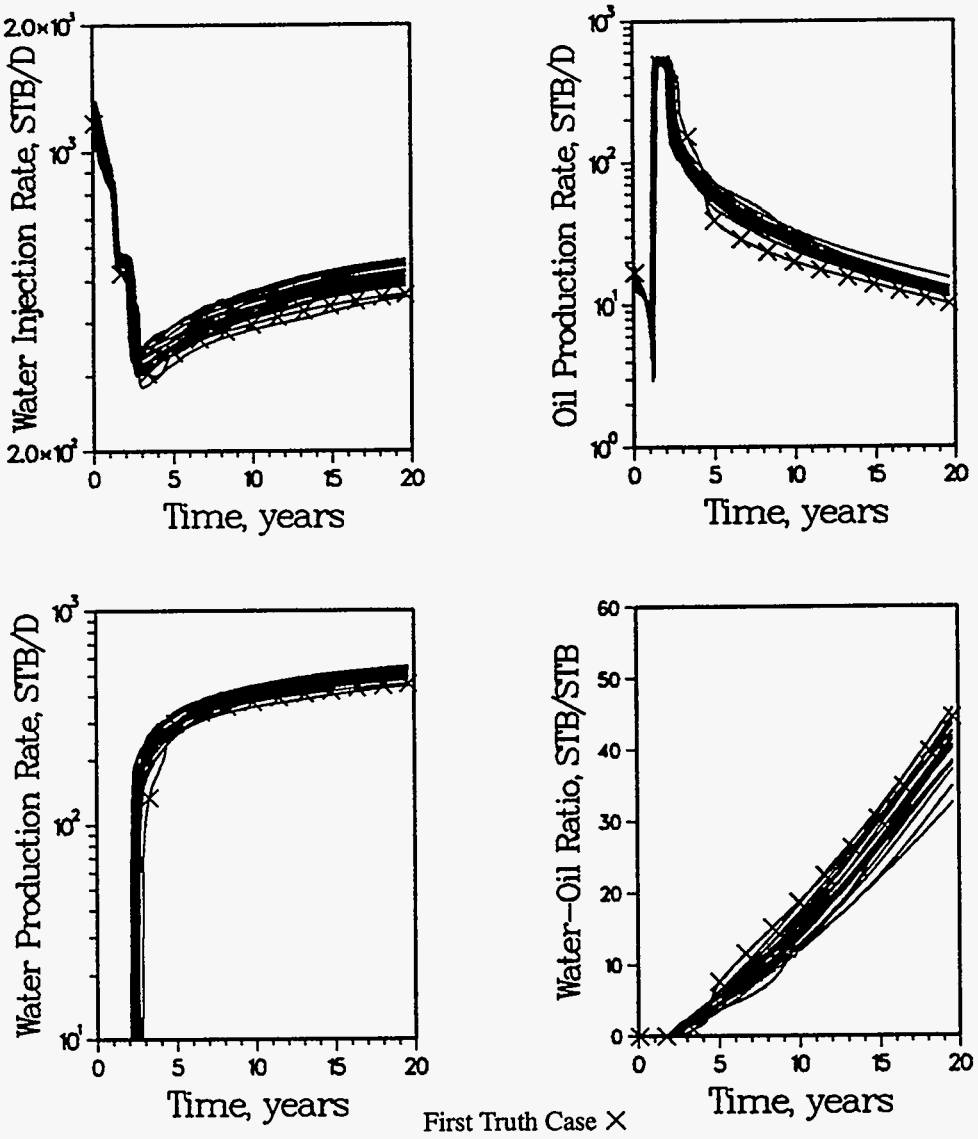

Figure 1.63: Simulated waterflood performance comparing the first truth case and 20 flow simulations based on k_{NWp} = 190 md, k_{NWi} = 370 md and p_{iH} = 0.319; one-quarter five-spot pattern system.

waterflood performance. However, the results are still biased compared to the truth case performance. Examination of the permeability realizations shows that the low permeability regions are located mostly in the diagonal corners of the pattern, as far as possible from the high permeability region surrounding each well. This is not true of the first truth case which has a region of high permeability surrounding the producer, quickly degrading into a low permeability region. This is the primary reason for the discrepancy between the truth case and all attempts to reproduce it.

The near-well permeabilities of the second, less heterogeneous truth case were used as additional constraints to generate 20 permeability realizations. The values of k_{NW} for the producer and injector for the second truth case are 340 and 575 md, respectively. Corresponding waterflood performance plots are illustrated in Fig. 1.64. An extremely good comparison is obtained between the second truth case and the other 20 flow simulations. Not only is performance from the second truth case reproduced very well, but the scatter between the 20 simulated waterflood performances is very small. This represents a significant improvement over the results obtained using just the connectivity threshold constraint. Unlike the first truth case, the regions of low permeability for the second, less heterogeneous truth case are located in the diagonal corners (see Fig. 1.22). This spatial distribution of permeability is a much more likely outcome and therefore is easier to reproduce.

k_{NW} and CV_{k*} Constraints Results

A total of 20 permeability fields were generated using simulated annealing, the more heterogeneous permeability frequency distribution and additional constraints of k_{NW} (k_{NWp} = 190 md and k_{NWi} = 370 md) and CV_{k*} (0.186). These values are characteristic of the first truth case. Inspection of the permeability images shows that the CV_{k*} constraint has reduced the connectivity between the injector and the producer by forcing the low permeability region to be spread out between the two wells, much like the first truth case permeability field (see Fig. 1.20). The corresponding waterflood performance is illustrated in Fig. 1.65. Variations in waterflood performance have been greatly reduced. Unlike previous attempts, the anomalous characteristics of the truth case waterflood performance are reproduced. The additional constraint of CV_{k*} has reduced the domain of possible solutions to a

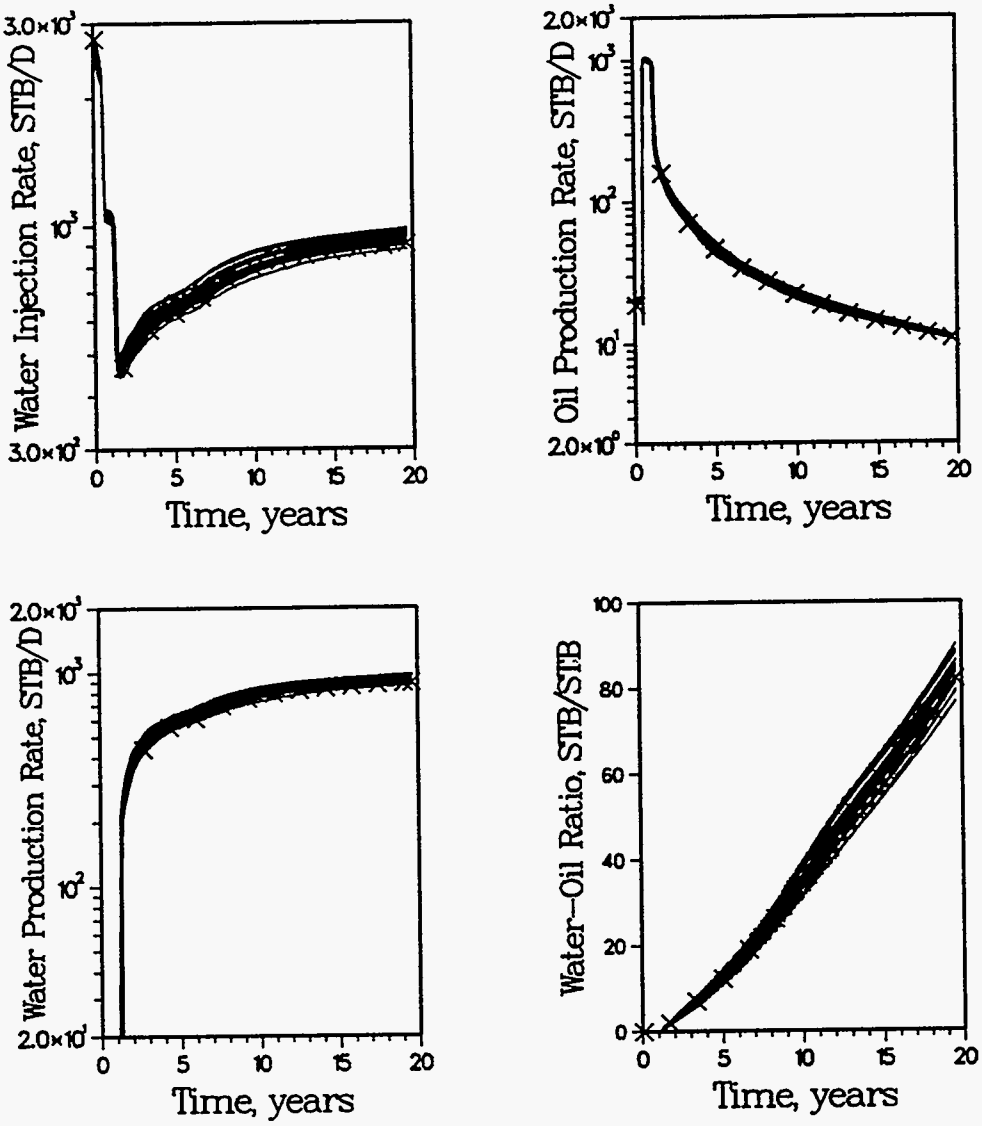

Figure 1.64: Simulated waterflood performance comparing the second truth case and 20 flow simulations based on k_{NWp} = 340 md, k_{NWi} = 575 md and p_{uH} = 0.298; one-quarter five-spot pattern system.

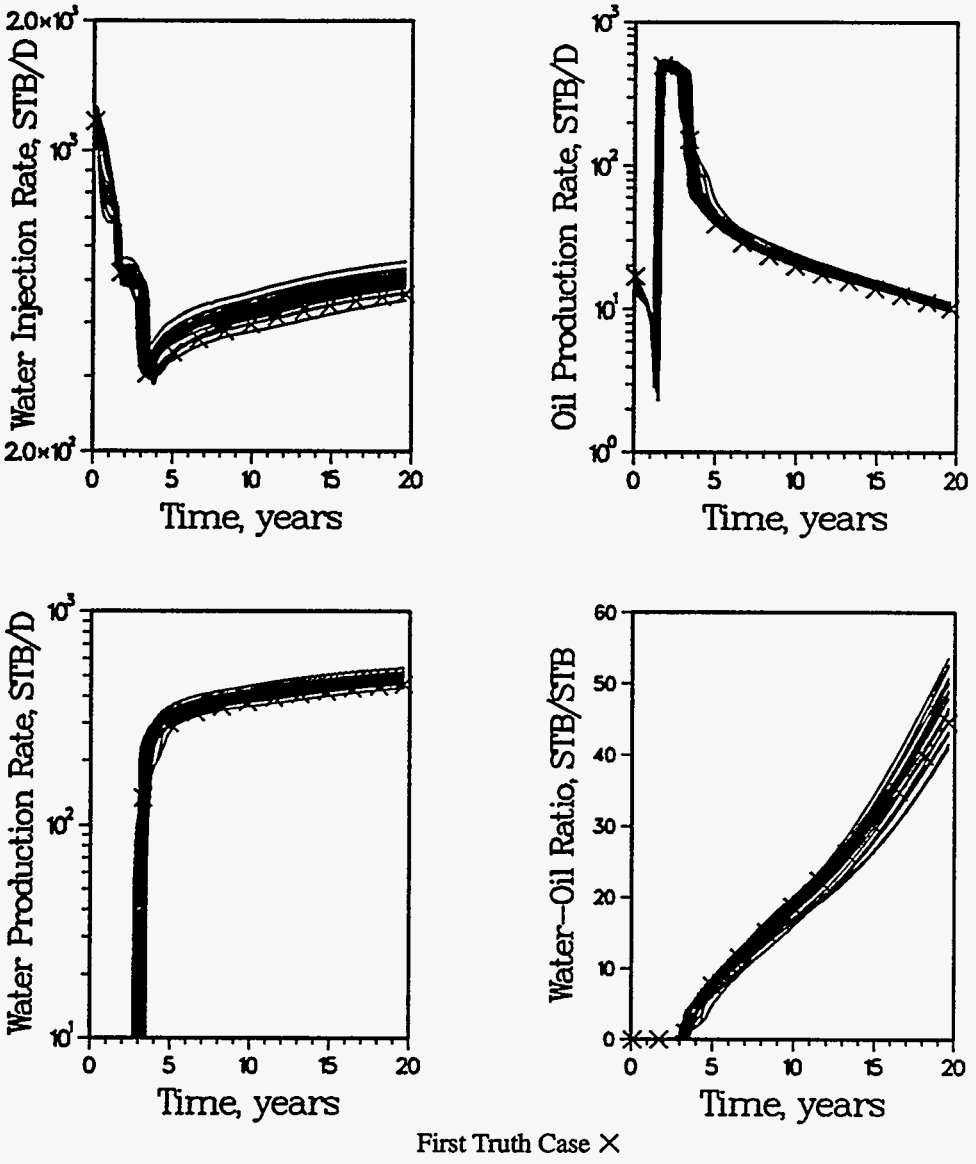

Figure 1.65: Simulated waterflood performance comparing the first truth case and 20 flow simulations based on k_{NWp} = 190 md, k_{NWi} = 370 md and CV_{k_*} = 0.186; one-quarter five-spot pattern system.

set with flow characteristics similar to the first truth case.

Analogous results, but based on characteristics of the second truth case, are shown in Fig. 1.66. Values of k_{NWp}, k_{NWi} and CV_{k*} for the second truth case and the other 20 permeability fields are 340 md, 575 md and 0.300, respectively. The locations of the low permeability regions for all 20 permeability fields compare very favorably with the second truth case. As a result, the waterflood performance of all 21 flow simulations also compare very well, especially oil rates. The reduction in the variation of waterflood performance in comparison to the base case results (Fig. 1.23) is significant.

Connectivity Estimation from Waterflood Performance

The above two synthetic case studies were performed with the assumption that the values of p_{dH} and CV_{k*} were known a priori. Since they cannot be measured directly, a correlation between waterflood performance parameters and the connectivity measures must be developed for estimation purposes. Sensitivities of CV_{k*} were performed over a wide range of values to illustrate the strong relationship between CV_{k*} and waterflood performance. Values of CV_{k*} were varied from 0.05 to 0.40 with five permeability realizations generated at each value of CV_{k*}. All other constraints were characteristic of the first truth case and were held constant. One-quarter of a five-spot pattern flow simulations were then performed using each permeability field. Fig. 1.67 contains waterflood performance plots for the CV_{k*} sensitivity flow simulations and the first truth case. For clarity, only one result per CV_{k*} value has been included in Fig. 1.67. The effect of varying CV_{k*} results in a decrease in water breakthrough time. Although not shown, flow simulations with equal values of CV_{k*} have similar waterflood performance behavior. The performance of the first truth case (highlighted) is about average compared to the other cases. This is expected since its value of CV_{k*} is approximately mid-range.

Fig. 1.68 better demonstrates the correlation between water breakthrough time and CV_{k*}. Data from all 21 flow simulation sensitivities have been plotted in Fig. 1.68. Note that as CV_{k*} is increased, the spread in breakthrough times for the same CV_{k*} is reduced. Larger values of CV_{k*} reflect stronger trends between the two wells.

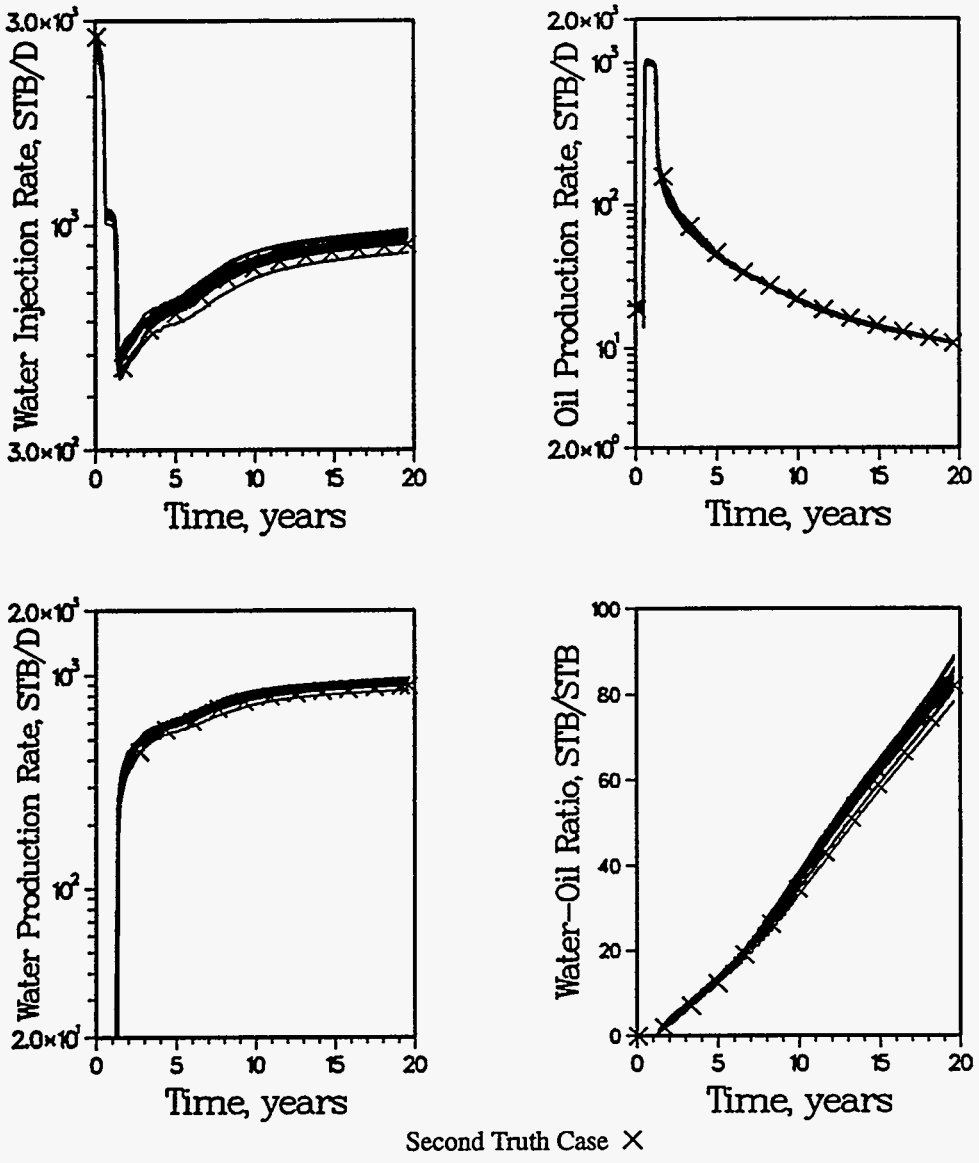

Figure 1.66: Simulated waterflood performance comparing the second truth case and 20 flow simulations based on k_{NWp} = 340 md, k_{NWi} = 575 md and CV_{k_*} = 0.300; one-quarter five-spot pattern system.

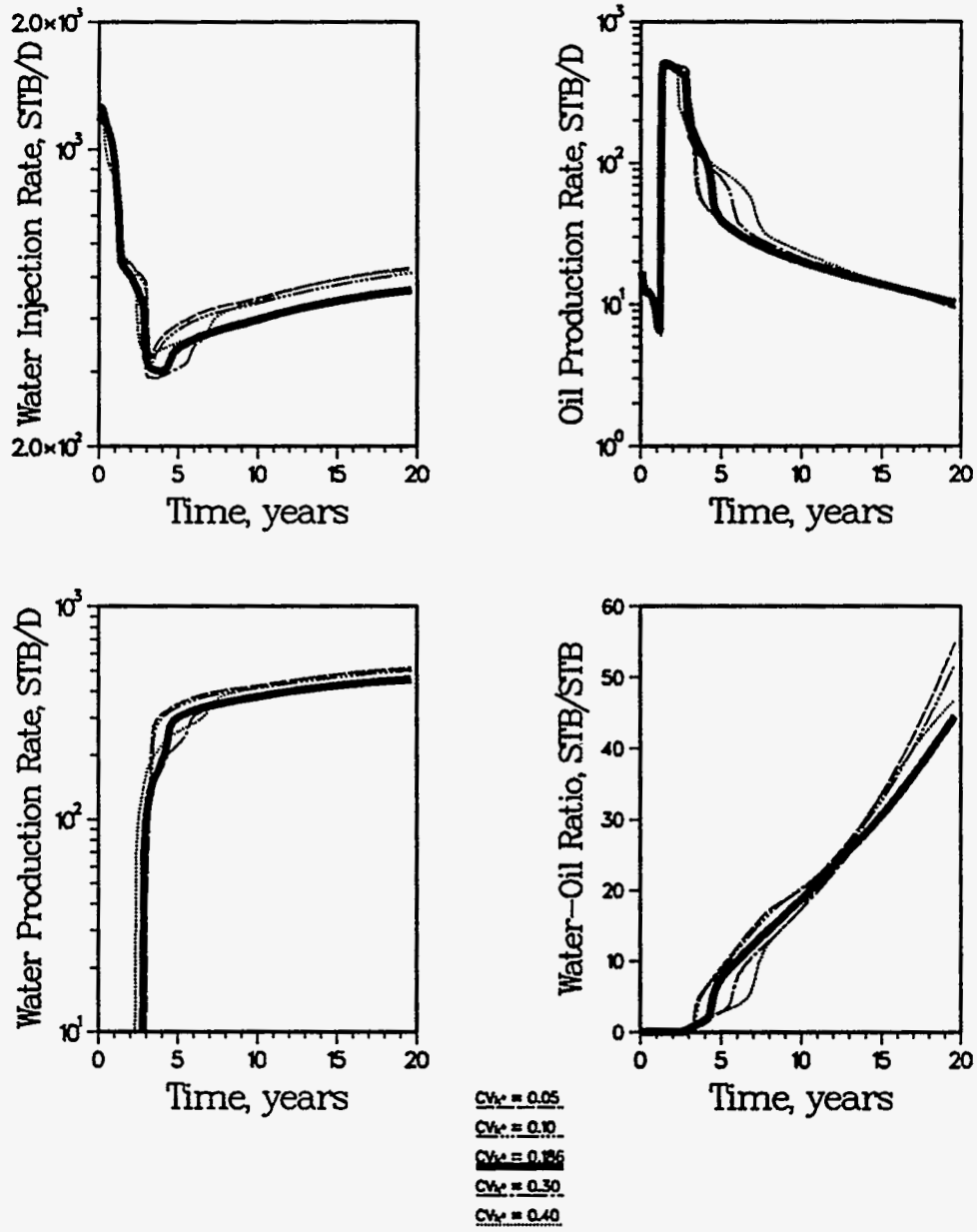

Figure 1.67: Simulated waterflood performance showing the sensitivity of waterflood response to CV_{k*}; one-quarter five-spot pattern system (first trough case highlighted).

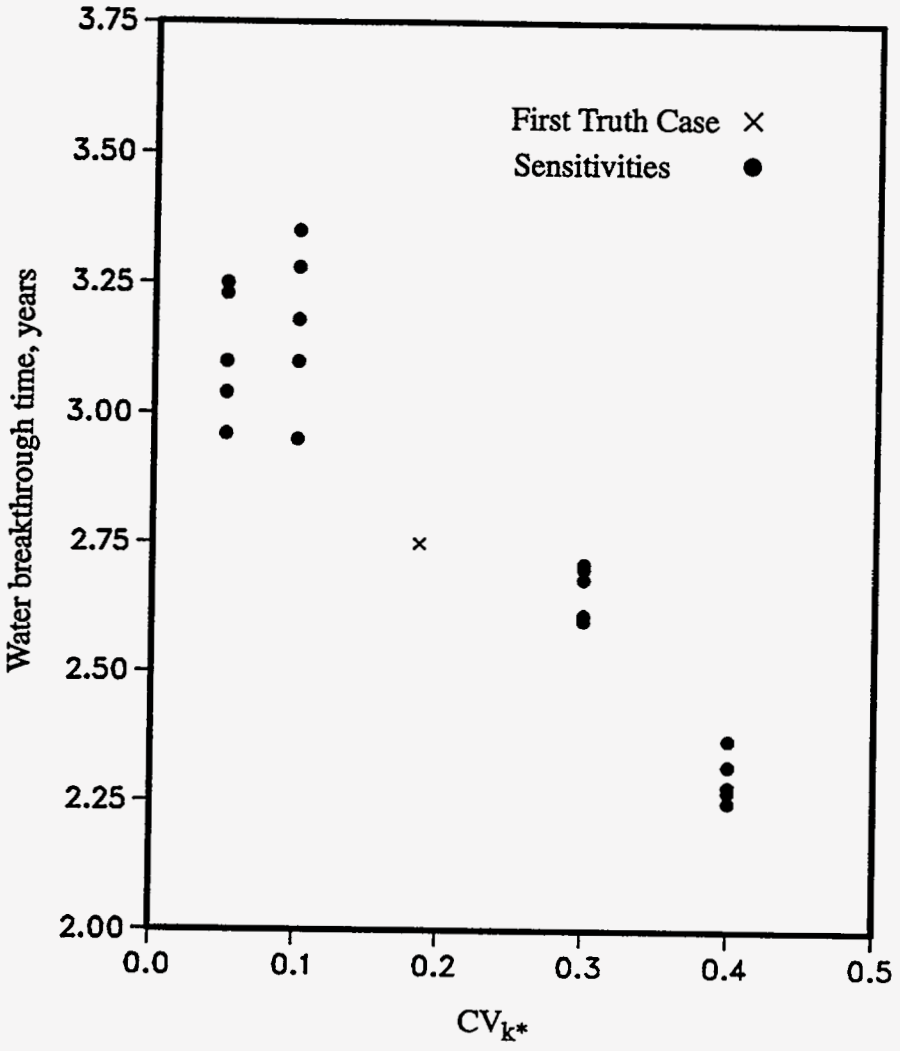

Figure 1.68: Sensitivity of water breakthrough time to CV_{k*}.

The effect of CV_{k*} on waterflood efficiency is illustrated in Fig. 1.69. Here, waterflood efficiency is represented by the cumulative WOR after one hydrocarbon pore volume of water injected (HCPVI). These results demonstrate that CV_{k*} does have a strong effect on waterflood performance. Hopefully, its value can be estimated by performing a sensitivity study.

Of course, the waterflood response of a producer is impacted by all neighboring injection wells. Therefore, the CV_{k*} estimated from water breakthrough time and cumulative WOR's is an average of the four associated one-quarter five-spot patterns. Sensitivity studies would have to account for the possibility of varying CV_{k*}'s within a five-spot pattern. More work is required to determine the best approach for estimating each injector/producer CV_{k*}.

The correlation between CV_{k*} and reservoir connectivity is also apparent when examining the 21 permeability fields generated for the sensitivity study. A permeability image representing each value of CV_{k*} investigated is depicted in Fig. 1.70. It can be seen that as CV_{k*} is increased, the high and low permeability trends become more aligned with the direction of fluid flow. Thus, higher values of CV_{k*} result in more continuous/conductive paths, decrease water breakthrough time and increase WOR trends, thereby decreasing waterflood efficiency.

Probability of Exceedance Maps

As more local reservoir constraints are defined, the variation in the spatial distribution of permeability between realizations is reduced. As a result, the uncertainty in defining regions of high and low permeability is also reduced. This becomes important when evaluating a reservoir for alternative operating strategies, e.g., infill drilling. Probability of exceedance maps can be used as a tool to quantify uncertainty. These maps are used to display the probability of exceeding a cutoff value at each grid block location. The probability of exceeding a cutoff at a grid block is calculated by determining the percentage of simulated values that exceed the cutoff at the particular grid block. This calculation is repeated for each grid block. A comparison of probability of exceedance maps representing the first truth case, the first base case and the corresponding results using k_{NW} and CV_{k*}

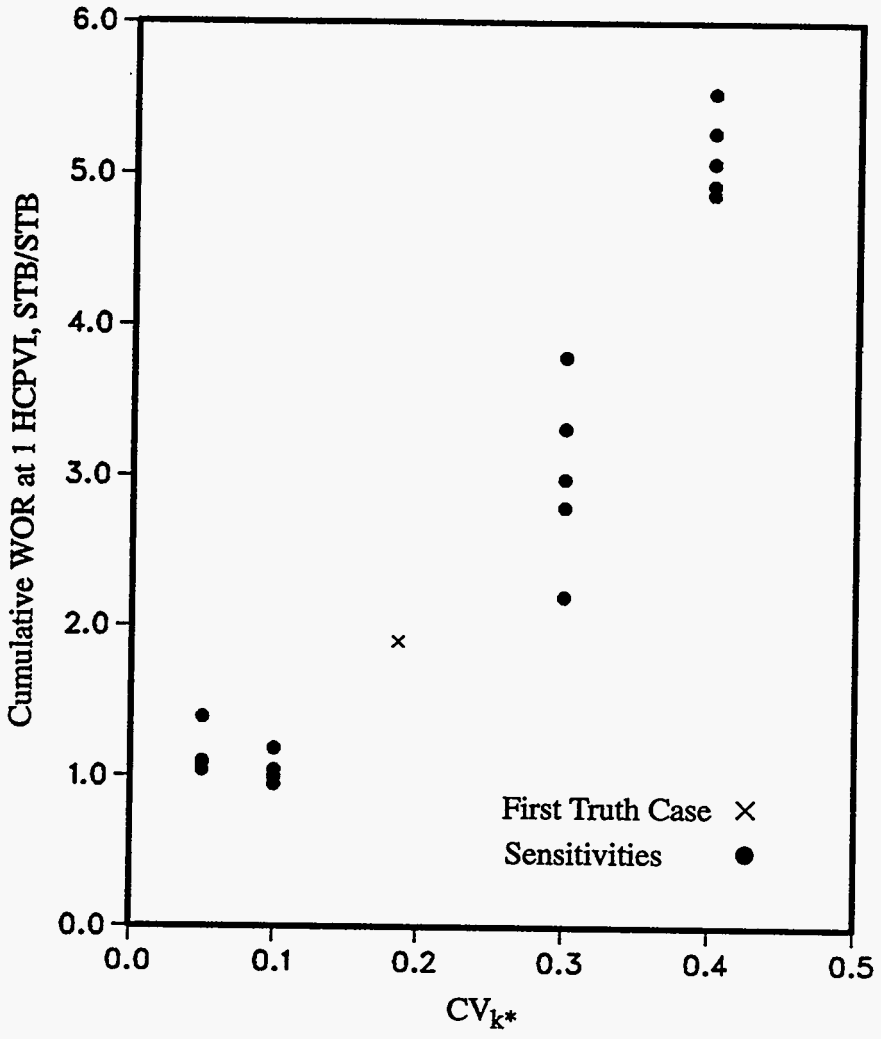

Figure 1.69: Sensitivity of cumulative water-oil ratio to CV_{k*}.

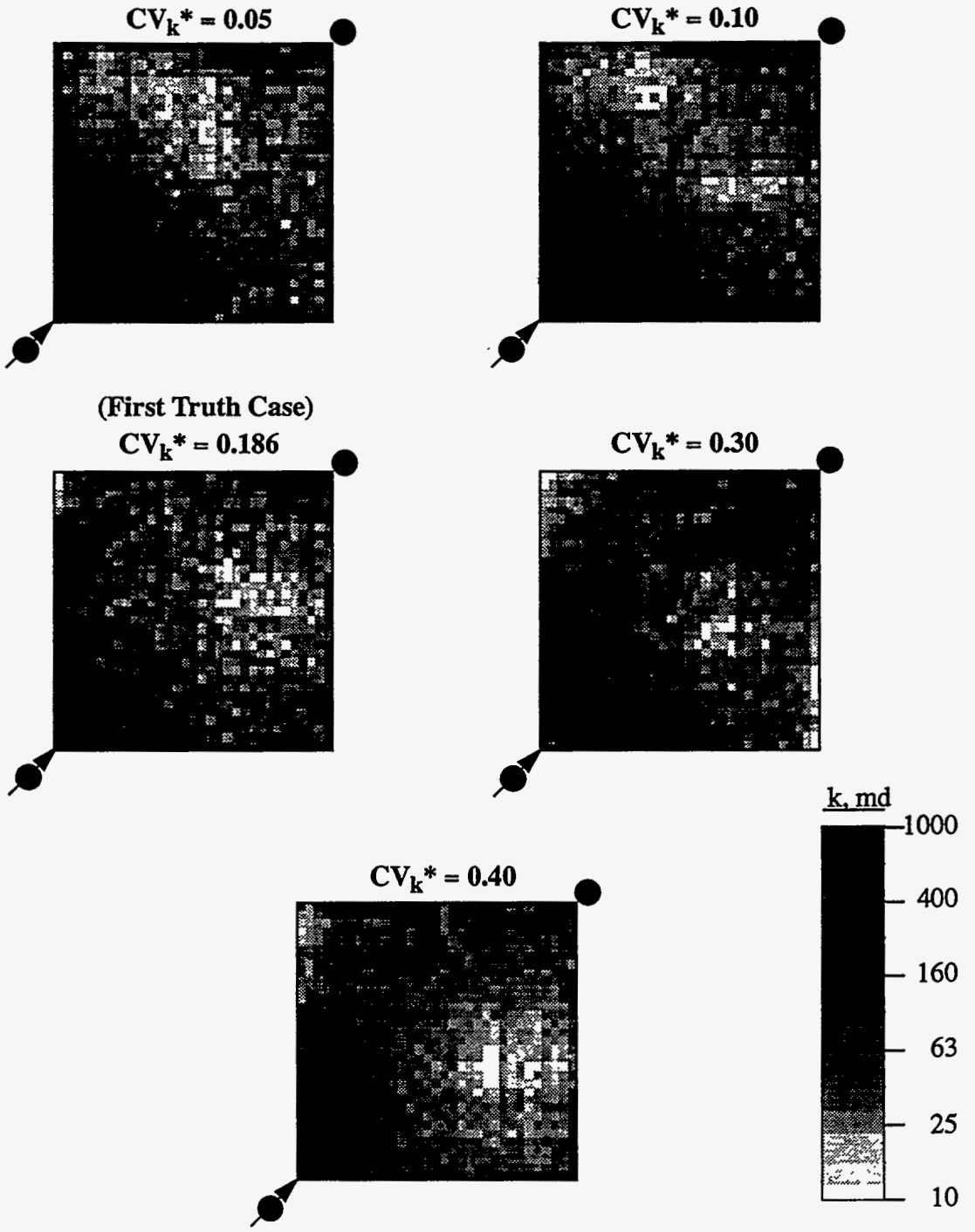

Figure 1.70: One-quarter five-spot pattern permeability realizations for various values of CV_{k^*}.

constraints is presented in Fig. 1.71. For this particular case, a low permeability percentile of 30% was used so that the regions which are most likely to have low permeability (but still floodable) would be highlighted. Such regions would most likely be good candidates for infill drilling in a mature waterflood. Since the permeability field for the truth case is known (i.e., deterministic), its grid blocks are either unshaded or darkly shaded, indicating a 100% certainty of their permeability values. On the other hand, the grid blocks for the other two cases are shades of gray, indicating some degree of uncertainty. Note that the regions exhibiting a low probability of exceedance for the connectivity constrained cases are consistent with the truth case. This is not true of the base case probability of exceedance map. The k_{NW} and CV_{k*} constraints are shown to reduce the uncertainty in identifying high and low permeability regions, and thus, potential infill drilling locations.

Extended Five-Spot Pattern - Less Heterogeneous Permeability Distribution

Base Case Results

The permeability field used for the first extended five-spot pattern truth case is shown in Fig. 1.72. The less heterogeneous permeability distribution ($\mu_{\log(k)}$ = 2.5, $\sigma_{\log(k)}$ = 0.2) was used to generate this truth case. The permeability correlation length was increased from 1000 ft to 1500 ft (λ_D = 0.803). All other pertinent data remain unchanged from the full five-spot pattern study. As before, 20 additional permeability fields were generated using conventional simulated annealing. The waterflood performance of the inner five-spot producer and four injectors are illustrated in Fig. 1.73 and Fig. 1.74. These base case results represent the typical range in simulated waterflood performance using conventional conditional simulation constraints for the given system. As expected, the variability exhibited by the flow simulation results is less than that obtained for the full five-spot pattern cases due to the reduced permeability variance. The injection rates vary more than production rates between simulations because the injectors have a much greater differential pressure (relative to the average reservoir pressure) than the producers.

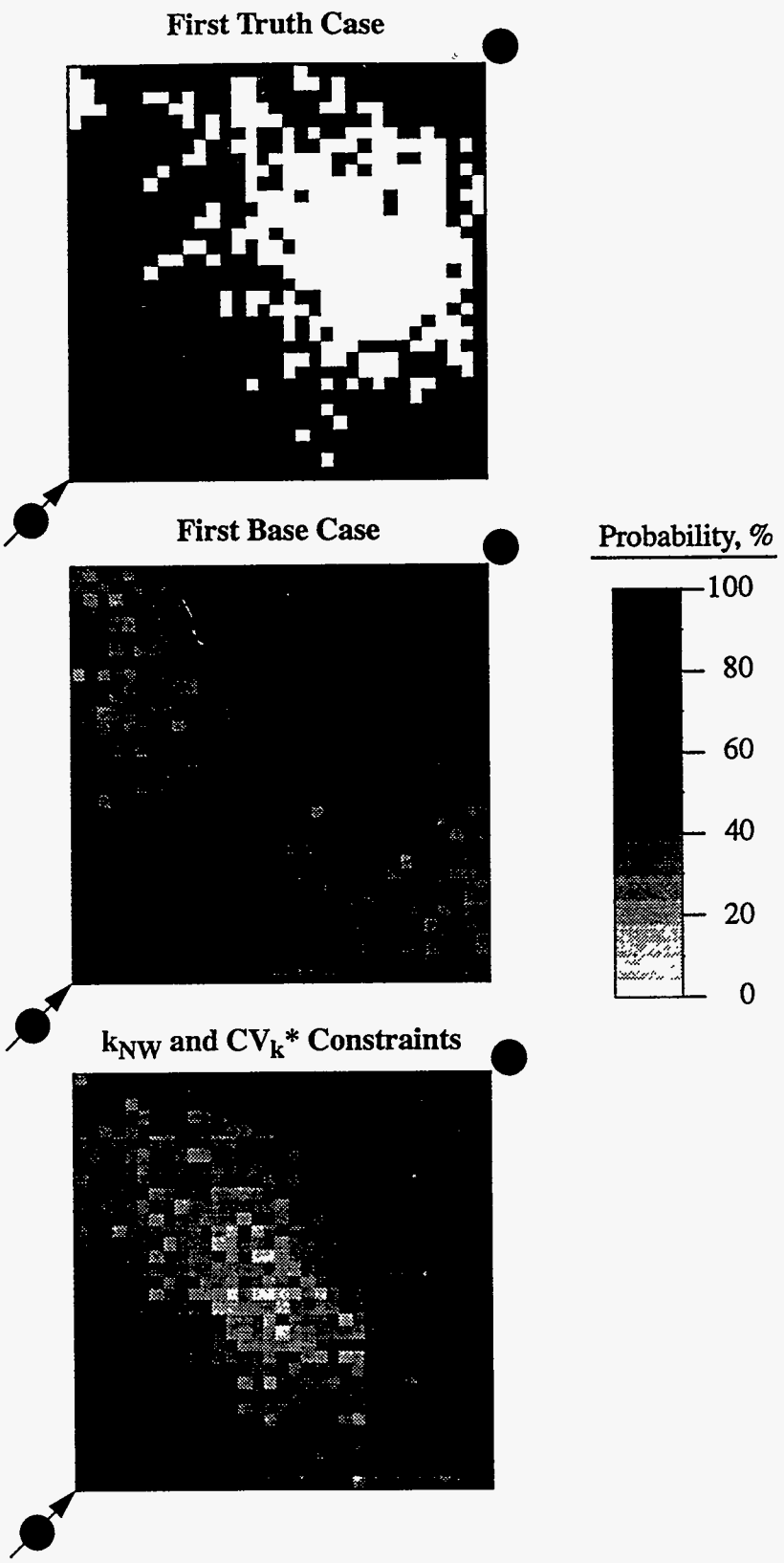

Figure 1.71: Comparison of one-quarter five-spot pattern permeability probability of exceedance maps, 30^{th} percentile.

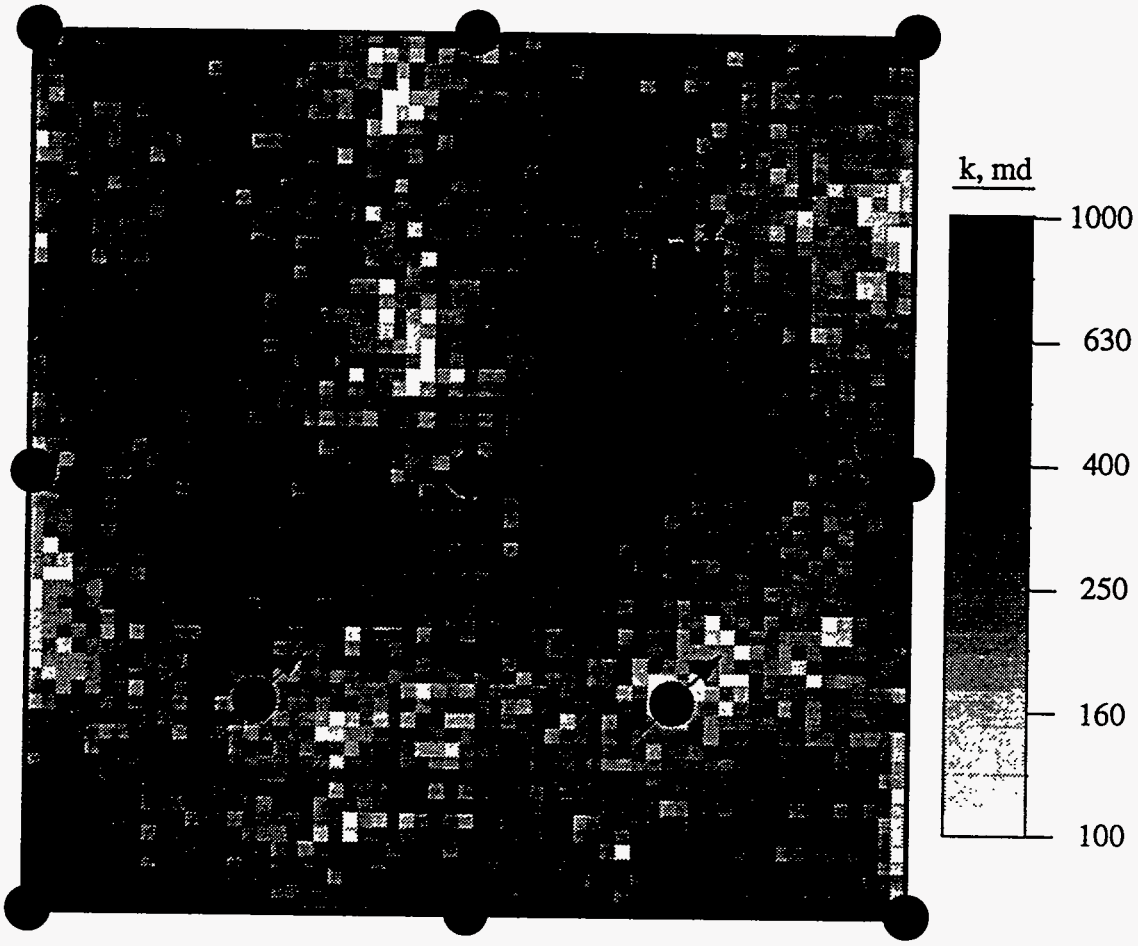

Figure 1.72: Truth case permeability field for extended five-spot pattern study; less heterogeneous permeability distribution.

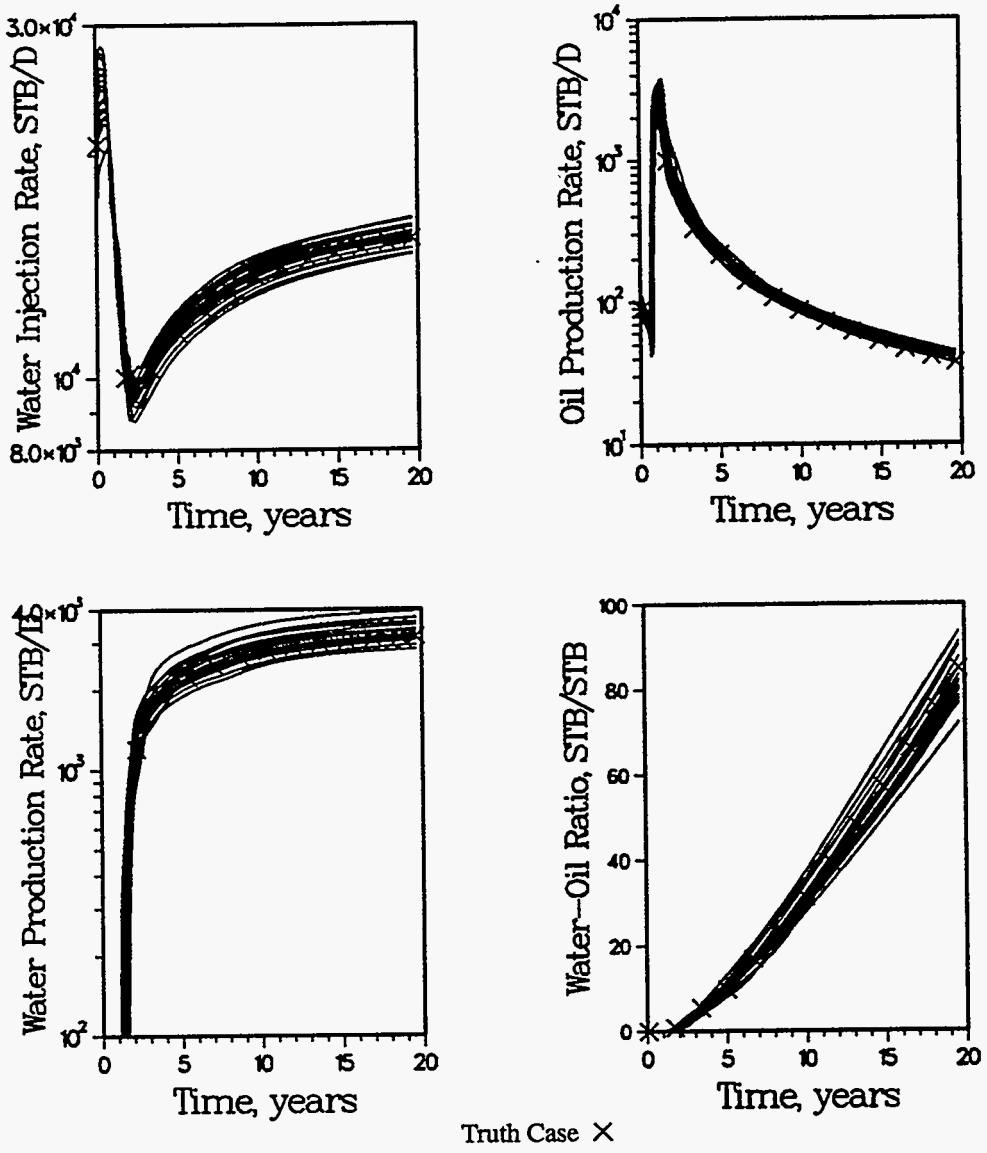

Figure 1.73: Base case waterflood performance for the inner five-spot pattern wells; extended five-spot pattern study using the less heterogeneous permeability distribution.

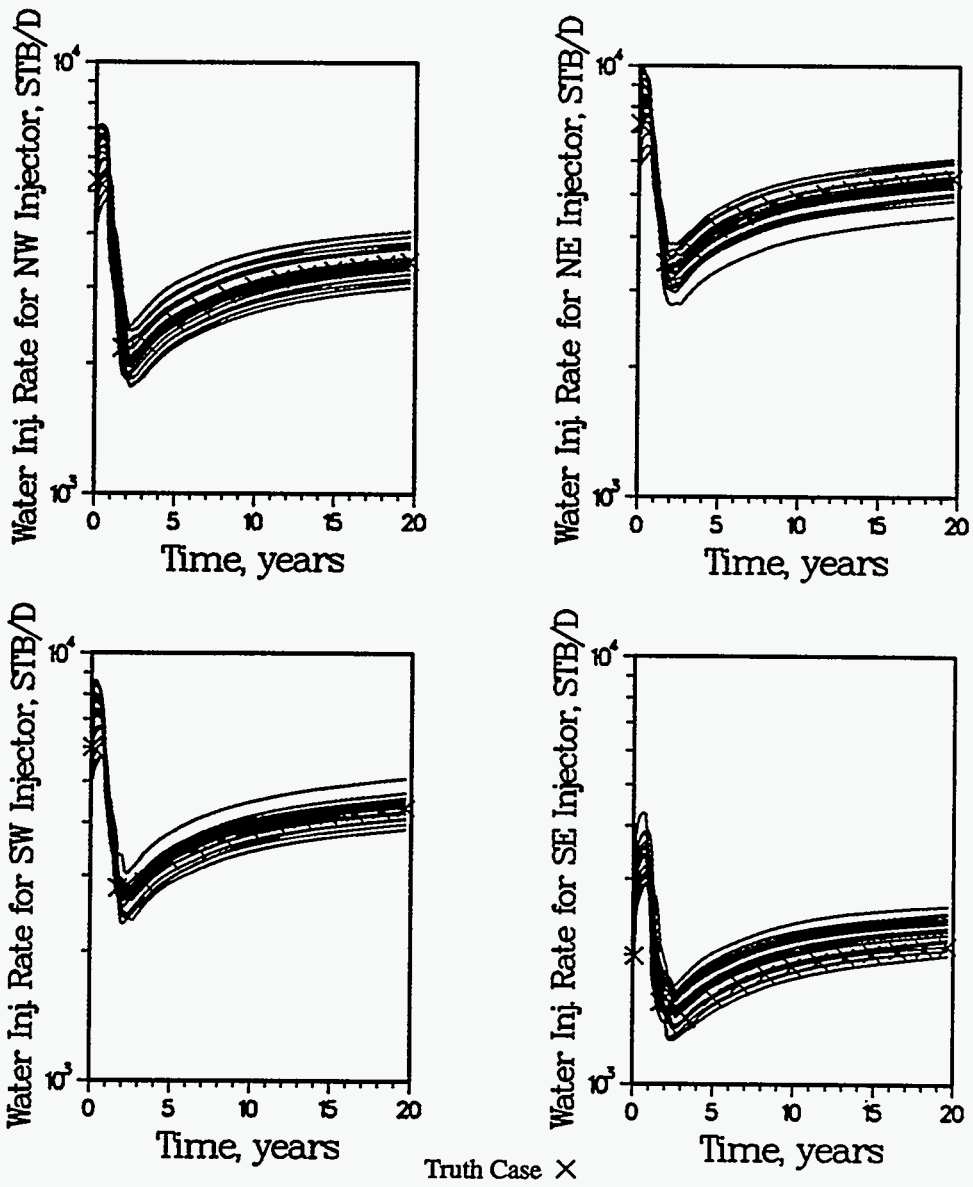

Figure 1.74: Base case waterflood performance for the inner five-spot pattern injection wells; extended five-spot pattern study using the less heterogeneous permeability distribution.

k_{NW} and CV_{k*} Results

The k_{NW} of each well and CV_{k*} of each injector/producer pair representing the truth case were used as constraints in generating 20 additional permeability fields. Waterflood performance of the inner five-spot wells are included in Fig. 1.75 and Fig. 1.76. A comparison of these two figures to their counterparts, Fig. 1.73 and Fig. 1.74, indicates that the inclusion of the constraints k_{NW} and CV_{k*} significantly increases the probability of generating a reservoir description with waterflood performance similar to the truth case. Several of the permeability fields have spatial characteristics very similar to the truth case (see Fig. 1.77). This is not the case for the 20 base case permeability fields. However, there are a few performance curves which do differ noticeably from the truth case performance. Probably of most concern is the tendency of the WOR curves of the inner five-spot producer (Fig. 1.75) to fall below the truth case WOR curve--two significantly more so than the others.

The permeability fields responsible for the anomalously-low WOR trends are shown in Fig. 1.78. Note that these two permeability fields are very similar. Also note that the most significant difference between these two permeability fields and the truth case (Fig. 1.77) is the spatial distribution of permeability between the central producer and the northeast injector. Although all three permeability fields have identical values of CV_{k*} for this injector/producer pair, the average permeability of the corresponding area of influence for the truth case is considerably higher. As a result, the truth case area of influence of these two wells is processed much faster. It should be noted that CV_{k*} represents the standard deviation of a permeability normalized by its mean. Therefore, two injector/producer pairs may have the same CV_{k*} but vastly different $k*$ means.

It is concluded that whereas k_{NW} constrains early time injectivity/productivity and CV_{k*} constrains reservoir connectivity, (relative) estimates of the average permeability between an injector/producer pair may be required to reproduce time-dependent variations in historical waterflood performance. This additional waterflood constraint, referred to as k_{PAT}, becomes significant only when large variations in average permeability of neighboring injector/producer areas of

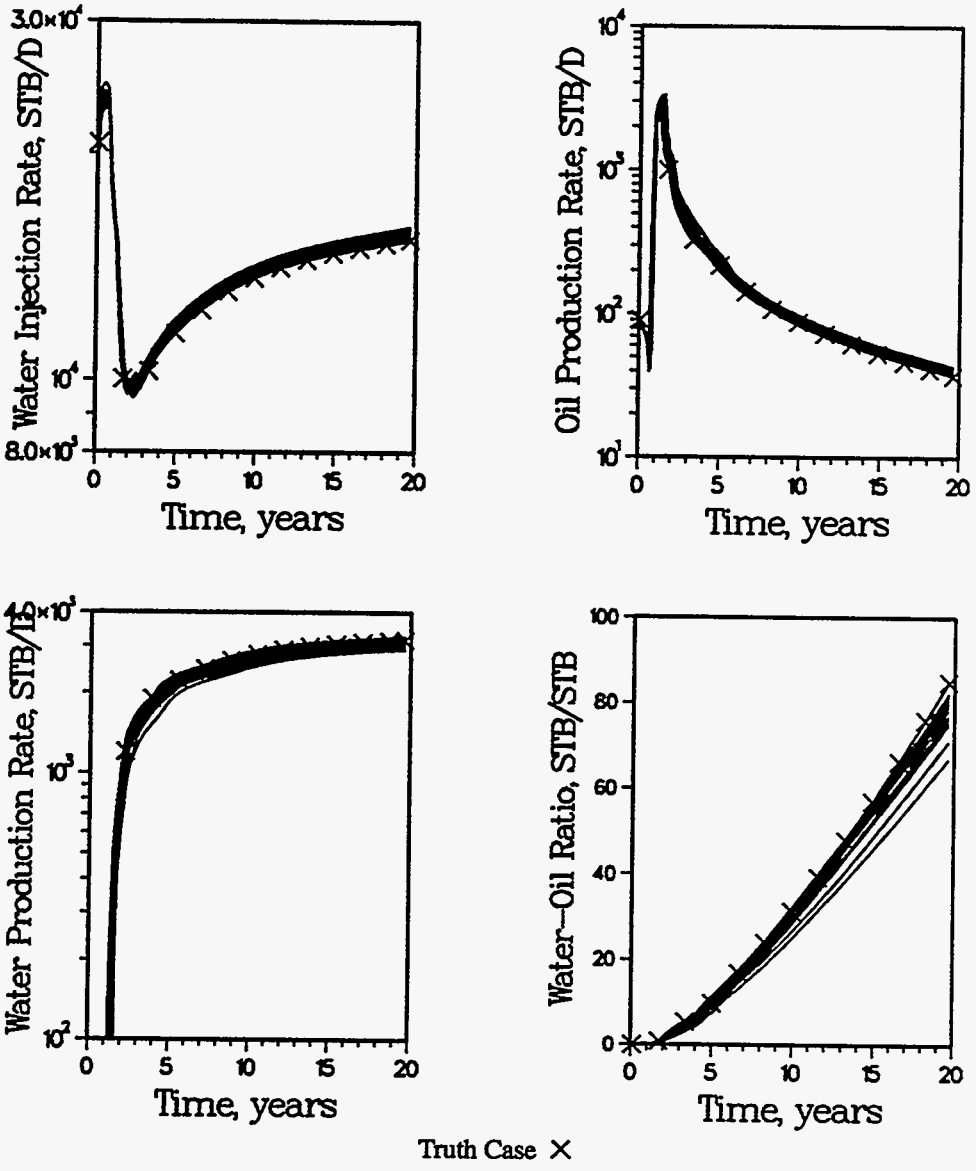

Figure 1.75: CV_{k_*} and k_{NW} contraints case waterflood performance for the inner five-spot pattern wells; extended five-spot pattern study using the less heterogeneous permeability distribution.

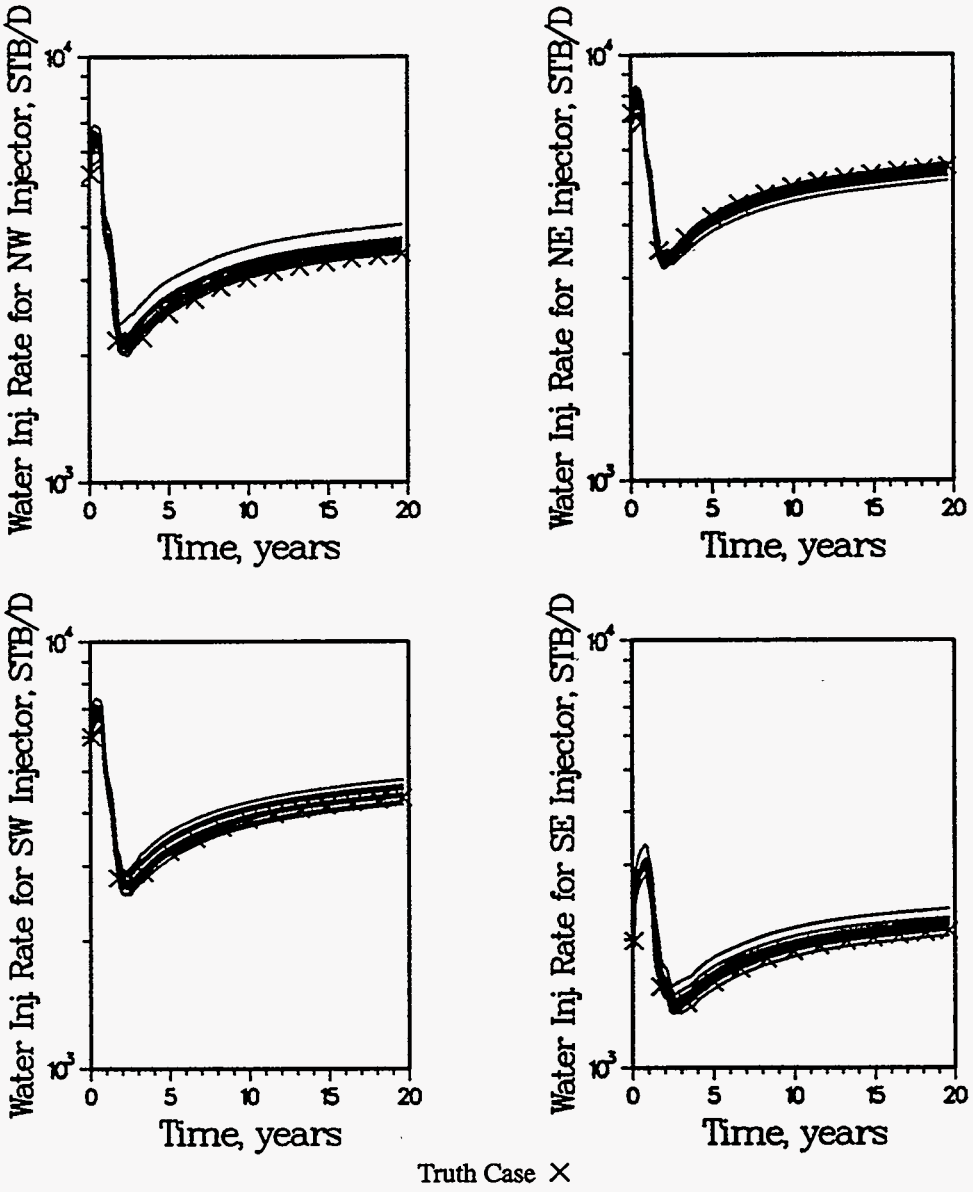

Figure 1.76: CV_{k_*} and k_{NW} contraints case waterflood performance for the inner five-spot pattern injection wells; extended five-spot pattern study using the less heterogeneous permeability distribution.

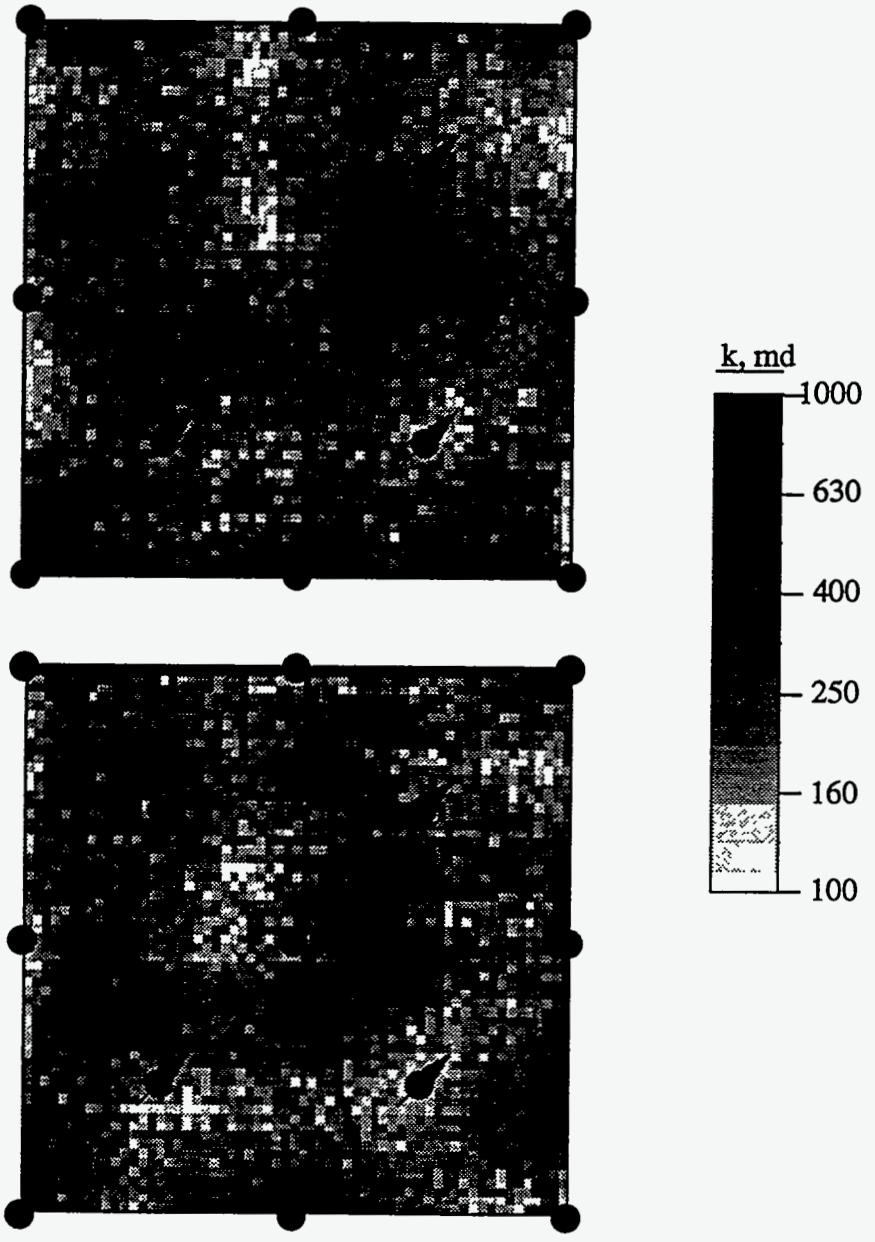

Figure 1.77: Comparison of truth case permeability field and an indirect performance contraints case permeability field; extended five-spot pattern study using the less heterogeneous permeability distribution.

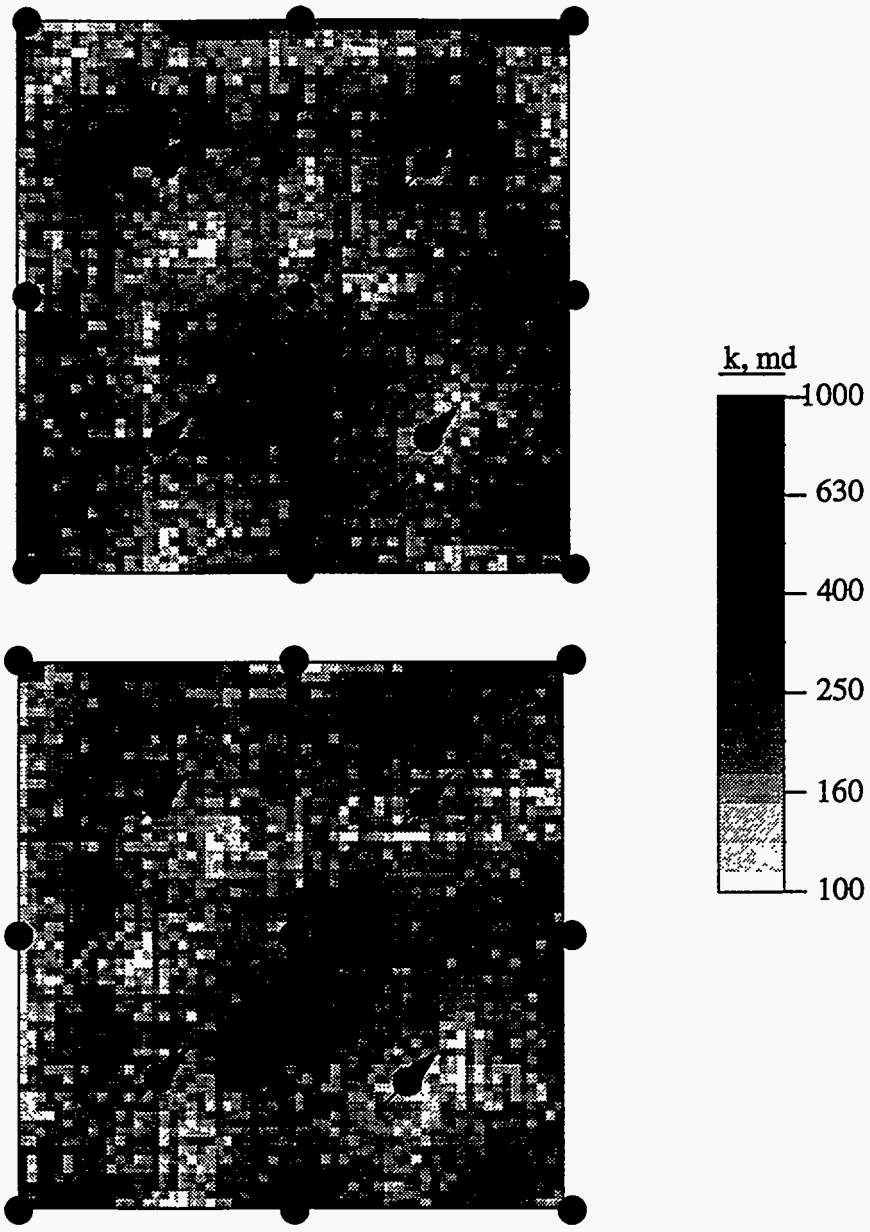

Figure 1.78: Permeability fields generated using indirect performance contraints and characterized by anomalous water-oil ratio trends; extended five-spot pattern study using the less heterogeneous permeability distribution.

influence exist. Otherwise, the parameter k_{PAT} has no more than a secondary effect. Although this study has studied the significance of k_{PAT}, it is not known how this parameter can be obtained from field data.

Extended Five-Spot Pattern - More Heterogeneous Permeability Distribution

The more heterogeneous permeability distribution was used to further investigate the impact of large variations in the average permeability for adjacent injector/producer pairs. It was felt that the large range in permeabilities would increase the potential of having large variations in the average permeability of injector/producer pairs. This would increase the likelihood of requiring k_{PAT} as a constraint. As before, base case results using conventional constraints are presented first. Subsequently, the results obtained when additional constraints are imposed are compared to the base case results to determine the degree of improvement.

Recall that the more heterogeneous permeability distribution is log-normally distributed having a mean $\log(k)$ of 2.0, or 100 md, and a standard deviation of 0.6. Consequently, 68% of the permeabilities lie between 40 and 250 md. The same 13-well, 80-acre well spacing, 160-acre five-spot waterflood pattern system will be used. All permeability realizations were generated using an omnidirectional spherical variogram having a 20% relative nugget and a correlation length of 1200 ft, or λ_D of 0.643.

Base Case Results

Conventional simulated annealing was used to generate 21 permeability realizations, all having the same permeability frequency distribution, variogram and wellblock permeability values. One of the permeability realizations was arbitrarily selected to represent the actual reservoir permeability field, i.e., to be the truth case permeability field. The truth case permeability field is shown in Fig. 1.79. Some of the more prominent features of the truth case permeability field are: 1) a high permeability zone surrounding the central producer, 2) a rim of low permeability surrounding the central producer high permeability zone, 3) a high permeability

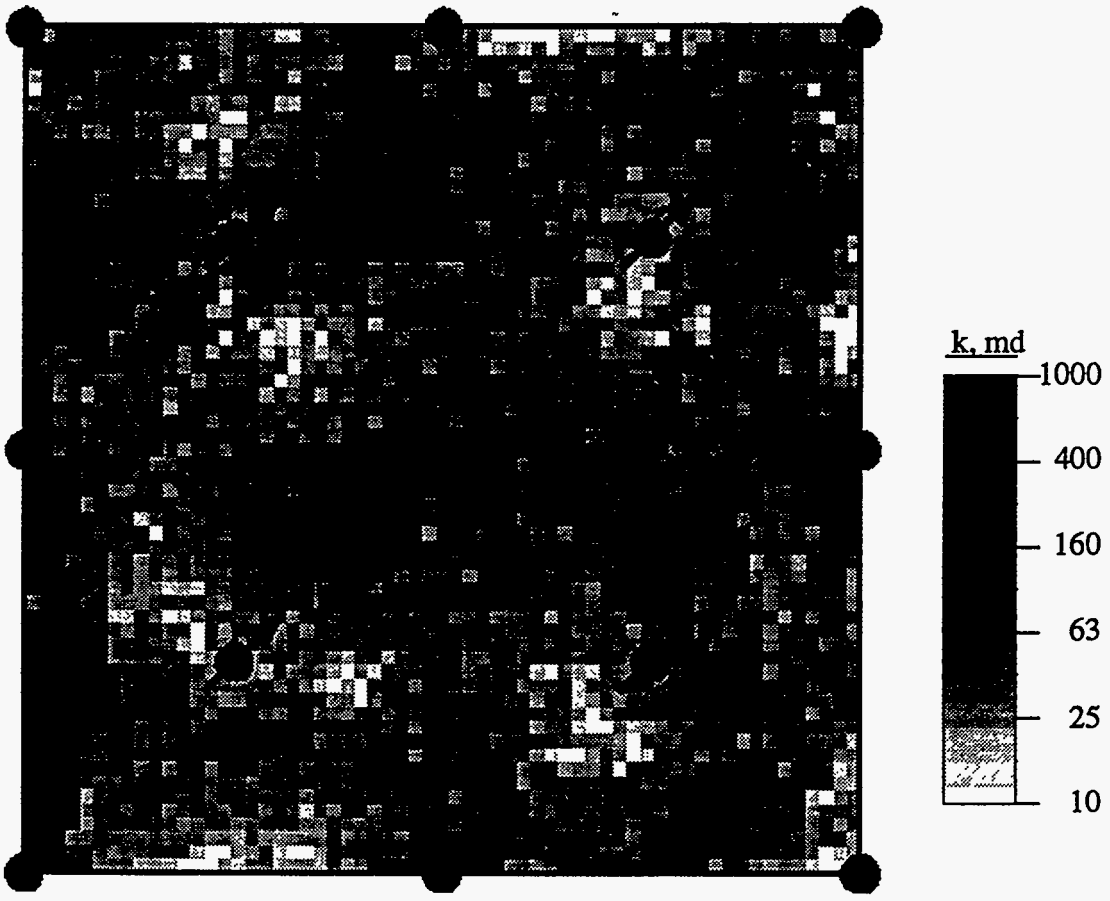

Figure 1.79: Truth case permeability field for the more heterogeneous permeability distribution; extended five-spot pattern.

streak connecting the central producer and the injection well offset to the southeast and 4) a high permeability connectivity streak running north/south along the west side.

Waterflood performance plots for the inner five-spot pattern wells are presented in Fig. 1.80 and Fig. 1.81. As expected for a highly heterogeneous system, performance varies considerably from realization to realization. For the central producer, water breakthrough time varies from less than 2 years to more than 4 years. The initial oil production rate for the central producer varies from 25 STB/D to 70 STB/D. The wells' WOR after 20 years ranges from 13 to 33 STB/STB. Similar variations are evident in the rate profiles of the four inner five-spot pattern injection wells (Fig. 1.81). Such large variations would result in extremely broad waterflood performance probability distributions. Additional information must be integrated into the reservoir description before realistic probability distributions can be obtained.

Variations in the spatial distribution of permeability between realizations are illustrated in Fig. 1.82. Three of the 20 permeability realizations generated using conventional simulated annealing are compared to the truth case image. Although the same degree of heterogeneity (permeability frequency distribution and spatial correlation) exists in all four realizations, local well-to-well heterogeneities differ greatly. This, of course, is the reason for the large variation in waterflood performance depicted in Fig. 1.80 and Fig. 1.81. For example, the central producer is surrounded by a high permeability region for both the truth case and Realization 3. However, the high permeability streak connecting the central producer to the northeast injection well does not exist for the truth case. As a result, the pore volume connecting these two wells will be processed much faster and less efficiently for Realization 3 than the truth case. Such adverse discrepancies exist throughout the 13 well area for all 20 realizations when compared to the truth case.

k_{NW}, $CV_{k\bullet}$ and k_{PAT} Results

For comparison, 20 additional permeability realizations were generated using the conventional constraints and the three indirect performance constraints - k_{NW}, $CV_{k\bullet}$

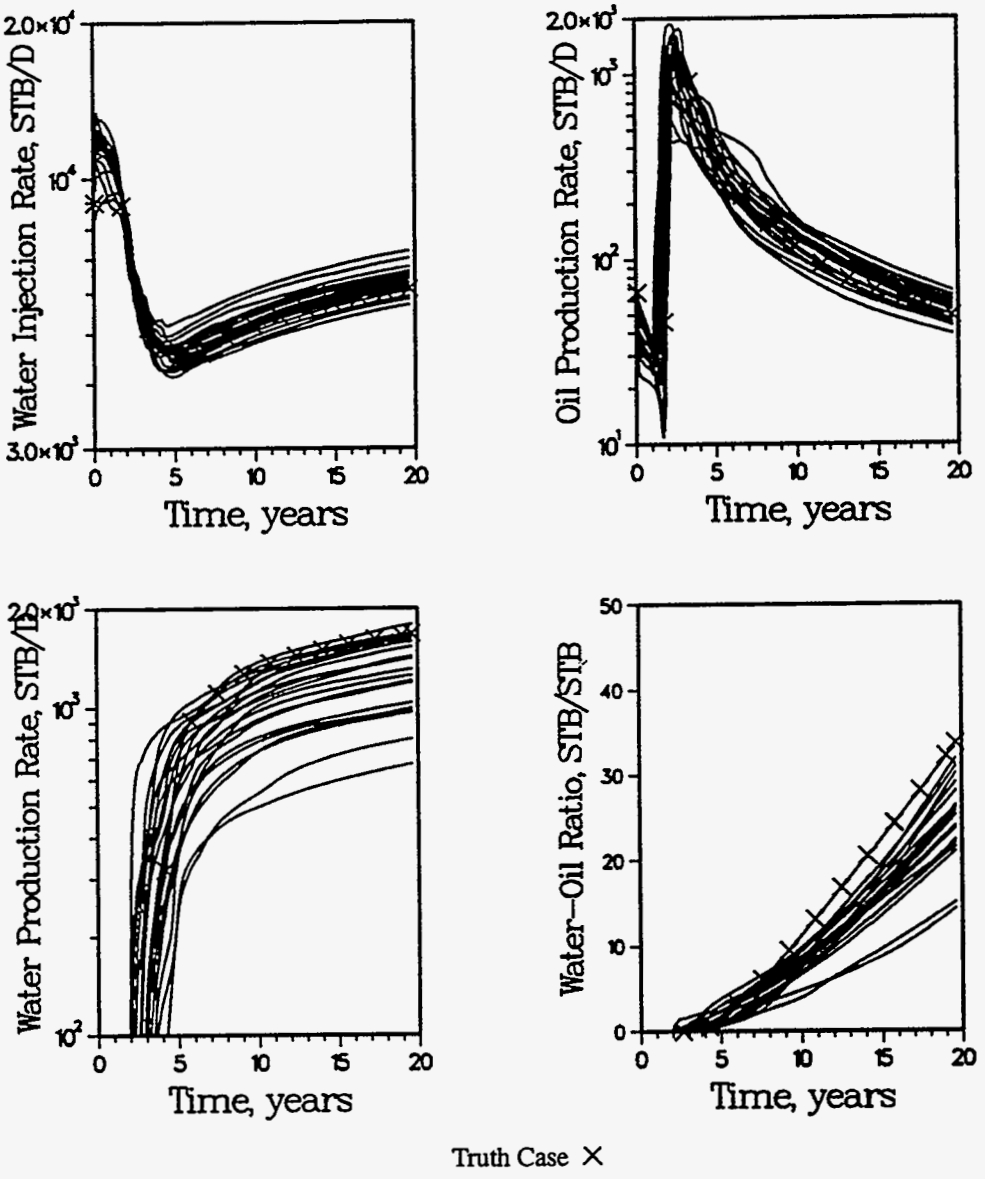

Figure 1.80: Base case waterflood performance for the inner five-spot pattern wells; extended five-spot pattern study using the more heterogeneous permeability distribution.

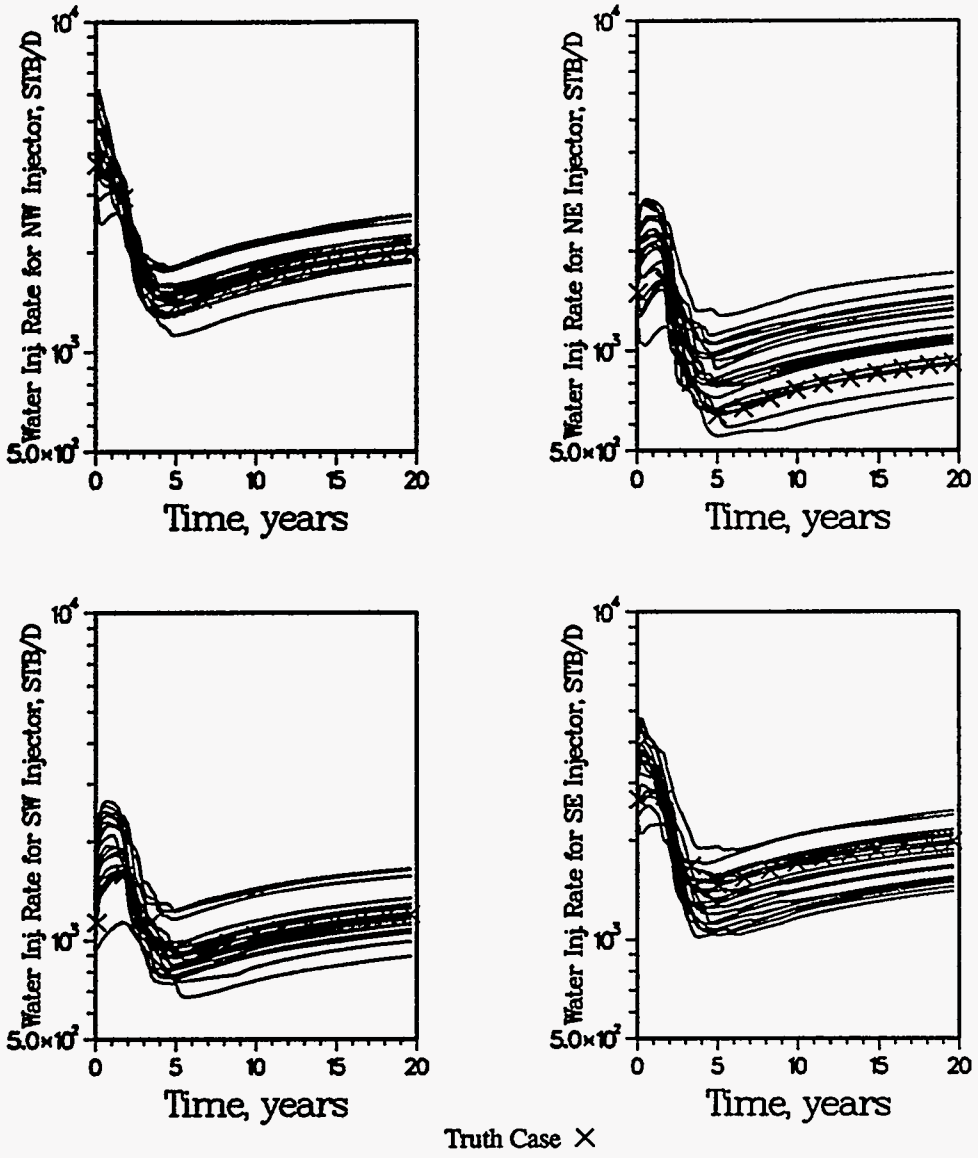

Figure 1.81: Base case waterflood performance for the inner five-spot pattern injection wells; extended five-spot pattern study using the more heterogeneous permeability distribution.

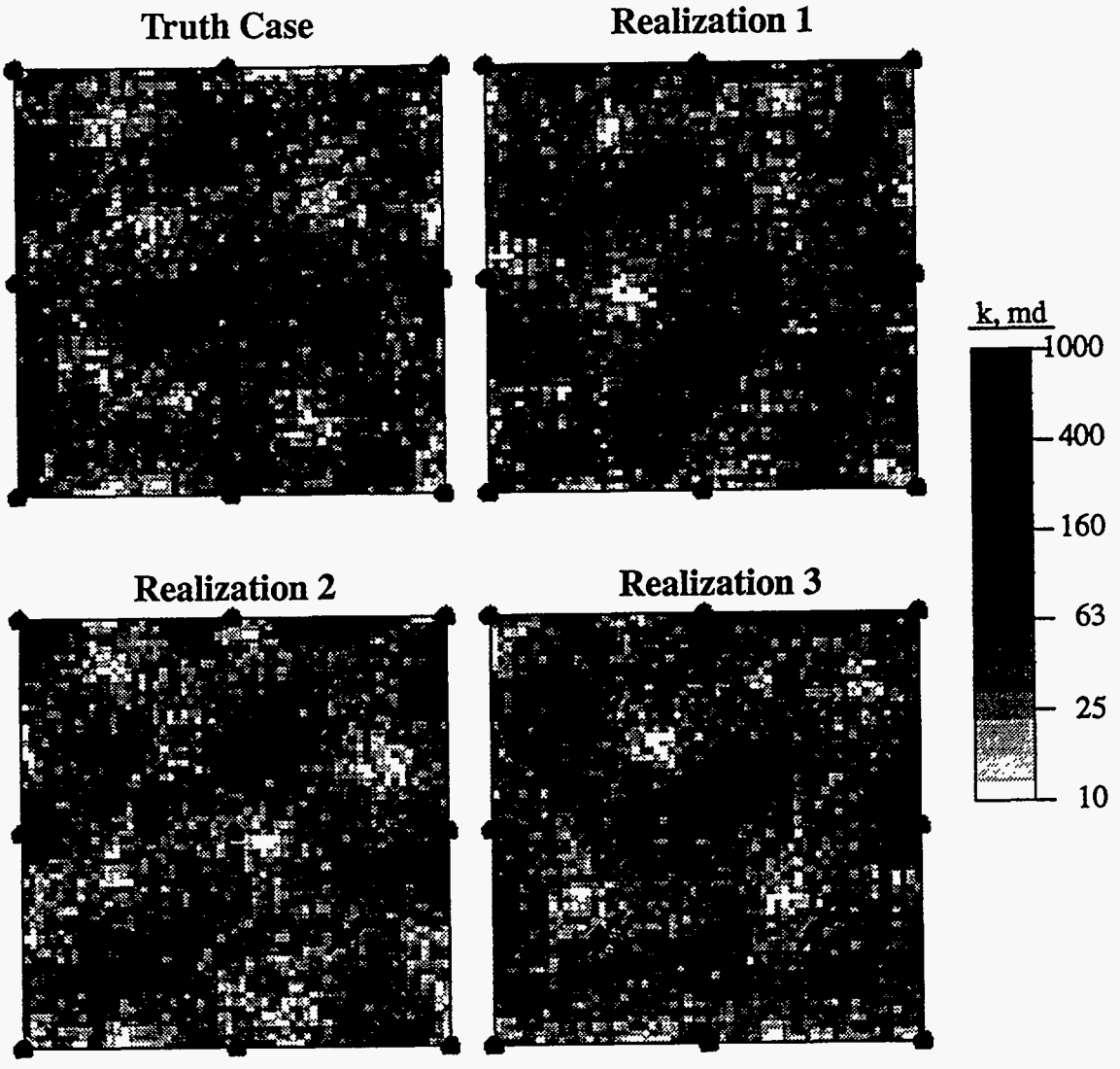

Figure 1.82: Comparison of extended five-spot pattern truth case permeability field to three permeability fields generated using conventional conditional simulation constraints.

and k_{PAT}. The waterflood performance of these 20 permeability realizations are depicted in Fig. 1.83 and Fig. 1.84. Also included in these figures are the results for the truth case. A comparison of these results to those obtained using conventional constraints (Fig. 1.80 and Fig. 1.81) shows the added benefit of including the indirect performance constraints. The permeability realizations generated with the indirect performance constraints have waterflood performance characteristics very similar to the truth case. This is true for the central producer and the four offset injection wells. All available data - geological, petrophysical and production--are now being integrated into the reservoir description.

Three permeability realizations obtained using the three indirect performance constraints are compared to the truth case permeability field in Fig. 1.85. Close inspection of these permeability images shows that most of the truth case high and low permeability regions are correctly reproduced by the three realizations. However, as would be expected considering the large number of unknowns, all three realizations do not perfectly reproduce the truth case permeability field. A probabilistic approach is still required to quantify uncertainty.

k_{NW} and CV_{k*} Results

It was previously concluded that inclusion of the k_{PAT} constraint would reduce the spread in simulated waterflood performance when large variations in the effective permeability of injector/producer regions of influence existed. To further examine this, permeability realizations were generated using the conventional constraints and the indirect performance constraints k_{NW} and CV_{k*} (not k_{PAT}). The corresponding waterflood performance of the inner five-spot pattern wells are depicted in Fig. 1.86 and Fig. 1.87. When comparing these results to those obtained using all three indirect performance constraints, there are many similarities. The only significant difference is the increased spread in water breakthrough times as a result of not including k_{PAT}. Water breakthrough times for the central producer range from 2.5 to 4.5 years when k_{PAT} is not included as a constraint (Fig. 1.86) and from 2.5 to 3.2 years when k_{PAT} is included. Because of the difficulty in estimating k_{PAT}, it is

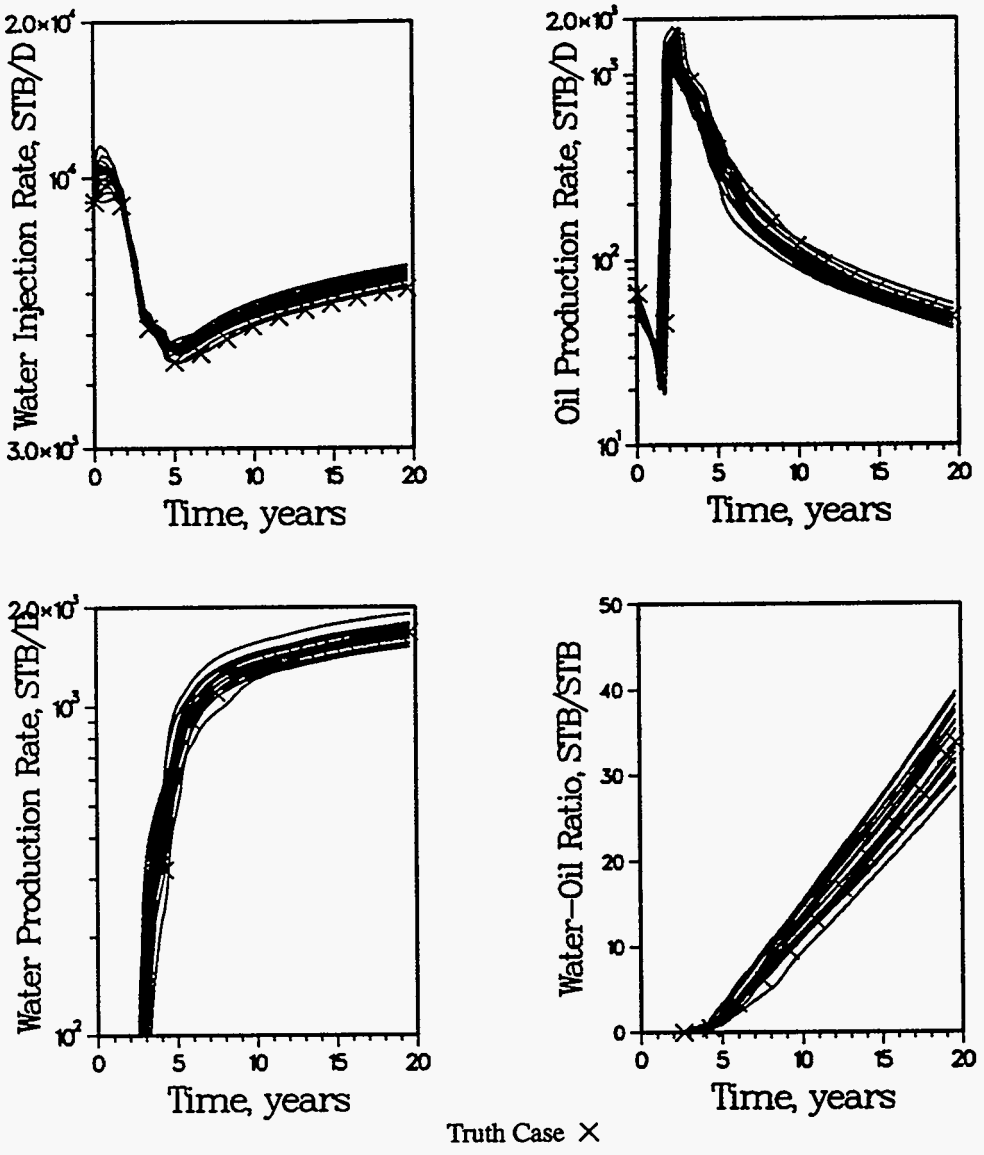

Figure 1.83: Conventional and k_{NW}, CV_{k*} and k_{PAT} indirect performance contraints case waterflood performance for the inner five-spot pattern wells; extended five-spot pattern study using the more heterogeneous permeability distribution.

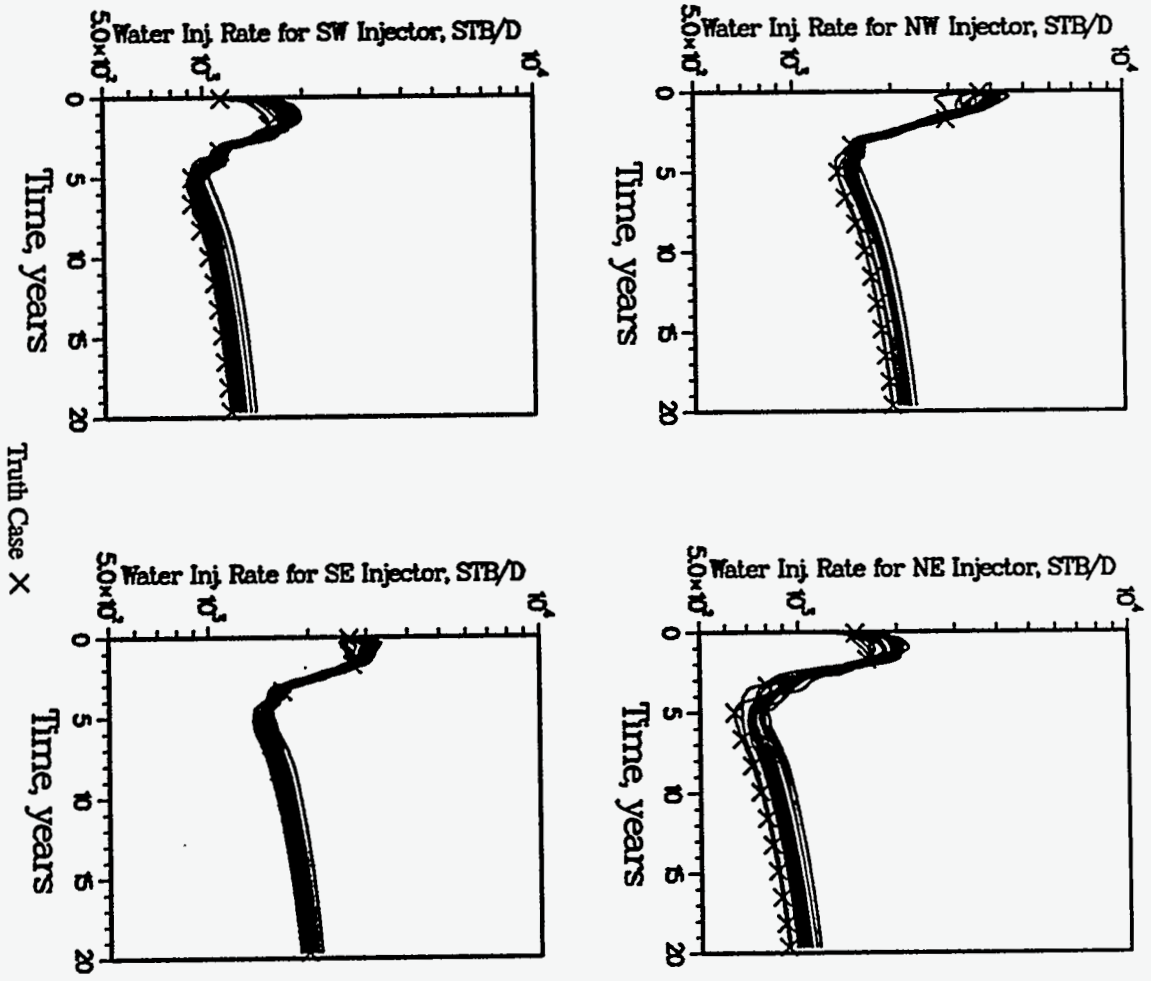

Figure 1.84: Conventional and k_{NW}, CV_{k*} and k_{PAT} indirect performance contraints case waterflood performance for the inner five-spot pattern injection wells; extended five-spot pattern study using the more heterogeneous permeability distribution.

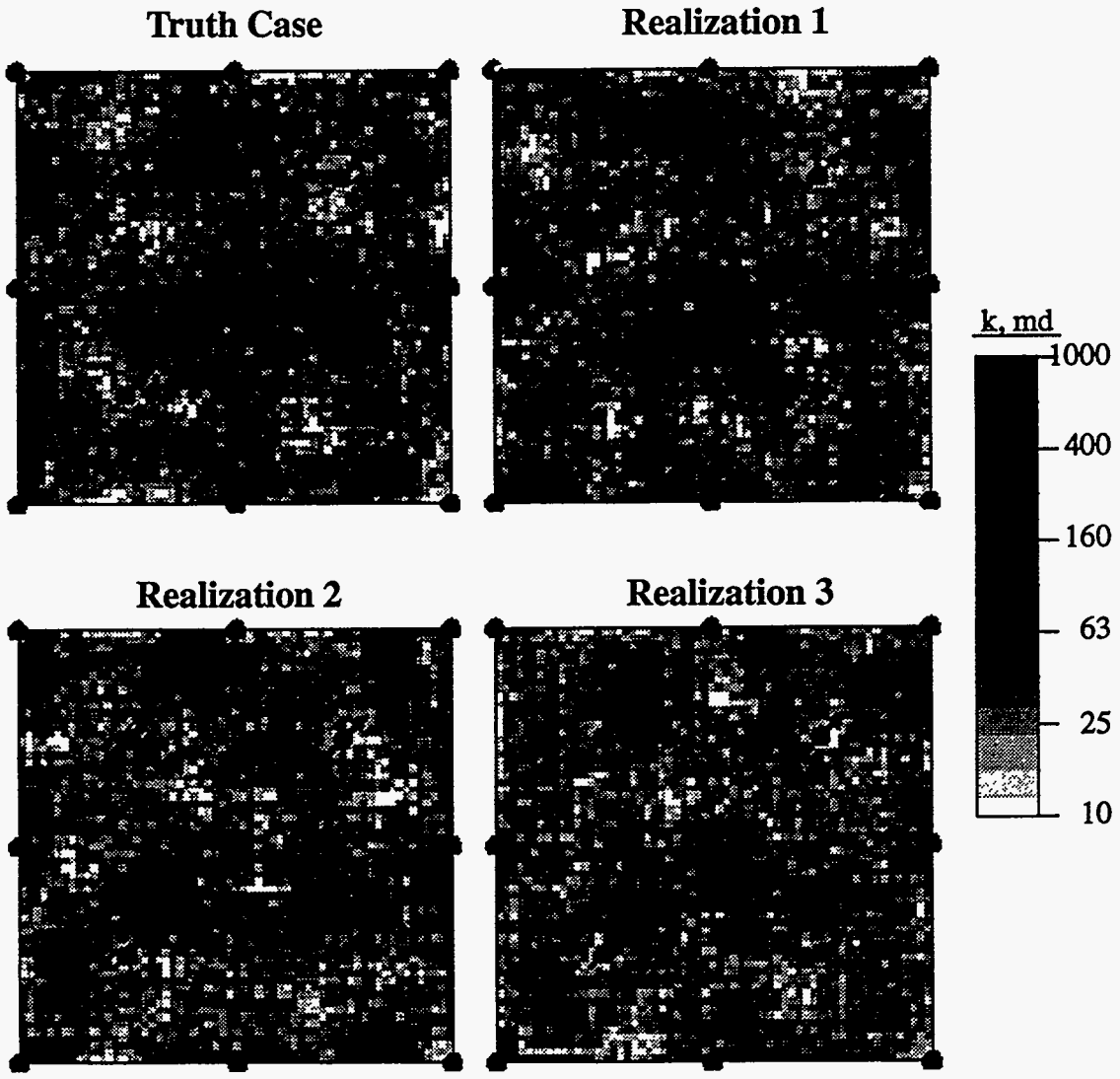

Figure 1.85: Comparison of extended five-spot pattern trugh case permeability field to three permeability fields generated using conventional and indirect performance constraints k_{NW}, CV_{k_*} and k_{PAT}.

reassuring to observe that the effect of k_{PAT} is not significant.

Indirect Performance Constraints Results Without Variogram Constraint

Considering the significant improvement obtained when including indirect performance constraints when generating permeability realizations, the necessity of the variogram constraint could be questioned. Realizing the difficulties involved in quantifying spatial correlation, especially for distances less than interwell distances, it would be of great benefit to eliminate its need. The time and money invested in acquiring and processing seismic data, studying outcrops and variogram analysis are very significant. The ability to extract spatial correlation characteristics from production data would greatly simplify reservoir characterization methodologies.

With this in mind, another synthetic case study was performed with all conventional and indirect performance constraints applied except for the permeability variogram constraint. As in previous case studies, the truth case properties were used to generate an additional 20 permeability realizations. Waterflood performance for the inner five-spot pattern wells for each realization and the truth case are shown in Fig. 1.88 and Fig. 1.89. Note the extremely small spread in each performance curve and the good reproduction of the truth case performance. These results are actually better than any of the previous results (see Fig. 1.80, Fig. 1.81, Fig. 1.83, Fig. 1.84, Fig. 1.86 and Fig. 1.87). The best reproduction, which is of obvious importance, is the oil production rate profile. It can be concluded from these results that waterflood performance can be simulated and predicted into the future using the indirect performance constraints without the aid of the permeability variogram constraint. This assumes that operating conditions are not altered during the course of the waterflood.

Three of the 20 corresponding permeability realizations are depicted in Fig. 1.90 and compared to the truth case permeability field. The absence of spatial correlation is obvious in each of the three realizations. In fact, the realizations appear almost to be completely random in nature. It is very surprising that these permeability fields are characterized by essentially the same waterflood performance as the truth case. This synthetic case study is a good example of the problem of non-uniqueness

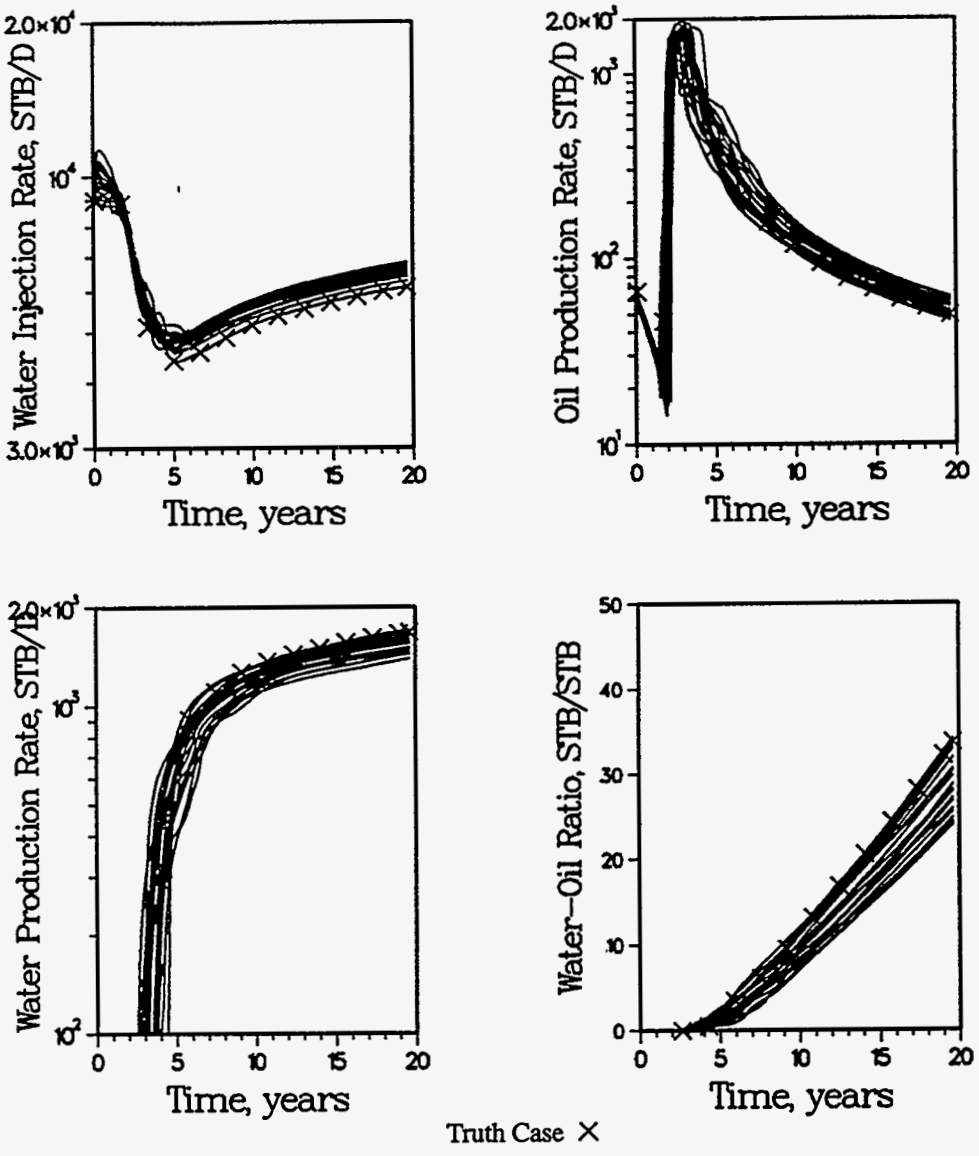

Figure 1.86: Conventional and k_{NW} and CV_{k*} indirect performance contraints case waterflood performance for the inner five-spot pattern wells; extended five-spot pattern study using the more heterogeneous permeability distribution.

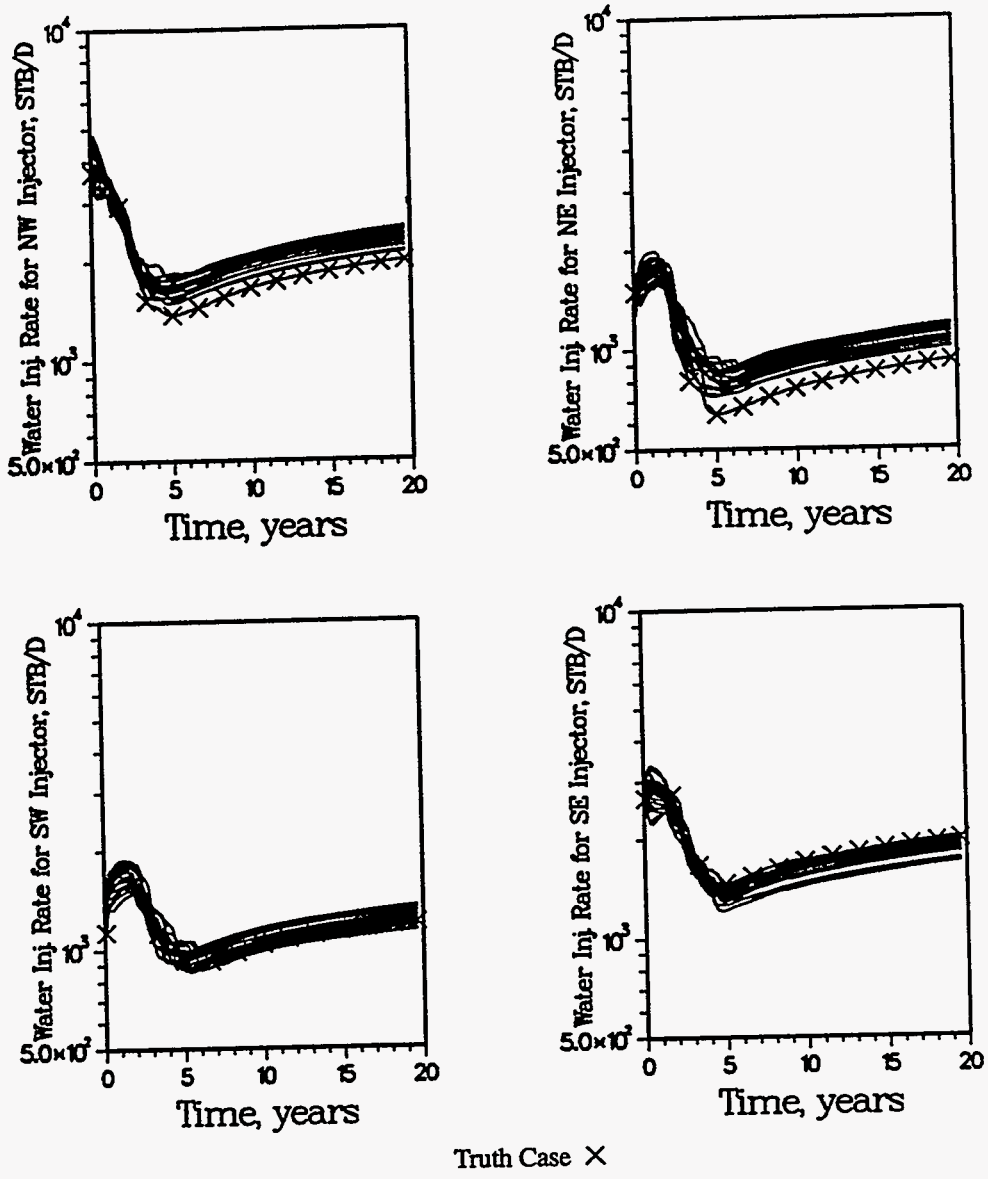

Figure 1.87: Conventional and k_{NW} and CV_{k*} indirect performance contraints case waterflood performance for the inner five-spot pattern injection wells; extended five-spot pattern study using the more heterogeneous permeability distribution.

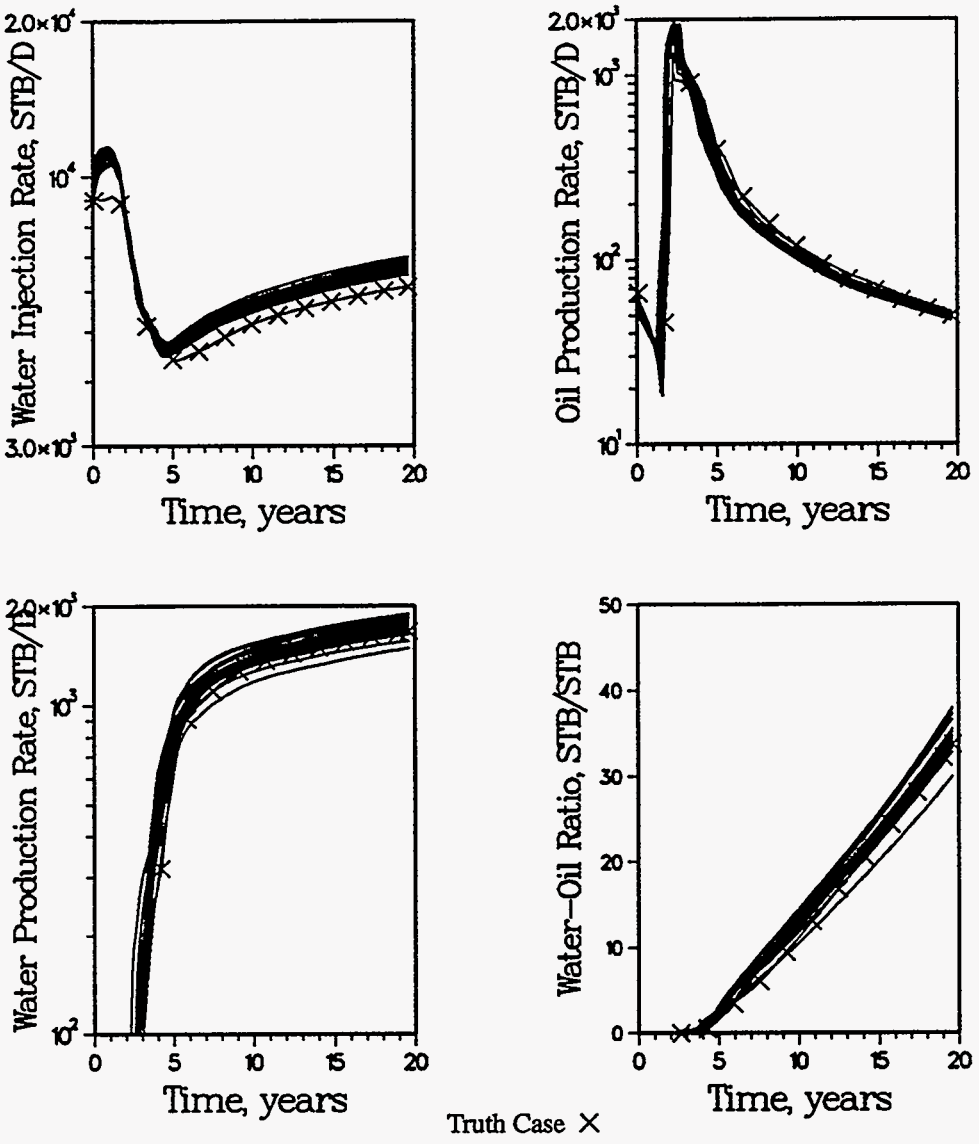

Figure 1.88: k_{NW}, CV_{k*} and k_{PAT} indirect performance contraints without variogram constraint case waterflood performance for the inner five-spot pattern wells; extended five-spot pattern study using the more heterogeneous permeability distribution.

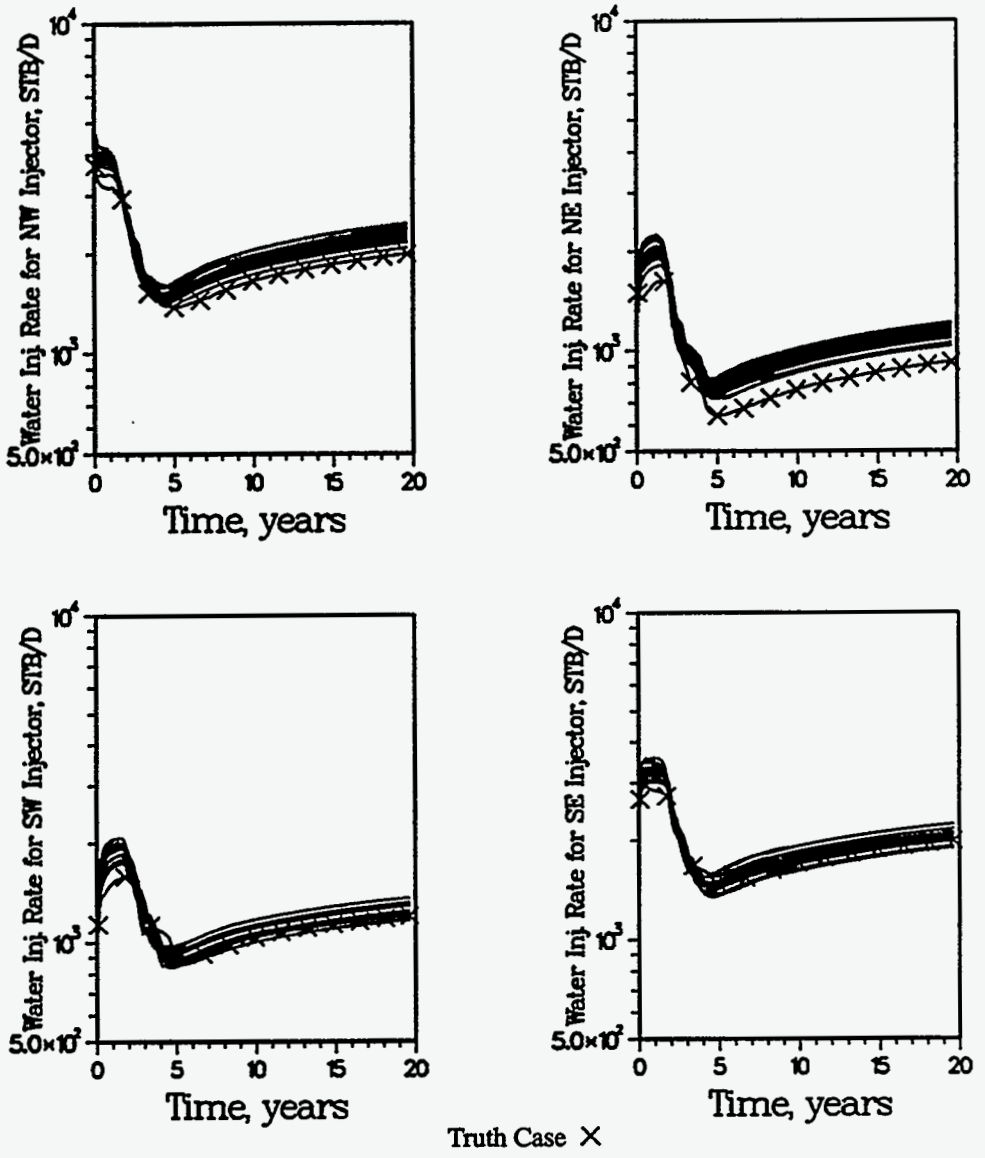

Figure 1.89: k_{NW}, CV_{k*} and k_{PAT} indirect performance contraints without variogram constraint case waterflood performance for the inner five-spot pattern injection wells; extended five-spot pattern study using the more heterogeneous permeability distribution.

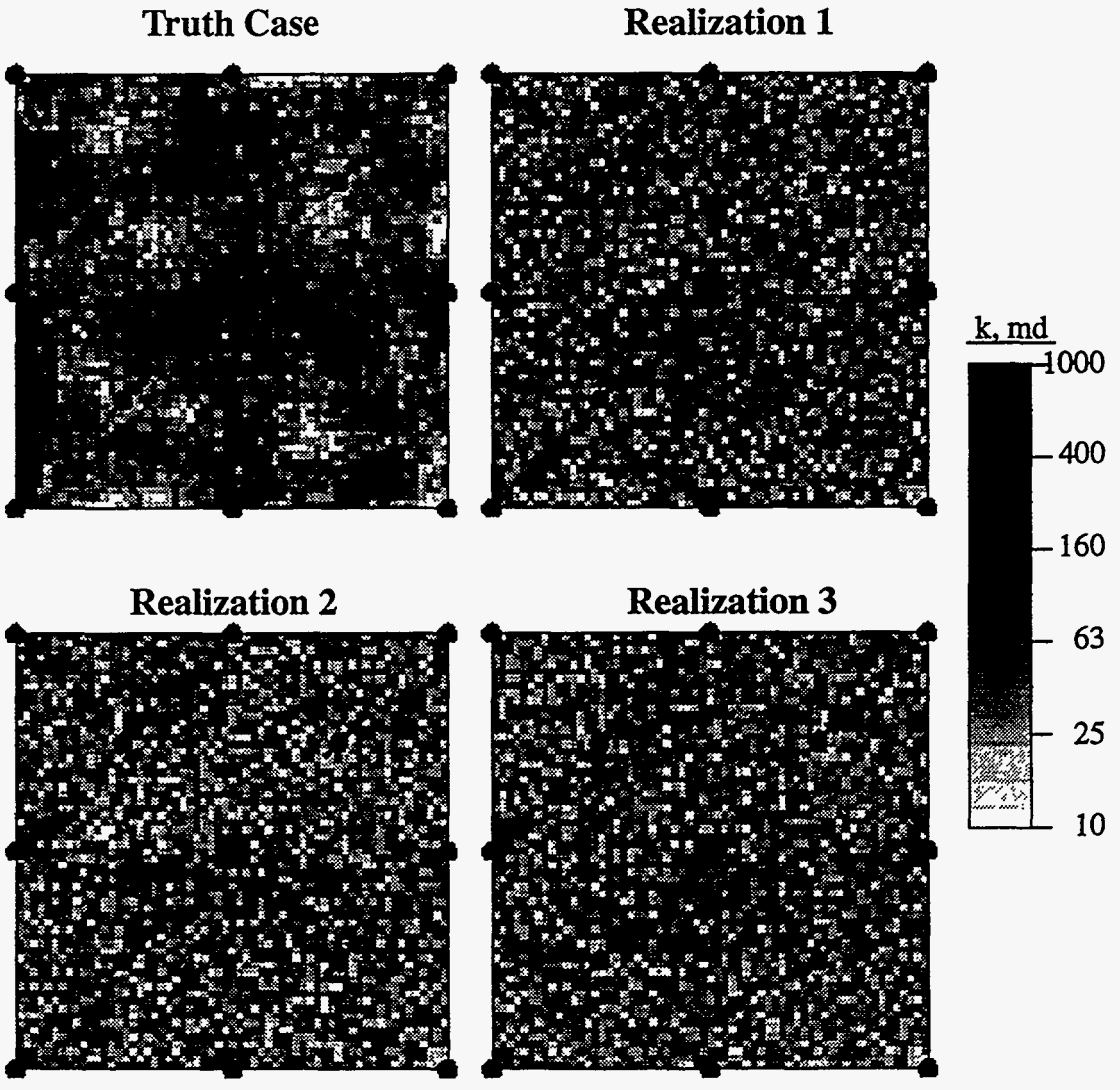

Figure 1.90: Comparison of extended five-spot patter truth case permeability field to three permeability fields generated using indirect performance constraints k_{NW}, CV_{k*} and k_{PAT} but not including variogram constraint.

encountered in history matching simulation studies. An unlimited number of permeability fields, similar to the three included in Fig. 1.90, can be generated having the same waterflood performance as the truth case but possessing extremely different spatial properties.

An important point to make is that these results all assume there aren't any changes in the operating conditions. If the above approach (i.e., no variogram constraint) was used to obtain a reservoir description via history matching waterflood performance, the success of the study would be totally dictated by the objectives. For example, if the study was being performed just to predict future waterflood rates and recoveries under existing operating conditions, it appears that the above approach should give realistic results. However, if the above approach was being used to develop a reservoir description for determining the optimum recovery scheme for future operations, the resulting conclusions could be misleading.

This particular synthetic waterflood case study emphasizes the value of geological information when characterizing a reservoir. Geological information, as represented by the variogram, is essential if the objective is to obtain a realistic spatial description of reservoir properties. This sort of information cannot be extracted from production data alone.

Summary of Results

Waterflood performance was shown to be more sensitive to reservoir heterogeneities than primary recovery. The reservoir characteristic identified as having the biggest impact on waterflood recovery efficiency was reservoir connectivity. Two reservoir connectivity parameters were defined, p_{tH} and CV_{k*}. The latter connectivity parameter was found to give better results when used as a conditional simulation constraint. The parameter CV_{k*} was determined to correlate strongly with water breakthrough time and cumulative water-oil ratio.

One-quarter five-spot pattern flow simulations were used to show that so-called "equally probable" realizations of permeability generated using conventional conditional simulation constraints were found to result in widely varying simulated well performance. When the CV_{k*} constraint was combined with conventional constraints and a near-well effective permeability constraint (referred to as "indirect

performance constraints"), the resulting permeability realizations exhibited very similar simulated waterflood performance. The indirect performance constraints were shown to significantly reduce the uncertainty in identifying high and low permeability regions.

Extended five-spot pattern simulations were performed to evaluate the effectiveness of the indirect performance constraints given the interaction of multiple injector/producer pairs. It was discovered that an additional indirect performance constraint, k_{PAT}, may be required for multiple injector/producer systems. This parameter becomes important when the average permeability for neighboring injector/producer areas of influence varies significantly. Permeability realizations generated using conventional constraints were found not to provide any assistance in identifying low and high permeability regions. Inclusion of the indirect performance constraints greatly reduced the uncertainty in spatial properties. An interesting discovery was that permeability fields could be generated having very similar waterflood performance by using the indirect performance constraints without including the variogram constraint. However, the resulting permeability realizations were nearly spatially random and poorly reproduced the desired spatial distribution of high and low permeabilities. It was concluded that spatial correlation structures cannot be inferred from production data; such information must be obtained from geological inferences.

Two-Dimensional Full-Field Study

The previous section investigated the impact porosity and permeability heterogeneities have on primary and secondary performance for an extended five-spot pattern. Only one petrophysical parameter was varied at a time; all others were assumed to be constant. Simulations were performed for limited areal coverage. Thus, only local spatial heterogeneities were considered. The impact of global trends superimposed on local variations were not addressed. The work included in this section has been performed to investigate these additional complications.

After summarizing the procedure used to generate the two-dimensional (2D) full-field truth case, its exhaustive reservoir properties will be described. Univariate and spatial statistical properties of the exhaustive data set will be compared with well values to identify important differences which directly impact conditional

simulation results. Truth case field and well performance are then compared to results obtained using varying degrees of available well performance data, most notably primary performance constraints versus primary and secondary performance constraints. Such a comparison illustrates the relative importance of the various constraints. This is important information considering certain performance constraints are obtainable only during specific phases of a well's life and are known with different degrees of certainty.

Procedure

This section briefly describes the development of a three-dimensional reservoir description and corresponding flow simulation results. Well and field data collected from the Burbank Field located in Osage County, Oklahoma, were used in developing the reservoir description. The reason for using the Burbank Field data was to construct a field description as close to reality as possible. The details regarding the three dimensional, exhaustive description are provided in the previous DOE report.[1.35]

The fluid properties, gas-oil relative permeability curves and water-oil relative permeability curves used in the flow simulation are shown in Table 1.10 and Fig. 1.91 and Fig. 1.92, respectively. Although the fluid properties are based on published Burbank Field data, the relative permeability curves are typical black oil, water-wet curves. A uniform initial pressure of 1200 psi was used. The bubble point pressure of the black oil is 1024 psi. A uniform initial connate water saturation of 20% was assumed.

In that report[1.35] we have discussed a detailed 10-layer description of the reservoir based on the Burbank reservoir. The 2D full-field reservoir description was generated by combining properties from Flow Units 3, 4 and 5 of the 3D truth case described in that report. These three flow units represent the main sand body and thus dominate the reservoir performance for the 3D truth case. The spatial distribution of sand thickness was obtained by summing the thickness of Flow Units 3, 4 and 5. Porosity values were obtained using thickness-weighted arithmetic averages from these same three flow units. Permeabilities were determined using a permeability-porosity correlation. Exhaustive reservoir properties were not defined on the fine-scale, but using flow simulation. Grid

Pressure, psi	B_o, RB/STB	μ_o, cp	B_g, RB/Mscf	μ_g, cp	R_s, Mscf/STB
14.7	1.0249	2.486	195.4	0.0086	0.000
50.0	1.0363	2.299	56.56	0.0099	0.022
100.0	1.0386	2.236	28.18	0.0108	0.031
150.0	1.0409	2.178	18.7435	0.0112	0.039
250.0	1.0471	2.059	11.1524	0.0116	0.057
350.0	1.0543	1.942	7.8864	0.0118	0.078
450.0	1.0617	1.837	6.0781	0.0119	0.099
700.0	1.0849	1.589	3.7942	0.0124	0.160
950.0	1.1128	1.380	2.7078	0.0129	0.229
1024.0	1.1215	1.326	2.4887	0.0131	0.250
1200.0	1.1197	1.341	2.0158	0.0136	0.250
1250.0	1.1192	1.345	1.9608	0.0143	0.250
1500.0	1.1168	1.366	1.6858	0.0150	0.250
1750.0	1.1146	1.386	1.4108	0.0157	0.250
2000.0	1.1124	1.407	1.1358	0.0164	0.250

Table 1.10: Black oil fluid properties used in flow simulations.

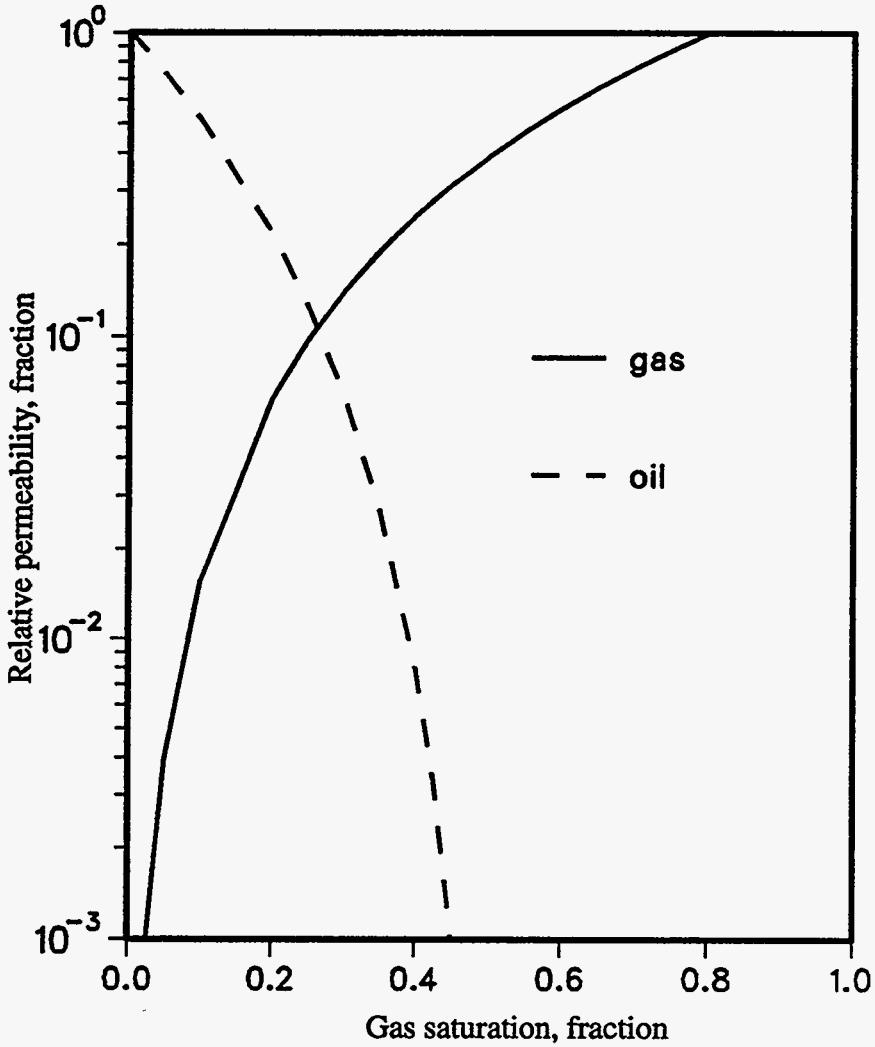

Figure 1.91: Gas-oil relative permeability curves used in flow simulations.

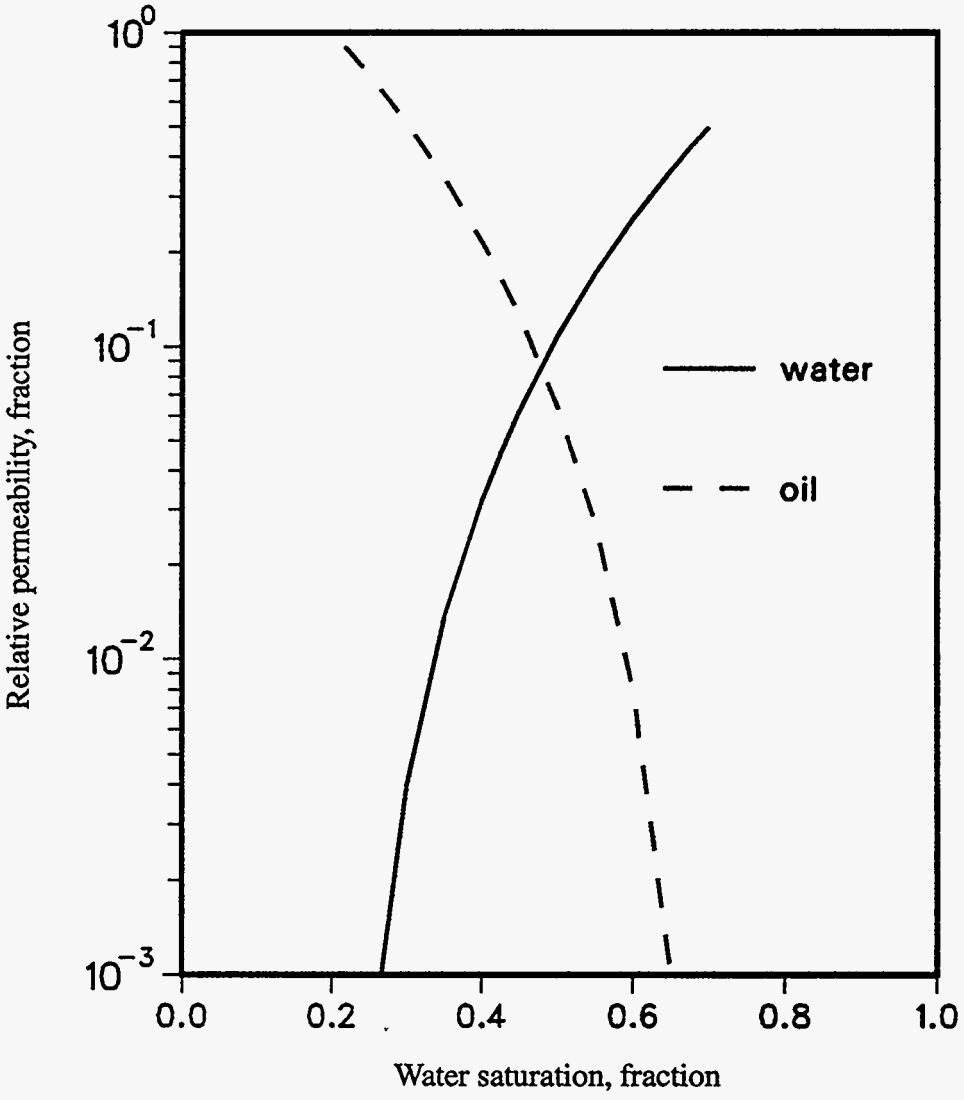

Figure 1.92: Water-oil relative permeability curves used in flow simulations.

blocks were 3888 (108 by 36) for the 4.5 mile by 1.5 mile system. Each block was 220 ft. × 220 ft. in size. Conditional simulations were performed using large grid blocks to make the study more manageable considering the large number of realizations and flow simulations generated.

Fig. 1.93 shows the location of the 59 wells used in the flow simulation. The wells were "drilled" on 80 acre spacing. These well locations do not correspond with the actual location of wells in the Burbank Field. All of the wells were operated at a constant bottomhole pressure of 200 psi. A total of 10 years of primary production was simulated. Following primary production, 32 of the producers were converted to water injection wells to form 27 five-spot patterns (Fig. 1.94). The injection pressure for all injection wells was set at 2000 psi. Water injection was continued for 10 years, resulting in a total simulation time of 20 years.

The study assumed conditioning data included well grid block porosities and sand thicknesses. Variograms for these two variables were estimated from the well data. It was also assumed that the grid block-scale permeability-porosity correlation was known. The spatial distribution of sand thickness was obtained using the well data-derived variogram and kriging. Unlike the spatial distributions of permeability and porosity, kriged sand thickness results were assumed to adequately represent the actual reservoir, i.e., the sensitivity of reservoir performance on alternative sand thickness relations was not investigated. Either well block porosities or permeabilities could be specified as conditioning data since a unique correlation between the two parameters was assumed. Swapping of paired values during the simulated annealing process required updating each objective function component because of the interdependency of porosity and permeability. The simulated annealing algorithm used for the full-field study is discussed in Section 1.2. Additional information regarding the conditional simulation program developed for performing this case study is given somewhere else.[1,2]

Univariate and Bivariate Distributions

Grid block thicknesses range from 14 to 72 feet with the mean thickness equaling 36.4 feet. Thickness values are essentially normally distributed having a standard

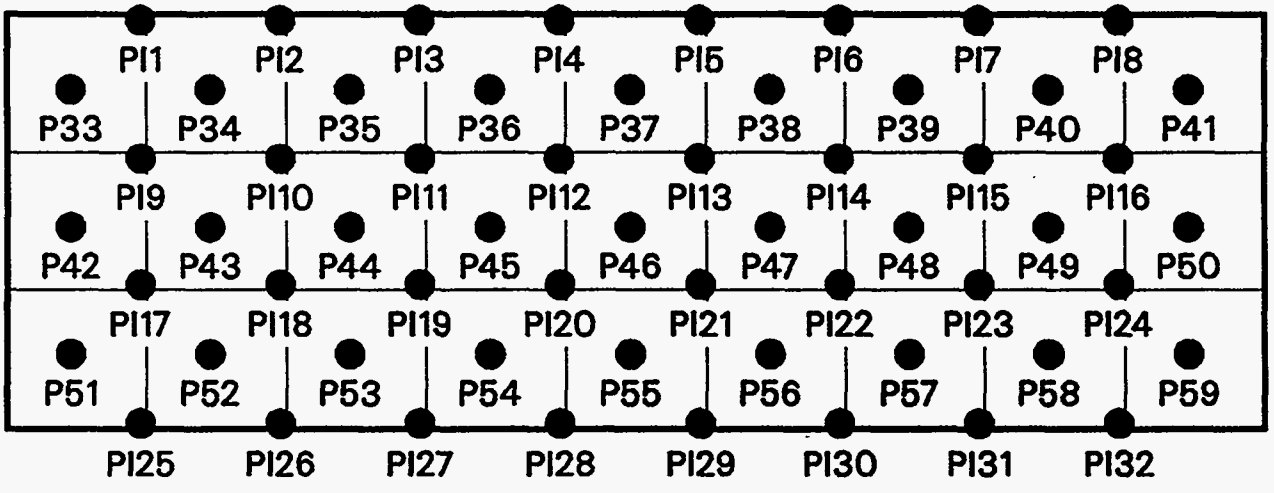

Figure 1.93: Location of producers during simulated primary recovery.

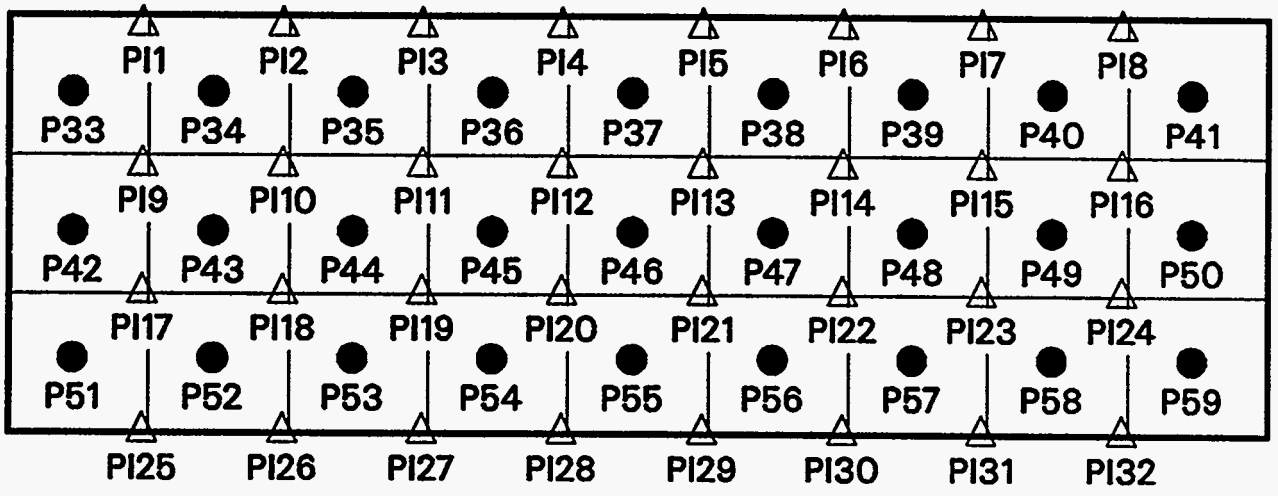

Figure 1.94: Location of producers and injectors during simulated waterflooding.

deviation of 10.4 feet. Half of the thickness values fall between 29 and 44 feet. Grid block porosities range from 0.12 to 0.28. Porosities are also normally distributed having a mean of 0.204 and a standard deviation of 0.027. The porosity interval 0.185 to 0.224 includes the middle 50 percent of the overall range. The linear regression coefficient of Flow Unit 3 log (permeability) vs. porosity core data were used to generate permeability values. The log-normally distributed permeabilities range from less than 1 md to more than 300 md. Approximately 75% of the permeability values are 100 md or less.

Spatial Correlations

The experimental variogram for sand thickness of the truth case grid block values is shown in Fig. 1.95. Two directional variograms are illustrated - one a N90°E, the major direction, and the other along the minor direction of N0°E. The sand thickness correlation length along the major direction is about 12,000 feet. This is about three times the correlation length of the minor direction. The nugget effect is essentially zero. Directional experimental porosity variograms are contained in Fig. 1.96. A correlation length in excess of 12,000 feet exists in the major direction of N90°E. The porosity variogram has an anisotropy ratio of about 5 with the minor direction of N0°E having a correlation length of only 3,000 feet. A nugget of about 20 percent exists for the variogram.

Spatial Properties

Fig. 1.97 contains a map of pay thickness for the full-field truth case. Locations of the 59 wells are also included in the figure. Sand thickness is seen to be the greatest in the northwest and thinnest to the southwest and east-central. Although the strong east-west correlation is evident in many areas of the field, some areas (e.g., the southeast region) is more isotropic. The exhaustive porosity field is depicted in Fig. 1.98. Note the strong east-west directional trend. The average porosity on the west side is approximately 0.23, decreasing to about 0.17 on the east side. The strong porosity trend branches off to the northeast and southeast near the east end of the field. Since permeabilities are derived directly from porosities, the spatial distribution of permeability is very similar to porosity. The exhaustive permeability field has similar characteristics as porosity.

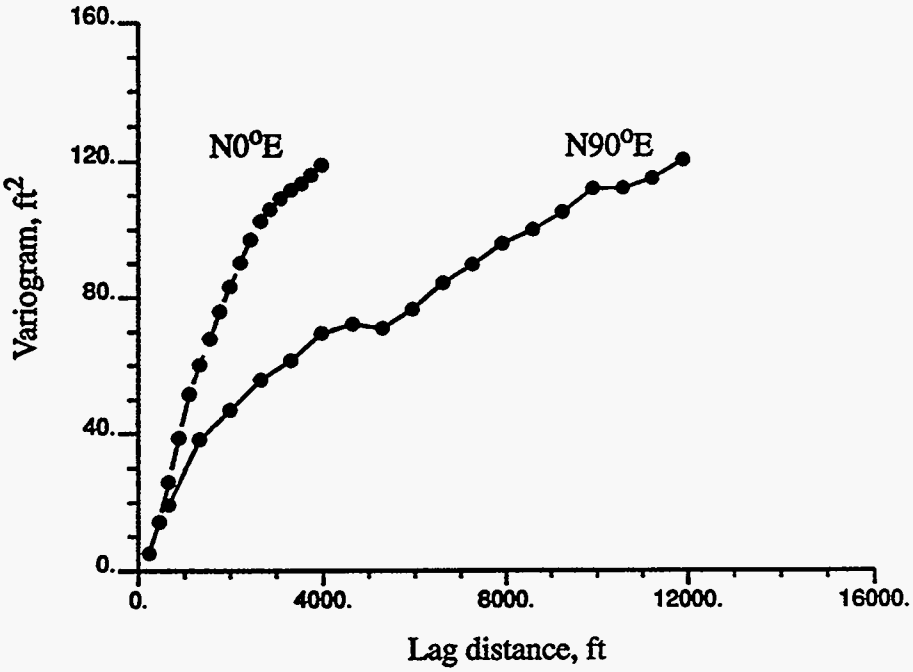

Figure 1.95: Variogram for sand thickness; full-field truth case.

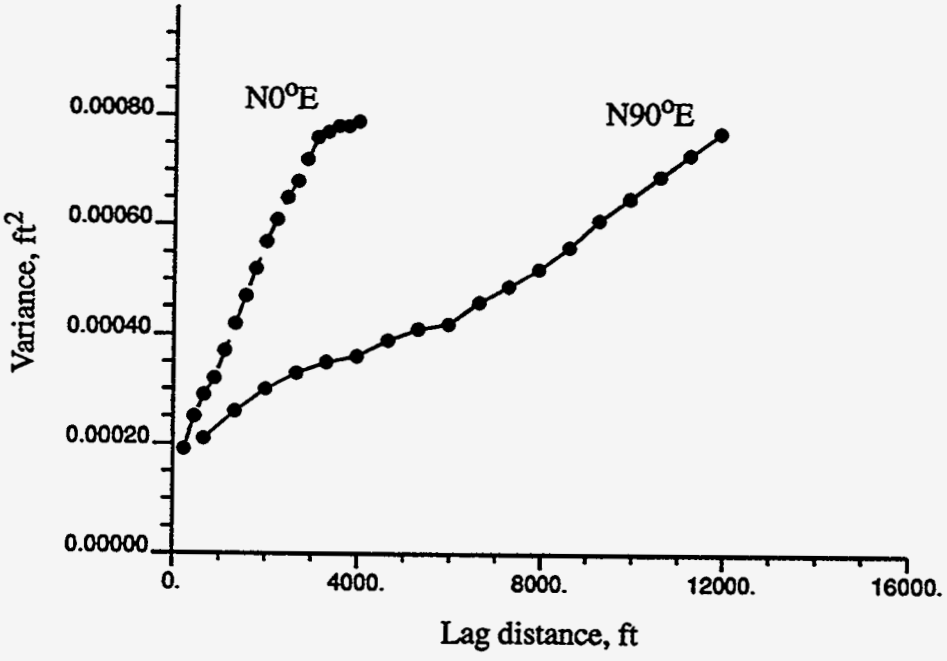

Figure 1.96: Variogram for porosity; full-field truth case.

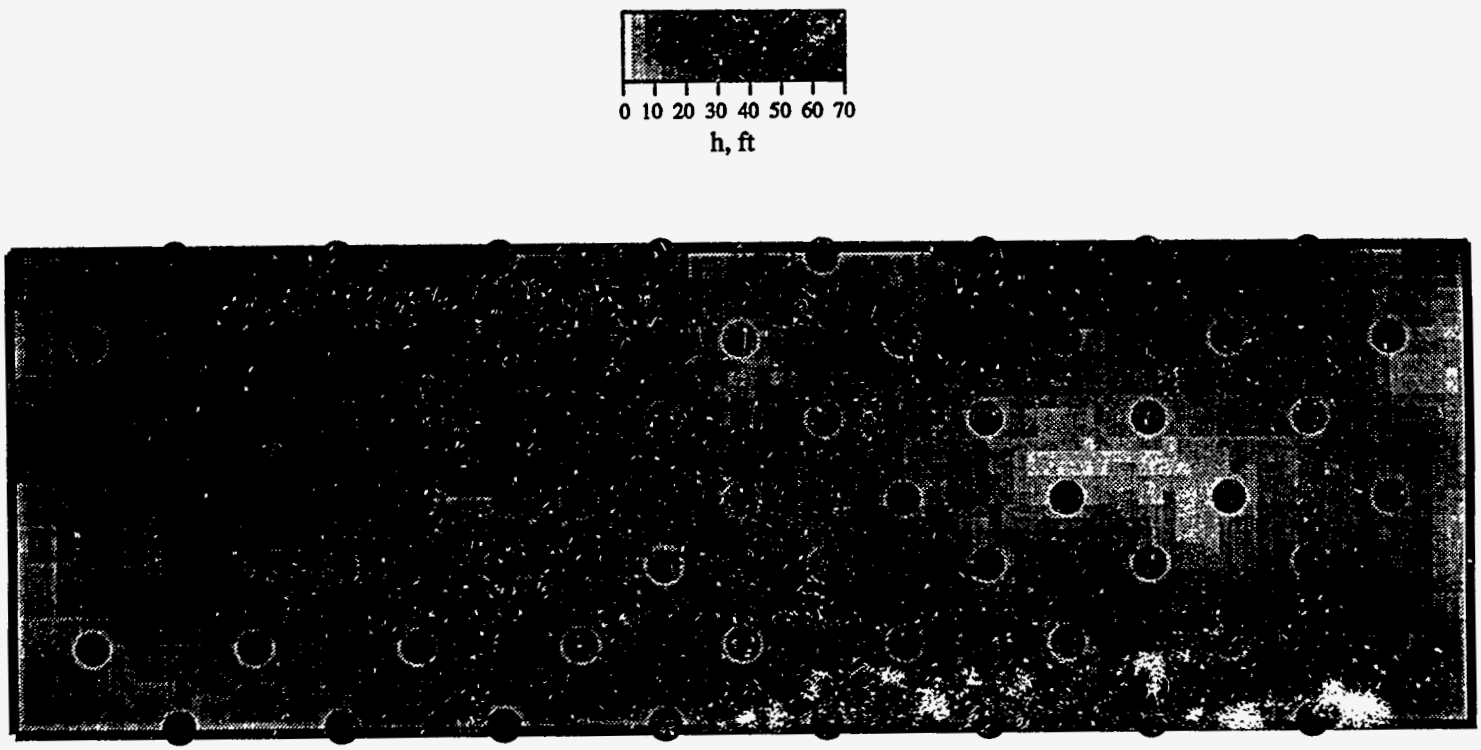

Figure 1.97: Exhaustive pay thickness map for the full-field truth case.

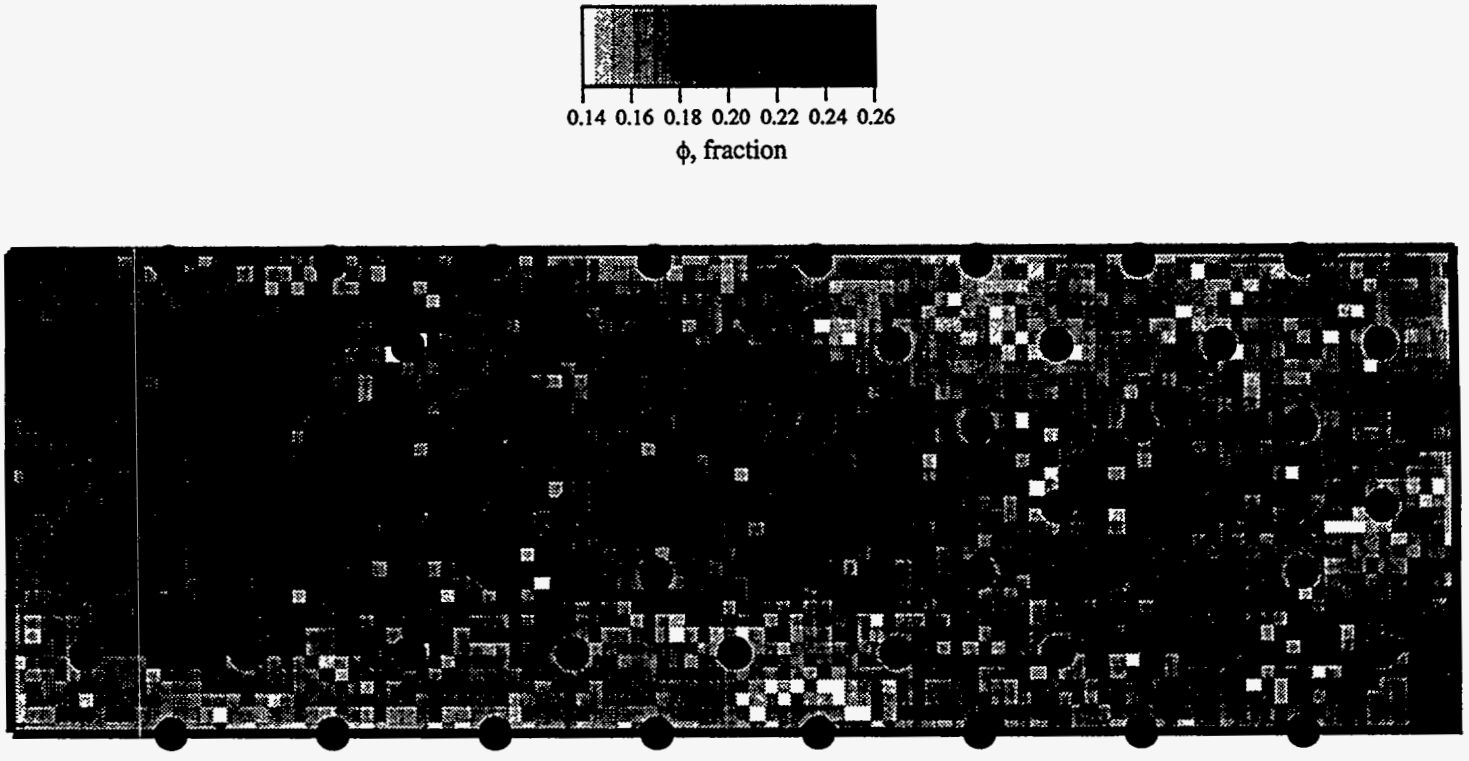

Figure 1.98: Exhaustive porosity field for the full-field truth case.

Well Derived Reservoir Properties

The 2D full-field case study was performed assuming that well block porosity, permeability and sand thickness values are statistically representative of the exhaustive properties. The porosity and sand thickness variograms used as constraints in the conditional simulations were based on analysis of the well data only. Therefore, many of the discrepancies between the exhaustive data set and the simulated reservoir properties are due to errors introduced by assuming exact statistical representation of the exhaustive properties by the well data, and not the inadequacies of the methodology. However, such an approach was selected because of its realistic nature. The amount of error introduced by assuming statistical representation by the well data can be estimated, or at least appreciated, by comparing field and well statistics. Such a comparison follows.

Univariate and Bivariate Distributions

When the histogram based on well grid blocks was compared to the exhaustive sand thickness histogram, the biggest discrepancy is in the disproportionate fraction of high values in the well data. Whereas only about 7 percent of the exhaustive sand thicknesses exceed 52 feet, this cutoff is exceeded by about 13 percent for the well data. A close comparison for porosity values indicates that the exhaustive porosity histogram is slightly positively skewed and the well porosity histogram is slightly negatively skewed. For the permeability data, the well block permeabilities do not contain the extreme high and low values existing in the exhaustive data set.

Spatial Correlations

The experimental variogram of well block sand thickness is depicted in Fig. 1.99. The correlation length in the major direction of N90°E is 9,000 feet, somewhat less than that of the exhaustive data set (Fig. 1.95). The minor direction sand thickness variograms of the well and exhaustive data are very similar. Based on the comparison of Fig. 1.95 and Fig. 1.99, it appears that little error is introduced by assuming the well-based thickness variogram is representative of the full-field. For porosity, variograms based on well data compare extremely well with the exhaustive porosity direction variograms.

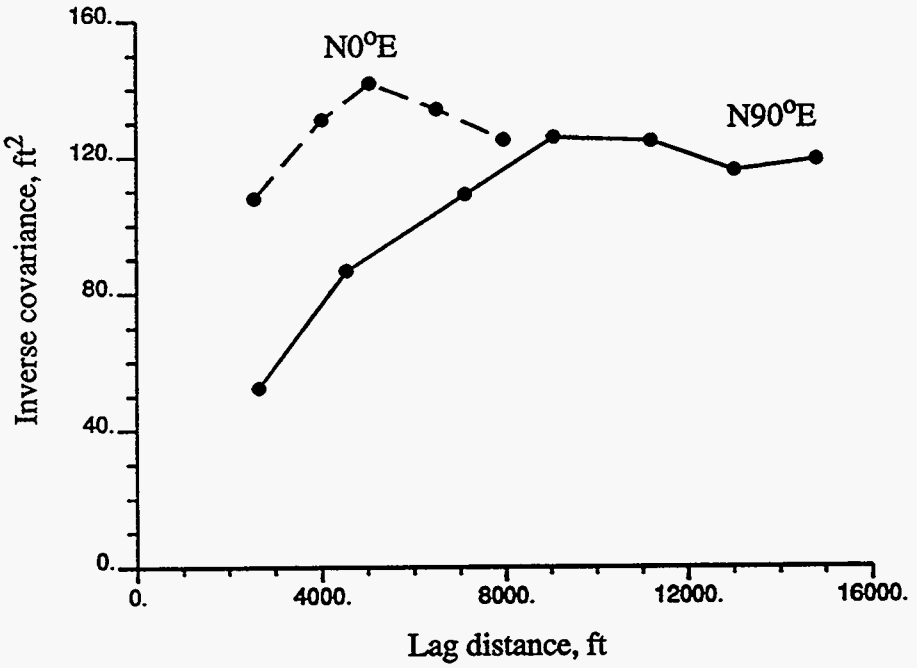

Figure 1.99: Inverse covariance for sand thickness based on the full-field truth case well data.

Spatial Properties - Kriged Sand Thickness

The sand thickness histogram and variogram derived from the well data were used to krige sand thickness. Although resulting thickness map does not capture many of the local variations exhibited by the exhaustive sand thickness map, most of the important sand thickness trends are honored.

Primary Constraints Results

Similar to previously-described synthetic case studies, the effectiveness of the performance constraints will be measured by the ability of resulting alternative reservoir descriptions to 1) simulate well performance which is similar to the truth case well performance and 2) have spatial characteristics which are similar to the truth case. In each case, ten alternative reservoir descriptions were generated using the same constraints. Well configurations, well operating conditions, rock properties and fluid properties are the same as previous case studies. Pertinent data are listed in Table 1.11. Flow simulations were performed assuming 10 years of primary production followed by 10 years of waterflooding. A total of 32 producers were converted to injection wells upon initiation of the waterflood, resulting in 27 five-spot patterns.

k_{NW} Constraint

Since large grid blocks (220 feet by 220 feet) were used for conditional simulation and well blocks were used as conditioning data, the base case results are equivalent to including a near-well effective permeability constraint. A comparison of the exhaustive permeability field to one of the permeability realizations generated using conventional and k_{NW} constraints is displayed in Fig. 1.100. Although many of the truth case global trends are captured using the k_{NW} constraint, this one performance constraint is not sufficient to identify local heterogeneties. Note the large permeability discrepancies in the northwest and northeast corners. These regions have estimated permeabilities which are in error by an order of magnitude or more. Similar results are also observed for porosity data. These results show that the k_{NW} constraint is not sufficient to accurately identify the location of high and low porosity/permeability regions.

Type of Simulation	2D Primary & Waterflood
Waterflood pattern type	1:1 five-spot
Well spacing	80 Ac
Waterflood pattern size	160 Ac
Areal grid dimensions	220 ft by 220 ft
Areal grid density	108 by 36
Thickness, porosity & permeability	variable
Number of primary wells	59
No. of waterflood producers/injectors	32/27
Mobility ratio	0.96
Initial/bubble point pressures	1200/1024 psi
Producing/injecting pressures	300/2000 psi

Table 1.11: Pertinent data used in two-dimensional full-field simulations.

Exhaustive

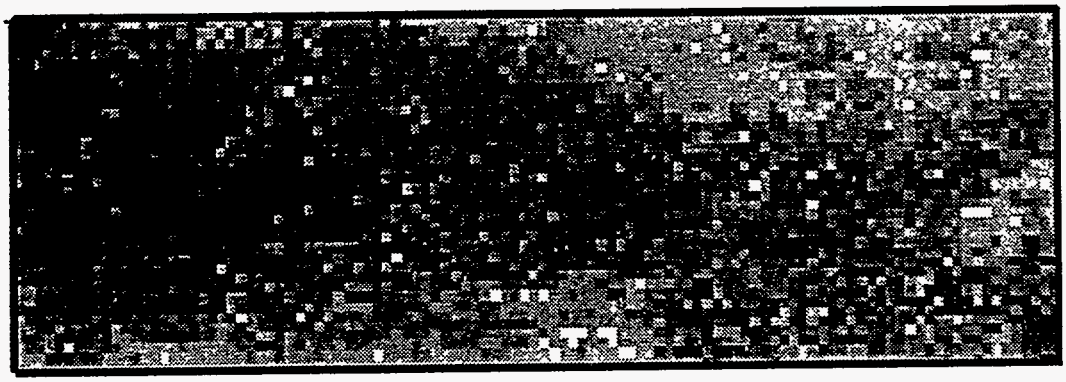

Conventional & k_{NW} Constraints

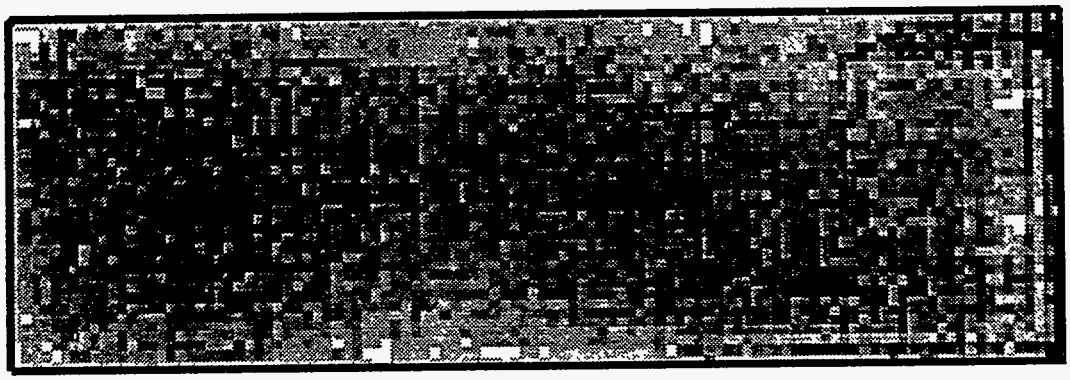

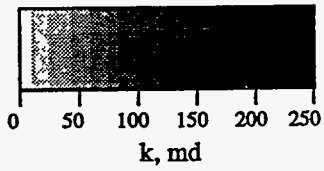

Figure 1.100: Comparison of full-field exhaustive permeability field to permeability field obtained using conventional and k_{NW} contraints.

The truth case and the 10 reservoir descriptions based on the k_{NW} constraint were flow simulated for comparison. The resulting field performances are illustrated in Fig. 1.101. The k_{NW} constraint is seen to do an excellent job in generating reservoir descriptions which behave similar to the truth case in terms of total field primary performance. These results show that it is possible to match historical total field primary performance by honoring near-well effective properties, univariate frequency distributions and general spatial variability characteristics. Also included in Fig. 1.101 is the waterflood performance for the truth case and the 10 k_{NW} constrained reservoir descriptions. The secondary total field oil rate curves are all fairly similar. The most noticeable discrepancies are the water breakthrough times and secondary water production rates. All of the realizations predict water breakthrough later than the truth case. One realization predicts water breakthrough approximately one year too late. At this time, actual water production had already increased to about 3000 STB/D. As expected, the k_{NW} constraint results in significant improvement in primary performance characteristics but is inadequate as a waterflood constraint.

Matching individual well performance is considerably more important than reproducing total field performance from a reservoir management viewpoint. Being able to make appropriate operational changes on a well-by-well basis is more economically effective than implementing global operational changes. Well performance for 8 producers distributed throughout the field were plotted to evaluate the effectiveness of the various performance constraints. The location of the 8 wells is depicted in Fig. 1.102. The corresponding performance plots for the wells are included in Fig. 1.103 and Fig. 1.104. Primary well performance for all reservoir descriptions compares favorably with the truth case performance. Such is not the case for individual well performances during water injection. Significant variability and truth case discrepancies exist for all of the wells during the 10 years of waterflooding. Note that the realizations can greatly overpredict (Well P50) and underpredict (Well P51) secondary response compared to the truth case performance. These well performance comparisons substantiate the conclusions reached based on comparing the spatial distributions of porosity and permeability, i.e., local reservoir characteristics are not captured using just the k_{NW} constraint.

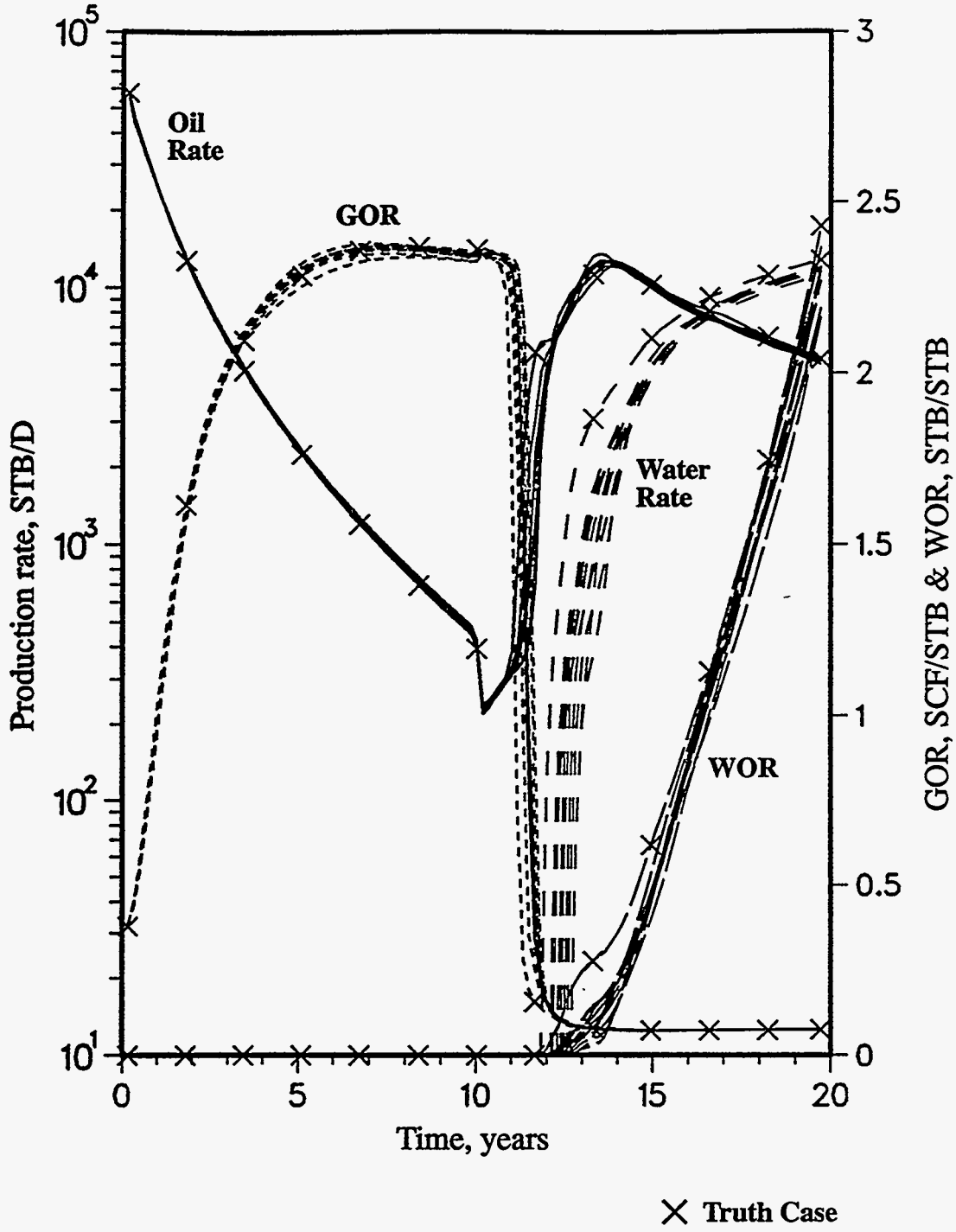

Figure 1.101: Comparison of full-field truth case performance vs. performance of 10 reservoir descriptions generated using conventional and k_{NW} constraints.

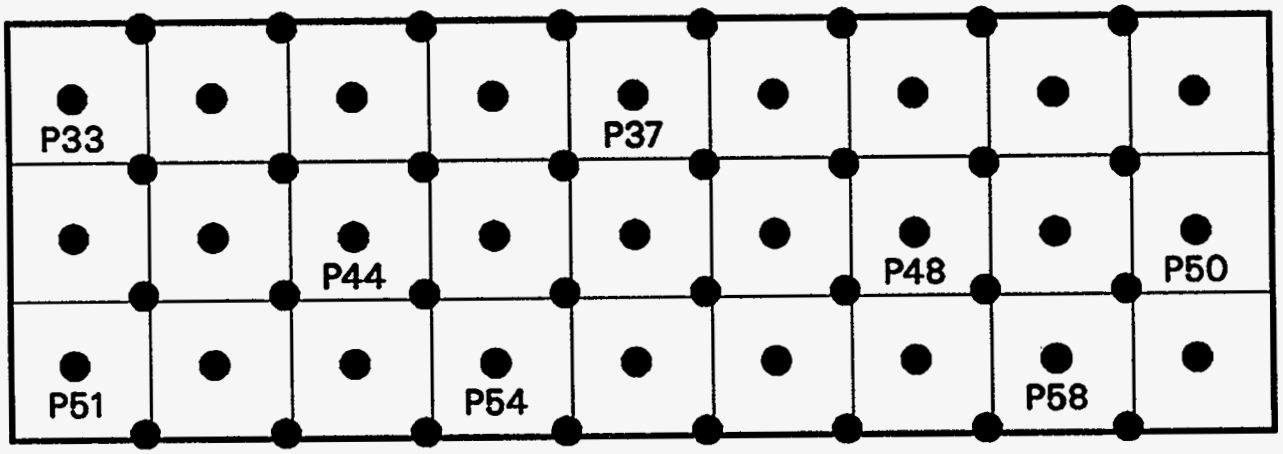

Figure 1.102: Location of selected full-field procedures.

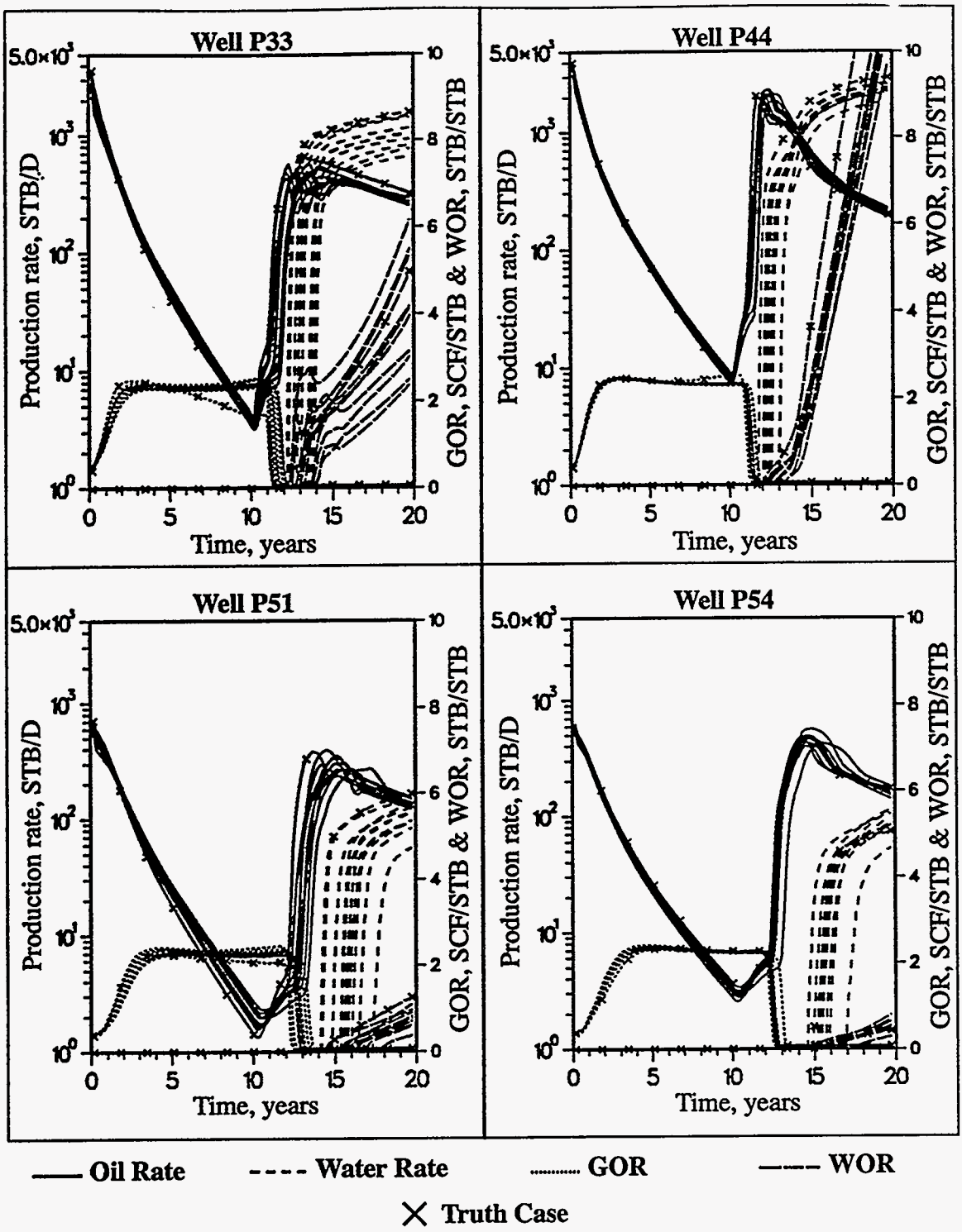

Figure 1.103: Performance plots for Wells P33, P44, P51 and P54; full-field reservoir descriptions based on conventional and k_{NW} constraints.

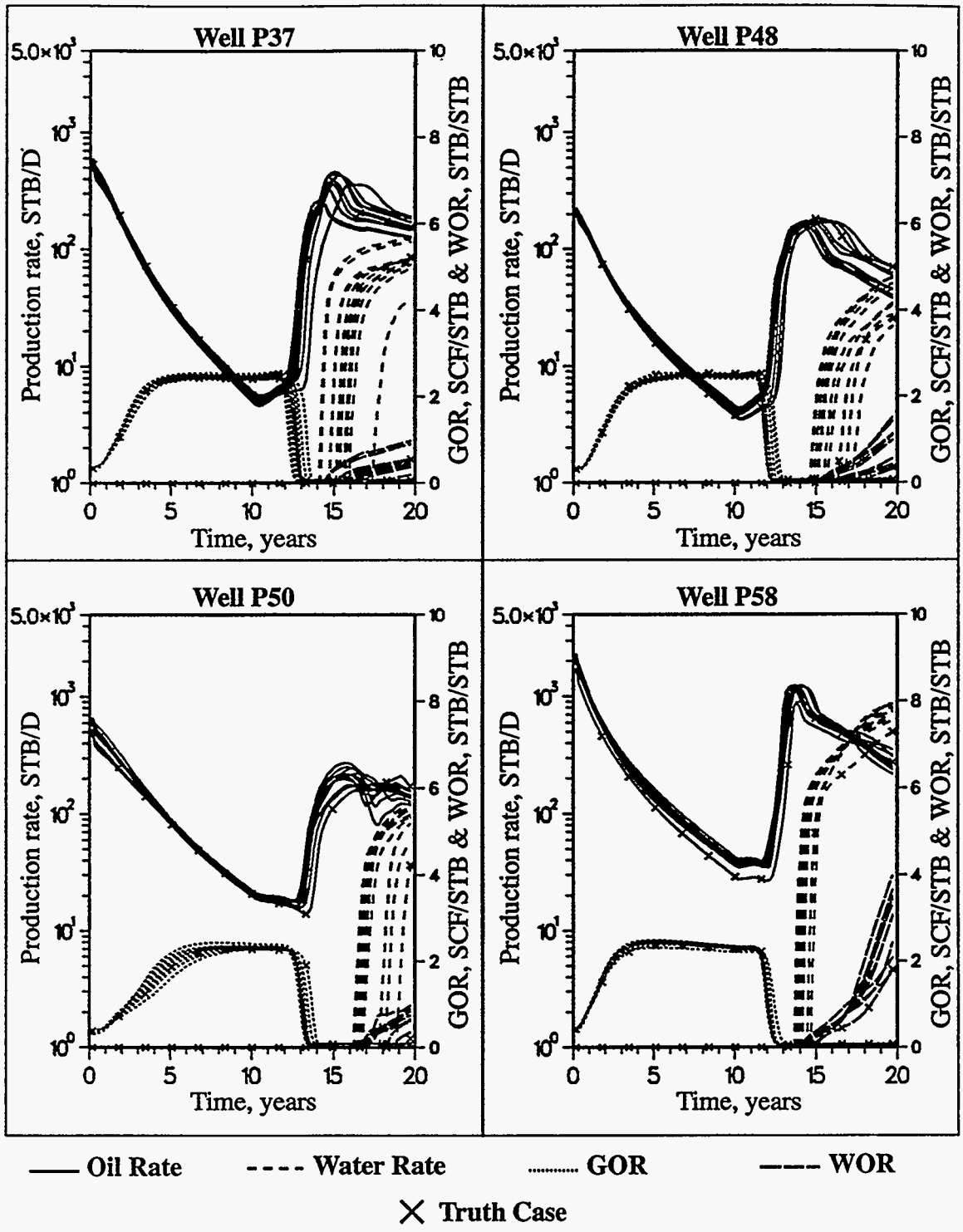

Figure 1.104: Performance plots for Wells P37, P48, P50 and P58; full-field reservoir descriptions based on conventional and k_{NW} constraints.

k_{NW}, PV_T, and PV_{DA} Constraints

Near-well permeability is frequently the first well performance characteristics that can be estimated from field data (well tests). As more primary production data is collected, pore volume estimates can be made through material balance calculations. Sometimes volumetric calculations can be made from structure and fluid contact contours even before any significant production has occurred. With this in mind, additional reservoir descriptions were generated assuming total field pore volume and individual well drainage area pore volume estimates were available as constraints, in addition to conventional and k_{NW} constraints. For simplicity, these constraints will be referred to as primary (production) constraints.

The truth case permeability field is compared to a permeability realization generated using all of the primary constraints in Fig. 1.105. This comparison is significantly better than previous results based on the k_{NW} constraint by itself. The global permeability trends are reasonably reproduced. There is still room for improvement in honoring local high and low permeability regions.

Full-field performance comparisons are made in Fig. 1.106. When compared to Fig. 1.101, the most obvious improvement is to more consistently predict water production rates during secondary recovery. For this case study, predicting total field performance during primary and secondary recovery is not a problem when all primary constraints are employed. The performance of the same 8 wells previously illustrated for the k_{NW} constraint results are depicted in Fig. 1.107 and Fig. 1.108. Consistent with the improvement in the estimation of spatial properties, individual well performance results are also better than when just including the k_{NW} constraint. However, significant spread in waterflood performance still exists for several of the wells. Much of the improvement in waterflood performance is due to assuming the direct one-to-one correlation between porosity and permeability; i.e., specifying each well's pore volume also specifies the average permeability of the region drained by the well. This average permeability has some commonality with the effective permeability of nearby injector/producer areas of influence.

Exhaustive

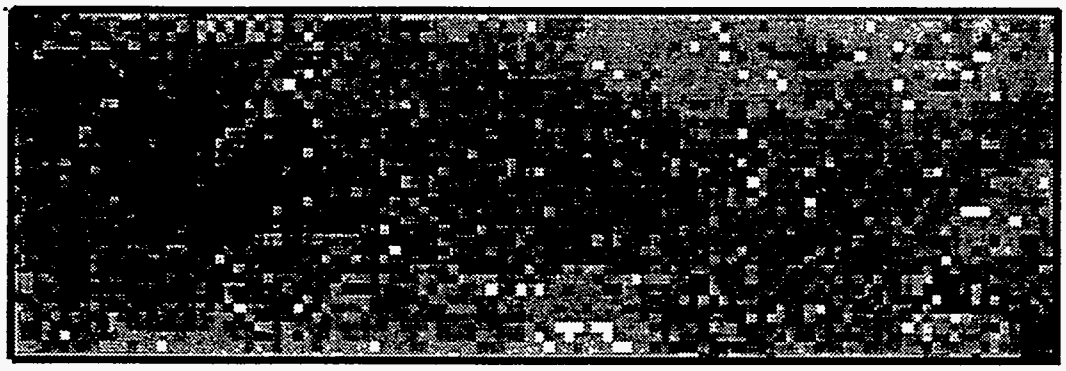

Conventional, k_{NW}, PV_T and PV_{DA} Constraints

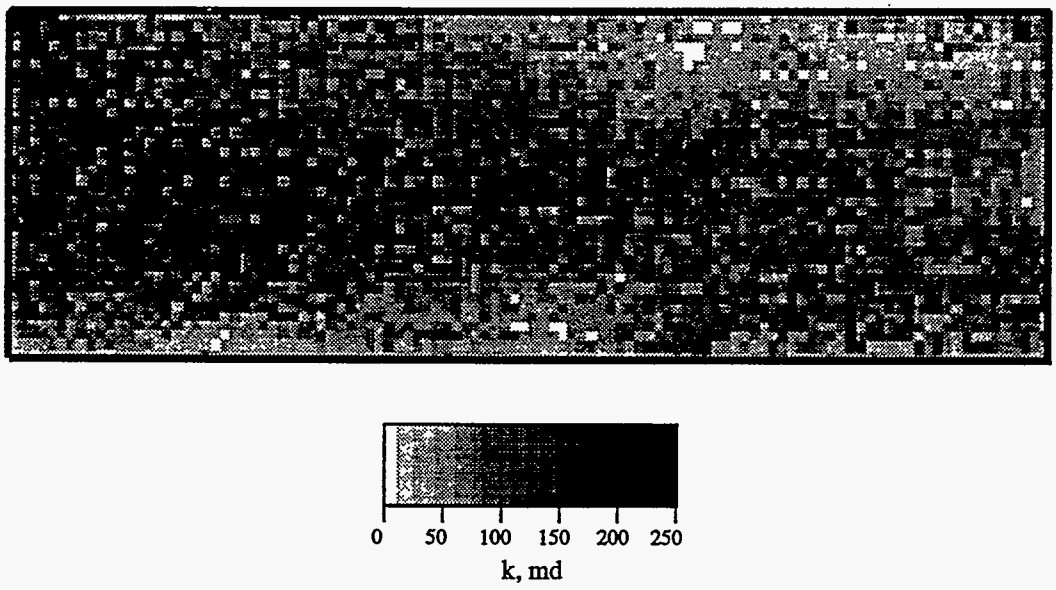

Figure 1.105: Comparison of full-field exhaustive permeability field to permeability field obtained using conventional, k_{NW}, PV_T and PV_{DA} constraints.

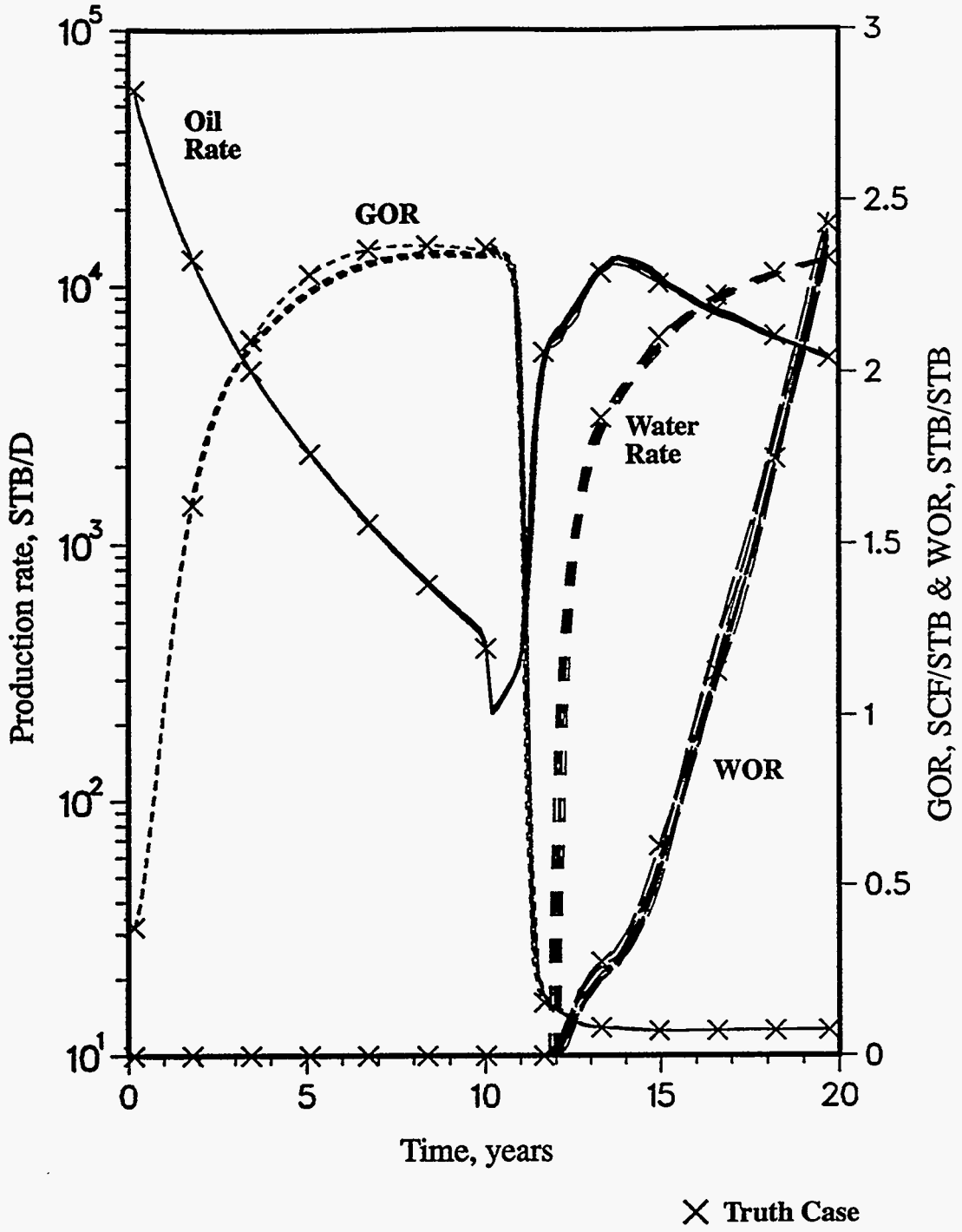

Figure 1.106: Comparison of full-field truth case performance vs. performance of 10 reservoir descriptions generated using conventional, k_{NW}, PV_T and PV_{DA} constraints.

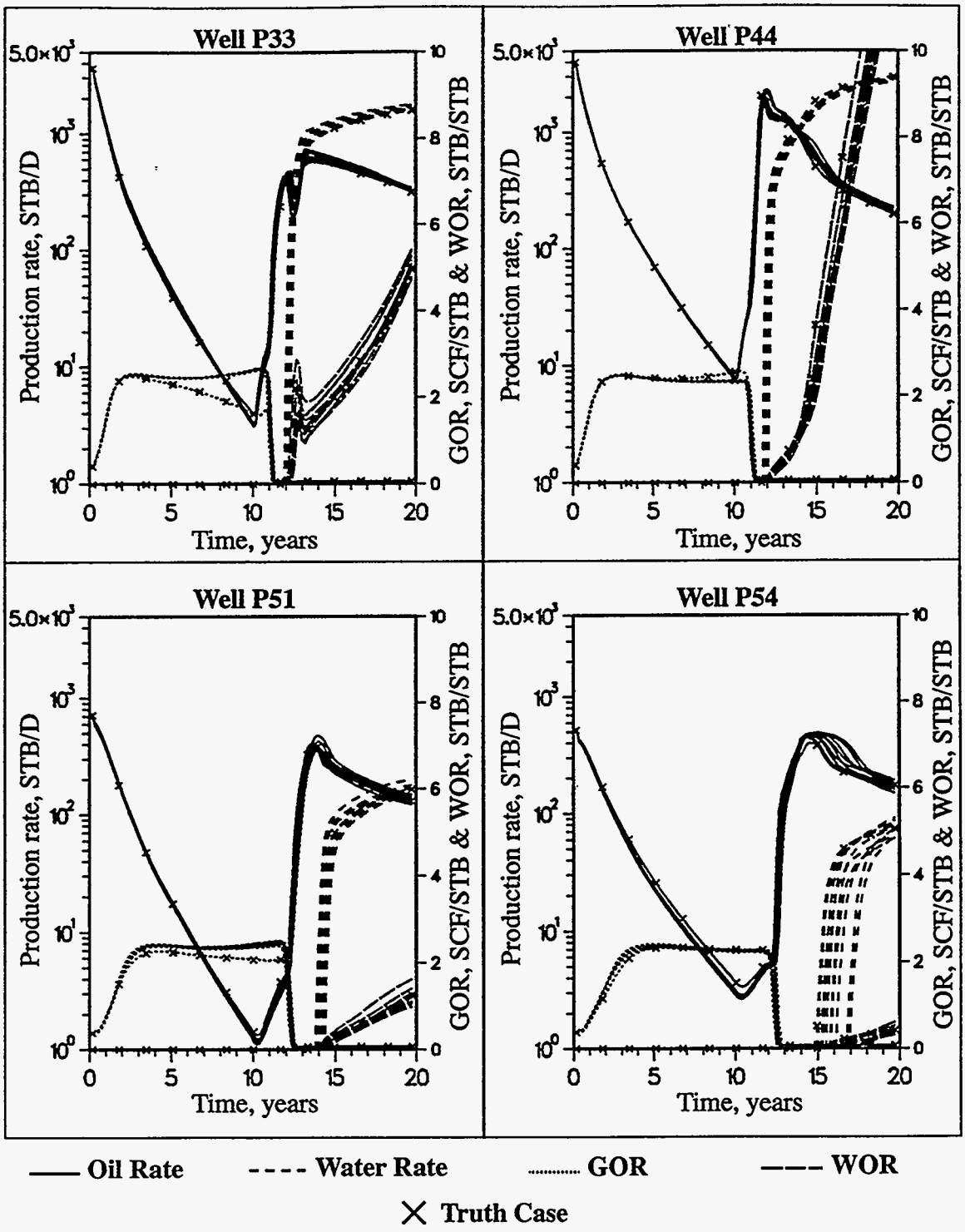

Figure 1.107: Performance plots for Wells P33, P44, P51 and P54; full-field reservoir descriptions based on conventional, k_{NW}, PV_T and PV_{DA} constraints.

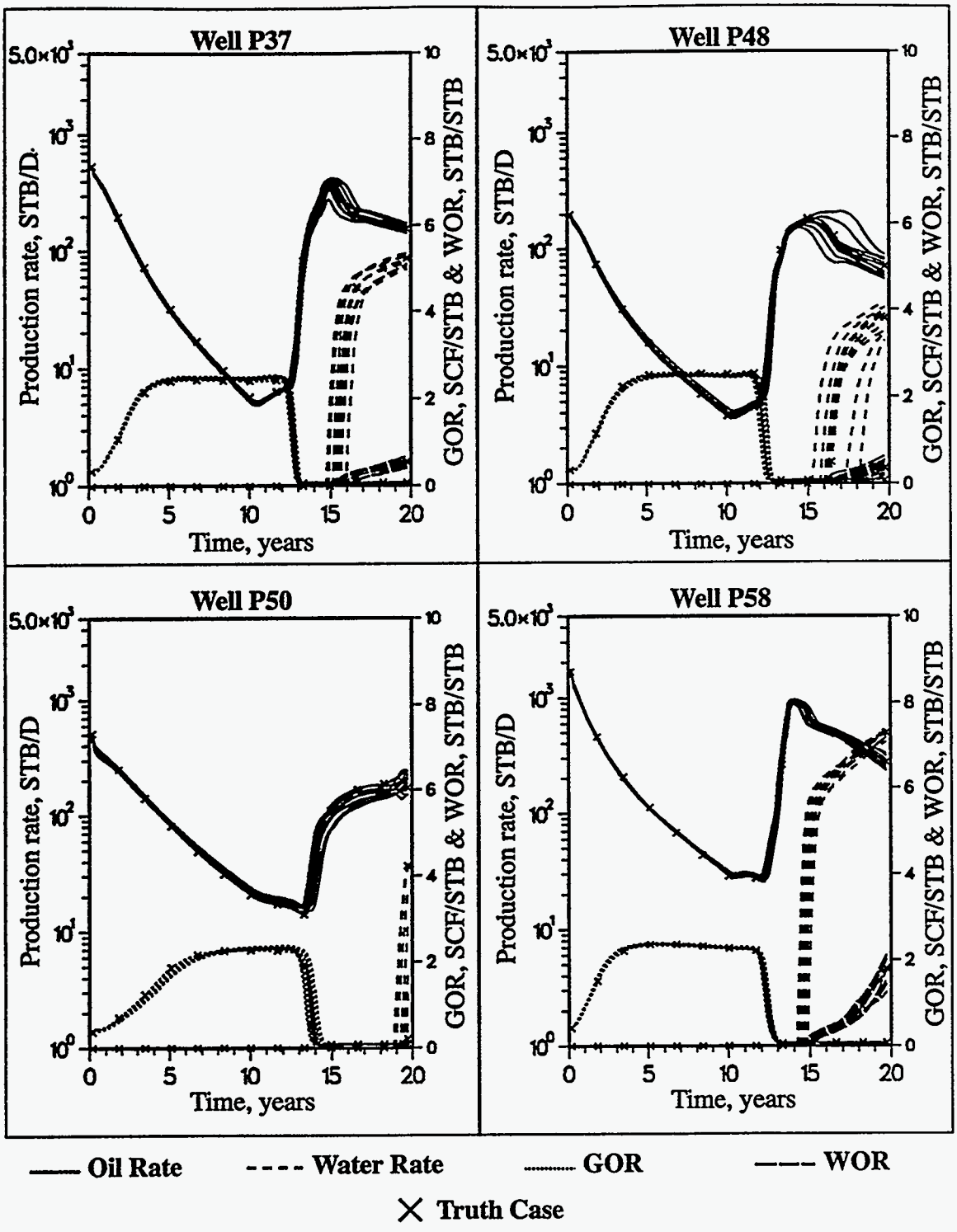

Figure 1.108: Performance plots for Wells P37, P48, P50 and P58; full-field reservoir descriptions based on conventional, k_{NW}, PV_T and PV_{DA} constraints.

Primary and Secondary Constraints Results

The above results were based on the use of conventional and primary performance constraints only. As expected, the resulting field and well performance behaved very similar to the truth case performance during primary production; however, some discrepancies existed during waterflooding. The following case studies assume sufficient secondary performance data is available to make accurate estimates of the secondary performance constraints $CV_{k\bullet}$ and k_{PAT}. These two constraints relate to connectivity between wells and pattern permeability between wells respectively.

Primary, $CV_{k\bullet}$ and k_{PAT} Constraints

All conventional, primary and secondary performance constraints have been utilized in the particular study. Fig. 1.109 contains a comparison of the truth case permeability field and one of the resulting permeability fields. Both global and local spatial characteristics of the truth case are well reproduced in both figures. It appears that a sufficient number of constraints have been imposed to allow the generation of realistic reservoir descriptions. It should be noted that the simulated annealing objective function contains 327 components for this particular case study: 1 PV_T constraint, 59 PV_{DA} constraints, 59 k_{NW} constraints, 96 $CV_{k\bullet}$ constraints, 96 k_{PAT} constraints and 16 variogram constraints (2 directions, 8 lags each). It is highly unlikely that this much information would be available for a real field study; however, these results emphasize the flexibility and robustness of the method.

Total field performance for the 10 alternative reservoir descriptions and the truth case are shown in Fig. 1.110. The responses for all cases are nearly indistinguishable. The only inconsistency is in the GOR curve during part of primary production. The reason for this GOR anomaly is unknown. Nearly as impressive is the individual well performances shown in Fig. 1.111 and 1.112. The most difficult waterflood parameters to match, water breakthrough time and WOR trend, are well reproduced for each well; extremely well reproduced for some wells. The total field and individual well performance results are consistent with the spatial distribution results, i.e., the primary and secondary performance

Exhaustive

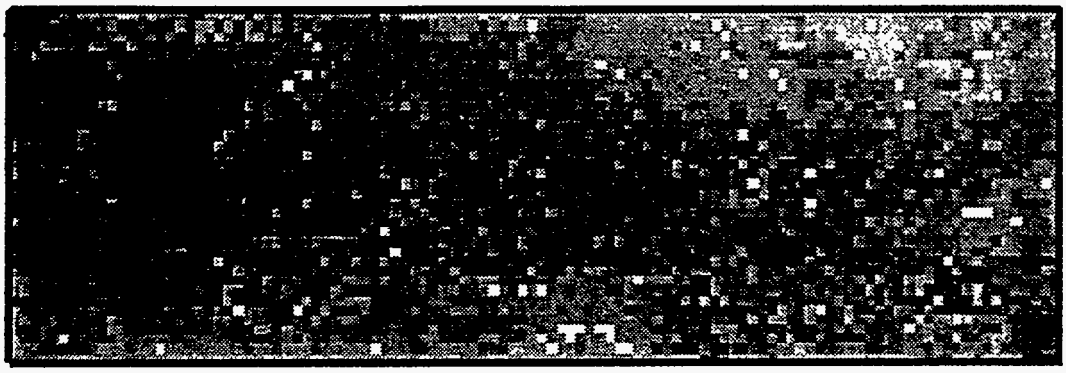

All Indirect Performance Constraints

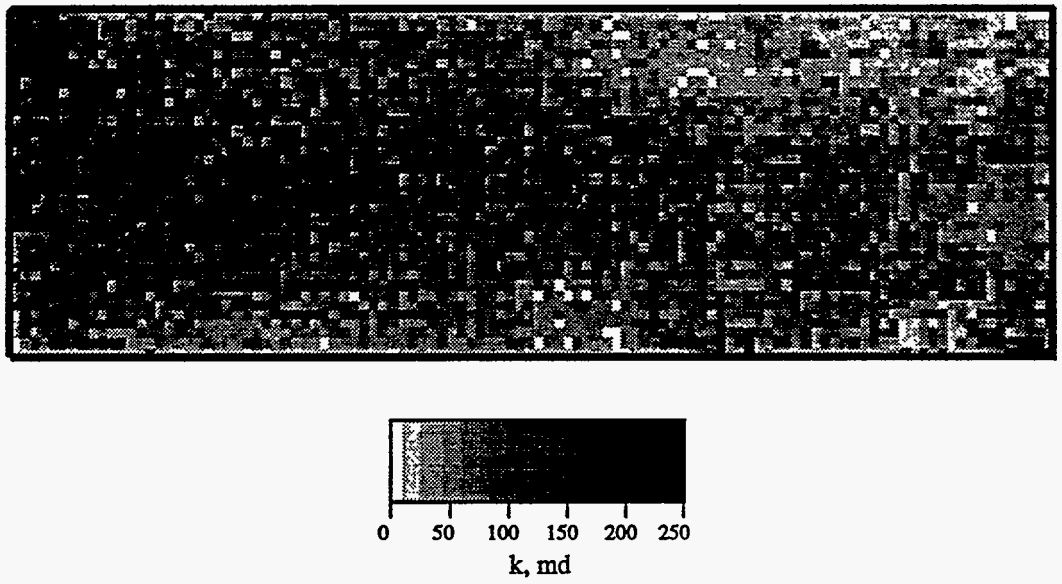

Figure 1.109: Comparison of full-field exhaustive permeability field to permeability field obtained using conventional, k_{NW}, PV_T, PV_{DA}, CV_{k*} and k_{PAT} constraints.

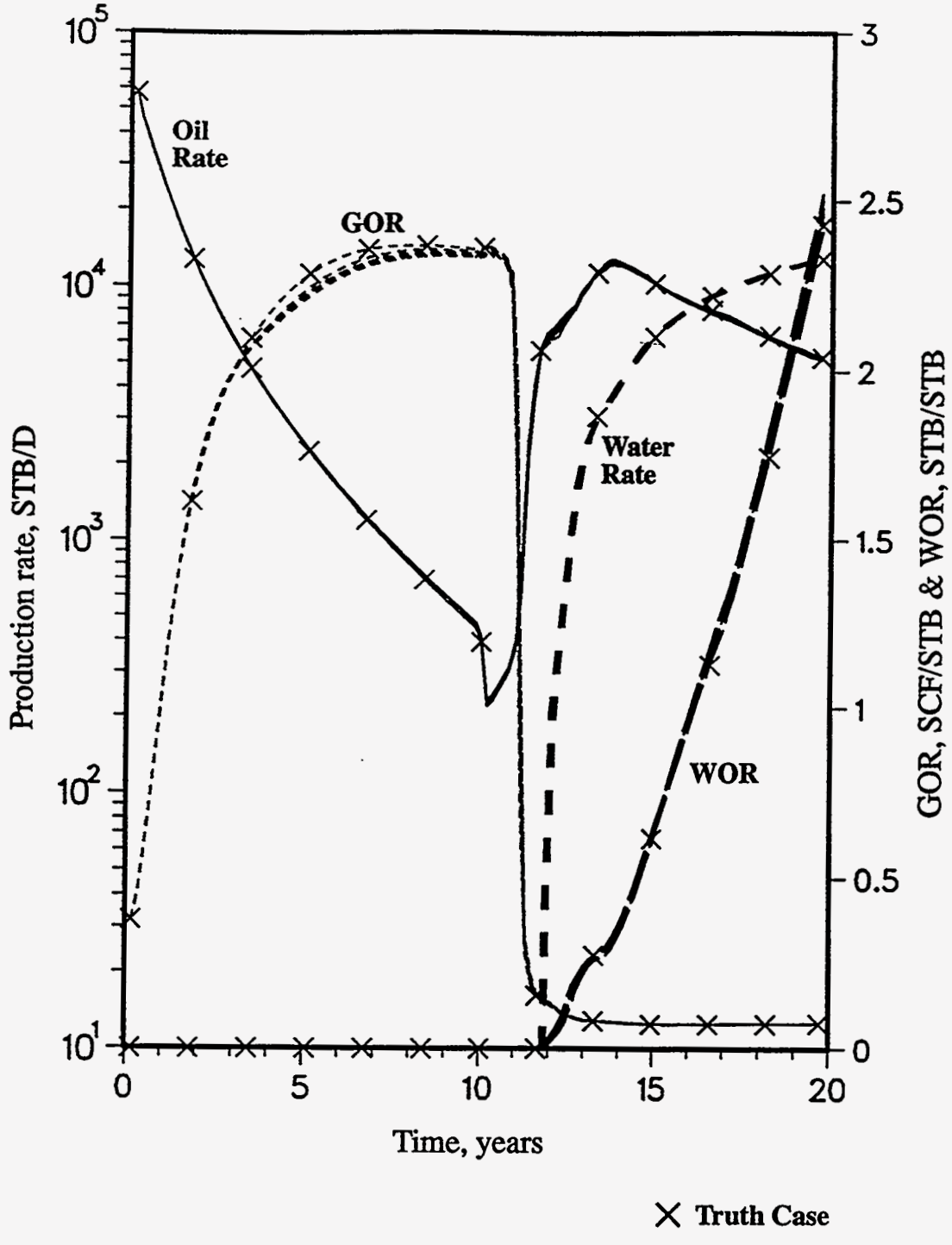

Figure 1.110: Comparison of full-field truth case performance vs. performance of 10 reservoir descriptions generated using conventional, k_{NW}, PV_T, PV_{DA}, CV_{k*} and k_{PAT} constraints.

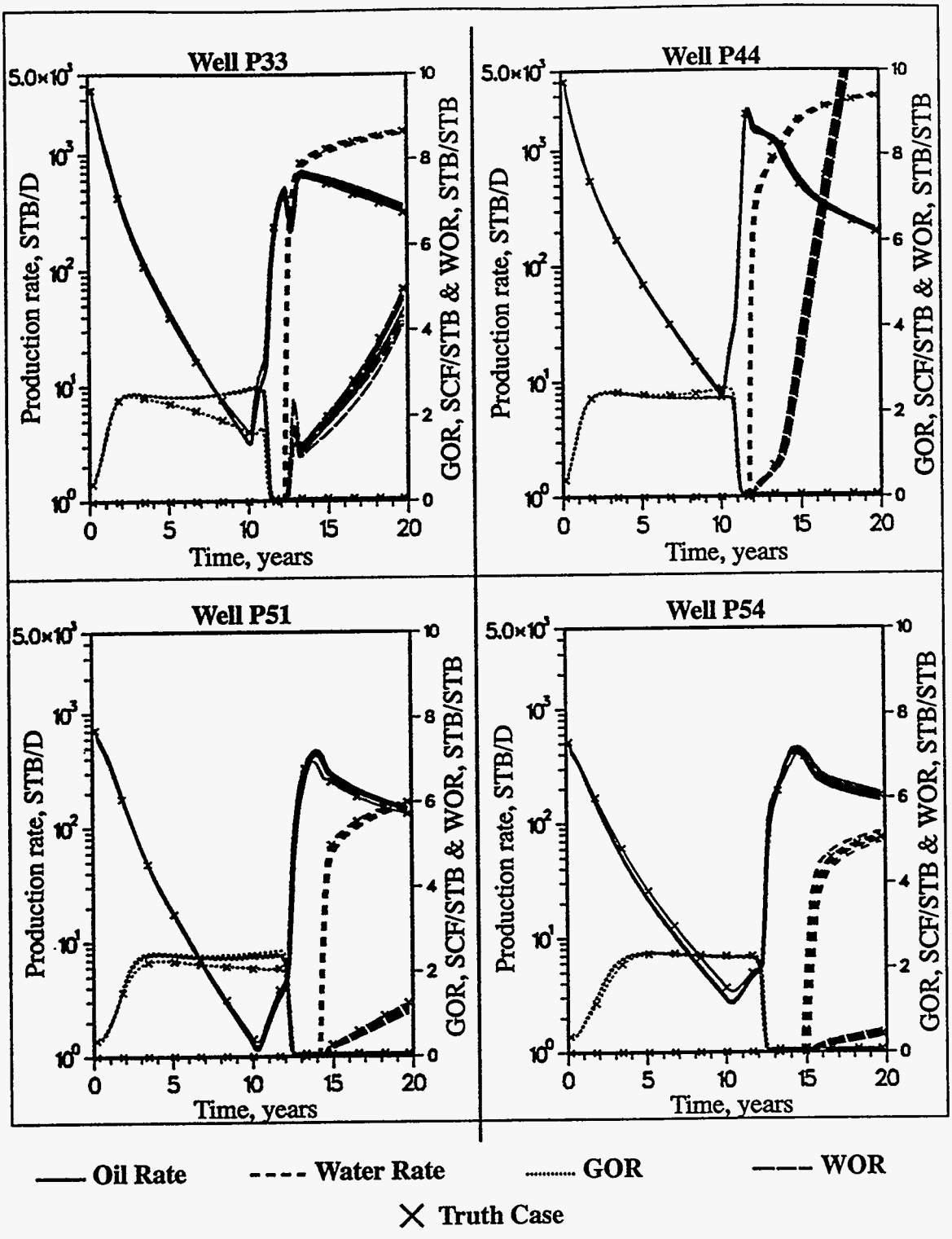

Figure 1.111: Performance plots for Wells P33, P44, P51 and P54; full-field reservoir descriptions based on conventional, k_{NW}, PV_T, PV_{DA}, CV_{k*} and k_{PAT} constraints.

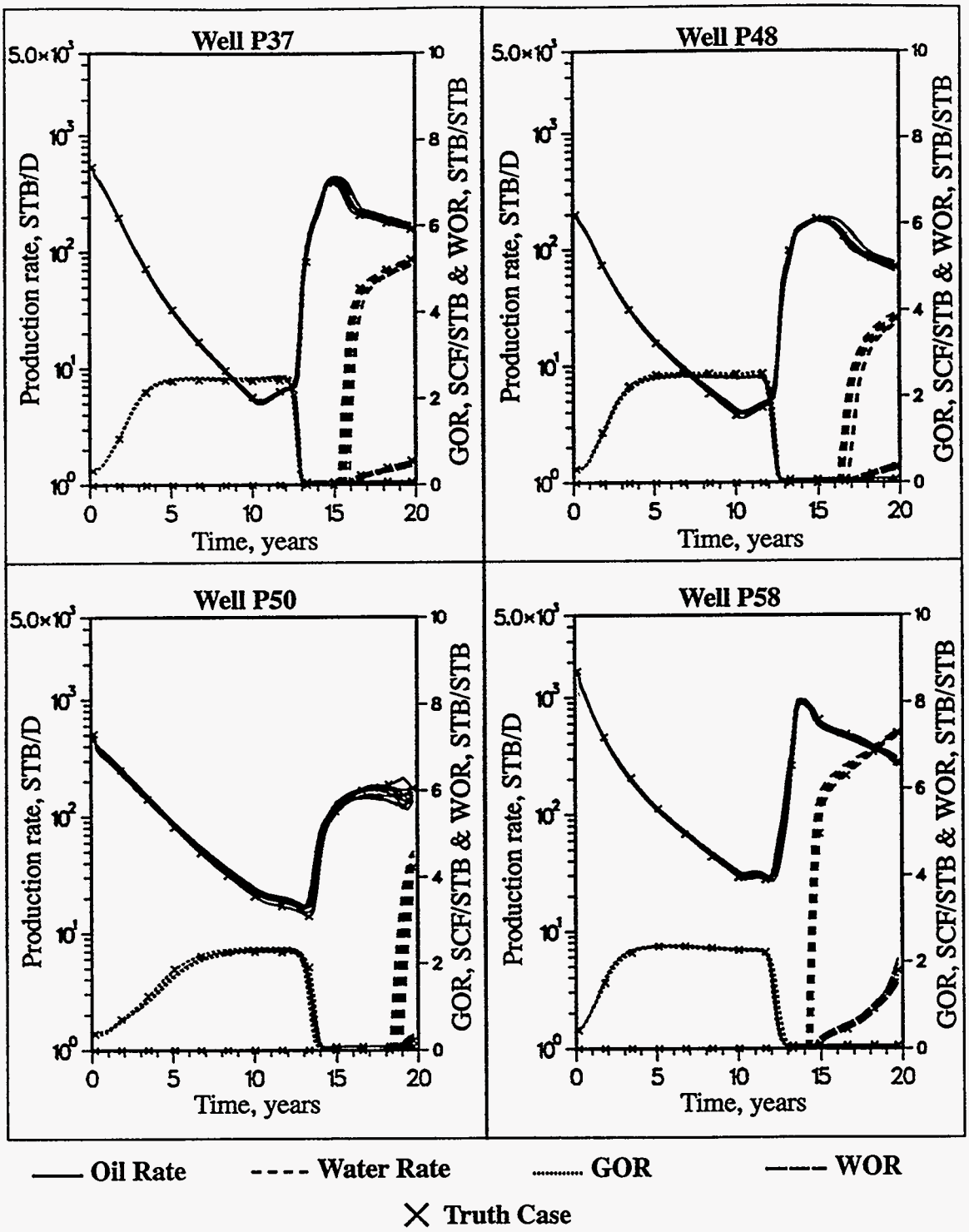

Figure 1.112: Performance plots for Wells P37, P48, P50 and P58; full-field reservoir descriptions based on conventional, k_{NW}, PV_T, PV_{DA}, CV_{k*} and k_{PAT} constraints.

constraints are sufficient for the purpose of generating reservoir descriptions which are very similar to the actual reservoir description and have very similar well performance.

Primary and CV_{k_*} Constraints

One additional case study was made, this time all primary and secondary constraints were included except k_{PAT}. The spatial distribution maps for permeability (not shown) indicate that there are a few more local inconsistencies between the truth case spatial distributions and the resulting realizations when compared to the results obtained when all performance constraints are included.

Total field and individual well performance plots are included in Fig. 1.113 through Fig. 1.114. Although the total field performance for the 10 alternative reservoir descriptions compare as favorably with the truth case as the previous case study (no CV_{k_*} constraint) did, some of the individual well performances do not compare as favorably. These results support the conclusion that the relative importance of the two secondary performance constraints, CV_{k_*} and k_{PAT}, is case-dependent. In some cases it is more important to honor the effective permeability level of an injector/producer area of influence than the connectivity between the two wells. In other cases, it is more important to honor the connectivity. This will depend not only on the reservoir properties directly between two wells, but will also be dependent on the properties of adjacent wells since the effect of an injector/producer k_{PAT} value is dependent on offset injector/producer pair k_{PAT} values.

Summary of Results

This two-dimensional full-field study used the results from previous sections and reports to develop and test an integrated conditional simulation approach. Conventional and indirect performance constraints were used to simultaneously generate porosity and permeability fields. Sensitivities were performed to determine the relative contribution of the various indirect performance constraints. The results were evaluated by comparing simulated primary and waterflood performance and spatial distributions of porosity and permeability to the "truth case" results. Probability of exceedance maps were used to quantify the degree of spatial distribution uncertainty.

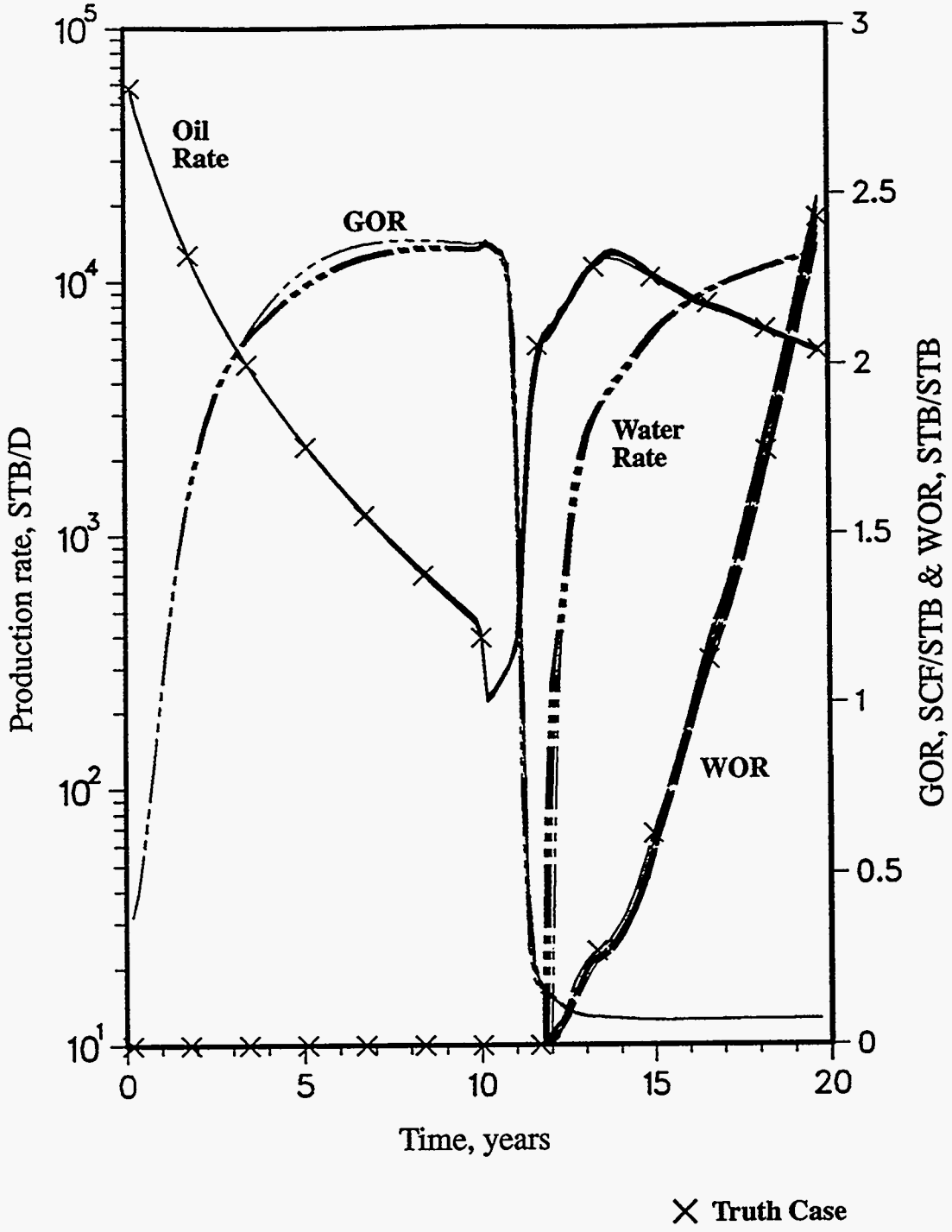

Figure 1.113: Comparison of full-field truth case performance vs. performance of 10 reservoir descriptions generated using conventional, k_{NW}, PV_T, PV_{DA} and CV_{k*} constraints.

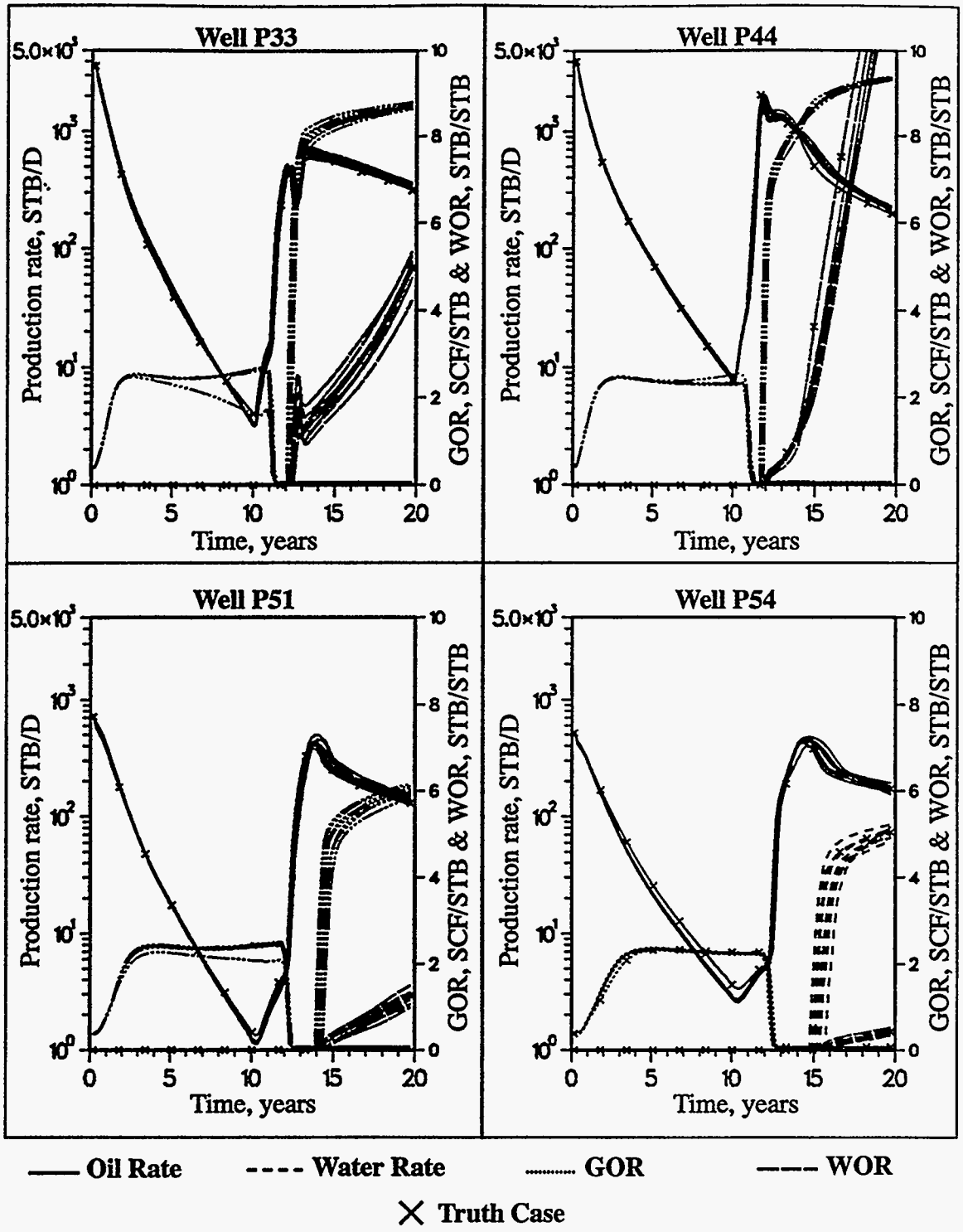

Figure 1.114: Performance plots for Wells P33, P44, P51 and P54; full-field reservoir descriptions based on conventional, k_{NW}, PV_T, PV_{DA} and CV_{k_x} constraints.

Well data were found to provide reasonable estimates of the exhaustive univariate statistics and spatial correlation structures of pay thickness, permeability and porosity. The spatial distributions of permeability and porosity and simulated well performance compared extremely well with the truth case when all conventional and indirect performance constraints were applied. Considering the large number of constraints (327 objective function components), this particular evaluation underscores the flexibility and robustness of the developed methodology.

The various combinations of indirect performance constraints investigated were consistent with the order in which the appropriate information would typically become available. The results obtained when just conventional and the near-well effective permeability constraint were imposed were sufficient for honoring primary performance but inadequate for reproducing waterflood performance and spatial distributions of porosity and permeability. Total field performance was well reproduced in each case, indicating that it is only necessary to honor global spatial characteristics if the objectives do not include matching individual well performances. The addition of pore volume constraints greatly reduced the spread in individual well waterflood performance and the correctness of the porosity and permeability realizations. It was noted that this improvement was greatly influenced by the assumed one-to-one correlation between porosity and permeability. The relative importance of the two waterflood constraints, CV_{k*} and k_{PAT}, was found to be case- and well-dependent. Injector/producer pairs which have unusually high or low reservoir connectivity would require a CV_{k*} constraint and those pairs which have anomalously high or low k_{PAT} values would require a k_{PAT} constraint. In either case, the inclusion of at least one of the waterflood indirect performance constraints improves results compared to when only primary indirect performance constraints are used.

Symbol

a_f = anisotropy ratio

A = radius of investigation coefficient

$A_{\vec{s}}$ = area of grid block in the annular ring at location vector $\vec{s}$, ft^2

A_r = area of annular region, ft^2

B = formation volume factor, bbl/STB

C = class interval for the sample cdf

c_t = total compressibility psi^{-1}

E = objective or energy function

E' = objective function after an update

E_0 = normalizing constant for objective function

h = thickness, ft

$\vec{h}$ = lag distance vector for variograms

HI = heterogeneity index

$\bar{k}$ = average permeability, *md*

$\bar{k}_a$ = arithmetic permeability average within an annular region, *md*

k_D = dimensionless permeability

$\bar{k}_e$ = equivalent permeability, *md*

$\bar{k}_g$ = geometric permeability average within an annular region, *md*

$\bar{k}_h$ = harmonic permeability average within an annular region, *md*

k_{ISA} = *ISA* derived equivalent radial permeability, md

$k(r,\theta)$ = permeability at location (r,θ) for a radial heterogeneous reservoir

k_{ref} = arbitrary reference permeability, md

$k_{\vec{s}}$ = grid block permeability, md

$\bar{k}_{wt}$ = well test permeability from the semilog straight line, md

$\hat{k}$ = instantaneous well test permeability, md

$K(r_D,t_D)$ = weighting or kernel function

l' = index defining the transformed grid block at, $\vec{s}'$, for the muti-well study

m = semilog straight line slope

M = number of iterations

N_c = number of conditioning data

N_d = number of variogram directions

N_f = number of classes for distribution function

N_h = number of variogram lag distances

N_o = number of constraints for a conditional simulation

N_p = number of pairs in a variogram

N_s = number of grid blocks in the simulation domain

N_r = number of radial divisions in the simulation grid

N_t = total number of time points valid for Oliver's solution

N_w = total number of well test constraints

N_x = number of grid blocks in x

N_y = number of grid blocks in y

O_x = coordinate of x-origin of the reservoir, ft

O_y = coordinate of y-origin of the reservoir, ft

p_D = dimensionless pressure

p_i = initial reservoir pressure, psia

p_0 = central grid block pressure, psia

p_{wf} = well flowing pressure, psia

p_{wd} = dimensionless well flowing pressure

p'_{wd} = dimensionless pressure derivative

q = rate, STB/D

r = radius, ft

$r_{c\max}$ = radius from the well to furthest corner of the gridblock, ft

$r_{c\min}$ = radius from the well to closest corner of the grid block, ft

r_D = dimensionless radius

$r_{D\max}$ = maximum dimensionless radius defined by the weighting function

$r_{D\min}$ = minimum dimensionless radius defined by the weighting function

r_e = reservoir radius to nearest no flow boundary, ft

r_w = wellbore radius, ft

R = random number

s = skin

$\vec{s}$ = grid block location vector

$\vec{s}'$ = transformed grid block location vector for the multi-well study

S_{wi} = initial water saturation

t = time, days

t_D = dimensionless time

$\hat{t}_D$ = instantaneous dimensionless time

T^r = temperature control parameter

T^o = initial temperature control parameter

V = simulation variable

V = Dykstra-Parson's coefficient

w_i = weight of annular region

$W_{1/2,1/2}$ = Whitaker function

x = x-direction grid block coordinate, ft

y = y-direction grid block coordinate, ft

α = convergence rate factor

ε_a = convergence tolerance based on acceptance ratio

ε_v = convergence tolerance based on objective function

γ = variogram

γ_o = specified variogram model for a conditional simulation

γ_s = sample variogram of simulation variable

λ = variogram correction term

ω = power for permeability averaging

ϕ = porosity

ψ = weight of objective function component

$\sigma^2_{\ln k}$ = variance of the logarithm of the permeability distribution

μ = viscosity, cp

μ_k = mean permeability, md

ΔE^k = change in objective function at iteration k

$\Delta p'_w$ = instantaneous logarithmic pressure derivative, psi

Δx = grid block dimension in x, ft

Δy = grid block dimension in y, ft

1.1 Sagar, R.,K.: "Reservoir Description by Integration of Well Test Data and Spatial Statistics." Ph.D. Dissertation, The University of Tulsa, Tulsa, OK (1993)

1.2 Hird, K.: "A Conditional Simulation Method for Reservoir Description Using Geological and Well Performance Constraints." Ph.D. Dissertation, The University of Tulsa, Tulsa, OK (1993)

1.3 Earlougher, R.C. Jr.: *Advances in Well Test Analysis*, Monograph Series, SPE, Richardson, TX (1977).

1.4 Van Poolen, H.K.: "Radius of Drainage and Stabilization-Time Equations," *Oil and Gas J.* (September 14, 1964) pp 138-146.

1.5 Lee, John: *Well Testing*, SPE, Dallas (1982).

1.6 Matthews, C.S. and Russell, D.G.: *Pressure Buildup and Flow Tests in Wells*, Monograph Series, SPE, Richardson, TX (1967)

1.7 Oliver, D.S.: "The Averaging Process in Permeability Estimation from Well-Test Data," *SPEFE* (September, 1990) pp 319-324.

1.8 Feitosa, G.: "Well Test Analysis for Heterogeneous Reservoirs," Ph.D. Dissertation, The University of Tulsa, Tulsa, OK (1993).

1.9 Whittaker, E.T. and Watson, G.N.: *A Course in Modern Analysis*, Cambridge University Press, Cambridge (1952).

1.10 Mantoglou, A. and Wilson, J.L.: "The Turning Bands Method for Simulation of Random Fields Using Line Generation by a Spectral Method," Water Resources Research (October, 1982) pp 1379-94.

1.11 Yang, A.: "Program TBM-Turning Bands Method to Generate 2-D Random Fields with Autocorrelation," FORTRAN Source Code, University of Texas, Austin, TX (1987).

1.12 *ECLIPSE 100 - Black Oil Simulator*, ECL-Bergeson Petroleum Technologies, Inc., Oxfordshire, England (1990).

1.13 Peaceman, D.W. : "Interpretation of Well-Block Pressures in Numerical Reservoir Simulation," *SPE of AIME* (1978).

1.14 MacDonald, R.C., and Coats, K.H.: "Methods for the Numerical Simulation of Water and Gas Coning." paper SPE 2796, presented at the Second Symposium on Numerical Simulation of Reservoir Performance, Dallas, TX, (February, 5-6, 1970).

1.15 Burden, R.L. and Faires, J.D: *Numerical Analysis*, Prindle, Weber, and Schmidt, Boston, MA (1985).

1.16 Young, L. C. and Stephenson, R. E.: "A Generalized Compositional Approach for Reservoir Simulation," *SPE Journal* (October, 1983) pp. 727-42.

1.17 Journal, A.G. and Alabert, F.G.: "A New Method for Reservoir Mapping," *JPT* (February, 1990) pp 212-218.

1.18 Deutsch, C.V. and Journel A.G.: GSLIB Oxford University Press

1.19 Shibli, S. " An Approach to Generating Reservoir Property Descriptions Using a Stochastic Conditional Simulation Method", MS Thesis, The University of Tulsa, Tulsa, OK (1992).

1.20 Pérez, G.: "Stochastic Conditional Simulation for Description of Reservoir Properties," Ph.D. Dissertation, The University of Tulsa, Tulsa, OK (1991).

1.21 Huang, X.: "Application of the Genetic Algorithm to Reservoir Description," MS Thesis, The University of Tulsa, Tulsa, OK (1993).

1.22 Sen, M., Datta Gupta, A., Stoffa, P.L., Lake, L.W., Pope, G.A.: "Stochastic Reservoir Modeling Using Simulated Annealing and Genetic Algorithms," paper SPE 24754 presented at the 1992 Annual Technical Conference and Exhibition, Washington, D.C. (October, 3-7, 1992).

1.23 Farmer, C.L.: "Numerical Rocks, The Mathematical Generation of Reservoir Geology," paper presented at the 1989 Joint IMA/SPE European Conference Cambridge University (July 25-27, 1989).

1.24 Ouenes, A.: "Application of Simulated Annealing to Reservoir Characterization and Petrophysics Inverse Problems," Ph.D. Dissertation, The New Mexico Institute of Mining and Technology, Socorro, NM (1992).

1.25 Deutsch, C.V. and Journel, A.G.: "Annealing Techniques Applied to the Integration of Geological and Engineering Data," Report for the Stanford Center for Reservoir Forecasting (1992). Stanford University.

1.26 Doyen, P.M. and Guidish, T.M.: "Seismic Discrimination of Lithology: A Bayesian Approach," Western Atlas International, Middlesex, England.

1.27 Kirkpatrick, S., Gelatt, C.D. Jr., and Vecchi, M.P.: "Optimization by Simulated Annealing," Science (May 13, 1983) pp 671-680.

1.28 Metropolis, N., Rosenbluth, A.W., Rosenbluth, M.N., Teller, A.G., and Teller, E. "Equation of State Calculations by Fast Computing Machines," The Journal of Chemical Physics (June, 1953) pp 1087-92.

1.29 Aarts, E. and Korst, J.: *Simulated Annealing and Boltzman Machines: A stochastic Approach to combinatorial Optimization and Neural Computing*, John Wiley & Sons Ltd., Chichester (1989).

1.30 Craig, F.F., Jr.: *Reservoir Engineering Aspects of Waterflooding*, Monograph Volume 3, SPE of AIME, Dallas, TX (1971).

1.31 Mishra, S., Brigham, W.E., and Orr, F.M. Jr.: "Tracer and Pressure Test Analysis for Characterization of Areally Heterogeneous Reservoirs," paper SPE/DOE 17365 presented at the 1988 SPE/DOE Enhanced Oil Recovery Symposium, Tulsa, OK, (April 17-20, 1988).

1.32 *Log Interpretation Charts*, Schlumberger Educational Services, USA (1991).

1.33 Isaaks, E.H. and Srivastava, R.M.: *Applied Geostatistics*, Oxford University Press, New York (1989).

1.34 Muskat, Morris: *Physical Principles of Oil Producation*, International Human Resources Development Corporation, Boston, MA (1981), pp 262-263.

1.35 Kelkar, Mohan: Reservoir Characterization of Pennyslvanian Sandstone Reservoirs, DOE Annual Report (December, 1991).

CHAPTER 2

Effective Properties of Simulator Grid Blocks

J. Lee, E. Kasap and M. Kelkar

2.1 Summary

The purpose of this study is to develop an analytical method to calculate an effective permeability tensor for a coarse-scale grid block in three dimensions. An analytical method to estimate the effective permeability in both two- and three-dimensions is presented. The results from this method are compared with numerical results based on a finite element simulator. The results compare favorably. For two-dimensional upscaling, additional flow simulation results are presented which show the superiority of the proposed method over the other methods. Since the work related to two-dimensional upscaling has been presented in the prior reports, only a brief description is provided. A detailed upscaling procedure for three-dimensional grid block is presented. Future work will include improvement of the analytical solution for three-dimensional upscaling. Additional flow simulation will also need to be conducted in 3 dimensions.

2.2 Introduction

For a successful field development and reservoir management, field-scale large numerical simulations are required. Reservoir performance simulators require input data on a scale that is much larger than the scale of inter-well laminations and cross beddings. Small-scale heterogeneities in the reservoir have been observed to influence reservoir performance. To properly account for their effect, permeability upscaling is often performed. The general form of permeability is as a tensor and consequently the effective-upscaled-permeability is also a tensor. Tensorial representation of permeability becomes important when the driving force is not aligned with one of the principal directions of the permeability[2.1] thereby the velocity vector along each principal axis is affected by transverse pressure gradients.

White and Horne[2.2] showed the necessity of the permeability tensor in the case of local permeability variations. Kasap and Lake[2.3] calculated an effective tensor for a rectangular system with a perturbation. The perturbation is a region with a different permeability value from the rest of the system. Aasum[2.4] developed an analytical tensor method which calculates the effective permeability of a two-dimensional simulator grid block under generalized anisotropic conditions. The method divides the grid block into four local blocks to account for the location of heterogeneity and uses the cross flow concept in calculating effective permeability for the entire grid block. The method showed good agreement with numerical simulation results and handles complex permeability heterogeneities efficiently.

This procedure can be extended to three-dimensional grid blocks. Instead of dividing the entire grid block into four local blocks, we are dividing the three-dimensional block into eight blocks. The purpose of doing this is to incorporate the local permeability variation and location of heterogeneities within the simulation block. The results of this analytical method are compared with finite element numerical results.

In the next section, some of the previous work are reviewed along with application results. These results have been presented in detail in previous DOE Reports[2.7]. Next, the procedure for the development of analytical method in three dimensions is presented along with the numerical calculation procedure. Preliminary results are compared and discussed. Finally, future work for the improvement of analytical method is included.

2.3 Review

2.3.1 Development Of Analytical Method In Two Dimensions

The analytical method developed for a two-dimensional system combines the advantages of numerical and analytical methods. Complex permeability heterogeneities are handled at a relatively high computational speed. The location and size of small-scale heterogeneities within a simulator grid block and the orientation of anisotropic permeability structures are accounted for using the developed method. The method estimates effective coarse-scale permeability yielding a tensorial form of effective permeability.

The procedure for developing an effective permeability can be described by following steps. Since the detailed procedures for the equations follow were already reported in the previous annual reports[2.7], the final form of the equations are presented.

1. Divide the grid block containing small-scale permeability heterogeneities into four quadrants or local blocks as shown in Fig. 2.1. The next step is to determine the effective permeability tensor in each of the four quadrants. To calculate the effective permeability for each quadrant, we determine the permeabilities along the principal directions by sweeping the directions between -90^{o} and 90^{o} relative to the horizontal x-axis. When a sweep is performed, we calculate permeabilities along the specified direction (k'_{xx}) and the direction perpendicular to that direction (k'_{yy}) and determine the principle directions (x' and y') in which direction k'_{xx} / k'_{yy} is the largest.

After calculating the permeabilities along the principal directions we perform coordinate rotation to obtain the effective permeability tensor for each local block. Since k'_{xx}, k'_{yy} and the orientation angle, α, were determined, the effective permeability tensor for the simulation coordinate system are calculated by following equations.

$$k_{xx} = (\cos\alpha)^2 \, k'_{xx} + (\sin\alpha)^2 \, k'_{yy} \tag{2.1}$$

$$k_{xy} = \sin\alpha\cos\alpha(k'_{xx} - k'_{yy}) \tag{2.2}$$

$$k_{yx} = \sin\alpha\cos\alpha(k'_{xx} - k'_{yy}) \tag{2.3}$$

$$k_{yy} = (\sin\alpha)^2 \, k'_{xx} + (\cos\alpha)^2 k'_{yy} \tag{2.4}$$

where k_{xx}, k_{xy}, k_{yx}, and k_{yy} are the effective permeability tensor elements in the original x, y - coordinate system. α is the angle by which the x' -, y'-coordinates are rotated from the x-, y -coordinate system.

2. Determine the effective permeability tensor for the entire grid block. The physical system consists of four grid blocks or quadrants as shown in Fig. 2.2. Each of the four blocks may have different, but possibly full permeability tensors

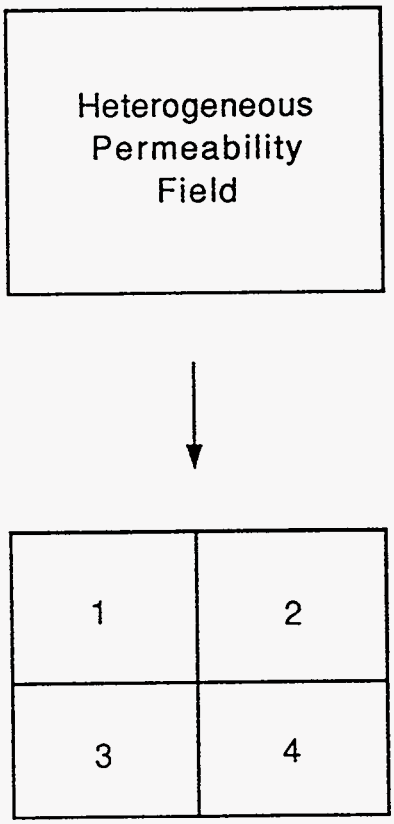

Figure 2.1: Field of small scale heterogeneities divided into four quadrants

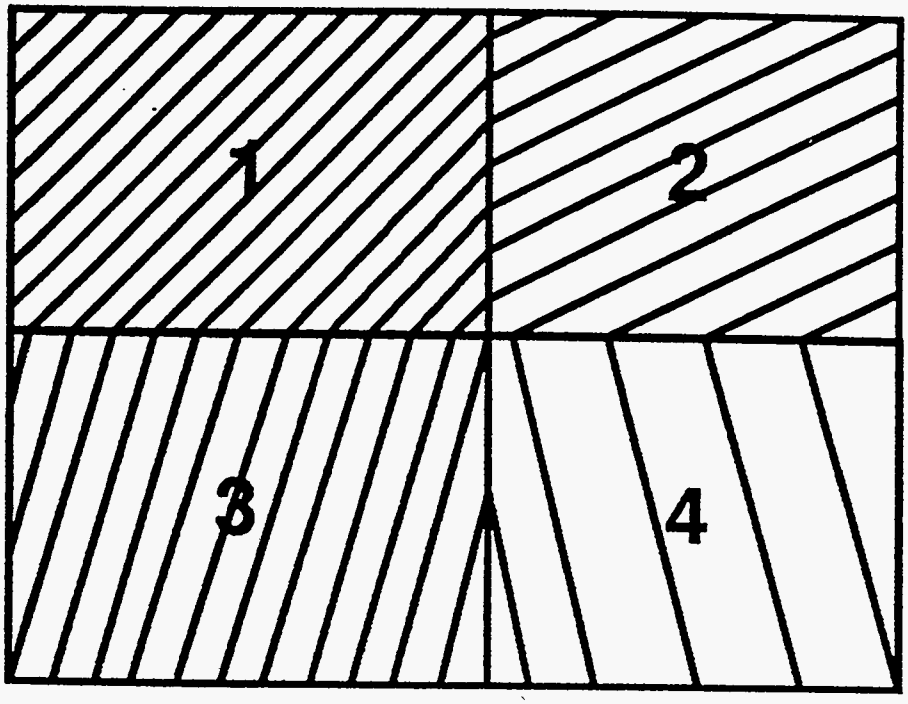

Figure 2.2: System containing four blocks and four permeability tensors

obtained from the previous step. Permeability anisotropy and varying block sizes are also permitted and accounted for in the determination of the elements of the effective permeability tensors. The elements of the effective permeability tensors are obtained from the following equations:

$$\bar{k}_{xx} = \frac{\bar{k}_{xapp}}{1 - \left(\left[\left(\frac{\partial \bar{p}}{\partial x} \right)_Y \Big/ \left(\frac{\partial \bar{p}}{\partial y} \right)_Y \right] \times \left[\left(\frac{\partial \bar{p}}{\partial y} \right)_X \Big/ \left(\frac{\partial \bar{p}}{\partial x} \right)_X \right] \right)} \tag{2.5}$$

$$\bar{k}_{yy} = \frac{\bar{k}_{yapp}}{1 - \left(\left[\left(\frac{\partial \bar{p}}{\partial x} \right)_Y \Big/ \left(\frac{\partial \bar{p}}{\partial y} \right)_Y \right] \times \left[\left(\frac{\partial \bar{p}}{\partial y} \right)_X \Big/ \left(\frac{\partial \bar{p}}{\partial x} \right)_X \right] \right)} \tag{2.6}$$

$$\bar{k}_{xy} = -\bar{k}_{xx} \left(\frac{\partial \bar{p}}{\partial x} \right)_Y \Big/ \left(\frac{\partial \bar{p}}{\partial y} \right)_Y \tag{2.7}$$

$$\bar{k}_{yx} = -\bar{k}_{yy} \left(\frac{\partial \bar{p}}{\partial y} \right)_X \Big/ \left(\frac{\partial \bar{p}}{\partial x} \right)_X \tag{2.8}$$

In Eq. 2.5 through Eq. 2.8, $\bar{k}_{xapp}$ and $\bar{k}_{yapp}$ are the apparent permeabilities along the x- and y-axis, respectively. Apparent permeabilities are used as effective permeabilities if the numerical simulator is not equipped to handle a tensor formulation of permeability. The pressure gradient ratio is defined as the ratio of transverse to longitudinal pressure gradient. $\left(\frac{\partial \bar{p}}{\partial x} \right)_Y \Big/ \left(\frac{\partial \bar{p}}{\partial y} \right)_Y$ is the pressure gradient ratio induced from injection along y-axis whereas $\left(\frac{\partial \bar{p}}{\partial y} \right)_X \Big/ \left(\frac{\partial \bar{p}}{\partial x} \right)_X$ is the pressure gradient ratio induced from injection along x-axis. In both cases, boundaries transverse to the principal direction of fluid injection are closed.

The apparent permeabilities and the pressure gradient ratios in Eq. 2.5 through Eq. 2.8 must be determined to obtain the elements of the effective permeability tensor. The detailed procedures for those two terms can be found in the previous annual report[2.7].

2.3.2 Comparisons Between Analytical and Numerical Effective Permeabilities

Case 1

This case is presented to illustrate the effect on effective permeability of a low permeability region ("perturbation") located off-center in a permeability field. The local grid blocks contain anisotropic permeabilities with non-zero off-diagonal elements in their permeability tensors. Fig. 2.3 shows the arrangement of the local permeability tensors.

Local anisotropy exists and the analytical method yields a good prediction of the effective permeability tensor. Notice that the off-diagonal elements of the effective permeability tensor are non-symmetric using both analytical and numerical methods. This phenomena is a result of anisotropic and full local permeability tensors. The two methods agree in both form and existence of non-symmetry of the effective permeability tensors, as shown in Fig. 2.3.

Case 2

The cross-bedded permeability distribution shown Fig. 2.4 is analyzed where the light and the dark grid blocks initially have isotropic permeabilities of 1000 md and 20 md, respectively. Fig. 2.4 also shows the effective permeability obtained from the numerical and analytical methods. The results agree well. Both methods predict isotropic diagonal elements of the effective permeability tensor, which is correct since the cross-beds are oriented at a -45° angle from the horizontal x axis. The off-diagonal elements are correctly predicted to be negative and symmetric. For this particular permeability distribution, the exact effective permeability tensor can be obtained through simple coordinate rotation since the permeabilities along the principal axes are simple arithmetic and harmonic averages of the two permeability values in this distribution, 1000 md and 20 md, and the angle of the cross-beds, -45°, is known. The analytical method agrees exactly with the tensor obtained from simple coordinate rotation. This results show that the directional search for k'_{xx}/k'_{yy} is successful in determining the principal axes of permeability. Therefore, the directional search method may also be a useful tool in detecting permeability structures in minipermeameter-measured permeability data from outcrops.

1	0.1	1000	100
0.1	0.1	100	100
1000	100	1000	100
100	100	100	100

Analytical Method:	
495	36
48	62
Numerical Method:	
501	34
44	61

Figure 2.3: Effective permeability tensors calculated by analytical and numerical methods for anisotropic and full local permeability tensors (units: md)

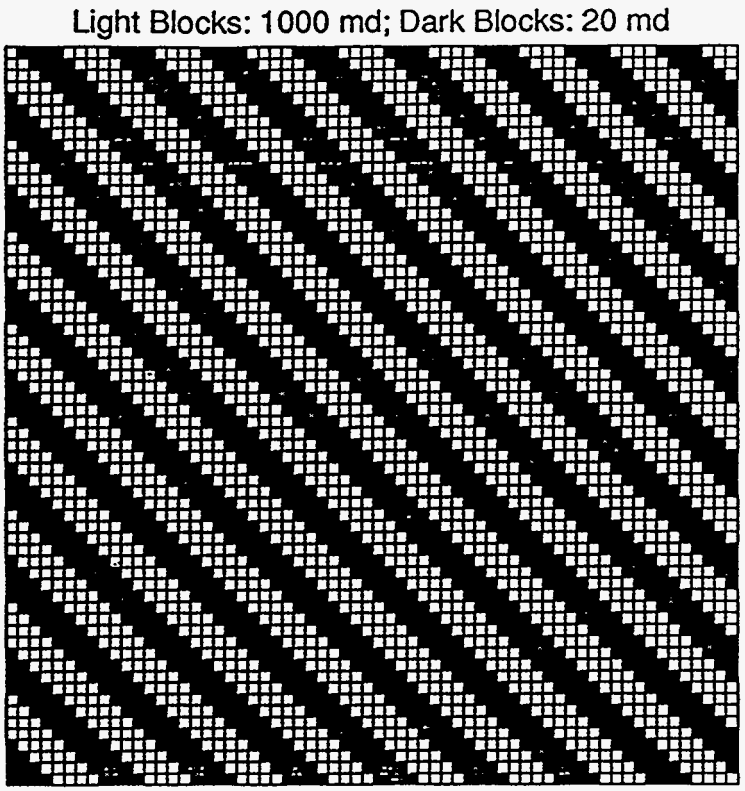

Analytical Method:	
275	-235
-235	275
Numerical Method:	
271	-224
-224	271

Figure 2.4: Effective permeability tensors calculated by analytical and numerical methods for cross-bedded permeability distribution (units: md)

Case 3

In this case, the effective permeability is determined from minipermeameter-measured permeability data from a small section of a San Andres carbonate outcrop in Algerita, New Mexico. The distribution of these data is shown in Fig. 2.5. Comparing the permeability distributions of Fig. 2.4 and Fig. 2.5, it is evident that the permeabilities in Fig. 2.5 have less structure or correlation. In Fig. 2.4, there are complete high and low permeability layers whereas the outcrop data in Fig. 2.5 appear to be more random in their distribution. This observation is supported by the analytical and numerical effective permeabilities calculated for the outcrop data. The off-diagonal elements in the permeability tensor are small compared to their respective diagonal elements. The ratios of k_{xy}/k_{xx} and k_{yx}/k_{yy} are indications of the sizes of the transverse-to-longitudinal pressure gradient ratios. Both numerical and analytical methods show ratios ranging from about 0.0 to 0.08. In Fig. 2.4 however, the ratios are -0.83 and -0.85. In other words, the cross-bedded heterogeneities in Fig. 2.4 induce much higher transverse pressure gradients than the more random heterogeneities in Fig. 2.5. There appears to be a difference in the prediction of k_{xy} in Fig. 2.5 but the difference is negligible considering the low pressure gradient ratios obtained both numerically and analytically.

2.3.3 Comparisons Between Results From Field Flow Simulations

Case 1 - Miscible Displacements

In this case the result from unit-mobility-ratio miscible-displacement simulation is presented. The convection-dispersion equation is solved for an incompressible fluid using a finite element simulator.

Fig. 2.6a shows the permeability distribution used in the simulation. It is essentially the same distribution as in Fig. 2.4, except that in Fig. 2.6a the aspect ratio is 8 to 1 rather than 1 to 1 as in Fig. 2.4. The following boundary conditions are used: a constant pressure potential of 2.5 atm is specified along the entire left vertical boundary; 1.0 atm is specified along the entire right vertical boundary; both horizontal boundaries are closed to flow.

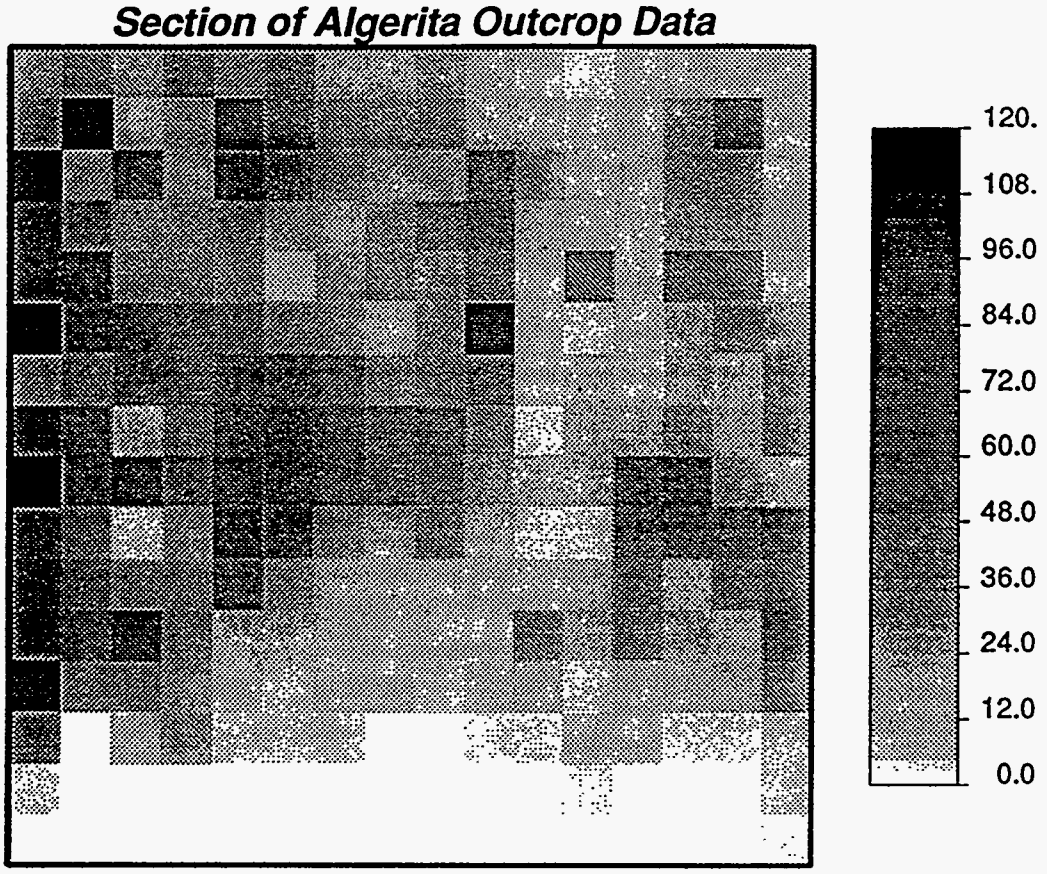

Analytical Method:	
11.9	0.0
0.1	1.7
Numerical Method:	
11.8	0.9
0.1	1.7

Figure 2.5: Effective permeability tensors calculated by analytical and numerical methods for minipermeameter measured permeability data from the Algerita outcrop (units: md)

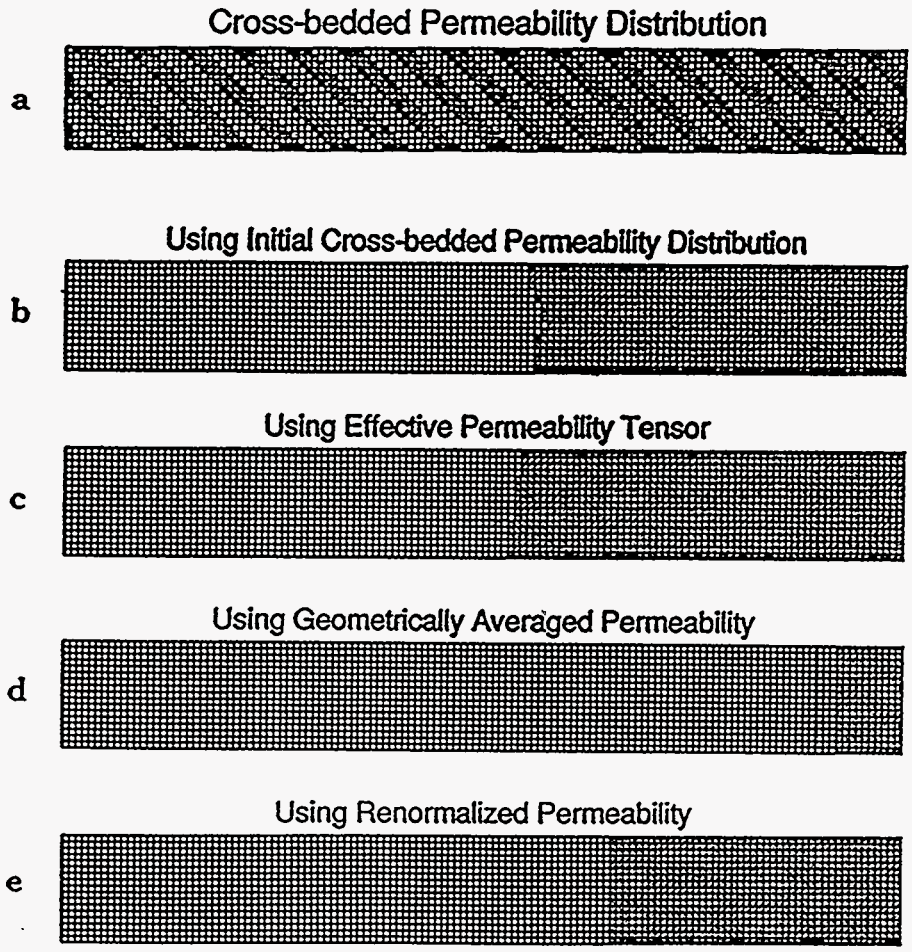

Figure 2.6: Initial permeability distribution (dark: 20 md; light: 1000 md) and 0.5 concentration contours after 49.7 days of injection using the initial permeability distribution and the permeability distributions obtained using various upscaling methods

Fig. 2.6b through Fig. 2.6e show 0.5 concentration contours of the flood fronts after 49.7 days of injection. Fig. 2.6b shows the location of the front using initial permeability distribution. This figure is used as the base case. The analytical effective permeability tensor method (Fig. 2.6c) yields the best prediction of the location of the flood front. The geometric mean predicts a flood front which is advancing too fast (Fig. 2.6d). Thus, the geometric mean overpredicts the effective permeability. The renormalization method (Fig. 2.6e) also predicts a flood front which is advancing too fast, although the overprediction of the effective permeability is not as severe as when using the geometric mean.

Case 2 - Waterfloods

This case involves a comparison of results from simulating a waterflood using initial permeability distributions and upscaled effective permeability distributions generated based on the analytical effective permeability method, and the geometric average. A two-phase oil and water system is simulated. The simulator used is a point-centered finite difference simulator which has the option of inserting separately-computed transmissibilities[2.8].

This case represents waterflooding in a quarter of a 5-spot pattern. The permeability distribution is anisotropic and oriented at a 45° angle to the horizontal x-axis. In other words, the orientation of the anisotropic permeability structures is parallel to the general flow direction from the injector in the southwest corner and the producer on the northeast corner of the field. The dimensionless correlation lengths are $\lambda_{Dl} = 1.0$ and $\lambda_{Dt} = 0.025$ along the layers and transverse to the layers, respectively. The Dykstra-Parsons coefficient is $V = 0.7$. There are 64×64 permeability values in the initial permeability distribution shown in Fig. 2.7. Injection pressure is 3000 psi and production pressure is 100 psi.

The water saturation fronts after 20 days of injection are shown in Fig. 2.8. Fig. 2.8a shows the water saturation front using the initial, generally anisotropic permeability distribution. Water breakthrough has already occurred because of the preferential flow paths created by the cross-bedded arrangement of the permeability values in the field. The microscale permeability distribution is upscaled or homogenized from 64×64 to 8×8 permeability values. Comparing to Fig. 2.8b

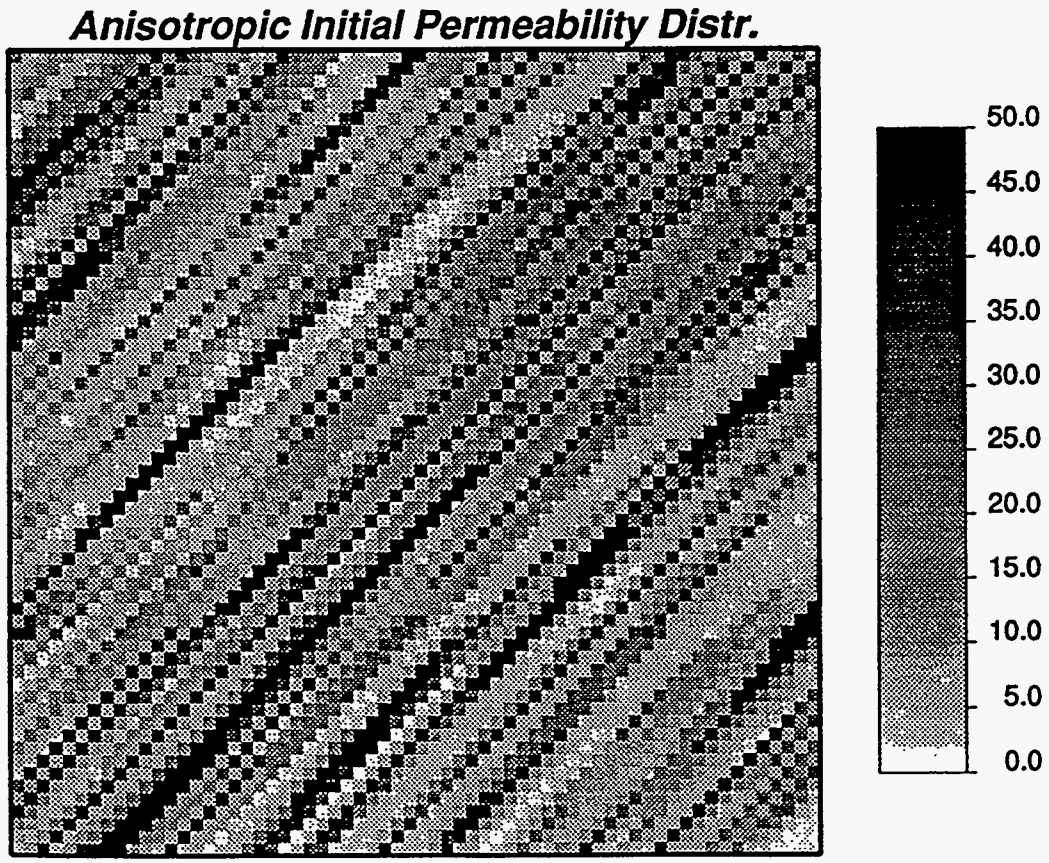

Figure 2.7: Anisotropic (cross-bedded) stochastic permeability distribution ($\lambda_{DI} = 1.01$, $\lambda_{Dt} = 0.025$, $V = 0.7$, 45° structure orientation, 64 × 64 values)

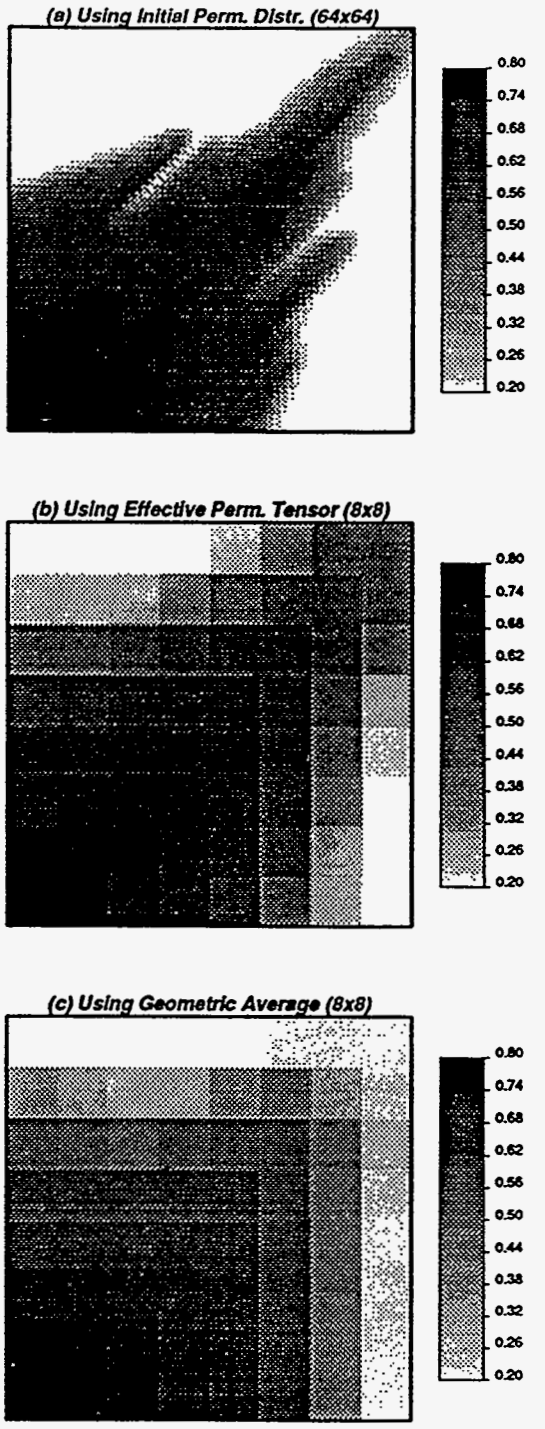

Figure 2.8: Water saturation maps after 20 days of water injection using (a) the initial permeability distribution (b) the effective permeability tensor and (c) the geometrically averaged permeability

and Fig. 2.8c, it is evident that using the effective permeability tensor, the water saturation front agrees better in terms of shape and amount of water broken through (Fig. 2.8b) than using the geometric average of permeability values (Fig. 2.8c). The geometric average method is not able to capture the anisotropic nature of the initial permeability distribution.

In Fig. 2.9, the cumulative oil recovery is plotted as a function of pore volumes of water injected for waterflooding through the microscale and the upscaled permeability distribution. From this figure, it can be observed that the recovery curve related to the effective permeability tensor shows excellent agreement with the recovery curve associated with the initial microscale permeability distribution. The recovery curve associated with the geometric average of the initial permeability distribution is too optimistic.

To summarize the results obtained in two-dimensional medium, the effective tensor upscaling method work well in simulating the flow behavior compared to the other upscaling methods which do not account for the non-diagonal elements in a permeability tensor.

2.4 Approach

For this section, we extend our approach to three-dimensional grid blocks.

2.4.1 Part 1 - Analytical Method

This section contains the procedures used for the analytical method. The system consists of eight blocks as shown in Fig. 2.10. Extending the procedure presented by Aasum[2.4], we arrive at following apparent effective permeability for homogenized system in three dimensions.

$$\bar{k}_{xapp} = \bar{k}_{xx} + \bar{k}_{xy}\left(\frac{\bar{k}_{zx}\bar{k}_{yz} - \bar{k}_{yx}\bar{k}_{zz}}{\bar{k}_{yy}\bar{k}_{zz} - \bar{k}_{yz}\bar{k}_{zy}}\right) + \bar{k}_{xz}\left(\frac{\bar{k}_{zy}\bar{k}_{yx} - \bar{k}_{zx}\bar{k}_{yy}}{\bar{k}_{yy}\bar{k}_{zz} - \bar{k}_{yz}\bar{k}_{zy}}\right) \tag{2.9}$$

$$\bar{k}_{yapp} = \bar{k}_{yy} + \bar{k}_{yx}\left(\frac{\bar{k}_{zy}\bar{k}_{xz} - \bar{k}_{xy}\bar{k}_{zz}}{\bar{k}_{xx}\bar{k}_{zz} - \bar{k}_{zx}\bar{k}_{xz}}\right) + \bar{k}_{yz}\left(\frac{\bar{k}_{xy}\bar{k}_{zx} - \bar{k}_{zy}\bar{k}_{xx}}{\bar{k}_{xx}\bar{k}_{zz} - \bar{k}_{xz}\bar{k}_{zx}}\right) \tag{2.10}$$

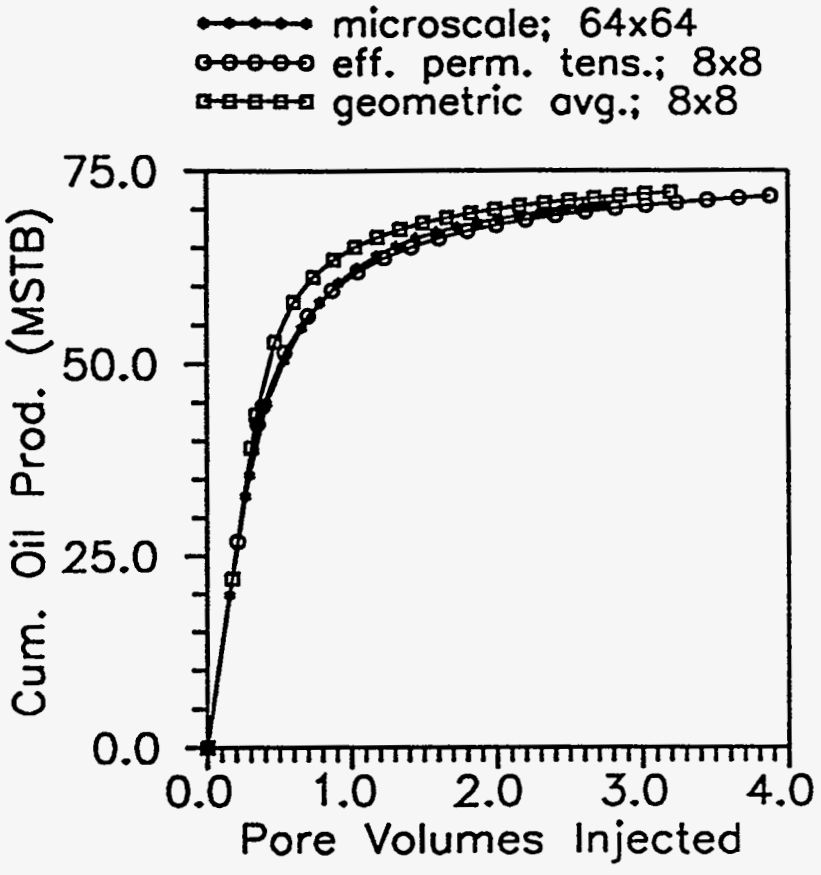

Figure 2.9: Cumulative oil recovery versus pore volumes injected for waterflood in a 1/4 of a 5-spot. Anisotropic (cross-bedded) initial permeability distribution. Effect of permeability upscaling.

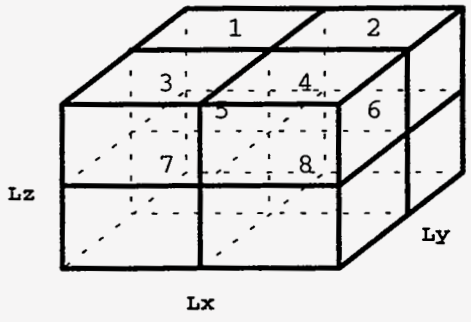

Figure 2.10: System containing 8 blocks

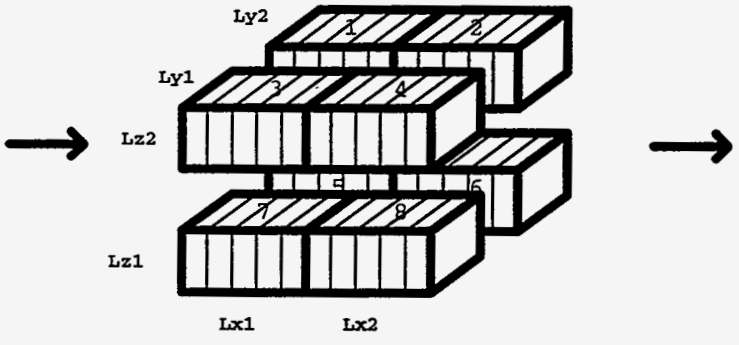

Figure 2.11: No communication along the y and z directions, flow in the x direction

$$\bar{k}_{zapp} = \bar{k}_{zz} + \bar{k}_{zx}\left(\frac{\bar{k}_{yz}\bar{k}_{xy} - \bar{k}_{xz}\bar{k}_{yy}}{\bar{k}_{xx}\bar{k}_{yy} - \bar{k}_{xy}\bar{k}_{yx}}\right) + \bar{k}_{zy}\left(\frac{\bar{k}_{xz}\bar{k}_{yx} - \bar{k}_{yz}\bar{k}_{xx}}{\bar{k}_{xx}\bar{k}_{yy} - \bar{k}_{xy}\bar{k}_{yx}}\right) \qquad (2.11)$$

$\bar{k}_{xapp}$, $\bar{k}_{yapp}$ and $\bar{k}_{zapp}$ are calculated in the following procedures.

Since the procedure for each apparent permeability is same, only the one for $\bar{k}_{xapp}$ is presented. The details can be found in Appendix A.

1. We divide the entire system into four two-block systems allowing no communication along the y- and z-directions (Fig. 2.11) and calculate two-block effective permeability for each two-block system using Darcy's law applying constant pressure gradient in the x-direction. Then, we get $\bar{k}_{xapp12}$, $\bar{k}_{xapp34}$, $\bar{k}_{xapp56}$ and $\bar{k}_{xapp78}$. The subscripts represent the block numbers and this notation will be used through out this report. Since these blocks are parallel to each other, we take an arithmetic average of the results for top and bottom two-block systems to get $\bar{k}_{xxappt}$, $\bar{k}_{xxappb}$. Then, $\bar{k}_{xxapp}$ is calculated as an arithmetic average of those two effective permeabilities.

2. We divide the system into four two-block systems assuming perfect communication along the y-direction (Fig. 2.12) and calculate two-block effective permeability to get $\bar{k}_{xapp13}$, $\bar{k}_{xapp24}$, $\bar{k}_{xapp57}$ and $\bar{k}_{xapp68}$. By taking the harmonic average of those, we calculate effective permeabilities of top and bottom two-block systems which are in series, $\bar{k}_{xyappt}$ and $\bar{k}_{xyappb}$. We combine these two effective permeability in parallel to get $\bar{k}_{xyapp,s}$. By taking arithmetic average, we calculate effective permeability of the left and right two-block systems which are in parallel, $\bar{k}_{xyappl}$ and $\bar{k}_{xyappr}$, to get $\bar{k}_{xyapp,p}$. Then, we take a weighted average of $\bar{k}_{xyapp,s}$ and $\bar{k}_{xyapp,p}$ to get $\bar{k}_{xyapp}$.

3. We divide the system into four two-block systems assuming perfect communication along the z-direction (Fig. 2.13) and calculate two-block effective permeability to get $\bar{k}_{xapp15}$, $\bar{k}_{xapp26}$, $\bar{k}_{xapp37}$ and $\bar{k}_{xapp48}$. By taking the harmonic average, we calculate effective permeabilities of the first and second two-block systems which are in series, $\bar{k}_{xzappf}$ and $\bar{k}_{xzapps}$. We combine these two effective permeabilities in parallel to get $\bar{k}_{xzapp,s}$. By taking the arithmetic average, we calculate effective permeabilities of the left and right two-block systems which are

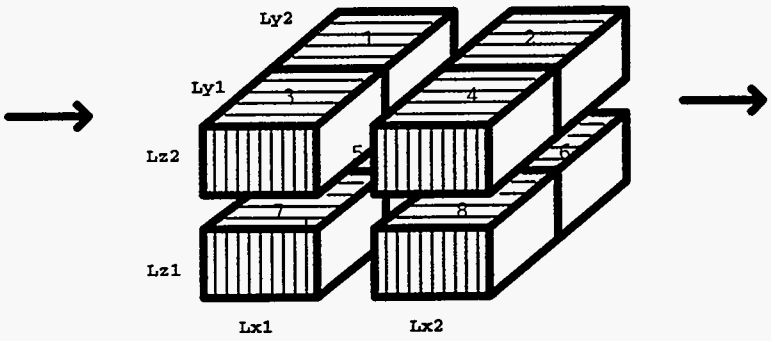

Figure 2.12: Communication along the y direction, flow along the x direction

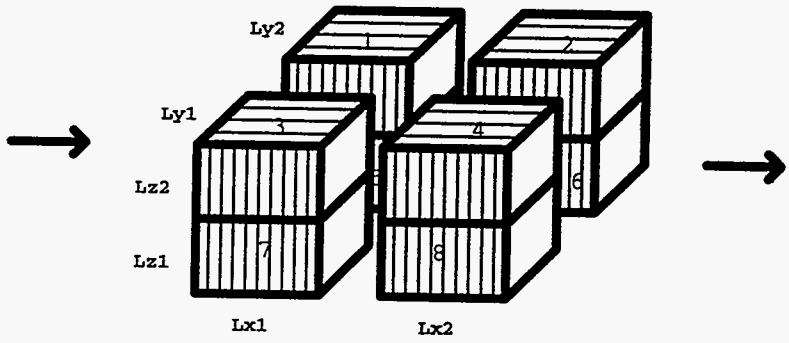

Figure 2.13: Communication along the z direction, flow along the x direction

in parallel, $\bar{k}_{xzappl}$ and $\bar{k}_{xzappr}$, to get $\bar{k}_{xzapp,p}$. Then, we take a weighted average of $\bar{k}_{xzapp,s}$ and $\bar{k}_{xzapp,p}$ to get $\bar{k}_{xzapp}$.

The final step involves the calculation of $\bar{k}_{xapp}$ from the weighted average of $\bar{k}_{xxapp}$, $\bar{k}_{xyapp}$ and $\bar{k}_{xzapp}$. $\bar{k}_{yapp}$ and $\bar{k}_{zapp}$ are calculated by following the same steps described above, and changing the direction of the applied pressure gradient. The equation for $\bar{k}_{xapp}$ is given below.

$$\bar{k}_{xapp} = \frac{\bar{k}_{xxapp}\bar{k}_{xapp} + \bar{k}_{xyapp}\bar{k}_{yapp} + \bar{k}_{xzapp}\bar{k}_{zapp}}{\bar{k}_{xapp} + \bar{k}_{yapp} + \bar{k}_{zapp}} \tag{2.12}$$

where

$$\bar{k}_{xxapp} = \frac{Lz_2}{Lz}\bar{k}_{xxt} + \frac{Lz_1}{Lz}\bar{k}_{xxb} \tag{2.13}$$

$$\bar{k}_{xyapp} = \frac{\bar{k}_{xyapp,s}\bar{k}_{xapp} + \bar{k}_{xyapp,p}\bar{k}_{zapp}}{\bar{k}_{xapp} + \bar{k}_{zapp}} \tag{2.14}$$

$$\bar{k}_{xzapp} = \frac{\bar{k}_{xzapp,s}\bar{k}_{xapp} + \bar{k}_{xzapp,p}\bar{k}_{yapp}}{\bar{k}_{xapp} + \bar{k}_{yapp}} \tag{2.15}$$

We manipulate Darcy's law applying constant pressure at the inlet and outlet with closed boundary conditions at transverse directions to the principal direction of flow to get the expressions for $\bar{k}_{xy}$, $\bar{k}_{xz}$, $\bar{k}_{yx}$, $\bar{k}_{yz}$, $\bar{k}_{zx}$ and $\bar{k}_{zy}$.

$$\bar{k}_{xy} = \left| \frac{\left(\frac{\partial \bar{p}}{\partial x}\right)_z \left(\frac{\partial \bar{p}}{\partial z}\right)_y - \left(\frac{\partial \bar{p}}{\partial x}\right)_y}{\left(\frac{\partial \bar{p}}{\partial z}\right)_z \left(\frac{\partial \bar{p}}{\partial y}\right)_y - \left(\frac{\partial \bar{p}}{\partial y}\right)_y} \right| \left(\left| 1 - \frac{\left(\frac{\partial \bar{p}}{\partial z}\right)_y \left(\frac{\partial \bar{p}}{\partial y}\right)_z}{\left(\frac{\partial \bar{p}}{\partial y}\right)_y \left(\frac{\partial \bar{p}}{\partial z}\right)_z} \right| \right) \bar{k}_{xx} \tag{2.16}$$

$$\bar{k}_{xz} = \left(\frac{\left(\frac{\partial \bar{p}}{\partial x}\right)_y \left(\frac{\partial \bar{p}}{\partial y}\right)_z - \left(\frac{\partial \bar{p}}{\partial x}\right)_z}{\left(\frac{\partial \bar{p}}{\partial y}\right)_y \left(\frac{\partial \bar{p}}{\partial z}\right)_z - \left(\frac{\partial \bar{p}}{\partial z}\right)_z} \right) \bar{k}_{xx} \left(1 - \frac{\left(\frac{\partial \bar{p}}{\partial z}\right)_y \left(\frac{\partial \bar{p}}{\partial y}\right)_z}{\left(\frac{\partial \bar{p}}{\partial y}\right)_y \left(\frac{\partial \bar{p}}{\partial z}\right)_z} \right) \tag{2.17}$$

$$\bar{k}_{yx} = \left(\frac{\left(\frac{\partial \bar{p}}{\partial z}\right)_x \left(\frac{\partial \bar{p}}{\partial y}\right)_z - \left(\frac{\partial \bar{p}}{\partial y}\right)_x}{\left(\frac{\partial \bar{p}}{\partial x}\right)_x \left(\frac{\partial \bar{p}}{\partial z}\right)_z - \left(\frac{\partial \bar{p}}{\partial x}\right)_x} \right) \bar{k}_{yy} \left(1 - \frac{\left(\frac{\partial \bar{p}}{\partial x}\right)_x \left(\frac{\partial \bar{p}}{\partial z}\right)_z}{\left(\frac{\partial \bar{p}}{\partial x}\right)_x \left(\frac{\partial \bar{p}}{\partial z}\right)_z} \right) \tag{2.18}$$

$$\bar{k}_{yz} = \left(\frac{\left(\frac{\partial \bar{p}}{\partial y}\right)_x \left(\frac{\partial \bar{p}}{\partial x}\right)_z - \left(\frac{\partial \bar{p}}{\partial y}\right)_z}{\left(\frac{\partial \bar{p}}{\partial x}\right)_x \left(\frac{\partial \bar{p}}{\partial z}\right)_z - \left(\frac{\partial \bar{p}}{\partial z}\right)_z} \right) \bar{k}_{yy} \left(1 - \frac{\left(\frac{\partial \bar{p}}{\partial z}\right)_x \left(\frac{\partial \bar{p}}{\partial x}\right)_z}{\left(\frac{\partial \bar{p}}{\partial x}\right)_x \left(\frac{\partial \bar{p}}{\partial z}\right)_z} \right) \tag{2.19}$$

$$\bar{k}_{zx} = \left(\frac{\left(\frac{\partial \bar{p}}{\partial y}\right)_x \left(\frac{\partial \bar{p}}{\partial z}\right)_y - \left(\frac{\partial \bar{p}}{\partial z}\right)_x}{\left(\frac{\partial \bar{p}}{\partial x}\right)_x \left(\frac{\partial \bar{p}}{\partial y}\right)_y - \left(\frac{\partial \bar{p}}{\partial x}\right)_x} \right) \bar{k}_{zz} \left(1 - \frac{\left(\frac{\partial \bar{p}}{\partial y}\right)_x \left(\frac{\partial \bar{p}}{\partial x}\right)_y}{\left(\frac{\partial \bar{p}}{\partial x}\right)_x \left(\frac{\partial \bar{p}}{\partial y}\right)_y} \right) \tag{2.20}$$

$$\bar{k}_{zy} = \left(\frac{\left(\frac{\partial \bar{p}}{\partial z}\right)_x \left(\frac{\partial \bar{p}}{\partial x}\right)_y - \left(\frac{\partial \bar{p}}{\partial z}\right)_y}{\left(\frac{\partial \bar{p}}{\partial x}\right)_x \left(\frac{\partial \bar{p}}{\partial y}\right)_y - \left(\frac{\partial \bar{p}}{\partial y}\right)_y} \Bigg/ \left(1 - \frac{\left(\frac{\partial \bar{p}}{\partial y}\right)_x \left(\frac{\partial \bar{p}}{\partial x}\right)_y}{\left(\frac{\partial \bar{p}}{\partial x}\right)_x \left(\frac{\partial \bar{p}}{\partial y}\right)_y}\right) \right) \bar{k}_{zz} \tag{2.21}$$

Substituting Eq. 2.16 and Eq. 2.17 in Eq. 2.9 and rearranging the equation, we have an expression for $\bar{k}_{xx}$

$$\bar{k}_{xx} = \frac{\bar{k}_{xapp}}{\left(1 + \left(\frac{\left(\frac{\partial \bar{p}}{\partial x}\right)_z \left(\frac{\partial \bar{p}}{\partial z}\right)_y - \left(\frac{\partial \bar{p}}{\partial x}\right)_y}{\left(\frac{\partial \bar{p}}{\partial z}\right)_z \left(\frac{\partial \bar{p}}{\partial y}\right)_y - \left(\frac{\partial \bar{p}}{\partial y}\right)_y} \Bigg/ \left(1 - \frac{\left(\frac{\partial \bar{p}}{\partial z}\right)_y \left(\frac{\partial \bar{p}}{\partial y}\right)_z}{\left(\frac{\partial \bar{p}}{\partial y}\right)_y \left(\frac{\partial \bar{p}}{\partial z}\right)_z}\right) \right) \frac{\left(\frac{\partial \bar{p}}{\partial y}\right)_x}{\left(\frac{\partial \bar{p}}{\partial x}\right)_x} + \left(\frac{\left(\frac{\partial \bar{p}}{\partial x}\right)_y \left(\frac{\partial \bar{p}}{\partial y}\right)_z - \left(\frac{\partial \bar{p}}{\partial x}\right)_z}{\left(\frac{\partial \bar{p}}{\partial y}\right)_y \left(\frac{\partial \bar{p}}{\partial z}\right)_z - \left(\frac{\partial \bar{p}}{\partial z}\right)_z} \Bigg/ \left(1 - \frac{\left(\frac{\partial \bar{p}}{\partial z}\right)_y \left(\frac{\partial \bar{p}}{\partial y}\right)_z}{\left(\frac{\partial \bar{p}}{\partial y}\right)_y \left(\frac{\partial \bar{p}}{\partial z}\right)_z}\right) \right) \frac{\left(\frac{\partial \bar{p}}{\partial z}\right)_x}{\left(\frac{\partial \bar{p}}{\partial x}\right)_x} \right)} \tag{2.22}$$

Substituting Eq. 2.18 and Eq. 2.19 in Eq. 2.10 and rearranging the equation, we get an expression for $\bar{k}_{yy}$

$$\bar{k}_{yy} = \frac{\bar{k}_{yapp}}{\left(1 + \left(\frac{\left(\frac{\partial \bar{p}}{\partial z}\right)_x \left(\frac{\partial \bar{p}}{\partial y}\right)_z - \left(\frac{\partial \bar{p}}{\partial y}\right)_x}{\left(\frac{\partial \bar{p}}{\partial x}\right)_x \left(\frac{\partial \bar{p}}{\partial z}\right)_z - \left(\frac{\partial \bar{p}}{\partial x}\right)_x} \Bigg/ \left(1 - \frac{\left(\frac{\partial \bar{p}}{\partial x}\right)_x \left(\frac{\partial \bar{p}}{\partial x}\right)_z}{\left(\frac{\partial \bar{p}}{\partial x}\right)_x \left(\frac{\partial \bar{p}}{\partial z}\right)_z}\right) \right) \frac{\left(\frac{\partial \bar{p}}{\partial x}\right)_y}{\left(\frac{\partial \bar{p}}{\partial y}\right)_y} + \left(\frac{\left(\frac{\partial \bar{p}}{\partial y}\right)_x \left(\frac{\partial \bar{p}}{\partial x}\right)_z - \left(\frac{\partial \bar{p}}{\partial y}\right)_z}{\left(\frac{\partial \bar{p}}{\partial x}\right)_x \left(\frac{\partial \bar{p}}{\partial z}\right)_z - \left(\frac{\partial \bar{p}}{\partial z}\right)_z} \Bigg/ \left(1 - \frac{\left(\frac{\partial \bar{p}}{\partial z}\right)_x \left(\frac{\partial \bar{p}}{\partial x}\right)_z}{\left(\frac{\partial \bar{p}}{\partial x}\right)_x \left(\frac{\partial \bar{p}}{\partial z}\right)_z}\right) \right) \frac{\left(\frac{\partial \bar{p}}{\partial z}\right)_y}{\left(\frac{\partial \bar{p}}{\partial y}\right)_y} \right)} \tag{2.23}$$

Substituting Eq. 2.20 and Eq. 2.21 in Eq. 2.11 and rearranging the equation, we get an expression for $\bar{k}_{zz}$.

$$\bar{k}_{zz} = \frac{\bar{k}_{zapp}}{\left(1+\left(\frac{\left(\frac{\partial\bar{p}}{\partial y}\right)_x\left(\frac{\partial\bar{p}}{\partial z}\right)_y-\left(\frac{\partial\bar{p}}{\partial z}\right)_x}{\left(\frac{\partial\bar{p}}{\partial x}\right)_x\left(\frac{\partial\bar{p}}{\partial y}\right)_y-\left(\frac{\partial\bar{p}}{\partial x}\right)_x}\right)\frac{\left(\frac{\partial\bar{p}}{\partial x}\right)_z}{\left(\frac{\partial\bar{p}}{\partial z}\right)_z}\right)\left(1-\frac{\left(\frac{\partial\bar{p}}{\partial y}\right)_x\left(\frac{\partial\bar{p}}{\partial x}\right)_y}{\left(\frac{\partial\bar{p}}{\partial x}\right)_x\left(\frac{\partial\bar{p}}{\partial y}\right)_y}\right)+\left(\frac{\left(\frac{\partial\bar{p}}{\partial z}\right)_x\left(\frac{\partial\bar{p}}{\partial x}\right)_y-\left(\frac{\partial\bar{p}}{\partial z}\right)_y}{\left(\frac{\partial\bar{p}}{\partial x}\right)_x\left(\frac{\partial\bar{p}}{\partial y}\right)_y-\left(\frac{\partial\bar{p}}{\partial y}\right)_y}\right)\frac{\left(\frac{\partial\bar{p}}{\partial y}\right)_z}{\left(\frac{\partial\bar{p}}{\partial z}\right)_z}\right)\left(1-\frac{\left(\frac{\partial\bar{p}}{\partial y}\right)_x\left(\frac{\partial\bar{p}}{\partial x}\right)_y}{\left(\frac{\partial\bar{p}}{\partial x}\right)_x\left(\frac{\partial\bar{p}}{\partial y}\right)_y}\right)} \quad (2.24)$$

To complete the calculation of these permeability tensors we need to find the following six terms for transverse pressure gradient ratios.

Injection along the x-direction:

$$\frac{\left(\frac{\partial\bar{p}}{\partial y}\right)_x}{\left(\frac{\partial\bar{p}}{\partial x}\right)_x} \quad \text{and} \quad \frac{\left(\frac{\partial\bar{p}}{\partial z}\right)_x}{\left(\frac{\partial\bar{p}}{\partial x}\right)_x} \quad (2.25)$$

Injection along the y-direction:

$$\frac{\left(\frac{\partial\bar{p}}{\partial x}\right)_y}{\left(\frac{\partial\bar{p}}{\partial y}\right)_y} \quad \text{and} \quad \frac{\left(\frac{\partial\bar{p}}{\partial z}\right)_y}{\left(\frac{\partial\bar{p}}{\partial y}\right)_y} \quad (2.26)$$

Injection along the z-direction;

$$\frac{\left(\frac{\partial\bar{p}}{\partial x}\right)_z}{\left(\frac{\partial\bar{p}}{\partial z}\right)_z} \quad \text{and} \quad \frac{\left(\frac{\partial\bar{p}}{\partial y}\right)_z}{\left(\frac{\partial\bar{p}}{\partial z}\right)_z} \quad (2.27)$$

For the cases tested in this report, the off-diagonal elements of the permeability tensor are assumed to be zero. Therefore the pressure gradient ratio due to permeability contrasts between the eight grid blocks are considered. The procedures for calculating these pressure gradient ratios are presented in Appendix B.

2.4.2 Part 2 - Numerical Method

This part of the study is carried out using a finite element simulator to check the validity of the analytical method. The simulator can handle simple heterogeneities such as single or multiple disturbances in the system. The system shown in Fig. 2.14 was simulated. In each simulation, pressure distribution and three components of the velocity vector, $\bar{v}_x$, $\bar{v}_y$ and $\bar{v}_z$, were calculated. After getting that information, pressure gradients in each direction were calculated and then Eq. 2.28 through Eq. 2.36 were solved for the nine components of the permeability tensor, $\bar{k}_{xx}, \bar{k}_{xy}, \bar{k}_{xz}, \bar{k}_{yx}, \bar{k}_{yy}, \bar{k}_{yz}, \bar{k}_{zx}, \bar{k}_{zy}$ and $\bar{k}_{zz}$.

Injection along the x-direction:

$$\bar{v}_x = -\frac{1}{\mu}\left(\bar{k}_{xx}\frac{\partial \bar{p}}{\partial x} + \bar{k}_{xy}\frac{\partial \bar{p}}{\partial y} + \bar{k}_{xz}\frac{\partial \bar{p}}{\partial z}\right)_x \tag{2.28}$$

$$\bar{v}_y = -\frac{1}{\mu}\left(\bar{k}_{yx}\frac{\partial \bar{p}}{\partial x} + \bar{k}_{yy}\frac{\partial \bar{p}}{\partial y} + \bar{k}_{yz}\frac{\partial \bar{p}}{\partial z}\right)_x = 0 \tag{2.29}$$

$$\bar{v}_z = -\frac{1}{\mu}\left(\bar{k}_{zx}\frac{\partial \bar{p}}{\partial x} + \bar{k}_{zy}\frac{\partial \bar{p}}{\partial y} + \bar{k}_{zz}\frac{\partial \bar{p}}{\partial z}\right)_x = 0 \tag{2.30}$$

Injection along the y-direction:

$$\bar{v}_x = -\frac{1}{\mu}\left(\bar{k}_{xx}\frac{\partial \bar{p}}{\partial x} + \bar{k}_{xy}\frac{\partial \bar{p}}{\partial y} + \bar{k}_{xz}\frac{\partial \bar{p}}{\partial z}\right)_Y = 0 \tag{2.31}$$

$$\bar{v}_y = -\frac{1}{\mu}\left(\bar{k}_{yx}\frac{\partial \bar{p}}{\partial x} + \bar{k}_{yy}\frac{\partial \bar{p}}{\partial y} + \bar{k}_{yz}\frac{\partial \bar{p}}{\partial z}\right)_Y \tag{2.32}$$

$$\bar{v}_z = -\frac{1}{\mu}\left(\bar{k}_{zx}\frac{\partial \bar{p}}{\partial x} + \bar{k}_{zy}\frac{\partial \bar{p}}{\partial y} + \bar{k}_{zz}\frac{\partial \bar{p}}{\partial z}\right)_Y = 0 \tag{2.33}$$

Injection along the z-direction;

$$\bar{v}_x = -\frac{1}{\mu}\left(\bar{k}_{xx}\frac{\partial \bar{p}}{\partial x} + \bar{k}_{xy}\frac{\partial \bar{p}}{\partial y} + \bar{k}_{xz}\frac{\partial \bar{p}}{\partial z}\right)_z = 0 \tag{2.34}$$

$$\bar{v}_y = -\frac{1}{\mu}\left(\bar{k}_{yx}\frac{\partial \bar{p}}{\partial x} + \bar{k}_{yy}\frac{\partial \bar{p}}{\partial y} + \bar{k}_{yz}\frac{\partial \bar{p}}{\partial z}\right)_z = 0 \tag{2.35}$$

$$\bar{v}_z = -\frac{1}{\mu}\left(\bar{k}_{zx}\frac{\partial \bar{p}}{\partial x} + \bar{k}_{zy}\frac{\partial \bar{p}}{\partial y} + \bar{k}_{zz}\frac{\partial \bar{p}}{\partial z}\right)_z \tag{2.36}$$

For each case study, we have to run the simulator three times changing the direction of injection. Changing the injection direction was extremely complex when we worked with large a number of elements in each block because we have to define the elements which are at flow the boundary. Instead of changing the injection direction, we decided to rotate the location of the disturbance k,eeping the x-direction as the injection direction for all cases. Calculated pressure gradients and velocity vectors were re-rotated to assign the calculated values to the original place which gives the same effect as changing injection direction. A system which is equivalent to injection along the y-direction for a system shown in Fig. 2.14 is depicted in Fig. 2.15. Fig. 2.16 is an equivalent system to a case of injection along the z-direction.

To minimize the constraining effect of the boundary conditions, we tested the simulator by increasing the number of elements in each block up to 15 × 15 × 15 elements resulting in a total of 3375 elements. By doing this, the effect of the boundary on transverse pressure gradient can be reduced.

2.5 Preliminary Results

2.5.1 Part 1 - Numerical Results

To test the simulator, we assigned permeability to each block and recalculated the effective permeability from the simulation results. The difference between input and calculated permeabilities was 0.04% for the diagonal tensor element and 3.4% for the off-diagonal elements when 8 × 8 × 8 elements for each block were used. For a case of calculating effective permeability with a disturbance in the system, we

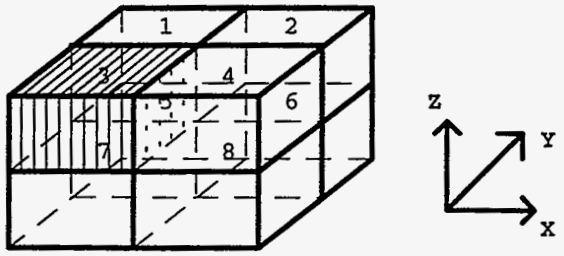

Figure 2.14: Disturbance at block #3. Injection along the x direction.

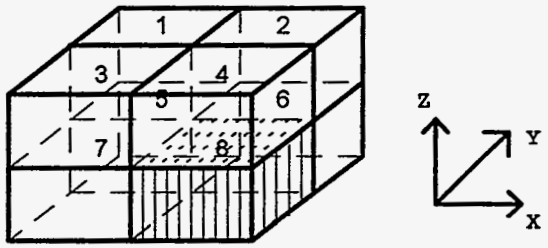

Figure 2.15: Disturbance at block #8. Equivalent to injection along the y direction.

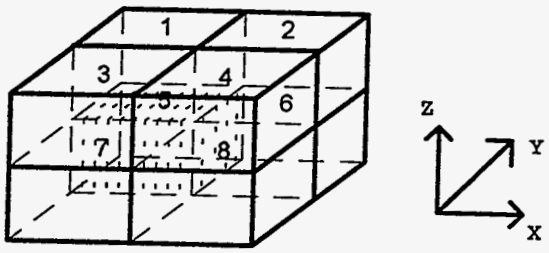

Figure 2.16: Disturbance at block #5. Equivalent to injection along the z direction.

ran the simulator several times increasing the number of elements expecting our results will converge to the exact solution based on the concept of *convergence of a sequence of approximate solutions*[2-5]. Whereas the magnitude of diagonal effective permeability element changed little, the magnitude of off - diagonal elements changed significantly as shown in Fig. 2.17. In this case the block #3 in Fig. 2.14 has $\bar{k}_{xx} = \bar{k}_{yy} = \bar{k}_{zz} = 1$ md, the other seven blocks have $\bar{k}_{xx} = \bar{k}_{yy} = \bar{k}_{zz} = 1000$ md. Local off - diagonal permeabilities are assumed to be zero. From the graph, we see that the slope is progressively decreasing which means that the difference between two successive runs is getting smaller and the results are converging to the exact solution. The actual dimension of the system in Fig. 2.14 is 20 cm in each direction and the disturbance is 10 × 10 × 10 cm. The pressure distributions at three different locations: x = 5.0 cm which is the center line of disturbance, x =10 cm which is the boundary line of disturbance and x =15 cm which is the center line of neighboring homogeneous block are depicted in Figs. 2.18 through Fig. 2.20. In these examples, an isotropic permeability of 1 md is assigned to a disturbance and 1000 md is assigned to the other seven blocks. This permeability configuration is maintained through out this report. These figures show pthe ressure distribution according to the presence of disturbance which induces transverse pressure gradient ratio resulting in cross-flow. On the contrary, the system shown in Fig. 2.21 which is a two-layer case, shows no transverse pressure gradient, see Fig. 2.22. The calculated effective permeability for a system containing a disturbance results in a symmetric matrix with different signs depending on the location of disturbance. The obtained results are as follows:

Disturbance at block #1 = Disturbance at block #8,

$$\bar{k} = \begin{vmatrix} 0.818 & -0.053 & -0.053 \\ -0.053 & 0.818 & 0.053 \\ -0.053 & 0.053 & 0.818 \end{vmatrix}$$

Disturbance at block #2 = Disturbance at block #7,

$$\bar{k} = \begin{vmatrix} 0.818 & 0.053 & 0.053 \\ 0.053 & 0.818 & 0.053 \\ 0.053 & 0.053 & 0.818 \end{vmatrix}$$

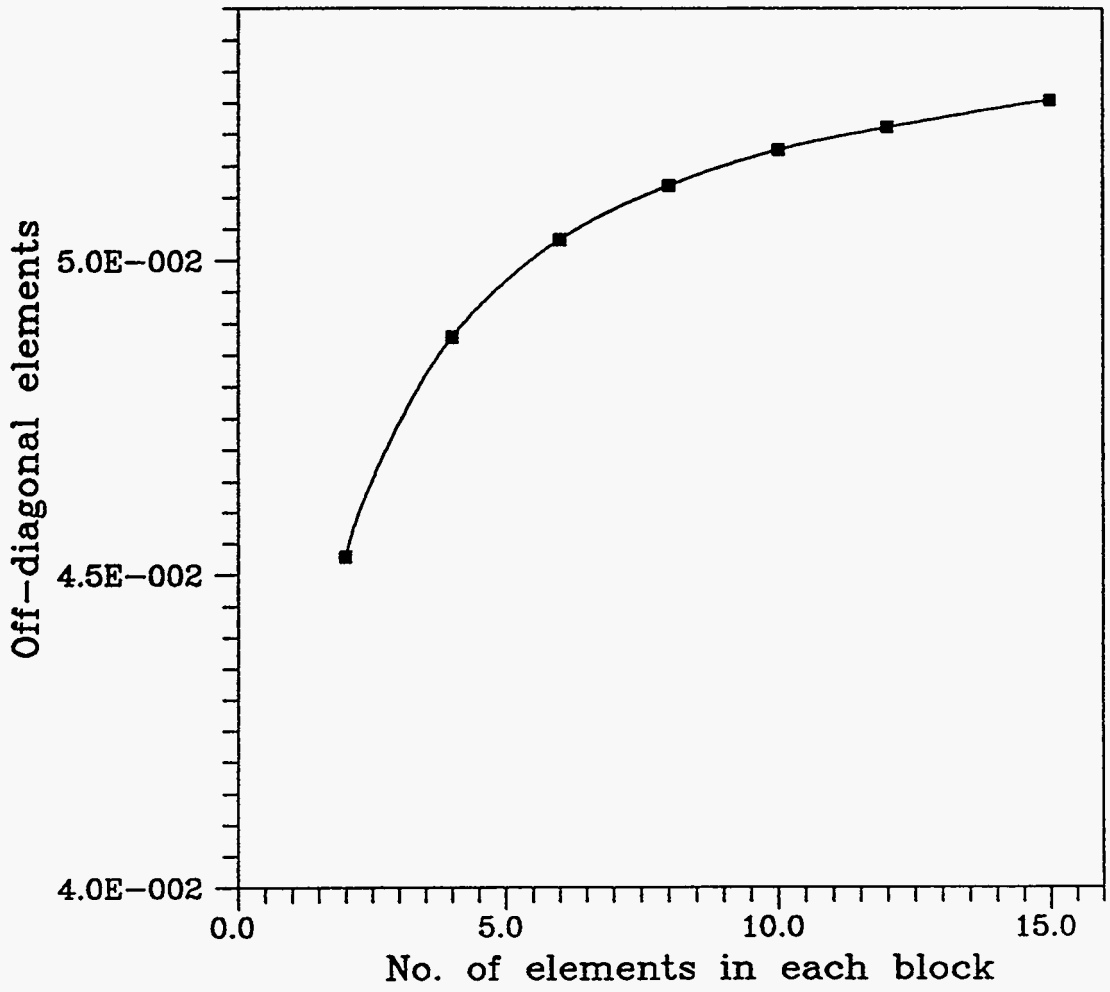

Figure 2.17: Changes in magnitude of off-diagonal elements with the number of simulator elements.

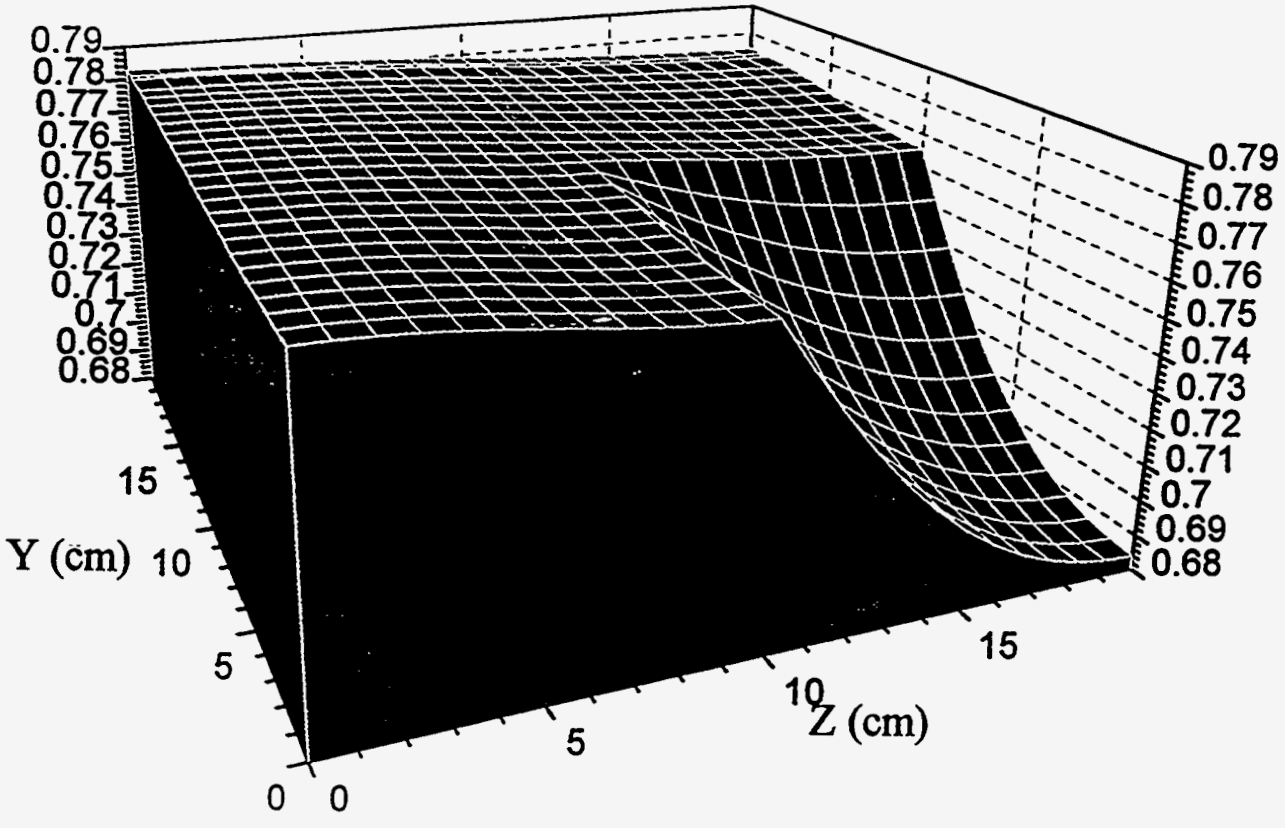

Figure 2.18: Pressure distribution (atm) at x = 5 cm, at the center line of the disturbance.

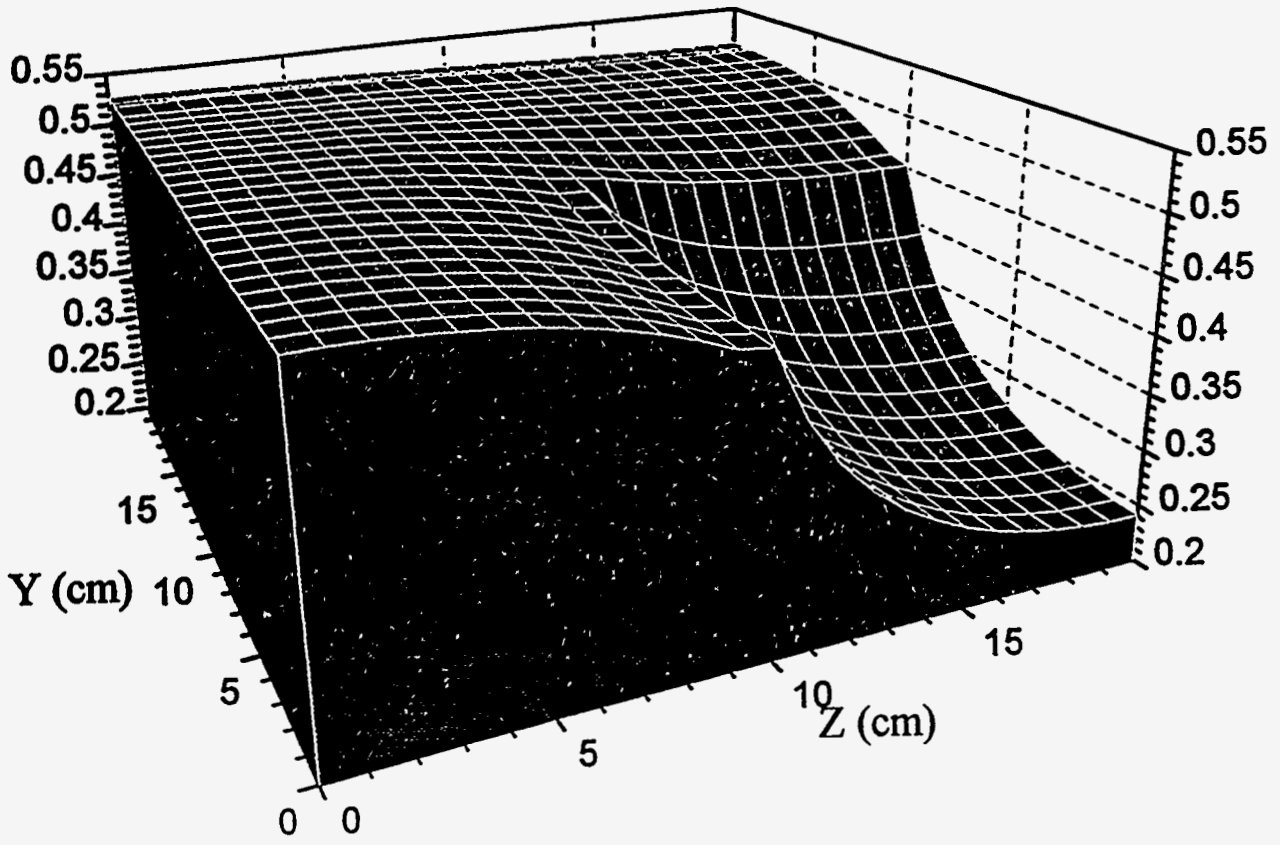

Figure 2.19: Pressure distribution (atm) at x = 10 cm, at the boundary line of disturbance.

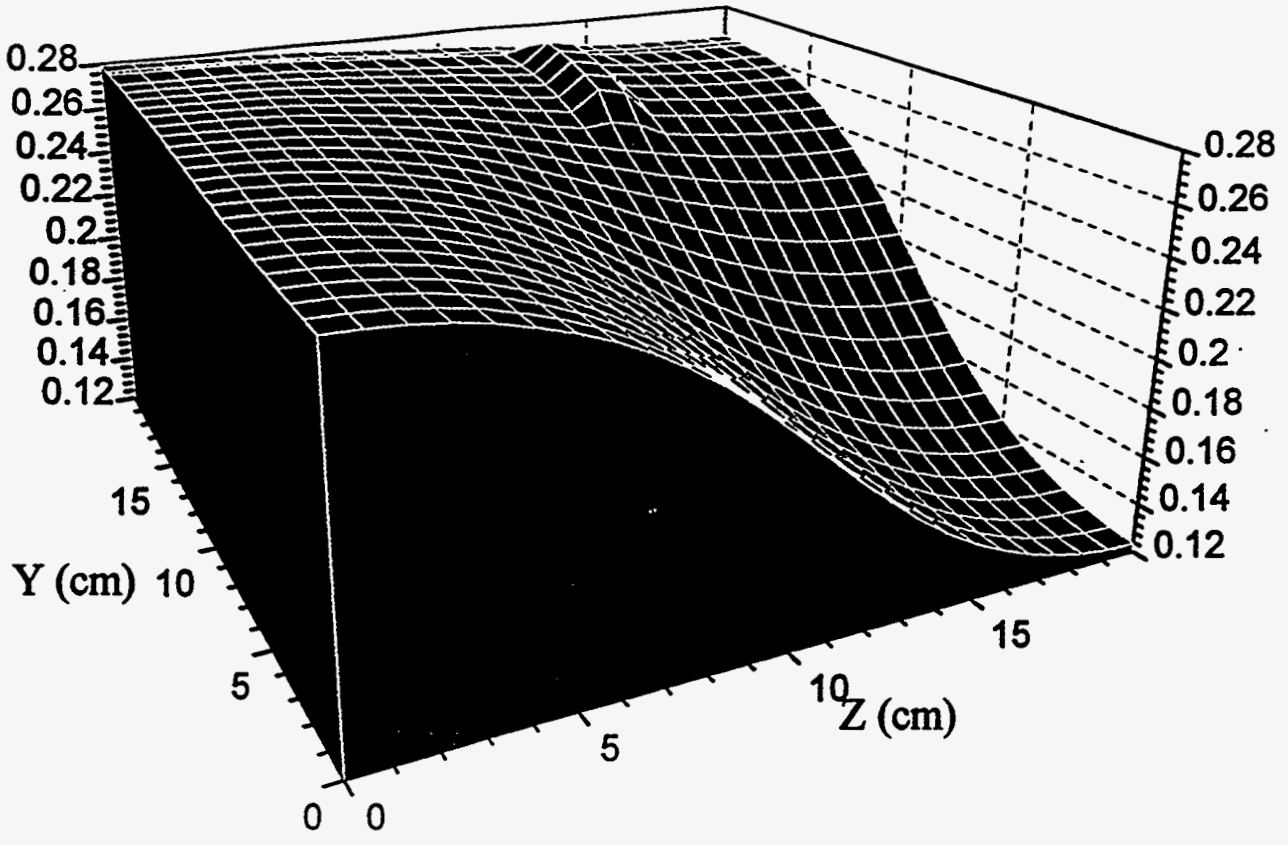

Figure 2.20: Pressure distribution (atm) at x = 15 cm, at the center line of the neighboring block.

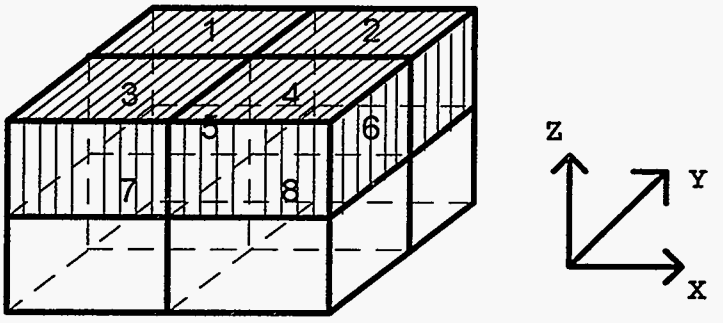

Figure 2.21: System containing disturbances at top four blocks (two layer case).

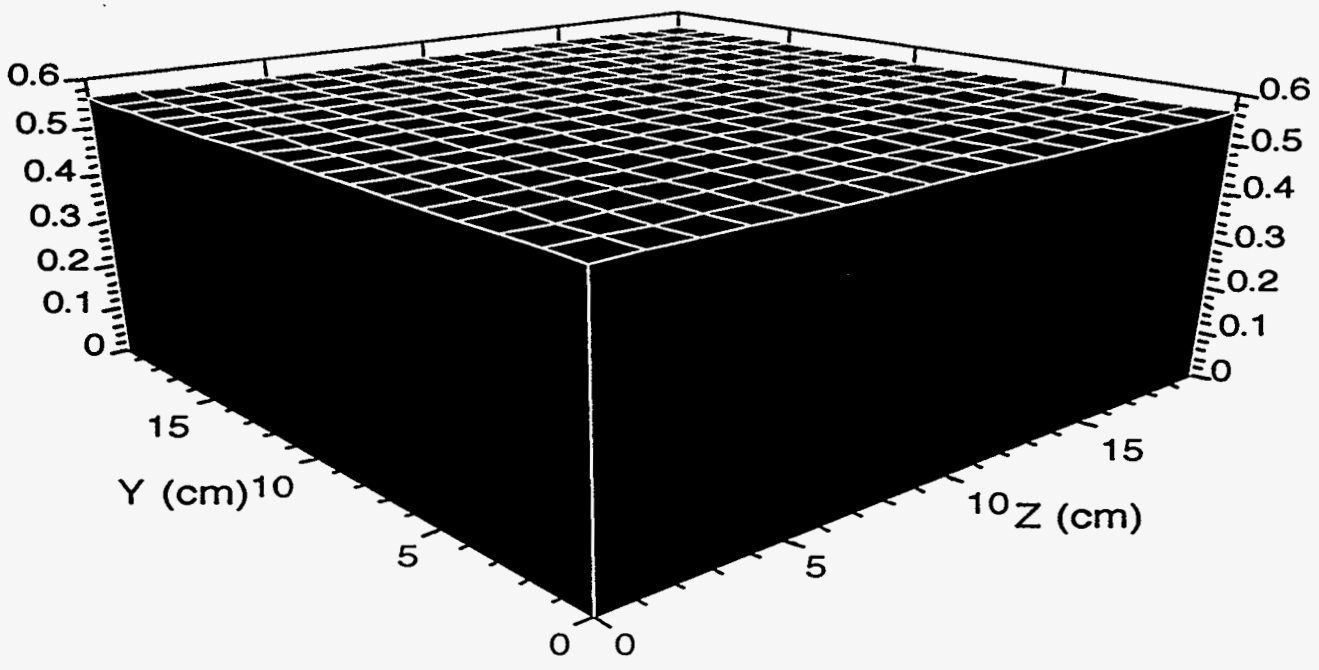

Figure 2.22: Pressure distribution (atm) at $x = 10$ cm for two layer case.

Disturbance at block #3 = Disturbance at block #6,

$$\bar{\bar{k}} = \begin{vmatrix} 0.818 & -0.053 & 0.053 \\ -0.053 & 0.818 & -0.053 \\ 0.053 & -0.053 & 0.818 \end{vmatrix}$$

Disturbance at block #4 = Disturbance at block #5,

$$\bar{\bar{k}} = \begin{vmatrix} 0.818 & 0.053 & -0.053 \\ 0.053 & 0.818 & -0.053 \\ -0.053 & -0.053 & 0.818 \end{vmatrix}$$

2.5.2 Part 2 - Analytical Results

The system in Fig. 2.21 is analyzed, the following results are obtained.

$$\bar{\bar{k}} = \begin{vmatrix} 0.500 & 0.000 & 0.000 \\ 0.000 & 0.500 & 0.000 \\ 0.000 & 0.000 & 0.002 \end{vmatrix}$$

The numerical results for the corresponding system are as follows

$$\bar{\bar{k}} = \begin{vmatrix} 0.500 & 0.000 & 0.000 \\ 0.000 & 0.500 & 0.000 \\ 0.000 & 0.000 & 0.002 \end{vmatrix}$$

These two results show that when there is no transverse pressure gradient, both methods match very well. In this system $\bar{k}_{xapp} = \bar{k}_{xx}, \bar{k}_{yapp} = \bar{k}_{yy}$ and $\bar{k}_{zapp} = \bar{k}_{zz}$.

A system with a disturbance is analyzed. A disturbance is placed at block #1 with a small permeability of 1 md and the analytical method yields the following permeability tensor.

$$\bar{\bar{k}} = \begin{vmatrix} 0.822 & -0.060 & -0.060 \\ -0.060 & 0.822 & 0.060 \\ -0.060 & 0.060 & 0.822 \end{vmatrix}$$

Comparing with the numerical results presented in part 1, the diagonal elements are very close, the relative difference which is defined by Aasum et al.[2.6] is 0.5%, but the off-diagonal elements are not as close as the main diagonal terms, with a relative difference of 11.7%. When a disturbance is located at block #3, the analytical method yields following permeability tensor;

$$\bar{k} = \begin{vmatrix} 0.822 & -0.060 & 0.060 \\ -0.060 & 0.822 & -0.060 \\ 0.060 & -0.060 & 0.822 \end{vmatrix}$$

This case also shows same results as the previous example when compared with the numerical results. Even though the magnitude of the off-diagonal elements do not match well, the signs are identical which means that the flow directions are properly determined by the analytical method. These results indicate that the magnitude of transverse pressure gradient to the principal flow direction is not correctly determined by the current analytical method. At this stage, we think that the transverse pressure gradient computation in three dimensions needs to be modified compared to the values calculated in two dimensions.

2.6 Future Work

The next step in this study will be to investigate the correct way to calculate transverse pressure gradients by which we can match the numerical results. Also a more complex case, such as a block containing an anisotropic permeability distribution, will be tested. To be applicable to an outcrop study, the method to determine the principal directions of permeability from field data such as minipermeameter measurements will be also developed. In addition, the finite element simulator will be revised in order to handle more general and complex permeability systems.

Symbol

k = permeability (Darcy)

q = flow rate (cm^3/sec)

p = pressure (atm)

v = Darcy velocity (cm/sec)

μ = fluid viscosity (cp)

Lx_1, Lx_2 = Length of system block in the x-direction (cm)

Ly_1, Ly_2 = Length of system block in the y-direction (cm)

Lz_1, Lz_2 = Length of system block in the z-direction (cm)

Subscripts

x = x-direction

y = y-direction

z = z-direction

NC = no communication along transverse direction to the direction of flow

VE, Y = vertical equilibrium along the y-direction

VE, Z = vertical equilibrium along the z-direction

t = top layer

b = bottom layer

f = first column

s = second column

r = right column

l = left column

1, 2, 3, 4, 5, 6, 7, 8 = number of blocks

$app1$, $app2$, ... = effective apparent permeability of each block

$app12$, $app34$, ... = effective apparent permeability of two-block system

app, s = effective apparent permeability combined in order of serial - parallel

app, p = effective apparent permeability combined in order of parallel - series

$xxapp$, $xyapp$, $xzapp$ = effective apparent permeability of the system, flow in the x-direction, communication only in the x, y and z direction respectively

$yxapp$, $yyapp$, $yzapp$ = effective apparent permeability of the system, flow in the y-direction, communication only in the x, y and z direction respectively

$zxapp$, $zyapp$, $zzapp$ = effective apparent permeability of the system, flow in the z-direction, communication only in the x, y and z direction respectively

2.1 Kasap, E.: "Analytic Methods To Calculate An Effective Permeability Tensor And Pseudo Relative Permeability For Cross-Bedded Flow Units," Ph.D. Dissertation, University of Texas, Austin, Texas (1990).

2.2 White, C. D. and Horne, R. N.: "Computing Absolute Transmissibility in the Presence of Fine - Scale Heterogeneity," paper SPE 16011, presented at the Ninth SPE Symposium on Reservoir Simulation, San Antonio, Texas (February 1 - 4, 1987).

2.3 Kasap, E. and Lake, L. W.: "Calculating the Effective Permeability Tensor of a Grid Blocks," *SPE Form. Eval.* (June, 1990) pp 192 - 200.

2.4 Aasum, Y.: "Effective Properties of Reservoir Simulator Grid Blocks," Ph.D. Dissertation, The University of Tulsa, Tulsa, Oklahoma (1992).

2.5 Burnett, D. S.: *Finite Element Method,* Addison Wesley, Inc. (1987).

2.6 Aasum, Y., Kasap, E. and Kelkar, M. G.: "Analytical Upscaling Of Small Scale Permeability Using A Full Tensor," paper SPE 25913, presented at the SPE Rocky Mountain Regional/Low Permeability Reservoirs Symposium, Denver, Colorado (April 25-28, 1993).

2.7 Kelkar, Mohan: Reservoir Characterization of Pennyslvanian Sandstone Reservoirs, DOE Annual Report (December, 1991).

2.8 M.O.R.E. Simulator, Black-Oil Version, Reservoir Simulation Research Corporation, Tulsa, Oklahoma (May, 1992).

This section contains the procedures to calculate $\bar{k}_{xapp}$, $\bar{k}_{yapp}$ and $\bar{k}_{zapp}$ which are calculated by following similar steps. Fig. A.1 shows a schematic of the system considered. This system is divided into four two-blocks depending on the flow direction and effective permeabilities for two-block systems are calculated, and then combined to yield the apparent permeability for each direction.

Calculation procedure for $\bar{k}_{xapp}$:

A. The system in Fig. A.1 is divided into four two-block systems considering no communication in the y- and z-directions as shown in Fig. A.2.

Velocity components along the x-direction for blocks 1 and 2:

$$v_{x1} = -\frac{1}{\mu}\left(\bar{k}_{xx1}\left(\frac{\partial p}{\partial x}\right)_1 + \bar{k}_{xy1}\left(\frac{\partial p}{\partial y}\right)_1 + \bar{k}_{xz1}\left(\frac{\partial p}{\partial z}\right)_1\right) \tag{A.1}$$

$$v_{x2} = -\frac{1}{\mu}\left(\bar{k}_{xx2}\left(\frac{\partial p}{\partial x}\right)_2 + \bar{k}_{xy2}\left(\frac{\partial p}{\partial y}\right)_2 + \bar{k}_{xz2}\left(\frac{\partial p}{\partial z}\right)_2\right) \tag{A.2}$$

Velocity components along the x-axis for block 1 and 2 combined:

$$\bar{v}_{x12} = -\frac{1}{\mu}\left(\bar{k}_{xx12}\left(\frac{\partial p}{\partial x}\right)_{12} + \bar{k}_{xy12}\left(\frac{\partial p}{\partial y}\right)_{12} + \bar{k}_{xz12}\left(\frac{\partial p}{\partial z}\right)_{12}\right) \tag{A.3}$$

Velocity components along the y-axis for blocks 1 and 2 are zero because of closed boundary conditions.

$$v_{y1} = -\frac{1}{\mu}\left(\bar{k}_{yx1}\left(\frac{\partial p}{\partial x}\right)_1 + \bar{k}_{yy1}\left(\frac{\partial p}{\partial y}\right)_1 + \bar{k}_{yz1}\left(\frac{\partial p}{\partial z}\right)_1\right) = 0 \tag{A.4}$$

$$v_{y2} = -\frac{1}{\mu}\left(\bar{k}_{yx2}\left(\frac{\partial p}{\partial x}\right)_2 + \bar{k}_{yy2}\left(\frac{\partial p}{\partial y}\right)_2 + \bar{k}_{yz2}\left(\frac{\partial p}{\partial z}\right)_2\right) = 0 \tag{A.5}$$

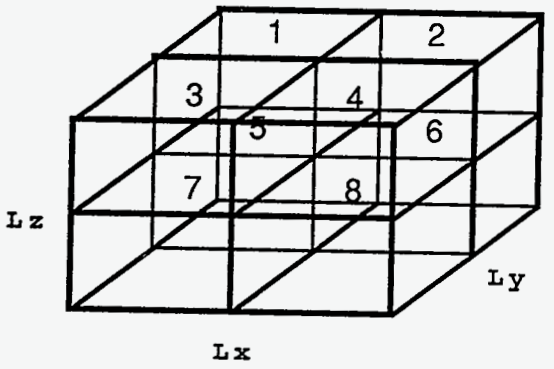

Figure A.1: System containing 8 blocks

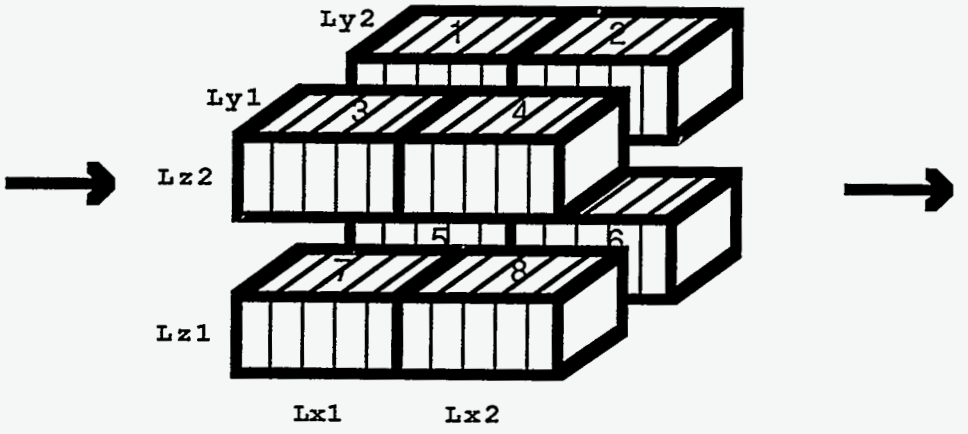

Figure A.2: No communication in the y and z directions, flow in the x direction

Velocity components along the y-axis for blocks 1 and 2 combined:

$$\bar{v}_{y12} = -\frac{1}{\mu}\left(\bar{k}_{yx12}\left(\frac{\partial p}{\partial x}\right)_{12} + \bar{k}_{yy12}\left(\frac{\partial p}{\partial y}\right)_{12} + \bar{k}_{yz12}\left(\frac{\partial p}{\partial z}\right)_{12}\right) = 0 \qquad \text{(A.6)}$$

Velocity components along the z-axis for blocks 1 and 2 are zero because of closed boundary conditions.

$$v_{z1} = -\frac{1}{\mu}\left(k_{zx1}\left(\frac{\partial p}{\partial x}\right)_1 + k_{zy1}\left(\frac{\partial p}{\partial y}\right)_1 + k_{zz1}\left(\frac{\partial p}{\partial z}\right)_1\right) = 0 \qquad \text{(A.7)}$$

$$v_{z2} = -\frac{1}{\mu}\left(k_{zx2}\left(\frac{\partial p}{\partial x}\right)_2 + k_{zy2}\left(\frac{\partial p}{\partial y}\right)_2 + k_{zz2}\left(\frac{\partial p}{\partial z}\right)_2\right) = 0 \qquad \text{(A.8)}$$

Velocity components along the z-axis for blocks 1 and 2 combined:

$$\bar{v}_{z12} = -\frac{1}{\mu}\left(\bar{k}_{zx12}\left(\frac{\partial p}{\partial x}\right)_{12} + \bar{k}_{zy12}\left(\frac{\partial p}{\partial y}\right)_{12} + \bar{k}_{zz12}\left(\frac{\partial p}{\partial z}\right)_{12}\right) = 0 \qquad \text{(A.9)}$$

Rearranging Eq. A.1 through Eq. A.9:

$$\left(\frac{\partial p}{\partial y}\right)_1 = \frac{k_{zx1}k_{yz1} - k_{yx1}k_{zz1}}{k_{yy1}k_{zz1} - k_{zy1}k_{yz1}}\left(\frac{\partial p}{\partial x}\right)_1 \qquad \text{(A.10)}$$

$$\left(\frac{\partial p}{\partial y}\right)_2 = \frac{k_{zx2}k_{yz2} - k_{yx2}k_{zz2}}{k_{yy2}k_{zz2} - k_{zy2}k_{yz2}}\left(\frac{\partial p}{\partial x}\right)_2 \qquad \text{(A.11)}$$

$$\left(\frac{\partial \bar{p}}{\partial y}\right)_{12} = \frac{\bar{k}_{zx12}\bar{k}_{yz12} - \bar{k}_{yx12}\bar{k}_{zz12}}{\bar{k}_{yy12}\bar{k}_{zz12} - \bar{k}_{zy12}\bar{k}_{yz12}}\left(\frac{\partial \bar{p}}{\partial x}\right)_{12} \qquad \text{(A.12)}$$

$$\left(\frac{\partial p}{\partial z}\right)_1 = \frac{k_{yx1}k_{zy1} - k_{zx1}k_{yy1}}{k_{yy1}k_{zz1} - k_{zy1}k_{yz1}}\left(\frac{\partial p}{\partial x}\right)_1 \qquad \text{(A.13)}$$

$$\left(\frac{\partial p}{\partial z}\right)_2 = \frac{k_{yx2}k_{zy2} - k_{zx2}k_{yy2}}{k_{yy2}k_{zz2} - k_{zy2}k_{yz2}}\left(\frac{\partial p}{\partial x}\right)_2 \qquad \text{(A.14)}$$

$$\left(\frac{\partial \bar{p}}{\partial z}\right)_{12} = \frac{\bar{k}_{yx12}\bar{k}_{zy12} - \bar{k}_{zx12}\bar{k}_{yy12}}{\bar{k}_{yy12}\bar{k}_{zz12} - \bar{k}_{zy12}\bar{k}_{yz12}}\left(\frac{\partial \bar{p}}{\partial x}\right)_{12} \qquad \text{(A.15)}$$

Total pressure gradient is:

$$\left(\frac{\partial \bar{p}}{\partial x}\right)_{12} = \frac{Lx_1}{Lx}\left(\frac{\partial p}{\partial x}\right)_1 + \frac{Lx_2}{Lx}\left(\frac{\partial p}{\partial x}\right)_2 \tag{A.16}$$

Insert Eq. A.10 and Eq. A.13 into Eq. A.1, Eq. A.11 and Eq. A.14 into Eq. A.2, and Eq. A.12 and Eq. A.15 into Eq. A.3. After rearranging the equations, we get:

$$v_{x1} = -\frac{1}{\mu}\left(\begin{array}{l} k_{xx1} + k_{xy1}\left(\dfrac{k_{zx1}k_{yz1} - k_{yx1}k_{zz1}}{k_{yy1}k_{zz1} - k_{yz1}k_{zy1}}\right) \\ +k_{xz1}\left(\dfrac{k_{yx1}k_{yz1} - k_{xx1}k_{yz1}}{k_{yy1}k_{zz1} - k_{yz1}k_{zy1}}\right) \end{array}\right)\left(\frac{\partial p}{\partial x}\right)_1 \tag{A.17}$$

$$v_{x2} = -\frac{1}{\mu}\left(\begin{array}{l} k_{xx2} + k_{xy2}\left(\dfrac{k_{zx2}k_{yz2} - k_{yx2}k_{zz2}}{k_{yy2}k_{zz2} - k_{yz2}k_{zy2}}\right) \\ +k_{xz2}\left(\dfrac{k_{yx2}k_{yz2} - k_{xx2}k_{yz2}}{k_{yy2}k_{zz2} - k_{yz2}k_{zy2}}\right) \end{array}\right)\left(\frac{\partial p}{\partial x}\right)_2 \tag{A.18}$$

$$\bar{v}_{x12} = -\frac{1}{\mu}\left(\begin{array}{l} \bar{k}_{xx12} + \bar{k}_{xy12}\left(\dfrac{\bar{k}_{zx12}\bar{k}_{yz12} - \bar{k}_{yx12}\bar{k}_{zz12}}{\bar{k}_{yy12}\bar{k}_{zz12} - \bar{k}_{zy12}\bar{k}_{yz12}}\right) \\ +\bar{k}_{xz12}\left(\dfrac{\bar{k}_{yx12}\bar{k}_{zy12} - \bar{k}_{zx12}\bar{k}_{yy12}}{\bar{k}_{yy12}\bar{k}_{zz12} - \bar{k}_{yz12}\bar{k}_{zy12}}\right) \end{array}\right)\left(\frac{\partial \bar{p}}{\partial x}\right)_{12} \tag{A.19}$$

Substituting Eq. A.17, Eq. A.18 and Eq. A.19 in Eq. A.16 and rearranging the equation that $\bar{v}_{x12} = v_{x1} = v_{x2}$, we get:

$$\frac{\bar{v}_{x12}}{\bar{k}_{xappl12}} = \frac{Lx_1}{Lx}\frac{v_{x1}}{k_{xappl1}} + \frac{Lx_2}{Lx}\frac{v_{x2}}{k_{xappl2}} \tag{A.20}$$

$$\bar{k}_{xappl12} = \frac{Lxk_{xappl1}k_{xappl2}}{Lx_1k_{xappl2} + Lx_2k_{xappl1}} \tag{A.21}$$

One block effective apparent permeability is

$$k_{xappl1} = k_{xx1} + k_{xy1}\left(\frac{k_{zx1}k_{yz1} - k_{yx1}k_{zz1}}{k_{yy1}k_{zz1} - k_{yz1}k_{zy1}}\right) + k_{xz1}\left(\frac{k_{zy1}k_{yx1} - k_{zx1}k_{yy1}}{k_{yy1}k_{zz1} - k_{yz1}k_{zy1}}\right) \tag{A.22}$$

$$k_{xapp2} = k_{xx2} + k_{xy2}\left(\frac{k_{zx2}k_{yz2} - k_{yx2}k_{zz2}}{k_{yy2}k_{zz2} - k_{yz2}k_{zy2}}\right) + k_{xz2}\left(\frac{k_{zy2}k_{yx2} - k_{zx2}k_{yy2}}{k_{yy2}k_{zz2} - k_{yz2}k_{zy2}}\right) \quad \text{(A.23)}$$

Following the same procedures, Eq. A.1 through Eq. A.23, for blocks 3 and 4:

$$\bar{k}_{xapp34} = \frac{Lxk_{xapp3}k_{xapp4}}{Lx_1k_{xapp4} + Lx_2k_{xapp3}} \quad \text{(A.24)}$$

where

$$k_{xapp3} = k_{xx3} + k_{xy3}\left(\frac{k_{zx3}k_{yz3} - k_{yx3}k_{zz3}}{k_{yy3}k_{zz3} - k_{yz3}k_{zy3}}\right) + k_{xz3}\left(\frac{k_{zy3}k_{yx3} - k_{zx3}k_{yy3}}{k_{yy3}k_{zz3} - k_{yz3}k_{zy3}}\right) \quad \text{(A.25)}$$

$$k_{xapp4} = k_{xx4} + k_{xy4}\left(\frac{k_{zx4}k_{yz4} - k_{yx4}k_{zz4}}{k_{yy4}k_{zz4} - k_{yz4}k_{zy4}}\right) + k_{xz4}\left(\frac{k_{zy4}k_{yx4} - k_{zx4}k_{yy4}}{k_{yy4}k_{zz4} - k_{yz4}k_{zy4}}\right) \quad \text{(A.26)}$$

For blocks 5 and 6:

$$\bar{k}_{xapp56} = \frac{Lxk_{xapp5}k_{xapp6}}{Lx_1k_{xapp6} + Lx_2k_{xapp5}} \quad \text{(A.27)}$$

where

$$k_{xapp5} = k_{xx5} + k_{xy5}\left(\frac{k_{zx5}k_{yz5} - k_{yx5}k_{zz5}}{k_{yy5}k_{zz5} - k_{yz5}k_{zy5}}\right) + k_{xz5}\left(\frac{k_{zy5}k_{yx5} - k_{zx5}k_{yy5}}{k_{yy5}k_{zz5} - k_{yz5}k_{zy5}}\right) \quad \text{(A.28)}$$

$$k_{xapp6} = k_{xx6} + k_{xy6}\left(\frac{k_{zx6}k_{yz6} - k_{yx6}k_{zz6}}{k_{yy6}k_{zz6} - k_{yz6}k_{zy6}}\right) + k_{xz6}\left(\frac{k_{zy6}k_{yx6} - k_{zx6}k_{yy6}}{k_{yy6}k_{zz6} - k_{yz6}k_{zy6}}\right) \quad \text{(A.29)}$$

For blocks 7 and 8:

$$\bar{k}_{xapp78} = \frac{Lxk_{xapp7}k_{xapp8}}{Lx_1k_{xapp8} + Lx_2k_{xapp7}} \quad \text{(A.30)}$$

where

$$k_{xapp7} = k_{xx7} + k_{xy7}\left(\frac{k_{zx7}k_{yz7} - k_{yx7}k_{zz7}}{k_{yy7}k_{zz7} - k_{yz7}k_{zy7}}\right) + k_{xz7}\left(\frac{k_{zy7}k_{yx7} - k_{zx7}k_{yy7}}{k_{yy7}k_{zz7} - k_{yz7}k_{zy7}}\right) \quad \text{(A.31)}$$

$$k_{xapp8} = k_{xx8} + k_{xy8}\left(\frac{k_{zx8}k_{yz8} - k_{yx8}k_{zz8}}{k_{yy8}k_{zz8} - k_{yz8}k_{zy8}}\right) + k_{xz8}\left(\frac{k_{zy8}k_{yx8} - k_{zx8}k_{yy8}}{k_{yy8}k_{zz8} - k_{yz8}k_{zy8}}\right) \qquad \text{(A.32)}$$

Since these four two-block systems are in parallel with respect to the direction of flow, the effective apparent permeability of the top and bottom blocks are calculated as a weighted arithmetic average:

$$\bar{k}_{xxappt} = \frac{Ly_2}{Ly}\bar{k}_{xappt12} + \frac{Ly_1}{Ly}\bar{k}_{xapp34} \qquad \text{(A.33)}$$

$$\bar{k}_{xxappb} = \frac{Ly_2}{Ly}\bar{k}_{xapp56} + \frac{Ly_1}{Ly}\bar{k}_{xapp78} \qquad \text{(A.34)}$$

Top and bottom two-blocks are in parallel, so the overall effective apparent permeability for a system shown in Fig. A.2 is the weighted arithmetic average of Eq. A.33 and Eq. A.34.

$$\bar{k}_{xxapp} = \frac{Lz_2}{Lz}\bar{k}_{xappt} + \frac{Lz_1}{Lz}\bar{k}_{xappb} \qquad \text{(A.35)}$$

B. The system in Fig. A.1 is divided into four two-blocks considering communication only in the y-direction as shown in Fig. A.3.

Using calculated effective apparent permeability for one block, calculate effective apparent permeability for two-block systems (block 1 and block 3). The total pressure gradient for blocks 1 and block 3 are the same as for the individual blocks.

$$\left(\frac{\partial \bar{p}}{\partial x}\right)_{13} = \left(\frac{\partial p}{\partial x}\right)_1 = \left(\frac{\partial p}{\partial x}\right)_3 \qquad \text{(A.36)}$$

Velocity for two-block systems in terms of local velocities:

$$\bar{v}_{x13} = \frac{Ly_1}{Ly}v_{x3} + \frac{Ly_2}{Ly}v_{x1} \qquad \text{(A.37)}$$

Using Eq. A.36 and velocity components, such as Eq. A.17 through Eq. A.19 with changing subscripts, we get this expression for blocks 1 and 3.

$$\bar{k}_{xapp13} = \frac{Ly_1}{Ly}k_{xapp3} + \frac{Ly_2}{Ly}k_{xapp1} \qquad \text{(A.38)}$$

For blocks 2 and 4:

$$\bar{k}_{xapp24} = \frac{Ly_1}{Ly} k_{xapp4} + \frac{Ly_2}{Ly} k_{xapp2} \tag{A.39}$$

For blocks 5 and 7:

$$\bar{k}_{xapp57} = \frac{Ly_1}{Ly} k_{xapp7} + \frac{Ly_2}{Ly} k_{xapp5} \tag{A.40}$$

For blocks 6 and 8:

$$\bar{k}_{xapp68} = \frac{Ly_1}{Ly} k_{xapp8} + \frac{Ly_2}{Ly} k_{xapp6} \tag{A.41}$$

There are two combinations. First, combine the top and bottom two blocks in series then combine the results in parallel. Second, combine the left and right two-blocks in parallel then combine the results in series. The outcome of the two combinations were different. It is decided, therefore, to calculate both combinations and take weighted average of them as an effective apparent permeability for the system shown in Fig. A.3.

First combination:

$$\bar{k}_{xyappt} = \frac{Lx\bar{k}_{xapp13}\bar{k}_{xapp24}}{Lx_1\bar{k}_{xapp24} + Lx_2\bar{k}_{xapp13}} \tag{A.42}$$

$$\bar{k}_{xyappb} = \frac{Lx\bar{k}_{xapp57}\bar{k}_{xapp68}}{Lx_1\bar{k}_{xapp68} + Lx_2\bar{k}_{xapp57}} \tag{A.43}$$

$$\bar{k}_{xyapp,s} = \frac{Lz_1}{Lz}\bar{k}_{xyappb} + \frac{Lz_2}{Lz}\bar{k}_{xyappt} \tag{A.44}$$

Second combination:

$$\bar{k}_{xyappl} = \frac{Lz_1}{Lz}\bar{k}_{xyapp57} + \frac{Lz_2}{Lz}\bar{k}_{xyapp13} \tag{A.45}$$

$$\bar{k}_{xyappr} = \frac{Lz_1}{Lz}\bar{k}_{xyapp68} + \frac{Lz_2}{Lz}\bar{k}_{xyapp24} \tag{A.46}$$

$$\bar{k}_{xyapp,p} = \frac{Lx\,\bar{k}_{xyappr}\bar{k}_{xyappl}}{Lx_1\,\bar{k}_{xyappr} + Lx_2\,\bar{k}_{xyappl}} \tag{A.47}$$

Taking a weighted average of Eq. A.44 and Eq. A.47 for effective apparent permeability of this system:

$$\bar{k}_{xyapp} = \frac{\bar{k}_{xapp}\bar{k}_{xyapp,s} + \bar{k}_{zapp}\bar{k}_{xyapp,p}}{\bar{k}_{xapp} + \bar{k}_{zapp}} \tag{A.48}$$

C. System in Fig. A.1 is divided into four two-blocks considering communication only in the z-direction as shown in Fig. A.4.

Calculate the effective apparent permeability of the two-block system, blocks 1 and 5. The total pressure gradient for blocks 1 and 5 is same as for individual blocks.

$$\left(\frac{\partial \bar{p}}{\partial x}\right)_{15} = \left(\frac{\partial p}{\partial x}\right)_1 = \left(\frac{\partial p}{\partial x}\right)_5 \tag{A.49}$$

Velocity for the two-block system in terms of local velocities is:

$$\bar{v}_{x15} = \frac{Lz_1}{Lz} v_{x5} + \frac{Lz_2}{Lz} v_{x1} \tag{A.50}$$

Using Eq. A.49 and velocity components, such as Eq. A.17 through Eq. A.19 with changed subscripts, we get this expression for blocks 1 and 5.

$$\bar{k}_{xapp15} = \frac{Lz_1}{Lz} k_{xapp5} + \frac{Ly_2}{Ly} k_{xapp1} \tag{A.51}$$

For blocks 2 and 6:

$$\bar{k}_{xapp26} = \frac{Lz_1}{Lz} k_{xapp6} + \frac{Lz_2}{Lz} k_{xapp2} \tag{A.52}$$

For blocks 3 and 7:

$$\bar{k}_{xapp37} = \frac{Lz_1}{Lz} k_{xapp7} + \frac{Lz_2}{Lz} k_{xapp3} \tag{A.53}$$

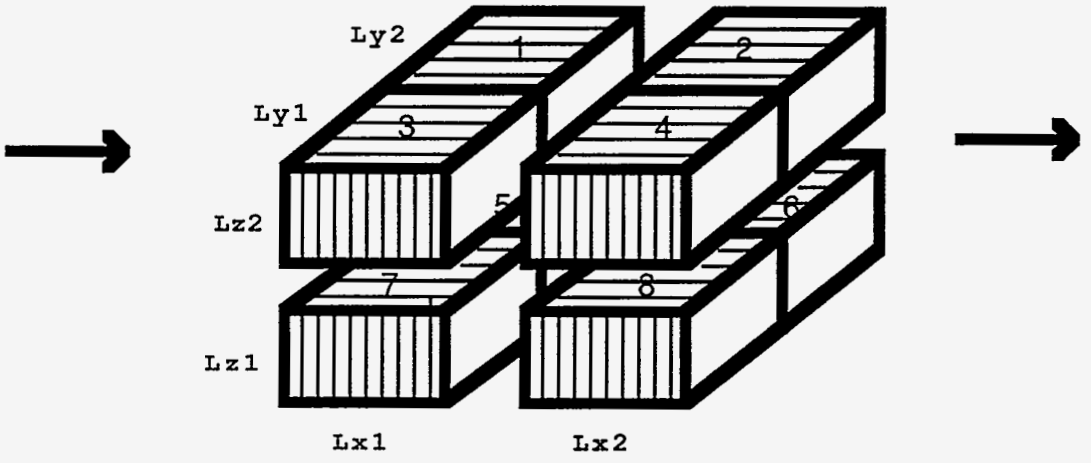

Figure A.3: Communication only in the y direction, flow in the x direction

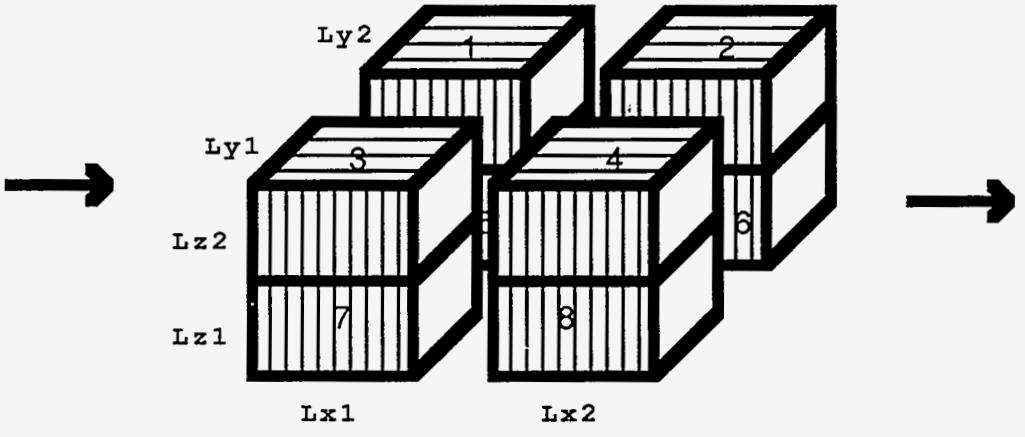

Figure A.4: Communication only in the z direction, flow in the x direction

For blocks 4 and 8:

$$\bar{k}_{xapp48} = \frac{Lz_1}{Lz} k_{xapp8} + \frac{Lz_2}{Lz} k_{xapp4} \tag{A.54}$$

There are two combinations here as well. The first permeability is obtained by combining the first and second two-blocks in series, then combining the results in parallel. The second is obtained by combining the left and right two-blocks in parallel, then combining the results in series. The effective apparent permeability for the system shown in Fig. A.4 is:

First combination:

$$\bar{k}_{xzappf} = \frac{Lx\,\bar{k}_{xapp37}\bar{k}_{xapp48}}{Lx_1\,\bar{k}_{xapp48} + Lx_2\,\bar{k}_{xapp37}} \tag{A.55}$$

$$\bar{k}_{xzapps} = \frac{Lx\,\bar{k}_{xapp26}\bar{k}_{xapp15}}{Lx_1\,\bar{k}_{xapp26} + Lx_2\,\bar{k}_{xapp15}} \tag{A.56}$$

$$\bar{k}_{xzapp,s} = \frac{Ly_1}{Ly}\bar{k}_{xzappf} + \frac{Ly_2}{Ly}\bar{k}_{xzapps} \tag{A.57}$$

Second combination:

$$\bar{k}_{xzappl} = \frac{Ly_1}{Ly}\bar{k}_{xzapp37} + \frac{Ly_2}{Ly}\bar{k}_{xzapp15} \tag{A.58}$$

$$\bar{k}_{xzappr} = \frac{Ly_1}{Ly}\bar{k}_{xzapp48} + \frac{Ly_2}{Ly}\bar{k}_{xzapp26} \tag{A.59}$$

$$\bar{k}_{xzapp,p} = \frac{Lx\,\bar{k}_{xzappr}\bar{k}_{xzappl}}{Lx_1\,\bar{k}_{xzappr} + Lx_2\,\bar{k}_{xzappl}} \tag{A.60}$$

Take a weighted average of Eq. A.57 and Eq. A.60 for effective apparent permeability of this system.

$$\bar{k}_{xzapp} = \frac{\bar{k}_{xapp}\bar{k}_{xzapp,s} + \bar{k}_{yapp}\bar{k}_{xzapp,p}}{\bar{k}_{xapp} + \bar{k}_{yapp}} \tag{A.61}$$

The effective apparent permeability of the x-direction is calculated as a weighted average of Eq. A.35, Eq. A.48 and Eq. A.61.

$$\bar{k}_{xapp} = \frac{\bar{k}_{xxapp}\bar{k}_{xapp} + \bar{k}_{xyapp}\bar{k}_{yapp} + \bar{k}_{xzapp}\bar{k}_{zapp}}{\bar{k}_{xapp} + \bar{k}_{yapp} + \bar{k}_{zapp}} \tag{A.62}$$

Following similar procedures for the y- and z-directions, we have nine non-linear equations corresponding to three equations for each direction.

For flow along the x-direction:

$$\bar{k}_{xyapp} = \frac{\bar{k}_{xapp}\bar{k}_{xyapp,s} + \bar{k}_{zapp}\bar{k}_{xyapp,p}}{\bar{k}_{xapp} + \bar{k}_{zapp}} \tag{A.63}$$

$$\bar{k}_{xzapp} = \frac{\bar{k}_{xapp}\bar{k}_{xzapp,s} + \bar{k}_{yapp}\bar{k}_{xzapp,p}}{\bar{k}_{xapp} + \bar{k}_{yapp}} \tag{A.64}$$

$$\bar{k}_{xapp} = \frac{\bar{k}_{xxapp}\bar{k}_{xapp} + \bar{k}_{xyapp}\bar{k}_{yapp} + \bar{k}_{xzapp}\bar{k}_{zapp}}{\bar{k}_{xapp} + \bar{k}_{yapp} + \bar{k}_{zapp}} \tag{A.65}$$

For flow along the y-direction:

$$\bar{k}_{yxapp} = \frac{\bar{k}_{yxapp,s}\bar{k}_{yapp} + \bar{k}_{yxapp,p}\bar{k}_{zapp}}{\bar{k}_{yapp} + \bar{k}_{zapp}} \tag{A.66}$$

$$\bar{k}_{yzapp} = \frac{\bar{k}_{yzapp,s}\bar{k}_{yapp} + \bar{k}_{yzapp,p}\bar{k}_{xapp}}{\bar{k}_{yapp} + \bar{k}_{xapp}} \tag{A.67}$$

$$\bar{k}_{yapp} = \frac{\bar{k}_{yxapp}\bar{k}_{xapp} + \bar{k}_{yyapp}\bar{k}_{yapp} + \bar{k}_{yzapp}\bar{k}_{zapp}}{\bar{k}_{xapp} + \bar{k}_{yapp} + \bar{k}_{zapp}} \tag{A.68}$$

For flow along z-direction:

$$\bar{k}_{zyapp} = \frac{\bar{k}_{zyapp,s}\bar{k}_{zapp} + \bar{k}_{zyapp,p}\bar{k}_{xapp}}{\bar{k}_{zapp} + \bar{k}_{xapp}} \tag{A.69}$$

$$\bar{k}_{zxapp} = \frac{\bar{k}_{zxapp,s}\bar{k}_{zapp} + \bar{k}_{zxapp,p}\bar{k}_{yapp}}{\bar{k}_{zapp} + \bar{k}_{yapp}} \tag{A.70}$$

$$\bar{k}_{zapp} = \frac{\bar{k}_{zxapp}\bar{k}_{xapp} + \bar{k}_{zyapp}\bar{k}_{yapp} + \bar{k}_{zzapp}\bar{k}_{zapp}}{\bar{k}_{xapp} + \bar{k}_{yapp} + \bar{k}_{zapp}} \tag{A.71}$$

These equations are solved by a successive substitution method.

Let

$$AC_1 = \frac{\bar{k}_{xapp}}{\bar{k}_{yapp}}, AC_2 = \frac{\bar{k}_{zapp}}{\bar{k}_{yapp}} \text{ and } AC_3 = \frac{\bar{k}_{xapp}}{\bar{k}_{zapp}} \tag{A.72}$$

These variables are initially assumed as:

$$AC_1 = \frac{\bar{k}_{xxapp}}{\bar{k}_{yyapp}}, AC_2 = \frac{\bar{k}_{zzapp}}{\bar{k}_{yyapp}} \text{ and } AC_3 = \frac{\bar{k}_{xxapp}}{\bar{k}_{zzapp}}$$

Rearranging Eq. A.63 and Eq. A.64. Using Eq. A.72:

$$\bar{k}_{xyapp} = \frac{AC_3\ \bar{k}_{xyapp,s} + \bar{k}_{xyapp,p}}{AC_3 + 1} \tag{A.73}$$

$$\bar{k}_{xzapp} = \frac{AC_1\ \bar{k}_{xzapp,s} + \bar{k}_{xzapp,p}}{AC_1 + 1} \tag{A.74}$$

Rearranging Eq. A.66 and Eq. A.67. Using Eq. A.72:

$$\bar{k}_{yxapp} = \frac{\bar{k}_{yxapp,s} + \bar{k}_{yxapp,p} AC_2}{1 + AC_2} \tag{A.75}$$

$$\bar{k}_{yzapp} = \frac{\bar{k}_{yzapp,s} + \bar{k}_{yzapp,p} AC_1}{1 + AC_1} \tag{A.76}$$

Rearrange Eq. A.69 and Eq. A.70. Using Eq. A.72:

$$\bar{k}_{zyapp} = \frac{\bar{k}_{zyapp,s} + \bar{k}_{zyapp,p} AC_3}{1 + AC_3} \tag{A.77}$$

$$\bar{k}_{zxapp} = \frac{\bar{k}_{zxapp,s} AC_2 + \bar{k}_{zxapp,p}}{AC_2 + 1} \tag{A.78}$$

Eq. A.65, Eq. A.68 and Eq. A.71 become:

$$\bar{k}_{xapp} = \frac{\bar{k}_{xxapp} AC_1 + \bar{k}_{xyapp} + \bar{k}_{xzapp} AC_2}{AC_1 + 1 + AC_2} \tag{A.79}$$

$$\bar{k}_{yapp} = \frac{\bar{k}_{yxapp}AC_1 + \bar{k}_{yyapp} + \bar{k}_{yzapp}AC_2}{AC_1 + 1 + AC_2} \tag{A.80}$$

$$\bar{k}_{zapp} = \frac{\bar{k}_{zxapp}AC_1 + \bar{k}_{zyapp} + \bar{k}_{zzapp}AC_2}{AC_1 + 1 + AC_2} \tag{A.81}$$

Divide Eq. A.79 and Eq. A.81 by Eq. A.80:

$$AC_1 = \frac{\bar{k}_{xxapp}\,AC_1 + \bar{k}_{xyapp} + \bar{k}_{xzapp}\,AC_2}{\bar{k}_{yxapp}\,AC_1 + \bar{k}_{yyapp} + \bar{k}_{yzapp}\,AC_2} \tag{A.82}$$

$$AC_2 = \frac{\bar{k}_{zxapp}\,AC_1 + \bar{k}_{zyapp} + \bar{k}_{zzapp}\,AC_2}{\bar{k}_{yxapp}\,AC_1 + \bar{k}_{yyapp} + \bar{k}_{yzapp}\,AC_2} \tag{A.83}$$

Solve Eq. A.82 for AC_1 and using the assumed value of AC_2 and solve Eq. A.83 for AC_2 using the assumed value of AC_1. Denote the solution values as C_1 and C_2.

$$C_1 = \frac{\left(\bar{k}_{zzapp} - \bar{k}_{yxapp}AC_2 - \bar{k}_{yyapp}\right) + \sqrt{\left(\left(\bar{k}_{yxapp}AC_2 + \bar{k}_{yyapp} - \bar{k}_{zzapp}\right)^2 + 4\bar{k}_{yzapp}\left(\bar{k}_{zxapp}AC_2 + \bar{k}_{zyapp}\right)\right)}}{2\bar{k}_{yzapp}} \tag{A.84}$$

$$C_2 = \frac{\left(\bar{k}_{xxapp} - \bar{k}_{yzapp}AC_1 - \bar{k}_{yyapp}\right) + \sqrt{\left(\left(\bar{k}_{yzapp}AC_1 + \bar{k}_{yyapp} - \bar{k}_{xxapp}\right)^2 + 4\bar{k}_{yzapp}\left(\bar{k}_{xzapp}AC_1 + \bar{k}_{xyapp}\right)\right)}}{2\bar{k}_{yxapp}} \tag{A.85}$$

Calculate $\bar{k}_{xapp}$, $\bar{k}_{yapp}$ and $\bar{k}_{zapp}$ using C_1 and C_2 then recalculate AC_1, AC_2 and AC_3. Compare with the assumed values. This completes the successive substitution loop.

Here the procedure for calculating pressure gradient ratios is presented. Two pressure gradient ratios for each direction will be calculated. Each pressure gradient ratio consists of two components, with and without vertical equilibrium along one of the transverse directions, and combined as a weighted average of those two. The derivations of pressure gradient ratios when the flow direction is along the x-direction are shown only. Two pressure gradient ratios for the x-direction follow.

$$\frac{\left(\frac{\partial \bar{p}}{\partial y}\right)_x}{\left(\frac{\partial \bar{p}}{\partial x}\right)_x} = \frac{\left|\frac{\left(\frac{\partial \bar{p}}{\partial y}\right)_x}{\left(\frac{\partial \bar{p}}{\partial x}\right)_x}\right|_{NC} \bar{k}_{xapp} + \left|\frac{\left(\frac{\partial \bar{p}}{\partial y}\right)_x}{\left(\frac{\partial \bar{p}}{\partial x}\right)_x}\right|_{VE,Z} \bar{k}_{zapp}}{\bar{k}_{xapp} + \bar{k}_{yapp} + \bar{k}_{zapp}} \tag{B.1}$$

$$\frac{\left(\frac{\partial \bar{p}}{\partial z}\right)_x}{\left(\frac{\partial \bar{p}}{\partial x}\right)_x} = \frac{\left|\frac{\left(\frac{\partial \bar{p}}{\partial z}\right)_x}{\left(\frac{\partial \bar{p}}{\partial x}\right)_x}\right|_{NC} \bar{k}_{xapp} + \left|\frac{\left(\frac{\partial \bar{p}}{\partial z}\right)_x}{\left(\frac{\partial \bar{p}}{\partial x}\right)_x}\right|_{VE,Y} \bar{k}_{yapp}}{\bar{k}_{xapp} + \bar{k}_{yapp} + \bar{k}_{zapp}} \tag{B.2}$$

Here NC means no communication along the transverse direction to the direction of flow and VE, Z (or VE, Y) means vertical equilibrium in specified direction. Each of these terms follows.

B.I The system shown in Fig. B.1 is considered for the pressure gradient ratio with no communication.

First, the pressures at the middle of each two-block are calculated.

1. Blocks 1 and 2

The flow rates for block 1 and 2 are:

$$q_{x1} = -\frac{k_{xapp1} Ly_2 Lz_2}{\mu} \frac{(P_1 - P_i)_x}{Lx_1} \tag{B.3}$$

$$q_{x2} = -\frac{k_{xapp2} Ly_2 Lz_2}{\mu} \frac{(P_o - P_1)_x}{Lx_2} \tag{B.4}$$

where k_{xapp1} and k_{xapp2} are effective apparent permeability for blocks 1 and 2 respectively. The effective flow rates for blocks 1 and 2 are combined:

$$\bar{q}_{x12} = -\frac{\bar{k}_{xxapp12} Ly_2 Lz_2}{\mu} \frac{(P_o - P_i)_x}{Lx} \tag{B.5}$$

where $\bar{k}_{xxapp12}$ is a weighted average of k_{xapp1} and k_{xapp2}, the Eq. B.3 and Eq. B.4 are rearranged.

$$(P_1 - P_i)_x = -\frac{\mu\, Lx_1\, q_{x1}}{k_{xapp1} Ly_2 Lz_2} \tag{B.6}$$

$$(P_o - P_1)_x = -\frac{\mu\, Lx_2\, q_{x2}}{k_{xapp2} Ly_2 Lz_2} \tag{B.7}$$

From the conservation of mass

$$q_{x1} = q_{x2} = \bar{q}_{x12} \tag{B.8}$$

Using Eq. B.8, subtract Eq. B.5 from Eq. B.4 and rearranging

$$P_1 = \frac{\bar{q}_{x12}\mu}{2\, Ly_2\, Lz_2}\left(\frac{Lx_2}{k_{xapp2}} - \frac{Lx_1}{k_{xapp1}}\right) + \frac{(P_i + P_o)}{2} \tag{B.9}$$

2. Blocks 3 and 4

The flow rates for block 3 and 4 are:

$$q_{x3} = -\frac{k_{xapp3} Ly_1 Lz_2}{\mu} \frac{(P_2 - P_i)_x}{Lx_1} \tag{B.10}$$

$$q_{x4} = -\frac{k_{xapp4} Ly_1 Lz_2}{\mu} \frac{(P_o - P_1)_x}{Lx_2} \tag{B.11}$$

where k_{xapp3} and k_{xapp4} are effective apparent permeabilities of blocks 3 and 4 respectively. The effective flow rates for blocks 3 and 4 are combined:

$$\bar{q}_{x34} = -\frac{\bar{k}_{xxapp34} Ly_1 Lz_2}{\mu} \frac{\left(P_o - P_i\right)_x}{Lx} \tag{B.12}$$

where $\bar{k}_{xxapp34}$ is a weighted average of k_{xapp3} and k_{xapp4}. Eq. B.10 and Eq. B11 are rearranged.

$$\left(P_2 - P_i\right)_x = -\frac{\mu\, Lx_1\, q_{x1}}{k_{xapp3} Ly_1 Lz_2} \tag{B.13}$$

$$\left(P_o - P_2\right)_x = -\frac{\mu\, Lx_2\, q_{x2}}{k_{xapp4} Ly_1 Lz_2} \tag{B.14}$$

From the conservation of mass

$$q_{x3} = q_{x4} = \bar{q}_{x34} \tag{B.15}$$

Using Eq. B.15, subtracting Eq. B.14 from Eq. B.13 and rearranging

$$P_2 = \frac{\bar{q}_{x34}\mu}{2\, Ly_1\, Lz_2}\left(\frac{Lx_2}{k_{xapp4}} - \frac{Lx_1}{k_{xapp3}}\right) + \frac{\left(P_i + P_o\right)}{2} \tag{B.16}$$

3. Blocks 5 and 6

The flow rates for blocks 7 and 8 are:

$$q_{x5} = -\frac{k_{xapp5} Ly_2 Lz_1}{\mu} \frac{\left(P_3 - P_i\right)_x}{Lx_1} \tag{B.17}$$

$$q_{x6} = -\frac{k_{xapp6} Ly_2 Lz_1}{\mu} \frac{\left(P_o - P_3\right)_x}{Lx_2} \tag{B.18}$$

where k_{xapp5} and k_{xapp6} are effective apparent permeabilities of blocks 5 and 6 respectively. The effective flow rates for blocks 5 and 6 are combined:

$$\bar{q}_{x56} = -\frac{\bar{k}_{xxapp56} Ly_2 Lz_1}{\mu} \frac{\left(P_o - P_i\right)_x}{Lx} \tag{B.19}$$

where $\bar{k}_{xxappb6}$ is a weighted average of k_{xappb5} and k_{xappb6}. Eq. B.17 and Eq. B18 are rearranged.

$$\left(P_3 - P_i\right)_x = -\frac{\mu\, Lx_1\, q_{x5}}{k_{xappb5} Ly_2 Lz_1} \tag{B.20}$$

$$\left(P_o - P_3\right)_x = -\frac{\mu\, Lx_2\, q_{x6}}{k_{xappb6} Ly_2 Lz_1} \tag{B.21}$$

From the conservation of mass

$$q_{x5} = q_{x6} = \bar{q}_{x56} \tag{B.22}$$

Using Eq. B.22, subtracting Eq. B.21 from Eq. B.20 and rearranging

$$P_3 = \frac{\bar{q}_{x56}\,\mu}{2\, Ly_2\, Lz_1}\left(\frac{Lx_2}{k_{xappb6}} - \frac{Lx_1}{k_{xappb5}}\right) + \frac{\left(P_i + P_o\right)}{2} \tag{B.23}$$

4. Blocks 7 and 8

The flow rates for blocks 7 and 8 are:

$$q_{x7} = -\frac{k_{xappb7} Ly_1 Lz_1}{\mu}\frac{\left(P_4 - P_i\right)_x}{Lx_1} \tag{B.24}$$

$$q_{x8} = -\frac{k_{xappb8} Ly_1 Lz_1}{\mu}\frac{\left(P_o - P_4\right)_x}{Lx_2} \tag{B.25}$$

where k_{xappb7} and k_{xappb8} are effective apparent permeabilities for blocks 7 and 8 respectively. The effective flow rates for blocks 7 and 8 are combined

$$\bar{q}_{x78} = -\frac{\bar{k}_{xxappb78} Ly_1 Lz_1}{\mu}\frac{\left(P_o - P_i\right)_x}{Lx} \tag{B.26}$$

where $\bar{k}_{xxappb78}$ is a weighted average of k_{xappb7} and k_{xappb8}. Eq. B.24 and Eq. B.25 are rearranged.

$$\left(P_4 - P_i\right)_x = -\frac{\mu\, Lx_1\, q_{x7}}{k_{xappb7} Ly_1 Lz_1} \tag{B.27}$$

$$(P_o - P_4)_x = -\frac{\mu\, Lx_2\, q_{x8}}{k_{xapp8}\, Ly_1 Lz_1} \tag{B.28}$$

From the conservation of mass

$$q_{x7} = q_{x8} = \bar{q}_{x78} \tag{B.29}$$

Using Eq. B.22, subtracting Eq. B.28 from Eq. B.27 and rearranging

$$P_4 = \frac{\bar{q}_{x78}\,\mu}{2\, Ly_1\, Lz_1}\left(\frac{Lx_2}{k_{xapp8}} - \frac{Lx_1}{k_{xapp7}}\right) + \frac{(P_i + P_o)}{2} \tag{B.30}$$

Using these mid-point pressures, the pressure gradient ratios are calculated.

$\left(\left(\frac{\partial \bar{p}}{\partial y}\right)_x \Big/ \left(\frac{\partial \bar{p}}{\partial x}\right)_x\right)_{NC}$ is obtained following these procedures.

Pressure gradient ratio for top two-blocks, blocks 1-2 and 3-4

$$\begin{aligned}\Delta P_{ymax1} &= P_1 - P_2 \\ &= \frac{\bar{q}_{x12}\,\mu}{2\, Ly_1\, Lz_2}\left(\frac{Lx_2}{k_{xapp2}} - \frac{Lx_1}{k_{xapp1}}\right) - \frac{\bar{q}_{x34}\mu}{2\, Ly_1\, Lz_2}\left(\frac{Lx_2}{k_{xapp4}} - \frac{Lx_1}{k_{xapp3}}\right)\end{aligned} \tag{B.31}$$

Effective flow rate for top two-block is:

$$\begin{aligned}\bar{q}_{xt} &= \bar{q}_{x12} + \bar{q}_{x34} \\ &= -\frac{\bar{k}_{xxappt}\, Ly\, Lz_2}{\mu}\frac{(P_o - P_i)}{Lx}\end{aligned} \tag{B.32}$$

$\bar{k}_{xxappt}$ is an effective apparent permeability of top two blocks. Rearranging Eq. B.32:

$$\begin{aligned}\bar{q}_{x12} &= \bar{q}_{xt} - \bar{q}_{x34} \\ &= -\frac{\bar{k}_{xxappt}\, Ly\, Lz_2}{\mu}\frac{\Delta P_x}{Lx} - \left(-\frac{\bar{k}_{xapp34}\, Ly_1\, Lz_2}{\mu}\frac{\Delta P_x}{Lx}\right)\end{aligned} \tag{B.33}$$

$$\bar{q}_{x12}\,\mu = \frac{\Delta P_x\, Lz_2}{Lx}\left(\bar{k}_{xapp34}\, Ly_1 - \bar{k}_{xxappt}\, Ly\right) \tag{B.34}$$

$$\bar{q}_{x34} = \bar{q}_{xt} - \bar{q}_{x12}$$

$$= -\frac{\bar{k}_{xxappt}\, Ly\, Lz_2}{\mu}\frac{\Delta P_x}{Lx} - \left(-\frac{\bar{k}_{xapp12}\, Ly_2\ Lz_2}{\mu}\frac{\Delta P_x}{Lx}\right) \tag{B.35}$$

$$\bar{q}_{x34}\,\mu = \frac{\Delta P_x\, Lz_2}{Lx}\left(\bar{k}_{xapp12}\, Ly_2 - \bar{k}_{xxappt}\, Ly\right) \tag{B.36}$$

Insert Eq. B.34 and Eq. B.36 into Eq. B.31:

$$\Delta P_{y\max 1} = \frac{\Delta P_x}{2\, Ly_2\, Lx}\left(\bar{k}_{xapp34}\, Ly_1 - \bar{k}_{xxappt}\, Ly\right)\left(\frac{Lx_2}{k_{xapp2}} - \frac{Lx_1}{k_{xapp1}}\right)$$
$$- \frac{\Delta P_x}{2\, Ly_1\, Lx}\left(\bar{k}_{xapp12}\, Ly_2 - \bar{k}_{xxappt}\, Ly\right)\left(\frac{Lx_2}{k_{xapp4}} - \frac{Lx_1}{k_{xapp3}}\right) \tag{B.37}$$

Using the relationship between the average and maximum pressure gradients[6], $\Delta P_{yavg} = 1/2\ \Delta P_{y\max}$, Eq. B.37 is rearranged:

$$\Delta P_{yavg1} = \frac{\Delta P_x}{4\, Ly_2\, Lx}\left(\bar{k}_{xapp34}\, Ly_1 - \bar{k}_{xxappt}\, Ly\right)\left(\frac{Lx_2}{k_{xapp2}} - \frac{Lx_1}{k_{xapp1}}\right)$$
$$- \frac{\Delta P_x}{4\, Ly_1\, Lx}\left(\bar{k}_{xapp12}\, Ly_2 - \bar{k}_{xxappt}\, Ly\right)\left(\frac{Lx_2}{k_{xapp4}} - \frac{Lx_1}{k_{xapp3}}\right) \tag{B.38}$$

Multiplying $(Lx/Ly)\,\Delta P_x$ by Eq. B.38, pressure gradient ratio in the top two-block is determined as follows:

$$\left(\left(\frac{\partial \bar{P}}{\partial y}\right)_x \Big/ \left(\frac{\partial P}{\partial x}\right)_x\right)_{NC,t} = \frac{1}{4\, Ly_2\, Ly}\left(\bar{k}_{xapp34}\, Ly_1 - \bar{k}_{xxappt}\, Ly\right)\left(\frac{Lx_2}{k_{xapp2}} - \frac{Lx_1}{k_{xapp1}}\right)$$
$$- \frac{1}{4\, Ly_1\, Ly}\left(\bar{k}_{xapp12}\, Ly_2 - \bar{k}_{xxappt}\, Ly\right)\left(\frac{Lx_2}{k_{xapp4}} - \frac{Lx_1}{k_{xapp3}}\right) \tag{B.39}$$

Pressure gradient ratio for the bottom blocks, blocks 5-6 and 7-8

$$\Delta P_{y\max 2} = P_3 - P_4$$

$$= \frac{\bar{q}_{x56}\,\mu}{2\, Ly_2\, Lz_1}\left(\frac{Lx_2}{k_{xapp6}} - \frac{Lx_1}{k_{xapp5}}\right) - \frac{\bar{q}_{x78}\mu}{2\, Ly_1\, Lz_1}\left(\frac{Lx_2}{k_{xapp8}} - \frac{Lx_1}{k_{xapp7}}\right) \tag{B.40}$$

Effective flow rate for the bottom two-blocks is:

$$\begin{aligned}\bar{q}_{xb} &= \bar{q}_{x56} + \bar{q}_{x78} \\ &= -\frac{\bar{k}_{xxappb} Ly\, Lz_1}{\mu} \frac{(P_o - P_i)}{Lx}\end{aligned} \tag{B.41}$$

$\bar{k}_{xxappb}$ is an effective apparent permeability of the bottom two-blocks. Rearranging Eq. B.41:

$$\begin{aligned}\bar{q}_{x56} &= \bar{q}_{xb} - \bar{q}_{x78} \\ &= -\frac{\bar{k}_{xxappb}\, Ly\, Lz_1}{\mu} \frac{\Delta P_x}{Lx} - \left(-\frac{\bar{k}_{xapp78}\, Ly_1\, Lz_1}{\mu} \frac{\Delta P_x}{Lx} \right)\end{aligned} \tag{B.42}$$

$$\bar{q}_{x56}\, \mu = \frac{\Delta P_x\, Lz_1}{Lx} \left(\bar{k}_{xapp78}\, Ly_1 - \bar{k}_{xxappb}\, Ly \right) \tag{B.43}$$

$$\begin{aligned}\bar{q}_{x78} &= \bar{q}_{xb} - \bar{q}_{x56} \\ &= -\frac{\bar{k}_{xxappb}\, Ly\, Lz_1}{\mu} \frac{\Delta P_x}{Lx} - \left(-\frac{\bar{k}_{xapp56}\, Ly_2\, Lz_1}{\mu} \frac{\Delta P_x}{Lx} \right)\end{aligned} \tag{B.44}$$

$$\bar{q}_{x78}\, \mu = \frac{\Delta P_x\, Lz_1}{Lx} \left(\bar{k}_{xapp56}\, Ly_2 - \bar{k}_{xxappb}\, Ly \right) \tag{B.45}$$

Insert Eq. B.43 and Eq. B.45 into Eq. B.40:

$$\begin{aligned}\Delta P_{ymax2} = &\frac{\Delta P_x}{2\, Ly_2\, Lx} \left(\bar{k}_{xapp78}\, Ly_1 - \bar{k}_{xxappb}\, Ly \right) \left(\frac{Lx_2}{k_{xapp6}} - \frac{Lx_1}{k_{xapp5}} \right) \\ &- \frac{\Delta P_x}{2\, Ly_1\, Lx} \left(\bar{k}_{xapp56}\, Ly_2 - \bar{k}_{xxappb}\, Ly \right) \left(\frac{Lx_2}{k_{xapp8}} - \frac{Lx_1}{k_{xapp7}} \right)\end{aligned} \tag{B.46}$$

Using the relationship between the average and maximum pressure gradients[6], $\Delta P_{yavg} = 1/2\, \Delta P_{ymax}$, Eq. B.46 is rearranged:

$$\begin{aligned}\Delta P_{yavg1} = &\frac{\Delta P_x}{4\, Ly_2\, Lx} \left(\bar{k}_{xapp78}\, Ly_1 - \bar{k}_{xxappb}\, Ly \right) \left(\frac{Lx_2}{k_{xapp6}} - \frac{Lx_1}{k_{xapp5}} \right) \\ &- \frac{\Delta P_x}{4\, Ly_1\, Lx} \left(\bar{k}_{xapp56}\, Ly_2 - \bar{k}_{xxappt}\, Ly \right) \left(\frac{Lx_2}{k_{xapp8}} - \frac{Lx_1}{k_{xapp7}} \right)\end{aligned} \tag{B.47}$$

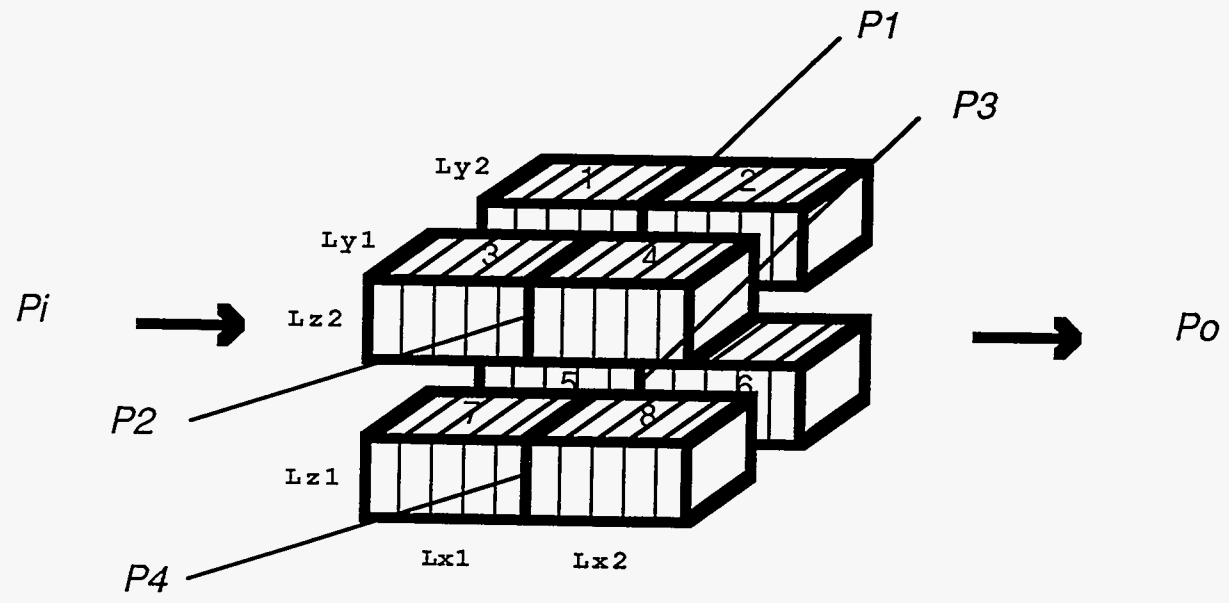

Figure B.1: No communication along the y and z direction, flow along the x direction

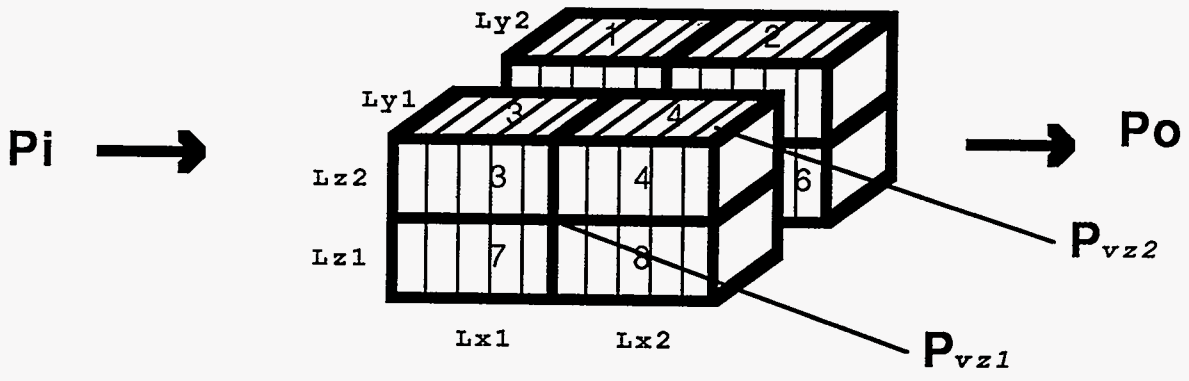

Figure B.2: Vertical equilibrium along the z direction, flow in the x direction

Multiplying $(Lx/Ly)\Delta P_x$ by Eq. B.47, the pressure gradient ratio in the bottom two-blocks is determined as follows:

$$\left(\left(\frac{\partial \bar{P}}{\partial y}\right)_x \Big/ \left(\frac{\partial P}{\partial x}\right)_x\right)_{NC,b} = \frac{1}{4\,Ly_2\,Ly}\left(\bar{k}_{xapp78}\,Ly_1 - \bar{k}_{xxappb}\,Ly\right)\left(\frac{Lx_2}{k_{xapp6}} - \frac{Lx_1}{k_{xapp5}}\right) - \frac{1}{4\,Ly_1\,Ly}\left(\bar{k}_{xapp56}\,Ly_2 - \bar{k}_{xxappb}\,Ly\right)\left(\frac{Lx_2}{k_{xapp8}} - \frac{Lx_1}{k_{xapp7}}\right) \quad \text{(B.48)}$$

$\left(\left(\frac{\partial \bar{p}}{\partial y}\right)_x \Big/ \left(\frac{\partial \bar{p}}{\partial x}\right)_x\right)_{NC}$ is determined as a weighted average of pressure gradient ratio of the top and bottom blocks according to the thickness.

$$\left(\left(\frac{\partial \bar{P}}{\partial y}\right)_x \Big/ \left(\frac{\partial P}{\partial x}\right)_x\right)_{NC} = \frac{\left(\left(\frac{\partial \bar{P}}{\partial y}\right)_x \Big/ \left(\frac{\partial P}{\partial x}\right)_x\right)_{NC,b} Lz_1 + \left(\left(\frac{\partial \bar{P}}{\partial y}\right)_x \Big/ \left(\frac{\partial P}{\partial x}\right)_x\right)_{NC,t} Lz_2}{Lz_1 + Lz_2} \quad \text{(B.49)}$$

B.II The system in Fig. B.2 is used in calculating $\left(\left(\frac{\partial \bar{p}}{\partial y}\right)_x \Big/ \left(\frac{\partial \bar{p}}{\partial x}\right)_x\right)_{VE,Z}$

Calculate mid point pressure of each combined block.

1. First, combine four blocks 3, 4, 7, 8

The flow rates for blocks 3, 7 and 4, 8 are:

$$\bar{q}_{x37} = -\frac{\bar{k}_{xapp37} Ly_1 Lz}{\mu}\frac{\left(P_{vz1} - P_i\right)_x}{Lx_1} \quad \text{(B.50)}$$

$$\bar{q}_{x48} = -\frac{\bar{k}_{xapp48} Ly_1 Lz}{\mu}\frac{\left(P_o - P_{vz1}\right)_x}{Lx_2} \quad \text{(B.51)}$$

where $\bar{k}_{xapp37}$ and $\bar{k}_{xapp48}$ are the combined effective apparent permeability of blocks 3, 7 and 4, 8 respectively. The effective flow rates for blocks 3, 7 and 4, 8 are combined.

$$\bar{q}_{x3748} = -\frac{\bar{k}_{xappf} Ly_1 Lz}{\mu} \frac{\left(P_o - P_i\right)_x}{Lx} \tag{B.52}$$

where $\bar{k}_{xzappf}$ is a weighted average of $\bar{k}_{xappB7}$ and $\bar{k}_{xapp48}$. Eq. B.50 and Eq. B.51 are rearranged.

$$\left(P_{vz1} - P_i\right)_x = -\frac{\mu\ Lx_1\ \bar{q}_{x37}}{\bar{k}_{xappB7} Ly_1 Lz} \tag{B.53}$$

$$\left(P_o - P_{vz1}\right)_x = -\frac{\mu\ Lx_2\ \bar{q}_{x48}}{\bar{k}_{xapp48} Ly_1 Lz} \tag{B.54}$$

From the conservation of mass

$$\bar{q}_{x3748} = \bar{q}_{x48} = \bar{q}_{x37} \tag{B.55}$$

Using Eq. B.55, subtracting Eq. B.54 from Eq. B.53 and rearranging.

$$P_{vz1} = \frac{\bar{q}_{x3748}\mu}{2\ Ly_1\ Lz}\left(\frac{Lx_2}{\bar{k}_{xapp48}} - \frac{Lx_1}{\bar{k}_{xappB7}}\right) + \frac{\left(P_i + P_o\right)}{2} \tag{B.56}$$

2. Second, combine blocks 1, 5, 2, 6

The flow rates for blocks 1, 5 and 2, 6 are:

$$\bar{q}_{x15} = -\frac{\bar{k}_{xapp15} Ly_2 Lz}{\mu} \frac{\left(P_{vz2} - P_i\right)_x}{Lx_1} \tag{B.57}$$

$$\bar{q}_{x26} = -\frac{\bar{k}_{xapp26} Ly_2 Lz}{\mu} \frac{\left(P_o - P_{vz2}\right)_x}{Lx_2} \tag{B.58}$$

where $\bar{k}_{xapp15}$ and $\bar{k}_{xapp26}$ are the combined effective apparent permeability of blocks 1, 5 and 2, 6 respectively. The effective flow rates for blocks 1, 5 and 2, 6 are combined.

$$\bar{q}_{x1526} = -\frac{\bar{k}_{xzapps} Ly_2 Lz}{\mu} \frac{\left(P_o - P_i\right)_x}{Lx} \tag{B.59}$$

where $\bar{k}_{xzapps}$ is a weighted average of $\bar{k}_{xapp15}$ and $\bar{k}_{xapp26}$. Eq. B.57 and Eq. B.58 are rearranged.

$$\left(P_{vz2} - P_i\right)_x = -\frac{\mu\, Lx_1\, \bar{q}_{x15}}{\bar{k}_{xapp15} Ly_2 Lz} \tag{B.60}$$

$$\left(P_o - P_{vz2}\right)_x = -\frac{\mu\, Lx_2\, \bar{q}_{x26}}{\bar{k}_{xapp26} Ly_2 Lz} \tag{B.61}$$

From the conservation of mass

$$\bar{q}_{x1526} = \bar{q}_{x15} = \bar{q}_{x26} \tag{B.62}$$

Using Eq. B.62, subtracting Eq. B.61 from Eq. B.60 and rearranging

$$P_{vz2} = \frac{\bar{q}_{x1526}\mu}{2\, Ly_2\, Lz}\left(\frac{Lx_2}{\bar{k}_{xapp26}} - \frac{Lx_1}{\bar{k}_{xapp15}}\right) + \frac{\left(P_i + P_o\right)}{2} \tag{B.63}$$

Maximum pressure gradient along the y-direction is determined as follows:

$$\begin{aligned}\left(\Delta P_{ymax}\right)_{VE,Z} &= P_{VZ2} - P_{VZ1} \\ &= \frac{\bar{q}_{x1526}\,\mu}{2\, Ly_2\, Lz}\left(\frac{Lx_2}{\bar{k}_{xapp26}} - \frac{Lx_1}{\bar{k}_{xapp15}}\right) - \frac{\bar{q}_{x3748}\mu}{2\, Ly_2\, Lz}\left(\frac{Lx_2}{\bar{k}_{xzapp48}} - \frac{Lx_1}{\bar{k}_{xapp37}}\right)\end{aligned} \tag{B.64}$$

Eq. (B.64) can be rearranged as follows,

$$\begin{aligned}\left(\Delta P_{ymax}\right)_{VE,Z} = &\frac{\Delta P_x}{2\, Ly_2\, Lx}\left(\bar{k}_{xzappf}\, Ly_1 - \bar{k}_{xzapps}\, Ly\right)\left(\frac{Lx_2}{\bar{k}_{xapp26}} - \frac{Lx_1}{\bar{k}_{xapp15}}\right) \\ &- \frac{\Delta P_x}{2\, Ly_1\, Lx}\left(\bar{k}_{xzappf}\, Ly_2 - \bar{k}_{xzapps}\, Ly\right)\left(\frac{Lx_2}{\bar{k}_{xapp48}} - \frac{Lx_1}{\bar{k}_{xapp37}}\right)\end{aligned} \tag{B.65}$$

Average pressure gradient ratio is determined:

$$\left(\Delta P_{yavg}\right)_{VE,Z} = \frac{\Delta P_x}{2\, Ly_2\, Lx}\left(\bar{k}_{xzappf}\, Ly_1 - \bar{k}_{xzapps}\, Ly\right)\left(\frac{Lx_2}{\bar{k}_{xapp26}} - \frac{Lx_1}{\bar{k}_{xapp15}}\right)$$

$$\left(\Delta P_{yavg}\right)_{VE,Z} = \frac{\Delta P_x}{2\,Ly_2\,Lx}\left(\bar{k}_{xzappf}\,Ly_1 - \bar{k}_{xzapps}\,Ly\right)\left(\frac{Lx_2}{\bar{k}_{xapp26}} - \frac{Lx_1}{\bar{k}_{xapp15}}\right) - \frac{\Delta P_x}{4\,Ly_1\,Lx}\left(\bar{k}_{xzappf}\,Ly_2 - \bar{k}_{xzapps}\,Ly\right)\left(\frac{Lx_2}{\bar{k}_{xapp48}} - \frac{Lx_1}{\bar{k}_{xapp37}}\right) \tag{B.66}$$

Multiplying $(Lx/Lz)\,\Delta P_x$ to Eq. B.66, pressure gradient ratio is determined as follows:

$$\left(\left(\frac{\partial \bar{P}}{\partial y}\right)_x \Big/ \left(\frac{\partial P}{\partial x}\right)_x\right)_{VE,Z} = \frac{1}{4\,Ly_2\,Ly}\left(\bar{k}_{xzappf}\,Ly_1 - \bar{k}_{xzapps}\,Ly\right)\left(\frac{Lx_2}{\bar{k}_{xapp26}} - \frac{Lx_1}{\bar{k}_{xapp15}}\right) - \frac{1}{4\,Ly_1\,Ly}\left(\bar{k}_{xzapps}\,Ly_2 - \bar{k}_{xzapps}\,Ly\right)\left(\frac{Lx_2}{\bar{k}_{xapp48}} - \frac{Lx_1}{\bar{k}_{xapp37}}\right) \tag{B.67}$$

CHAPTER 3

Outcrop Studies
Geological and Engineering Interpretation

I. Azof, G. Martinez, N. Hyne, D. Kerr and M. Kelkar

3.1 Summary

Investigation of outcrops allows description of rock properties at a scale which is not otherwise possible in typical reservoirs. This description includes the detailed geological investigation of depositional units and subfacies as well as the measurement of petrophysical properties such as permeability and porosity. This report presents a detailed investigation of the Bartlesville sandstone outcrop based on the outcrop surface measurements as well as measurements of information at wells drilled behind the outcrop. The detailed geological investigation allows us to identify four discrete genetic units and the presence of three subfacies within three of these units. Based on the geological description, a three-dimensional petrophysical properties description of the outcrop was constructed which honors the geological information. Flow simulation studies in this "constructed" reservoir revealed that the large-scale geological description has a much more significant impact on the performance than the detailed description of the reservoir properties. Also, one of the important parameters, but which is hard to measure, which has a significant impact on flow performance is the vertical permeability. This indicates the need to honor the geological units as faithfully as possible in the description process. Also, better techniques need to be investigated to measure the vertical continuity in the reservoir.

3.2 Introduction

One of the missing links in describing reservoirs in a proper fashion is the information at interwell scales. Typically, significant information can be collected at individual well locations. As a result we have an abundance of vertical

information. However, in the horizontal direction, we are limited by the well spacing. One way to circumvent the problem of limited horizontal data is to conduct an investigation of outcrop analogs of the reservoir. Outcrop analogs are the exposed rocks which were formed under the same depositional environment as the reservoir rock. Because of their exposure at the surface, it is much easier to study the outcrop at a very detailed scale. By studying the outcrop at a detailed level, we may be able to infer missing information, such as interwell distribution of properties, for an actual reservoir where such information is not available.

In this section, we discuss a detailed investigation of an outcrop analog of the Bartlesville sandstone. In addition, to study the outcrop surface, we also drilled several wells behind the outcrop to study the rock characteristics further. We investigated both the geological and petrophysical properties of the outcrop to understand the reservoir rock a little better.

The report is divided into several sections. Section 3.3 discusses the collection of data, including the surface properties as well as the information collected at the wells drilled behind the outcrop. Section 3.4 discusses the geological description and interpretation of the outcrop in three dimensions based on the surface and the well data. Section 3.5 discusses the procedure used to construct the three-dimensional description of the outcrop at very small scales. It involves the use of two conditional simulation methods. Section 3.6 presents preliminary flow simulation results based on the constructed three-dimensional description of the outcrop. The final Section is devoted to conclusions reached based on this investigation.

3.3 Data Collection

This section discusses the collection of data from cores and the outcrop face. The purpose of the data collection is to get detailed information about the reservoir properties and geologic description of the Bartlesville Sandstone in two and three dimensions. The location of the outcrop study is shown in Fig. 3.1.

In order to complete the study, several tasks were undertaken. The first task was to drill wells behind the outcrop face. This task was completed during October and

LOCATION OF STUDY AREA

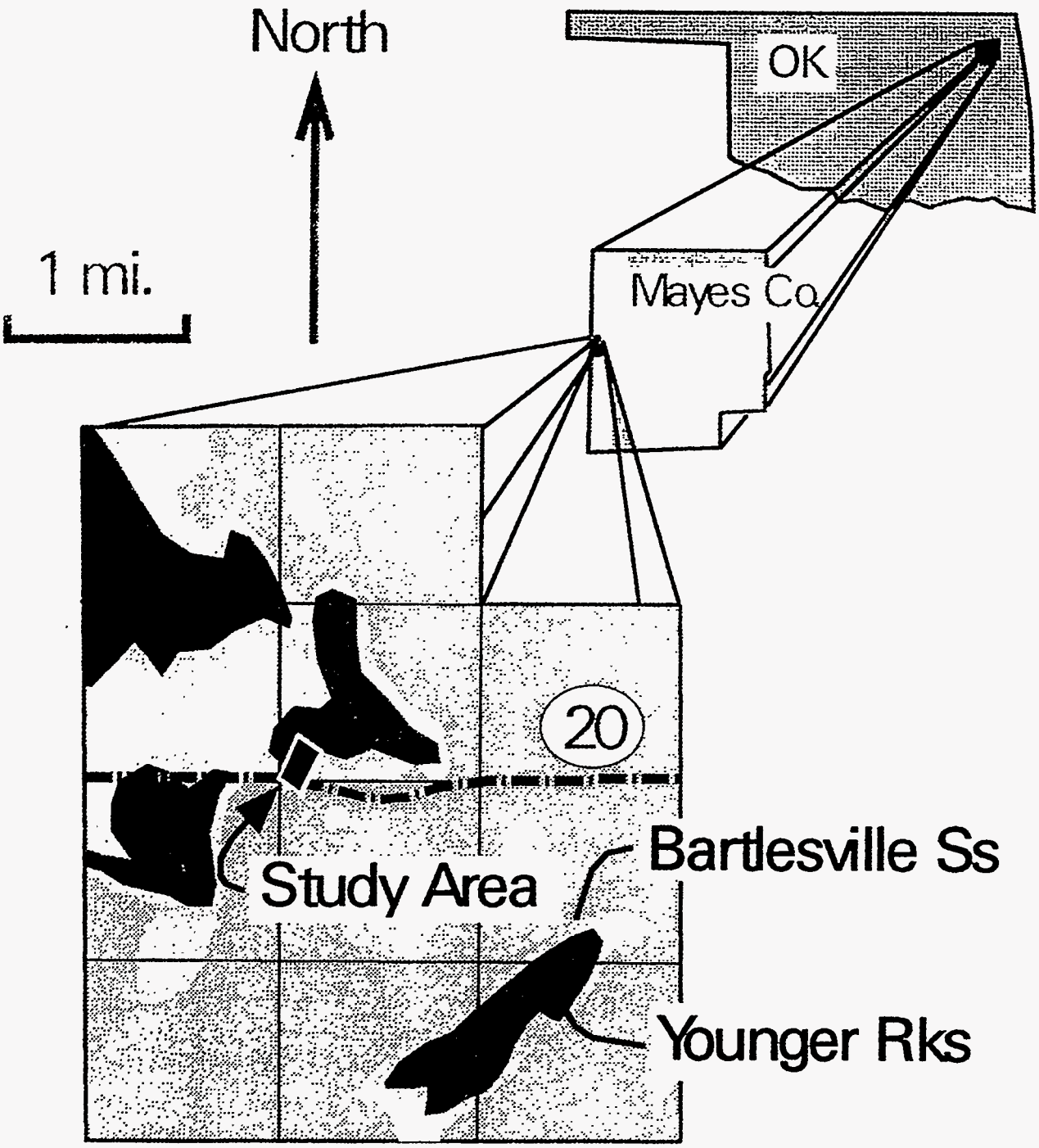

Figure 3.1: Location of outcrop study (from Berg, 1963).

November of 1991. Twelve of the proposed thirteen wells were drilled. The relative locations of these wells with respect to the outcrop are shown in Fig. 3.2.

The second stage of the investigation was completed in late November. All the sandstone cores were scanned using a gamma ray scanner and slabbed. We took 1388 permeability measurements using a minipermeameter and each core was photographed.

Staying as close as possible to the point where the minipermeameter readings were taken, about 200 core plugs, each of 1 inch in diameter were taken. The Holeman #3 core was selected for the cutting of 119 core plugs, all in the horizontal position, while the remaining 81 core plugs were distributed among the following cored wells: Holeman #4, Holeman #6 and Brown #1. Included were some vertical plugs, whose locations depended on geologic description. Of the 81 core plugs, 52 horizontal plugs and 21 of 29 planned vertical core plugs were taken. All the cores were measured for the porosity and permeability values.

The second set of permeability readings were taken on the outcrop face. The permeability measurements were taken in the vertical and horizontal directions. In the vertical direction, the readings were taken for every 1 foot on the grid surveyed on the outcrop face locations #1, #13 and #2. The readings in the horizontal direction were taken on the grid surveyed over 87 D to 12 D (Fig. 3.3). The measurements on the outcrop face were very difficult, due to the wet conditions on the outcrop face. It was difficult to get a good sealing between the tip and the rock surface when measurements were conducted in wet conditions.

The geological descriptions on the outcrop face and on the cores were also done. The geological data include the outcrop face description, the core description and the well log analysis. The detailed geological analysis is discussed next.

3.4 Geologic Description

In this study, the term facies is defined as a body of rock with specific characteristics, including texture, fossils, physical and/or biogenic structures and nature of contacts. It is considered here as a transferable entity, that with little

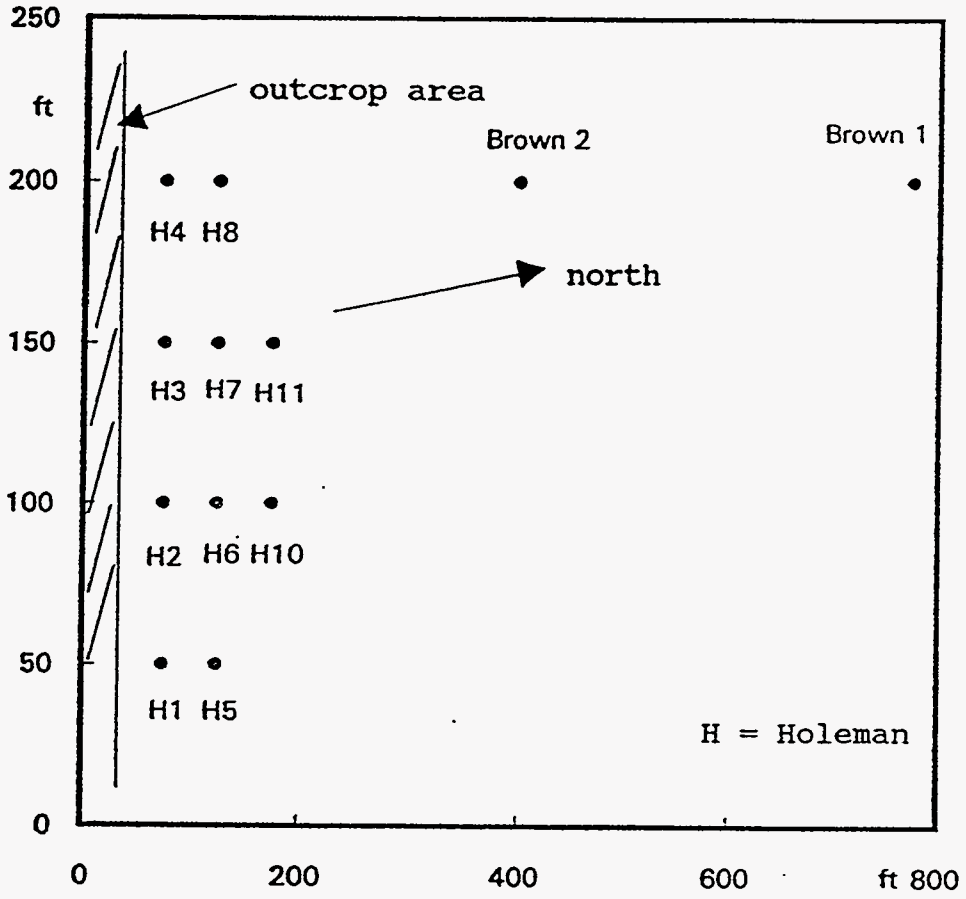

Figure 3.2: Well location.

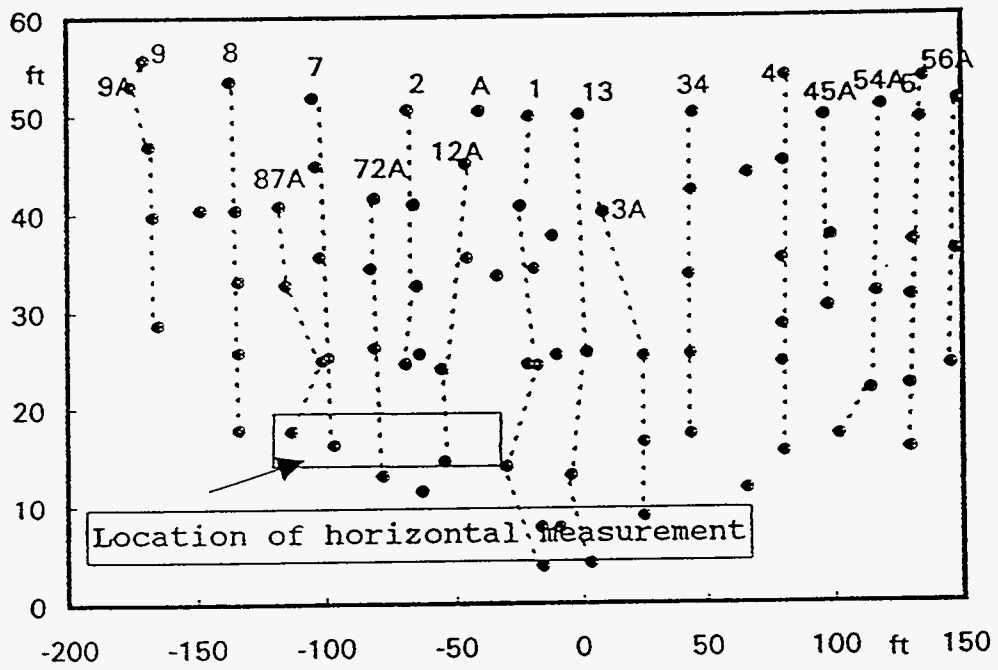

Figure 3.3: Outcrop grid surveyed.

modification, can be present in a variety of depositional processes, and that is not necessarily restricted to a given geologic time period (Kerr, personal comm., 1992).[3.1]

A very important aspect in applying the term facies is scale. Since a body of rock can have just about any dimensions, its use should be governed by the objectives of the study and the available information. In this sense, one can see that a seismic facies can be 2-3 orders of magnitude larger than the facies defined on an outcrop study. After defining the dimensions or coverage of facies in a specific study, subdivisions maybe appropriate. Subdivisions must not be attempted before becoming familiar with the facies. The objective of the study should still be kept in mind. In this study, facies subdivisions are based on vertical variations of sedimentological patterns within a facies.

The concept of a discrete genetic interval (DGI) is applied. Kerr and Jirik (1990)[3.2] defined a discrete genetic interval as a collection of contiguous facies that are deposited in brief discrete increment of time. Two facies are identified in the Bartlesville Sandstone, in the study area: 1) channel-fill facies, and 2) splay facies. The channel-fill facies are further subdivided into 3 subfacies.

3.4.1 Channel-Fill Facies

In study area, the channel-fill facies are represented by upward-fining texture profile that ranges from medium sandstones to mudstones. The scale of sedimentary structures decreases also from internally thickly laminated (up to 1.1 in; 3 cm.) through cross-stratification at the bottom to thin and ripple lamination at the top.

Channel-fill facies average 16 feet (5 m) in thickness, with a range from 10 to 24 feet (3 to 7 m) (Tables 3.1 and 3.3). Cross sections (Fig. 3.4 through Fig. 3.8) show the general thickness distribution of the channel-fill facies within the study area. Fig. 3.9 illustrates the facies/subfacies correlation, as exposed in the roadcut face.

The upward differentiation of texture and sedimentary structures allows for the sub-division of the channel-fill facies into 3 sub-facies (Fig. 3.4 through Fig. 3.9, and

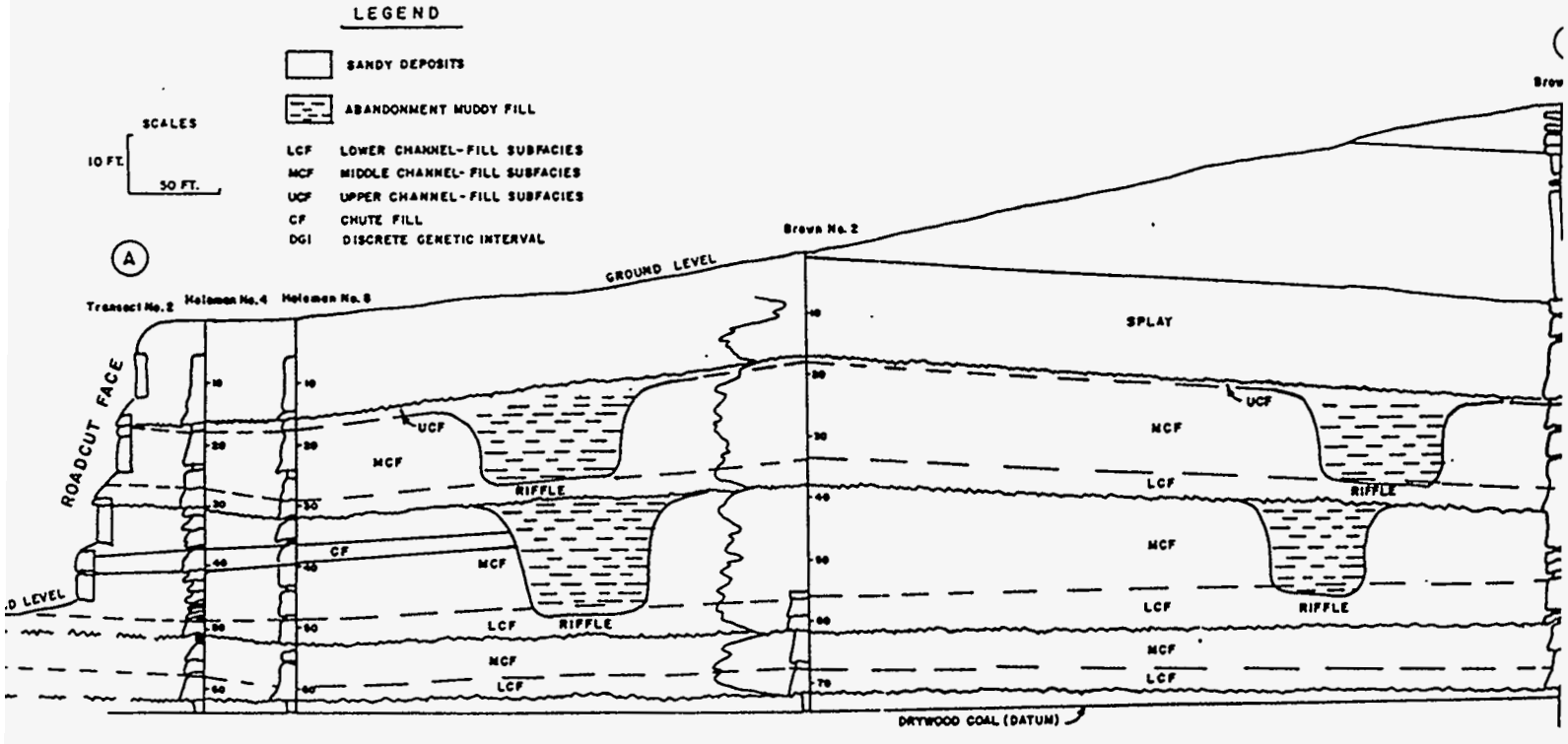

Figure 3.4: Stratigrapic cross section A-A'. Riffles are subenvironments where sandy deposits exist possibly connecting neighboring lateral accretion bars.

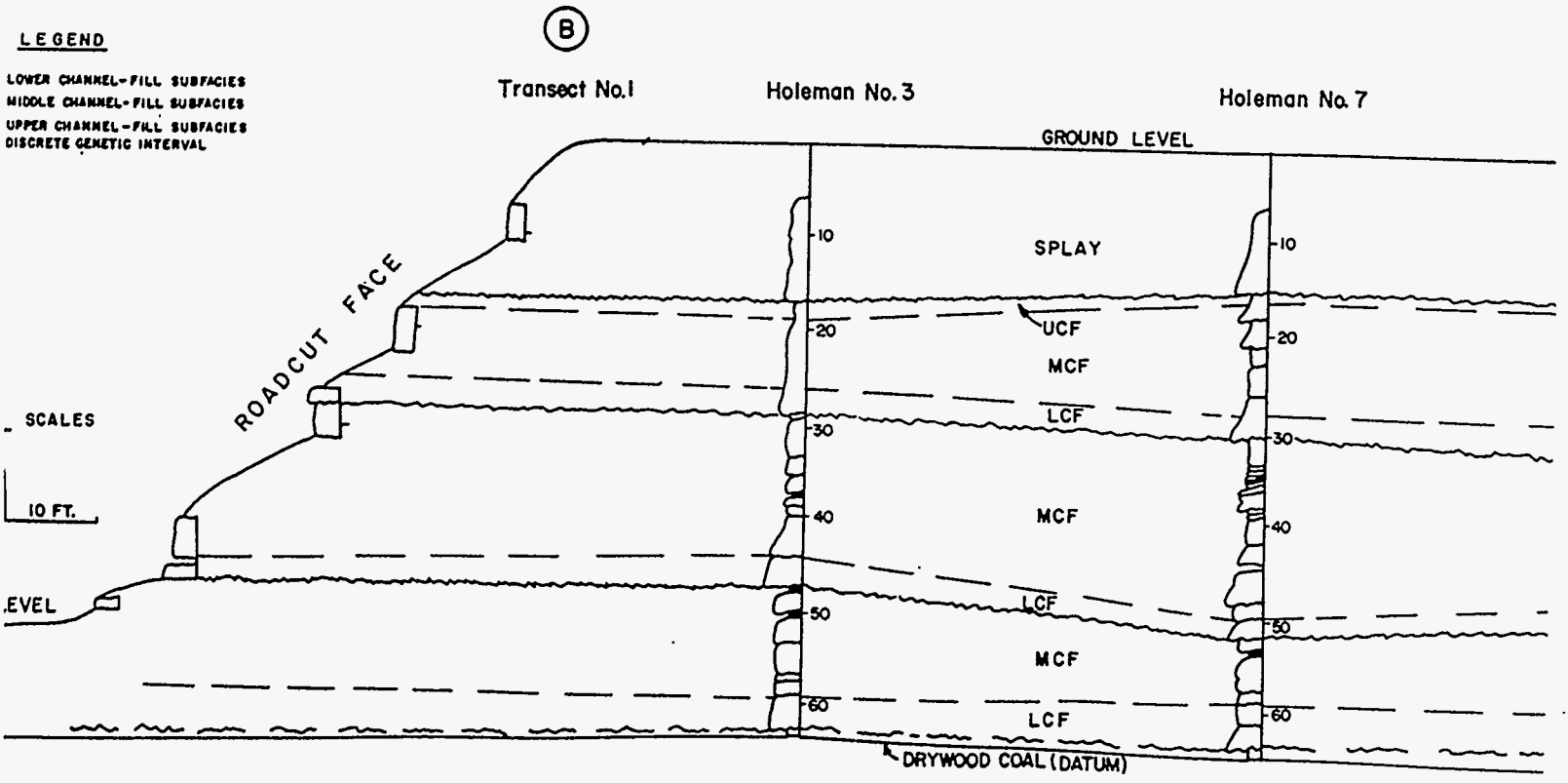

Figure 3.5: Stratigraphic cross section B-B'.

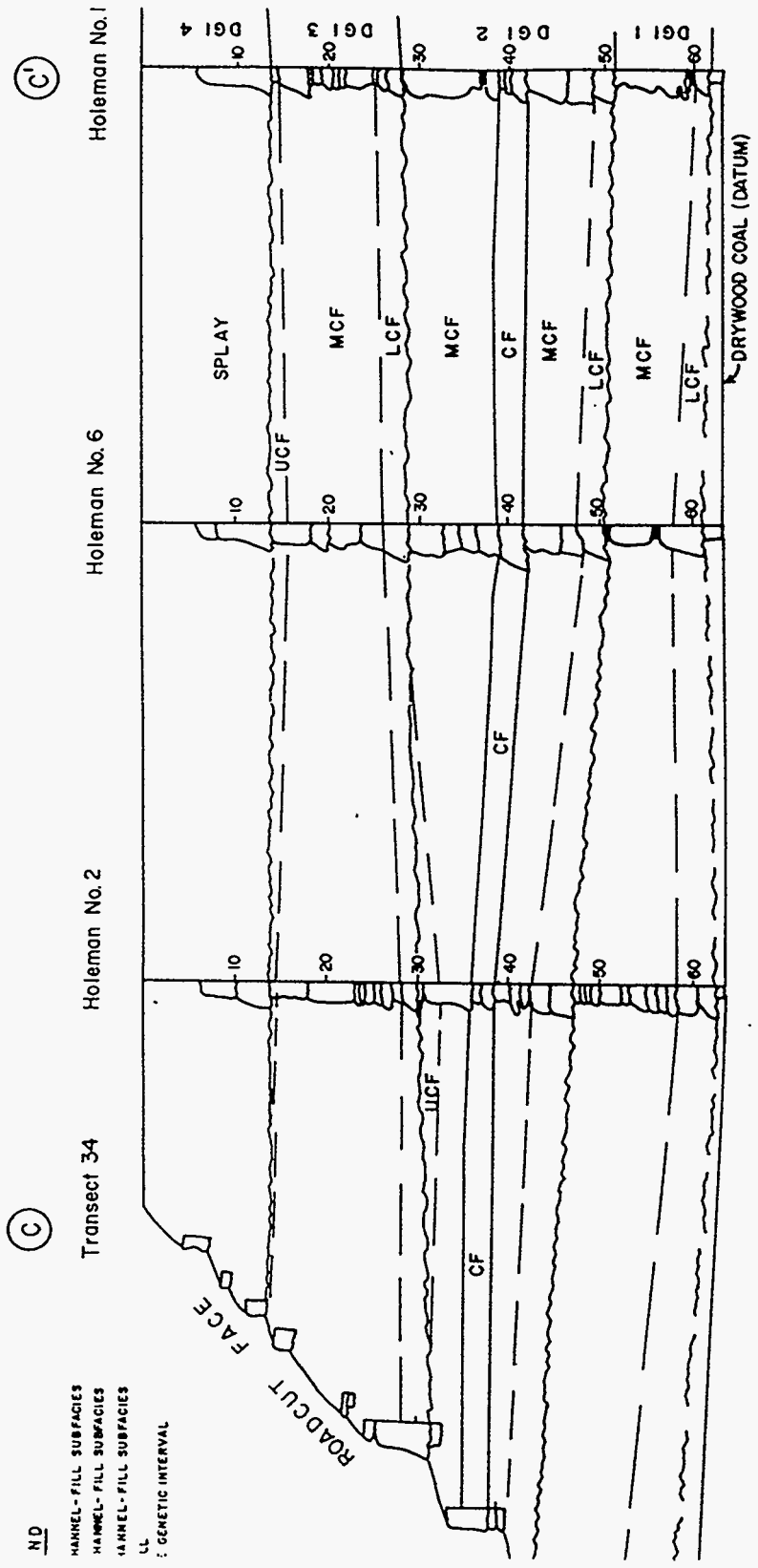

Figure 3.6: Stratigrapic cross section C-C'.

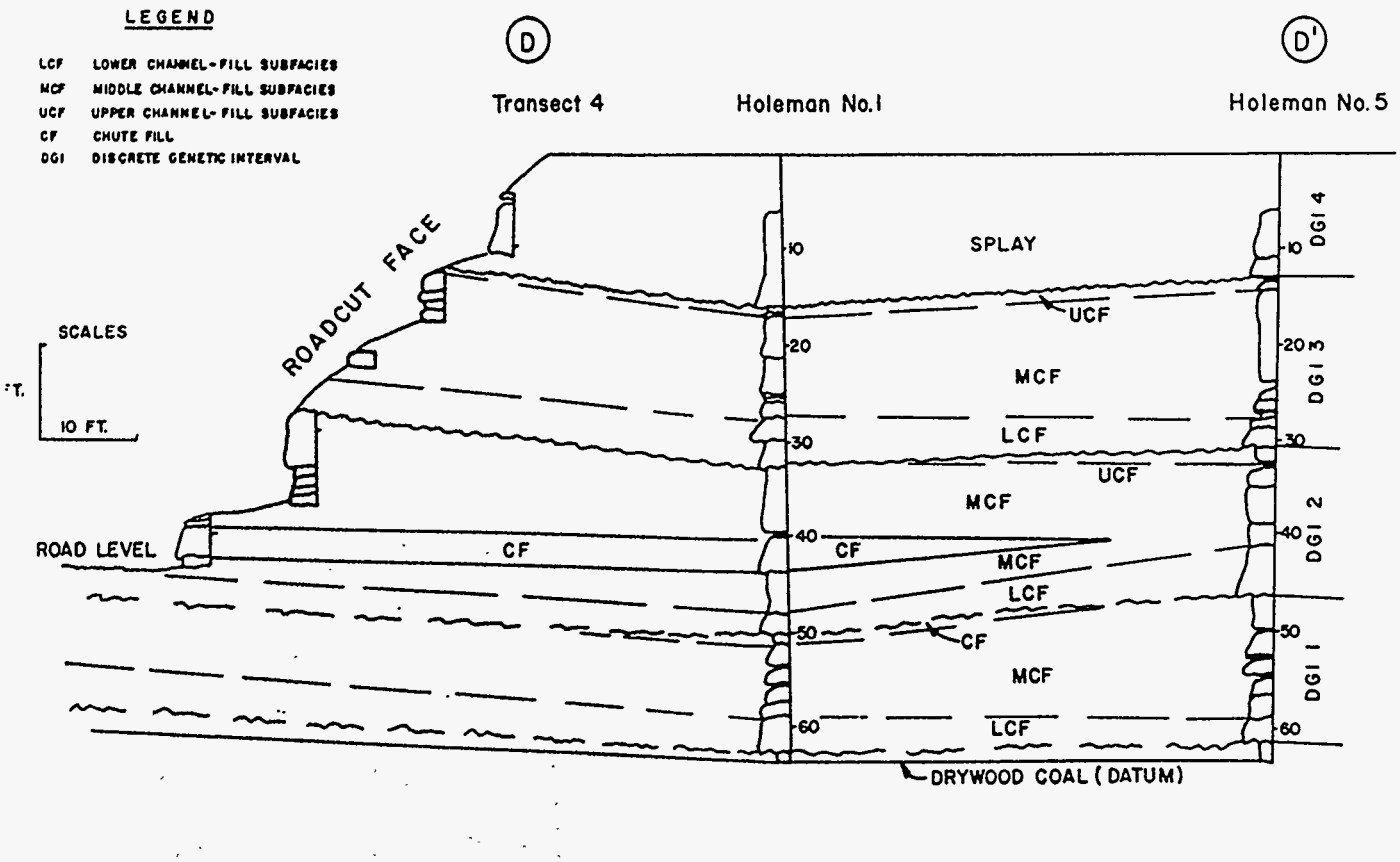

Figure 3.7: Stratigraphic cross section D-D'.

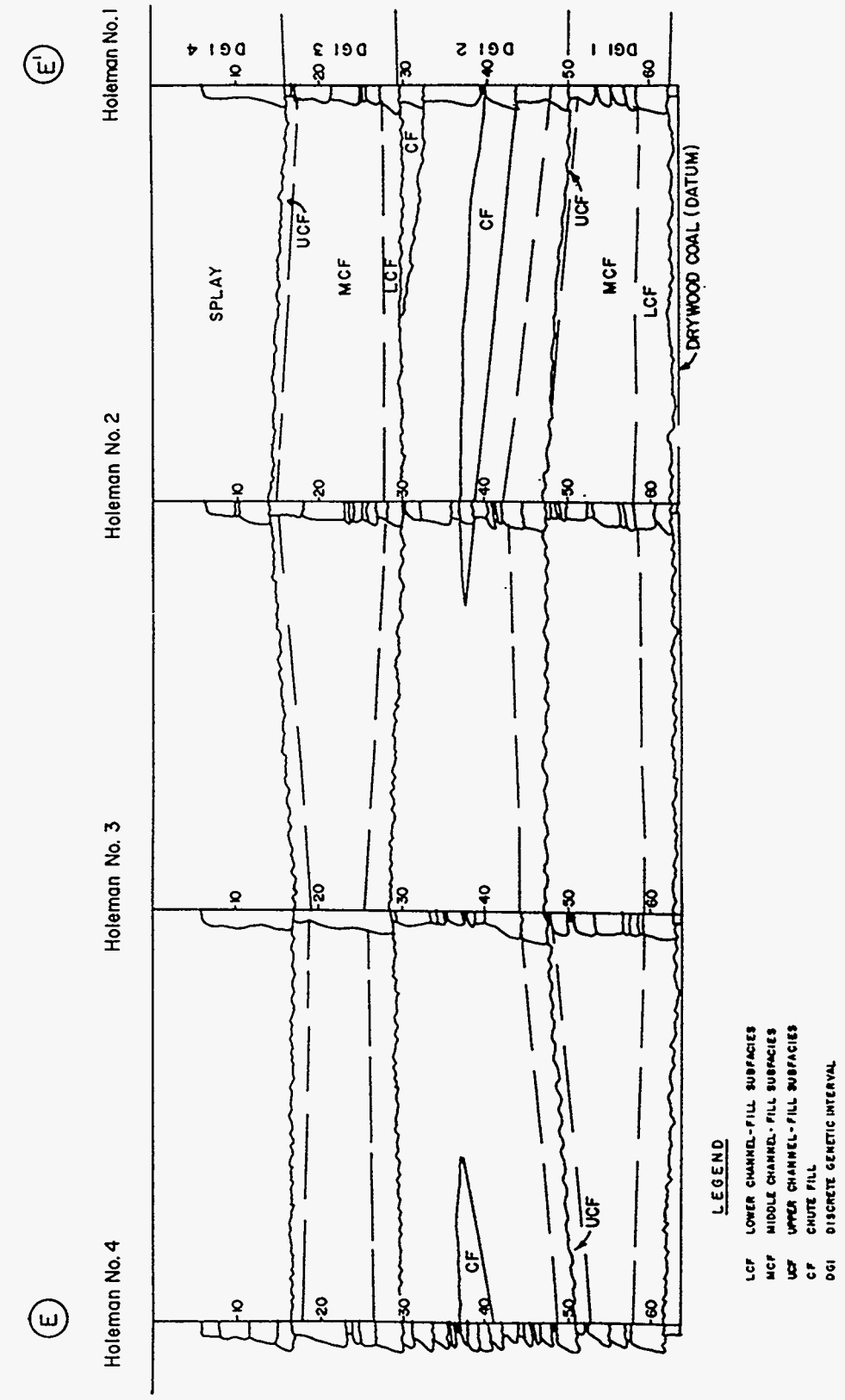

Figure 3.8: Stratigraphic cross section E-E'.

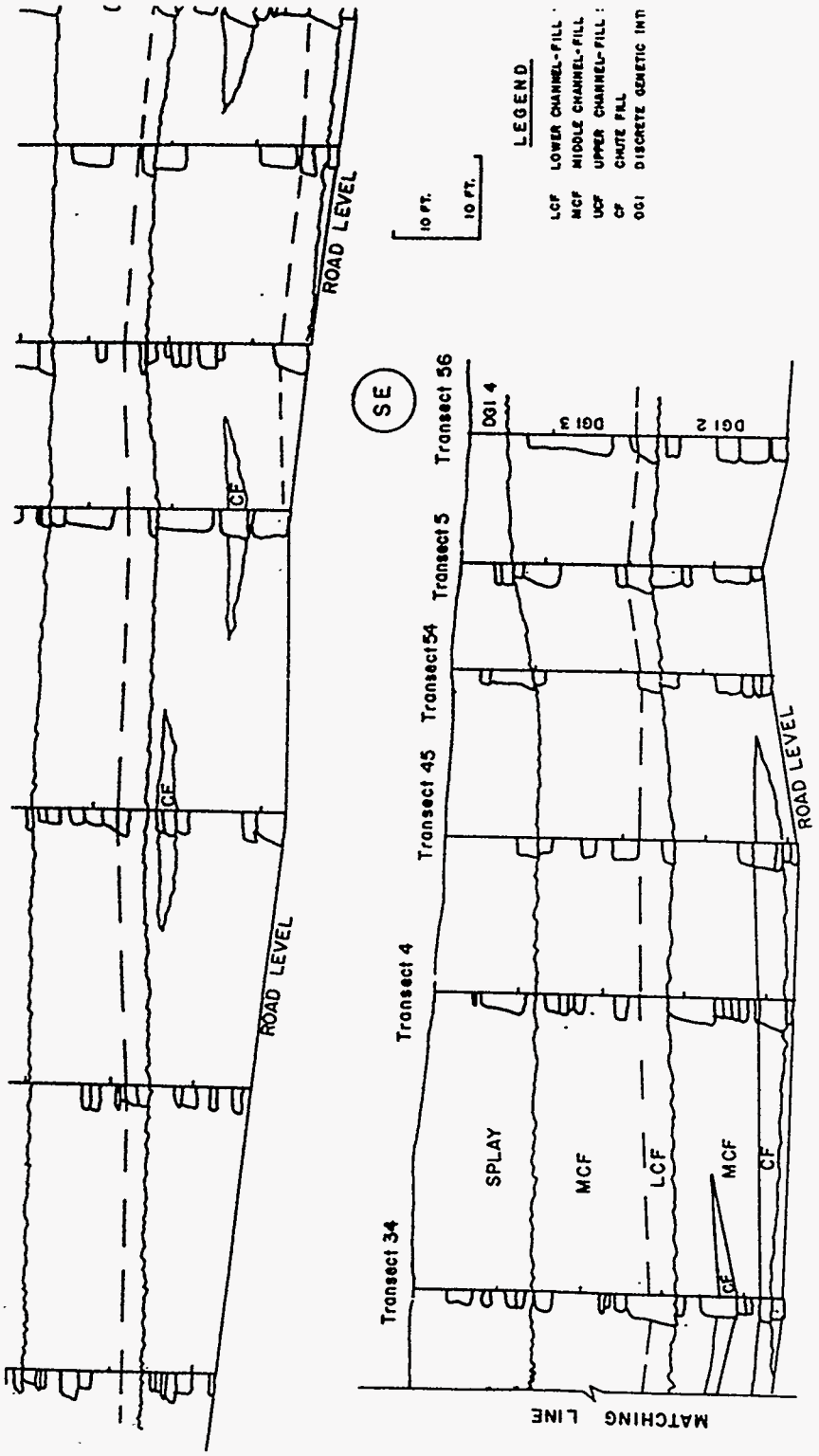

Figure 3.9: Facies/subfacies correlation along the roadcut face, showing geologic columns of transects.

Tables 3.1 to 3.3) that have been identified in this study in ascending order as the lower, middle and upper channel-fill subfacies. Successions are incomplete, because basal erosion of the overlying channel-fill presumably has removed part of underlying channel-fill deposits. This erosive character is less prominent on the uppermost channel-fill facies, which are overlain by splay facies.

Lower channel-fill subfacies are made up of subangular to subrounded, moderately to wellsorted, medium- to fine-grained sandstone (Table 3.3). The basal contact, which is the same as that of the channel-fill facies, is erosive. It is represented by an abrupt upward increase in grain size between underlying and overlying rocks, and common channel-lag deposit. Usually porous rocks are found on both sides of the contact.

The basal few inches (cm) of the lower channel-fill subfacies are characterized by poorly-developed stratification. Mud ripup clasts of variable sizes (up to 1 × 0.5 in, 2 × 1 cm) and shapes are present. Transported siderite nodules (Fig. 3.10) are also present towards the base of this subfacies, specially in the lowermost channel-fill facies succession. Matrix content is relatively low. Intergranular porosity can easily be recognized with a binocular microscope. Sand grains appear loosely cemented by clay alone or clay and calcite. Calcite cementation is mostly found around the areas of high iron oxide concentrations and thicker stratification. The average thickness is 3.3 feet (1 m) and range from 2 feet (0.6 m) to 5 feet (1.5 m). It represents 19% of the total thickness of the channel-fill facies.

Stratification is better developed in the overlying lower part of channel-fill subfacies. Trough cross-stratification is abundant (Fig. 3.10 and Fig. 3.11). Cross-strata are grouped in sets, with individual sets reaching up to 2.5 feet (0.76 m) thick. Cosets are locally separated by mud drapes (Fig. 3.10) that in places, as observed on the road cut face, cojoin with the mud drapes of the middle channel-fill subfacies. Individual cross-strata reach up to 1.5 in (3 cm) thick, separated by thin (<0.04 in; <1 mm) mud drapes or by intervals of finer-grained sandstone. Cross-strata dip angles reach as high as 250.

Well No.	Savana Fm.	D G I No. 1			D G I No.2			D G I No. 3			DGI No.4
		L	M	U	L	M	U	L	M	U	SPL
Holeman # 1	61.2	56.8	50.5	49.0	47.0	29.5	--	25.5	17.0	16.0	6.0
Holeman # 2	61.1	57.5	46.0	--	42.0	32.0	30.0	26.5	16.8	14.0	6.0
Holeman # 3	62.8	59.2	49.0	--	44.1	29.8	29.6	27.0	18.8	17.2	6.0
Holeman # 4	62.3	59.0	51.3	--	48.5	32.5	31.5	27.0	19.0	17.5	6.0
Holeman # 5	61.8	59.5	46.3	--	42.0	33.4	31.0	28.0	20.6	14.7	6.0
Holeman # 6	61.0	56.5	51.0	--	48.3	29.0	--	27	14.3	14.0	6.0
Holeman # 7	62.8	61.0	51.0	--	43.5	30.0	--	28.0	15.3	15.0	6.0
Holeman # 8	62.4	60.0	54.0	--	49.0	33.0	--	31.0	19.0	16.0	6.0
Holeman # 10	63.7	61.2	51.5	--	43.5	28.8	--	26.8	15.7	14.3	6.0
Holeman # 11	63.0	--	49.1	--	46.0	31.5	--	30.0	17.3	15.5	6.0
Brown # 1	95.0	93.5	84.3	83.8	79.0	65.4	--	63.5	49.5	48.5	34.3
Brown # 2	71.0	67.5	60.5	--	52.0	36.0	--	31.0	17.0	15.0	5.0

Table 3.1: Tops of Savanna Fm. and Bartlesville Sandstone facies/subfacies. Discrete Genetic Intervals (DGI) 1 - 3 are made up of channel-fill facies. DGI 4 is a splay facies. L, M and U refer to the 3 subdivisions, lower, middle and upper subfacies of the channel-fill facies. Top of the lower channel-fill subfacies of DGI 1 is missing due to core losses, other missing data refer to the erosion of the upper channel-fill subfacies by the overlying splay unit.

Well No.	DGI No. 1			DGI No.2			DGI No. 3			DGI No.4
	L	M	U	L	M	U	L	M	U	SPL
Holeman # 1	4.3	6.3	1.5	2.0	17.5		4.0	8.5	1.0	10.0
Holeman # 2	3.6	11.5	0.0	4.0	10.0	2.0	3.5	9.7	2.8	8.0
Holeman # 3	3.6	10.2	0.0	4.9	14.3	0.3	2.5	8.2	1.7	11.2
Holeman # 4	3.3	7.7	0.0	2.8	15.9	1.0	4.7	8.0	1.5	11.5
Holeman # 5	2.3	13.2	0.0	4.3	8.6	2.4	3.0	7.4	5.8	8.7
Holeman # 6	4.5	5.5	0.0	2.75	19.3	0.0	2.0	12.7	0.0	8.3
Holeman # 7	1.8	10.0	0.0	7.5	13.5	0.0	2.0	12.8	1.3	9.3
Holeman # 8	2.4	6.0	0.0	5.0	16.0	0.0	2.0	12.0	3.0	10.0
Holeman # 10	2.5	9.7	0.0	8.0	14.7	0.0	2.0	21.2	1.3	8.3
Holeman # 11	-	-	0.0	3.1	14.5	0.0	1.5	12.7	1.8	9.5
Brown # 1	1.5	9.3	0.4	4.8	13.6	0.0	1.9	14.0	1.0	14.2
Brown # 2	3.5	7.0	0.5	8.5	16.0	1.0	5.0	14.0	2.0	10.0
Mean	3.0	8.4	1.0	4.2	14.5	1.5	2.8	11.4	1.8	10.0

Mean thicknesses for channel-fill facies and subfacies

Subfacies	thickness	Channel-fill facies	thickness
Lower	3.3	DGI 1	12.4
Middle	11.4	DGI 2	20.2
Upper	1.4	DGI 3	16.0
		MEAN	16.0

Table 3.2: Summary of Bartlesvill Ss. facies/subfacies thickness (feet). The upper channel-fill subfacies are presumably eroded by the cutting process of the immediate overlying channel-fill facies in places of zero thickness. Well drilling design did not recover the upper 6 feet of core in the Holeman array, thus DGI 4 is likely thicker than presented in the Table. For the Holeman No. 11 well, the thickness of the lower and middle channel-fill subfacies of DGI 1 and 2 are missing due to core losses.

Facies	Texture	Physical Structures	Biogenic structures	Cementation Pattern
Channel-fill				
Lower	Sbang to sbrndd, mod to wl srt, med-to f-gr Sst. Carb frag concentrated along x-strat foresets. Transported sid nod are com.	Erosional basal surf. Internally structureless channel lag. Med-scale trough x-strat. Mud drapes along foresets.	Transported plt casts.	Sid nod in higher DGI's are ox. Fe-ox-rich calc cmt accumulates in thicker strat.
Middle	Sbang to sbrndd, mod srt, m-to very f-gr Ss. Carb frag concentrated along x-strat foresets.	Dominant low-angle parallel, med-scale strat, and subordinate med scale trough x-strat. Mud drapes are com also.	Transported plt frag.	Fe ox-rich cmt increases upward through the DGI's. Thicker strat contain calc cmt also.
Upper	Poorly to mod srt, f to v f Sst. and slty Mdst. Infiltrated Cl Mtrx.	Thinly lam Sst. intercal w/ Rpl and thinly lam Mdst. Highly cntrt.	In-place root casts and root turbation are com.	Fe Conc commonly have Calc rims.
Splay	Sbang to sbrndd mod to wl srt, f-to v f-gr Sst. Evenly distributed Cl Mtrx.	Low-angle parallel thickly lam at base. Transitioning upwards to Rpl and thinly lam Sst., intercal with Mdst drapes at Tp.	Root turbation.	Fe ox com to Mtrx rich Intvls.

Table 3.3: Summary of sedimentary characteristics of the Bartlesville Sandstone facies and subfacies.

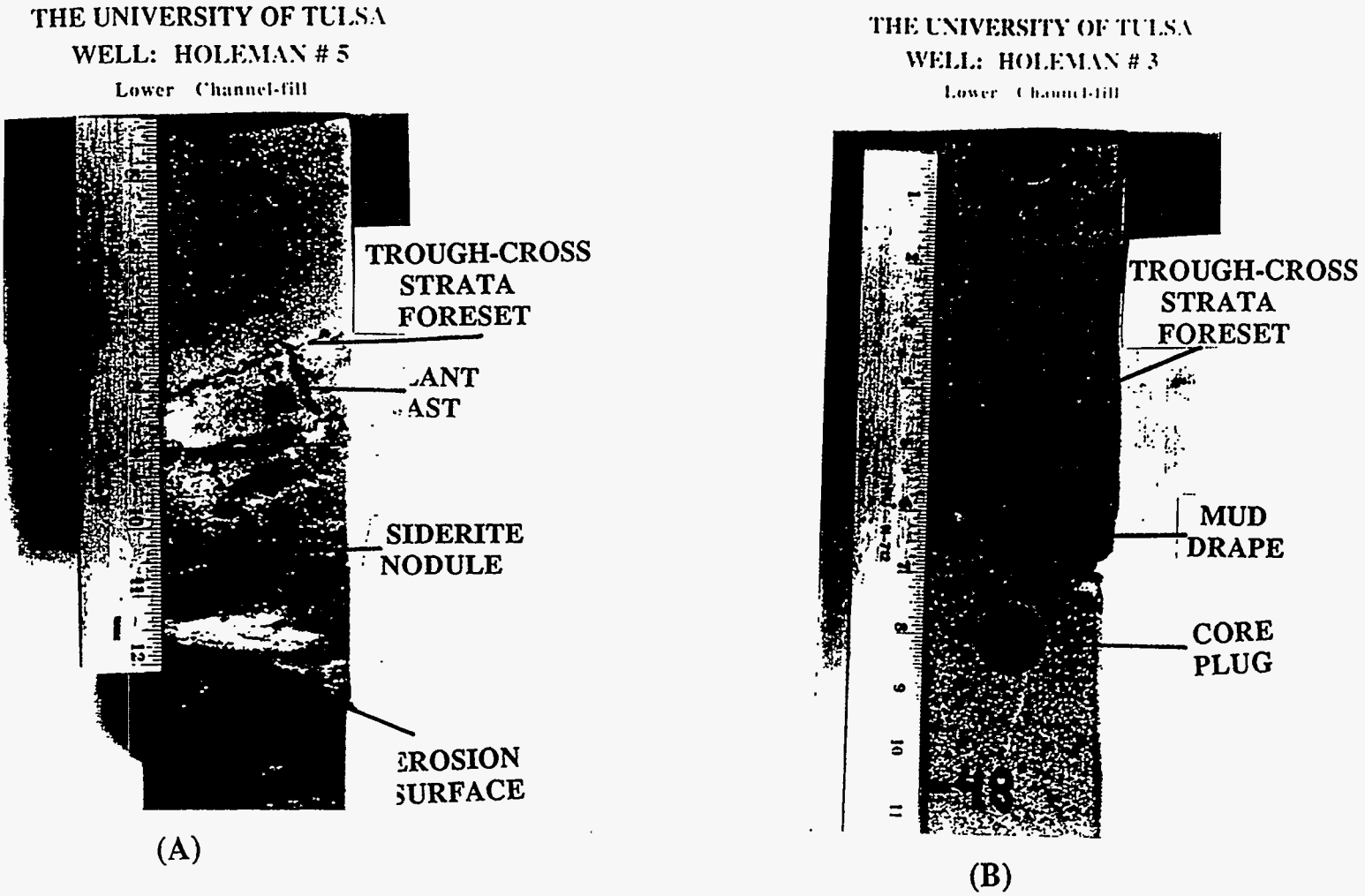

Figure 3.10: Lower channel-fill subfacies examples from cores. Scales are in inches.

(A)

(B)

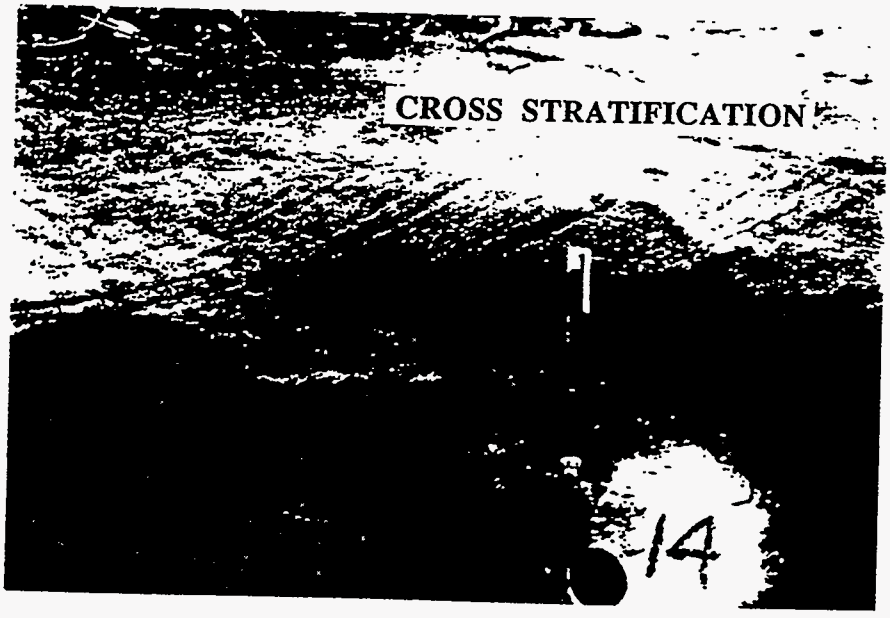

Figure 3.11: Lower channel-fill subfacies exposed in the roadcut face near station 1.E. (A) A general view shows an apparently structureless sandstones. (B) But at a closer view, abundance of trough cross stratification becomes evident.

Figure 3.12: General view of the roadcut face showing proportions of channel-fill subfacies, and vertical limits of some DGI's. Low-relief surfaces separating DGI's appear convex-up due to photo distortion.

Middle Channel-Fill Subfacies

Middle channel-fill subfacies are composed of sub-angular to sub-rounded, moderately- to well-sorted medium- to very fine-grained sandstones with less common mudstone drapes (Table 3.3). Generally, sorting has improved from the lower subfacies, but finer grains also become more abundant. Intergranular porosity can still be recognized on the binocular microscope.

Thickness averages 11.4 feet (3.5 m) and ranges from 8 to 21 feet (2.4 to 6.4 m). This subfacies makes up 70% of the total thickness of the channel-fill facies. Thus, it dominates the Bartlesville sandstone, which is evident in the exposure offered by roadcut face (Fig. 3.12).

In this subfacie, medium to thin beds (0.3 to 1 feet, 10 to 30 cm) dip at low angle (average of less than 100) separated by: (1) thinly-laminated (<0.04 in, <1 mm) silty mud drapes (Fig. 3.13A), that can be thick as 0.5 in (10 mm); or (2) ripple-laminated sets of similar thickness that are made up of very fine to silty sandstone stratification, thickly (0.5 in; 1 cm) to thinly parallel laminated (<0.04 in; < 1 mm). Stratification sets are separated by intervals of higher clay matrix content or micaceous mud drapes, where carbonaceous can also be present.

Commonly, high-angle trough cross-strata sets of thickness up to 1 feet (0.3 m), with stratification and texture patterns similar to those of the lower channel-fill subfacies and including basal lag deposits are grouped in cosets of 2 to 4 sets. These cosets appear as isolated units that cut across the lateral continuity of the middle subfacies (Fig. 3.13B).

Upper Channel-Fill Subfacies

It is thought to be under-represented in its thickness, probably as a result of erosion by younger channel-cutting processes. General characteristics are hard to draw because of its erratic presence in the study area. Average thickness is 1.4 feet (43 cm) and ranges from zero to 5 feet (1.5 m). It represents only 11% of the total facies thickness in the study area (Tables 3.1 to 3.3).

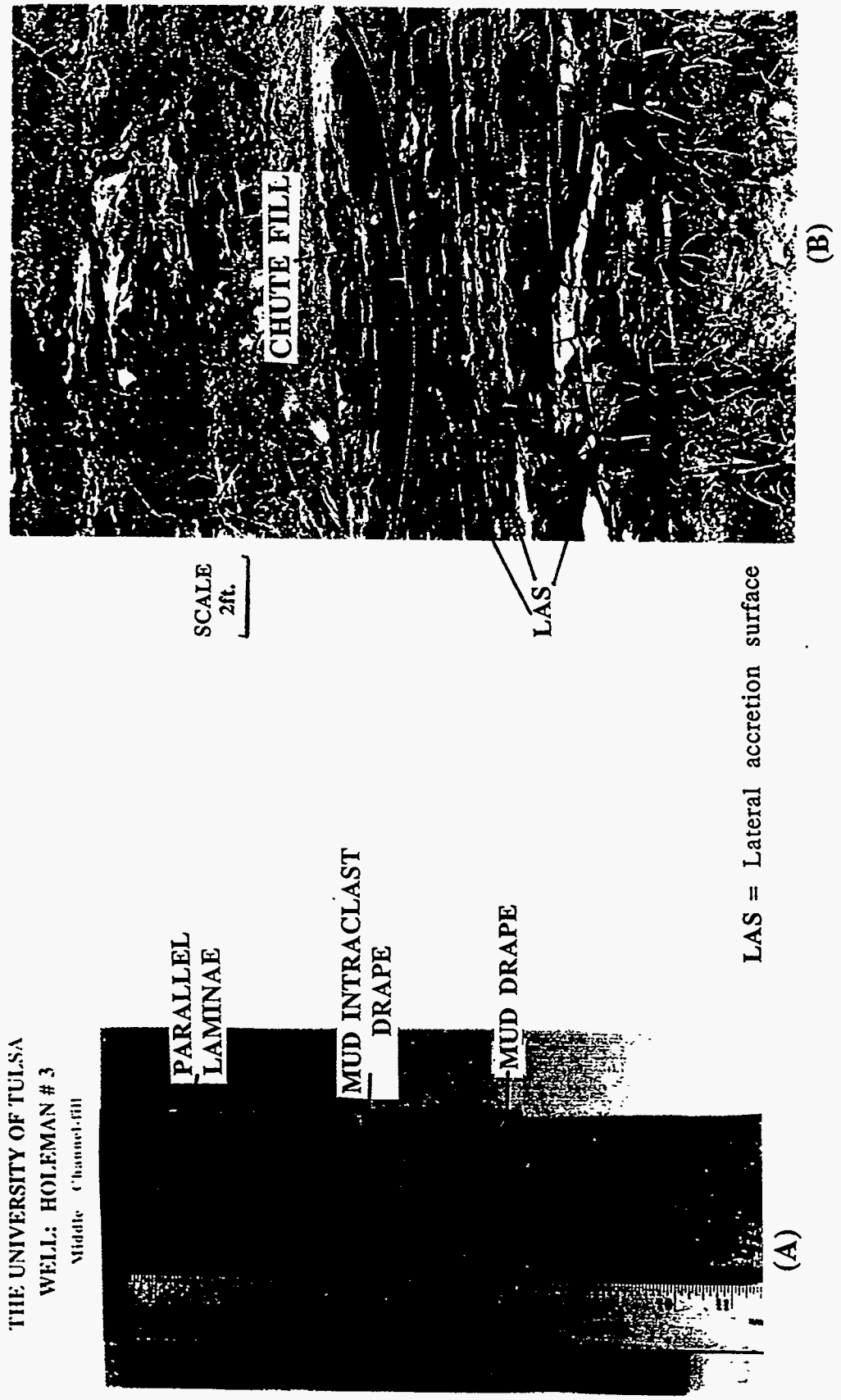

Figure 3.13: (A) Core example, and (B) outcrop view, between stations 3D and 34D, of the middle channel-fill subfacies.

In the sandy interval, sand grains are better rounded than in the other subfacies, and better sorted. However, the matrix content has increased to the point that it is very difficult to detect intergranular porosity with the binocular microscope. In the silty mudstones no intergranular porosity is observed with the binocular microscope.

Its contact with the underlying middle channel-fill subfacies is gradational and difficult to pinpoint. Fig. 3.14A shows the abrupt change of the very fine sediments of an upper channel-fill facies succession has eroded, making it difficult to assess the original thickness. Usually this subfacie is represented by a transition of upward decreasing grain size, that makes very fine sandy to silty sediments more abundant, while becoming increasingly intercalated with mudstones.

Bed contortion is abundant, and only relic structures can be observed in many cases. Stratification is parallel thinly-laminated to ripple- (<0.04 in; <1 mm) laminated. Water escape structures are also present.

Root casts, common to these subfacies (Walker[3.3]) are related to tube-like horizontal ironstone concertinas' structures that are observed on the roadcut face (Fig. 3.14B). These root casts have a yellow silty core with concentric rings of outward increasing lateritic iron oxide concentration and some calcite rims.

Wireline Log Character

Wireline logs from the Holeman No. 1 well are typical of the log response for the channel-fill facies (Fig. 3.15). The upward-fining textural profile for each of the facies, especially the channel-fill facies, is still recognizable on the Gamma ray curve, but briefly interrupted at the middle of DGI 2 by chute cut and fill (42 feet in Fig. 3.15).

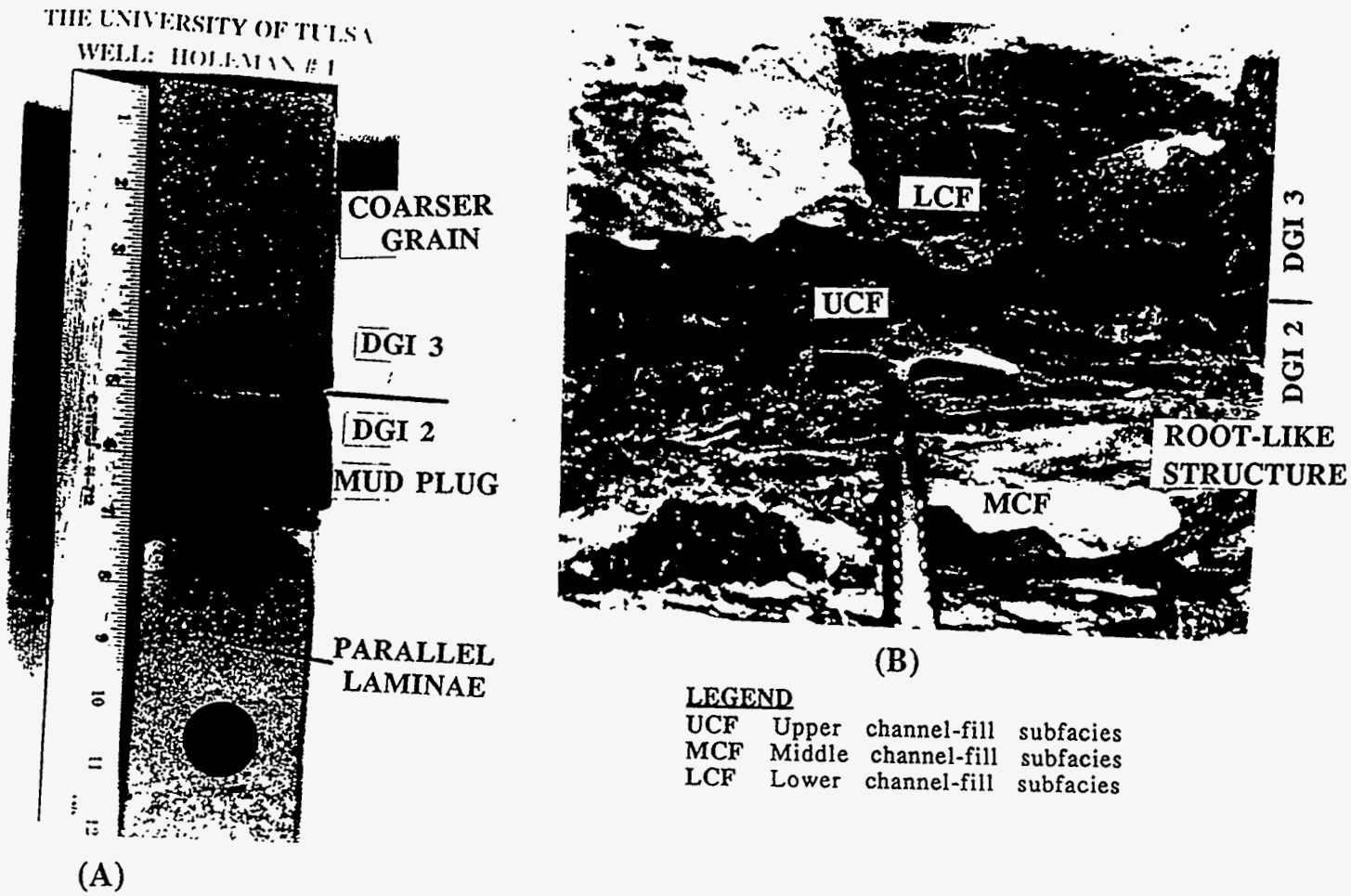

Figure 3.14: (A) Core examples of the upper channel-fill subfacies of DGI 2 and the lower channel-fill subfacies of DGI 3, and (B) outcrop views of the upper channel-fill subfacies of DGI 2 and the lower channel-fill subfacies of DGI 3 near station 12C.

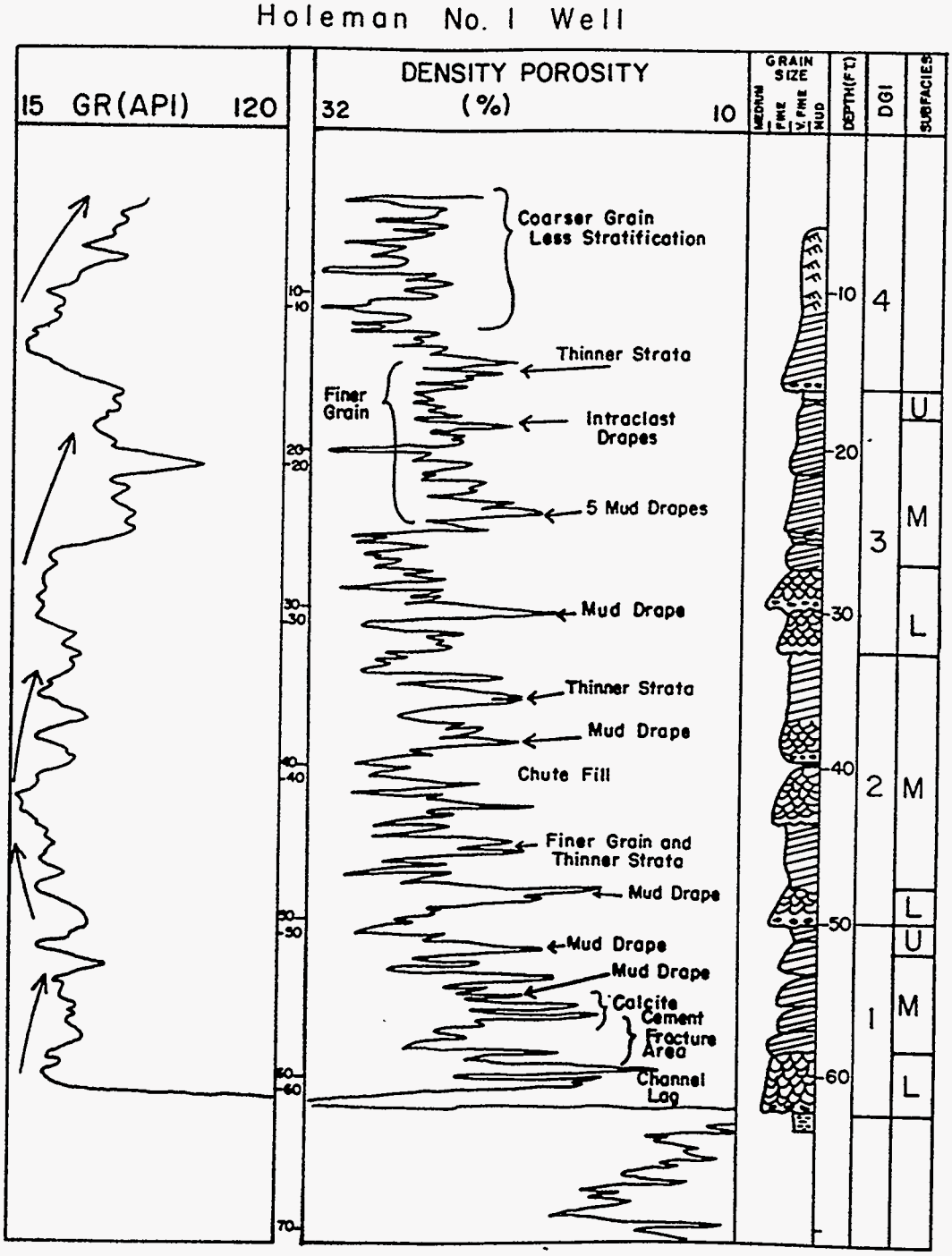

Figure 3.15: Type well log (Holeman No. 1), correlated with core graphic. Finer and coarser-grained sections on upper portion refer to relative grain size between the two sections.

At the bottom of the log, between 55 and 62 feet, calcite cementation and lag deposits, observed in the cores, appear to decrease porosity, while an intersecting fracture (between 56 and 58 feet) appears to increase porosity. Porosity log variations are not obviously correlative with channel-fill facies in the core.

The general wireline character of the lower channel-fill subfacies is difficult to separate from middle channel-fill subfacies in the well cores, the road-cut face and well logs. Generally, this subfacies shows the lowest amount of API units on the gamma ray log, among the 3 channel-fill subfacies (Fig. 3.15), but its small thickness (a couple of feet) might be used. The common smoothing processes of well log curves do not provide much information for differentiation of this subfacies either. In some cases, like between 26 and 30 feet in Fig. 3.15, a sharp contrast in porosity exists.

Generally, the middle channel-fill subfacies show an upward increase in API units detected by gamma ray tool, that is, it is usually more radioactive (argillaceous) than the lower subfacies. Closely-spaced radioactive deflections may be related to the lateral accretion surfaces, which are difficult to correlate from well to well due to tool resolution and curve smoothing. On the density porosity curve, there is not much difference when compared with the other channel-fill subfacies.

A distinguishing well log character is not obvious for the upper channel-fill subfacies. Its limited thickness makes it difficult to asses thickness for this subfacies, based on well logs only. As shown in Fig. 3.15, these subfacies are represented on the gamma ray curve as a simple radioactive interval at the end of the channel-fill facies successions.

Interpretation

The lower channel-fill subfacies are interpreted as having been deposited over the basal surface (channel floor under the thalweg) of the channel-fill facies, as migrating subaqueous crescentic dunes.

Typically, along the thalweg, a channel lag composed of the coarsest sediments being transported is deposited at the bottom of the channel-fill deposit (Reineck and Singh;[3.4] Walker[3.3]). According to Reineck and Singh,[3.4] the channel-lag deposits

are not very thick and concentrate wood debris, large sediment blocks of unconsolidated sediments, mud pebbles and dead organism, whenever coarse grain sediments are not available at the lower reaches of the stream. The main direction of sediment transport and deposition is downstream. The main direction of sediments is bedload in the form of sinuous crested dunes (Walker[3.3]), this resulting in trough cross-stratification.

The middle channel-fill subfacies is identified as the point bars described by Galloway and Hobday,[3.5] as being deposited by lateral accretion processes, on the inside of the meander bend of alluvial channels. Mud drapes that separated cross-strata sets dip at low angles and can be traced on the outcrop for tens of feet are regarded as lateral accretion surfaces. Chute channels cut across the point bar top. In the Bartlesville Sandstone, chute-cut and -fills are represented by isolated trough cross-stratified cosets that interrupt the lateral continuity. The middle channel-fill subfacies are, thus regarded as deposits of a chute-modified lateral-accretion bar.

Depending on discharge and bank stability, a parameter used commonly for differentiation of meandering (unstable bank) and braided streams (stable banks) (an issue not entirely supported by Jackson[3.6]), a meandering channel can migrate, laterally, downstream or both, by changing the amplitude or phase of its sinuous thalweg. When these migrations start, a process of lateral accretion deposition takes place in the inner side of the loop. Sediments that are separated from the streamflow during high flow stages tend to move upwards onto the inner banks of the stream. According to Walker,[3.3] higher water elevations on the outer side of the loop can cause flow currents that go down towards the channel floor and up onto the opposite side of the channel. These flow currents drive sediments that can show an upward decrease in grain size, by lateral accretion, forming the typical point bar, so well known in the literature, and mostly referred to in this study as a lateral accretion bar. McGowen and Garner[3.7] identified these deposits in 3 types of stratifications that suggest deposition under tranquil waters: trough-cross-stratification and foreset-cross-stratification are probably deposited under similar conditions. As water recedes from the lateral accretion bar, finer deposits are laid down as mud drapes. Accumulation of fine sediments closes the cycle of deposition of a single bar, forming mud layers, known as the lateral accretion surfaces (LAS). At times of aerial exposure, these drape deposits become cracked, showing desiccation marks, or become turbated by organic activity. Also, wind-

blown deposits can accumulate on top of the bar. Deposits between consecutive LAS dip towards the thalweg, perpendicular to stream flow, making up the epsilon cross-strata (ECS) of Allen.[3.8]

During high flood stages, a secondary thread of maximum surface flow may cut across lateral accretion bar (McGowen and Garner,[3.7] Walker[3.3]). Coarse sediments are then funneled through chutes that increase in depth as they erode towards the downstream side of the bar, where chute bars (Jackson[3.9]) are deposited (Fig. 3.16). Chute-fills interrupt the vertical preservation of lateral accretion deposits and show an erosive basal surface. Because chute-channels modify the depositional pattern of the lateral accretion bars, the term chute-modified lateral accretion bars is applied in such cases.

The upper channel-fill subfacies as interpreted as having been deposited under condition of low energy, by the process of channel abandonment. The deposits are regarded here as a channel-abandonment fill, with pedogenic cementation and overprinting of primary sedimentary structures.

At late stages a stream can become abandoned by upstream channel piracy, avulsion or meander-neck cutoff (Galloway[3.10]). When this happens, the main source of deposits in the old channel course, is the overbank flooding from the main channel, that now follows a different course, and the main type of deposition is by vertical accretion (Walker[3.3]), of sediments of upward decreasing grain size, including mostly muds and silts that can be thick as the underlying lateral accretionary deposits (middle channel-fill subfacies). It represents a diminishing trend in depositional energy and stream competence. However, this is a depositional cycle that does not have to be completed in order for the next channel-fill to reoccupy the older channel course. Organic debris and coal deposits can be an important part of these sediments.

These deposits tend to separate the sandy deposits of laterally-contiguous bars. However, Reineck and Singh[3.4] identified areas of sand deposits of the shallower portions of the meander loop and referred to them as riffles. They are located on the upstream and down stream sides of the loop, the deepest part of the channel presents no sand deposition, separating the riffles. This area is referred by Reineck and Singh[3.4] as the pool.

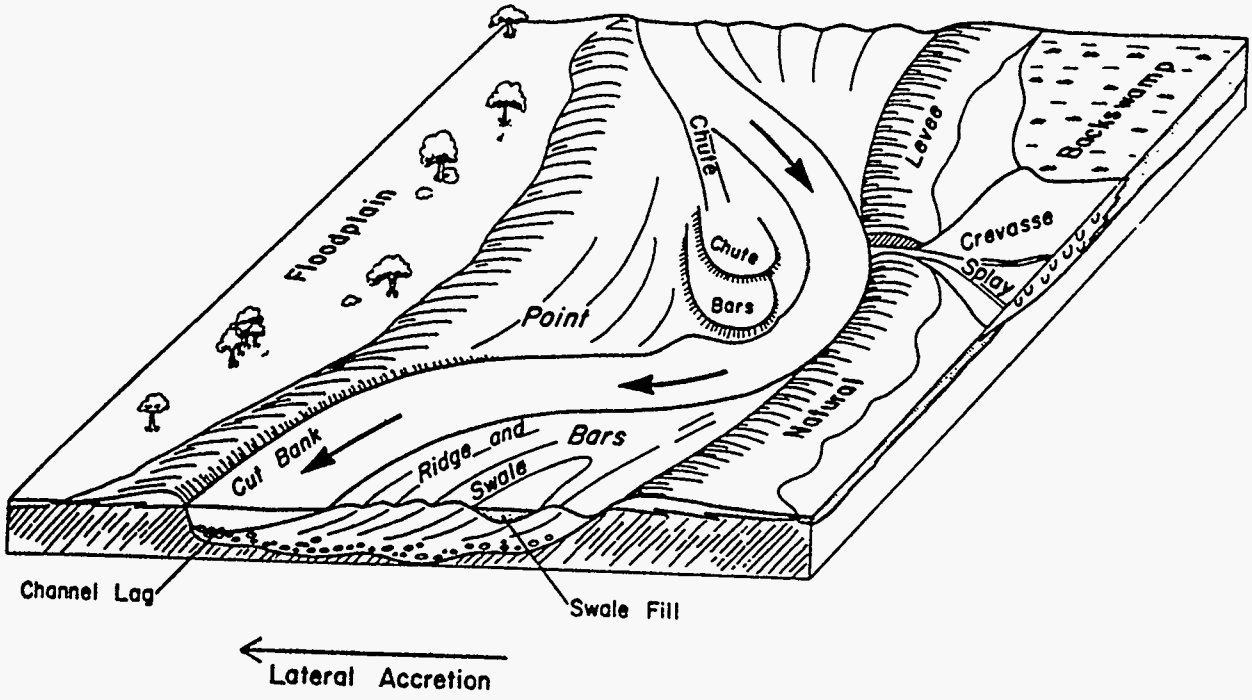

Figure 3.16: Schematic representation of fluvial deposits within a single discrete genetic interval (Galloway, 1985).

3.4.2 Splay Facies

Description

In the study area, DGI 4 (Fig. 3.4 through Fig. 3.9) is made up of a subangular to subrounded, moderately- to well-sorted, fine- to very fine-grained sandstone (Tables 3.1 to 3.3). Average thickness is 10 feet (3 m), ranging from 8 to 10 feet (2.4 to 3 m) around the roadcut area.

Stratification is not very clear at the base, where it appears as structureless, but usually it shows low-angle parallel, thick laminations (Fig. 3.17A). Mud ripup clasts are also common here (Fig. 3.17B). Mud drapes are erratic, but can be as thick as 1 in (2.5 cm) and thinly laminated. Ripple laminations become abundant mostly about mid-section, but are usually alternated by thinly horizontally-laminated deposits. Toward the top, bands and patches of highly cemented iron-oxide concentrations, appear with low angle to horizontal orientation and irregular shapes (Fig. 3.18A)

On the roadcut face, the top portion is not complete and it grades into the modern soil cover, after becoming highly intercalated with fissile, soft, iron oxide-rich clays that show ripple to thin (0.04 in, <1 mm) laminations. Here also, pedogenic structures, like root turbation and dewatering structures are common (Fig. 3.18B).

Wireline Log Character

The wireline log character of this subfacie is very similar to the one of the channel-fill facies (Fig. 3.15). Clay content, however, is definitely higher. It shows a general upward-fining texture, but the gamma ray signal generally shows higher mud content than the channel-fill facies.

Interpretation

The splay facies, like the one identified in DGI 4, are the result of unconfined flow deposition outside the main channel course. Splay deposits originate at periods of high flood. They can be formed by overtopping the river banks or by being funneled

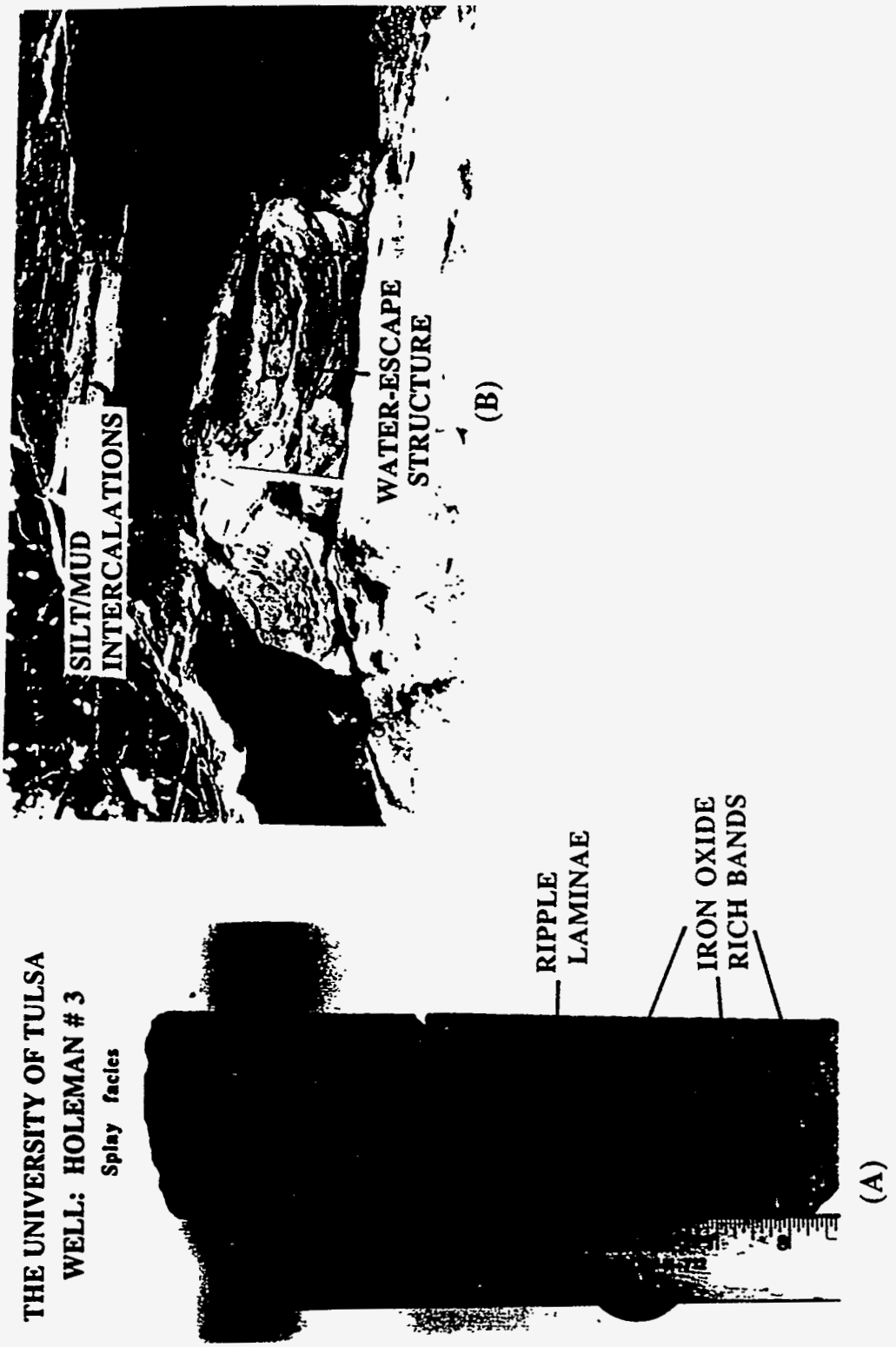

Figure 3.17: (A) Core view of the iron-rich bands in the splay facies, and (B) large-scale contortion of water-scape structure, in the roadcut face near Station 3.

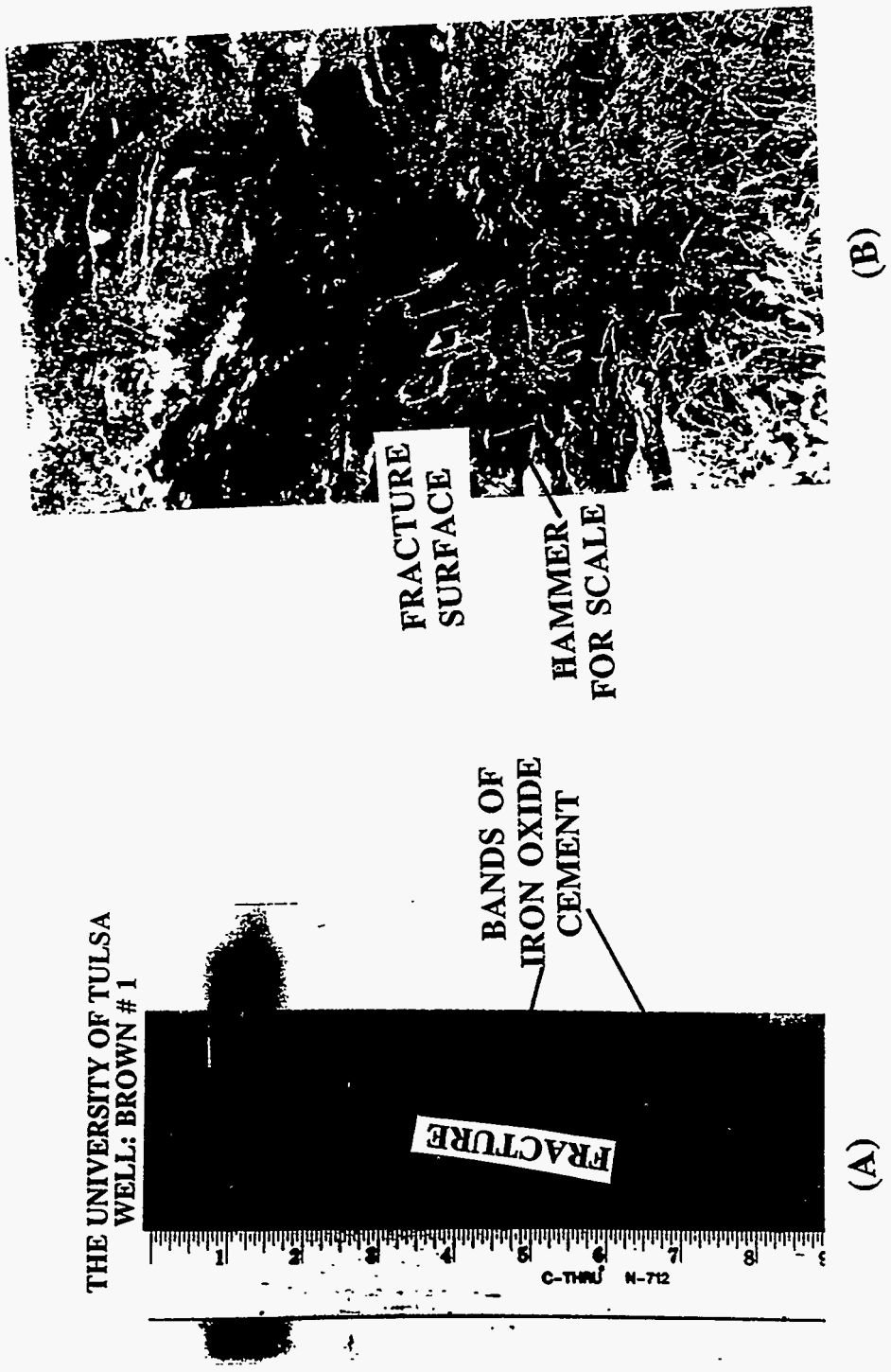

Figure 3.18: (A) Perpendicular view of a facture in cores. Notice absence of primary stratification. (B) Fracture surface in the roadcut face of stations 4C, 4D and 4E.

through channels cut across the natural levees (Walker[3.3]). The channels are called crevasses, and the deposits of unconfined flow are referred to as splays. When overtopping the river banks, there is a potential that splay sediment would not be connected to the main channel after deposition. But, when the levee is broken, sediment left in the crevasse channel may connect splays and channel sediments. Splay deposits can reach tens of feet in thickness, and become thinner in the direction away from the main channel. Sedimentary structures include small-scale cross-bedding, climbing ripple lamination and horizontal bedding (Walker[3.3]).

3.5 Petrophysical Data Analysis

This section discusses the analysis of the collected petrophysical data. We have divided this section into three parts. The first part discusses the well data set, the second part discusses the univariate and bivariate statistical analysis of the data, and the third part discusses the spatial statistics through variograms of the data. In this part, we also present the applicability of the variogram in detecting geological information.

3.5.1 Well Data Set

We divide the data into two sets; they are: 1) 10-well data set and 2) 5-well data set. The 10-well data set consists of the all the Holeman well data; the 5-well data set consists of 5 Holeman well data, these are the Holeman #2, #4, #5, #7 and #10. The purpose of dividing the data into two categories is to investigate the importance of data in quantifying the uncertainties. We do not use the Brown wells. Other than the distance between these well with the remaining wells, we have very limited information from the Brown #2 well.

3.5.2 Univariate and Bivariate Statistics

In this part, discussion about the permeability analysis of the sample data is divided into three categories. The first is the permeability of the entire Holeman well data set or 10-well data set, the second is the permeability data based on the geological unit description. The third is the permeability data based on the channel-fill subfacies.

Permeability Data Statistical Analysis

The univariate statistical parameters used in the analysis of permeability data are mean, variance, the coefficient of variation and the quartile distributions. Detailed permeability analysis is summarized in Table 3.4.

From Table 3.4, we can see that the mean permeability of all categories is around 50 md. The standard deviation for the overall data is similar to the standard deviation of individual discrete genetic intervals. The overall mean is also similar to the individual means of the geological units except the DGI 4 / unit 4. This indicates the DGI's represent the cyclicity in the system and reproduce the same petrophysical properties. Where the data are subdivided in terms of subfacies, the means are different for individual subfacies. Mean for the upper channel-fill subfacies is 45.6 md, and it increases to 56 md for the lower channel-fill subfacies. The standard deviations also increase as we move from upper to lower channel-fill subfacies.

The coefficient of variation (relative variation in permeability values) increases as we move from the upper to the lower channel-fill subfacies. For individual DGI 1-3 the coefficients of variation are similar to each other except the DGI 4 / splay. The discrepancy in DGI 4 may be due to a different geological environment.

Relationship Between Permeability and Porosity

Using all the data collected from wirelogs and core plugs in Fig. 3.19, the porosity values are plotted against the log of permeability. The relationship is linear up to a porosity value of 19%. Beyond 19%, the permeability value is constant and is independent of the porosity values. Since the relationship is not different for individual channel-fill facies, the same relationship is used for all the sub-facies.

Relationship Between Vertical Permeability and Horizontal Permeability

The relationship between vertical permeability and horizontal permeability is shown in the Fig. 3.20. We can see that the permeability data of the middle channel-fill subfacies show more variability than the others. Although data are limited, both the lower and upper subfacies indicate that the vertical permeability values are very

Name	Number	Mean (md)	Variance	CV	median	Q1	Q2
10-well data	1110	50.36	634.03	0.5	47.9	67	28
DGI 1	336	54.68	747.47	0.5	47.9	67.7	37.8
DGI 2	332	54.89	911.4	0.55	52	70.6	31.5
DGI 3	313	45.66	653.8	0.56	42	63.6	25.8
Splays	132	39.24	636.8	0.64	37.75	55.9	17.9
Upper	70	45.6	474.43	0.47	48.2	67.9	24.6
Medium	612	50.8	827.56	0.56	47.9	67.4	28.95
Lower	232	56.04	762.86	0.49	49.2	71.5	37.9

Table 3.4: Summarized statistical analysis of permeability of channel-fill subfacies, facies and 10-well data set.

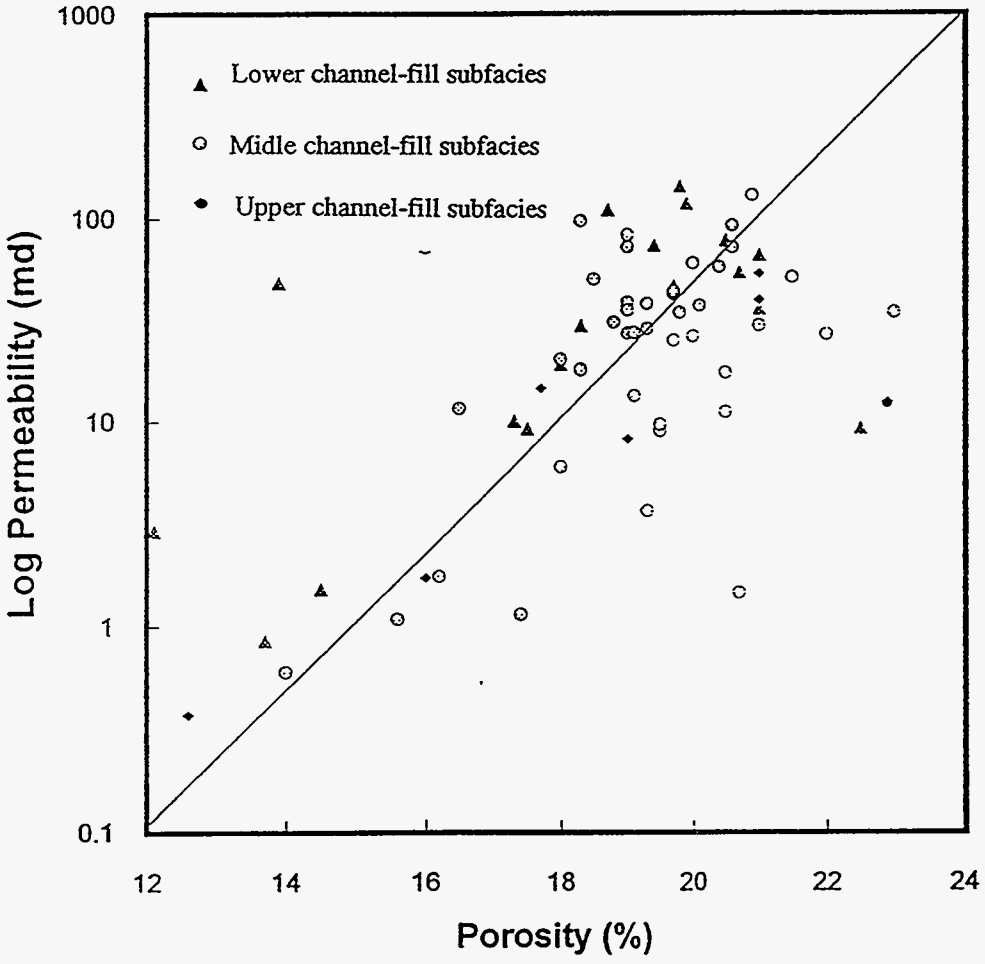

Figure 3.19: Log permeability vs. porosity.

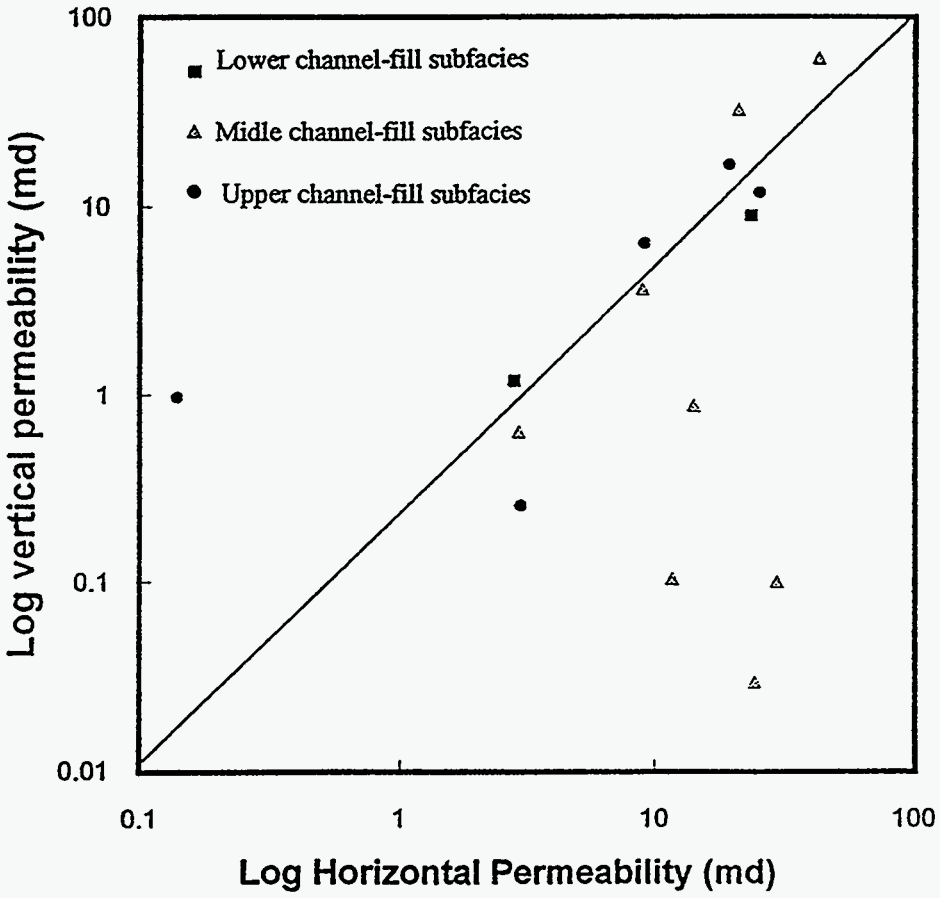

Figure 3.20: Log vertical permeability vs. log horizontal permeability.

similar to the horizontal permeability data. Overall, the log of vertical permeability values are close to the log of horizontal permeability values except for the middle subfacies, where the vertical permeability is lower than the horizontal permeability. However, there is a lot of variability in the data set to reach a definite conclusion. It is important to note that we could not collect vertical samples where we had thin (probably impermeable) laminations across horizontal planes. The effective vertical permeability for these cases may be very low. However, every time an attempt was made to collect a sample, the core plugs broke along the horizontal plane. If we had representative samples from these plugs, we may have seen smaller vertical permeability values that presented in Fig. 3.20.

3.5.3 Spatial Statistics

In this part, we first discuss the estimated variogram of permeability and gamma ray data. Next, we create synthetic variograms to understand the features observed in vertical variograms. Then we compare the synthetic variogram with the estimated variogram. Lastly, we model the variograms using the conventional methods.

Estimated Variogram

Spatial correlation and variability of the permeability of vertical and horizontal data are evaluated with the variogram analysis. The estimated variogram for horizontal data is shown in the Fig. 3.21. The horizontal data are collected from the outcrop face. Due to the difficulty in conducting measurements, some data at horizontal locations cannot be taken, so the estimated horizontal variogram values do not look smooth.

The estimated variogram from vertical permeability data of Holeman #1 well is shown in Fig. 3.22. It can be seen in the Fig. 3.22 that the variogram shows a high nugget value. The variogram exhibits hole effects and the cycle repeats at approximately a 15 feet distance. A consistent observation of the hole effects in both the permeability and the gamma ray vertical variograms indicates that the hole effects are not simply an artifact. Rather, it is an indication of a particular

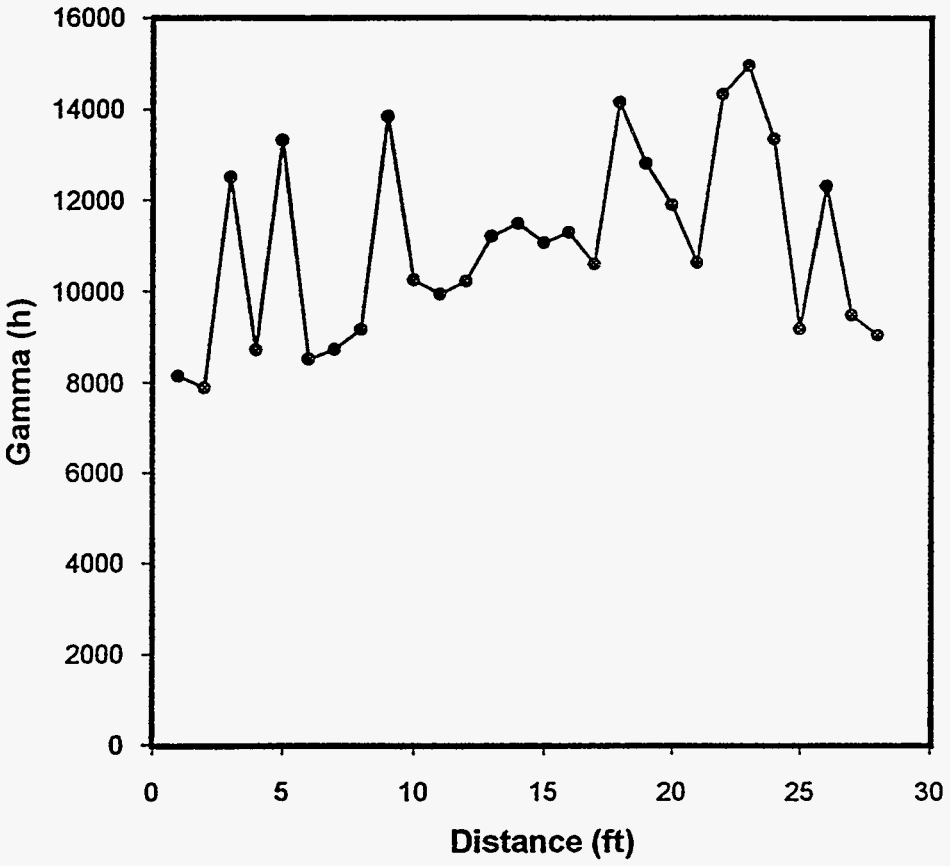

Figure 3.21: Estimated horizontal permeability data.

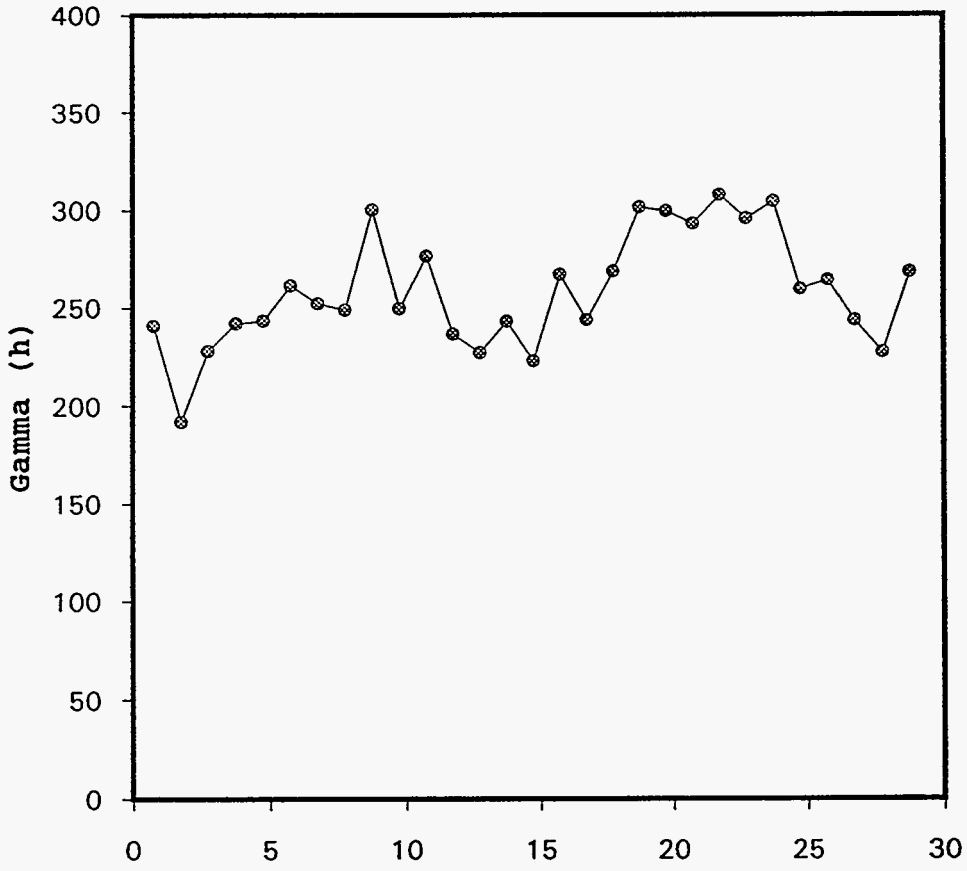

Figure 3.22: Estimated vertical permeability variogram of Holeman #1 well.

geological feature which may be captured by the variogram. To understand the impact of geological features clearly, variograms using synthetic data were created.

Synthetic Variogram

In many instances, the estimated variogram exhibits periodic behavior. As shown in the Fig. 3.22, this periodic behavior is expressed as hole effects. The hole effects are commonly found in variograms of the vertical data. It is believed that the hole effects occur because vertical data consist of several different layers having similar properties.

Using simple synthetic data, one can simulate vertical data that are similar to real vertical data and using those data one can define the boundaries of a layer. Fig. 3.23 shows the variogram and the synthetic data of two main layers. Each main layer consists of 3 sublayers. Sublayer "a" is assigned a value 1, sublayer "b" is assigned a value 2 and sublayer "c" is assigned a value 3. All the sublayers have the same thickness of 10 feet. The variogram changes the slope at 10 feet thickness, it reaches a maximum value at 20 feet which is the boundary of sublayer "b" and reaches a minimum value at 30 feet, which is exactly the thickness of the first main layer. In this variogram, we still can see very clearly the boundaries of the sublayers.

In Fig. 3.24, we use the same synthetic data model as for Fig. 3.23 but we use different thicknesses; sublayer "a" is 10 feet, sublayer "b" is 20 feet, and sublayer "c" is 15 feet. The variogram is different compared to the previous model. We see that the variogram reaches the maximum value at the boundary of sublayer "b" and reaches a minimum value at the boundary of sublayer "c". However, the evaluation of individual sublayers becomes increasingly difficult.

In Fig. 3.25, we try different variation in values. Using synthetic data from Fig. 3.23, we assign a value of 1 for sublayer "a" and a value of 0 for other sublayers. We repeat the procedure by assigning a value one to sublayers "b" and "c" respectively. Then the estimated variogram is obtained for each sublayer which is assigned a value of "1" to see the relationships between the sublayer to other

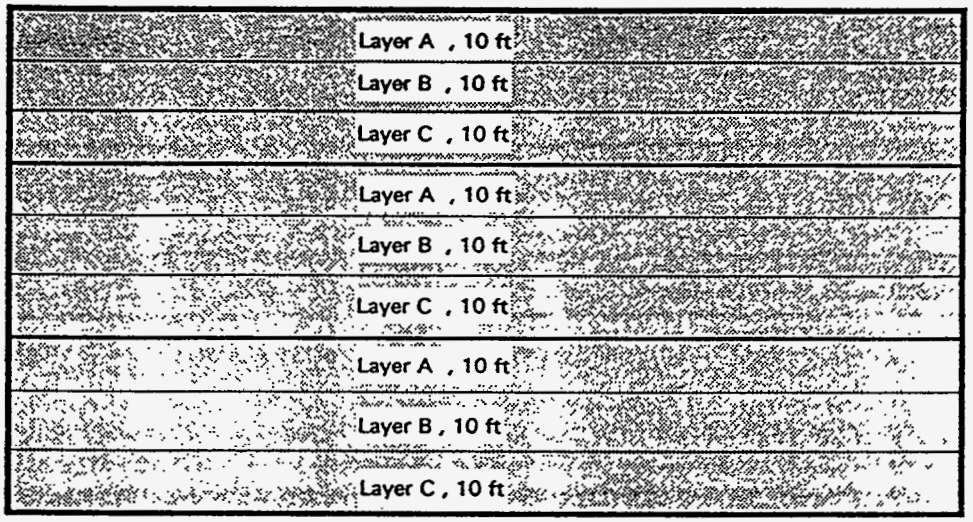

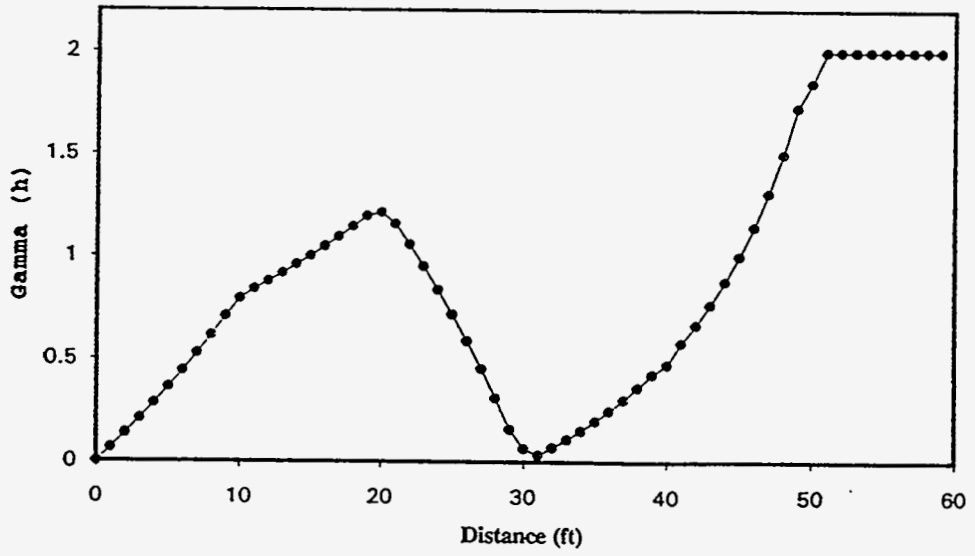

Figure 3.23: Synthetic data and variogram of synthetic data of 3 uniform layer thickness.

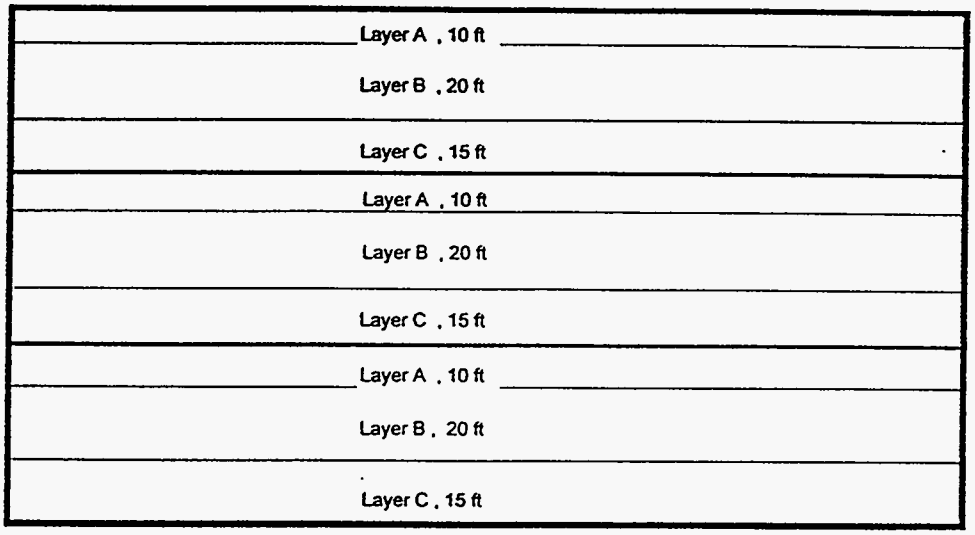

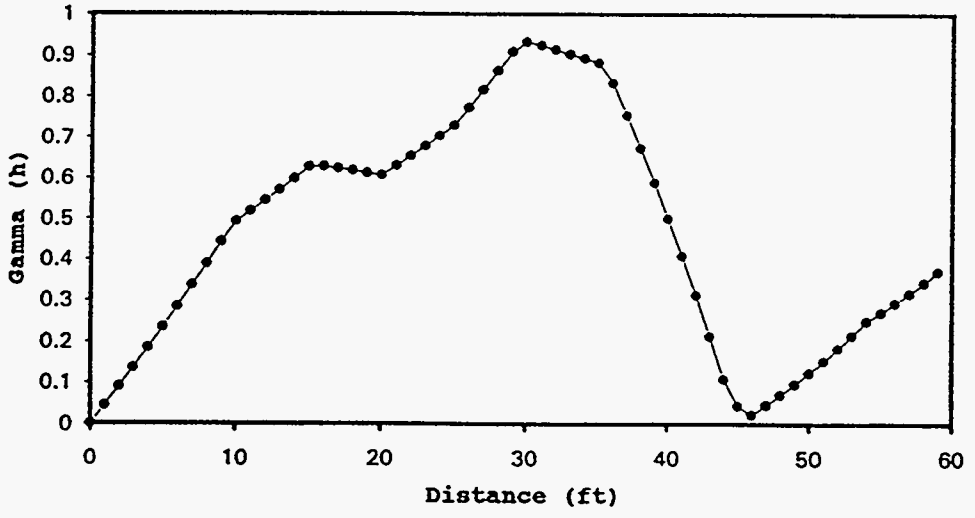

Figure 3.24: Synthetic data and variogram of synthetic data of 3 nonuniform layer thickness.

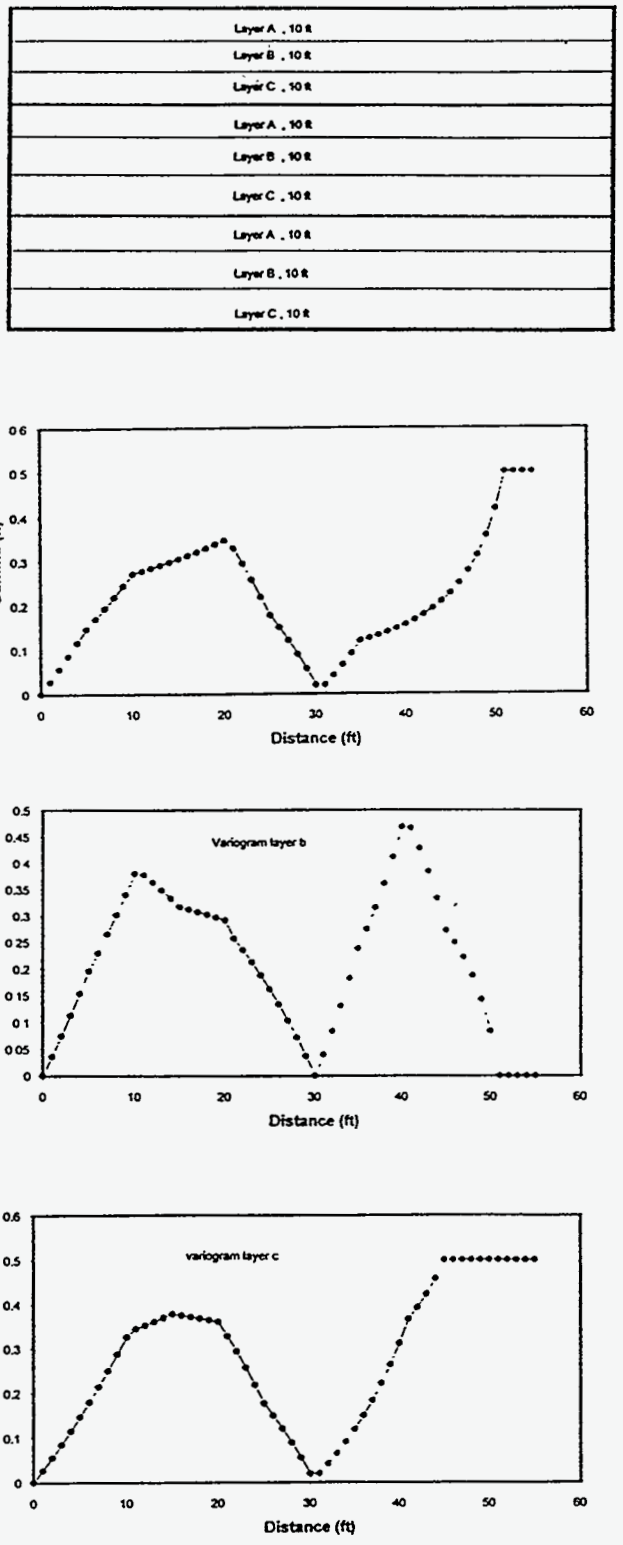

Figure 3.25: Synthetic data and variogram of synthetic data of 3 uniform sublayer thickness.

sublayers in the main unit. From Fig. 3.25, it can be seen that for sublayer "a", the variogram changes the value at 10 feet then reaches minimum at 30 feet which is exactly the boundary between main layers. In the variogram of sublayer "b", we can see the variogram reaches the maximum at 10 feet and can see the change in the variogram value at 20 feet which is the end of sublayer "b". The variogram reaches the minimum value at 30 feet which is the thickness of individual main layer. For sublayer "c", the only thing we can discern is the thickness of the main layer.

In general, we can obtain the thickness of the sublayers in the variogram if the thickness of each sublayer is the same. We still can define the boundary of the sublayer if the thicknesses are different. However, we may obtain nonunique solutions if the thicknesses of individual sublayers are not known. In the following section, we compare the synthetic variogram with real data.

Comparison Between Synthetic vs. Estimated Variogram

To compare synthetic and estimated variograms, we use the variogram of Holeman #1 in the Fig. 3.26. In the Fig. 3.26 it is shown that the variogram of synthetic data reaches the minimum value at a lag distance of 15 feet. This pattern is shown in the variogram of Holeman #1. In the variogram Holeman #1, the variogram reaches the minimum value at distance between 14 feet to 15 feet. Based on the conclusions from the previous section, the average thickness of a layer in Holeman 1 is 15 feet. The information about the sublayers is difficult to observe.

In general, the advantage of using synthetic variograms is that one can define the average thickness of the layers if the variogram shows the hole effects clearly. The cyclical unit thickness can be easily obtained. However, the individual sublayers are difficult to obtain using the existing technique. This technique needs to be refined further to obtain that additional information.

Modeling of Variograms

Once the variogram is estimated based on the collected sample data, the next step is the modeling of the variogram using certain functions. In modeling the estimated

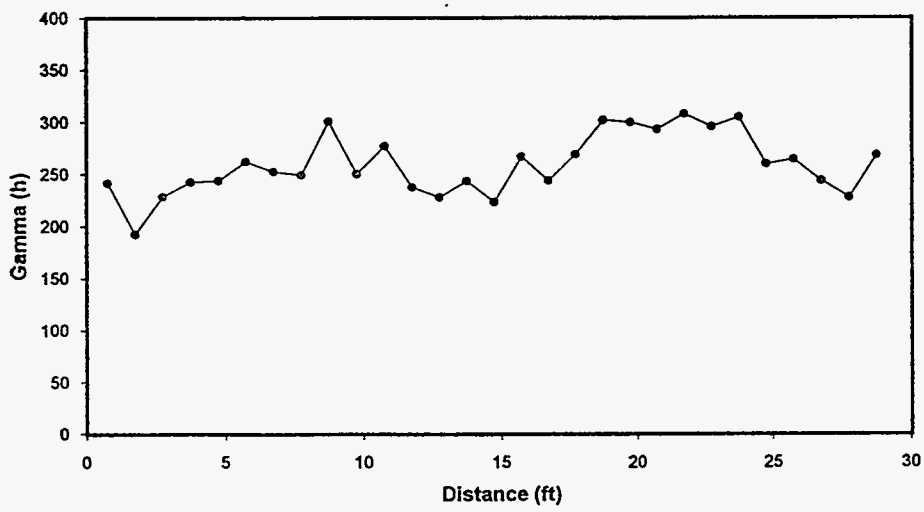

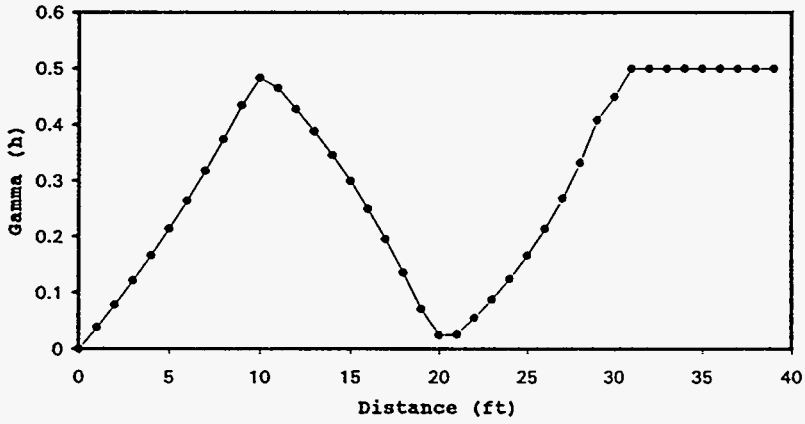

Figure 3.26: Comparison between estimated variogram of Holeman #1 with synthetic variogram.

variogram, it is important to capture the basic features observed.

We have already sub-divided the channel-fill subfacies into three segments, they are the upper, middle and lower subfacies. The upper channel-fill subfacies are assigned a value of 1, middle channel-fill is assigned a value of 2 and a value of 3 for the lower channel. Using these values, the variograms are estimated for all three subfacies, and are modeled using conventional methods.

The analysis shown in this part will be used in simulating the reservoir properties description. The detailed procedure used for simulating the values of the variables is explained in the next section.

3.6 Spatial Simulation Of Reservoir Properties

Before discussing the detailed simulation of geologic and petrophysical properties, we first briefly discuss the simulation techniques used in this simulation.

3.6.1 Background

In this section, two conditional simulation methods are discussed in more detail: 1) the sequential indicator simulation technique used to generate geological unit description in the reservoir, and 2) the simulation annealing method that is used to create reservoir properties distribution.

Sequential Indicator Simulation

This method is based on indicator variables and the simulation takes place in a sequential manner.

The sequential steps in this method are as follows:

•define indicator variables

•define univariate and bivariate statistics

•conduct sequential indicator simulation. Indicator simulation is a procedure which eliminates some of the drawbacks present in conventional kriging method. The indicator function can be written as:

$$i(\vec{\omega};V_{f,k}) = \begin{Bmatrix} 1, V(\vec{\omega}) \le V_{f,k} \\ 0, V(\vec{\omega}) > V_{f,k} \end{Bmatrix} \qquad (3.1)$$

The value $V_{f,k}$, is called a threshold value. The indicator variable is a binary function and takes only two values, 0 and 1. The number of values of indicator variables will depend on the number of threshold values chosen. Each random variable will be associated with an identical number of indicator variables. For example, if we choose three threshold values, each random variable will be defined in terms of three indicator values, one at each threshold.[3.11]

Once the indicator values are defined for the sample data, the next step is to define the univariate and bivariate statistics. These are prior distribution function, non-centered covariance, covariance, and indicator variogram.

The next step is sequential indicator simulation. In the simulation algorithm, the simulation takes place in a sequential manner, where all the unsampled locations are visited once by selecting a random path by which the sequence in which the points to be visited is established. In simulating successive nodes the previously-simulated node is also used. Once a node to be simulated is selected, the value of indicator function for a given threshold can be estimated by solving the equations which are based on simple or ordinary kriging. The number of estimations will depend on the number of thresholds. All the samples are visited to estimate the indicator value. These indicator values represent the posterior probability distribution of the variable at that location. Using a random selection method, we can assign a value at that point using the posterior distribution function. For example, we can assign facies 1, 2 or 3 at a particular location.

This method is not restricted to variables which can take continuous values. It can also be extended where a variable can only take finite number of values (such as facies distribution). For details, see Reference 3.11.

Simulated Annealing

To apply this technique requires that the system is divided into three categories: the objective function, which represents the "energy" of the system and is also the function to be minimized; the control parameter, which defines the rate at which the

system will reach equilibrium; and the interchange mechanism, which is a finite set of perturbations to the variables of the system which tends to result in a change in the objective function.

The goal of simulated annealing is to find a configuration of variables that will yield a global minimum of the objective function. Changes are applied to the system through the interchange mechanism, and the objective function is then evaluated; an increase in the magnitude of the objective function may or may not be accepted according to the probability function proposed by Metropolis et al.[3.12] Perez[3.13] presented a discussion of the use of Metropolis function.

The specification constraints in the simulated annealing method are the conditioning data, the distribution function, and the semi-variogram models for several directions. In the first set of constraints, the conditioning data values are assigned at specific locations. The conditioning data remain fixed at the specific locations throughout the conditional simulation. Mathematically, the constraints corresponding to a number, N_c, of conditioning data that can be expressed as,

$$V(\vec{\omega}_{c,l}) = V_c(\vec{\omega}_{c,l}) \tag{3.2}$$

where V_c is the value of the conditioning data and $\vec{\omega}_{c,l}$ for $l = 1, \ldots, N_c$ is the set locations corresponding to the conditioning data. The conditioning data are usually taken at a well location and are data such as wireline log values or core data.

The specified discrete cumulative distribution function, F_o, for the simulation should obey the following constraint[3.13]

$$F(V_{f,k}) = F_o(V_{f,k}) \tag{3.3}$$

For $k = 1,\ldots, N_f$. The cumulative distribution function represents the probability that the variable is smaller that a given value, and must be a strictly increasing function. In practice, the discrete cumulative distribution function is given by Eq. 3.4.

$$F(V_{f,k}) = \frac{1}{N_f}\sum_{i=1}^{N_f} i(\vec{\omega}_i V_{f,k}) \tag{3.4}$$

where N_f is the number of classes used to discretize the cumulative distribution function. The third set of constraints is the semi-variograms. The semi-variogram models specified in the conditional simulations are denoted by γ_o and require that

$$\gamma_s\left(\vec{h}_{l,i}\right) = \gamma_o\left(\vec{h}_{l,i}\right) \tag{3.5}$$

where, as noted previously, i is the direction of the variogram and l is the lag distance for that particular direction.

The objective function is the function to be minimized with the simulated annealing method. The objective function is defined as a function of the difference between the sample semi-variograms of the simulation variable and the required semi-variogram models. Therefore, by minimizing this objective function, the requirement in Eq. 3.5 can be satisfied.

The objective function, E, is defined as

$$E_k = \frac{1}{E_o}\sqrt{\sum_{i=1}^{N_d}\sum_{l=1}^{N_{h,i}}\left[\frac{\gamma_s^k\left(\vec{h}_{l,i}\right) - \gamma_o\left(\vec{h}_{l,i}\right)}{\gamma_o\left(\vec{h}_{l,i}\right)}\right]^2} \tag{3.6}$$

where, the index k refers to the iteration number within a step and E_o is a normalizing constant equal to[3.13]

$$E_o = \sqrt{\sum_{i=1}^{N_d}\sum_{l=1}^{N_{h,i}}\left[\frac{\gamma_s^0\left(\vec{h}_{l,i}\right) - \gamma_o\left(\vec{h}_{l,i}\right)}{\gamma_o\left(\vec{h}_{l,i}\right)}\right]^2} \tag{3.7}$$

In Eq. 3.7, $\gamma_s^0\left(\vec{h}_{l,i}\right)$ are the semi-variograms of the simulation variable at initial conditions calculated from the initial distribution of the variable. The purpose of the normalizing constant used in Eq. 3.6 is to assign a value of one to the objective function at the initial conditions for any distribution or specifications. In simulated annealing, the Metropolis condition is used to calculate the probability of the transition between states of the objective function at a given value of control parameter analogous to the temperature of the system. The Metropolis condition is given by

$$P(\Delta E^k, T^r) = \begin{cases} 1, & \Delta E^k \le 0 \\ \exp\left(\dfrac{-\Delta E^k}{T^r}\right) & \Delta E^k > 0 \end{cases} \tag{3.8}$$

where, the index k refers to an iteration within a step represented by the index r. In Eq. 3.9, the change of the objective function, ΔE^k, due to one interchange is

$$\Delta E^k = E' - E^k \tag{3.9}$$

where E' is the new objective function after the interchange and E^k is the objective function for iteration k within a step. The control parameter, T^r, in Eq. 3.8 is calculated according the following equation

$$T^r = \alpha T^{r-1} \tag{3.10}$$

where the index r is the step number, and α is the convergence rate factor. The convergence rate factor is a constant value in the range $0 < \alpha < 1$ throughout the simulation.

Each interchange is accepted or rejected depending on the Metropolis condition. The temperature is lowered in a stepwise manner after a fixed number of swaps is accepted. The program terminates when the objective function reaches a certain minimum value.

3.6.2 Property Simulation

The ultimate goal of this section is to generate the three-dimensional descriptions of reservoir properties which are constrained by both geological and petrophysical information. At present, we do not have a method which can simultaneously incorporate both the geological and petrophysical constraints. Therefore, as an approximation, we used a two-step process. In the first step, we created a geologic description which is consistent with the three channel-fill subfacies described in the previous chapter. In the second step, we created a three-dimensional petrophysical properties description by superimposing the petrophysical properties on the geological description.

Geologic Description

Using Sisimpdf program from the GSLIB software,[3.11] we created the geological description. To create the geological description, we went through several steps discussed below.

The first step is selecting the conditional data. The conditional data used in this case are a 10-well data set and a 5-well data set that are already selected based on channel-fill subfacies. The second step is obtaining the vertical and the horizontal estimated and model variograms for each subfacies. The parameters used and model variograms are shown in Table 3.5. We only have one horizontal permeability variogram at a particular horizontal location. It is also known that the actual correlation in the horizontal direction is longer than the correlation range along vertical direction. We use the same correlation length in the horizontal direction for lower and upper channel-fill subfacies. For middle channel-fill subfacies, the variogram range is inferred from geologic description. The individual parameters are adjusted to ensure that the anisotropic model for each subfacies satisfied the condition of positive definiteness.

After all the data are input, the simulation is run for three realizations, two of three realizations are from 10-well data set as conditional data and the other for 5-well data set as conditional data. One of the realizations is presented in Fig. 3.27. Fig. 3.27 shows a vertical cross section between Holeman #5 and Holeman #8 wells.

Description of Petrophysical Properties.

Permeability

In generating the petrophysical properties, it is important that we honor the geologic description. To assure that the properties generated will be consistent with the facies description, we use a "filtering" process. In this process, we generate the petrophysical properties for each facies at every grid location. To achieve this, we will have to run the conditional simulation program to generate petrophysical properties for each facies separately. We use the simulated annealing program for this purpose.

Name	direction	model	nugget	sill	range	periodic length
10-well data set						
Splays	x	spherical	0	0.144	100	
	y	spherical	0	0.144	100	
	z	spherical	0	0.144	20	
Upper channel	x	spherical	0	0.23	100	
subfacies	y	spherical	0	0.23	100	
	z	spherical	0	0.23	6.5	
		cosine		0.018		15
Middle channel-fill	x	spherical	0	0.2	20	
subfacies	y	spherical	0	0.2	20	
	z	spherical	0	0.2	0.4	
		cosine		0.003		16
Lower channel-fill	x	spherical	0	0.144	100	
subfacies	y	spherical	0	0.144	100	
	z	spherical	0	0.144	5	
		cosine		0.016		15

Table 3.5: Summarized variogram models of the channel-fill subfacies.

Figure 3.27: Vertical facies cross section of Holeman #5 and Holeman #8 wells.

In our case, since we have used three channel-fill subfacies and splay facies for geologic description, we will have to run the simulated annealing program four times. The splay facies and each subfacies may have separate spatial relationships as well as a separate histogram function as explained in the previous section. Once the simulation is run for each of the facies separately, we have four permeability values at each grid point corresponding to each subfacies. When "filtering", we will accept only one value at a given grid point based on the simulated subfacies at that point. Fig. 3.28 shows the filtering process. This way, our subfacies description will be preserved. Also, the permeability distribution as well as the variograms for individual subfacies will be honored. The step to generate permeability distribution is the same as the step to generate the geological channel-fill subfacies distribution. We separate each channel-fill subfacies to obtain the estimated permeability variogram for each subfacies. For particular subfacies, we use the permeability value that already exists in that subfacies and assign a missing value for other subfacies.

The estimated permeability variograms are modeled using conventional methods. To generate the model of the horizontal permeability variogram, we used the same procedure as facies model. One difference is that in simulated annealing program, we do not need to satisfy the condition of positive definiteness.

The simulated annealing conditional simulation is run for six different realizations, 3 realizations are based on 10-well data set and 3 of the realizations are from 5-well data set. One of the realization results is presented in the Fig. 3.29. Fig. 3.29 shows the results of the upper cross section of middle subfacies.

By running the program separately for each subfacies, we can honor the histogram as well as the variogram for permeability distribution for each subfacies. After completing the four simulations, we will have four permeability values at each grid point corresponding to each of the subfacies. By "filtering" these four simulations through the base geologic description at each grid point, we will accept an appropriate permeability value depending on which facies are present at a particular grid block. For example at certain grid location, if medium channel-fill subfacies are present based on geologic description, we will accept the permeability value corresponding

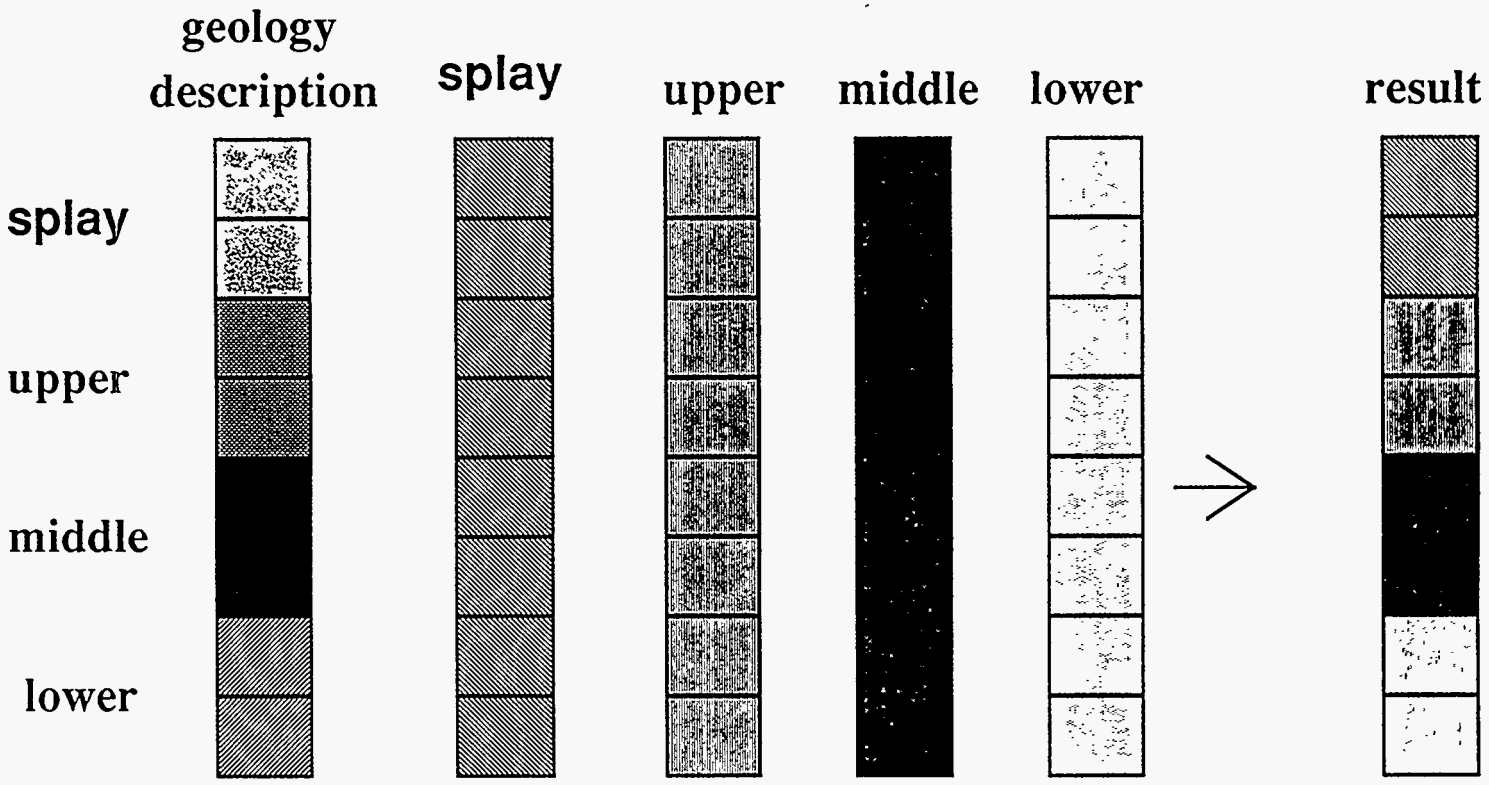

Figure 3.28: Filtering process.

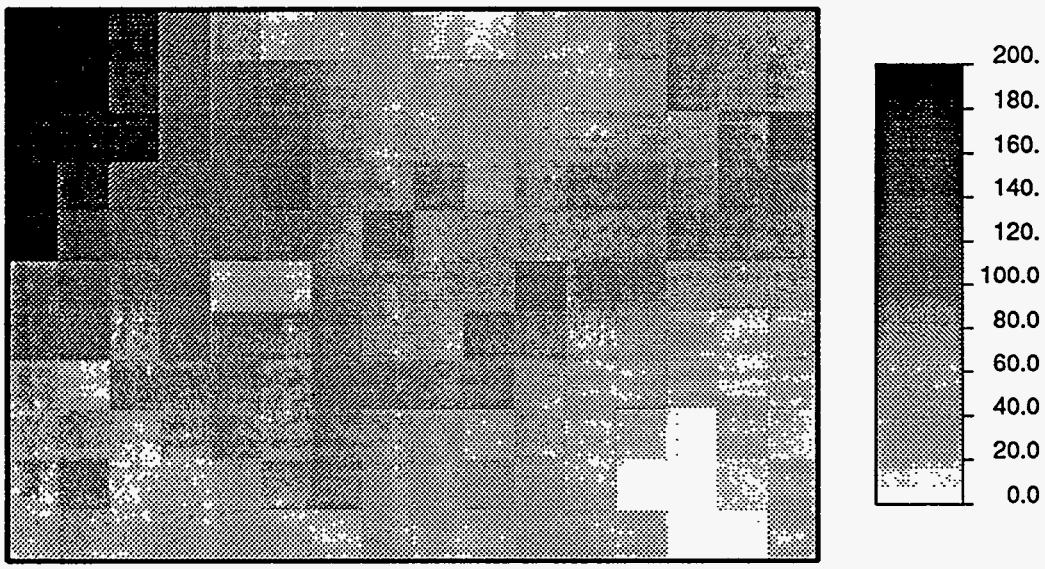

Figure 3.29: Upper cross section of middle channel-fill subfacies.

to that subfacies. After the assignment of permeabilities at each grid location is completed, we would have created a petrophysical properties description which is consistent with the underlying geologic description.

Porosity

The porosity data are collected from well logs and core plugs. Since the information collected is limited and we do not have enough data to generate porosity distribution using geostatistical techniques, we use the correlation between porosity and permeability to generate the porosity values.

By using this method the porosity distribution is relatively narrow, but consistent with the observed data. By generating porosity values based on permeability data, we honor the local relationship between the two variables as observed based on the well data. The porosity and the filtered permeability values will be used in the next section in order to define the flow performance of reservoir.

3.7 Flow Simulation

In this section, we investigate the effect of uncertainties with respect to input data on the flow performance of the reservoir. For this purpose, we will treat the outcrop subsurface as a representation of the actual reservoir. We will use both the descriptions created using the 10-well data and 5-well data sets. This allows us to evaluate the impact of additional information on the reservoir description.

Using the ECLIPSE 100 flow simulator, we obtained the model of oil production of the study area. The reservoir and flow properties data used for simulation purposes are based on typical data observed in Burbank field. The petrophysical properties are included in Table 3.6. The permeability and porosity values are generated using the method discussed in the previous section.

The permeability data selected to be used to generate the flow performance models are realizations of the 10-well data set and the 5-well data set. Table 3.7 shows the realizations constructed for both well data sets. As shown in the Table 3.7, for 10-well data set, two realizations were constructed using facies description and one

PVT oil data

Rs (Mscf/stb)	Pressure (psia)	Bo (Rb/stb)	Uo (cp)
0	14.7	1.0249	2.486
0.022	50	1.0363	2.299
0.031	100	1.0386	2.236
0.039	150	1.0409	2.178
0.057	250	1.0471	2.059
0.078	350	1.0543	1.942
0.099	450	1.0617	1.837
0.16	700	1.0849	1.589
0.229	950	1.1128	1.38
0.25	1024	1.1215	1.326
	1200	1.1197	1.341
	1250	1.1192	1.345
	1500	1.1168	1.366
	1750	1.1146	1.386
	2000	1.112	1.407

PVT gas data

Pressure (Psi)	Bg (Rb/Mscf)	Ug (cp)
14.7	195.3693	0.0086
50	56.5568	0.0099
100	28.1765	0.0108
150	18.7435	0.0112
250	11.1524	0.0116
350	7.8864	0.0118
450	6.0781	0.0119
700	3.7942	0.0124
950	2.7078	0.0129
1024	2.4887	0.0131
1200	2.0158	0.0136
1250	1.9608	0.0143
1500	1.6858	0.015
1750	1.4108	0.0157
2000	1.1358	0.0164

SGOF

Sg	Krg	Krog	Pcog
0	0	1	0
0.025	0.00098	0.8574	0
0.05	0.0039	0.729	0
0.1	0.0156	0.512	0
0.2	0.0625	0.216	0
0.25	0.0977	0.125	0
0.3	0.1406	0.064	0
0.35	0.1914	0.027	0
0.4	0.25	0.008	0
0.425	0.2822	0.0034	0
0.45	0.3164	0.001	0
0.5	0.3906	0	0
0.55	0.4727	0	0
0.6	0.5625	0	0
0.65	0.6602	0	0
0.7	0.7656	0	0
0.75	0.8789	0	0
0.8	1	0	0
1	1	0	0

SWOF

Sw	Krw	Krow	Pcow
0	0	1	0
0.2	0	1	0
0.225	0.00006	0.8574	0
0.25	0.0005	0.729	0
0.3	0.004	0.512	0
0.35	0.0135	0.343	0
0.4	0.032	0.216	0
0.425	0.0456	0.1664	0
0.45	0.0625	0.125	0
0.5	0.108	0.064	0
0.55	0.1715	0.027	0
0.6	0.256	0.008	0
0.65	0.3645	0.001	0
0.675	0.4287	0.00012	0
0.7	0.5	0	0
1	0.5	0	0

Table 3.6: Burbank field reservoir properties data.

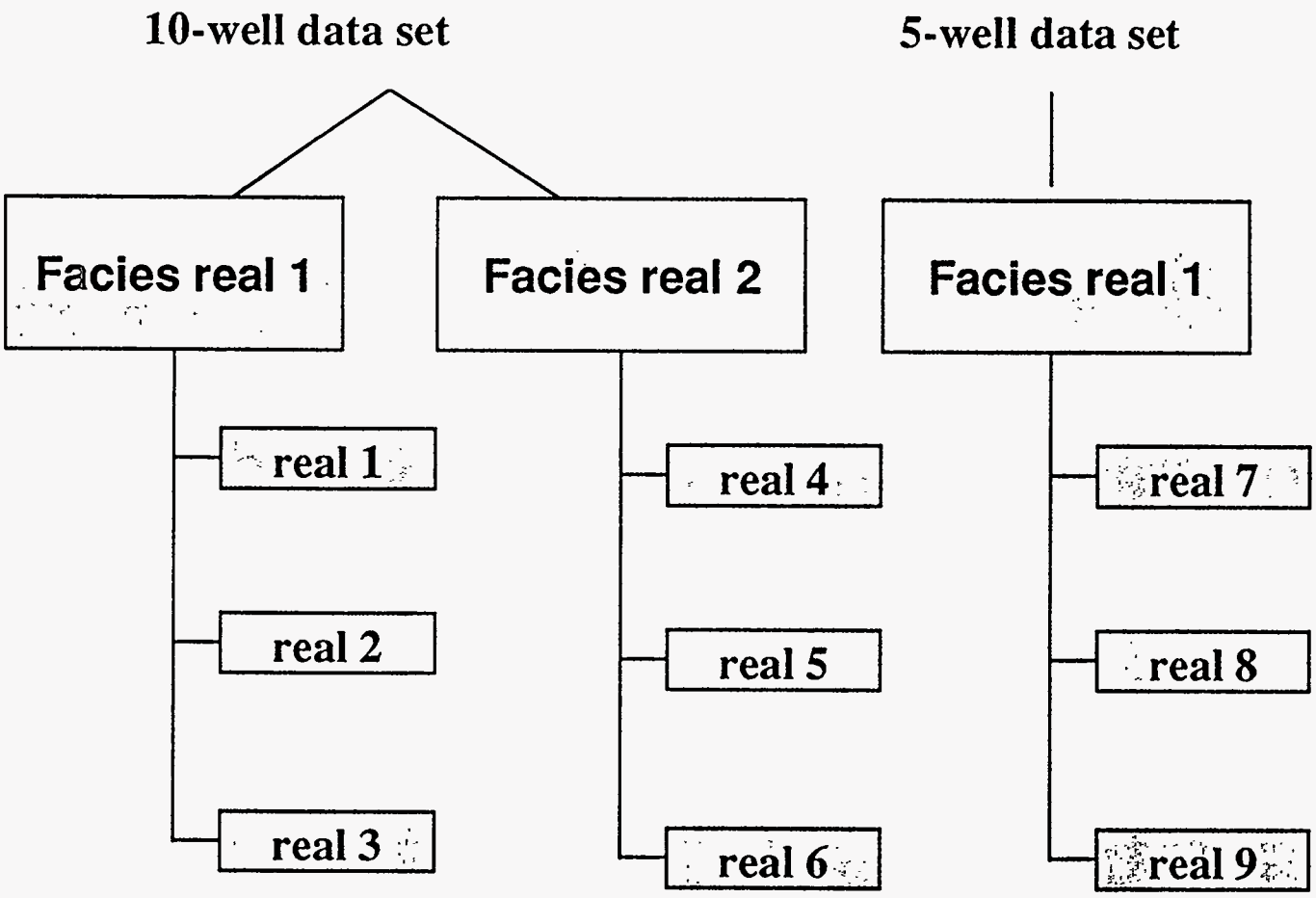

Table 3.7: The results of realization constructed of 10-well data set and 5-well data set.

realization for the 5-well data set. For each of the facies descriptions, we generated three realizations for varying petrophysical properties. Especially for realization 4 of the 10-well data set, we also investigated vertical averaging of permeability for one (realization 4), two and three feet vertical intervals. The purpose of using the average permeability data for certain average distance is to observe the impact of the vertical averaging on oil production. We use the arithmetic average of both permeability and porosity values. In a typical reservoir simulation, we cannot use detailed vertical description. We wanted to investigate the impact of loss of vertical detail on the flow performance. In another case, we investigate the impact of vertical permeability on the flow performance by assuming that the permeability in the z-direction is one half of the permeability in the x- and y-directions.

We conducted the simulation in two stages. In the first stage, the reservoir was produced using primary depletion. After the pressure reached close to the bottom hole pressure, water flooding was initiated. We set the bottomhole pressure at 500 psia; then we injected water into reservoir to see the increase in oil production. The wells used as production wells are Holeman #1, #3, #6, #8, and #10, and the wells used as injection wells are Holeman #2, #4, #5, #7 and #11.

In our study, the oil from each production well was produced using the maximum flow capacity. Typical time required to produced all the oil, using ECLIPSE flow simulator, is only 35 days of production. The purpose of using the maximum oil flow was to limit the computation time.

When the oil is produced during primary depletion the pressure dropped rapidly. When it approached close to 500 psia, the water flooding method was applied, and water flooding was conducted for additional 15 days of production.

Fig. 3.30.a, Fig. 3.30.b, Fig. 3.31.a, Fig. 3.31.b and Fig. 3.32 show the plots of the total oil production vs. total liquid production, in which the x-direction is the normalized cumulative liquid production (production divided by 12,000 bbls maximum amount produced for all realization), where liquid means oil and water, and the y-direction is normalized cumulative oil production.

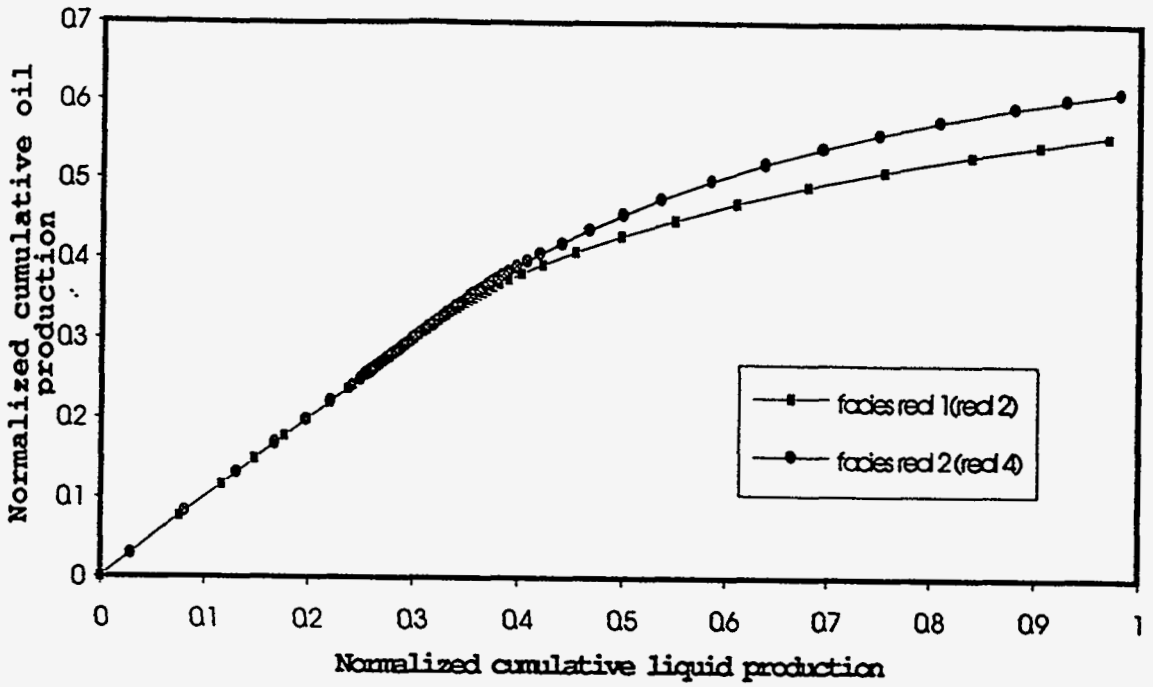

Figure 3.30a: Normalized cumulative oil production vs. normalized cumulative liquid production from two different facies description.

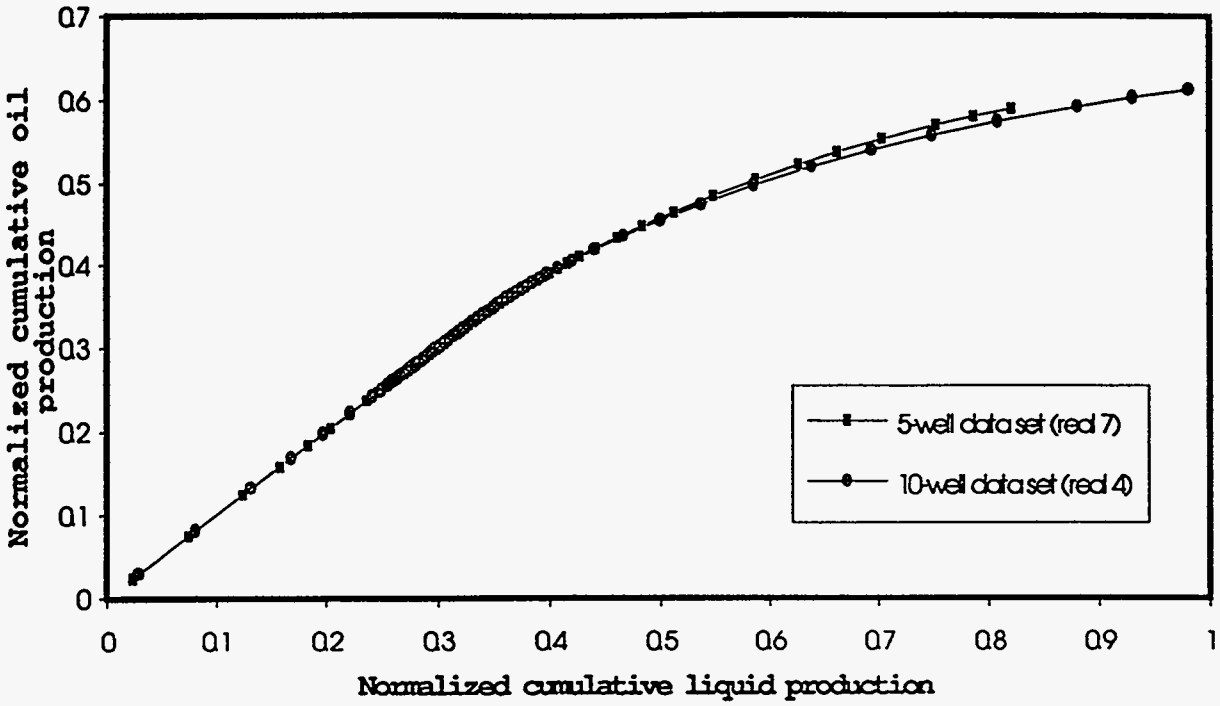

Figure 3.30b: Normalized cumulative oil production vs. normalized cumulative liquid production from two different petrophysical properties.

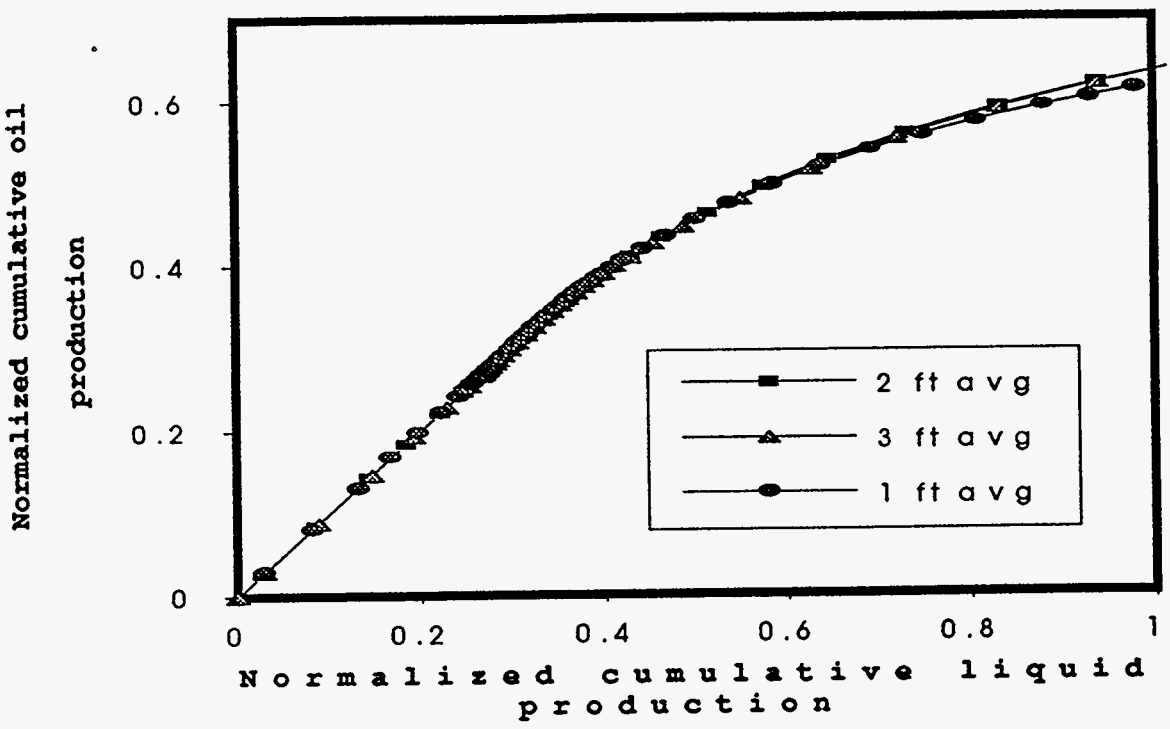

Figure 3.31a: Normalized cumulative oil production vs. normalized cumulative liquid production from two different facies description of 10-well data set.

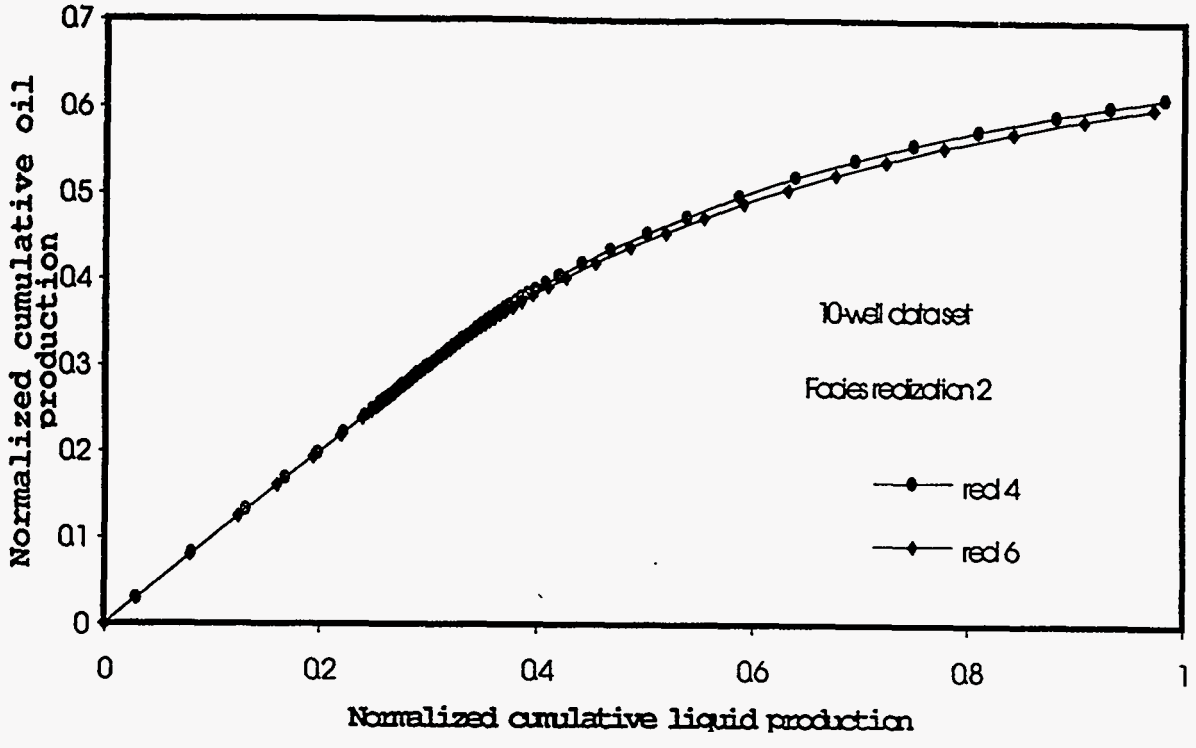

Figure 3.31b: Normalized cumulative oil production vs. normalized cumulative liquid production from two different realizations of 1, 2 and 3 feet vertical averaging.

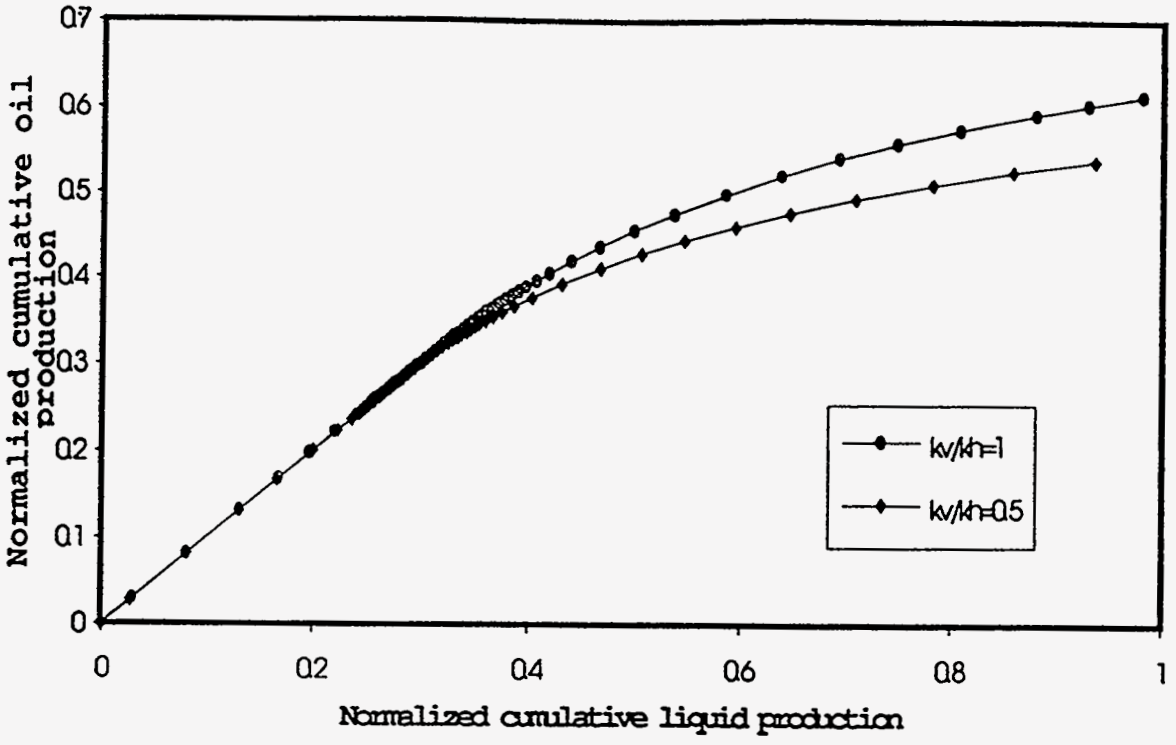

Figure 3.32: Normalized cumulative oil production vs. normalized cumulative liquid production from two different vertical permeability.

Fig. 3.30.a shows the impact of different realization for two different facies description. As can be seen, for a given well data set, the facies description does have an impact on reservoir performance. The performance after initiation of water flood is different for the two realizations. in contrast, figure 3.30.b shows the impact for the two different petrophysical properties realizations for the same facies description. Although there is a difference in the performance, it is not as significant as in Fig. 3.30.a. This indicates that the petrophysical properties description is secondary to the facies description in terms of impact on the flow performance.

Fig. 3.31.a shows the effect of vertical averaging on the flow performance for a given realization. As expected, as the permeability is vertically averaged, the performance becomes more optimistic. Surprisingly, however, the effect of 2 and 3 feet averaging is not significant. May be, additional averaging will eventually lead to further optimistic results.

Fig. 3.31.b shows the importance of well information on the description. As can be seen, the difference between the two realizations is very small. It appears that even 5-well data set is sufficient for reservoir description purposes. Additional information from 5-well data set does not lead to further reduction in reservoir uncertainty with respect to reservoir description.

Fig. 3.32 shows the effect of vertical permeability on the flow performance. As can be seen, the variation in the vertical permeability has the most impact on the reservoir performance. By reducing the vertical permeability, the effect of vertical heterogeneity is accentuated. Considering that vertical permeability may not be known, this effect points out the major uncertainty in the reservoir description process.

It should be noted that simulation results are based on very limited number of simulations. Further validation is needed by conducting additional simulation runs.

3.8 Conclusions

3.8.1 Geological Interpretation

A sedimentological characterization of the Bartlesville Sandstone is defined based on facies and subfacies subdivisions, which are identified as architecture elements arranged in an architectural hierarchy. Two facies are present in the study area: channel-fill facies and splay facies. The channel-fill facies are subdivided into lower, middle, and upper subfacies, each of which shows different patterns in grain size and sedimentary structures. Architectural elements are organized into a hierarchy of 5 scales. At the largest scale of rock volume the Bartlesville Sandstone in the study area is comprised of a group of 4 discrete genetic intervals (DGI). The second level is the individual DGI. The third level is represented by an individual facies within a DGI. Only one facies was encountered per DGI; three are channel-fill facies and one is a splay facies. Other contiguous genetically-related facies are not present in the study area because of its geographic limits. The fourth level is described here for the channel-fill facies only, and is represented by a subdivision of 3 subfacies, lower, middle and upper. The fifth level is represented by the different stratification patterns and scales within a channel-fill subfacies.

Facies and subfacies do not show diagnostic signatures on well log patterns. Conventional well logs, by themselves, do not provide enough information for the identification of contacts between DGI's, facies or subfacies, but interpretations can be considerably improved when these logs are combined with cores, outcrop or microscaled-log information.

Heterogeneities represented by mudstone drapes and intercalations can represent barriers at very small scales, but mostly they are the sites for baffles. It is possible that the Bartlesville Sandstone in the study area is one whole flow unit in the horizontal sense. After all, its average thickness represent one that is not uncommon to hydrocarbon reservoirs.

3.8.2 Engineering/Integrated Interpretation

In this study, we constructed a detailed outcrop description using appropriate geostatistical techniqueS. We developed a procedure for incorporating the geological and petrophysical information in constructing the reservoir description.

Using the generated reservoir description, we investigated the impact of reservoir heterogeneties on the flow performance. Based on the investigation, the following conclusions can be derived:

•Collection of detailed outcrop data is useful in understanding and supplementing detailed reservoir description. The univariate statistical analysis indicates that the permeability distribution for individual geological units is very similar to each other; however, the permeability distribution was different for individual subfacies. This indicates that the subfacies may have distinct properties; but the overall cyclical distribution is repeated in each cycle.

•The vertical variograms for both permeability and gamma rays exhibit hole effectS. These hole effects are consistent with the geological observation of cyclicity in the environment. This indicates that variogram may be a quantitative tool in identifying basic geologic features.

•Analysis of synthetic variograms indicates that the average thickness of individual units can be quantified using the variograms; however, information about the sublayers may be difficult to quantify due to non-unique nature of variogram values.

•A method was developed to capture both geologic and petrophysical features in a consistent manner. The method is a combination of facies generation followed by filtering of petrophysical properties consistent with underlying geologic description. The method preserves both the geologic and petrophysical features for individual subfacies.

•Simulated annealing was able to reproduce the model variograms for petrophysical properties. The only exception was the upper subfacies. This may be due to limited conditional data for that upper subfacies.

•Based on limited simulation runs, it was observed that:

•The effect of facies description is more significant than the effect of petrophysical properties description.

•Vertical averaging results in optimistic flow performance.

•The vertical permeability variation can significantly alter the flow performance. This may point out one of the most significant uncertainties in evaluating the reservoir behavior.

Symbol

C = correlation coefficient

Cnl = conpesated neutron log

Dil = dual induction log

DGI = discrete genetic interval

E = objective function

k = iteration number

N_p = number of pairs

F = cumulative distribution function

Fms = formation micro scanner

γ_s^0 = varigram at initial conditions

T = control parameter

V_c = conditioning data

$V(\vec{\omega})$ = data at location

$V(\vec{\omega}_j + \vec{h}_{i,i})$ = data at location $(\vec{\omega}_j + \vec{h}_{i,i})$

ϕ = porosity

3.1 Kerr, D. R.: Private Communication (1992).

3.2 Kerr, D. R., and Jirik, L. A.: "Fluvial Architecture and Reservoir Compartmentalization in the Oligocene Middle Frio Formation," South Texas: Gulf Coast Association of Geological Societies, v. XL (1990) pp 8.

3.3 Walker, R. G.: "Facies Models," Geoscience Canada Reprint Series 1 (1984) pp 317.

3.4 Reineck, H. E. and Singh, I. B.: *Depositional Sedimentary Environments,* Springer-Verlag, New York, New York (1980) pp 551.

3.5 Galloway, W. E. and Hobday, D. K.: "Terrigeneous Clastic Depositional Systems," *Applications to Petroleum, Coal, and Uranium Exploration,* Springer-Verlag, New York, New York (1983) pp 423.

3.6 Jackson, R. G., II: "Depositional Model of Point Bars in the Lower Wabash River," *Journal of Sedimentary Petrology,* v.46 (1976) pp 579-594.

3.7 McGowen, J. H. and Garner, L. E.: "Physiographic Features and Sedimentation Types of Coarse-Grained Point Bars: Modern and Ancient Examples," *Sedimentology,* v. 14 (1970) pp 77-111.

3.8 Allen, J. R. L: "Studies in Fluviatile Sedimentation: Bars, and Bar Complexes and Sandstone Sheets (Love Sinuosity Braided Streams) in the Brownstones (L. Devonian), Welsh Borders," *Sedimentary Geology,* v. 33 (1983) pp 237-293.

3.9 Jackson, R. G., II: "Preliminary Evaluation of Lithofacies Models for Meandering Alluvial Streams," *in* Miall, A. D., ed., *Fluvial Sedimentology: Geological Society of Canada,* Calgary, Alberta, Canada (1978) pp 577-586.

3.10 Galloway, W. E.: "Meandering Streams-Modern and Ancient," *in* Flores, R. M.; Ethridge, F. G.; Miall, A. D.; Galloway, W. E. and Fouch, T. D., eds., *Recognition of Fluvial Depositional Systems and Their Resource Potential,* SEPM Short Course No. 19, SEPM, Tulsa, Oklahoma (1985) pp 146-166.

3.11 Deutsch, C. V. and Journel, A. G.: *GSLIB: Geostatistical Software Library* , v. 2.0, Standford Center for Reservoir Forecasting, Standford University, Standford, California (1991).

3.12 Metropolis, N., Rosenbluth, A. W., Rosenbluth, M. N., Teller, A. G. and Teller, E.: "Equation of State Calculations by Fast Computing Machines," *The Journal of Chemical Physics,* (June, 1953) pp 1087-92.

3.13 Perez, G.: Stochastic Conditional Simulation for Description of Reservoir Properties," Ph.D. dissertation, The University of Tulsa, Tulsa, Oklahoma (1991).

3.14 Martinez, G.: "Reservoir Heterogeneities in a Portion of the Bartlesville Sandstone (Desmoinian), Mayes County, Northeastern Oklahoma," M.S. thesis, The University of Tulsa, Tulsa, Oklahoma (1993).

3.15 Azof, I.: "Geostatistical Analysis of Bartlesville Sandstone Outcrop," M. S. thesis, The University of Tulsa, Tulsa, Oklahoma (1993).

☆U.S. GOVERNMENT PRINTING OFFICE: 1995 - 660-029/20001